Study of the oxygen reduction on perovskite-type oxides in alkaline media

Tiphaine Poux

UNIVERSITÉ DE STRASBOURG

EDSC
Ecole Doctorale des Sciences Chimiques

ÉCOLE DOCTORALE SCIENCES CHIMIQUES

Institut de Chimie et Procédés pour l'Energie, l'Environnement et la Santé (ICPEES)

THÈSE

présentée par :

Tiphaine POUX

Ingénieur, Phelma, Grenoble-INP, France

soutenue le : **27 janvier 2014**

pour obtenir le grade de : **Docteur de l'Université de Strasbourg**

Discipline / Spécialité : Chimie / Chimie Physique et Electrochimie

Étude de la réduction d'oxygène sur les oxydes de type pérovskite en milieu alcalin

Study of the oxygen reduction on perovskite-type oxides in alkaline media

THÈSE dirigée par :
Mme. SAVINOVA Elena Professeur, Université de Strasbourg

THÈSE co-encadrée par :
Mme. KERANGUEVEN Gwénaëlle Maître de conférences, Université de Strasbourg

RAPPORTEURS :
M. SCHMIDT Thomas Justus Professeur, Institut Paul Scherrer – ETHZ (CH)
M. FELIU MARTINEZ Juan Miguel Professeur, Université d'Alicante (ES)

AUTRES MEMBRES DU JURY :
Mme. ROGER Anne-Cécile Professeur, Université de Strasbourg
M. CHATENET Marian Professeur, Grenoble INP

To my mother

Acknowledgement

This PhD story would not have been possible without the participation of a lot of people and organizations. I would like to thank all of them.

First of all, I am very grateful to the **Doctoral School "Sciences Chimiques"**, to **Université de Strasbourg** and to the **French Ministry** for attributing me this three years fellowship.
I also would like to thanks the **CNRS** and the **Region Alsace** for the financial support of the research projects.

This PhD thesis would have been really poor without my PhD supervisor **Elena Savinova**. Your passion, your ideas, our discussions allowed me to learn so much and help me to go in the right direction to be, today, proud of this work. Thank you so much. Many thanks also to **Gwénaëlle Kerangueven**, my co-supervisor, for showing me how to work in the lab, for reviewing my work several times and for her availability when I needed advice.
I should also thank **Antoine Bonnefont**, from Institut de Chimie, for his huge work to help us to understand the ORR mechanism and for being always ready to answer to my (numerous) questions.

I am particularly sensitive that **Prof. Thomas Schmidt**, from PSI, and **Prof. Juan Feliu**, from Alicante University, did the honor to be the reviewers of my thesis.
I also really appreciate that **Prof. Marian Chatenet**, from Phelma, and **Prof. Anne-Cécile Roger**, from Université de Strasbourg, accepted to be part of the jury of this thesis.

I am very grateful to our partners from the Chemistry Faculty of Moscow State University (RU), **Filipp Napolskiy**, **Sergey Istomin**, **Evgeny Antipov** and **Galina Tsirlina**, for supplying us the perovskite oxides but also for our scientific discussions.
Thanks also to **Pavel Simonov**, from Boreskov Institute of Catalysis in Novosibirsk (RU), for kindly supplying us Sibunit carbon, and to **Tokuyama Company** for the alkaline ionomer.

Part of the experiments would not have been possible without the help of the master trainees **Maximilien Huguenel** and especially **Elaine Dahlen**. Thank you for being enough patient for performing H_2O_2 decomposition measurements.

I also have a thought to all the people who help me for the material characterization – **Pierre Bernhardt** for XPS analysis, **Thierry Dintzer** for SEM/EDX analysis – and for technical aspects in the lab – **Alain Rach**, **Michel Wolf** and **Fabrice Vigneron**.
Thanks also to **Veronique Verkruysse** and **Francine Jacky** for the vast administrative staff they realized.

I have a particular gratitude to my colleagues who became my friends and without whom this PhD would have been a sad solitary experience.
First of all, thanks to **Marlène** and **Yassou**, for our Grey's Anatomy parties, our beauty events, our discussions on existential problems :) and your support everyday. You were always here for me, thank you so much for that.
Thank you, **Pierre-Alex** for being a so comprehensive friend, always ready to listen to me (even when I complain). Thanks also to **Alfonso**. Even if you enjoyed so much to shock me :P, you brought a lot of fun in the office. I miss your "Interesting…".
I also would like to thank **Sergey**, **Sebastien**, **Thomas** and **Anya**, for their kindness, and all the nice people I met during my PhD in the lab.
A great thanks to Addal for having given me the opportuny to meet people to share fun…and the difficulties of being a PhD student :). I think to **Elise**, **Olivier**, **Mike**, **Orphée**, **Isabelle**, **Neila**, **Kenneth**, **Lionel**, **Anis**, **Cécilia**, **Julien**, and all those I forget, thank you!.

This thesis is the result of the support and encouragement that **my family** - in particular **my mother** who always believes in me - offered me throughout my schooling. A special kiss to **my brothers**.
I can also not forget the support of my coach, **Jacqueline Fruh**, who knew how to adapt the sport to my stress level.
A thought to all the people who addressed me their encouragements and therefore helped me to stay motivated: **my "mother-in-law"**, **Laetitia & Fred** (for their "joie de vivre", but also for the beautiful nails I had even when my experiences were not working :P), **Claire V.**, etc.

Last but certainly not least, I would like to send all my love to **Jérôme** who always supported me and accepted my stress, my joy, my doubts. You never gave up and I am very grateful for that. Thank you for giving me the strength to achieve this work and for being my partner everyday.

Table of contents

List of abbreviations

AFC : Alkaline Fuel Cell

BET : Brunauer, Emett and Teller technique

CP : Carbon Paper

CV : Cyclic Voltammetry

DBFC : Direct Borohydride Fuel Cell

DFT : Density Functional Theory

DMFC : Direct Methanol Fuel Cell

EDX : Energy-Dispersive X-Ray spectroscopy

GC : Glassy Carbon

GDL : Gas Diffusion Layer

ICDD : International Centre of Diffraction Data

ICP : Inductively Coupled Plasma

LEI : Low secondary Electron Image

MEA : Membrane-Electrode Assembly

MS : Mass Spectrometry

OER : Oxygen Evolution Reaction

ORR : Oxygen Reduction Reaction

PEMFC : Proton-Exchange Membrane Fuel Cell

PTFE : Polytetrafluoroethylene

RDE : Rotating Disk Electrode

RHE: Reversible Hydrogen Electrode

RRDE : Rotating Ring Disk Electrode

SAFC : Solid Alkaline Fuel Cell

SEI : Secondary Electron Image

SEM : Scanning Electron Microscopy

SHE: Standard Hydrogen Electrode

SOFC : Solid Oxide Fuel Cell

XANES : X-ray Absorption Near Edge Structure

XAS : X-ray Absorption Spectroscopy

XPS : X-Ray Photoelectron Spectroscopy

XRD : X-Ray Diffraction

General Introduction

With the population growth, the increase of the new technologies and the transportation requirements, the energy demand was never as high as today. To fulfill this increasing energy need and to compensate the decreasing fossil fuel resources, new systems of energy production have to be developed. Moreover, the global warming and the desire to improve our life quality motivate the search of cleaner energies. Among possible energy conversion systems, fuel cells represent a good alternative. They can be used in various applications such as transport devices, cogeneration systems or mobil phone. In addition, the fuel cell system is one of the less polluting systems with water as only product.

Nevertheless, the commercialization of these devices is currently limited by their cost. Indeed, to get sufficient kinetics of the reactions occurring at the fuel cell electrodes, electrocatalysts are required. Today, the most used catalyst for the oxygen reduction reaction (ORR) is platinum which is highly active for this cathode reaction, but also very expensive. Therefore, the current research target is to develop cheaper catalysts with equivalent electrocatalytic activites. While in acidic media, only noble metals are stable and active for the ORR, various materials such as non noble metal oxides are suitable for the ORR electrocatalysis in alkaline media. Therefore, alkaline anion exchange membrane fuel cells represent interesting systems in terms of fuel cell cost.

Perovskite oxides are promising materials. Their flexible structure tolerates a wide range of oxide compositions and thus, offers a large window of properties. Then, perovskites are suitable for numerous applications in heterogenous catalysis and electrocatalysis, in particular, ORR electrocatalysis. To aim an alkaline anion exchange membrane fuel cell application, the electrocatalytic activity of this oxide for the ORR should be sufficiently high to get reasonable performances and they have to display long term stability. Also, in order to improve the cathode composition, the ORR mechanism and the role of each component of the catalytic layer have to be understood.

To answer these questions, the present thesis is divided in six chapters.

Chapter 1 gives a literature review on the ORR catalysts in general, and on perovskite oxides in particular.

The materials and methods used in this work to study the perovskite catalysts are discribed in **Chapter 2**.

Chapter 3 is devoted to the characterization of the oxides. It includes the material characterization and the investigation of the electrochemical properties of various perovskites.

Carbon is usually added to catalytic layers to improve their conductivity. Its role in the electrochemical and electrocatalytic behaviors of perovskite/carbon electrodes is studied in **Chapter 4**. In this chapter, the catalytic activity of perovskite electrodes for the ORR is also discussed according to their compositions.

Chapter 5 is focused on the understanding of the ORR mechanism on perovskite/carbon composites. For this, the ORR and the transformation of a reaction intermediate, the hydrogen peroxide, are studied experimentally on various perovskite-based electrodes and interepreted with the help of a mathematical model.

The chemical and electrochemical stabilities of the perovskite electrodes under various conditions are investigated in **Chapter 6**. In this chapter, the electrochemical response is discussed together with the material characterization of the oxides.

Finally, the **General conclusion and Outlook** concludes the work.

At the end of the thesis, additional data can be found in the **Appendix** section.

Chapter 1 :
Literature Review

1.1. Fuel cell technology and challenges

During the last decades, numerous studies were dedicated to the improvement and the commercialization of new systems of electricity production to fulfill the growing energy demand and the approaching lack of fossil fuel ressources.

With the purpose to develop clean energies, the fuel cell technology offers many environmental advantages - no or few CO_2 emission, no emission of NO_x, hydrocarbon or particles, water as only product for hydrogen fuel cells – as well as automotive, mobile and stationary applications.

In a fuel cell, the electricity is directly produced from chemical energy thanks to the oxidation of a fuel (e.g. hydrogen) at the anode coupled with the reduction of an oxidant (e.g. oxygen from air) at the cathode.

Depending on the nature of their fuel and of their electrolyte, several fuel cell systems exist. Some of them are listed in Table 1. The solid oxide fuel cells (SOFC) have high operating temperature – 700-1000°C – and are therefore only used for stationary applications. Low temperature fuels cells such as alkaline fuel cell (AFC) or proton-exchange membrane (PEMFC) are more suitable for transport applications.

Besides hydrogen, methanol in e.g. direct methanol fuel cells (DMFC) and borohydride in direct borohydride fuel cell (DBFC) can be used as fuels.

Table 1 : *Example of fuel cell systems*

Fuel cell name	**Fuel**	**Oxidant**	**Ion conducted**	**Electrolyte**	**Operating temperature, °C**
PEMFC	H_2	Air	H^+	Proton exchange membrane	60-100
AFC	H_2	Air + H_2O	OH^-	Alkaline electrolyte	60-90
SAFC	H_2, CH_3OH	Air + H_2O	OH^-	Alkaline anion exchange membrane	< 90
SOFC	CH_4, H_2, CO	Air	O^{2-}	Oxide	700-1000

The principal fuel cell component is the membrane electrode assembly (MEA) which is composed of three main elements. One of them is the electrolyte which can be a liquid electrolyte or a membrane and which serves as separator of the anode and the cathode reagents, electronic insulator and ionic conductor. On both sides of this electrolyte lie the cathodic and the anodic active layers where the electrochemical reactions occur. These layers contain the catalyst material, which, for low temperature fuel cells, is usually mixed with or deposited on carbon to ensure high particle dispersion and electronic conduction, and an ionomer to allow the triple – ion, electron, gas – contact. At the back of the active layers and for low temperature fuel cells, the gas diffusion layer (GDL), composed of a carbon paper and polytetrafluoroethylene (PTFE), allows the reagent feeding, the product draining and the current collecting.

Up to now, the main studied fuel cells are the PEMFC thanks to the existence of well-developed proton-exchange membranes such as Nafion®. However, acid fuel cells require the use of noble metal catalysts such as platinum, the price and availability of which limit the commercialization of these fuel cells. Moreover, the active layers suffer from degradation during PEMFC operation due to (i) Pt dissolution, (ii) carbon support corrosion and subsequent Pt agglomeration, (iii) Pt migration to the electrolyte [1]. It results in an accelerated decrease of the performance.

The alkaline fuel cells (AFC) present the advantage to allow the utilization of cheaper catalysts. Indeed, numerous non noble metals and oxides are stable and active in this medium. Nevertheless, carbon dioxide from air can react with the liquid electrolyte to form carbonate species. This results in a loss of the performance due to the decrease of the electrolyte conductivity and the blocking of the porous cathode by the carbonate precipitates.

The alkaline anion exchange membrane fuel cell - or solid alkaline fuel cell (SAFC) – offers a good compromise between PEMFC and AFC. First of all, the alkaline membrane is less affected by the carbonation since it does not contain mobile cations to form solid precipitates. Then, the use of a membrane results in a compact system, contrary to an AFC. Finally, the alkaline medium allows the utilization of less expensive catalysts than in a PEMFC. Even if the improvement of the alkaline anion exchange membrane properties is still required [2], SAFCs are considered as promising type of fuel cells.

1.2. Oxygen Reduction Reaction (ORR)

The oxygen reduction reaction (ORR) is one of the most important processes in low temperature fuel cells. However, the sluggish kinetics of the oxygen reduction reaction (ORR) is largely responsible for the overpotential in these devices, even on the most catalytically active Pt materials [3]. Therefore, intensive researches were performed during the last decades to find suitable catalysts. The main issues of the catalyst material concern the performance, but also the durability and the cost.

This section gives a succinct description of the ORR in acid and alkaline media, as well as a brief review of the materials active for the ORR electrocatalysis in alkaline media.

1.2.1. ORR pathways

1.2.1.1. ORR in acid medium

The ORR has a complex mechanism involving several steps and intermediate species such as $O_{2,ads}$, $HO_{2,ads}$, $H_2O_{2,ads}$, OH_{ads}, O_{ads} where "ads" stands for adsorbed species. Even if the ORR has been widely studied on Pt-based materials, the nature of these steps is still debated. Nevertheless, it is established that two main ORR pathways can occur, depending on the type of electrocatalyst and the experimental conditions.

The first one - the so-called "direct" pathway - is the reduction of O_2 into H_2O, written as (Equation 1):

$$\text{Reaction 1}: \ O_2 + 4\,e^- + 4H^+ \ \rightleftarrows \ 2\,H_2O, E° = 1.23\ V_{SHE} \text{ at } 298K \quad \text{(Equation 1)}$$

in acid media, where E° stands for the standard potential. It is however not the direct exchange of 4 electrons, but is called direct since none of the intermediate species of the elementary steps is stable in aqueous electrolytes.

This is not the case for the "series" pathaway where O_2 is reduced in a 2 electron reaction to H_2O_2 (Equation 2):

$$\text{Reaction 2}: \ O_2 + 2\,e^- + 2H^+ \ \rightleftarrows \ H_2O_2, E° = 0.7\ V_{SHE} \text{ at } 298K \quad \text{(Equation 2)}$$

This H_2O_2 intermediate is stable and can either:

- be reduced through a 2 electron reaction (Equation 3):

$$\text{Reaction 3}: \ H_2O_2 + 2\,e^- + 2H^+ \ \rightleftarrows \ 2H_2O, E° = 1.77\ V_{SHE} \text{ at } 298K \quad \text{(Equation 3)}$$

- be catalytically decomposed into O_2 and H_2O (Equation 4):

$$\text{Reaction 4}: \ 2H_2O_2 \ \rightleftarrows \ 2H_2O + O_2 \quad \text{(Equation 4)}$$

- or diffuse away from the electrode surface to the bulk of the electrolyte.

These processes are often represented through the following Wroblowa's scheme (Figure 1).

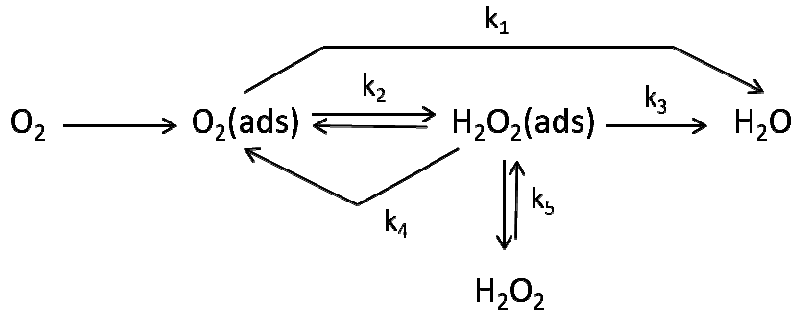

Figure 1 : *Simplified scheme of the ORR, adapted from [4], where k_i is the rate constant of the reaction i*

When the reduction or the decomposition of H_2O_2 occurs, the global number of exchanged electrons is 4, as for the "direct" pathway. However, the presence of H_2O_2 is detrimental for fuel cells since it degrades the catalyst layer and the membrane [5,6]. Therefore, if the ORR follows a "series" pathway, a high activity of the catalyst for H_2O_2 transformation is required to reduce the degradation caused by the H_2O_2 presence.

In order to study whether the ORR is a "series" or a "direct" pathway, researchers usually use the rotating-ring disk electrode (RRDE) technique. With this method, the ORR occurs at the disk, and eventual H_2O_2 species formed during a "series" ORR pathway will be oxidized at the ring, which therefore serves as a detector. It should however be noticed that if the H_2O_2 transformation is fast on the electrode surface, no H_2O_2 intermediate will be detected. In the case of a "series" pathway, it can also be useful to study the kinetics of the H_2O_2 reduction and H_2O_2 decomposition reactions.

1.2.1.2. ORR in alkaline medium

In alkaline electrolytes, the main ORR pathways are similar to those in acidic media. Neverthelss, in alkaline solution, H_2O_2 is transformed into HO_2^- according to (Equation 5):

$$H_2O_2 + OH^- \rightleftarrows HO_2^- + H_2O \quad \text{(Equation 5)}$$

The pK_A of this reaction is 11.7 [7]. Then, the ORR "direct" pathway is (Equation 6):

$$O_2 + 4\,e^- + 2H_2O \rightleftarrows 4\,OH^-, E° = 0.401\ V_{SHE} \text{ at } 298K \quad \text{(Equation 6)}$$

and the main steps of the "series" pathway are (Equation 7) (Equation 8) (Equation 9):

$$O_2 + H_2O + 2e^- \rightleftarrows HO_2^- + OH^-, E° = -0.065\ V_{SHE} \text{ at } 298K \quad \text{(Equation 7)}$$

$$HO_2^- + 2e^- + H_2O \rightleftarrows 3OH^-, E° = 0.867\ V_{SHE} \text{ at } 298K \quad \text{(Equation 8)}$$

$$2HO_2^- \rightleftarrows 2OH^- + O_2 \quad \text{(Equation 9)}$$

Also, HO_2^- species may diffuse in the electrolyte.

It should be noticed that, by misuse of language, HO_2^- intermediate species are often referred to H_2O_2 in the literature.

1.2.2. ORR electrocatalysts in alkaline media

The ORR kinetics is strongly sensitive to the type of the catalyst surface. Therefore, highly active materials have to be chosen. Besides, the catalysts should also be stable, selective and able to reduce O_2 to OH^-, producing as little as possible HO_2^-.

This section gives a non exhaustive review of ORR catalysts in alkaline media.

1.2.2.1. Noble metals

The high ORR activity of platinum motivated intensive researches on reaction kinetics and mechanism. Fundamental studies were perfomed on Pt single crystals. In 0.1M KOH, Pt(111) demonstrated the highest ORR activity [8,9]. The lower activity of Pt(110) and Pt(100) was attributed, with the help of the study of the temperature dependence of the HO_2^- yield and modeling, to the irreversible adsorption of OH species which limits the reaction kinetics. The study of the HO_2^- reaction suggested that, despite the low amount of HO_2^- detected, the ORR is mainly a "series" pathway on Pt single crystals, with the reduction of HO_2^- intermediate. The latter is inhibited in the hydrogen underpotential deposition region, leading to high yields of HO_2^-. The "series" pathway was also reported for polycrystalline Pt surfaces [10,11].

For practical applications, it is necessary to reduce the Pt loading to decrease the catalyst cost. Therefore, Pt in fuel cells is usually used in the form of carbon supported Pt nanoparticles. Genies et al. [12] studied the effect of the Pt loading and the particle size in Pt/C electrodes on the ORR electrocatalysis. They found that the specific activity - normalized to the surface area - decreases with the particle size. Indeed, the kinetic currents at -0.06 V vs Hg/HgO in 1M NaOH was 290 $\mu A.cm^{-2}_{Pt}$ for the Pt/C electrodes with 80% Pt (particle size of ca. 25 nm), while only 70 $\mu A.cm^{-2}_{Pt}$ was measured on the electrode containing 5% Pt (particle size of ca. 2 nm). Using the RRDE technique, they measured very little amount of HO_2^- produced during the ORR. The higher amount detected for the electrode with the lower Pt loading was attributed to the reduction of O_2 into HO_2^- on the carbon support.

Another way to decrease the catalyst cost is to use other noble metals. For instance, Lima et al. investigated the ORR on various noble metals in 0.1M NaOH [13]. They observed that, in alkaline media, the most active single crystal surfaces were Pt(111) and, interestingly, Pd(111), followed by Rh(111), Ag(111), and further, Ir(111) and Ru(0001) which display significantly lower onset potentials. While Au(111) demonstrated high ORR kinetic currents, it involves only 2 electrons in the ORR whereas other noble metals catalyse a 4 electron pathway. The same trends were observed for noble metal nanoparticles deposited on high surface area carbon. By plotting the kinetic current for single crystals, carbon-supported nanoparticles as well as Pt monolayers on single crystal surfaces versus the d-band center energies, a Volcano relationship was observed [13]. The d-band center should have an optimum value. High values of the d-band center lead to strong O_2 bonding. Then the O_2 splitting – assuming a “direct pathway” - easily occurs, but the surface is covered by oxygenated species which are strongly adsorbed. On the other side, low values of the d-band center allow a weaker adsorption of oxygen-containing species but the bonding is not sufficient to perform the O_2 splitting.

Reviews on Pt-based catalysts including alloys can be found in the literature [14,15].

To conclude, noble metals are highly active for the ORR. Nevertheless, their price is a limiting factor. Alternative candidates are carbon materials (see section 1.2.2.2) and non noble metal oxides (see section 1.2.2.3) which are more interesting from the point of view of cost and availability.

Much interest has been attracted to FeN_x/C materials which will not be considered in this review.

1.2.2.2. Carbon materials

While not active in acid medium, carbon is able to catalyse the oxygen reduction in alkaline medium. As reported in some reviews [16,17], several mechanisms were proposed for the ORR on carbon materials. They depend on the allotropic form of carbon but also on the eventual pretreatment (e.g. polishing, fracturing, reduction/oxidation [18,19]) of the surface. Despite the mechanistic differences, the authors agree that the ORR on carbon catalysts results in HO_2^-, which is not suitable for fuel cell applications.
The characteristic two wave shape of the ORR voltammograms on glassy carbon (GC) electrodes was attributed to two consequitive 2 electron reductions of O_2 into HO_2^-. At low overpotential, this reaction occurs on the most active sites. Thanks to the comparison of the ORR on bare GC and on quinone-modified GC electrodes, Tammeveski et al. determined that these actives sites are the quinone groups [20]. On bare GC, the surface concentration of these sites is limited, leading to a decrease of the current at high overpotentials.

With the purpose to improve its ORR activity, carbon can be doped with heteroatoms. For instance, Pan et al. [21] doped graphene with N and observed very high ORR activity in 0.1M KOH, comparable to that of Pt/C. Besides, P-doped carbon materials were also reported to be active towards the ORR in alkaline media [22]. Moreover, they display some activity for the HO_2^- reduction. Also, almost 4 electrons were involved in the ORR on graphene-based carbon nitride electrodes [23].

1.2.2.3. Non noble metal oxides

In alkaline solutions, contrary to acid media, non noble metal oxides are stable and can serve as ORR electrocatalysts. Simple oxides such as spinel or manganese oxides, as well as complexe oxides including pyrochlore and perovskite oxides demonstrated significant ORR activities.

1.2.2.3.1. Spinel oxides

Oxides with spinel structure – $X^{2+}Y^{3+}{}_2O^{2-}{}_4$ general formula – have shown activity for both the ORR and the oxygen evolution reaction (OER) electrocatalysis in alkaline media.

The most common spinel catalyst for these applications is the Co-based spinel. Compared to carbon, Co_3O_4 displays higher ORR activity with four global electrons involved in the mechanism [24-26]. This is due to the high activity of this spinel catalyst for the decomposition or the reduction of HO_2^-. Although NiO is not capable to reduce or decompose HO_2^- species [25], the substitution of Co^{2+} by Ni^{2+} to form $NiCo_2O_4$ oxide does not affect the number of electrons which remains equal to 4 [24,25]. Also, the Mn-substituted $MnCo_2O_4$ spinel shows higher ORR activity than carbon [26] and De Koninck et al. [27] demonstrated that the highest ORR activity of $Mn_xCu_{1-x}Co_2O_4$ compounds is obtained when both Mn and Cu cations are present.

Besides, the electrocatalytic activities of AMn_2O_4 spinels were investigated using the RRDE technique. Ortiz et al. [28] studied the ORR on $Cr_{1-x}Cu_xMn_2O_4$ oxides and measured the lowest amount of HO_2^- release when x=0.75. Later, Ponce et al. [29] observed that the ORR kinetic currents of $NiMn_2O_4$ were significantly higher than those of $Ni_{0.5}Al_{0.5}Mn_2O_4$ and $AlMn_2O_4$ compounds, showing the detrimental effect of the Al substitution. Regarding the high amount of HO_2^- measured, the authors concluded that the ORR on the studied spinel oxides was a "series" pathway.

Usually, spinel electrodes contain the spinel oxide physically mixed with a carbon material. With the purpose to increase the catalytic activity, some authors directly grow spinel oxides on graphene. For instance, Liang et al. [30] have investigated the ORR activity of Co_3O_4 grown on graphene in alkaline electrolyte and measured enhanced activity compared to spinel alone or graphene alone. This activity was even higher when graphene was doped with N. Then, the hybrid Co_3O_4/N-doped graphene displayed comparable current densities to Pt/C and, more importantly, higher stability. The authors also compared the ORR and OER activities of Co_3O_4/graphene to that of $MnCo_2O_4$/grapheme [31]. Both act as bifunctional catalysts but $MnCo_2O_4$ is the most active for the ORR. When grown on N-doped graphene, $MnCo_2O_4$ catalyst has a halfwave potential at only 20 mV below that of Pt/C electrodes for the same catalyst loading in 1M KOH. Moreover, the activity of the spinel/graphene hybrid catalyst was stable for at least 6h while the ORR current on Pt/C decreased by ca. 30%. In addition, little amount of HO_2^- was detected in the course of ORR on the spinel electrode, proving efficient reduction to OH^-. The activity of the hydrid material was significantly higher

than that of $MnCo_2O_4$ alone and $MnCo_2O_4$ physically mixed with N-doped graphene. This was attributed to the intimate interaction between the two components in the hybrid electrode which ensures high conductivity and electrochemical activity.

1.2.2.3.2. MnO_x

Without carbon, Mn oxides are not very active for the ORR [32]. However, when supported on carbon materials, they display very high electrocatalytic activity, comparable to Pt/C [32,33]. Although the authors generally agree on the involvement of the redox transitions of Mn and of 4 global electrons involved in the ORR, conclusions on the reaction mechanism are contradictory. Some of the authors suggested that the ORR follows a "direct" pathway on MnO_x [33,34] at least at low overpotentials, while others proposed a "series" pathway, either exclusively on the Mn oxide [35] or with the reduction of O_2 into HO_2^- on the carbon material, followed by the HO_2^- reduction/decomposition on MnO_x [32,36-38]. This could explain why the number of involved electrons, and thus, of the HO_2^- release, strongly depend on the MnOOH to carbon ratio [39].

The electrocatalytic activity of Mn material could be improved by doping. For example, Roche et al. [33] showed that the amount of HO_2^- produced could be decreased by doping of MnO_x/C by Ni or Mg. Also, Wu et al. [40] reported that the ORR activity of MnO_x/C catalysts was not stable. A loss of kinetic currents and a decrease of the number of electrons were observed after cycling. This could be avoided by doping the catalyst with $Ni(OH)_2$.

1.2.2.3.3. Pyrochlore oxides

Pyrochlores are complex oxides of the general formula $A_2B_2O_7$, where A is often a trivalent rare-earth cation, and B, a tetravalent transition metal cation. These species were also studied for the ORR electrocatalysis and display quite high activity.

For instance, Saito et al. [41] investigated the ORR on various $Ln_2Ru_2O_{7-\delta}$ (Ln=Pr, Nd, Sm, Gd, Dy, Yb) oxides in 0.1M KOH using the RRDE technique and measured substantial electrocatalytic activity and less than 20% of released HO_2^- species. Moreover, this activity could be increased by partially substituting Ru by Mn cation. Indeed, the ORR onset potential on $Nd_2Ru_{1.75}Mn_{0.25}O_{7-\delta}$ pyrochlore is only 50 mV below that of Pt/C and less than 10% of

HO_2^- was detected on the pyrochlore electrode. Interestingly, it was also demonstrated that pyrochlores show higher selectivity towards the ORR than Pt/C. By adding methanol in the alkaline electrolyte, the ORR onset potential of Pt/C drops due to the methanol oxidation, while the ORR activity of $Nd_2Ru_{1-x}Mn_xO_{7-\delta}$ remains stable.

The ORR activity of $Ln_2B_2O_{7-\delta}$ pyrochlores was also studied with Zr or Sn in B position [42]. For both cations, the most interesting pyrochlore structures regarding the HO_2^- release were those with La as the A cation, while almost 80% were measured at the ring of the RRDE on the Yb-based electrode. In fact, the activity of $Yb_2Zr_2O_{7-\delta}$ was very similar to that of ZnO_2 in the mentioned work, suggesting low influence of the structure on the electrocatalytic activity in that case. The authors also reported that the incorporation of $LaMnO_3$ perovskite in $La_2Zr_2O_{7-\delta}$ significantly enhances its electrocatalytic activity by positively shifting its onset potential.

1.2.2.3.4. Perovskite oxides

The perovskite structure is particularly interesting considering its flexibility (see section 1.3). Then, it allows the tuning of the oxide properties by varying its composition, giving promising materials for various catalysis applications.

Peroskite oxides have been intensively used as heterogenous catalysts for e.g. hydrocarbon combustion [43-55], Fischer-Tropsch synthesis [56,57], oxidation of ethanol [55,58] or toluene [59], CO oxidation [60-63], NO and N_2O decomposition [64,65], but are also suitable for electrochemical applications.

For example, they serve as cathode materials for solid oxide fuel cells (SOFC) [66-71] thanks to their mixed conductivity and thermal stability. Since the seminal work of Matsumoto et al. [72,73] and Bockris et al. [74,75] on the study of the OER and ORR electrocatalysis on perovskite pellets, there is also an increasing interest for perovskite oxides as OER [76-81], ORR [82-95] or bifunctional electrocatalysts [96-102] for low temperature applications such as liquid and solid alkaline fuel cells, water splitting and metal-air batteries.

The perovskite oxides are indeed highly active for the ORR electrocatalysis since activities close to that of Pt/C were reported for some perovskite electrodes [84,85,103]. Their applications as ORR catalysts will be discussed in more detail in section 1.4.

1.3. Perovskite structure

This section gives a brief description of the perovskite structure. Reviews on this structure can be found in [104-106].

1.3.1. Ideal structure

The general formula of perovskite oxides is ABO_3, where A is a large cation with low valence (usually 3+ or 2+) and B is a smaller cation, in general a transition metal cation, with a similar or higher valence (usually 3+ or 4+). A wide range of cations can be inserted in A and B sites thanks to the structure flexibility.

The ideal structure of perovskites is cubic. As represented in Figure 2, BO_6 octahedra form a three dimensions array by sharing their corners, and A cations lie in the cavity created by eight octahedra. From another point of view, the structure can be seen as being composed of cubes of A with O in the center of the faces and B in the center of the octahedron formed by O ions. Thus, the angle formed by B-O-B is equal to 180°.

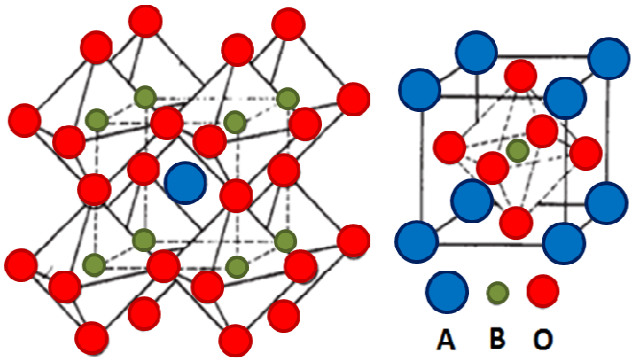

Figure 2 : *Two views of the ideal cubic structure of perovskite, adapted from [106]*

In the ideal cubic structure, the distances between B and O atoms (D_{B-O}), and A and O atoms (D_{A-O}) follow the relationship: $\sqrt{2}\ (D_{B-O}) = D_{A-O}$. However, in practice, few ABO_3 structures respect this rule due to various cation sizes. Therefore, Goldschmidt [107] introduced the tolerance factor t given by (Equation 10) to estimate the deviation from the ideal structure (t=1).

$$t = \frac{R_A + R_O}{\sqrt{2}\,(R_B + R_O)}$$ (Equation 10)

with R_A : ionic radius of A, R_O : ionic radius of O anion, and R_B: ionic radius of B cation.

If t is different from 1 but is comprised between 0.75 and 1.05, the structure is perovskite but experiences internal strains. Thus distortions are required to stabilize the structure and structures with lower symmetry, such as orthorhombic or rhombohedral, are obtained.

In the 70's, Glazer proposed a table of predicted structures for distorted compounds which display cation ordering and octahedral tilting [108,109]. This table was further improved by Woodward [110,111].

1.3.2. Distortions

A tolerance factor t below 1 often indicates that the cation in A-sites is too small, leading to a too large cavity and therefore an unstable cubic structure. Thus, the BO_6 octahedra tilt around a crystallographic axis in order to lower the strain by reducing the site size. This tilting is performed without changing the size of the octahedra, neither the connectivity, in order to minimize the distortion energy. The resulting B-O-B bonds are bended.

For t above 1, some octahedra share their faces instead of their corners, leading to both cubic and hexagonal layers. The latter layers can be stable without cations in the B-sites.

When the electronic configuration of a component presents a degeneracy, the structure breaks this degeneracy by displacing cations and distorting octahedra. It is the Jahn-Teller effect which allows the structure to reduce the energy involved by the degeneracy.

1.3.3. Cation ordering

If some A or B cations are substituted by cations of similar size and charge, the different cationic species will be randomly distributed in the structure, each site being equivalent. However, if the two cationic species present sufficiently distinct charge and/or size, a cation ordering will occur.

Generally, in $A_{1-x}A'_xBO_3$ structures, A-site species are ordered in the layer arrangement, each layer containing one type of cations. In $AB_{1-x}B'_xO_3$ structures, the preferential order is the NaCl arrangement where the two species B and B' alternate in the octahedral site. The

obtained structure is often called “double perovskite” since the cell unit is doubled. When the two species do not have the same size, a displacement of O is required to adjust the bond length.

1.3.4. Atomic vacancies

Perovskite structures can involve A or O atomic vacancies (□), whereas B-defictive perovskites are not stable, except in face-sharing octahedra layers as mentioned above. Also, interstitial ions are not thermodynamically favorable in perovskite structures. The oxygen excess reported in $LaMnO_{3+\delta}$ compounds should rather be viewed as cation deficiencies.

In the bronze structures $\square_x A_{1-x}BO_3$, the ordering of the vacancies is generally accompanied by the tilting of BO_6 octahedra. The A cation may also be totally absent in the structure since the array formed by B and O atoms is very stable. The remained $\square BO_3$ structure either keeps the cubic structure, as for $\square ReO_3$, or is distorted.

Besides, several structures of anion-deficient perovskites were reported [112,113]. When present in high quantity – up to ABO_2 structures - the oxygen vacancies lead to a cation ordering depending on the Jahn-Teller effect, but also on the coordination preference of the B cations. B can lie in a square planar configuration, like $ACuO_2$ [113], or in the tetragonal pyramids and octahedra of brownmillerite $A_nB_nO3_{n-1}$ structure.

When the structure presents both O and A vacancies ($\square BO_{3-\delta}$), it might translate along an axis which does not contain oxygen atoms to eliminate the vacancies. Then, the structure - crystallographic shear structure - is constituted of edge-sharing octahedra.

One should also mention the existence of the layered perovskites. These structures are composed of 2D layers of corner-sharing octahedra separated by layers of cations. The most common layers perovskites are the Ruddlesden-Poper $A_{n+1}B_nX_{3n+1}$ and the Dion-Jacobson $A_nB_nX_{3n+1}$ structures, where n is the number of octahedra layers. This type of structure is the only one which can support interstitial ions.

The extended perovskite composition and structure possibilities result in a large spectrum of properties such as magnetic properties, electrical and ionic conductivities, thermal stabilities or adsorption properties [114] which allow the utilization of perovskites for various catalytic applications.

1.4. Perovskites as ORR catalysts

In this section, the reported results concerning the electrode configuration, the ORR activity and mechanism as well as the stability of perovskite catalysts will be discussed.

1.4.1. Configuration of perovskite electrodes

Various electrode configurations have been applied to study the ORR/OER electrocatalysis on perovskites, including gas-diffusion electrodes, pellets, films obtained by painting the oxide slurry on a metal foil, or by spreading oxide particles and a binder, with or without carbon, on a glassy carbon support. This section is a brief review of the perovskite electrodes reported in the literature.

1.4.1.1. Gas diffusion electrodes

With the increase of the interest to fuel cells, gas diffusion layers (GDL) became more frequently used for perovskite oxides [83,86,87,94-96,99-102,115,116]. A GDL electrode consists of a gas supply layer and of a reaction layer. The gas supply layer is a hydrophobic layer usually made of carbon and PTFE which allow electronic connection and reactant diffusion, and the reaction layer contains a catalyst, in this case perovskite oxide. To build these layers, a mixture of a catalyst, carbon and PTFE in an organic solvent is rolled into a layer of ca. 200 µm and heated. Finally the active and gas supply layers are rolled together with a metallic mesh (Ni, stainless steel …) in between.

For GDL electrodes, perovskite oxide is usually mixed with carbon black particles, eventually treated at high temperature to obtain graphitized carbon. However, some authors reported also the use of carbon nanotubes (CNT) [115] and carbon nanocapsules (CNC) [116] instead of carbon black. Moreover, perovskite oxides of GDLs can be directly supported on a carbon material, as found in [83,86,87].

In order to measure ORR activities in fuel cell conditions, perovskite-based gas diffusion cathodes are prefered. However, the complex configuration of these electrodes makes difficult the study of ORR mechanism and the electrochemical behavior of the perovskite. Therefore other electrodes such as pellets or thin layers, more suitable for electrochemical studies, are often utilized to investigate perovskite materials.

1.4.1.2. Pellet electrodes

For the first studies with perovskites, researchers mostly used pellets to investigate the OER and ORR. In the 70s, Matsumoto et al. studied the ORR activity of $LaNiO_3$ [72], as well as of $LaTiO_3$, $SrFeO_3$, $SrVO_3$, $SrRuO_3$, $V_{0.2}Ti_{1.8}O_3$ and $La_{1-x}Sr_xMnO_3$ perovskite pellets [73]. In the 80s, Bockris et al. [74,75] studied a wide range of perovskite compositions both for the OER and the ORR using pellet configuration. Pellet electrodes consist of a perovskite powder pressed into disk electrodes, connected to a metallic wire. In general, only one face of the pellet is in contact with the electrolyte. Other faces are isolated with epoxy material.
Nowadays, only few authors reported the use of perovskite pellets [91,92]. Indeed, the pellet electrodes have the advantages to avoid binders or other additives, but their disadvantage lies in the high porosity and concomitant internal diffusion complications. For example, Bockris et al. [75] estimated the roughness factor of perovskite pellets prepared by solid state synthesis as ca. 1000 and El Baydi et al. [117] found a roughness factor of ca. 1500 for $LaNiO_3$ pellets prepared using the malic acid method. Moreover, electrode formulations containing perovskites alone usually suffer from high Ohmic losses, posing problems for the ORR investigation.

1.4.1.3. Thin layer electrodes

Very thin layers (ca. 1 µm) of perovskite oxides can be obtained by drop casting on inert support, for example on glassy carbon (GC) surface [78,82,84,85,88,89,93,103]. The thin film approach is compatible with the rotating disc (RDE) and the rotating ring disc electrode (RRDE), the advantage compared to the gas-diffusion electrode consisting of a more reliable separation of kinetic and mass transport contributions. However, the drop casting of perovskite particles is a very sensitive technique for which the particle dispersion on the GC

surface strongly depends on the perovskite suspension preparation and on the drying method. Several solvents were utilized for preparing perovskite suspensions, such as water [85], 2-propanol [82,93], 1-hexanol [89] or tetrahydrofuran (THF) [78,88,103]. Moreover, some researchers speed up the drying by placing deposits under light [82,93] while other authors reported a slow drying under a close jar [78,88,103]. Except for a few publications [85], perovskites are usually mixed with carbon particles or eventually supported on carbon materials (e.g. [89]) to improve the electrode conductivity. In order to fix catalyst particles on the GC surface, a binder such as Nafion transformed from protonated into a cationic form is usually used. It can be directly mixed with the catalyst suspension [78,85,103] or deposited on a dried catalyst layer [82,88,93].

1.4.1.4. Alternative electrodes

Besides the mentioned electrode configuration, some authors utilized other electrode types. One example is the layer of perovskite with [90] or without carbon [80,117] painted on a metal foil (Ti, Ni…).

Another type of electrode is the paste electrode. It consists of a mixture of perovskite, carbon and oil pressed into a porous material, as used in references [77,118,119]. The resulting electrode is highly dense, contrary to pellet electrodes.

1.4.2. ORR activity of perovskite oxides

After the electrode preparation, ORR activites of perovskite-based cathodes are measured in an O_2-containing alkaline electrolyte by taking polarization curves for gas diffusion layer electrodes and by RDE technique for thin layers. Thanks to these electrochemical techniques, it was demonstrated that perovskite-based electrodes display higher ORR activities – higher currents at lower overpotential - than the corresponding carbon support [82,83,100,115,116]. For example, Hayashi et al. reported ORR current densities of 300 $mA.cm^{-2}_{geo}$ at -80 mV vs. Hg/HgO for carbon supported $LaMnO_{3+\delta}$, while similar current densities are only reach at ca. -230 mV vs. Hg/HgO for carbon alone [83]. It proves that perovskites are good candidates for ORR electrocatalysis. More interestingly, some authors reported ORR activity of perovskite electrodes close to the “state-of-the-art” Pt/C. Indeed, at the benchmark potential of 0.9 V vs.

RHE and in 0.1M KOH, ORR current densities of 40 $\mu A.cm^{-2}_{oxide}$ were measured on $LaNiO_3$ electrodes while Pt/C reaches 320 $\mu A.cm^{-2}_{Pt}$ [103]. Therefore only one order of magnitude separated the perovskite material from the Pt electrode. Moreover, low cost of oxide materials allows one to increase the catalyst loading in the fuel cell electrode to reach higher currents. ORR activites comparable to that of Pt/C were also reported for Mn-perovskites, such as $LaMnO_{3+\delta}$ [84], $La_{0.4}Sr_{0.6}MnO_3$ [85] and $La_{0.6}Ca_{0.4}Mn_{0.9}Fe_{0.1}O_3$ [86].

It is generally accepted that the active site for the ORR on ABO_3 perovskites is the B cation, while the choice of an A cation and its partial substitution by a lower valence cation indirectly impact the catalytic activity by changing the B oxidation state and the oxygen stoichiometry. For low temperature applications, the most studied perovskites for the ORR are the La-based oxides. They were studied either without doping [72,83,87,88,118] or doped with Sr [85,89,115] or Ca [82,86,90-93,95,96,99,100,102,116]. Besides La-based perovskites, some authors also investigated Pr-based [94] and Nd-based [119] perovskite oxides. For all these perovskites, partial doping of the perovskite by a low valence A cation leads to an improved ORR electrocatalysis [85,91,92,94,119]. For example, non doped $NdCoO_3$ reaches 40 $mA.cm^{-2}_{geo}$ at ca. -340 mV vs. Hg/HgO while $Nd_{0.8}Sr_{0.2}CoO_3$ reaches same ORR current densities at a lower overpotential, i.e. at ca. -60 mV vs. Hg/HgO [119]. According to Tulloch et al., for $La_{1-x}Sr_xMnO_3$, about one order of magnitude separates current densities for non doped $LaMnO_3$ from Sr-doped perovskites, the latter one being more active for the ORR [85]. Moreover, while current densities of ca. 185 $mA.cm^{-2}_{geo}$ for $PrMnO_3$ and ca. 220 $mA.cm^{-2}_{geo}$ for $CaMnO_3$ are reported in reference [94], $Pr_{0.6}Ca_{0.4}MnO_3$ displays ORR current densities of ca. 320 $mA.cm^{-2}_{geo}$ at -150 mV vs. Hg/HgO.

In the reported studies, the perovskites which display significant ORR activities are those containing Mn [83,85,87,89,93,94], Co [77,82,90-92,95,96,99,100,102,115] and Ni [72,88,101,119]. Ir might also be a good candidate according to Chang et al. who partially substituted Co by Ir in $La_{0.6}Ca_{0.4}CoO_3$ perovskites and observed an increase of the ORR activity [116]. However, Fe cation should be avoided in perovskite electrodes. Indeed, by gradually incorporating Fe in $La_{0.4}Ca_{0.6}Mn_{1-y}Fe_yO_3$ structure, Yuasa et al. [86] demonstrated that Fe-based perovskites are less active than Mn-based perovskites for the ORR electrocatalysis.

It should be noticed however that there is no agreement in the literature concerning the best B-cation for the ORR in alkaline media. On the one hand, Suntivich et al. studied a wide range of $LaBO_3$ perovskites in 0.1M KOH and reported the highest activity for $LaMnO_{3+\delta}$ and $LaNiO_3$, which was at only one order of magnitude inferior to that of Pt/C [84,103]. On the

other hand, Sunarso et al. [88] investigated Ni, Co, Fe, Mn, and Cr as B cations for $LaBO_3$ perovskites in 0.1M KOH too, and showed that $LaCoO_3$ is the most active in terms of the ORR onset potential, in contradiction with the above mentioned publication. This emphasized difficulties in comparing published results since the authors use different ways to prepare and study perovskite electrodes. These differences concern material parameters such as the perovskite synthesis, the electrode type and preparation, the nature of the carbon support, the nature of the electrolyte, as well as the way the electrocatalytic activity is determined which depends on the electrochemical method utilized for the study, the correction of the mass transport contribution, and the normalization of the current by the oxide surface.

Among the mentioned parameters, the presence and the nature of the carbon support have a great effect on the ORR performance of perovskite electrodes. Indeed, by varying the perovskite to carbon ratio and by varying the carbon morphologies, several authors showed that the composition of perovskite electrodes strongly impacts the perovskite utilization, and, a fortiori, the ORR activities. Indeed, perovskite electrodes without carbon [82,88] or with an insufficient carbon content [83,87] show very little ORR activities due to their low electronic conductivity. This highlights that the addition of carbon powders significantly improves the electrical contact between perovskite particles. On the other hand, Miyazaki et al. [89] compared composites of $La_{1-x}Sr_xMnO_3$/carbon nanotubes (CNT) with electrodes of $La_{1-x}Sr_xMnO_3$ mixed with carbon black particles with a similar perovskite loading, and found that the former leads to higher ORR activities. Similar behavior was observed for $La_{0.6}Sr_{0.4}CoO_3$ electrodes by Thiele et al. [115] who compared perovskites mixed with CNT and perovskites mixed with acetylene black particles. Electrodes containing CNT displayed larger ORR activities, attributed to a better electrical contact between the perovskite particles. Therefore, an optimization of the perovskite based electrodes concerning both the perovskite/carbon ratio and the electrode composition and morphology is required to increase the electrocatalytic efficiency.

Recently [120], it was reported that the nature of the cation of the alkaline electrolyte plays a significant role in the ORR mechanism. In the mentioned work, the use of NaOH, KOH or LiOH electrolyte results in very different ORR activities for $LaMnO_{3+\delta}$, the highest activity being measured in KOH and the lowest – one order of magnitude lower - for LiOH. This points out to the fact that the use of different electrolytes may lead to different activities for a given catalyst.

To conclude, ORR activites of perovskite electrodes reported by different groups are difficult to compare since researchers use various methodologies. Nevertheless, perovskite oxides

seem to be promising candidates for the cathode of an alkaline fuel cell. This brings up the question of the ORR mechanism.

1.4.3. ORR mechanisms on perovskite electrodes

In order to investigate the ORR mechanism on perovskite oxides, several approaches have been applied in the literature. First of all, the presence of HO_2^- intermediate, proof of a "series" ORR pathway, was investigated by the rotating ring-disk electrode (RRDE). This intermediate can then be further reduced or decomposed (see section 1.2.1). Thus, the kinetics of both HO_2^- electrochemical reduction and HO_2^- chemical decomposition were studied by a few groups to determine the predominant ORR mechanism on perovskite oxides. Carbon being an almost indispensable component of perovskite-based electrodes, it is also interesting to investigate its exact role in the ORR electrocatalysis on composite electrodes. Finally, the relationship between the electronic properties of the oxide and its electrocatalytic activity will be discussed.

1.4.3.1. Identification of "series" versus "direct" ORR pathway by RRDE studies

Thanks to the RRDE method, any stable HO_2^- intermediates produced at the disk during the ORR can be oxidized at the ring, resulting in a positive current at the ring. With this technique, the amount of HO_2^- formed during the ORR on $LaMnO_3$ measured by Konishi et al. [42] as well as on various $LaMO_3$ and $LaNi_{0.5}M_{0.5}O_3$ oxides (M = Ni, Co, Fe, Mn, Cr) measured by Sunarso et al. [88] was very low. Therefore, the authors suggested that the ORR mainly occurs through a "direct" ORR pathway without formation of HO_2^- on perovskite oxides. On the other hand, Tulloch et al. [85] found that the amount of HO_2^- detected – and thus the percentage of the "direct" pathway - is strongly dependent on the Sr doping by studying various $La_{1-x}Sr_xMnO_3$ perovskites. Indeed, up to 80% of HO_2^- were measured during the ORR on $LaMnO_3$ while $La_{0.4}Sr_{0.6}MnO_3$ displayed only 15% of HO_2^-. Different amounts of HO_2^- were also measured for $La_xCa_{0.4}MnO_3$ perovskites by Yuan et al. [93] with ca. 24% of HO_2^- for stoichiometric perovskites and around 10% for non-soichiometric oxides in both 1M and 6M KOH. The authors attributed these differences to a more pronounced participation of

Mn reduction/oxidation transitions in the ORR mechanism in non stoichiometric perovskites which would favor the "direct" ORR pathway. According to Matsumoto et al. [72], a low amount of HO_2^- detected at the ring of a RRDE may be due to a fast transformation of HO_2^- on perovskite oxides rather than a "direct" ORR pathway. They proposed that after being formed through the adsorption and reduction of O_2, HO_2^- stayed adsorbed on $LaNiO_3$ surface and was rapidly reduced by a rearrangement on oxygen vacancies. High reactivity of HO_2^- and its concomitant short life time did not allow it to desorb and to diffuse away from the diskelectrode to be detected at the ring.

Besides, the ORR on $La_{0.6}Ca_{0.4}CoO_3$ was studied using a channel flow cell [90] where eventual intermediate species are formed on a generator electrode, transported by the laminar flow of an electrolyte and collected by a downstream electrode. The presence of HO_2^- in the ORR mechanism was evidenced, and the comparison of the kinetics of the reductions of O_2 into OH^- and of O_2 into HO_2^- led the authors to discard a possible "direct" ORR pathway on the perovskite. The results obtained on $La_{0.6}Ca_{0.4}CoO_3$/carbon electrodes also proved the ability of this perovskite to reduce or decompose HO_2^- contrary to carbon electrodes. The "series" ORR pathway was also highlighted by Li et al. [82] on the same perovskite ($La_{0.6}Ca_{0.4}CoO_3$) for various concentrated alkaline electrolytes using the RRDE method. The currents measured on the ring during the ORR were non-negligible, suggesting a significant amount of HO_2^- formed on this perovskite. The authors finally suggested an ORR mechanism with two possible ways for the HO_2^- intermediate. HO_2^- can either stay adsorbed and be reduced on perovskite surface or desorbs and be detected by the ring of RRDE. This is consistent with the ORR mechanism proposed by Matsumoto et al. [72].

In conclusion, while some authors mentioned the "direct" ORR pathway on perovskite oxides, it seems reasonable to also consider the "series" ORR pathway on these electrodes, the low amount of HO_2^- detected being possibly attributed to the fast transformation of HO_2^- without its desorption. Therefore, it is essential to study the kinetics of possible HO_2^- transformations to identify the mechanism.

1.4.3.2. Study of HO_2^- decomposition kinetics

The catalytic decomposition of HO_2^- was studied on various perovskite oxides using the gasometric method. It consists of placing a H_2O_2 aliquot in a catalyst-containing solution and to measure the volume of O_2 evolved during the catalytic HO_2^- decomposition reaction. With

this method and regardless the perovskite composition, the HO_2^- decomposition was generally found to be a first order reaction with respect to the H_2O_2 concentration [121-127].

The rate constant was then calculated by different ways depending on the authors which makes comparison difficult. Normally the heterogeneous rate constant is calculated in $cm.s^{-1}$ by multiplying the first order constant by the solution volume and normalizing it by the surface area of the catalysts [122,123,125]. This way, Soleymani et al. [125] measured a kinetic constant of ca. 5 10^{-5} $cm.s^{-1}$ for $La_{1-x}Ca_xMnO_3$ while Falcon et al. [123] found more than 10^{-3} $cm.s^{-1}$ for $LaFe_{1-x}Ni_xO_3$. When the surface area of the perovskite oxides is unknown, an alternative way to compare catalyst activities is to normalize the first order constant by the catalyst mass since the activity increases linearly with the latter [127]. This was performed in references [121,124,126,128]. Depending on the perovskite composition and the temperature, the obtained kinetic constants range between 10^{-2} and ca. 7. 10^{-1} $g^{-1}.s^{-1}$(the largest was measured for $La_{0.9}Sr_{0.1}NiO_3$ [121,124]) and the corresponding activation energy, between 20 and 50 $kJ.mol^{-1}$ [121,124,126], showing the differences of catalytic activities of various perovskites.

It is generally accepted that cations in A position do not directly affect the activity of perovskites for HO_2^- decomposition. However, the nature of B cations may strongly influence the catalytic activity. For example, it was highlighted that Cr-based perovskites are less active than Ni-based for HO_2^- decomposition since the reaction rate decreases by substituting Ni by Cr in $La_{0.9}Sr_{0.1}Ni_{1-x}Cr_xO_3$ perovskites [121]. Magalhaes et al. [129] found that the presence of Mn in $LaMn_xFe_yMo_zO_3$ (x+y+z=1) perovskites is essential to achieve high activity for HO_2^- decomposition while the increase of Fe and/or Mo contents leads to a decreasing catalytic activity. The reasons of the higher activity of Mn and Ni cations are not understood yet but were investigated by several authors. In general, the activity of Mn-perovskites for HO_2^- decomposition is related to Mn^{4+}/Mn^{3+} mixed valence ratio [125,126,130]. However, the same authors also mentioned that the presence of oxygen vacancies might play a role in the catalytic reaction. Lee et al. [127] studied various $Ln_{1-x}A'MnO_3$ and concluded that the activity for the HO_2^- decomposition is not determined by Mn surface concentration or Mn^{4+}/Mn^{3+} ratio, contrary to conclusions of other authors, but only by the oxygen non-stoichiometry of the perovskites. They therefore proposed a HO_2^- decomposition mechanism involving the oxygen vacancies. By studying various Ni-based perovskites, the activity for the HO_2^- decomposition was attributed to the facile redox transition of Ni cations [121-124].

Numerous studies demonstrated the activity of perovskites for HO_2^- decomposition, but the kinetics of this reaction is strongly influenced by the perovskite composition and, in particular, by the oxidation state of the B-cation and the presence of oxygen vacancies.

1.4.3.3. Study of HO_2^- reduction kinetics

While several researchers studied the HO_2^- decomposition on perovskite oxides, very few published results can be found for the study of the electrochemical reduction of HO_2^- on perovskite oxides.

In order to learn about the ORR mechanism in alkaline media, Wang et al. [131] and Zhuang et al. [132] investigated the electrocatalysis of HO_2^- reduction using cyclic voltammetry in H_2O_2-containing 3M KOH electrolytes on $La_{1-x}Sr_xMnO_3$ and $La_{1-x}Ca_xCoO_3$. Both perovskite types showed activity for the mentioned reaction but conclusions on the reaction mechanism and kinetics could hardly be obtained with the method applied. Nevertheless, it was found that the amount of perovskite doping does not have any effect on the mixed potential of the reaction. Moreover, Wang et al. [131] by varying the H_2O_2 concentration from 0.4M to 1M demonstrated that, at low potentials, the HO_2^- reduction is controlled by diffusion on $La_{1-x}Sr_xMnO_3$ electrodes. Previously, Matsumoto et al. [72] proved with the RDE method in 1M NaOH + 0.01M H_2O_2 that $LaNiO_3$ pellets display significant activity for HO_2^- reduction. They therefore suggested a "series" ORR mechanism where HO_2^- is rapidly reduced on perovskite electrode thanks to the participation of oxygen vacancies. This fast transformation of HO_2^- into OH^- avoids its desorption from perovskite surface and thus this intermediate cannot be detected by the ring of the RRDE, leading to an apparent "direct" ORR pathway. In his PhD thesis, Hermann investigated the electrocatalysis of HO_2^- reduction on $La_{0.6}Ca_{0.4}CoO_3$ [133]. Both RDE and flow cell methods were used and several electrode configurations were tested for various H_2O_2 concentrations in 1M KOH electrolytes. For all tested electrodes, HO_2^- reduction occurred in a mixed regime on the studied perovskites. Indeed, the measured currents suggest that the perovskite can indeed reduce HO_2^- but the currents were only slightly dependent on the mass transport, indicating that the reaction kinetics was slow. The author concluded that the perovskite rather transformed HO_2^- by a chemical decomposition for which the perovskite showed significant activity, followed by the reduction of the formed O_2.

Besides the ORR investigations, the H_2O_2 reduction/oxidation electrocatalysis was also studied with the aim to build perovskite-based H_2O_2 sensors [134-136]. However, these

researches were performed in neutral solutions and thus can differ from the reactions actually occurring during the ORR in alkaline media. The activity of $La_{0.66}Sr_{0.33}MnO_3$ for H_2O_2 reduction/oxidation was demonstrated thanks to a great increase of the measured current in the presence of H_2O_2 compared to graphite electrodes [135]. The same authors observed that Sr-doping of $La_{1-x}A_xMnO_3$ leads to more efficient activity than Ca-doping. Shimizu et al. [134] tested the activity of several $La_{0.6}Ca_{0.4}B_{1-x}B'_xO_3$ oxides (B=Cr, Mn, Fe, Co, Ni, B'=Fe) and concluded that $La_{0.6}Ca_{0.4}Ni_{0.7}Fe_{x0.3}O_3$ is the most active for the H_2O_2 reaction electrocatalysis and that carbon is required in the electrode to achieve a good H_2O_2 response. Others authors [136] proposed the involvement of oxygen vacancies in the H_2O_2 reduction on $La_{0.5}Sr_{0.5}CoO_{3-\delta}$, in agreement with the mechanism proposed by Matsumoto on $LaNiO_3$ [72]. Ahn et al. also evidenced differences in the catalytic behavior for the reduction and the oxidation of H_2O_2.

In conclusion, it appearss that HO_2^- can be reduced on perovskite oxides but further work has to be performed to investigate the reduction mechanism and kinetics in more detail.

1.4.3.4. Carbon contribution in the ORR mechanism

It was shown in sections 1.4.1 and 1.4.2 that most perovskite electrodes currently contain a certain amount of carbon in order to improve the perovskite utilization. However, as mentioned in section 1.2.2.2, carbon is known to be active for the O_2 reduction into HO_2^- in alkaline media. Therefore it brings up a question on the separation of contributions from the two components in the perovskite/carbon composite materials.

Most studies of the ORR on perovskite oxides neglect the contribution of carbon into the ORR kinetics, even if the latter is added to the thin film electrodes. For example, Suntivich et al. [103] reported a methodology to quantify specific ORR activies of perovskites without considering carbon contribution to the ORR electrocatalysis, and normalizing the kinetic current by the oxide surface area. On the other hand, some authors have investigated the ORR mechanism by the RDE [82,88] or channel flow cell [90] on carbon and $La_{0.6}Ca_{0.4}CoO_3$/carbon electrodes to identify the role of each component. By comparing the ORR onset potential and the number of involved electrons for both electrodes, it appeared that the role of carbon may not be limited to the improvement of an electrical contact in the catalytic layer. In fact, carbon probably participates in the first steps of the ORR, i.e. the O_2 reduction into HO_2^-. Then, the role of oxide may indeed be limited to the decomposition or

reduction of HO_2^- into OH^- in the presence of carbon, leading to a higher number of electrons than carbon alone.

1.4.3.5. Influence of electronic structure of perovskite oxides on the ORR electrocatalytic activity

In the 70's, Matsumoto et al. [73] proposed a relationship between the ORR electrocatalytic activity and the electronic structure of perovskites. They observed that the ORR activity increased with the doping of $LaMnO_3$ by Sr and suggested that it is related to the availability of a localized e_g orbital on the transition metal ion of the doped perovskite to form a σ* bond with the surface oxygen. They also observed that perovskites with empty σ* bonds display low ORR activity and proposed therefore that an electron is required in this bond to allow the exchange of an electron in the rate-determining step of the ORR. For these authors, the O_2 adsorption is an end-on type adsorption on perovskite surface and therefore occurs through the orientation of the π* orbital of O_2 toward the e_g orbital of the transition metal. If the overlap of these orbitals is high, the electron transfer probability will be high. In other words, the reaction rate will be high and the perovskite will be highly active for the ORR. When the perovskite structure is distorted due to a small A cation, the random direction of e_g orbitals complicates their overlap with the π* orbital of O_2 and leads to low activity.

Some years later, Bockris et al. [75] studied the OER on perovskite oxides ant arrived at important conclusions which can be applied to the ORR as well. First of all, they showed that, in alkaline media, perovskite oxides are highly covered by OH species. Secondly, they plotted the OER activity in function of the number of d-electrons and found a direct correlation between them, suggesting that the transition metal determines the electrocataytic activity. Also, they observed that the OER current decreases when the bond strength between the transition metal cation and OH species increases. Thus, the breaking of this bond was proposed to be the rate determining step of the OER. According to the molecular-orbital approach and knowing that, at the perovskite surface, the e_g orbital is split into the d_{z^2} level at a lower electron energy and a $d_{x^2-y^2}$ level at a higher electron energy, the authors proposed that the filling of the d_{z^2} orbital determines the OER activity. When electrons are present in this orbital, the occupancy of the antibonding σ* orbitals of B-OH increases, resulting in a weaker bond, and thus, to higher OER rate.

By using the density functional theory (DFT), Fernandez et al. [137] demonstrated that the adsorption energies for O and OH on transition metals and transition metal oxides is determined by the strength of the coupling of the valence states of the adsorbates with the d states of the transition metal.

Very recently, after the start of the present thesis, Suntivich et al. [84] studied a wide range of perovskites and found a M-shape relationship between the ORR activity and the number of d electrons. The maximal activity was measured at high spin d^4 and low spin d^7. This corresponds to an e_g-filling of 1. By plotting the electrocatalytic activity of perovskites in the ORR in function of their e_g-filling, a volcano shape was observed, as shown in Figure 3.

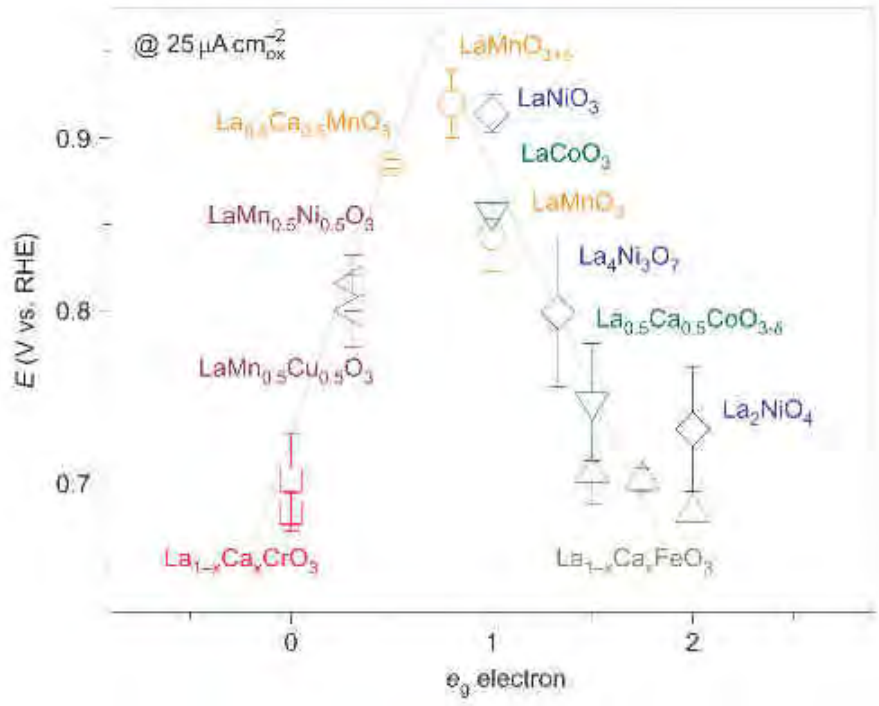

Figure 3 : *ORR potentials at 25 μA.cm$^{-2}_{ox}$ as function of e_g orbital in perovskite-based oxides. Data symbols vary with type of B ions (Cr, red; Mn, orange; Fe, grey, Co, green; Ni, blue; mixed compounds, purple), where x = 0 and 0.5 for Cr, and 0, 0.25 and 0.5 for Fe. Error bars represent standard deviations. Reprinted from [84] with the permission of Nature Publishing Group.*

To account for the observed volcano-type relationship, the authors proposed the following explanation. When the e_g-filling is equal to one, one electron lies in the d_{z^2} orbital which is directed towards the surface oxygen. This is therefore an σ* electron which can destabilize the B-OH bond in favour of the B-O_2 bond. When the e_g-filling is higher than 1, the B-O_2 bond is weak – it was confirmed by the O_2 temperature-programmed desorption. Then the replacement of OH by O_2 hardly occurs and is therefore the rate determining step of the ORR.

On the contrary, when the e_g-filling is lower than 1, the B-O_2 is strong, leading to a difficult regeneration of the surface OH.

To conclude, the authors proposed the filling of the e_g orbital of the transition metal at the perovskite surface as the ORR activity descriptor. Nevertheless, this volcano relationship should be taken with caution, first of all because the determination of the e_g-filling was not precise, and secondly because the contribution of carbon in the ORR activity is neglected in the mentioned study despite the fact that carbon was present in the thin layer electrodes in high quantities.

1.4.4. Stability of perovskite electrodes

With the purpose to use perovskites as catalysts in SAFCs, sufficient stability of the oxide properties is required. It includes the (i) thermodynamic stability of the perovskite structure, (ii) chemical stability of perovskites in alkaline media, (iii) reversible transformations of perovskites with the electrode polarization and (iv) sustainable ORR activity with stable oxide properties after electrocatalysis.

1.4.4.1. Structure stability

As mentioned in section 1.3, AMO_3 oxides with a tolerance factor between 0.75 and 1.05 have stable perovskite structure. These considerations are based on the cation radii, but thermodynamic data can also give information about the structure stability.

With this purpose, Calle-Vallejo et al. [138] calculated the formation energies of various perovskites using the DFT and found values in very good agreement with reported experimental free energy values. Two mains conclusions emerge from the comparison of the free energies for different perovskites (Figure 4). First of all, it is observed that the stability decreases with the increase of the atomic number of transition metal M. This is attributed to the relative ease to exchange atoms, which is the easiest for the cation with the lowest number of electrons in the 3d band, Ti, and the hardest for the one with the highest number of electrons in the 3d band, Cu. Secondly, it is noticed that perovskites with A and M cations of the same oxidation state, e.g. $LaMO_3$ and YMO_3 with A and M in the oxidation state (3+), are

more stable than those which have different oxidation state for the two cations, e.g. $BaMO_3$, $CaMO_3$ and $SrMO_3$ with A in oxidation state (2+) and M in the oxidation state (4+). This trend is supported by the values for doped $La_{1-x}Sr_xMO_3$ perovskites. Indeed, they have intermediate formation energies, consistent with their doping degree, showing that the oxidation states of the perovskite components are determining factors in the structure stability.

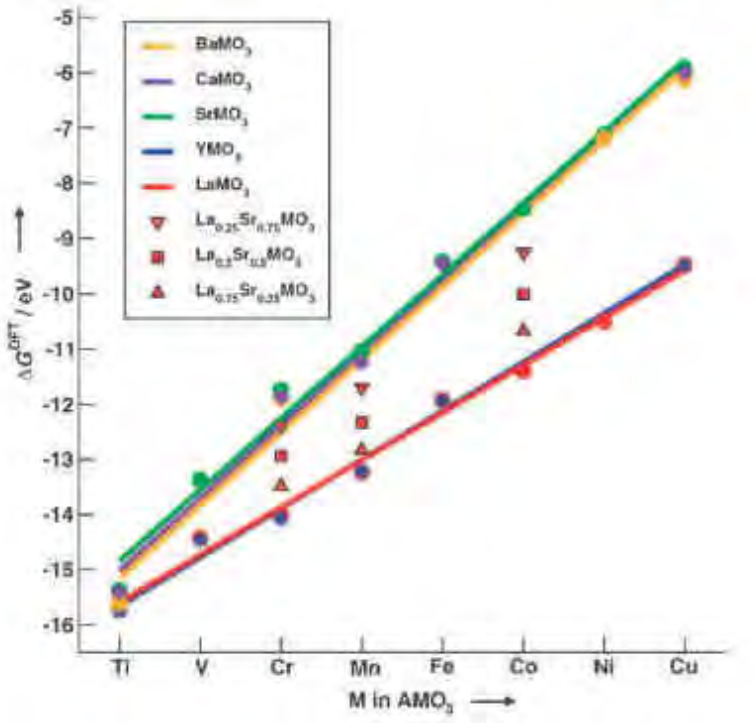

Figure 4 : *Trends in formation energies from elements for various families of perovskites (AMO_3), in terms of the atomic number of M. Symbols indicate calculated values for individual perovskites, and lines show the best fit for each family. Reprinted from [138] with the permission of John Wiley and Sons.*

1.4.4.2. Chemical stability

As SAFCs require the use of alkaline membranes, the stability of perovskite oxides in concentrated alkaline media is necessary.

Towards this goal, the chemical stability of La-based perovskite oxides was investigated by XRD after 12h in 9M NaOH at 80°C [139]. After this treatment in the strong alkaline medium, $LaCoO_3$ was almost completely transformed into lanthanum hydroxide. $LaMnO_3$ and $LaNiO_3$ also showed some traces of lanthanum hydroxide while $LaCrO_3$, $LaFeO_3$ and $La_{0.6}Sr_{0.4}FeO_3$ demonstrated a stable perovskite structure. Interestingly, it was found that a

partial substitution of Fe by Co or Mn in $La_{0.6}Sr_{0.4}FeO_3$ perovskite does not alter its chemical stability.

On the other hand, several researchers worked with perovskite electrodes in alkaline media and did not report such significant changes. In particular, the stability of both ORR [83,94,100] (see section 1.4.4.4) and OER [75,100,101] activities in alkaline media indirectly prove the stability of Co-based and Mn-based perovskite oxides in these media.

1.4.4.3. Electrochemical stability

The ORR occurs under a cathodic polarisation of an electrode. Therefore, it is desirable to study eventual transformations of perovskite oxide with the electrode potential.

In order to investigate the electrochemical stability of $Ca_{1-x}Ce_xMnO_3$ perovskite, Lucas et al. [140] performed XRD, SEM and roughness factor measurements before and after CVs in alkaline media. They found that an increase of the roughness of the electrode occurs with the polarization, and, from a careful study of peak dependencies and from the change of the electrolyte color, attributed these to the dissolution of high oxidation state Mn^{x+} cation ($x > 4$) at high potentials (ca. +0.4 V vs Hg/HgO). Despite this dissolution, XRD analysis proved that the perovskite structure was preserved in the bulk after CV measurements. On their side, Carbonio et al. [118] studied the effect of polarization on $LaFe_{0.25}Ni_{0.75}O_3$ and $SrFeO_3$ perovskites using the *in-situ* Mössbauer effect spectroscopy analysis in 0.1M KOH. For the former, no modifications occur in the perovskite bulk with electrode polarization, while for the latter, the perovskite is irreversibly reduced to $Fe(OH)_2$ at potentials below -0.7 V vs Hg/HgO. $LaNiO_3$ also demonstrates an irreversible transformation with decreasing potential. Indeed, Karlsson [141] observed an increase of the ohmic resistance of the mentioned perovskite upon electrode reduction in 1M KOH at 55°C and, by employing the XRD analysis, concluded that $LaNiO_3$ is reduced to a poorly conductive layer of $La(OH)_3$ and $Ni(OH)_2$.

When possible and depending on the nature of the B cation of perovskites, the ORR should be studied in a restricted potential window to avoid irreversible modifications of the oxides.

1.4.4.4. Electrocatalytic stability

Usually, the electrocatalytic stability of a material is investigated by potentiostatic or galvanostatic experiments in the presence of a reactant.

By these methods, the stability of the ORR activity was studied on various perovskite catalysts. For example, galvanostatic measurements at -300 $mA.cm^{-2}_{geo}$ were performed in 8M KOH at 60°C in the presence of air and showed that $LaMnO_3$ demonstrated a stable ORR activity for at least 140h [83]. In the same electrolyte and at similar cathodic current densities, Hyodo et al. [94] reported a stable ORR activity for ca. 200h of a $Pr_{0.6}Ca_{0.4}MnO_3$ electrode. By performing XRD analysis before and after electrocatalysis, the authors showed that this perovskite did not show noticeable changes in the structure. It is not the case of $La_{0.6}Ca_{0.4}CoO_3$ which, according to XRD, is largely decomposed into $La(OH)_3$ probably due to the interaction with the alkaline electrolyte (see section 1.4.4.2). This transformation results in an increase of the overpotential of ca. 110 mV in 120h. These results are however not in agreement with Zhuang et al. [100] who also studied $La_{0.6}Ca_{0.4}CoO_3$ and observed a rather stable ORR activity during 120h at -50 $mA.cm^{-2}_{geo}$. Interestingly, it was found that $Nd_{0.8}Sr_{0.2}CoO_3$ perovskite demonstrates higher durability towards the ORR with pure O_2 than with air [119], showing the importance of the partial pressure of oxygen on the mass transport resistance and thus on the ORR activity. In this work, the stability of the ORR activity was significantly improved with the partial substitution of Co by Ni. However, Karlsson [141] showed that the ORR activity of $LaNiO_3$ in 1M KOH at 55°C decreases significantly with the time due to the irreversible reduction and transformation of the perovskite into $La(OH)_3$ and $Ni(OH)_2$ species with the polarization (see section 1.4.4.3).

Besides, some authors have studied the stability of perovskite electrodes in the HO_2^- reduction reaction, as a possible step of the ORR. For instance, Wang et al. [131] by chronoamperometry measurements at various potentials showed that a Mn-based perovskite ($La_{0.4}Sr_{0.6}MnO_3$) has a stable activity for the HO_2^- reduction in 3M KOH + 0.6M H_2O_2 at 25°C. A Co-based perovskite - $La_{0.6}Ca_{0.4}CoO_3$ – also displays stable activity for this reaction, as demonstrated by galvanostatic measurements at various cathodic current densities in 3M KOH + 0.4M H_2O_2 at 25°C [132]. However, the durations of the tests – 30 min – is too short to conclude on the long-term stability versus HO_2^- reactions.

In conclusion, no clear tendency of the electrocatalytic stability of perovskite oxides emerges from the literature. Moreover, the stability of perovskite catalysts is not systematically investigated although required for practical applications. Thus, search of on active ORR catalysts should be accompanied by stability tests.

1.5. Conclusions of Chapter 1 and Objectives

Regarding the increasing electricity production requirements and the environmental concerns, fuel cells represent an attractive energy conversion technology. In particular, the solid alkaline fuel cell (SAFC) is a promising system which allows the use of inexpensive materials.

Although the oxygen reduction reaction in the alkaline medium is often faster than in the acidic, it is still a very slow process which largely limits the performance of fuel cells. Thus, numerous studies have been performed to search for the most active and stable catalysts for this reaction. In alkaline media, besides noble metals, various materials, including metal free materials and transitions metal oxides, demonstrate noticeable ORR activity. Among these materials, perovskite oxides appear to be suitable catalyst regarding their ORR activities and their price. The present thesis is therefore focused on the investigation of perovskite oxides, the catalytic behavior of which is not fully understood yet.

The flexible perovskite structure tolerates a wide range of $A_{1-x}A'_xB_{1-y}B'_yO_3$ compositions, and thus, allows tuning of the oxide properties. The nature of the B cation was reported to have a great impact on the ORR activity and doping of the A cation by cation of lower valence may increase the ORR kinetics. Among perovskites of various transition metals Mn and Co-containing perovskites have shown the most attractive catalytic activities. This work therefore includes the study of several doped and non-doped perovskites of Mn and Co to determine the relationship between their material properties and their catalytic activities.

In the literature, a large range of electrode configurations were used to measure the ORR activities of perovskite materials. However, only one – the thin layer approach – is compatible with the rotating (ring) disk (R(R)DE) techniques. Thanks to these techniques, careful measurement of the kinetic activities and mechanistic studies of the ORR are possible in liquid media. Therefore, liquid electrolyte and thin layers of perovskites are utilized in this work.

However, perovskite-based electrodes generally suffer from high resistance between the oxide particles (or agglomerates), which limits the ORR studies but also the application of these oxides as cathode materials in fuel cells. The addition of carbon significantly improves the conductivity of perovskite electrodes and thus, their performance. While carbon materials show significant ORR activities in alkaline media which might interfere with that of

perovskites, the role of carbon in perovskite/carbon composite electrodes is still unclear. In this thesis, the impact of the carbon on the ORR mechanism will be investigated by systematically varying the perovskite to carbon ratio in composite electrodes. Also, the possibility to evaluate the intrinsic activity of perovskites in the ORR is an important issue which will be addressed in this work.

The ORR has a complex multi-step mechanism which may involve the HO_2^- intermediates if it occurs through the "series" pathway. In the literature, some contradictions about the ORR mechanism appear for perovskite-based electrodes. Indeed, both the "series" and the "direct" pathways were reported. This might be the result of the utilization of different electrode configurations, compositions and catalyst loadings. Therefore, the impact of the electrode composition in terms of perovskite and carbon loadings as well as the oxide nature on the HO_2^- production during the ORR will be studied in this work using the RRDE technique.

If the ORR is indeed a "series" pathway with production of the HO_2^- intermediates, the investigation of the kinetics of its transformations is mandatory for the understanding of the mechanism. From the literature, it is known that the HO_2^- decomposition kinetics is strongly dependent on the nature of the B cation. Besides, little work has been performed on the HO_2^- reduction on perovskites, therefore the kinetics of this reaction remains largely unknown. The present work includes the study of the HO_2^- reduction/oxidation and the HO_2^- decomposition for various perovskites to extend the understanding of the ORR.

Finally, with the purpose to use perovskite oxides as cathode materials in fuel cells, long term performance stability is required. Literature data indicate that some perovskites might not be stable in alkaline media. On the other hand, the stability of the electrocatalytic activity of perovskites is not always performed, while being vital for fuel cell applications. Therefore, the chemical and the electrochemical stability of perovskite oxides will be investigated in this work. It includes not only the monitoring of the electrocatalytic activity but also the characterization of the perovskite material after its eventual degradation.

To sum up, the present thesis will regroup kinetic, mechanistic and stability studies on various electrode compositions. These studies are rarely combined in the literature but are required to fully understand the ORR electrocatalysis. The present work therefore links fundamental studies of the ORR to potential applications of perovskites as cathode materials for SAFCs.

Chapter 2 :
Materials and Methods

2.1. Synthesis of perovskite oxides

2.1.1. Synthesis procedure

The most commonly used method to prepare oxides with perovskite structure is the solid state synthesis in which oxides are mixed in stoichiometric amounts and heated at high temperature (1000-1400^{o}C). However, for electrocatalysis purpose, this method is not suitable since only powders with low surface area can be prepared.

The perovskite oxides studied in this work were all synthesized in the Moscow State University by F. Napolskiy [142] with a soft chemistry method using polyacrylamide gel. This method was described by Douy [143] and provides materials with higher surface areas than conventional high temperature approaches.

For this synthesis, nitrate and acetate of the desired components are required. In case they are only available in the form of oxides or carbonates, the latter were reacted with nitric acid to form nitrates. Precursors - nitrate and acetate solutions - were weighted according to the required stoichiometry, mixed with a solution of acrylamide and bis-acrylamide and heated at around 300°C to form a polyacrylamide gel. Then, this gel was heated in air from 25°C to 650°C at 5°C.min^{-1} and annealed at 650°C for 1h to decompose the gel and form perovskite oxides. This temperature was chosen since it usually results in smaller particle size than higher temperature synthesis [143]. After cooling, the oxides were milled in a planetary mill in the presence of ethanol for 3 h at 120 rpm using WC balls to separate particles and thus to obtain microfine oxide powder.

2.1.2. Choice of studied compositions

In this work, various perovskite compositions were studied in order to understand the influence of the B cation, the A cation and the perovskite doping on the ORR mechanism and on the perovskite stability.

It is known from literature that ORR activity is mainly linked to the nature and the oxidation state of the B cations. That is why it was chosen to study two different B cations to confirm

this behavior: Co and Mn, which demonstrated ORR activity in the literature (see section 1.4.2). One of the most common A cation for ORR catalysts being La, the main studied components were therefore $LaCoO_3$ and $LaMnO_3$ to allow comparison with the literature data. In order to vary the oxidation state of Mn and/or the number of oxygen vacancies and a fortiori the ORR activity, the effect of partial substitution of La^{3+} by a A^{2+} cation in $LaMnO_3$ oxides was also investigated by thoroughly studying $La_{0.8}Sr_{0.2}MnO_3$. Finally, $PrCoO_3$, $PrMnO_3$ and $La_{0.8}Ca_{0.2}MnO_3$ were tested as ORR catalysts and compared to $LaCoO_3$ and $LaMnO_3$ to check the influence of the nature of the A and A' cations and their effect on the perovskite structure and on the ORR activity.

Beside perovskite oxides, simple oxides of Co – Co_3O_4 spinel – and Mn – Mn_2O_3 – were also synthesized by the polyacrylamide gel method and studied for ORR electrocatalysis in order to verify the importance of the perovskite structure.

Other components studied in this work – La oxide (La_2O_3, 99.99%, Aldrich) and carbonate ($La_2(CO_3)_3$, xH_2O, Aldrich), Co hydroxide ($Co(OH)_2$, 99.9%, Alfa Aesar), Na hydroxide (NaOH, >99%, SDS) and carbonate (Na_2CO_3, >99.5%, SDS) , and Pt/C (40 wt. % Pt on carbon black, Alfa Aesar) – are commercial materials.

2.2. Material characterization

Several techniques were used to characterize the studied catalysts before and after electrocatalysis. They gave access to volume properties - crystallographic properties from X-Ray Diffraction (XRD), morphologic properties from Scanning Electron Microscopy (SEM), and composition properties from Energy-Dispersive X-Ray Spectroscopy (EDX) – as well as to surface properties - surface composition from X-Ray Photoelectron Spectroscopy (XPS) and specific surface from Brunauer, Emett and Teller (BET) technique. This section describes the methods employed and their principles.

2.2.1. X-Ray Diffraction (XRD)

2.2.1.1. XRD principle

Nature and structure of cristalline phases of a material can be determined by X-ray diffraction (XRD) technique. This technique is based on the Bragg diffraction, which is a consequence of the interference between waves reflecting from different crystal planes of a solid. When a X-ray beam reaches the sample to study, it is diffracted according to the Bragg's law (Equation 11):

$$2d\sin\theta = n\lambda \quad \text{(Equation 11)}$$

with d, spacing between two cristallographic plans, θ, Bragg angle, which is half of the angle between the incident beam and the detector direction, n, the order of reflection, and λ, the wavelength of the incident wave. Then the diffracted X-rays are collected in function of the 2θ angle. The pattern produced by XRD therefore gives information on the inter-layer spacing of atoms in the crystal structures of the sample.

Unless specified, X-Ray powder diffractions were recorded with D8 Advance Brucker diffractometer equipped with a copper anticathode using the Kα1 radiation. For powder samples, the oxide powders were first ground in a mortar to break down eventual agglomerates, then deposited as a powder thin layer on a glass support, and finally immobilized thanks to ethanol which is evaporated before analysis. For carbon paper samples

(see section 2.5.4.1), the samples were placed as received on the glass support in the presence of ethanol. The sample holder was rotated at 15 rpm during analysis to measure X-Ray intensities in each direction. Diffraction patterns were collected at room temperature for 2θ between 20 and 100°. The acquisition time was 2 h for powder samples and 8 h for carbon paper samples in order to distinguish perovskite peaks from the background contribution of the carbon paper.

2.2.1.2. Determination of bulk composition and structure

Each cristalline phase leads to a unique diffraction pattern. Thus reference cards of the International Centre of Diffraction Data (ICDD) database were used to determine the structures present in the studied samples. The cards containing the expected elements – such as La, Co and O in the case of $LaCoO_3$ - were collected and compared to experimental diffraction patterns after the background correction. Those which present similar position peaks and peak intensity ratio were considered corresponding to the bulk structure of the sample. When peaks could not be identified with this method, the search/match procedure was repeated with other possible components such as WC traces, NaOH traces or carbonates. This method has however its limits: peaks can be shifted compared to reference cards when the sample is too thick, for example, and the relative height of the peaks can be different from theory due to preferential orientation, insufficient number of crystallites or peak superposition. Moreover, amorphous phases cannot be identified by the XRD technique.

Previously to this work and immediately after the perovskite synthesis, unit cell parameters and quantification of the phases present in the initial oxides were determined by F. Napolskiy at the Moscow State University (142). The X-ray powder diffractions for this refinement were recorded with Huber G670 Image plate Guinier diffractometer (CuKα1 radiation, curve) and the unit cell parameters were refined by the full profile Rietveld analysis [144,145]. This method consists of simulating a diffraction pattern from a crystallographic model of the sample, and then of adapting the parameters of this model to fit the experimental diffraction pattern.

2.2.1.3. Determination of the crystallite size

The particle size of a crystalline material, or, more precisely, the size of a coherently scattering domain, can be estimated from the Scherrer equation which relates the mean crystallite size to the broadening of a peak in a diffraction pattern.
This equation can be written as (Equation 12):

$$t = \frac{k\lambda}{b\cos\theta} \quad \text{(Equation 12)}$$

with t, the mean size of crystallites in nm, k, the shape factor, which is 0.89 for D8 Advance Brucker diffractometer, λ, the X-Ray wavelength which is 0.15418 nm for Cu, b, the peak width at half of maximal intensity in radian, and θ, the Bragg angle in radian. It is only valid for nano-scale particles. The crystallite size obtained with this equation is smaller or equal to the grain size. Therefore, one can estimate the particle size and surface area of the studied material, assuming that particles are spherical. In this study, crystallite sizes were determined at low θ values to have more precision, with single peaks.

2.2.2. Particle Size Distribution

Particle size distribution was determined in the Moscow State University by a laser diffraction analysis. This technique is based on the principle that particles passing through a laser beam will scatter light at an angle and intensity that is directly proportional to their size. It therefore gives the distribution of the relative amount of particles or agglomerates present in the studied material according to their size.

2.2.3. Scanning Electron Microscopy (SEM) and Energy-Dispersive X-Ray Spectroscopy (EDX)

2.2.3.1. SEM principle

Morphology, particle size, and distribution homogeneity of a sample can be observed by the scanning electron microscopy (SEM). This technique produces largely magnified image of a

sample thanks to the interactions between electrons and matter. Indeed, an electron beam scans the sample surface, which produces elementary particles in response. These particles are then accelerated to detectors which amplify the electrical signal. The signal intensity depends on the sample nature at the point of impact, as well as its morphology. Nanometer size objects can be observed by this technique.

The particles produced by the excited sample include secondary electrons, backscattered electrons and photons. Whereas photons are used for the elemental analysis of the sample, secondary and backscattered electrons are used for imaging the material. The secondary electrons show the morphology and topography of the sample since the number of secondary electrons is function of the angle between the surface and the beam. The detection of these electrons is made by secondary electron image (SEI) and low secondary electron image (LEI) detectors. The SEI mode gives better resolved images, but LEI is preferred in case of charging of the sample. The backscattered electrons through a COMPO detector illustrate contrasts in the composition of the sample. Indeed, their intensity is strongly related to the atomic number of the beamed species.

The morphology of perovskite samples was analyzed with a Jeol 6007F apparatus at IPCMS, Strasbourg on ground perovskite powders and on perovskite/carbon thin layers on glassy carbon support (see section 2.3.2) as well as on carbon paper (see section 2.5.4.1). Perovskite powders were analyzed as received, without a conductive layer addition.

2.2.3.2. EDX principle

The energy-dispersive X-ray (EDX) spectroscopy is an analytical technique used for the elemental analysis of a sample from the detection of the photons produced by the excited sample. Indeed, the X-ray energy produced during the relaxation of excited atoms is dependent on their chemical nature. Therefore, by selecting energies, one can identify the atoms present in the sample at the point of impact. If the beam scans the whole screen, it is possible to make an elemental mapping of the sample and thus, to observe the distribution of various components over the surface.

The elemental distribution of the composite perovskite/carbon electrodes was studied in parallel to the SEM analysis with the Jeol 6007F apparatus at IPCMS, Strasbourg.

2.2.4. Brunauer, Emett and Teller (BET) technique

The specific surface area of a solid sample, i.e. the accessible surface for gas molecules per mass unit, is a determining factor for catalytic activity. While it can be evaluated thanks to hydrogen underpotential deposition for Pt samples (see section 2.3.4.3), other techniques are required for perovskites. The most common technique for oxide samples is the Brunauer, Emmet, and Teller (BET) method, developed in 1938 for the gas physisorption [146]. The physisorption phenomenon is the adsorption of gas molecules on the solid surface involving only Van der Waals forces. The BET model is based on three hypotheses: (i) adsorption enthalpy of molecules other than those in the first layer is equal to the liquefaction enthalpy, (ii) there is no interaction between adsorbed molecules, and (iii) the number of adsorbed layers is infinite at the saturated vapor pressure.

The BET equation is (Equation 13):

$$\frac{P}{V(P^o - P)} = \frac{1}{V_m C} + \frac{C-1}{V_m C} \times \frac{P}{P^o} \text{ (Equation 13)}$$

with P: equilibrium pressure, P°, vapor pressure of the adsorbate at the test temperature, V, adsorbed gas volume per gram of the solid at P, V_m, gas volume required to completely cover the solid surface with a molecular monolayer of the adsorbate, and C, characteristic constant of the system gaz - solid. Thus, by plotting P / [V(P° – P)] versus P/P°, one can determine V_m and C from the slope and y-intercept of the obtained straight line. Then, the specific surface area S_{BET} of the studied sample can be determined from (Equation 14):

$$S_{BET} = \frac{V_m N_a \sigma}{V_M} \text{ (Equation 14)}$$

with N_a, Avogadro number, 6.022 10^{23} mol^{-1}, σ, surface area occupied by a gas molecule, which is 0.162 nm^2 for N_2 at 77K, and V_M, molar volume.

The specific surface area of perovskite powders was determined by BET method using a Micrometrics Tristar 3000 apparatus. A certain amount of oxide was first degassed at 200° for ca. 8h to remove moisture and adsorbed species from the sample. The exact mass was measured after this degassing step. The measurements were then performed at 77 K using liquid nitrogen to achieve the adsorption of the introduced nitrogen gas on the sample. The successive measurements of the adsorbed gas volume and of the equilibrium pressure gave the adsorption isotherm from which the specific surface of the catalyst could be determined, knowing its mass.

2.2.5. X-Ray Photoelectron Spectroscopy (XPS)

2.2.5.1. XPS principle

When a solid is irradiated by a beam of X photons, its atoms emit photoelectrons. The principle of X-ray photoelectron spectroscopy (XPS) consists of analyzing the kinetic energy E_K of these photoelectrons. Then the binding energy E_B, which characterizes an electron at a given electronic level, can be calculated from the relationship of energy conservation (Equation 15):

$$E_B = h\nu - E_K \quad \text{(Equation 15)}$$

with $h\nu$, the energy of the incident X photons. As binding energies of core electrons are specific to an atom, it is then possible to identify and quantify the atoms present on the surface of a sample thanks to this technique.

When an atom is involved in a chemical compound, its core levels are modified compared to the levels of the isolated atom. In particular, orbital energies are shifted of some eV since they depend on the chemical bonds established by the atom, as well as its nature and its coordination number. This chemical shift allows for example the identification of the chemical bonds involved in chemical species, or the oxidation state of an element.

One should note that the apparent binding energy of photoelectrons is function of the conductivity of the studied sample. Actually, for an insulating material, a positive charge is created by photoemission, leading to a decrease of the kinetic energy, and thus to an increase of the apparent binding energy. This charge effect is usually compensated by using the C1s peak of adventitious carbon as reference.

XPS is a surface analysis since thicknesses of only 1 to 5 nanometers can be studied. Indeed, the analyzed thickness is limited by the mean free path of the photoelectrons – the distance crossed between two collisions – which is dependent on E_K and on the composition and density of the studied material. Identification of the surface composition is particularly important in catalysis since most reactions occur at the surface.

In this work, XPS analysis was performed with a Multilab 2000 Thermoelectron spectrometer with Al Kα ($h\nu$ = 1486.6 eV) source under the pressure of 10^{-9} mbar. Spectrum analysis was performed with the Avantage software, and the binding energy of adventitious carbon was set at 284.6 eV to calibrate the peak positions. Perovskite powders were ground before being

applied on the carbon scotch of the sample holder to break down agglomerates and thus minimize charge effects, and to get a fresh surface.

2.2.5.2. Identification of the present species

In a typical XPS analysis, a survey scan was first operated in a large binding energy window – usually from ca. 1200 eV to 0 eV - to check the elements present. For reference, the Handbook of X-ray Photoelectron Spectroscopy [147] was used. Once the elemental composition was determined, more detailed scans of each element were performed in the corresponding binding energy window, and the background signal was subtracted using the Shirley method. C1s peak was first analyzed in order to perform the calibration of the peak position. Then other components were labeled according to their electronic structure, and their corresponding peaks were identified thanks to deconvolution.

The deconvolution process of a photoelectron peak consists of simulating a theoretical spectrum close to the experimental one by varying (i) the number of individual components – element or chemical components, (ii) their binding energy, (iii) their peak width, and (iv) their intensity. The choice of these parameters was based on the literature.

In addition to photoelectrons emitted in the photoelectric process, Auger electrons can be emitted because of the relaxation of the excited ions remaining after photoemission. These Auger electrons can have binding energy close to the binding energy of the photoelectrons and high intensities. Therefore, they should also be taken into account in the deconvolution process.

2.2.5.3. Quantitative analysis

The quantification of an element or a chemical component can be achieved from the intensity I of a photoemission peak. Indeed, after background subtraction and peak deconvolution, this intensity is dependent on the atomic concentration N of the considered component on the surface according to the relationship (Equation 16):

$$I = KN\sigma\lambda \quad \text{(Equation 16)}$$

with K, a constant dependent on the detection of the signal, λ, the mean free path of photoelectrons which varies with the kinetic energy, and σ, the photoelectron cross section - section where the photoionisation is efficient - which is dependent on the electronic structure and can be determined from the Scofield's tables [148].

One can therefore easily obtain the atomic ratio of two components A and B according to (Equation 17):

$$\frac{N_A}{N_b} = \frac{I_A}{I_B} \times \frac{\sigma_B \lambda_B}{\sigma_A \lambda_A} \quad \text{(Equation 17)}$$

The error of the quantification thanks to this technique is about 10%.

2.2.6. Inductively Coupled Plasma - Mass Spectrometry (ICP-MS)

Inductively coupled plasma - Mass spectrometry (ICP-MS) was used to quantify the eventual dissolved species in electrolyte. This technique combined an ICP source which converts the atoms of the elements present in the sample into ions, and a mass spectrometer, which separates and quantifies these ions. It was performed at IPHC, Strasbourg.

2.3. Electrochemical techniques

2.3.1. Cleanliness of experiments

Very clean equipments and solutions have to be used for electrochemical analysis to avoid any troubles with impurities and therefore to increase reproducibility of the experiments. This was achieved by using very pure water and by thoroughly cleaning electrochemical cells.

2.3.1.1. Ultrapure water

The water used in the following experiments was ultrapure water. To obtain water of this purity, demineralized water was first distillated to remove main impurities, and then filtered and deionized with a Purelab Ultra apparatus (ELGA). The resulting water displays the typical resistivity of 18.2 MΩ.cm at 25°C and the amount of total organic carbon (TOC) inferior to 3 ppb.

2.3.1.2. Piranha solution

Piranha solution was used to clean glassware. This solution is obtained by adding hydrogen peroxide solution (H_2O_2, 35% in solution, stabilized, Acros Organics) to concentrated sulfuric acid (H_2SO_4, 95-98%, Sigma-Aldrich) in the volume ratio 1:1 under magnetic mixing. The resulting reaction is (Equation 18):

$$H_2SO_4 + H_2O_2 \rightarrow H_2SO_5 + H_2O \quad \text{(Equation 18)}$$

This reaction being exothermic, the addition of H_2O_2 to H_2SO_4 should be performed slowly and the reaction vessel should be surrounded by ice to avoid overheating of the mixture. The obtained solution is a strong oxidizing agent which can remove most organic matter. Its high acidity also allows the dissolution of oxides.

The prepared solution was active for around 6 months – proof of activity can be checked by presence of bubbles in the solution – and was stored under the hood in not tightly closed bottles.

2.3.1.3. Cleaning procedure

Glassware as well as plastic material such as Teflon cell should first be carefully rinsed with ultrapure water to remove for example alkaline and most catalysts traces. Under the hood, piranha solution is added in the item to be washed when possible, or the material is placed in a large beaker containing piranha solution. This material is covered to avoid solution evaporation, but not tightly closed to avoid internal pressure. After one night, the piranha solution is recovered and the material is washed several times with ultrapure water to remove piranha solution traces. Any remaining traces can lead to unexpected behavior such as dissolution of catalyst due to acidic traces or reduction current due to H_2O_2 traces. After careful rinsing of the material, it can be used for experiments.

2.3.2. Electrode preparation

Thin layers of perovskite/carbon were prepared following the procedure adapted from Schmidt et al. [149]. This method allows a good reproducibility, a complete utilization of the catalyst for sufficiently thin layers and is adapted for RDE and RRDE studies.

2.3.2.1. Carbon choice

Thin layers of perovskite usually suffer from low conductivity, therefore carbon material was added into the catalytic layer. Carbon of the Sibunit family was chosen for its high purity (ash content <0.4 wt%), avoiding reactions catalyzed by impurities, and high electron conductivity (around 10 $S.cm^{-1}$) [150-152].

Sibunit carbons are obtained by pyrolysis of hydrocarbons onto a template such as carbon black. Then a steam activation leads to the formation of the porous structure of Sibunit carbon by burning off the carbon black particles. By carefully choosing the template, i.e. the size of

carbon black particles, and by controlling the activation step, i.e. the manner and the duration of the activation, one can obtain carbon with the desired surface area and pore size.
The carbon used in this study was mainly Sibunit carbon of BET surface area of 65.7 $m^2.g^{-1}$ supplied by P. Simonov of the Boreskov Institute of Catalysis. Sibunit carbon of lower surface area (6 $m^2.g^{-1}$) from the same supplier was also studied for comparison.

2.3.2.2. Catalyst thin layer

The perovskite oxide powders (black powders) were first ground with a pestle in a mortar to break down agglomerates. For each experiment, controlled amounts of oxide and carbon powder were mixed together and ultrapure water (18.2 MΩ cm, Purelab) was added to get the desired suspension of the powder. The suspension was then treated in an ultrasonic bath during 30 minutes to break down remaining agglomerates and disperse particles. Making fresh suspensions for each experiment is preferable for two reasons: (i) an eventual error in the preparation of a suspension will not be reproduced; (ii) oxide suspensions might not be stable during time, as discussed in section 6.2.2.
A glassy carbon (GC) rotating-disc electrode (RDE) (0.07 cm² geometric area, Autolab) or a GC rotating ring-disc electrode (RRDE) (0.2 cm² geometric area, PINE) was successively polished with 1.0, 0.3 and 0.05 µm alumina slurry (Escil) and rinsed with ultrapure water to get a mirror finish. When GC disc was dried, 3.2 µL of the catalyst suspension for RDE experiments or 10 µL for RRDE experiments were taken under sonication to keep a homogeneous mixture, drop cast onto the GC support, and dried under N_2. This last operation – deposition and drying - was repeated three times in order to get a homogeneous coverage of the electrode and to improve the reproducibility. Thus, one should for example prepare a suspension containing 0.67 $g.L^{-1}$ of perovskite and 0.27 $g.L^{-1}$ of carbon to get a catalytic layer of 91 $\mu g.cm^{-2}$ perovskite and 37$\mu g.cm^{-2}$ carbon on RDE GC of 0.07 cm^2 via 3 depositions of 3.2 µL.
The obtained thin layer was observed with an optical microscope (IPCMS, Strasbourg) to check the distribution of the particles. Optical photograph in Figure 5 shows that perovskite and carbon particles cover rather homogeneously the whole glassy carbon surface.

Figure 5 : *Perovskite/carbon thin layer on glassy carbon observed by optical microscopy*

The apparent thickness t_{CL} of the catalytic layer was estimated using (Equation 19)

$$t_{CL} = \frac{m_1}{\pi r^2 \rho_1} + \frac{m_2}{\pi r^2 \rho_2} \quad \text{(Equation 19)}$$

with m_1 and m_2 - the mass of the perovskite oxide and carbon, respectively; ρ_1 and ρ_2 - the powder density of the perovskite oxide and carbon, respectively; r – the radius of the RDE (0.15 cm) or RRDE (0.3 cm). The powder densities were estimated by measuring the volume of water added to a known mass of powder material to reach a desired volume. No setting of the powder were performed. The obtained powder densities were 0.65 and 0.4 $g.cm^{-3}$ for perovskite oxides and the Sibunit carbon, correspondingly.

Both RDE and RRDE experiments were performed with various amounts of perovskite and carbon to study the role of each component in electrocatalysis (see sections 4 and 5). RRDE experiments were performed with thinner catalytic layers than RDE to facilitate diffusion, and thus increase the probability of detection, of the H_2O_2 intermediate out of the layer. In order to better identify the contribution of carbon, electrodes containing only Sibunit carbon - no perovskite - were prepared following the same procedure and quantity as perovskite/carbon thin layers. The contribution of the support was also evaluated by using polished GC electrode without any deposition.

Pt/C is usually utilized as a benchmark of the ORR activity [3]. Therefore, electrodes were prepared from suspensions containing Pt/C (40 wt. % Pt on carbon black, Alfa Aesar). For the ORR RDE study, the Pt/C electrodes contained 91 $\mu g.cm^{-2}$ Pt to be compared to perovskite electrodes, and for RRDE and HO_2^- reduction/oxidation RDE experiments, Pt/C electrodes with lower thickness were utilized to avoid strong capacitive contribution. No Sibunit carbon was added for these electrodes. The roughness factor of Pt particles on the electrode was estimated using the coulometry of the hydrogen underpotential deposition and found to be 26

$cm^2_{Pt}.cm^{-2}_{geo}$ for ORR RDE study and 6 $cm^2_{Pt}.cm^{-2}_{geo}$ for RRDE calibration (see section 2.3.5.2) and HO_2^- reduction/oxidation RDE study (see section 2.3.5.1).

2.3.2.3. Binder layer

Thin layers prepared from perovskite oxides were unstable when the electrode was placed in an alkaline electrolyte. In order to improve the adhesion of the particles onto the GC support, a binder layer was then added on the dried catalyst layer. Nafion is often used as binder for thin layer applications. Nevertheless, as experiments were performed in alkaline media, an alkaline ionomer was preferred to allow diffusion of OH^- ions through the binder, and to avoid any dissolution of oxide in contact with acidic medium of Nafion. The chosen ionomer is AS-4 from Tokuyama Company. It has a linear hydrocarbon backbone with quaternary ammonium group (Figure 6) [153].

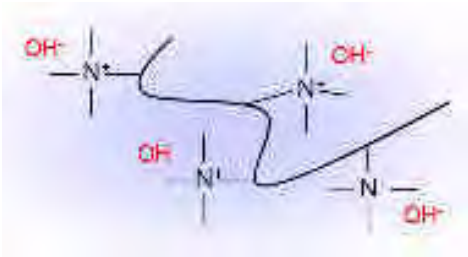

Figure 6 : *Schematic representation of the structure of AS-4 ionomer [153]*

RDE and RRDE experiments were performed with different catalyst layer thicknesses and therefore required different amounts of ionomer. Thus, AS-4 ionomer solution (5 wt% in 1-Propanol) was diluted in water to obtain a 2.2 10^{-3} vol% solution (8.68 µL AS-4 ionomer solution in 4 mL water) for RDE and a 1 10^{-3} vol% solution (5.2 µL AS-4 ionomer solution in 5 mL water) for RRDE. An aliquot of 2 µL of 2.2 10^{-3} vol% solution for RDE and of 6 µL of 1 10^{-3} vol% solution for RRDE was deposited on the dried layer of a catalyst. The final apparent thickness of the binder t_B was estimated to be around 15 nm for RDE and 7.5 nm for RRDE. Schmidt et al. [149] and Paulus et al. [154] showed that the film diffusion resistance is negligible for thin Nafion layers (below 0.1 µm). After extrapolation of this conclusion to alkaline ionomer, and as the binder thickness was very low compared to the thickness of the catalyst layer (> 0.4 µm, see sections 4 and 5), the diffusion resistance into the binder layer was neglected in this work. Moreover, one can assume that such a thin binder layer did not lead to the blocking of the catalyst surface.

When the ionomer layer was dried, the electrode was immersed in a beaker containing electrolyte and it appeared that the depositions with the binder layer were stable.

2.3.3. Setup for electrochemical measurements

2.3.3.1. Three electrode cell

A standard three electrode cell was used for electrochemical measurements. All parts of the electrochemical cell in contact with the alkaline electrolyte – such as the bottom of the cell or the reference electrode - were in Teflon whereas the rest was in Pyrex. The electrolyte was 100 mL of 1 M NaOH prepared from extra pure NaOH solution (50 wt. % solution in water, Acros Organics) and ultrapure water, at 25°C. The temperature was controlled by a thermostat bath. Since the preparation was performed in air, carbonate impurities cannot be completely excluded. Depending on the type of experiments, the working electrode was RDE, RRDE or carbon paper with perovskite/carbon thin layer. The counter electrode was a platinum wire in a separated compartment to avoid side reactions such as HO_2^- decomposition on Pt. This counter electrode should have a higher surface area than the working electrode to avoid current limitation by the counter electrode. The reference electrode - to which the applied potential was referred - was a Hg/HgO electrode (IJ Cambria Scientific) filled with 1M NaOH.

The electrolyte resistance was measured by potential electrochemical impedance spectroscopy (PEIS) at open circuit potential (OCP) from 100 kHz to 1 Hz and was equal to ca. 15 Ω. For the currents measured during electrochemical experiments, the IR correction was negligible - less than 2 mV shift for highest currents - and was therefore not applied.

2.3.3.2. Reference electrode calibration

The potential of the Hg/HgO/1M NaOH electrode was calibrated vs. the reversible hydrogen electrode (RHE). The utilization of this electrode allows to correct for thermodynamic effect of pH on electrochemical processes. For this electrode, the relation between the potential and the pH is given by (Equation 20).

$$E_o(\mathrm{RHE}) = 0.000 - 0.059 \times \mathrm{pH} \quad \text{(Equation 20)}$$

Therefore, electrochemical processes appear at the same potentials vs. RHE in electrolytes of different pH, unless pH influences the process kinetics. For calibration, 1M NaOH electrolyte was saturated with H_2 – after N_2-purging to remove any oxygen traces – and the open circuit potential was measured between a working electrode of platinum (typically a Pt wire or a platinized Pt foil) and the Hg/HgO/1M NaOH electrode. This open circuit potential was equal to +0.93V vs. RHE. In what follows the electrode potentials are given in the RHE scale.

2.3.3.3. Typical electrochemical experiments

All electrochemical measurements were performed using Autolab potentiostat with an analog scan generator, and the scan rate was usually 10 $mV.s^{-1}$ (unless otherwise stated). Each experiment was made at least two (but in general three or four) times to check the reproducibility of the catalyst loading and of its electrocatalytic behavior. Some of the repeated experiments can be seen in Appendix 1.

For all experiments, the 1M NaOH electrolyte was first purged with N_2 gas during at least 1h to remove oxygen traces. Then the working electrode – RDE or RRDE - was immersed in the N_2-purged electrolyte and cyclic voltammetry (CV) measurements were performed without electrode rotation until a stable voltammogram was obtained – usually 10 cycles. The potential window was restricted to +0.43 V / +1.23 V vs. RHE in order to avoid the irreversible oxide reduction at more negative potentials (see section 3.3.1), or the carbon oxidation at more positive potentials. The obtained voltammogram was used as a background for the ORR rotating disk electrode (RDE) and rotating ring-disk electrode (RRDE) as well as for HO_2^- reduction/oxidation RDE measurements. These reactions were then studied with hydrodynamic methods, description of the experiments is given in the corresponding sections (see section 2.3.5).

2.3.4. Cyclic voltammetry (CV)

2.3.4.1. CV principle

The voltammetry is a method to study the electrode processes by controlling the potential variation (Equation 21):

$$E(t) = E_i \pm v_s t \quad \text{(Equation 21)}$$

with E_i, the initial electrode potential in V vs. the reference electrode, v_s, the sweep rate in $V.s^{-1}$, and t, the time in s. The evolution of the current passing in an electrochemical system is then measured in function of the time and plotted versus the applied potential to give a voltammogram (Figure 7). Thus, if the potential is swept in the negative direction, the reduction of the electroactive species which can be reduced in this potential window will occur, giving a negative faradaic current which increases when the potential decreases. Due to consumption of species in the vicinity of the electrode surface and mass transport limitations, the absolute current will then decrease if the potential is kept decreasing. A current peak will therefore appear in the voltammogram. Usually, the electrode is immobile during voltammetry, but this technique can also be combined with hydrodynamic methods such as rotating disk electrode to change mass transport conditions.

The voltammetry is called cyclic voltammetry when the sweep direction is inverted at a chosen potential. Therefore, if the potential was first swept in the negative direction, the products of the reduction can be oxidized when the potential is swept in the positive direction. Several cycles between two potential values – E_{min} and E_{max} - can be performed during an experiment (Figure 7).

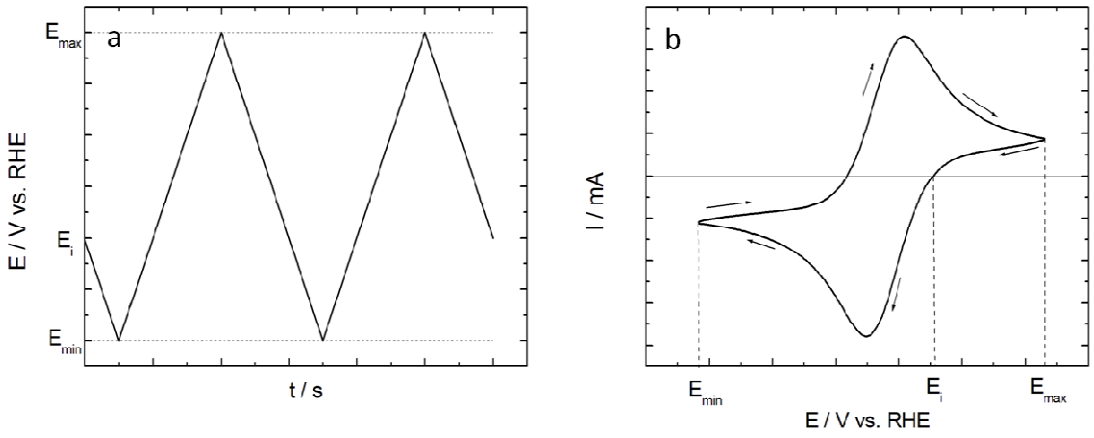

Figure 7 : *(a) Variation of the applied potential with time in cyclic voltammetry and (b) schematic current response versus applied potential. The arrows indicate the potential sweep direction.*

The total current I(t) measured during voltammetry is given by (Equation 22):

$$I(t) = I_f(t) + I_{dl}(t) \quad \text{(Equation 22)}$$

with I_f, the faradaic current, and I_{dl}, the capacitive current. The faradaic current is due to electrochemical processes and is directly proportional to their reaction rates. The capacitive current is due to the double layer charging – modification of the electrical charge distribution at the electrode-electrolyte interface - and increases with increasing the sweep rate (Equation 23).

$$I_{dl}(t) = C_{dl} \frac{dE(t)}{dt} \quad \text{(Equation 23)}$$

with C_{dl}, the capacity of the double layer, in Farad. In order to study only faradaic processes, one should subtract the capacitive current from the total current. The charge – in Coulomb – of the double layer Q_{dl} can be evaluated by integrating the capacitive current in function of the time, and the charge associated to an electrochemical reaction Q_{farad}, by integrating the faradaic current.

In order to study the interfacial properties of the studied oxides, CV measurements were performed in the N_2-purged electrolyte in various potential windows and at various scan rates. With this method, the potential window in which the oxides were electrochemically stable was investigated, as well as the roughness of the catalyst layer and the reversibility of the perovskite redox transitions.

2.3.4.2. Reversibility of electrochemical systems

The notion of reversibility in electrochemistry differs from that one in thermodynamics.

Various physico-chemical processes can be involved at the electrodes, such as the electron transfer between the current collector and a redox couple, i.e. the redox reaction, the mass transport of the species in the electrolyte and the adsorption and desorption processes – i.e. electrosorption reactions – occurring on electrode surface. Electrochemical systems can be classed into three categories, depending on their kinetics. A system is called fast when it is controlled by diffusion. When both diffusion and electron transfer control the electrode process, the system is considered as moderate. Finally, a process exclusively limited by the charge transfer is considered as slow. According to Matsuda's criteria, reversible redox systems – i.e. systems which are controlled by mass transport and have almost identical reduction and oxidation reaction rates - have kinetics constant in $cm.s^{-1}$ superior to $0.3\ v_s^{1/2}n^{1/2}$ while irreversible systems display kinetics constant below $2.10^{-5}\ v_s^{1/2}n^{1/2}$. Kinetic constants between these two values correspond to quasi-reversible systems. Clearly, the reversibility of

a reaction depends on the time constant of a method, and for linear sweep and cyclic voltammetry, on the sweep rate. Indeed, high sweep rates lead to too short time to reach equilibrium at the electrode surface, thus slow sweep rates should be applied such that a reaction satisfies the reversibility conditions.

Considering the redox reaction $O + ne \rightleftarrows R$ from species in solution, several equations were obtained – as for example demonstrated by Bard et al. [155] and Diard et al. [156] – to calculate the peak currents and potentials in function of the reaction kinetics.

For a reversible redox system in solution, the peak current $I_{f,peak}^{redox,rev}$ is proportional to $v_s^{1/2}$ (Equation 24):

$$I_{f,peak}^{redox,rev} = -0.446nFAC_O\sqrt{\frac{nFv_sD_O}{RT}} \text{ (Equation 24)}$$

with n, the number of involved electrons, F, the Faraday constant, A, the electrode surface area, C_O, the initial concentration of O in the solution, D_O, the diffusion coefficient of O, R, the gas constant, and T, the temperature in Kelvin. Moreover, the peak potential $E_{peak}^{redox,rev}$ of a reversible system does not depend on the sweep rate (Equation 25):

$$E_{peak}^{redox,rev} = E_{O/R}^{\circ} + \frac{RT}{nF}\ln\left(\frac{\sqrt{D_R}}{\sqrt{D_O}}\right) - \frac{1.109RT}{nF} \text{ (Equation 25)}$$

with $E_{O/R}^{\circ}$, the standard potential of the redox couple O/R, and D_R, the diffusion coefficient of R ; and the reduction peak – cathodic peak $E_{peak}^{redox,c}$ – and the oxidation peak - anodic peak $E_{peak}^{redox,a}$ - are separated by a constant potential gap for any sweep rate. This potential gap is equal to (Equation 26):

$$\left|E_{peak}^{redox,c} - E_{peak}^{redox,a}\right| = \frac{2.3\ RT}{nF} \text{ (Equation 26)}$$

which is 59/n mV at 25°C. For an irreversible redox system, however, the oxidation of the R species hardly occurs, and the peak potential gap between anodic and cathodic peaks is higher than this value. Indeed, peak potentials $E_{peak}^{redox,irrev}$ depend on v_s for irreversible systems (Equation 27):

$$E_{peak}^{redox,irrev} = E_{O/R}^{\circ} + \frac{RT}{\alpha_r nF}\left[\ln\left(\frac{k^{\circ}RT}{\sqrt{\alpha_r nFv_sD_O}}\right) - 0.780\right] \text{ (Equation 27)}$$

with k°, the standard constant of electronic transfer, and α_r, the symmetry factor, which indicates the feasibility in terms of enthalpy of the considered half-reaction – here, the reduction. Peak currents are proportional to $v_s^{1/2}$, as for reversible systems, but the equation which gives the peak current $I_{f,peak}^{redox,irrev}$ contains the symmetry factor (Equation 28):

$$I_{f,peak}^{redox,irrev} = -0.496nFAC_O\sqrt{\frac{\alpha_r nFv_s D_O}{RT}}$$ (Equation 28)

Finally, quasi-reversible redox systems are characterized by a peak current which is not proportional to $v_s^{1/2}$ and by peak potentials as well as a peak potential gap which are dependent on v_s. In particular, the potential gap between anodic and cathodic peaks is higher than for reversible systems.

For the electrosorption reaction $A^- + * \rightleftarrows A,ads + e^-$, where * is a free site on the electrode surface, and A,ads stands for A adsorbed on the electrode surface, it was shown [156] that peak potential of reversible electrosorption reactions $E_{peak}^{electros,rev}$ does not depend on the sweep rate (Equation 29) while peak potential of irreversible electrosorption reactions $E_{peak}^{electros,irrev}$ does (Equation 30), as for redox processes:

$$E_{peak}^{electros,rev} = \frac{RT}{F}\ln\left(\frac{k_r}{k_o A^{-*}}\right)$$ (Equation 29)

$$E_{peak}^{electros,irrev} = \frac{RT}{\alpha_o F}\ln\left(\frac{\alpha_o F v_s}{RTk_o A^{-*}}\right)$$ (Equation 30)

with A^-*, the initial concentration of A^- in the bulk, and k_o and k_r, the kinetic constant of electronic transfer in the oxidation direction and in the reduction direction, respectively. However, contrary to redox processes from species in solution, the peak current of electrosorption reactions varies linearly with v_s for reversible (Equation 31) as well for irreversible (Equation 32) reactions:

$$I_{f,peak}^{electros,rev} = \frac{F^2 A\Gamma v_s}{4RT}$$ (Equation 31)

$$I_{f,peak}^{electros,irrev} = \frac{F^2 A\Gamma\alpha_o v_s}{eRT}$$ (Equation 32)

with Γ, number of sites per surface unit, and e, electron charge.

Therefore, by studying the dependence of the peak current and potential on the sweep rate, it is possible to determine the nature and the kinetics of an electrode process.

2.3.4.3. CV of platinum electrodes

Polycrystalline platinum electrodes display a typical voltammogram on which three regions may be distinguished. At high potentials, the “oxygen region” is characterized by an anodic current of hydroxide anions adsorption and Pt oxide formation and by a cathodic peak of

reduction of this Pt oxide - hydroxide layer. A region of very low current is found in the center of the voltammogram. This is the double layer region where only capacitive processes occur. This region is narrower in alkaline media than in acidic media due to an earlier surface oxide/hydroxide formation. Finally, the "hydrogen region" appears at low potentials. With the decrease of the potential, the adsorption of hydrogen – also called hydrogen underpotential deposition - takes place, until hydrogen evolution near 0 V vs. RHE. When the potential is inverted and increased again, hydrogen is then desorbed. This interpretation was based on works on Pt single crystals in alkaline media [8,157].

Figure 8 presents the CV of a Pt/C electrode in N_2-purged 1M NaOH electrolyte. This CV is very similar to the CV found for Pt/C electrodes in alkaline media in the literature [12,158,159].

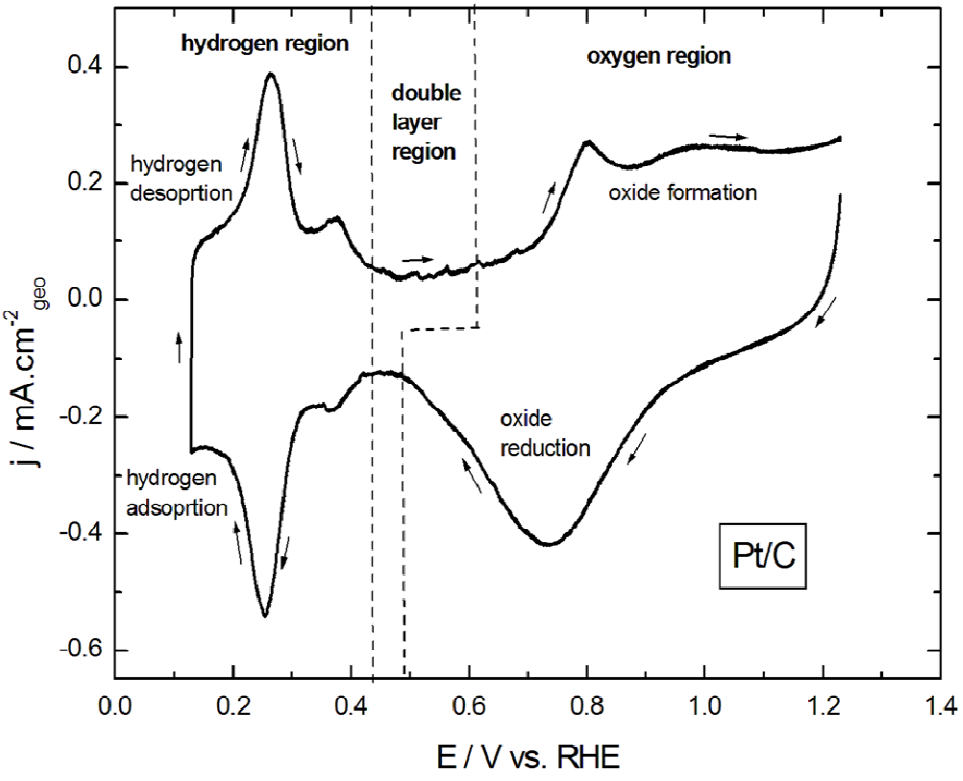

Figure 8 : *CV of GC-supported thin films of Pt/C in N_2-purged 1M NaOH electrolyte at 10 $mV.s^{-1}$. Measurements were performed with 91 $\mu g.cm^{-2}_{geo}$ Pt. Currents are normalized to the geometric area of the electrode*

The hydrogen adsorption process is often used to evaluate the real Pt surface area. Indeed, the real surface area $A_{coulomb}$ can be calculated as (Equation 33):

$$A_{coulomb} = N_a a_H n_H \text{ (Equation 33)}$$

with N_a, the Avogadro's number, a_H, the area occupied by each adsorbed hydrogen atom, and n_H, the amount in moles of adsorbed hydrogen atoms. n_H can be estimated assuming a one-electron charge transfer process (Equation 34):

$$n_H = \frac{Q_H}{F} \text{ (Equation 34)}$$

with Q_H, the charge associated with the formation of a monolayer of adsorbed hydrogen. Then, the real Pt surface area is (Equation 35):

$$A_{coulomb} = \frac{N_a a_H Q_H}{F} \text{ (Equation 35)}$$

in which $N_a a_H/F$ is usually equal to 210 µC.cm_{Pt}^{-2} for polycrystalline platinum [160]. The charge Q_H can be measured by integrating the faradaic current - capacitive currents can be deduced from the double layer region - between t_i, the time when the hydrogen adsorption starts, and t_f, the time when the monolayer is completed.

With this method, the surface areas of Pt particles of Pt/C electrodes were estimated as 1.8 cm^2_{Pt} for 91 µg.cm^{-2} loading used for the ORR RDE study and 0.4 cm^2_{Pt} for 20 µg.cm^{-2} loading used for the HO_2^- reduction/oxidation RDE study. The corresponding roughness factors of these electrodes were therefore 26 $cm^2_{Pt}.cm^{-2}_{geo}$ and 6 $cm^2_{Pt}.cm^{-2}_{geo}$, respectively.

2.3.5. Hydrodynamic methods

2.3.5.1. Rotating disk electrode (RDE)

2.3.5.1.1. Principle

RDE consists of a conductive disk electrode – in this work glassy carbon with perovskite/carbon thin layer – surrounded by an insulating ring (Figure 9). By rotating this electrode at various rotation rates, the mass transport conditions near the electrode surface are set due to forced convection and well defined. Therefore the activity of an electrocatalytic system can be determined by separating mass transport limitations and charge transfer losses. This correction is not possible in stagnant electrolyte where diffusion is the main transport process.

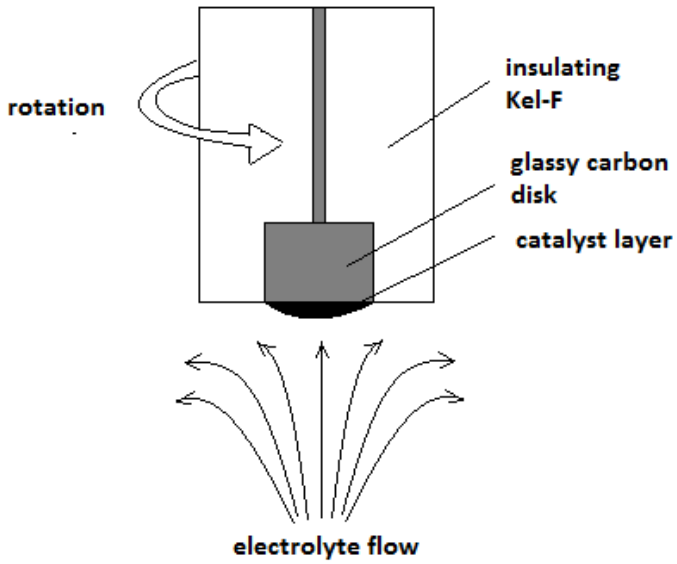

Figure 9 : *Schematic cross view of a RDE*

For a RDE experiment, cyclic voltammetries are performed at various rotation rates in an electrolyte containing the studied reactant. In order to obtain the faradaic current by removing the capacitive contribution to the total current (Equation 22), the capacitive current was approximated as being the current of the CV in the electrolyte without reactant. In this study, this corresponds to the CV in N_2-purged 1M NaOH electrolyte. An example of background corrected RDE voltammograms is shown in Figure 10.

The qualitative and quantitative interpretations of these curves were discussed in [155,156,161] and are summarized below.

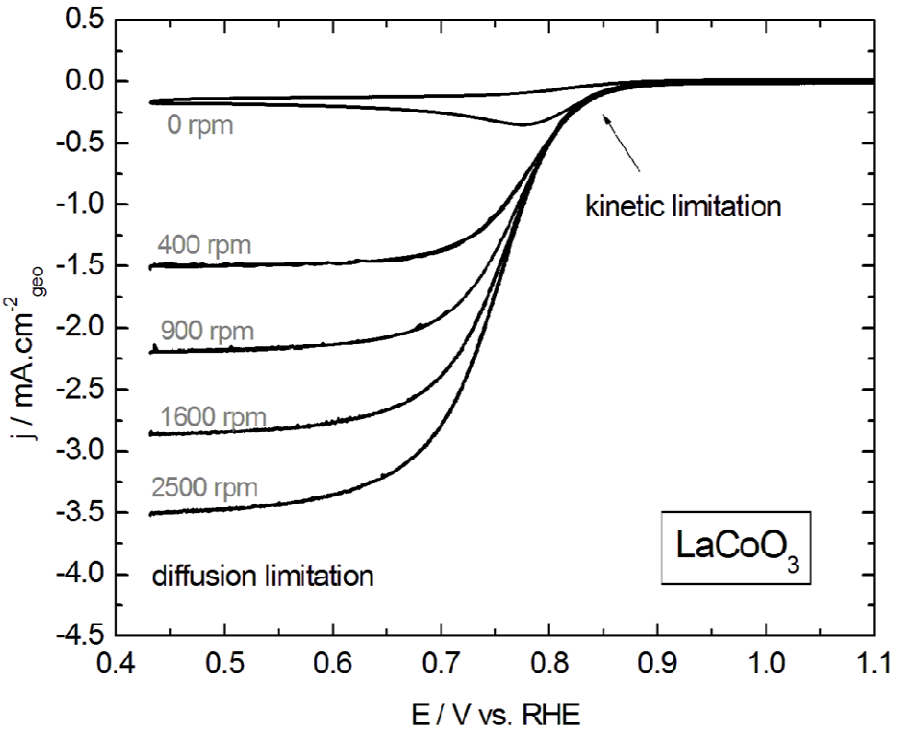

Figure 10 : *RDE voltammograms of GC-supported thin films of $LaCoO_3$ + Sibunit carbon in O_2-saturated 1M NaOH electrolyte at various rotation rates and at 10 mV.s^{-1}. Measurements were performed with 91 µg.cm$^{-2}_{geo}$ perovskite and 37 µg.cm$^{-2}_{geo}$ Sibunit carbon. Currents are normalized to the geometric area of the electrode and corrected to the background currents measured in the N_2 atmosphere.*

When the applied potential moves away from the equilibrium potential of the studied reaction (1.23 V_{RHE} for the ORR at 25°C), it reaches the onset potential where the reaction starts, leading to an increase of the absolute faradaic current. The faster the reaction kinetics, the smaller is the overpotential. In other words, for a reduction reaction, the faster the kinetics, the more positive is the onset potential. The reaction is exclusively limited by the reaction kinetics at these low overpotentials and the current does not depend on the rotation rate.

When the overpotential is gradually increased, the reaction becomes limited by both reaction kinetics and mass transport. And at low potentials for reduction processes and at high potentials for oxidation processes, i.e. at high absolute overpotentials, the charge transfer kinetics becomes very fast and the reaction is exclusively limited by the mass transport of reactants. This results in a current plateau I_D on the RDE voltammograms, which is dependent

on the concentration of reactants and increases linearly with the square root of electrode rotation rate ω according to Levich equation (Equation 36):

$$|I_D| = 0.62\ n\ A\ F\ D^{\frac{2}{3}}\ \nu^{-\frac{1}{6}}\ C_{O2}\ \omega^{\frac{1}{2}} \quad \text{(Equation 36)}$$

with the following parameter values in 1M NaOH at 25 °C: the concentration of O_2 in the saturated electrolyte, C_{O2} = 8.4 x 10^{-7} mol.cm^{-3}, the diffusion coefficient of O_2, D_{O2} = 1.65 x 10^{-5} cm².s^{-1} [163], the kinematic viscosity of electrolyte, ν = 0.011 cm².s^{-1} and the electrode geometric surface area A = 0.07 cm^2. The RDE voltammograms are usually plotted with normalization of the current by the geometric surface area to have direct access to the diffusion limited current density. According to the Levich equation, the slope of the linear curve of I_D versus $\omega^{1/2}$ gives the number of electrons involved in the studied reaction. However, the RDE technique is only valid for uniformly accessible thin layers. For too thick or not well dispersed catalytic layers, Levich equation is not applicable. In particular, the layer thickness should be lower than the diffusion layer thickness δ (Equation 37):

$$\delta = 1.61\ D^{\frac{1}{3}}\ \omega^{-\frac{1}{2}}\ \nu^{\frac{1}{6}} \quad \text{(Equation 37)}$$

The electrode rotation rates used in this study were usually 400, 900, 1600 and 2500 rpm. The corresponding δ values were therefore 30, 20, 15 and 12 µm, respectively. Thus, all perovskite/carbon electrodes used in this study, except the one containing the highest amount of carbon (820 µg.cm$^{-2}_{geo}$), present a catalytic layer thickness lower than the diffusion layer thickness (see sections 4 and 5).

According to Koutecky-Levich, the faradaic current I_f is related to the kinetic current I_k which determines the electrocatalytic activity, i.e. charge transfer limitation, by (Equation 38):

$$\frac{1}{|I_f|} = \frac{1}{|I_k|} + \frac{1}{|I_D|} \quad \text{(Equation 38)}$$

with I_D, the current from mass transport limitations, determined by Levich equation (Equation 36). The kinetic currents are usually normalised by the real surface area of catalyst (j_k) to obtain the specific catalytic activity, and plotted in logarithmic scale versus the applied potential, i.e. in a Tafel representation.

It is possible to determine I_k with two methods. The first one consists in plotting $|I_f|^{-1}$ in function of $\omega^{-1/2}$ for various potentials. The obtained curves should be linear with a slope directly linked to the number of electrons and the y-interecept (extrapolation to ω=0) gives the value of $|I_k|^{-1}$ at the corresponding potential. In particular, at high overpotentials, $|I_k|^{-1}$ should

be equal to zero due to the very fast reaction kinetics. Kinetic currents obtained with this method are presented in Figure 11 with the red curve for a glassy carbon disk.

The second method is the mass transport correction with direct application of the Koutecky-Levich equation at a given rotation rate. Indeed, for a rotation rate, I_D can be determined from the current plateau value, and therefore its inverse can be substracted to the inverse of the faradaic current at this rotation rate to obtain the inverse of the kinetic current. Kinetic currents obtained for the glassy carbon disk with this second method are presented in Figure 11 with the green curve. The kinetic currents obtained with the two different methods are close (Figure 11), but the second method was preferred in this work since the first method is hardly applicable at low overpotentials, the curves $|I_f|^{-1}$ versus $\omega^{-1/2}$ being not parallele anymore at low overpotentials.

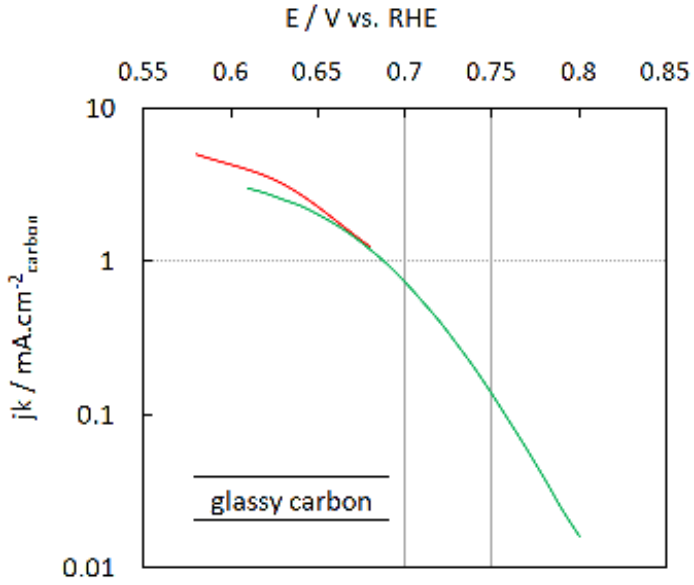

Figure 11 : *Tafel plots from mass-transport corrected positive-going scans of GC in O_2-saturated 1 M NaOH at 10 mV.s^{-1}. Color codes: kinetic currents obtained from y-intercepts of Koutecky-Levich plots (red), kinetic currents obtained with direct application of Koutecky-Levich equation to a RDE curve at a single rotation rate (green). Currents are normalized to the geometric surface area for GC.*

For the one electron redox system $O + e \rightleftarrows R$, the kinetic current densities j_k are related to the overpotential $\eta = E - E_{eq}$ by the Butler-Volmer relationship (Equation 39):

$$j_k = j_o \left[\exp\left(\frac{\alpha_O F}{RT}\eta\right) - \exp\left(-\frac{\alpha_R F}{RT}\eta\right)\right] \quad \text{(Equation 39)}$$

with, α_O and α_R, the symmetry coefficient of the oxidation and reduction, respectively ($\alpha_O + \alpha_R = 1$), F, the Faraday constant, R, the gas constant, and T, the temperature in Kelvin. j_o is the exchange current density (Equation 40):

$$j_o = Fk°R^{*\alpha_R}O^{*\alpha_O} \text{ (Equation 40)}$$

in which k° is the standard constant of electronic transfert kinetics in the redox system in $cm.s^{-1}$, and R* and O*, the oxidant and reductant concentration in the solution, supposed constant. However, this relationship is valid for a one electron redox system while ORR is a multi electron process involving several electrochemical, chemical and adsorption steps. For multistep reactions such as ORR, the kinetic currents are governed by the rate determining step, i.e. the elemental step with significantly lower reaction rate than the other steps.
With the purpose to compare the electrocatalytic activity of various catalysts, the ORR kinetic currents of the different catalysts are determined thanks to the RDE technique and plotted in Tafel plots. The most active catalyst is then that which displays higher kinetic currents at the lowest overpotential.

2.3.5.1.2. Experimental study of the ORR by the RDE

After acquisition of the background voltammogram in N_2-purged 1M NaOH electrolyte, O_2 gas was bubbled through the electrolyte for at least 45 minutes to get a O_2-saturated solution in order to study the ORR. Depending on the stability of the voltammogram, 3 to 5 cycles were performed without rotation in O_2-saturated electrolyte. RDE voltammograms were then taken at various rotation speeds of 400, 900, 1600, 2500 rpm with 2 cycles at each rotation. At 10 $mV.s^{-1}$ scan rate, the difference of the positive and the negative ORR scans after the background correction – a CV under N_2 atmosphere – was negligible and therefore, unless specified, only anodic scans were used for determining the ORR activity.

2.3.5.1.3. Experimental study of the HO_2^- reduction/oxidation by the RDE

As HO_2^- reduction might be a step in the ORR mechanism on perovskite oxides, this reaction was also investigated. For that, an aliquot of SupraPur H_2O_2 (H_2O_2 30 wt% solution in water, SupraPur, Merck) previously titrated with standardized $KMnO_4$ (see section 2.4.1) was added to the N_2-purged 1M NaOH after measuring the background voltammogram. For this study, it

was chosen to mainly work with a concentration of H_2O_2 of 0.84mM, which corresponds to the concentration of O_2 in O_2 saturated electrolyte and thus, the maximum concentration of HO_2^- which can be formed during the ORR. The addition of H_2O_2 was made under rotation of the working electrode and during bubbling of N_2 to achieve convection and thus good mix of solutions. RDE voltammograms were then taken at various rotation speeds of 400, 900, 1600, 2500 rpm with 2 cycles at each rotation with as low as possible waiting time between each rotation to minimize the effect of HO_2^- decomposition in the electrolyte.

2.3.5.2. Rotating ring-disk electrode (RRDE)

2.3.5.2.1. Principle

A RRDE is a rotating setup constituted of a disk and a ring, separated by an insulating ring to keep them electrically isolated (Figure 12). The disk behaves like a RDE, but the ring is polarized at a different potential than the disk in order that the products formed at the disk can be, depending on the ring potential, reduced or oxidized at the ring after diffusion through the electrolyte. Then, the current measured at the ring gives an indication of the quantity of transformed species. It is particularly useful for quantifying stable intermediates of multistep reactions. For example, it is possible to quantify HO_2^- formation during the ORR if the potential of the ring is sufficiently high to oxidize HO_2^- (Figure 12).

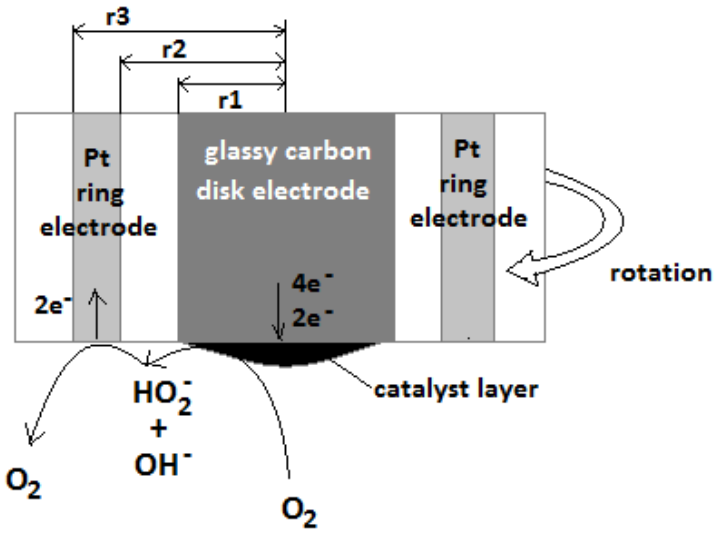

Figure 12 : *Schematic cross view of a RRDE during the ORR*

Indeed, during the ORR, the disk current I_D is the sum of the current of the "direct" pathway I_{OH^-} - from O_2 to OH^- - and of the current of the "series" pathway I_{HO2^-} - from O_2 to HO_2^- (Equation 41):

$$I_D = I_{OH-} + I_{HO2-} \text{ (Equation 41)}$$

I_{HO2^-} can be determined from the ring current I_R after its normalization by the collection factor N (Equation 42), which represents the amount of diffused species which can be detected by the ring:

$$I_{HO2-} = \frac{I_R}{N} \text{ (Equation 42)}$$

N is lower than 1 since a part of generated species escape to the bulk solution and thus, are not accessible to be detected at the ring. Then, the percentage of the "series" pathway, i.e. HO_2^- yield, can be calculated from the molar flux rates of O_2 ($\dot{n}_{O2}(4e^-)$) and HO_2^- ($\dot{n}_{O2}(2e^-)$) (Equation 43):

$$HO_2^- \text{ yield} = 100\frac{\dot{n}_{O2}(2e^-)}{\dot{n}_{O2}(2e^-)+\dot{n}_{O2}(4e^-)} \text{ (Equation 43)}$$

The molar flux rates are given by (Equation 44) (Equation 45):

$$\dot{n}_{O2}(2e) = \frac{I_{HO2-}}{2F} \text{ (Equation 44)}$$

$$\dot{n}_{O2}(4e) = \frac{I_{OH-}}{4F} \text{ (Equation 45)}$$

Then, the HO_2^- yield can be determined directly from the disc and the ring current thanks to (Equation 46):

$$HO_2^- \text{ yield} = 100\frac{2\frac{I_R}{N}}{I_D+\frac{I_R}{N}} \text{ (Equation 46)}$$

It should however be noticed that HO_2^- has to desorb and diffuse away from the working electrode to be detected at the ring. Thus, if HO_2^- formed during the ORR is reduced without desorption or desorbs and the readsorbs at neighbor site, the ORR mechanism will appear – incorrectly - as a direct 4 electron pathway.

In this work, the disk electrode was a GC disk with a thin layer of perovskite/carbon deposited as usually, the insulating ring was a Teflon tube and the ring electrode was a Pt ring. Before use, the Teflon tube was cleaned with Piranha solution for one night and rinsed carefully with water. As the Pt ring could not be detached from the RRDE support, strong chemical or thermal treatment could not be applied to clean Pt surface. Thus, an

electrochemical cleaning was applied to the ring by performing at least 100 cycles at 200 $mV.s^{-1}$ in N_2-purged 1M NaOH electrolyte in the potential window [+0.13 ; +1.23 V vs. RHE]. The resulting CV presented well defined hydrogen adsorption/desorption peaks, showing that the Pt surface was cleaned.

After ring cleaning and acquisition of the disk background voltammogram in N_2-purged 1M NaOH electrolyte, O_2 gas was bubbled through the electrolyte for at least 45 minutes to get a saturated solution and RRDE voltammograms were then taken at various rotation speeds of 400, 900, 1600, 2500 rpm with 2 cycles at each rotation. A +1.23V vs. RHE potential was applied on the ring to oxidize HO_2^- species, while the potential at the disc was swept between +0.43 V and +1.23 V vs. RHE.

2.3.5.2.2. RRDE calibration

The collection factor N of the RRDE used in this work was determined both experimentally and theoretically. The theoretical value of N is obtained from geometry parameters by (Equation 47) [155]:

$$N = 1 - F\left(\frac{\alpha}{\beta}\right) + \beta^{\frac{2}{3}}[1 - F(\alpha)] - (1 + \alpha + \beta)^{\frac{2}{3}} \left\{1 - F\left[\left(\frac{\alpha}{\beta}\right)(1 + \alpha + \beta)\right]\right\} \text{ (Equation 47)}$$

with (Equation 48)(Equation 49) (Equation 50):

$$F(\theta) = \left(\frac{\sqrt{3}}{4\pi}\right) \ln\left\{\frac{\left(1+\theta^{\frac{1}{3}}\right)^3}{1+\theta}\right\} + \frac{3}{2\pi} \arctan\left(\frac{2\theta^{\frac{1}{3}}-1}{3^{\frac{1}{2}}}\right) + \frac{1}{4} \text{ (Equation 48)}$$

$$\alpha = \left(\frac{r_2}{r_1}\right)^3 - 1 \text{ (Equation 49)}$$

$$\beta = \left(\frac{r_3}{r_1}\right)^3 - \left(\frac{r_2}{r_1}\right)^3 \text{ (Equation 50)}$$

and r_1, radius of the disk (2.5 mm), r_2, radius of the disk and insulating ring (3.25 mm) and r_3, radius of the disk, insulating ring and ring (3.75 mm) (Figure 12). The obtained N was 0.255, independently of the electrode rotation rate.

N was also estimated experimentally using the reversible $Fe(CN)_6^{3-}$/ $Fe(CN)_6^{4-}$ redox couple. Indeed, N is directly related to the disk and the ring current for reversible reactions (Equation 51):

$$N = -\frac{I_R}{I_D} \text{ (Equation 51)}$$

In order to simulate the thickness of the perovskite/carbon electrodes, the calibration was performed with a thin layer of Pt/C deposited on the GC disk rather than on a polycrystalline Pt disk. After ring cleaning and acquisition of the disk background voltammogram in N_2-purged 1M NaOH electrolyte, the RRDE was placed in another electrochemical cell containing 10 mM $K_3Fe(CN)_6$ and 1M NaOH, purged with N_2. Alkaline solution was also chosen in references [90,154,164] and its use avoids Prussian blue formation which occurs more likely in acidic media [162]. CVs were first performed without rotation on disk and ring electrodes, independently. The CV obtained in the potential window [+0.98 V ; +1.53 V vs. RHE] at various sweep rates displayed a cathodic and a anodic peak with similar coulombic charge (not shown). As (i) the peak potential was independent of the sweep rate, (ii) the potential gap between anodic and cathodic peaks was 59 mV, and (iii) the peak current increased linearly with the square root of the sweep rate, the reversible behavior of $Fe(CN)_6^{3-}$/ $Fe(CN)_6^{4-}$ was confirmed. RRDE voltammograms were then taken at various electrode rotation rates at 10 $mV.s^{-1}$ in the same potential range and a +1.48V vs. RHE potential was applied on the ring to achieve $Fe(CN)_6^{4-}$ oxidation. The results are shown in Figure 13,a.

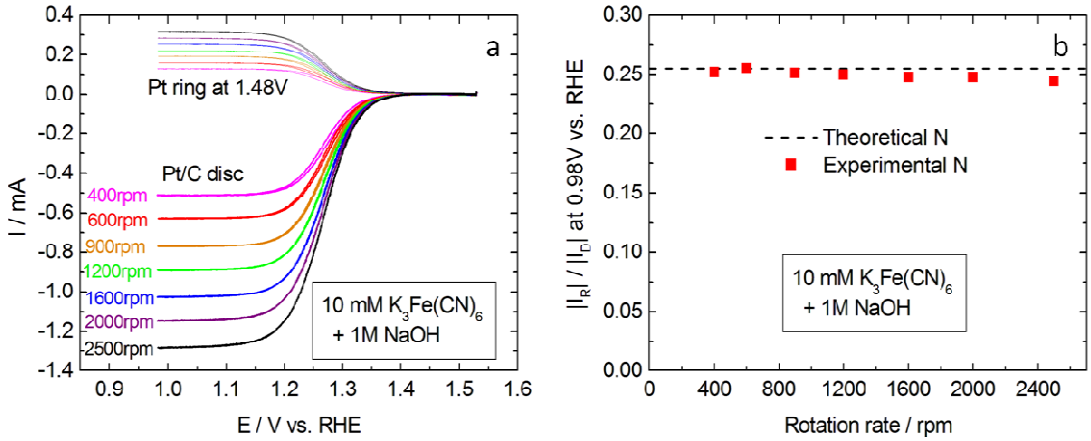

Figure 13 : *(a) RRDE voltammograms of GC-supported thin film of Pt/C and corresponding currents on Pt ring polarized at +1.48 V vs. RHE, in N_2-purged 10 mM $K_3Fe(CN)_6$ + 1M NaOH electrolyte at various electrode rotation rates and at 10 $mV.s^{-1}$. Measurements were performed with 20 $\mu g.cm^{-2}_{geo}$ Pt. Color codes for rotation rates : 400 (pink), 600 (red), 900 (orange), 1200 (green), 1600 (blue), 2000 (purple), and 2500 rpm (black). Disk currents are corrected to the background currents measured in the N_2 atmosphere in the absence of $K_3Fe(CN)_6$. (b) Corresponding $|I_R|/I_D|$ ratio at +0.98 V vs. RHE versus rotation rate.*

The disk and ring currents reach a plateau at low potential values. At 0.98 V vs. RHE, both disk and ring currents increase linearly with the square root of the rotation rate, showing that

the current is limited by diffusion at this potential. By plotting the ratio $|I_R|/|I_D|$ at this potential (Figure 13,b), N appears to be 0.25 and nearly constant with the rotation rate. This value is close to the theoretical N value – 0.255 – calculated from (Equation 47) and was therefore used for the RRDE analysis.

2.4. HO_2^- decomposition study

During the ORR electrocatalysis on oxides, eventual HO_2^- intermediates might decompose. Therefore this decomposition reaction was investigated using a volumetric technique to determine its kinetics.

2.4.1. Titration of H_2O_2

As H_2O_2 might already decompose into O_2 and H_2O during its storage, it should be titrated before being used for HO_2^- decomposition and HO_2^- reduction/oxidation experiments.

2.4.1.1. Preparation of $KMnO_4$ solution

Solutions of approximately 0.02 M $KMnO_4$ were prepared by dissolving 1.6 g of potassium permanganate ($KMnO_4$, Prolabo) into an Erlenmeyer containing 500 mL of ultrapure water under magnetic mixing at 95°C during 2 hours. The Erlenmeyer was then protected from light with aluminum foil and cooled at ambient temperature during the night. Then, the solution was filtered with a Buchner funnel containing a filter paper (Verlabo) to remove undissolved species. The filtered solutions were finally kept in opaque bottles to protect them from light.
The day before each standardization, the $KMnO_4$ solutions were heated at 95°C during 2 hours again, cooled at ambient temperature during one night and filtered.

2.4.1.2. Standardization of $KMnO_4$ solution

The prepared $KMnO_4$ solution was standardized with sodium oxalate in the presence of an excess of sulfuric acid to ensure a stoichiometric reaction. Thus a 250 mL-solution containing 1M H_2SO_4 and 0.006 M $Na_2C_2O_4$ was prepared with 14 mL of H_2SO_4 (H_2SO_4, 95-98%, Sigma-Aldrich), 30 mL of $Na_2C_2O_4$ ($Na_2C_2O_4$, 0.05M, Fluka) and ultrapure water in order to

have a equivalence volume of around 30 mL, and placed in an Erlenmeyer with a magnetic stirrer. The prepared $KMnO_4$ solution was then placed in a burette, and the titration was performed at around 80°C under magnetic mixing.

The reaction which occurs during this titration is (Equation 52)

$$2\,MnO_4^- + 5\,H_2C_2O_4 + 6\,H^+ = 2\,Mn_2^+ + 10\,CO_2 + 8\,H_2O \quad \text{(Equation 52)}$$

Therefore, the exact concentration in MnO_4^- of the $KMnO_4$ solution C_{MnO4-}° can be determined thanks to V_{MnO4-}^{eq}, the volume of $KMnO_4$ added at the equivalence point (Equation 53):

$$C_{MnO_4^-}{}^{o} = \frac{\frac{2}{5} n_{H_2C_2O_4}{}^{o}}{V_{MnO_4^-}{}^{eq}} \quad \text{(Equation 53)}$$

with n_{H2C2O4}°, the initial mole quantity of $H_2C_2O_4$ in the Erlenmeyer. This standardization was performed before each H_2O_2 titration.

2.4.1.3. Titration of H_2O_2 with standardized $KMnO_4$ solution

For HO_2^- decomposition and HO_2^- reduction/oxidation experiments, SupraPur H_2O_2 (H_2O_2 30 wt% solution in water, SupraPur, Merck) was used to avoid impurities and stabilizers often found in H_2O_2 solutions of lower purity. This SupraPur solution was titrated with the standardized $KMnO_4$ solution in the presence of an excess of sulfuric acid to ensure stoichiometric reaction. Thus a 250 mL-solution was prepared with 4 mL of H_2SO_4 (H_2SO_4, 95-98%, Sigma-Aldrich), 100 µL of SupraPur H_2O_2 (H_2O_2 30 wt% solution in water, SupraPur, Merck) and ultrapure water in order to have an equivalence volume of around 20mL, and placed in an Erlenmeyer with a magnetic stirrer. The standardized $KMnO_4$ solution was then placed in a burette, and the titration was performed at ambient temperature under magnetic stirring.

The reaction which occurs during this titration is (Equation 54):

$$2\,MnO_4^- + 5\,H_2O_2 + 6\,H^+ = 2\,Mn_2^+ + 5\,O_2 + 8\,H_2O \quad \text{(Equation 54)}$$

Therefore, the exact concentration of H_2O_2 solution C_{H2O2}° can be determined thanks to V_{MnO4-}^{eq}, the volume of $KMnO_4$ added at the equivalence point (Equation 55):

$$C_{H_2O_2}{}^{o} = \frac{\frac{5}{2} V_{MnO_4^-}{}^{eq}\, C_{MnO_4^-}{}^{o}}{V_{H_2O_2}{}^{o}} \quad \text{(Equation 55)}$$

with $C_{MnO4-}°$, the concentration of the standardized $KMnO_4$ solution and $V_{H2O2}°$, the initial volume of H_2O_2 added in the Erlenmeyer (100µL).
This titration was performed each week and shows that H_2O_2 concentration is indeed quite stable - around 10 M - with time in the bottle.

2.4.2. Volumetric follow-up of the O_2 formation

In this section, the study of HO_2^- decomposition reaction is described.

2.4.2.1. Theory and approximations

The reaction studied in this section is the HO_2^- decomposition into OH^- and O_2 (Equation 56):

$$HO_2^- = OH^- + \frac{1}{2}O_2 \quad \text{(Equation 56)}$$

Therefore, the number of O_2 moles, n_{O2}, is (Equation 57):

$$n_{O_2} = \frac{\left(n_{HO_2^-}{}^{o}\right) - \left(n_{HO_2^-}\right)}{2} \text{ (Equation 57)}$$

with n_{HO2-}, the number of HO_2^- moles at a given time and $n_{HO2-}°$, the initial number of HO_2^- moles. It is possible to estimate the volume of O_2, V_{O2}, thanks to the perfect gas approximation (Equation 58):

$$PV_{O_2} = n_{O_2}RT \text{ (Equation 58)}$$

with P, the atmospheric pressure, 1.013 x 10^5 Pa, R, the gas constant, 8.314 $J.K^{-1}.mol^{-1}$, and T, the temperature in Kelvin which was taken as equal to 289K – 25°C, the temperature of the cell – even though the temperature of the gas was not controlled. Thus, the volume of O_2 produced during the reaction is (Equation 59):

$$V_{O_2} = \frac{\left[\left(C_{HO_2^-}{}^{o}\right) - \left(C_{HO_2^-}\right)\right]V_{solution}RT}{2P} \text{ (Equation 59)}$$

with C_{HO2-}, the HO_2^- concentration at a given time, $C_{HO2-}°$, the initial HO_2^- concentration (which is equal to the initial H_2O_2 concentration), and $V_{solution}$, the volume of the solution. In

particular, the maximum volume of O_2 - V_{O2}^{max} - formed when all HO_2^- is consumed is (Equation 60):

$$V_{O_2}^{max} = \frac{C_{HO_2^-}{}^{o} V_{solution} RT}{2P} \text{ (Equation 60)}$$

In conclusion, one can follow the HO_2^- concentration evolution by measuring the O_2 volume at various states of advancement (Equation 61):

$$C_{HO_2^-} = C_{HO_2^-}{}^{o} \left(1 - \frac{V_{O_2}}{V_{O_2}^{max}}\right) \text{ (Equation 61)}$$

Several works showed that HO_2^- decomposition is a first order reaction on perovskite oxides [121-127] and it was confirmed in this work (see section 5.4.2). Therefore, the reaction rate can be expressed as (Equation 62):

$$-\frac{dC_{HO_2^-}}{dt} = kC_{HO_2^-} \text{ (Equation 62)}$$

with k, the first-order constant in s^{-1}. This expression can be integrated as (Equation 63) since $C_{HO2-} = C_{HO2-}{}^{\circ}$ at t = 0:

$$\ln \frac{C_{HO_2^-}}{C_{HO_2^-}{}^{o}} = -kt \text{ (Equation 63)}$$

which finally gives (Equation 64):

$$\ln \left(1 - \frac{V_{O_2}}{V_{O_2 max}}\right) = -kt \text{ (Equation 64)}$$

By plotting $\ln(1-V_{O2}/V_{O2}^{max})$ versus the time, one can determine the first order constant k from the slope of the straight line. The heterogeneous rate constant k_{het}, expressed in $cm.s^{-1}$, can be calculated thanks to (Equation 65):

$$k_{het} = \frac{k\, Vsolution}{m\, S_{BET}} \text{ (Equation 65)}$$

with m, the mass of catalyst utilized for the study, and S_{BET}, the BET surface of the catalyst. Then, the catalytic activity per unit surface area of different catalysts can be compared.

2.4.2.2. Setup used for the study of HO_2^- decomposition

As suggested by the previous equations, the kinetic rate of the catalytic HO_2^- decomposition can be determined by the follow-up of O_2 formation. Therefore, a setup was built to measure the volume of O_2 during the decomposition of HO_2^- on perovskite oxides. A photograph of the

setup can be found in Figure 14. It was inspired by setups described by Deren et al. [165] and Minami et al. [166]. As O_2 was evolved during the decomposition reaction, O_2 formation was visualized in the manometer. Water was then run down from the burette to measure the O_2 volume.

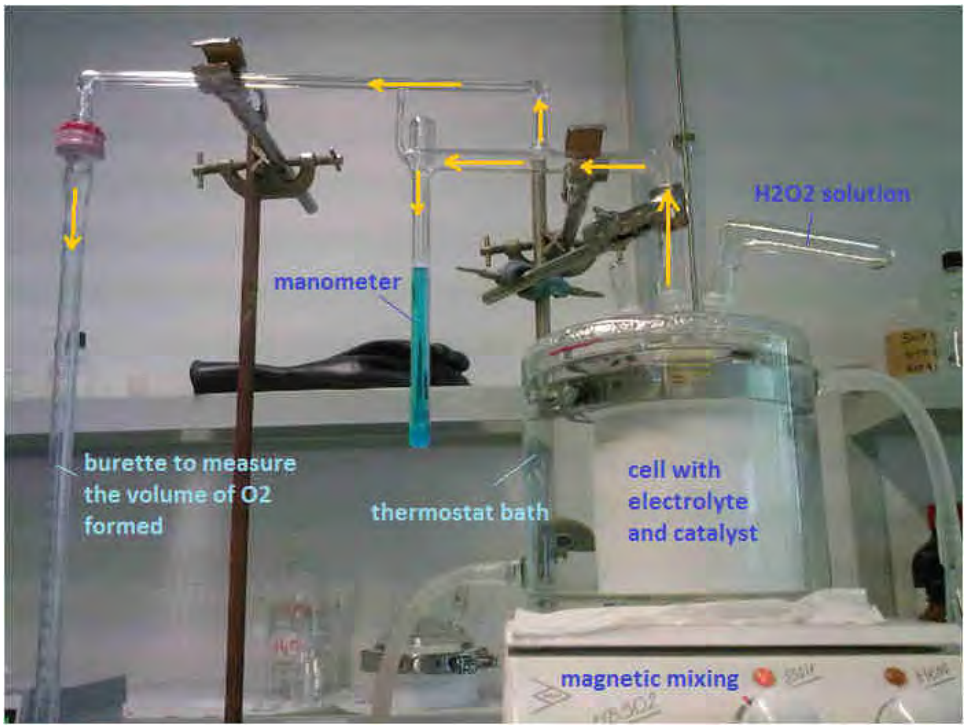

Figure 14 : *Setup of volumetric follow-up of O_2 formation, inspired from [165,166]*

As glass is attacked by NaOH to form sodium silicates, the reaction cell was made of Teflon. This cell was built with a round-shape bottom to avoid that catalyst particles stick to the edges and an oval magnetic stirrer was placed in the bottom of this cell to avoid mass transport limitations. The cell was immersed into a thermostat bath at 25°C. The control of the solution temperature is essential since the kinetic constant is dependent on the temperature T according to Arrhenius law (Equation 66):

$$k = A \exp\left(-\frac{E_a}{RT}\right) \text{ (Equation 66)}$$

with R, the gas constant, A, the pre-exponential factor and E_a, the activation energy.

In a typical experiment, the desired amount of a milled catalyst was placed into the cell through a funnel and the electrolyte was added through the same funnel to avoid loss of the catalyst. A 10 mL-solution containing a certain amount of H_2O_2 was prepared, placed in the V-shaped tube and protected from light with an aluminium foil. The electrolyte was then saturated with O_2 during at least 1h. Thanks to this O_2 saturation, all O_2 formed during the HO_2^- decomposition will be transferred from an electrolyte to the gas phase and can be

measured by the volumetric method. When the electrolyte was saturated, the cell was closed with caps and the gas-tight behavior was ensured with the presence of grease and paraffin film around the caps. The level in the U-manometer is initialized by removing water from the burette – initially full of water - until the levels in the two tubes are identical, and the corresponding volume in the burette is marked as the initial volume. Then, the V-shaped tube is turned around to discharge the H_2O_2-containing solution in the electrolyte and the chronometer is started. Finally, the O_2 volume formed during the HO_2^- decomposition was measured regularly by running down water from the burette.

It should be noted that, with this setup, the temperature of the gas was unfortunatelly not controlled, therefore the gas volume might be slightly different from theory. Moreover, some gas diffusion through the liquid filling the manometer – colored water – could not be excluded.

2.4.2.3. Electrolyte and H_2O_2-containing solution

The electrolyte used in this work was 1 M NaOH prepared from extra pure NaOH solution (50 wt. % solution in water, Acros Organics) and ultrapure water in polypropylene volumetric flasks. The volume initially placed in the reaction cell was 100 mL.

The V-tube was containing a 10 mL-solution prepared with ultrapure water and the H_2O_2 volume V_{H2O2} of (Equation 67):

$$V_{H_2O_2} = \frac{{C_{H_2O_2}}^{\text{reaction}} {V_{H_2O_2}}^{\text{reaction}}}{{C_{H_2O_2}}^{\text{titration}}} \quad \text{(Equation 67)}$$

with ${C_{H2O2}}^{\text{reaction}}$, the desired concentration in the reaction cell, ${V_{H2O2}}^{\text{reaction}}$, the final volume of electrolyte in the reaction cell which is 110 mL (100 mL + 10 mL), and ${C_{H2O2}}^{\text{titration}}$, the concentration of the source H_2O_2 solution, which was obtained by titration. This solution was prepared in an opaque bottle to protect it from light.

According to (Equation 60), the maximum volume of O_2 which can be formed during HO_2^- decomposition can be estimated. Most of experiements were therefore performed with a 0.03 M H_2O_2 concentration since it corresponds to a maximum volume of ca. 40 mL. Higher concentrations would have led to higher O_2 volumes and thus, no plateau could be reached in the 50 mL burette used in the setup. Lower concentrations could be used but the small volume changes with time would have caused imprecise volume determination.

2.4.2.4. Determination of the kinetic constant

Various experiments were performed to thorouhgly study the HO_2^- decomposition reaction. First of all, the non catalytic HO_2^- decomposition was studied by adding an H_2O_2-containing solution in a cell without catalyst. Various H_2O_2 concentrations were tested in order to determine the rate order of this reaction. These experiments were also used as a background to correct the experiments performed in the presence of a catalyst since non catalytic reaction can also occur during these experiments. Secondly, the reaction order of the catalytic decomposition reaction was investigated on $LaMnO_3$ and extrapolated to other perovskites. For that, various catalyst masses and H_2O_2 concentrations were studied. By varying the catalyst mass, one can verify if the reaction is indeed limited by the kinetics. Thanks to the various H_2O_2 concentrations, the reaction order of the catalytic reaction could be determined and the accuracy of the perfect gas law could be verified by comparing the experimental maximal O_2 volume with the theoretical one. Finally, the catalytic activity of various perovskite oxides, simple oxides, Pt/C and carbon were measured in presence of 0.03M H_2O_2 and the heterogeneous constants were compared.

2.5. Perovskite stability study

Various stability tests were performed on perovskite catalyst to validate their possible fuel cell application.

2.5.1. Thermal treatment of perovskites

Perovskite powders were stored in air for several months after the synthesis, and thus formation of the carbonates on perovskite surface can occur. To remove eventual carbonates, a thermal treatment was applied. This thermal treatment was similar to the annealing step of the synthesis. Indeed, the powder placed in a crucible was heated in air from room temperature to 650°C at 5°C.min^{-1} and annealed at 650°C for 1h. An annealing temperature of 700°C was also tested. After cooling, the treated powders were analyzed by XPS to determine the surface composition, and their electrochemical properties were investigated by CV and RDE techniques.

2.5.2. Chemical stability of perovskite suspensions

The stability of aqueous suspensions of oxides was also studied. XPS characterization was performed for four different suspensions of 2g.L^{-1} of $LaCoO_3$. The first one – suspension A - was made from unground $LaCoO_3$ powder, whereas the three others – suspensions B, C and D - were prepared with ground powder as usually. This was done to detect eventual influence of the grinding - obtaining of fresh surface - on the stability of the perovskite surface in water. Suspensions A, B and C were placed in ultrasonic bath for 30 minutes, while suspension D received a 2 h-ultrasonic bath treatment in order to identify the impact of this violent treatment on the perovskite state. Suspensions A, B and D were analyzed immediately after preparation and suspension C after one week to determine the effect of the storage time. Table 2 summarizes the studied suspensions. It should be noted that suspension B represents the usual way to prepare the catalyst suspension.

For XPS analysis, a 100 µL drop of a desired suspension was directly deposited on the carbon scotch placed on a XPS sample holder.

Table 2 : *Aqueous suspensions of $LaCoO_3$ tested by XPS*

Suspension	Grinding in a mortar	Duration of ultrasonic treatment (min)	Storage time
Suspension A	No	30	(no storage)
Suspension B	Yes	30	(no storage)
Suspension C	Yes	30	7 days
Suspension D	Yes	120	(no storage)

2.5.3. Chemical stability of perovskite in alkaline media

The chemical stability of the perovskite oxides was tested by immersing 100 mg of a perovskite powder in 50 mL of 1M NaOH in a Nalgene bottle. The bottles were closed, shaken by hand to obtain a homogeneous suspension, and placed on a roller-mixer with a rotation speed of 60 rpm. These experiments were performed at room temperature. After the desired duration, the samples were shaken by hand and filtered through a filter paper placed in a plastic funnel. The filter paper was then dried in air during one night. The filtered solution was analyzed by ICP-MS to detect eventual dissolved species, whereas the perovskite powder recovered on the dried filter paper was scrubbed to be detached and characterized by XPS and XRD as soon as possible. The immersion durations were 2 days, 7 days, 18 days and 1 month. One can expect sodium hydroxide precipitation or sodium carbonates formation on perovskite surface during the filtration step. Thus, the effect of rinsing was investigated by rinsing the powders with various amounts of ultrapure water and analyzing them by XPS. However, the results were irreproducible due to possible surface modification by the rinsing. It was therefore chosen not to rinse the samples for further experiments. Results shown in section 6 correspond to samples without rinsing before the characterization.

2.5.4. Electrochemical stability of perovskite/carbon composites

2.5.4.1. Electrode preparation for stability tests

As RDE and RRDE display too small geometric surface area to perform material characterization after electrocatalysis, another working electrode type was used for stability experiments.

2.5.4.1.1. Carbon paper choice

The Toray carbon paper TGP-H-60 (Alfa Aesar) usually used as a gas-diffusion layer (GDL) in fuel cells was chosen as support. The carbon paper used in this work does not contain any PTFE, and thus can display hydrophilic properties after an appropriate treatment. It is supplied in a foil form, from which any size of electrode can be cut, depending on the application. In order to have sufficient surface area to perform material characterization, electrodes of 1 cm x 1 cm were cut with a scalpel. The thickness of 0.19 mm of the carbon paper is small enough to have negligible impact on the material characterization such as XRD.

2.5.4.1.2. Hydrophilic treatment on the carbon paper

Electrodes of 1 cm^2 were attached to a gold wire through a hole made in the carbon paper and immersed in ca. 50 mL of 1M NaOH - prepared from extra pure NaOH solution (50 wt. % solution in water, Acros Organics) and ultrapure water - at ambient temperature during one night in order to make carbon paper hydrophilic. The rigidity of the gold wire allows the carbon paper to stay immersed in the alkaline solution despite its initial hydrophobic properties. Then, electrodes were rinsed by immersing them several times in fresh ultrapure water. It was observed than carbon paper electrodes can be more easily immersed in water after this treatment.

2.5.4.1.3. Catalyst thin layer

The treated carbon paper was placed on a support with contact only on the edges to allow gas circulation through the electrode. 9 aliquots of 20 µL of a suspension of 0.33 $g.L^{-1}$ of perovskite and 0.14 $g.L^{-1}$ of Sibunit carbon were taken under sonication of the suspension and drop casted on the dried carbon paper, each drop deposited in a different area to completely cover the carbon paper. The electrode was then dried under N_2. This last operation – deposition of 9 drops and drying - was repeated three times in order to get a homogeneous coverage of the electrode and to improve the reproducibility. Finally, the total amount of suspension deposited was 540 µL (3 x 9 x 20 µL), which gives a loading of 180 $\mu g.cm^{-2}$ perovskite and 74 $\mu g.cm^{-2}$ Sibunit carbon on the 1 cm^2 electrode. This loading was low enough to avoid loss of particles from the porous and rough carbon paper without addition of an ionomer. Moreover, this low loading allowed a lower ohmic resistance and a more uniform electrical contact between carbon paper, oxide particles and Sibunit carbon than for thicker catalyst layers.

2.5.4.1.4. Material characterization

These electrodes were prepared to allow material characterization after chemical and electrochemical treatments. This characterization was performed using XRD and XPS techniques to check stabilities of the bulk and surface composition, respectively. Each stability test was therefore performed on two identical samples in order to carry out both analyses simultaneously. In parallel, the stability was performed on carbon paper without thin layer deposition to get the support signal. All analyses were made the same day as the treatment to avoid modification of the catalyst with atmosphere. As XRD is a non-destructive method, the samples could be recovered when required for successive SEM characterization to detect eventual modification of morphologies and agglomeration. Unfortunately ICP technique could not be used to detect eventual dissolved species since the catalyst quantities were small.

2.5.4.2. Stability after polarization and electrocatalysis

Electrochemical stability of oxides was investigated after polarization in inert atmosphere, after ORR and after HO_2^- reduction/oxidation since all these processes were utilized for ORR studies. For all experiments, the carbon paper sample with perovskite/carbon thin layers was attached to a gold wire soldered in by Pyrex to avoid gas leakage and immersed in 1M NaOH electrolyte at 25°C. Then the solution was purged with N_2 gas during at least 1h to remove oxygen traces from electrolyte and from carbon paper and 10 CV cycles were performed at 10 $mV.s^{-1}$ between +0.43 V and +1.23 V vs. RHE using Autolab potentiostat. No agitation was performed in the cell during CV measurements to avoid loss of electrical contact between the carbon paper and the gold wire.

For the polarization stability study, additional 20 CV cycles were performed in the N_2-purged electrolyte. At 10 $mV.s^{-1}$ in the studied potential window, this corresponds to around 1h of polarization. For the ORR stability study, O_2 gas was bubbled through the electrolyte for at least 2h to get a saturated solution and to allow O_2 molecules to enter the porous structure of the carbon paper. 20 CV cycles were then performed in this media. For HO_2^- reduction/oxidation stability study, an aliquot of titrated SupraPur H_2O_2 (H_2O_2 30 wt% solution in water, SupraPur, Merck) was added in the N_2-purged 1M NaOH to get a 0.84mM H_2O_2-containing electrolyte. The addition of H_2O_2 was made during bubbling of N_2 to achieve convection and thus good mix of solutions. 20 CV cycles were then performed in this media.

For all experiments, the samples were removed from solution after CV measurements, placed on a tissue to remove liquid traces and characterized immediately. No rinsing was applied.

2.5.4.3. Stability in alkaline media

To be used as a background and to separate perovskite modifications due to chemical instabilities from modifications due to electrochemical instabilities, the chemical stability of the perovskite/carbon composites was investigated in 1M NaOH solution.

For these tests, carbon paper samples with perovskite/carbon thin layers were placed in Nalgene bottles containing around 50 mL of 1M NaOH. The bottles were closed and placed on a roller-mixer with a rotation speed of 60 rpm at room temperature. After 3h – corresponding to the duration of an electrochemical experiment - the samples were removed

from the alkaline solution, placed on a tissue to remove liquid traces and characterized immediately. No rinsing was applied.

2.5.5. Stability of the ORR activity studied by chronoamperometry

2.5.5.1. Principle of the test

Chronoamperometry was used to check the stability of the activity, i.e. the current, with time at a given potential. This was performed with RDE GC-supported thin layer electrodes. Three different potentials were tested. The first one corresponded to the kinetic region – ORR current of ca. 0.01 mA - the second one, to the halfwave potential and thus to the mixed kinetic-diffusion region, and the last one was taken at the lower potential limit - +0.43V vs. RHE – to correspond to the diffusion region. The potential values were determined from the RDE curves of the studied sample. These tests were performed in O_2- and H_2O_2-containing media to determine the stability of the ORR activity and of activity for the HO_2^- reduction, respectively, and in N_2-purged electrolyte to study the effect of polarisation. Before and after each chronoamperometry measurement, CV in inert atmosphere was recorded to follow eventual modification of interfacial properties of perovskite, and RDE voltammogram at 2500 rpm in the studied media – O_2 or H_2O_2-containing – was carried out to have an overview of the electrocatalytic stability. The experiments were performed with a rotation rate of the electrode of 2500 rpm to avoid mass transport limitation, except for chronoamperometry measurements in N_2-purged electrolyte which was performed without rotation to minimize the influence of eventual O_2 traces.

2.5.5.2. Typical chronoamperometry experiment

The 1M NaOH electrolyte was first purged with N_2 gas during at least 1h to remove oxygen traces and the temperature was controlled at 25°C. Afterwards the working electrode was immersed in the N_2-purged electrolyte and CV measurements were performed at 10 $mV.s^{-1}$ in the potential window of +0.43 V / +1.23 V vs. RHE with the Autolab potentiostat. Then, the electrolyte was prepared for the reaction study. For the ORR stability study, O_2 gas was

bubbled through the electrolyte for at least 45 minutes to get a saturated solution, and for HO_2^- reduction stability study, an aliquot of titrated SupraPur H_2O_2 (H_2O_2 30 wt% solution in water, SupraPur, Merck) was added in the N_2-purged 1M NaOH to get a 0.84mM H_2O_2-containing electrolyte. RDE voltammograms were then recorded at 2500 rpm before applying the desired potential and performing the chronoamperometry at 2500 rpm during 10,000 seconds with interval time of 1s. Immediately after the chronoamperometry measurement, RDE voltammograms at 2500 rpm were recorded again. Finally, CV measurements were perfomed in N_2 atmosphere. In the case of the ORR studies, the same electrolyte was purged with N_2 for 1h to remove O_2. In case of the HO_2^- reduction studies, the working electrode with the used catalyst was removed from the first cell and immersed in the second cell containing N_2-purged 1M NaOH.

In order to study the effect of polarisation during these stability experiments, chronoamperometry in N_2-purged electrolyte was performed at the desired potential without rotation immediately after the CV measurement. No RDE voltammogram was recorded in this case.

Chapter 3 :
Properties of perovskite catalysts

3.1. Introduction

Before being used as ORR catalysts, the perovskite oxides should be characterized to check if they display the expected structure and to learn about their surface composition. This was investigated by XRD and XPS techniques, respectively. Moreover, it is necessary to know the available surface area of a catalyst to normalize its electrocatalytic activity. SEM analysis of the oxide morphology, with the help of BET measurements, gave an estimation of the accessible surface. In order to learn about the distribution of particles in the perovskite/carbon composite electrodes, SEM was associated to EDX. Finally, the interfacial properties of the oxides were studied by CV. This technique permits to identify the potential window of the perovskite stability, essential for further electrochemical measurements, but also to investigate the redox transitions occurring in the studied oxides.

All these characterizations will help to understand the catalytic behavior of the perovskite oxides.

3.2. Physical and chemical properties

3.2.1. Structure of the bulk

3.2.1.1. Identification of the cristalline phases

XRD characterization for each of the samples was performed twice. Firslty, XRD patterns (not shown) were taken by our project partner F. Napolskiy at the Moscow State University [142] right after the synthesis in order to confirm the formation of the expected perovskite structure and check the possible presence of impurity phases. The structure symmetry as well as the unit cell parameters were determined using the Rietvield refinement [144,145] and can be found in Table 3 for the studied oxides.

Secondly, the XRD characterization was repeated in Strasbourg after a few months storage of the samples under ambient conditions and shortly before performing electrochemical measurements in order to check possible perovskite modification during storage (Figure 15). For this second set of measurements, the Rietvield refinement was not applied and the unit cell parameters were estimated by comparing the peak positions and peak intensity ratio with the ICDD reference cards. The ICDD reference cards which fitted the most closely to the experimental patterns are indicated on Figure 15 and reported in Table 3.

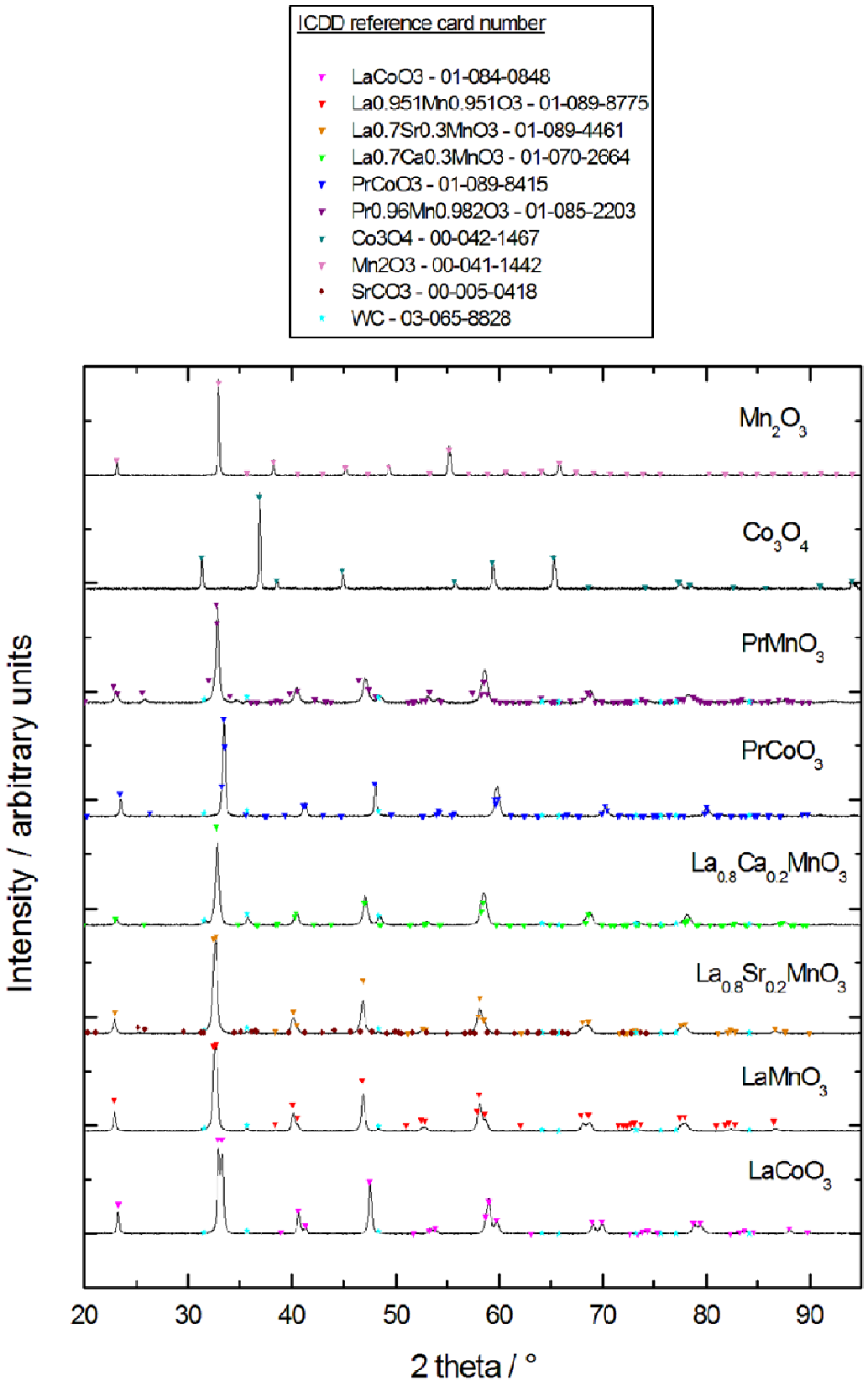

Figure 15 : *X-Ray powder diffraction pattern (step size = 0.0223°, step time = 1s) of perovskite and simple oxide powders after storage under ambient conditions, and the corresponding ICDD reference cards. The diffraction patterns were corrected from the background signal.*

Table 3 : *Structure and unit cell parameters of oxide powders determined Rietveld refinement right after synthesis and from comparison with ICDD reference cards after atmospheric storage*

Compounds	Structure determined by Rietveld refinement right after synthesis [142]	Structure reported in ICDD reference cards fitting with XRD patterns after atmospheric storage (Figure 15)
$LaCoO_3$	$LaCoO_3$, rhombohedral R-3c, a = 5.385 Å, α = 60.68°	$LaCoO_3$ (01-084-0848), rhombohedral R-3c, a = 5.378 Å, α = 60.80° WC traces (03-065-8828)
$LaMnO_3$	$LaMnO_3$, rhombohedral R-3c, a = 5.465 Å, α = 60.52° WC traces	$La_{0.951}Mn_{0.951}O_3$ (01-089-8775), rhombohedral R-3c, a = b = 5.515 Å, c = 13.34 Å, α = β = 90°, γ = 120° WC traces (03-065-8828)
$La_{0.8}Sr_{0.2}MnO_3$	$La_{0.8}Sr_{0.2}MnO_3$, rhombohedral R-3c, a = 5.473 Å, α = 60.42° WC 2%	$La_{0.7}Sr_{0.3}MnO_3$ (01-089-4461), rhombohedral R-3c, a = b = 5.502 Å, c = 13.35 Å, α = β = 90°, γ = 120° WC traces (03-065-8828) $SrCO_3$ traces (00-005-0418)
$La_{0.8}Ca_{0.2}MnO_3$	$La_{0.8}Ca_{0.2}MnO_3$, orthorhombic Pnma, a=5.459, b=7.724, c=5.498	$La_{0.7}Ca_{0.3}MnO_3$ (01-070-2664), orthorhombic Pmna, a = 5.462 Å, b = 7.719 Å, c = 5.483 Å WC traces (03-065-8828)
$PrCoO_3$	$PrCoO_3$, orthorhombic Pbnm, a = 5.378 Å, b = 5.343 Å, c = 7.580 Å WC <1%	$PrCoO_3$ (01-089-8415), orthorhombic Pmna, a = 5.340 Å, b = 7.574 Å, c = 5.375 Å WC traces (03-065-8828)
$PrMnO_3$	$PrMnO_3$, orthorhombic Pbnm, a = 5.461 Å, b = 5.496 Å, c = 7.713 Å WC 3%	$Pr_{0.96}Mn_{0.982}O_3$ (01-085-2203), orthorhombic Pbnm, a = 5.456 Å, b = 5.594 Å, c = 7.663 Å WC traces (03-065-8828)

Co_3O_4	Co_3O_4, cubic Fd-3m, a = 8.083 Å	Co_3O_4 (00-042-1467), cubic Fd-3m, a = 8.084 Å
Mn_2O_3	Mn_2O_3, cubic Ia-3, a = 9.412 Å	Mn_2O_3 (00-041-1442), cubic Ia-3, a = 9.409 Å

First of all, it was observed right after synthesis that all the synthesized perovskites present perovskite characteristic crystalline peaks, as expected, and no precursors traces were remaining. Therefore, the soft chemistry synthesis using polyacrylamide gel is appropriate to obtain perovskite compounds. After storage, no perovskite phase decomposition could be observed showing the stability of the perovskite structure under ambient conditions. As rhombohedral structure is characterized by a doublet peak around 33°, while orthorhombic structure presents a simple peak at this angle, one can see from XRD patterns and corresponding ICDD reference cards that the crystal symmetry is function of the nature of the A cation of the perovskite. Indeed, non-doped and Sr-doped La-based perovskites show rhombohedral structure, in agreement with the literature for $LaCoO_3$ [47,55,59,60,88,97,167-171] and for $La_{1-x}Sr_xMnO_3$ [45,58,83,167-169,171,172] whereas $La_{0.8}Ca_{0.2}MnO_3$ and Pr-based perovskites present orthorhombic structure, as found in reference [65] for $PrMnO_3$. This can be explained from the Goldschmidt tolerance factor (Equation 10) (see section 1.3). The ionic radii of A cation are in the order $Pr^{3+} < Ca^{2+} < La^{3+} < Sr^{2+}$. Therefore, since the ionic radii of Pr^{3+} and Ca^{2+} are smaller than the ionic radii of La^{3+} and Sr^{2+}, the tolerance factors of Pr-based oxides and $La_{0.8}Ca_{0.2}MnO_3$ are smaller than those of $LaCoO_3$, $LaMnO_3$ and $La_{0.8}Sr_{0.2}MnO_3$. In other words, the former present lower symmetry (orthorhombic structure) than the latter (rhombohedral structure).

As shown in Table 3, some differences in the perovskite structure are observed between the results obtained right after the synthesis and those obtained after a few months storage. This is partially due to the less precise method using the ICDD reference cards. Indeed, for a given compound, the theoretical and the experimental diffraction patterns can differ since theoretical diffraction patterns were either calculated or measured for an ideal structure under ideal conditions, contrary to experimental diffraction patterns. Thus, the experimental diffraction pattern may appear closer to another compound than the one it really belongs and would lead in a wrong interpretation. It might be the case for $La_{1-x}A'_xMnO_3$ (A' = Sr or Ca) perovskites, for which the ICDD reference cards with x = 0.3 are the closest to the experimental patterns, whereas x is expected to be 0.2. Moreover, there is a lack of ICDD reference cards for some compounds, in particular for $PrMnO_3$ perovskites which were rarely

studied. Nevertheless, one can notice in Table 3 that $LaMnO_3$ and $PrMnO_3$ samples are closer to non stoichiometric compounds than to stoichiometric ones after storage. This is in agreement with the literature since Mn-perovkites often present oxygen excess or cation vacancies, especially for synthesis in oxygen containing atmospheres [58,83,88,167-169,171-173]. From this observation, one may infer that Mn probably exists in both Mn^{3+} and Mn^{4+} oxidation states in non-doped Mn perovskites, as for A^{2+}-doped perovskites.

After storage under ambient conditions, the $La_{0.8}Sr_{0.2}MnO_3$ compound shows the presence of $SrCO_3$ traces which were not present in the fresh powder and thus which do not originate from the synthesis precursors but rather from the interaction of the sample with atmospheric CO_2. Such $SrCO_3$ traces were also found by XRD analysis in the literature for $La_{1-x}Sr_xCoO_3$ compounds [43,59,174].

One can notice that WC traces resulting from the ball milling are found in the studied compounds. However, this component is in trace form and is not expected to be active for ORR [175]. This phase was therefore neglected for electrocatalysis studies and the perovskite oxides were considered as single phase compounds.

The simple oxides Co_3O_4 and Mn_2O_3 present different structure from the perovskite oxides. Indeed, these compounds display strong and sharp peaks showing high cristallinity, and their structures are cubic according to both Rietvield refinement and ICDD reference cards.

3.2.1.2. Oxide crystallite size

The crystallite size of the studied oxides was determined from Scherrer equation (Equation 12). The equation was applied to two single peaks at low θ values of the diffraction pattern (Figure 15), and the mean crystallite size is presented in Table 4.

Table 4 : *Crystallite size from experimental diffractograms, particle density from corresponding ICDD reference cards and calculated XRD surface area of perovskite and simple oxide powders*

Compounds	Mean crystallite size determined by Scherrer equation (nm)	Particle density ρ from corresponding ICDD reference cards ($g.cm^{-3}$)	Calculated XRD surface area S_{XRD} ($m^2.g^{-1}$)
$LaCoO_3$	31	7.29 ($LaCoO_3$ 01-084-0848)	27
$LaMnO_3$	27	6.59 ($La_{0.951}Mn_{0.951}O_3$ 01-089-8775)	34
$La_{0.8}Sr_{0.2}MnO_3$	22	6.45 ($La_{0.7}Sr_{0.3}MnO_3$ 01-089-4461)	43
$La_{0.8}Ca_{0.2}MnO_3$	15	6.10 ($La_{0.7}Ca_{0.3}MnO_3$ 01-070-2664)	66
$PrCoO_3$	26	7.57 ($PrCoO_3$ 01-089-8415)	32
$PrMnO_3$	16	6.74 ($Pr_{0.96}Mn_{0.982}O_3$ 01-085-2203)	57
Co_3O_4	49	6.06 (Co_3O_4 00-042-1467)	20
Mn_2O_3	53	5.04 (Mn_2O_3 00-041-1442)	22

The perovskite crystallite sizes are between ca. 15 and 30 nm according to Scherrer equation. However, from the particle size distribution performed on perovskite with laser diffraction analysis [142], it was observed that most of particle sizes lied between 300 nm and 30 µm (Figure 16 for $La_{0.8}Sr_{0.2}MnO_3$). This showed that the perovskite crystallites are agglomerated. The simple oxides Co_3O_4 and Mn_2O_3 show bigger crystallites than perovskite with a mean crystallite size of ca. 50 nm.

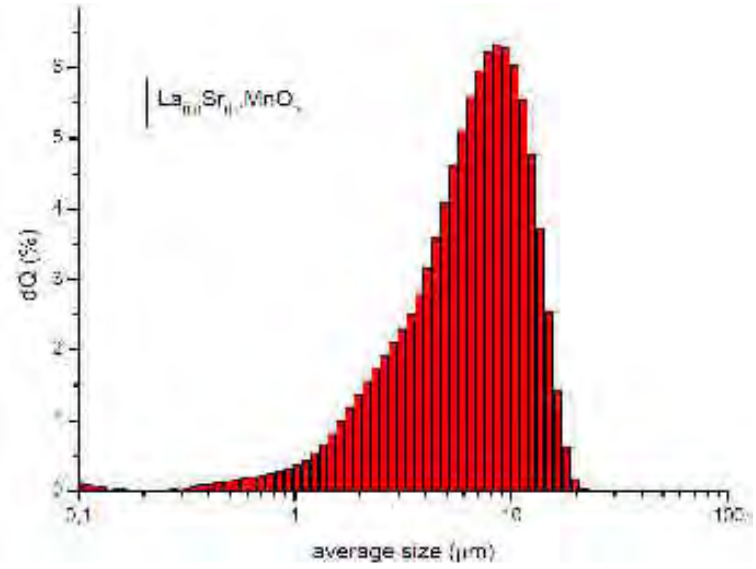

Figure 16 : *Particle size distribution of $La_{0.8}Sr_{0.2}MnO_3$ determined by laser diffraction analysis [142]*

The XRD surface area S_{XRD} of the studied material can be calculated from crystallite size thanks to (Equation 68) if particles are considered as spherical and if the grain size diameter is supposed to be equal to the crystallite size. Thus, S_{XRD} represents the maximal possible surface area of the oxide which would have been observed if crystallites were not agglomerated.

$$S_{XRD} = \frac{3}{r\rho} \quad \text{(Equation 68)}$$

with r: the radius of the spherical particle which is equal to the half of the crystallite size, and ρ, the particle bulk density, estimated from corresponding ICDD reference cards. Table 4 shows that the XRD surface area of perovskite oxides is between 30 and 70 $m^2.g^{-1}$. In order to estimate the extent of crystallite agglomeration, these surface areas will be compared to BET values in section 3.2.3. Due to their smaller crystallite size, simple oxides have XRD surface area of only ca. 20 $m^2.g^{-1}$.

3.2.2. Morphology and dispersion of particles

3.2.2.1. Oxide powder

In order to validate the particle size estimated from XRD and to learn about morphological aspects, perovskite powders were examined by SEM technique. Typical SEM images are

presented in Figure 17 and in Figure 18 in larger resolution for some ground La-based perovskites, and in Figure 19 for simple oxides.

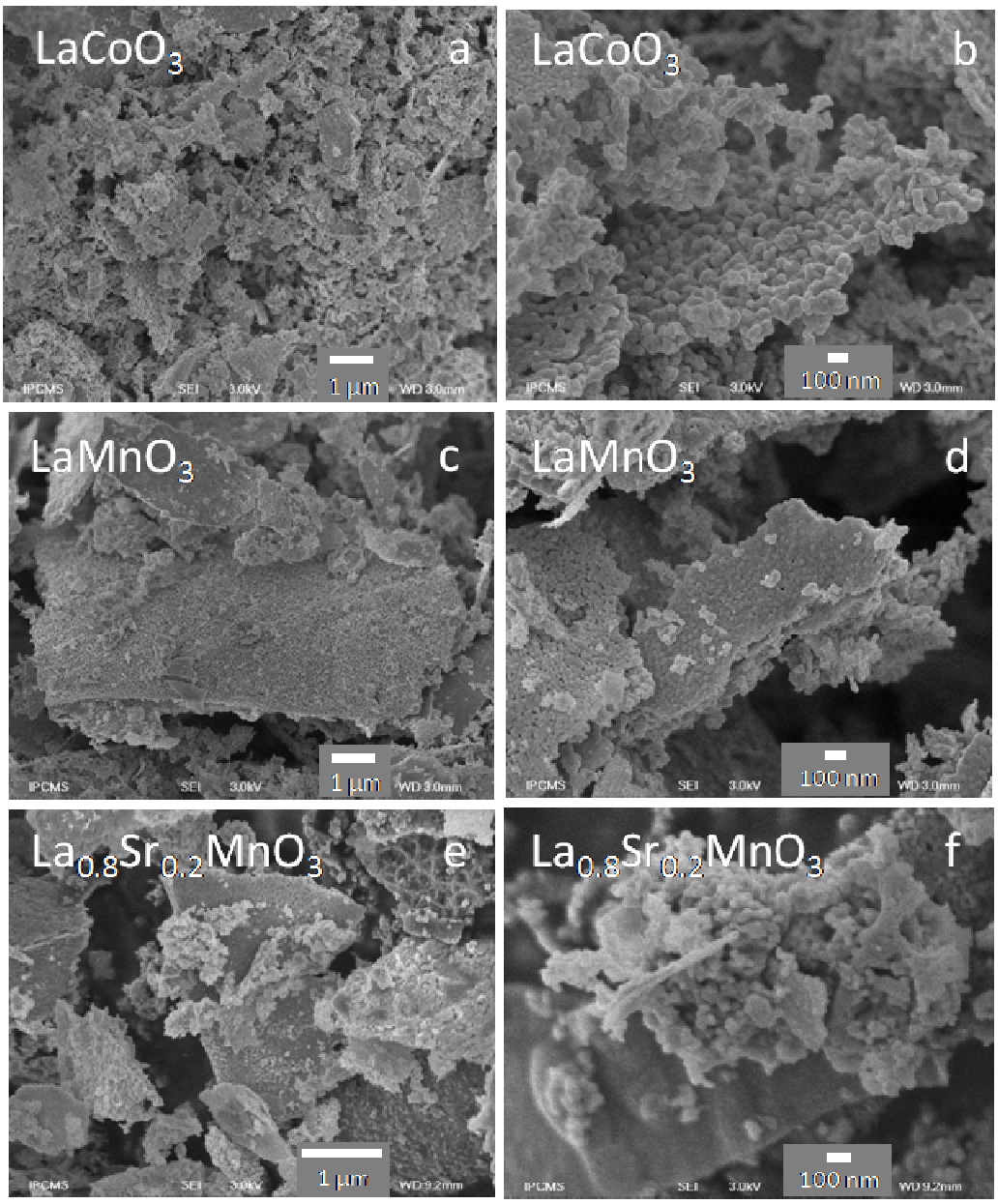

Figure 17 : *SEM images (SEI) of (a),(b) $LaCoO_3$, (c),(d) $LaMnO_3$ and (e),(f) $La_{0.8}Sr_{0.2}MnO_3$ perovskite powders*

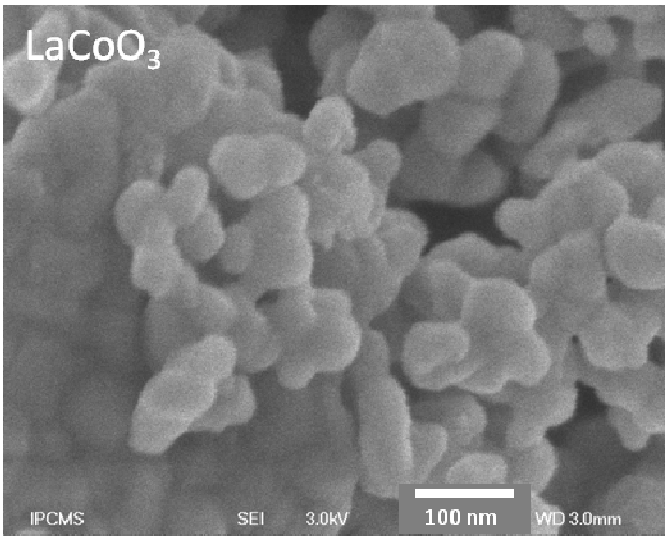

Figure 18 : *SEM image (SEI) of $LaCoO_3$ perovskite powder in higher resolution*

SEM analysis (Figure 17) revealed that perovskite oxides have a porous morphology composed of agglomerates, in agreement with the particle size distribution. These agglomerates are not uniform in size and shape. Indeed, some platelet agglomerates can be observed as well as more complex structures, and agglomerate size ranges from several hundred nanometers to a few micrometers. They consist of spherical nanoparticles of 50-100 nm size (Figure 18), which is larger than the particle size estimated from XRD. This can be explained by the fact that one grain can contain several crystallite domains. No significant differences in morphology were noticed between doped and undoped La perovskites.

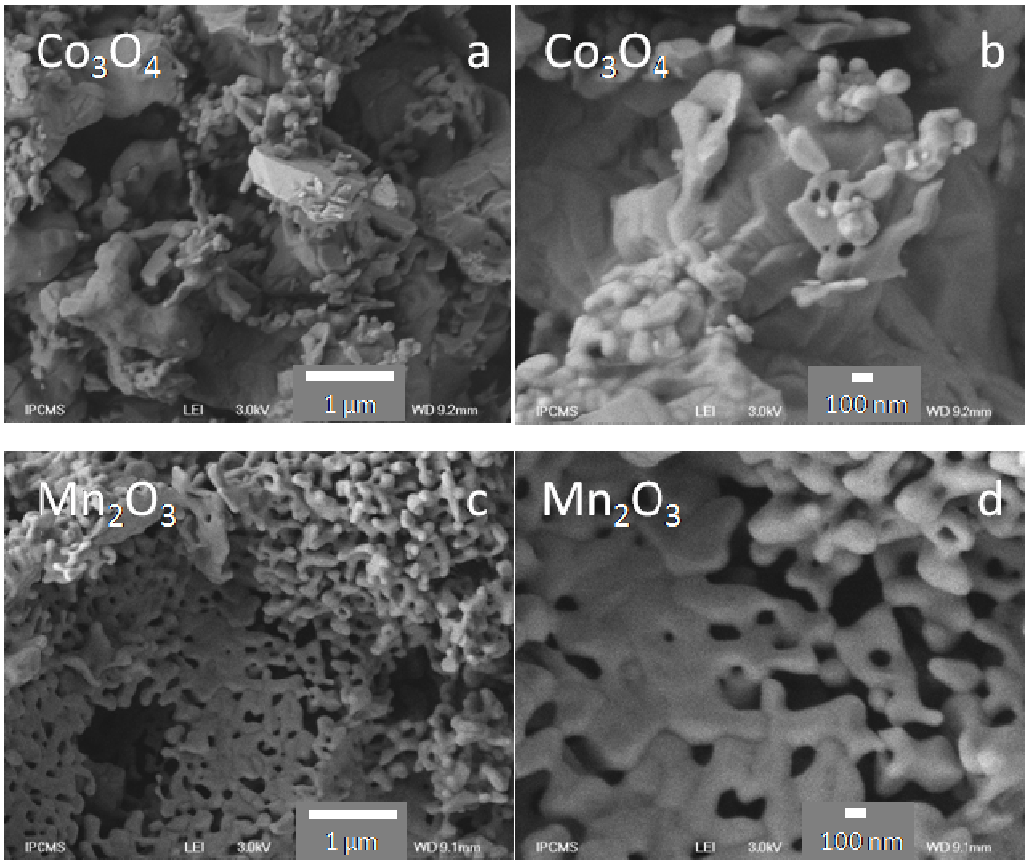

Figure 19 : *SEM images (LEI) of (a),(b) Co_3O_4 and (c),(d) Mn_2O_3 simple oxide powders*

It can be seen from Figure 19 that simple oxides present a very different microstructure from perovskite oxides. Indeed, the particles seem to be bigger, in agreement with XRD results, and strongly agglomerated with not well-defined grain boundaries, i.e. particles are interconnected. Therefore, one can expect that the accessible surface for these simple oxides is very low, and, considering that these oxides have low conductivity, that it would probably lead in high ohmic drop in the catalytic layer.

3.2.2.2. Oxide/carbon composite

In order to explore the homogeneity of the composite oxide/carbon electrodes, a thin layer of $LaCoO_3$/carbon was deposited on a glassy carbon support in the same manner as for electrochemical experiments and studied with SEM/EDX technique. Figure 20 shows a SEM image of this composite electrode, and the EDX spectrum and elemental mapping of various components across this image.

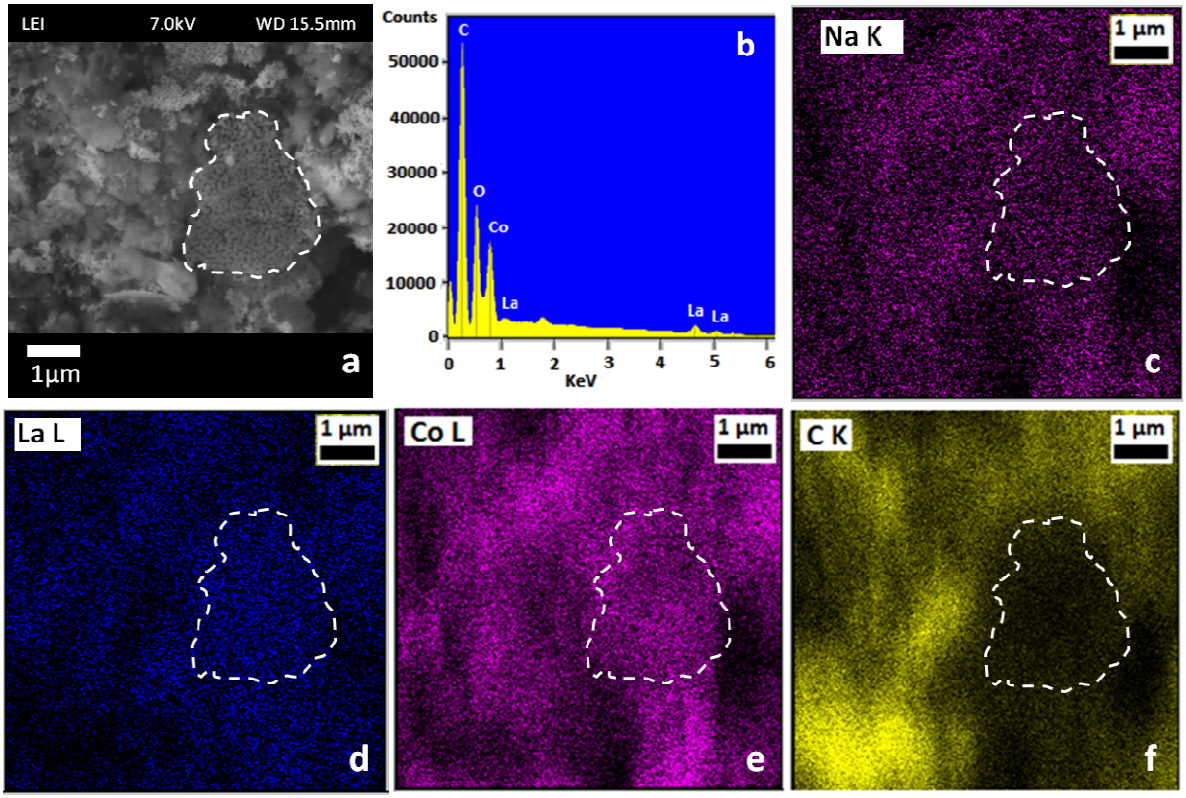

Figure 20 : *(a) SEM image (LEI), (b) EDX spectrum averaged across the frame and elemental mapping of (c) Na, (d) La, (e) Co and (f) C for $LaCoO_3$/Sibunit carbon composite deposited on glassy carbon. The dotted line delimits an aggregate of $LaCoO_3$ particles*

According to the EDX spectrum (Figure 20, b), C, O, Co and La are present in the sample meaning that both Sibunit carbon and perovskite are represented. La and Co (Figure 20, d,e) as well as C (Figure 20, f) elemental mappings were therefore performed across the frame to visualize the distribution of perovskite and Sibunit carbon agglomerates, respectively. A background measurement was performed through the elemental mapping of Na (Figure 20, c). Figure 20 shows that La, Co and C are well dispersed and suggests that the perovskite is well intermixed with carbon in the catalytic layer. Thus, the thin layer preparation method used in this study is valid to get homogeneous (on the micrometer scale) perovskite/carbon composites.

The elemental mapping also allows to distinguish areas enriched either in perovskite or in carbon. For example, one may notice a perovskite agglomerate (Figure 20, dotted line delimited area) featuring high concentration of Co but impoverished in C. Indeed, the micrometer size of this agglomerate makes difficult its mixing with carbon. Although the presence of carbon in the electrode is confirmed by EDX, Sibunit particles could not be clearly visualized and distinguished from the perovskite.

3.2.3. Specific surface area

Further to SEM analysis, a more precise accessible surface determination was required. Thus the specific surface of various compounds was determined using the BET technique. The obtained specific surface areas are listed in Table 5 and compared to XRD specific surface (see section 3.2.1.2).

Table 5 : *Comparison of specific surfaces of perovskite and simple oxide powders measured by BET and calculated from XRD patterns*

Compounds	BET specific surface S_{BET} ($m^2.g^{-1}$)	Calculated XRD surface area S_{XRD} ($m^2.g^{-1}$)
$LaCoO_3$	10	27
$LaMnO_3$	14	34
$La_{0.8}Sr_{0.2}MnO_3$	17	43
$La_{0.8}Ca_{0.2}MnO_3$	20	66
$PrCoO_3$	10	32
$PrMnO_3$	18	57
Co_3O_4	2	20
Mn_2O_3	3	22

First of all, it can be observed that the tendency is the same between the surfaces determined by BET and the one determined by XRD. Indeed, oxides with the lowest XRD specific surface are also those which possess the lowest BET specific surface. The BET surface area of perovskite oxides is between 10 and 20 $m^2.g^{-1}$, close to BET values found for similar perovskite syntheses in the literature [45,59,98,169,172]. There is a factor of ca. 3 between BET and XRD surfaces, showing the extent of crystallite agglomeration, in agreement with SEM and laser scattering analysis. In what follows, BET surface area was used to calculate the specific electrocatalytic activity since it corresponds to the accessible surface area.

Concerning simple oxides, a factor of 10 is found between XRD and BET surfaces, the latter being around 2 $m^2.g^{-1}$. It can be explained on the basis of a SEM observation where it was observed that these oxides present a strong particle agglomeration (see section 3.2.2.1).

3.2.4. Surface composition

The nature of the species on the perovskite surface was first investigated by a XPS scan in a large binding energy window. From this survey spectrum, the presence of A and B cations as well as of O anions on the perovskite surface was confirmed. High resolution spectra of each component were then studied.

3.2.4.1. Presence of A and B cations on the perovskite surface

Figure 21 shows the XPS spectra of various A cations – La3d, Pr3d, Sr3d and Ca2p – potentially present in the studied perovskites. It is clear from these results that these species are indeed present in the corresponding perovskite compounds. The dashed lines indicate the peak positions and the corresponding binding energies are reported in Table 6 for perovskite oxides and in Table 7 for other oxides and carbonates.

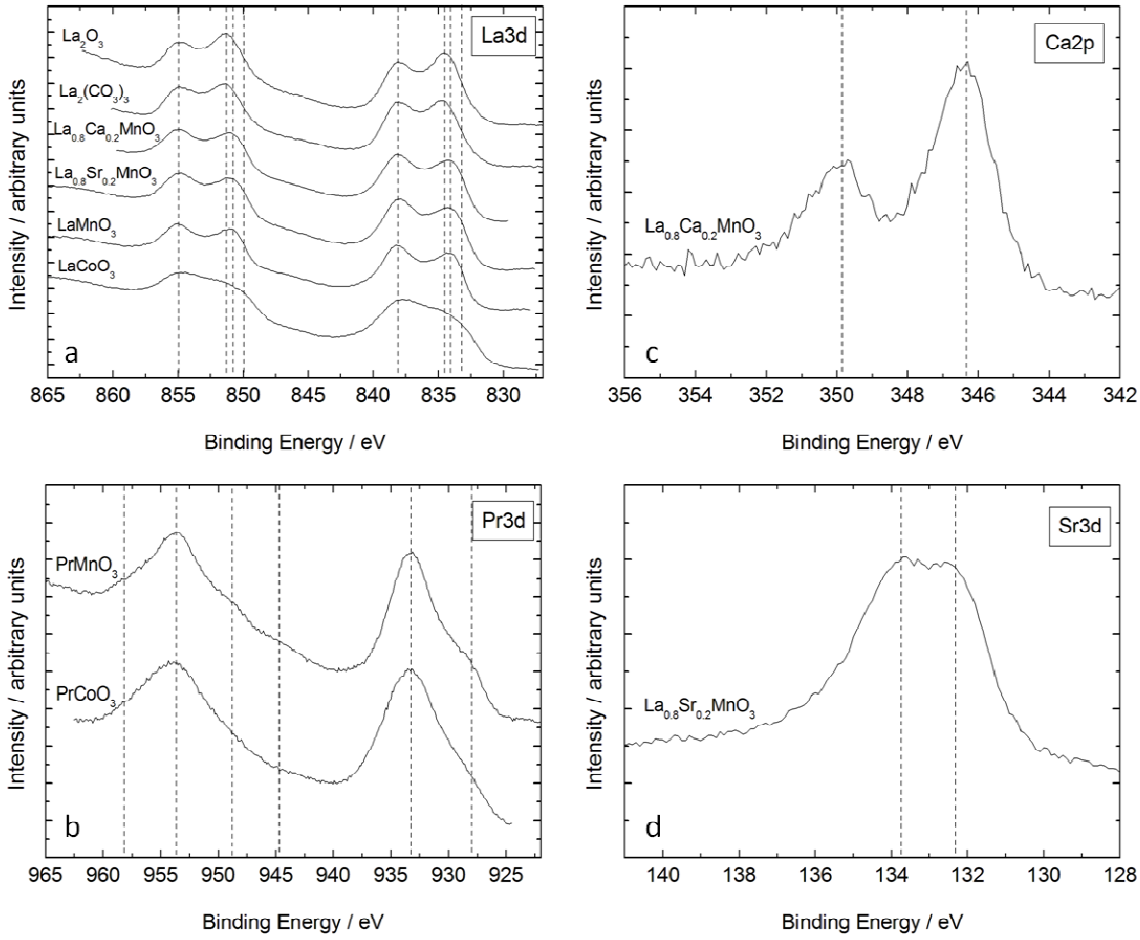

Figure 21 : *XPS spectra of (a) La3d, (b) Pr3d, (c) Ca2p and (d) Sr3d of perovskite and lanthanum oxide and carbonate powders. Lines are guides for the eye and indicate the experimental positions.*

La3d spectrum (Figure 21,a) presents two double peaks for $La_{1-x}A'_xMnO_3$ perovskites. The split of $La3d_{5/2}$ and $La3d_{3/2}$ peaks into two components may be due to the charge transfer from the valence band of oxygen to the unfilled La4f level [176]. The La peak positions for Mn-perovskites are 834.1 eV and 838.1 eV for $La3d_{5/2}$ and 850.7 eV and 854.9 eV for $La3d_{3/2}$. This is very similar to other XPS studies performed on La-based perovskites [43,52,58,60,174,177,178]. La3d spectrum of perovskites is also very close to La3d spectra of commercial lanthanum oxide (La_2O_3, 99.99%, Aldrich) and lanthanum carbonate ($La_2(CO_3)_3$, xH_2O, Aldrich), the peak positions of which are 834.5 eV and 838.1 eV for $La3d_{5/2}$ and 851.3 eV and 854.9 eV for $La3d_{3/2}$, as shown in Figure 21,a. The spectra of these lanthanum species are in agreement with the literature [46,52,60,179,180] and lead to the conclusion that it is difficult to distinguish lanthanum from the perovskite structure from lanthanum oxides or carbonates. Moreover, for all perovskites, La Auger peaks can interfere with La3d peaks, thus

deconvolution can hardly be performed on La spectrum. For $LaCoO_3$, however, the double peaks are not well defined and a shoulder can be distinguished at lower binding energies. Similar La3d shape was found for Co-perovskites in the literature [43,46,47,170] but is not fully understood yet. It can be due to different peak positions between La peaks from Co-perovskite (at lower binding energies) and La peaks from lanthanum oxide and carbonate (at higher binding energies), contrary to perovskites made with other transition metals where La3d peaks from perovskites and carbonates appear at the same binding energy. This is well illustrated by Milt et al. [46] as shown in Figure 98 (see Appendix 2).
One can also not exclude some contributions of Co Auger peaks which occur at similar binding energies.

Peak positions in Pr3d spectrum (Figure 21,b) are in agreement with other XPS studies of Pr-based perovskites [65,181]. Yaremchenko et al. [181] suggested that both Pr^{3+} and Pr^{4+} cations display peaks at ca. 929 and 933 eV in $Pr3d_{5/2}$ spectrum, and by peaks at ca. 950, 954 and 958 eV in $Pr3d_{3/2}$ spectrum. However, a contribution at ca. 946 eV is attributed to Pr^{4+} species. Such a contribution is visible in $PrMnO_3$ spectra. Thus, one can propose that differences observed in Pr3d spectra for $PrCoO_3$ and $PrMnO_3$ compounds are linked to differences in the Pr oxidation states. In $PrCoO_3$, Pr^{3+} is the only oxidation state of Pr, while Pr^{3+} and Pr^{4+} coexist in $PrMnO_3$. Coexistence of Pr^{3+} and Pr^{4+} was also observed in simple Pr-oxides [182].

Concerning the Ca2p spectrum of $La_{0.8}Ca_{0.2}MnO_3$ (Figure 21,c), two distinct peaks are visible. The first one at 346.3 eV is attributed to $Ca2p_{3/2}$ whereas the second one at 349.9 eV is $Ca2p_{1/2}$, in agreement with XPS analysis of $La_{0.8}Ca_{0.2}Mn_{0.9}Fe_{0.1}O_3$ [86].

Sr3d spectrum (Figure 21, d) reveals a broad peak composed of at least two peaks corresponding to $Sr3d_{5/2}$ and $Sr3d_{3/2}$. As the peak area of $Sr3d_{3/2}$ peak is expected to be lower than that of the $Sr3d_{5/2}$ peak, other contributions must be present to give the observed shape of Sr3d spectrum. According to references [62,67,174,177,183], one of these contributions can be due to $SrCO_3$ species, the presence of which was confirmed by XRD in $La_{0.8}Sr_{0.2}MnO_3$.

Figure 22 shows the XPS spectra of various B cations – Co2p and Mn2p – potentially present in the studied perovskites. As for A cations, it is clear that these species are indeed present in the corresponding perovskite compounds. The dashed lines indicate the peak positions and the

corresponding binding energies are reported in Table 6 for perovskite oxides and in Table 7 for other oxides and carbonates.

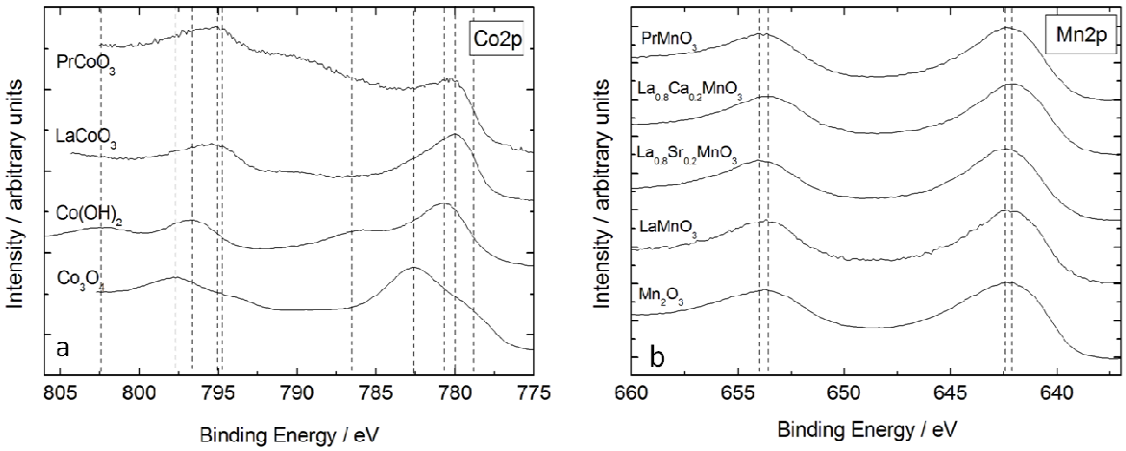

Figure 22 : *XPS spectra of (a) Co2P and (b) Mn2p of perovskite, cobalt oxide and hydroxide, and manganese oxide powders. Lines are guides for the eye and indicate the experimental positions.*

Figure 22,a presents the Co2p spectra of $LaCoO_3$, of $PrCoO_3$, of commercial cobalt hydroxide ($Co(OH)_2$, 99.9%, Alfa Aesar) and of Co_3O_4. For both perovskites, $Co2p_{3/2}$ appears at 779.9 eV and $Co2p_{1/2}$ at 795.2 eV, as found for some Co-perovskites in the literature [43,55,59,60,67,174,184]. Work on simple cobalt oxides [185-187] and on doped cobalt perovskites [188,189] showed that Co oxidation state can hardly be determined from the main peaks but Co^{2+} presence leads to a satellite peak between 785 and 788 eV. This is confirmed by the Co2p spectrum of $Co(OH)_2$ - containing mainly Co^{2+} - (Figure 22,a) on which the main peak positions are 780.6 eV for $Co2p_{3/2}$ and 796.7 eV for $Co2p_{1/2}$, and satellite peaks are found at 786.5 and 802.4 eV, respectively. Thus, from the peak positions and the absence of satellite peaks in Co2p spectra, one can reasonably assume that no Co^{2+} species are present in perovskite compounds, Co existing mainly in Co^{3+} form. Eventual Co^{4+} cannot be excluded due to the asymmetric shape of the peak, but is not likely regarding the low stability of this cation.

One should note that deconvolution of the Co spectrum is difficult because of various possible Co oxidation states, but also due to Co Auger peaks which appear in the same binding energy range. Moreover, it can be supposed that the intensity shift of Co spectrum of $PrCoO_3$ at high binding energies is linked to the Pr Auger peaks occurring at around 788 eV.

The Co2p spectrum obtained for Co_3O_4 is quite unusual. In theory, both Co^{2+} and Co^{3+} are present in this compound, but the spectrum shape and the peak positions do not correspond to these oxidation states of Co. This might mean that the surface is covered by a layer of another Co oxide. However, the bulk is definitely Co_3O_4, as confirmed by XRD (see section 3.2.1.1).

No significant differences between various Mn-perovskites and Mn_2O_3 can be observed from Mn2p spectra (Figure 22,b). The peak positions observed are 642.1 eV for $Mn2p_{3/2}$ and 653.5 eV for $Mn2p_{1/2}$ for Mn_2O_3, $LaMnO_3$, $PrMnO_3$ and $La_{0.8}Ca_{0.2}MnO_3$, and 642.4 eV for $Mn2p_{3/2}$ and 653.8 eV for $Mn2p_{1/2}$ for $La_{0.8}Sr_{0.2}MnO_3$. Similar peak positions were found for Mn-perovskites in the literature [45,53,58,65,86,127,171] as well as for Mn_2O_3 [190]. According to these authors, the broad and assymetric shape of Mn2p peaks may be explained by the presence of at least two different Mn oxidation states – Mn^{3+} at low energies and Mn^{4+} at high energies – in the doped and non doped Mn-perovskites. The slight shift of the peak position for $La_{0.8}Sr_{0.2}MnO_3$ compared to other Mn-oxides in the Mn2p spectra may indicate that the amount of Mn^{4+} is larger in this compounds, thanks to the Sr^{2+} doping. No differences due to Mn^{2+} presence to balance the eventual existence of Pr^{4+} can be found in the Mn2p spectrum of $PrMnO_3$.

3.2.4.2. Presence of carbonates on perovskite surfaces

For all the studied perovskites, a strong peak at low binding energies and a smaller one at higher binding energies were present in the C1s spectra (Figure 23,a). The first peak can be separated in two contributions, one for adventious carbon which is also the reference at 284.6 eV, and one for C=O bonds (arising from the partial oxidation of carbon) at 286 eV. The peak around 288-289 eV is attributed to carbonate species after comparison with the C1s spectrum of $(La_2(CO_3)_3$ (Figure 23,a) and considering XPS spectra of A cations which evidence the presence of La and Sr carbonates. This deconvolution, shown in (Figure 23,a), is based on the literature [44,46,60,69,174,177,191] and proves the presence of carbonate species at the perovskite surfaces.

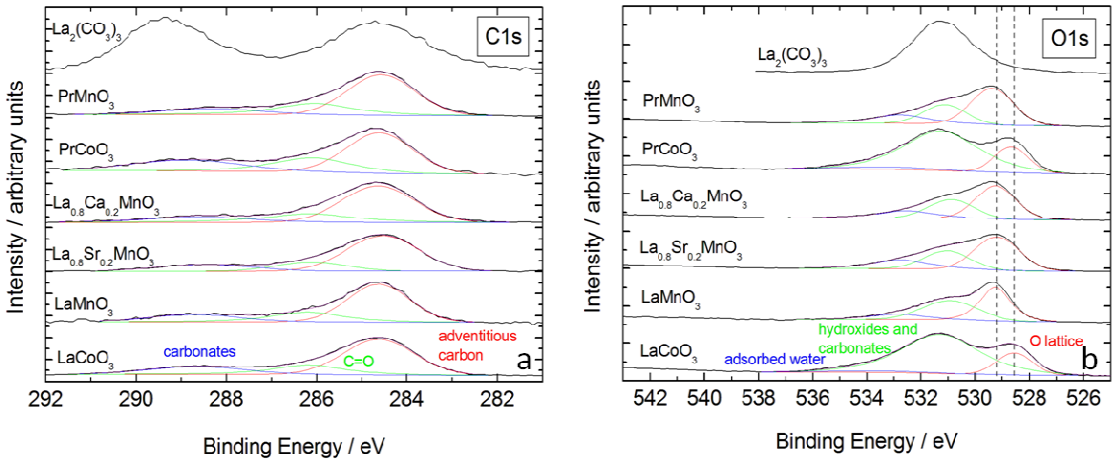

Figure 23 : *XPS spectra of (a) C1s and of (b) O1s of perovskite and lanthanum carbonate powders, and corresponding peak deconvolution. Lines are guides for the eye and indicate the experimental positions.*

As these carbonate species contain oxygen, they are also present in the O1s spectra and should therefore be separated from the lattice oxygen. O1s spectra of the studied perovskites are presented in Figure 23,b. Three main contributions can be distinguished according to the literature [43,44,46,51,54,62,64,171,174,191]. The first one, occurring at 528.6 eV for Co-perovskites and at 529.2 eV for Mn-perovskites, corresponds to the lattice oxygen. The second O1s contribution around 531 eV is characteristic of hydroxide and carbonates species. This is confirmed by O1s spectrum of $La_2(CO_3)_3$. By calculating the atomic ratio from C1s and from O1s spectra thanks to Scofield factors, a ratio of ca. 1:3 was found, corresponding to carbonate CO_3^{2-} species. Thus, hydroxide fraction is indeed low compared to the carbonate fraction on the perovskite surface. Finally, adsorbed water appears at around 533 eV in the O1s spectra. This deconvolution gives access to the lattice oxygen and therefore allows a comparison of its atomic concentration to those of A and B cations in a given perovskite.

Table 6 : *Binding energies of XPS peaks (in eV) of perovskite oxides*

Compounds	$La3d_{5/2}$	$Pr3d_{5/2}$	$Ca2p_{3/2}$	$Sr3d_{5/2}$	$Co2p_{3/2}$	$Mn2p_{3/2}$	C1s	O1s
$LaCoO_3$	833.2 834.1 838.1	-	-	-	779.9	-	284.6 286.2 288.7	528.6 531.3 532.7
$LaMnO_3$	834.1 838.1	-	-	-	-	642.1	284.6 286.2 288.7	529.3 531.0 532.8
$La_{0.8}Sr_{0.2}MnO_3$	834.1 838.1	-	-	132.3	-	642.4	284.6 286.1 288.5	529.2 531.0 532.7
$La_{0.8}Ca_{0.2}MnO_3$	834.1 838.1	-	346.3	-	-	642.1	284.6 286.1 288.6	529.2 530.9 532.5
$PrCoO_3$	-	928.0	-	-	779.9 795.2	-	284.6 286.1 288.8	528.7 531.2 533.2
$PrMnO_3$	-	928.0	-	-	-	642.1	284.6 286.1 288.5	529.3 531.1 532.8

Table 7 : *Binding energies of XPS peaks (in eV) of simple oxides and carbonates*

Compounds	$La3d_{5/2}$	$Co2p_{3/2}$	$Mn2p_{3/2}$
La_2O_3	834.5 838.1	-	-
$La_2(CO_3)_3$	834.5 838.1	-	-
$Co(OH)_2$	-	780.7 786.5	-
Co_3O_4	-	778.8 782.6	-
Mn_2O_3	-	-	642.1

3.2.4.3. Surface atomic ratio

The atomic ratio of various perovskite components were calculated using the peak area after the background correction and considering Scofield factors. Results are displayed in Figure 24 for various perovskites and compared to an ideal ABO_3 perovskite phase (first column).

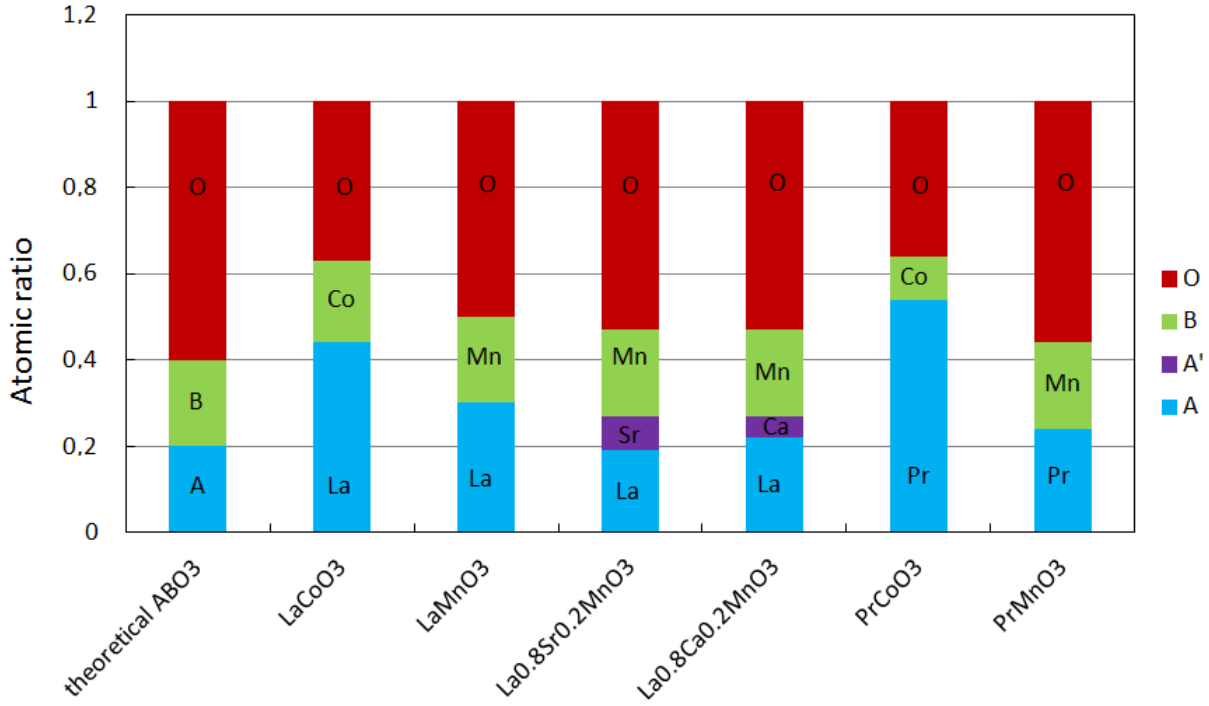

Figure 24 : *XPS atomic ratio of A (blue), A' (purple), B (green) and O from perovskite lattice (red) in perovskite oxides calculated with Scofield factors after background correction of XPS spectra.*

First of all, one can notice that atomic ratios of Mn-perovskites are closer to theory, with a A:B:O ratio of about 1.5:1:2.5, than Co-perovskites which present a A:B:O ratio of 5:1:4. Then, it can be observed that all perovskites, and especially Co-perovskites, present an enrichment of the A cation on the surface. This is probably due to the formation of carbonates of A cation, as emphasized by detailed analysis of C, O and A XPS spectra. It is also supported by numerous studies which showed that perovskites [43,44,46,51,52,54,55,58,60,62,69,170,174,177,191-193] as well as lanthanum oxides [46,180,194] tend to form carbonates on their surfaces when exposed to ambient conditions, leading to a non stoichiometric A:B atomic ratio. According to the atomic ratio obtained for various perovskites, A cation seems to be less stable and to form more carbonates in Co-perovskites than in Mn-perovskites.

All conclusions from the XPS analysis concern the surface – some nanometers depth - rather than the bulk, which is mainly composed of perovskite as shown by XRD (see section 3.2.1.1). However, this surface composition raises some questions. First, the formation of a carbonate layer on the perovskite surface can lead to an increase of the ohmic drop in the

catalytic layer, hampering electron transfer processes, and to a decrease of the available surface area. Secondly, this carbonate layer is composed of A cation, whereas the ORR active site is rather B cation as it will be highlighted later in this work. Thus the segregation of A on the perovskite surface can decrease its catalytic activity and also suggests that only the surface and the near surface region of perovskite oxides is only partially represented by the perovskite ABO_3 structure.

3.3. Interfacial properties

The electrochemical properties of the oxide materials were studied using cyclic voltammetry without electrode rotation in N_2-purged 1M NaOH electrolyte. Various potential windows as well as various sweep rates were used to investigate the interfacial behavior of the catalysts. These experiments were performed with carbon addition in the catalytic layer to avoid any conductivity limitations, but the exact role of carbon will be investigated in section 4.

3.3.1. Potential window stability of perovskite oxides

The open circuit potentials (OCP) of various perovskite/carbon electrodes studied in this work were between 0.9 and 1V vs. RHE in N_2-purged electrolyte. Therefore, a first CV cycle was performed between 0.93 V vs. RHE (close to OCP) and 1.23 V vs. RHE. The positive potential limit (1.23 V vs. RHE) was chosen to minimize the oxidation of the carbon contained in the electrodes. The potential window stability of the electrodes was then investigated by decreasing progressively the lower potential limit down to 0.13 V vs. RHE. After each CV cycle, a reference CV was performed in the initial potential range of [0.93 ; 1.23 V vs. RHE] to check the stability of the voltammogram. The results are shown in Figure 25 for the $LaCoO_3$/C, $LaMnO_3$/C and $La_{0.8}Sr_{0.2}MnO_3$/C electrodes, to represent non doped Co-perovskites, non doped Mn-perovskites and doped Mn-perovskites, respectively. The first cycle, performed in the potential range [0.93 ; 1.23 V vs. RHE], is represented in black with the number one. Then, the increasing numbers indicate the order in which the cycles were made, and the same number and color was used for the reference CV in the interval [0.93 ; 1.23 V vs. RHE] after a given cycle. For example, the fifth cycle (green in Figure 25,a,b,c) was performed in the potential range [0.53 ; 1.23 V vs. RHE], and before the sixth cycle (light blue in Figure 25,a,b,c) in the range [0.43 ; 1.23 V vs. RHE], a reference cycle was recorded in the range [0.53 ; 1.23 V vs. RHE], and is represented in green in Figure 25,d,e,f.

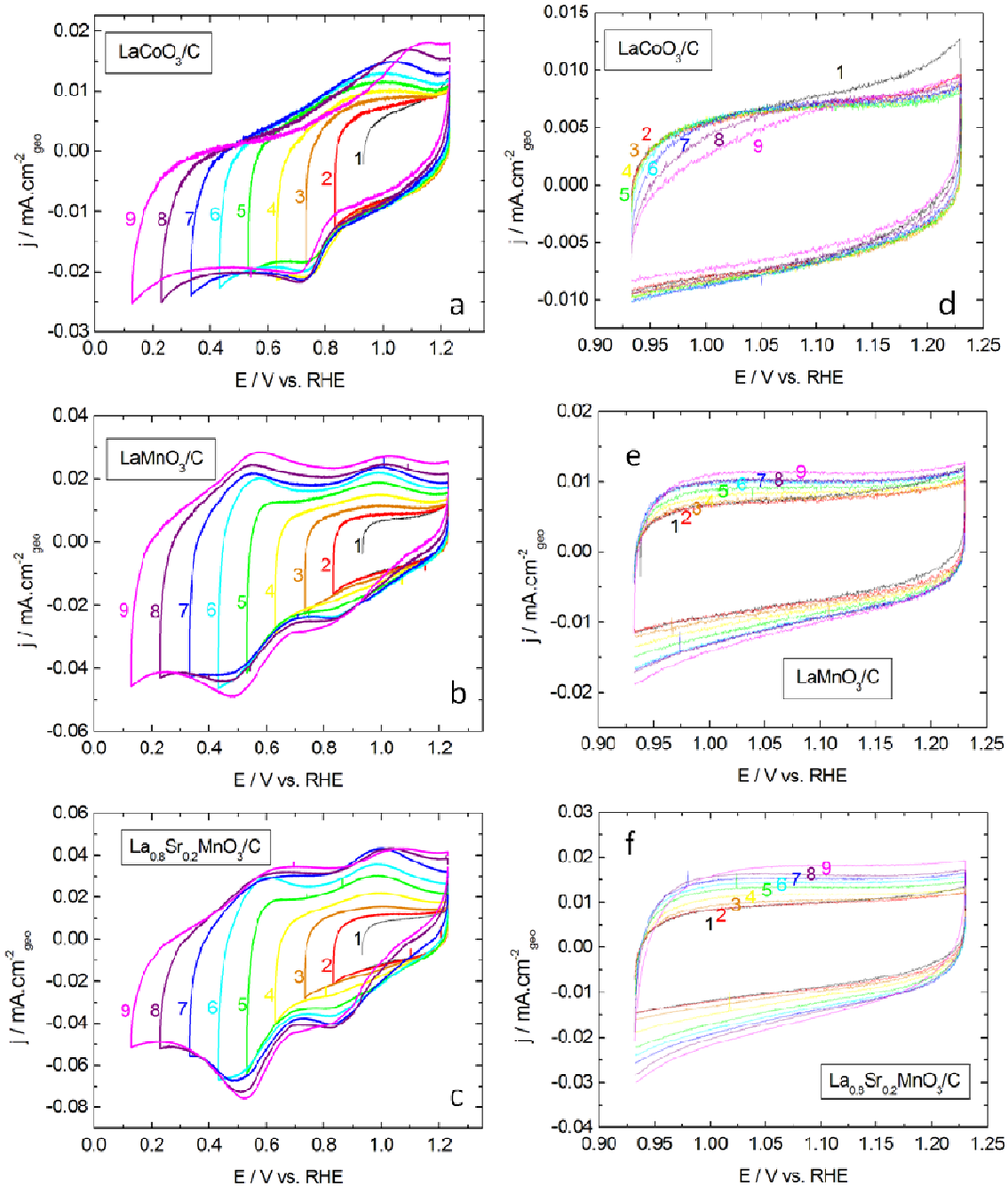

Figure 25 : *(a,b,c) CVs in various potential windows and (d,e,f) corresponding reference CVs of GC-supported thin films of (a,d) $LaCoO_3$ + Sibunit carbon, (b,e) $LaMnO_3$ + Sibunit carbon, (c,f) $La_{0.8}Sr_{0.2}MnO_3$ + Sibunit carbon in N_2-purged 1M NaOH electrolyte at 10 mV.s^{-1}. Measurements were performed with 91 µg.cm$^{-2}_{geo}$ perovskite and 18 µg.cm$^{-2}_{geo}$ Sibunit carbon. Currents are normalized to the geometric area of the electrode. The number and color indicate the sequence of the scans.*

For $LaCoO_3$ electrodes (Figure 25,a,d), it can be observed that, up to 0.43 V vs. RHE, the absolute current increases with decreasing the lower potential limit leading to an appearance

of an anodic and a cathodic peaks. Moreover, reference voltammograms are stable after these cycles. Thus, the perovskite is stable in the range [0.43 ; 1.23 V vs. RHE]. However, when the potential is decreased to lower values, the anodic peak is shifted and reference voltammograms are modified, showing the irreversibility of $LaCoO_3$ reduction below 0.43 V vs. RHE.

Non-doped (Figure 25,b,e) and doped (Figure 25,c,f) $LaMnO_3$ perovskites display similar behavior. When the lower potential limit is gradually decreased, the absolute current increases and a first anodic peak is visible around 1 V vs. RHE. By decreasing further this potential, two cathodic peaks and an additional anodic peak appear. For potentials below 0.43 V vs. RHE, the electrochemical behavior of the perovskites is irreversibly modified, showing lower cathodic currents at high potential values. One can note that the reference voltammograms in the potential range [0.93 ; 1.23 V vs. RHE] show an irreversible increase of the absolute current with the number of cycles. The cause of this behavior is not understood yet but might be linked to a modification in the capacitive properties, such as an increase of the roughness. One may also suppose that a distortion of the perovskite oxide is occurring when the potential is decreasing, leading to an increase of the number of available electrochemically active sites.

The potential window kept in the following experiments was [0.43 ; 1.23 V vs. RHE] in which stable voltammograms were observed for both Co-based and Mn-based perovskites.

3.3.2. Perovskite redox transitions

3.3.2.1. Identification of the redox transitions

The CV of various oxides studied in this work are presented in Figure 26. Three distinct behaviors can be observed, the CV of perovskites being strongly dependent on the nature of the B cation. Indeed, perovskites with the same A cation and different B cations, such as $LaCoO_3$ and $LaMnO_3$, have very different electrochemical behavior, while perovskites with the same B cations show similar CVs. It can already be concluded that the redox transitions occurring at the surface of perovskite oxides are related to B cations rather than to the structure symmetry or to A cations, even if the latter are in high quantities on the perovskite surface in the carbonate form, as shown by the XPS analysis (see section 3.2.4.3). The electrochemical stability of the A cations is in agreement with Pourbaix diagrams [195,196]

which show that the La^{3+}, Ca^{2+}, Sr^{2+} and Pr^{3+} oxidation states are stable in the studied potential range at pH14 (1M NaOH).

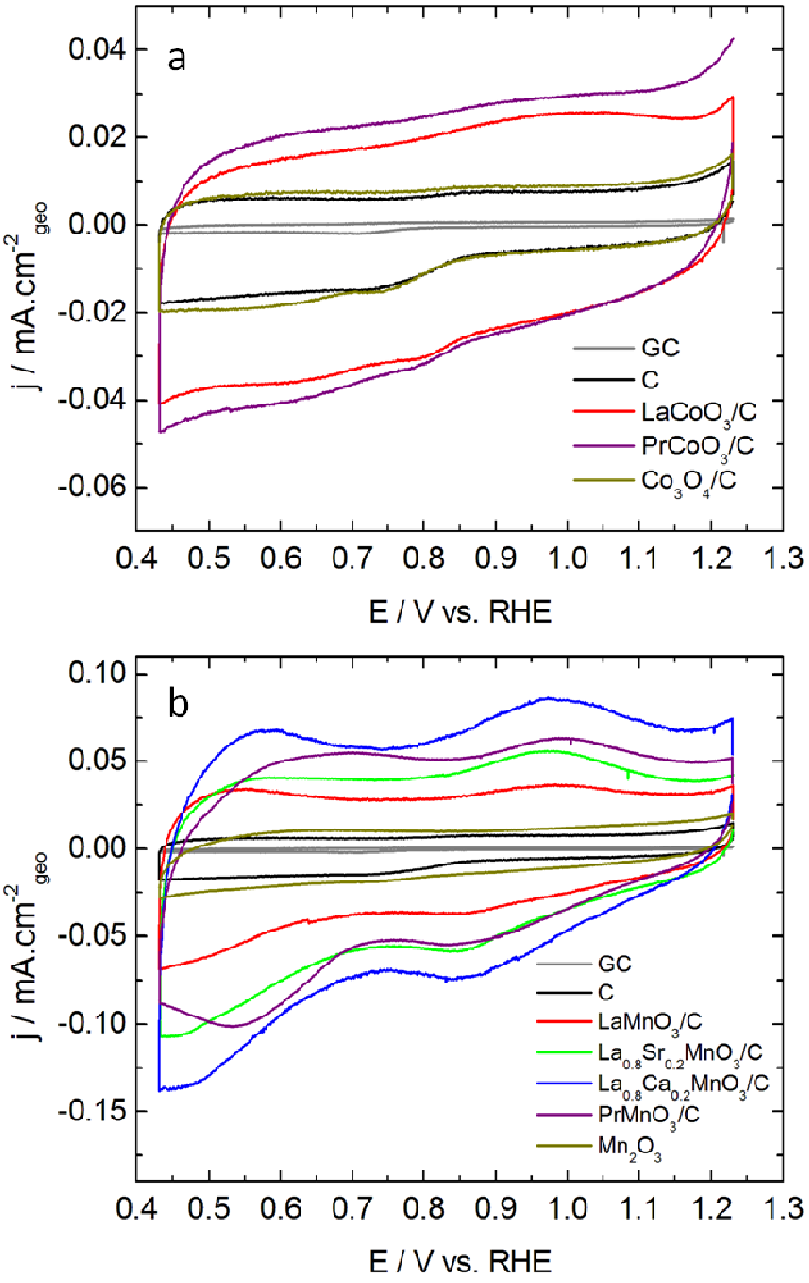

Figure 26 : *CVs of GC-supported thin films of (a) Co-based oxides + Sibunit carbon and (b) Mn-based oxides + Sibunit carbon in N_2-purged 1M NaOH electrolyte at 10 mV.s^{-1}. Measurements were performed with 91 µg.cm$^{-2}_{geo}$ oxide and 37 µg.cm$^{-2}_{geo}$ Sibunit carbon. Grey and black lines show CV for GC and 37 µg.cm$^{-2}_{geo}$ Sibunit carbon, respectively. Currents are normalized to the geometric area of the electrode.*

First, the two Co-based perovskites – $LaCoO_3$ and $PrCoO_3$ – display an identical voltammogram with poorly defined pair of peaks (Figure 26,a). As mentioned above, the OCP of various perovskite/carbon electrodes were between 0.9 and 1V vs. RHE. According to the Pourbaix diagrams [195] of Co-oxides at this potential and at pH14, the surface equilibrium of Co-perovskites is expected to be determined by the Co^{3+}/Co^{2+} redox couple. This interpretation should be taken with caution since potential/pH diagrams were calculated for simple oxides only, but the presence of Co^{3+} on the perovskite surface is in agreement with the XPS results (see section 3.2.4.1). Thus the pair of peaks observed in the voltammogram can be tentatively attributed to Co^{3+}/Co^{2+} transitions. The reduction of Co^{3+} into Co^{2+} might lead to the formation of oxygen deficient perovskite structure on the surface and probably also in the near surface region [197].

Secondly, it can be noticed that all Mn-based perovskites – $LaMnO_3$, $La_{0.8}Sr_{0.2}MnO_3$, $La_{0.8}Ca_{0.2}MnO_3$ and $PrMnO_3$ – present two cathodic and two anodic peaks (Figure 26,b). However, the peaks at lower potentials values are shifted towards positive potentials for $PrMnO_3$ compared to La-perovskites. The OCP observed for these perovskites can correspond to the Mn^{4+}/Mn^{3+} redox couple according to Pourbaix diagrams [195] for Mn-oxides. This is consistent with the XPS results which suggested the presence of both oxidation states on the surface of the studied perovskites (see section 3.2.4.1). Moreover, the cathodic peak at 0.85 V vs. RHE and the anodic peak at 1 V vs. RHE may correspond to the reduction of Mn^{4+} and the oxidation of Mn^{3+}, respectively. Similar CV peak attributions were made for doped-$CaMnO_3$ perovskites in the literature [140,198]. The cathodic and anodic peaks appearing at lower potentials might be linked to the Mn^{3+}/Mn^{2+} redox couple since the latter oxidation state appears below 0.7 V vs. RHE in Pourbaix diagrams [195]. These assumptions are supported by *in-situ* characterization of simple Mn oxides. Indeed, Lima et al. [199] combined *in-situ* X-ray absorption near edge structure (XANES) to CV characterization of Mn oxides and, by comparing to reference Mn oxides, found that Mn^{4+}/Mn^{3+} transitions occur at high potentials (between -0.1 and 0.4 V vs. Hg/HgO, corresponding to ca. 0.8 V and 1.3 V vs. RHE in 1M KOH) and Mn^{3+}/Mn^{2+} at low potentials (between -0.7 and -0.1 V vs. Hg/HgO, corresponding to ca. 0.2 V and 0.8 V vs. RHE in 1M KOH). This is also in agreement with *in-situ* Raman results on Mn electrodes of Messaoudi et al. [200]. During electrochemical reduction of MnO_2, it is generally accepted that protons and electrons are inserted into the oxide bulk [201-203]. These inserted protons compensate the Mn^{4+} vacancies ("Ruetshi" protons) or are associated with Mn^{3+} cations ("Coleman" protons). They become associated with O_2^- ion to

form OH^- ion in the solid phase. However, regarding the CV charge (see sections 3.3.3 and 4.2 for further details), the transitions are likely to occur only at the oxide surface for the perovskites studied in this work.

The broad character of the peaks suggests that several contributions are involved. It can be due to heterogeneities in the surface sites, identical redox transitions occurring at slightly different potentials on the different sites. Moreover, from Figure 25, it seems that the peaks are not independent. The cathodic peak around 0.85 V vs. RHE (presumably reduction of Mn^{4+} to Mn^{3+}) appears only when the lower potential limit is decreased, and thus, when the peaks corresponding to Mn^{3+}/Mn^{2+} are visible. This might be a proof that the amount of Mn^{4+} cation is small in the initial samples, and that a reductive transformation of the surface is required to favor its further creation. The positive shift of the peaks of presumably Mn^{3+}/Mn^{2+} redox couple in $PrMnO_3$ cannot be explained yet. Anyhow, it cannot be due to an eventual presence of Mn^{2+} in the initial perovskite since it would have shifted the potential of the Mn^{3+}/Mn^{2+} redox couple towards smaller potential values according to the Nernst equation. Indeed, at equilibrium, the potential E_{eq} of the redox reaction $\sum_i \nu_i A_i + \nu_e e \rightleftarrows 0$, with ν_i and ν_e, the algebric stoichimetric coefficients, is given by (Equation 69):

$$E_{eq} = E° + \frac{RT}{\nu_e F} \ln\left(\prod_i a_i^{\nu_i}\right) \quad \text{(Equation 69)}$$

with E°, the standard potential of the redox couple, R, the gas constant, T, the temperature in Kelvin, F, the Faraday constant (96485 $C.mol^{-1}$), a_i, the species activities.

Finally, a yet distinct behavior was found for Co_3O_4 (Figure 26,a) and Mn_2O_3 (Figure 26,b) electrodes. They display very low currents and a voltammogram very close to the one of the carbon contained in the electrodes. These compounds are known to display very low electrical conductivities [204,205], hampering their participation in electrochemical processes.

3.3.2.2. Reversibility of the redox transitions

From the dependence of the peak current and potential with the sweep rate, one can get information on the reversibility of the redox transitions occuring in perovskites. In this section, Co-based perovskites are not considered since their redox peaks are not clearly defined in CVs. CVs at various sweep rates were therefore performed for $La_{0.8}Sr_{0.2}MnO_3$, as an example for Mn-based perovskites. The results are shown in Figure 27,a.

For all sweep rates, the two cathodic peaks (C1 and C2) and the two anodic peaks (A1 and A2) already mentioned in the previous section are observed. An additional cathodic peak appears at 5 $mV.s^{-1}$ at 0.73 V vs. RHE. The nature of the process involved at this potential is not understood yet, but it is undoubtly an irreversible process since it can be observed only at a slow sweep rate and since no corresponding anodic peak is visible.

In order to better visualize the modification of the CV shape, the CVs were normalized by the sweep rate in Figure 27,b. It is observed that both the CV charge and the peak current densities are almost proportional to the sweep rate, as expected for a surface process (see section 2.3.4). Therefore the peaks correspond neither to diffusion nor to bulk processes.

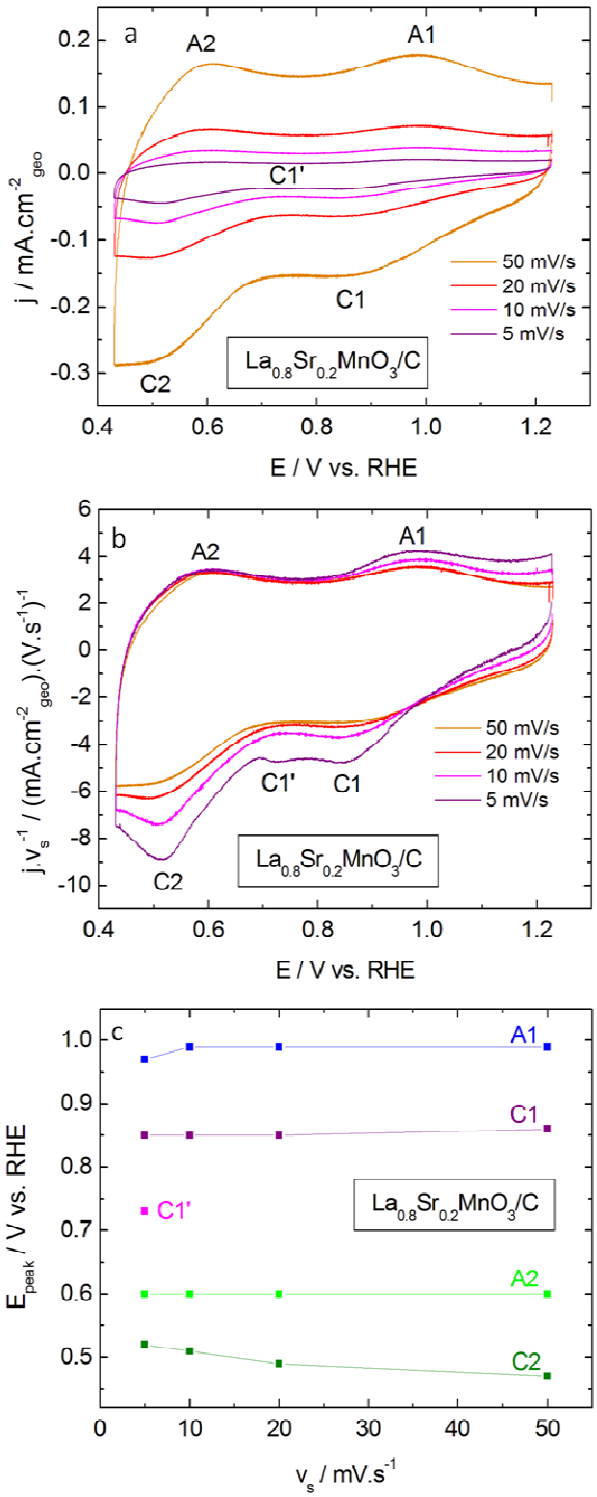

Figure 27 : *(a) CVs of GC-supported thin films of $La_{0.8}Sr_{0.2}MnO_3$ + Sibunit carbon in N_2-purged 1M NaOH electrolyte at various sweep rates. Corresponding (b) CVs normalized by the sweep rate and (c) peak potential versus the sweep rate. Measurements were performed with 91 $\mu g.cm^{-2}_{geo}$ perovskite and 18 $\mu g.cm^{-2}_{geo}$ Sibunit carbon. Currents are normalized to the geometric area of the electrode.*

The potentials of the various peaks observed on the CV are plotted versus the sweep rate in Figure 27,c. The determination of these potentials were however not precise due to the large breadth of the peaks. As the peak potentials of peaks A1 and C1 do not change with the sweep rate and as anodic and cathodic peak currents are similar, one may suggest that the redox couple involved at this potential (probably Mn^{4+}/Mn^{3+}) is a reversible process. However, the potential splitting between the two peaks is higher than expected. Indeed, a splitting of ca. 140 mV is found whereas reversible processes involving one electron should display a peak splitting of 59 mV at 25°C. Such a behavior is not fully understood yet but might be related to the complexity of the redox transition involved and probably some slow chemical steps associated to the electrochemical process.

For A2/C2 peak couple, both peak potential and potential peak splitting are dependent on the sweep rate. Therefore this redox transition is rather an irreversible process. This intepretation is emphasized by the difference in coulombic charge of the two peaks. Indeed, the charge under C2 peak is greater than the charge of A2 peak. The reason of this irreversibility is not clear yet, but might be a proof of a rearrangement of the perovskite structure near the surface which accompanies the reduction of B^{3+} into B^{2+}. In particular, it can be expected that oxygen vacancies are formed to ensure the electroneutrality of the perovskite structure. Also, studies on simple Mn oxides with RRDE [200] and *in-situ* XANES [206] proved that the formation of Mn in the low oxidation state results in a dissolution of Mn from the electrode. However, these low valence cations might be more stable in the perovskite structure than in simple oxides. Indeed, no current loss was observed upon 30 minute cycling.

3.3.3. Roughness of the perovskite electrode

Knowing the BET surface area S_{BET} (see section 3.2.3) of a perovskite, the roughness of the perovskite electrode can be determined with (Equation 70):

$$R_f = S_{BET} \times \frac{m_p}{S_{geo}} \text{ (Equation 70)}$$

where $\frac{m_p}{S_{geo}}$ is the perovskite loading in the electrode. Therefore, for an electrode containing for example a loading of 91 $\mu g.cm^{-2}_{geo}$ $La_{0.8}Sr_{0.2}MnO_3$, the roughness factor is ca. 15 $cm^2_{perovskite}.cm^{-2}_{geo}$ (S_{BET} = 17 $m^2.g^{-1}$ for $La_{0.8}Sr_{0.2}MnO_3$).

The roughness factor of an electrode can be related to its double layer capacity C_{dl}. The method to estimate the double layer capacity of perovskites was inspired by the literature [75,140,160,198,207]. CVs were performed on perovskite/carbon electrodes at various sweep rates in a restricted potential window of 100 mV size where few faradaic processes occur. However, these processes cannot be totally excluded since the redox peaks are broad. CVs in the same potential range were also measured for carbon electrodes and subtracted from the corresponding CVs of perovskite/carbon electrodes in order to remove the pseudocapacitive contribution of carbon. The obtained corrected CVs are presented in Figure 28,a for $La_{0.8}Sr_{0.2}MnO_3$.

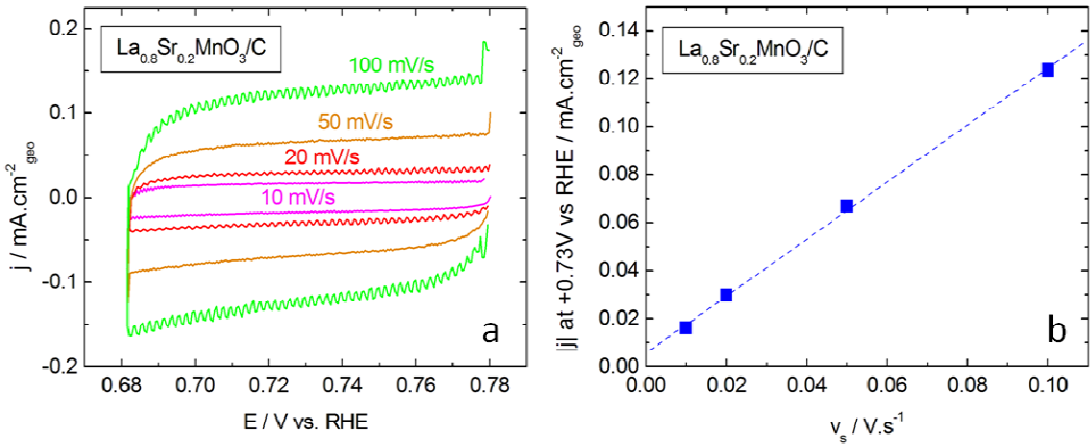

Figure 28 : *(a) CVs in the capacitive region of GC-supported thin films of $La_{0.8}Sr_{0.2}MnO_3$ + Sibunit carbon in N_2-purged 1M NaOH electrolyte at various sweep rates, and (b) corresponding absolute current density at +0.73V vs. RHE versus the sweep rate. Measurements were performed with 91 $\mu g.cm^{-2}_{geo}$ perovskite and 37 $\mu g.cm^{-2}_{geo}$ Sibunit carbon. Currents are normalized to the geometric area of the electrode.*

The rectangular shape of the CV indicates a typical capacitive behavior. By plotting the current versus the sweep rate (Figure 28,b), a linear relationship is obtained as expected from (Equation 23). The capacity per geometric surface area can therefore be estimated from the slope of this curve and was found to be 1.2 $mF.cm^{-2}_{geo}$ for the studied perovskite. Then the capacity per surface area of the oxide was calculated using $R_f = 15$ (see above) and found to be 80 $\mu F.cm^{-2}_{perovskite}$ (Equation 71):

$$C_{dl} = \frac{1.2\ mF.cm^{-2}_{geo}}{R_f} = 80\ \mu F.cm^{-2}_{perovskite} \quad \text{(Equation 71)}$$

This value is close to the theoretical capacity of a smooth oxide surface – ca. 60 $\mu F.cm^{-2}_{oxide}$ - found thanks to modeling of the double layer of non porous oxides by Levine et al. [208] and

therefore suggests that the perovskite surface is not significantly blocked by carbonates. Moreover, it demonstrates that only the perovskite surface is involved in the electrochemical processes, bulk participation would have led to a higher capacity.

3.4. Conclusions of Chapter 3

Thanks to the XRD analysis, it was shown that the perovskites synthesized for this study displayed a perovskite structure without precursor traces and that the bulk of the phase was stable under an atmospheric storage. The symmetry of the structure appeared to be strongly dependent on the size of the A cation. The perovskite oxides observed by SEM were constituted of small particles of 50-100 nm arranged in micrometer size agglomerates. This particle agglomeration led to a BET specific surface area of 10-20 $m^2.g^{-1}$, lower than expected from XRD for non-agglomerated crystallites. From SEM, it was also observed that the perovskite/carbon thin layers prepared for electrochemical measurements were well dispersed with a good mix of both electrode components. The perovskite surface, important for electrocatalysis, was studied by XPS. It confirmed the presence of A cation, B cation and O from the lattice since the binding energies of the various components were in agreement with the literature data on perovskite oxides. However, the atomic ratio of these components did not match the stoechiometry atomic ratio. Indeed an enrichment of A cation was observed for all perovskite samples. This was probably due to the presence of carbonates, according to C1s and O1s spectra.

From CV measurements, the perovskites were found to be stable in the potential window [0.43 ; 1.23 V vs. RHE]. In this potential range, redox transitions were attributed to B cations rather than to A cations, and no effect of carbonates species was visible. For Co-based perovskites, redox transitions were poorly resolved in CVs, while Mn-based perovskites presented two anodic and two cathodic peaks. The redox couples involved in these peaks were supposed to be Mn^{4+}/Mn^{3+} at high potentials and Mn^{3+}/Mn^{2+} at lower potentials, the former transition is most likely reversible while the latter is probably irreversible. The ORR activity of these perovskite oxides will be studied in the following chapter.

The oxides synthesized for comparison displayed a cubic structure, but their surface area was significantly lower than the perovskite one – factor of ca. 5 – due to a high degree of the particle agglomeration. Moreover, their low conductivity hampers their investigation with electrochemical methods.

Chapter 4 :
Dual role of carbon in the catalytic layers of perovskite/carbon composites

4.1. Introduction

Although numerous oxides of perovskite type display intrinsic electronic conductivities sufficient to be used in electrochemical systems, perovskite catalytic layers suffer and a fortiori, from low catalyst utilization factor. This high resistance of the perovskite catalytic layers may be attributed to the contact ohmic drop between perovskite aggregates. Several studies [82,83,87-89,115] have proven that addition of carbon powders is required to increase the electrocatalytic efficiency of perovskite materials for ORR by significantly improving the conductivity of oxide-based electrodes (see section 1.4). However, carbon materials are known to be active for ORR electrocatalysis in alkaline media by reducing O_2 into HO_2^- [209,210]. This brings up a question on the separation of contributions from the two components in the composite oxide/carbon electrodes. A recent study of the ORR on perovskite oxides proposed a methodology to determine ORR activity from RDE measurements by neglecting the contribution of carbon into the ORR kinetics, even if the latter is added to the thin film electrodes [103].

Therefore, the objectives of this chapter are to determine the role of carbon in perovskite/carbon composite cathodes, and to verify the correctness of conventional approaches to quantify the activity of perovskites by either neglecting or subtracting the contribution of carbon to the ORR kinetics. In order to achieve this goal, the oxide to carbon ratio was varied systematically and electrochemical and electrocatalytic properties of thin film composite electrodes were studied using cyclic voltammetry and the RDE method.

This chapter is based on the published article : **Poux, T., Napolskiy, F.S., Dintzer, T., Kéranguéven, G., Istomin, S.Ya., Tsirlina, G.A., Antipov, E.V., Savinova, E.R.** Dual role of carbon in the catalytic layers of perovskite/carbon composites for the electrocatalytic oxygen reduction reaction. *Catalysis Today.* 2012, Vol. 189, 83-92 [211] and completed with unpublished results.

The contribution of the author of the present thesis in this publication was comprised of the following: the entirety of the experimental part except perovskite synthesis, the analysis and the discussion of the experimental data, as well as the participation in the preparation of the manuscript for the publication.

4.2. CV in supporting electrolyte: influence of carbon on the electrical contact

In order to investigate the role of carbon on the electrical properties of perovskite/carbon catalytic layers, electrodes with constant amount of perovskite (91 $\mu g.cm^{-2}_{geo}$) and various amounts of carbon were prepared for $LaCoO_3$, $LaMnO_3$ and $La_{0.8}Sr_{0.2}MnO_3$. The tested compositions are listed in Table 8, where the roughness factors were calculated from BET surface area values (see section 3.2.3 and 3.3.3). The three perovskites were chosen to represent non doped Co-perovskites, non doped Mn-perovskites and doped Mn-perovskites, respectively. Electrodes containing only carbon were prepared with the same amount of carbon and were used for comparison.

Table 8 : *Loading, roughness factors and estimated thickness (calculated with (Equation 19)) of RDE thin layers with constant perovskite loading*

Electrodes	**Constant perovskite loading**					
Perovskite loading ($\mu g.cm^{-2}_{geo}$)	91	91	91	91	91	91
$LaCoO_3$ roughness factor ($cm^2_{oxide}.cm^{-2}_{geo}$)	9.1	9.1	9.1	9.1	9.1	9.1
$LaMnO_3$ roughness factor ($cm^2_{oxide}.cm^{-2}_{geo}$)	13	13	13	13	13	13
$La_{0.8}Sr_{0.2}MnO_3$ roughness factor ($cm^2_{oxide}.cm^{-2}_{geo}$)	16	16	16	16	16	16
Carbon loading ($\mu g.cm^{-2}_{geo}$)	0	18	37	140	270	820
Carbon roughness factor ($cm^2_{carbon}.cm^{-2}_{geo}$)	0	12	24	90	178	540
Content of perovskite in the composite (wt%)	100	83	71	40	25	10
Estimated layer thickness (μm)	1.5	1.9	2.3	4.8	8.2	22

Figure 29 shows representative CVs in N_2-purged 1M NaOH electrolyte. It should be noticed however that repeated independent experiments were performed for each electrode to check the reproductibility of the results. Some of the repeated CVs can be seen in Appendix 1 (Figure 94).

From Figure 29,b,c,d, it was observed that the addition of carbon strongly affects CV of perovskite oxides with an increase of the current density with the carbon loading. However, similar effect was found for carbon electrodes (Figure 29,a). Thus, in order to better visualize the influence of carbon on the current originating from perovskite oxides, difference voltammograms were constructed by subtracting the CV of carbon electrodes from the CV of the composite perovskite/carbon electrodes containing the same amount of carbon (Figure 30). For electrodes containing very large fraction of carbon (> 75 wt.%), such procedure leads to a very large error and is therefore not shown.

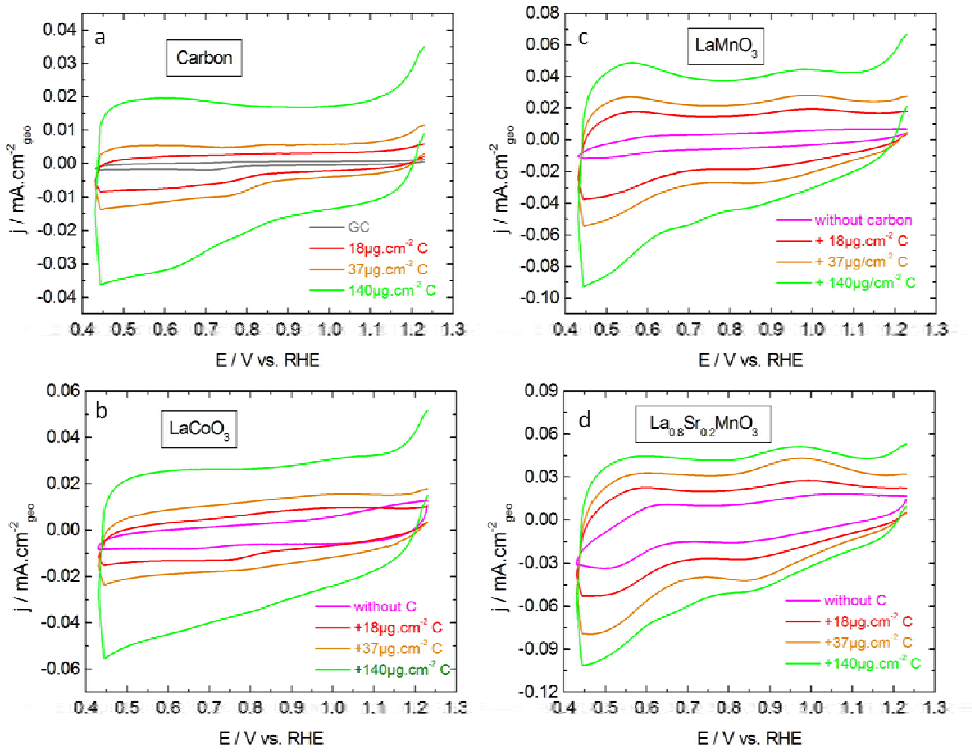

Figure 29 : *CVs of GC-supported thin films of (a) Sibunit carbon, (b) $LaCoO_3$ + Sibunit carbon, (c) $LaMnO_3$+ Sibunit carbon, (d) $La_{0.8}Sr_{0.2}MnO_3$+ Sibunit carbon in N_2-purged 1M NaOH electrolyte at 10 mV.s^{-1}. Measurements were performed with a constant amount of perovskite (91 µg.cm$^{-2}_{geo}$), except for carbon electrodes which do not contain perovskite, and variable amount of Sibunit carbon. Color codes for Sibunit carbon loading: 0 (pink), 18 (red), 37 (orange) and 140 µg.cm$^{-2}_{geo}$ (green). GC is displayed in grey. Currents are normalized to the geometric area of the electrode.*

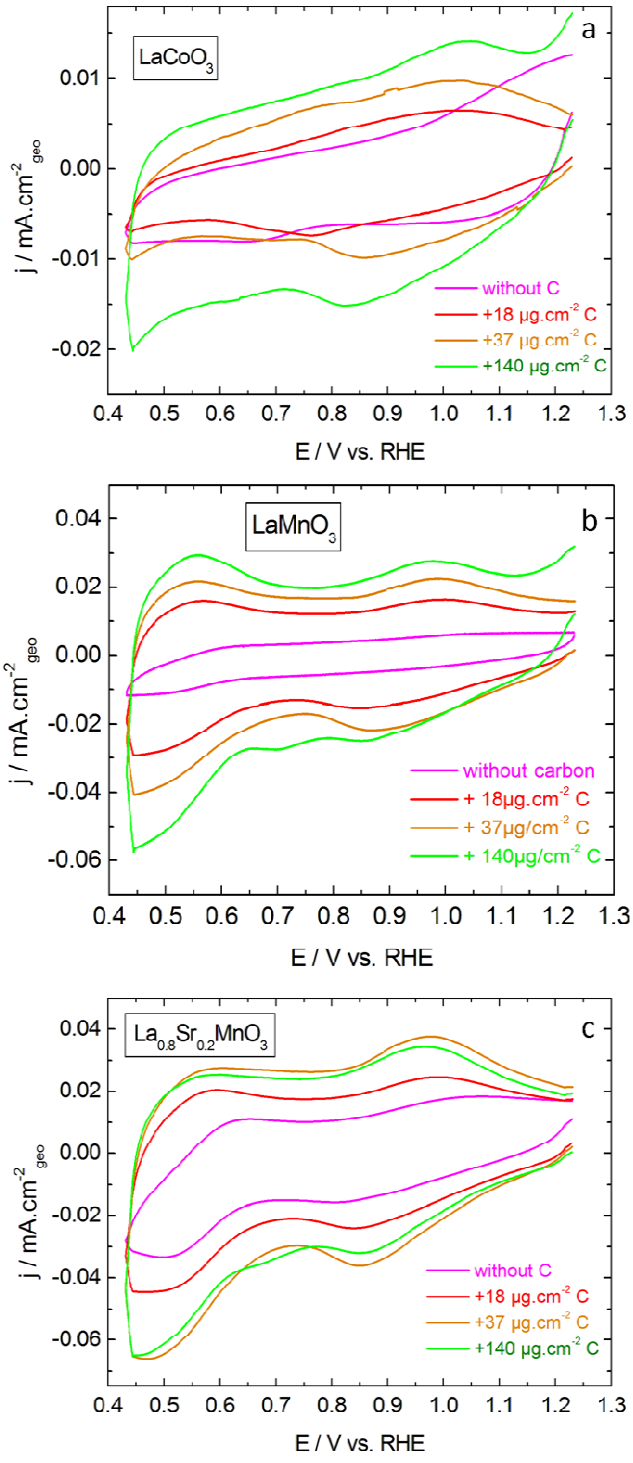

Figure 30 : *Difference voltammograms obtained by substracting CV of Sibunit carbon (*Figure 29*,a) from corresponding CV of perovskite + Sibunit carbon electrodes (*Figure 29*,,b,c,d) in N_2-purged 1M NaOH electrolyte at 10 mV.s^{-1} for (a) $LaCoO_3$, (b) $LaMnO_3$, (c) $La_{0.8}Sr_{0.2}MnO_3$. Measurements were performed with a constant amount of perovskite (91 µg.cm$^{-2}{}_{geo}$) and variable amount of Sibunit carbon. Color codes for Sibunit carbon loading: 0 (pink), 18 (red), 37 (orange) and 140 µg.cm$^{-2}{}_{geo}$ (green). Currents are normalized to the geometric area of the electrode.*

Two effects are observed with the addition of carbon to the thin film electrodes. First, the total charge under the CV increases for the three perovskites with the quantity of carbon even after subtraction of the carbon contribution. One may assume that carbon improves the contact of perovskite particles – which are agglomerated (see section 3.2.2.1) - with the current collector and thus allows higher utilization of their surface. It was noticed that even higher carbon quantities are required when perovskite powder was not ground before use, since agglomerates where even bigger. In order to quantify the improvement of the catalytic layers with the addition of carbon, the total charge was calculated by integrating the current of the corrected CV in function of the time and normalizing it by the BET surface (Table 5) and plotted versus carbon loading (Figure 31).

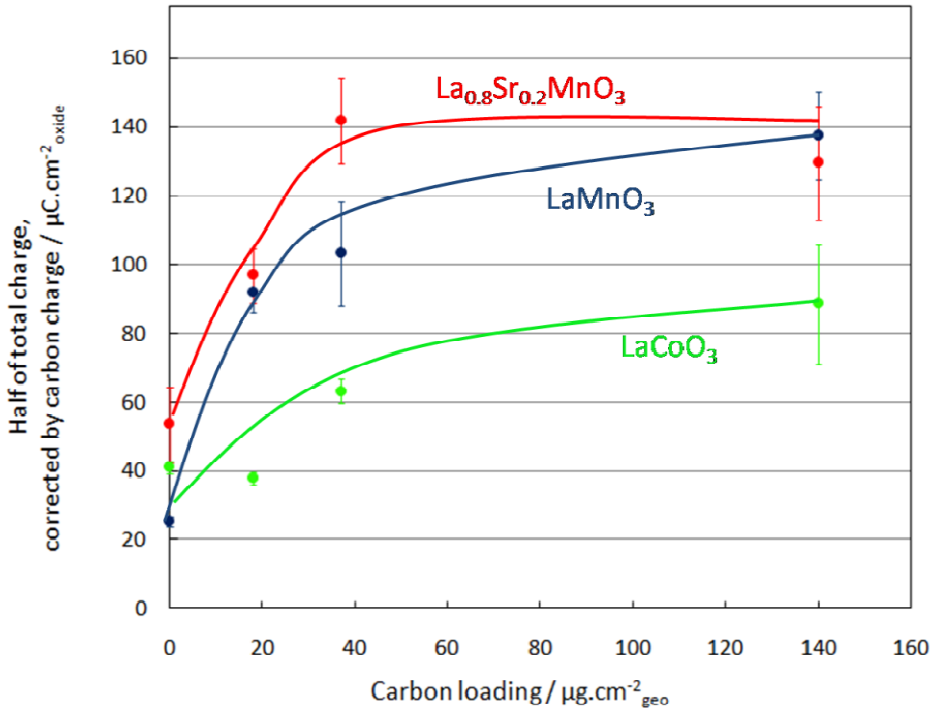

Figure 31 : *Half of the total charge calculated from difference voltammograms of perovskite + Sibunit carbon electrodes in N_2-purged 1M NaOH electrolyte at 10 mV.s^{-1}(Figure 30) and normalized by oxide surface area (Table 5), versus the carbon loading. Measurements were performed with a constant amount of perovskite (91 µg.cm$^{-2}_{geo}$) and variable amounts of Sibunit carbon. Color codes: $LaCoO_3$ (green), $LaMnO_3$ (blue), $La_{0.8}Sr_{0.2}MnO_3$ (red). Error bars represent standard deviation from at least two independent repeated measurements.*

It is clear from this figure that increasing the carbon loading leads to an increased access to the perovskite surface by at least a factor of two. For $La_{0.8}Sr_{0.2}MnO_3$, the charge seems to level off around 37 µg.cm$^{-2}_{geo}$ of carbon whereas, for $LaCoO_3$ and $LaMnO_3$, it keeps

increasing. This difference in behavior of the three studied oxides upon carbon addition is related to the oxide conductivity. Indeed, $La_{0.8}Sr_{0.2}MnO_3$ has a lower intrinsic resistivity (ca. 2 10^{-1} Ω.cm [73]) than $LaMnO_3$ (ca. 2 Ω.cm [73,75]) or $LaCoO_3$ (ca. 4 Ω.cm [75]), due to Sr doping which insures the presence of electronic and ionic defects. Therefore, the doped perovskite required less carbon to achieve sufficient layer conductivity.

In order to evaluate the amount of perovskite responsible for the electrochemical currents, the charge involved on the surface of one monolayer was approximated. The surface area of one rhombohedral unit cell is a^2, thus, according to XRD results (a is about 5.4 Å, see section 3.2.1) the surface area is ca. 30 10^{-16} cm^2. The number of surface sites in one unit cell is 1 (4 B cations which are shared between 4 unit cells). For a 1 electron transfer, i.e. for a charge exchanged of 1.6 10^{-19} C, the expected charge for one monolayer may therefore be approximated as : $\frac{1*1.6*10^{-19}}{3*10^{-15}} \approx 60\ \mu C.\ cm^{-2}$, and for a 2 electron transfer, the charge is about 120 µC.cm^{-2}. Thus, with this approximation, the measured charge indicates that one monolayer is involved in the redox transitions of $LaCoO_3$ (1 electron exchanged during the CV cycle) and of Mn-perovskites (2 electrons exchanged during the CV cycle, see section 3.3). The electrochemical processes are therefore surface rather than bulk processes, consistent with section 3.3.3.

The second effect observed with the addition of carbon is the decrease of the splitting between the anodic and the cathodic peak potentials. This suggests that the presence of carbon decreases the ohmic resistance of the layer. Indeed, although intrinsic conductivities of perovskites are relatively high, the ohmic resistance of compacted oxide powders is dominated by the contact resistance between agglomerated particles, and the presence of carbonate surface layer exacerbates this resistance. Addition of small carbon particles allows "wiring" oxide particles and improves "particle – particle" as well as "particle - current collector" electrical contact. This leads to a strong decrease of the ohmic resistance and an enhancement of the surface utilization. For example, redox peaks of $LaCoO_3$ shift by more than 100 mV when carbon is added. According to the Ohm law (Equation 72):

$$U = R_l \times I \quad \text{(Equation 72)}$$

with U, the potential shift, the layer resistance R_l was estimated to be above 100 kΩ in the CV current region (ca. 0.01 mA.cm^{-2} * 0.07 cm^2). Simultaneously, the total charge increases by more than a factor of 2 suggesting ca. twice higher utilization of the perovskite surface.

Thus, CV in supporting electrolyte confirm that, in agreement with the literature data [82,83,87-89,115], carbon is indeed required for improving the quality of the thin film

perovskite electrodes. The increase of the number of accessible active sites is expected to affect the measured catalytic activity in the ORR and will be discussed in the following sections.

4.3. RDE study in O_2-saturated electrolyte: influence of carbon/ perovskite ratio on ORR electrocatalysis

4.3.1. Influence of carbon loading

The ORR activity of $LaCoO_3$, $LaMnO_3$ and $La_{0.8}Sr_{0.2}MnO_3$ oxides was studied with various quantities of carbon (Table 8) using the RDE in O_2-saturated 1M NaOH. Different rotation rates were applied to separate kinetic from diffusion limitations. Typical anodic sweeps shown in Figure 32 for thin film RDE electrodes containing 91 $\mu g.cm^{-2}_{geo}$ perovskite and 37 $\mu g.cm^{-2}_{geo}$ carbon, other electrodes presenting similar evolution with the rotation rate. It is clear that the absolute limiting current density increases with the rotation rate, as expected from Levich thoery. However, while $LaCoO_3$ electrodes show constant kinetic current densities, it seems that the kinetic current densities of Mn-perovskites is not stable and decrease with cycles/rotation. This behavior will be studied in more detail in the stability section (see section 6.3), and will be neglected in this chapter.

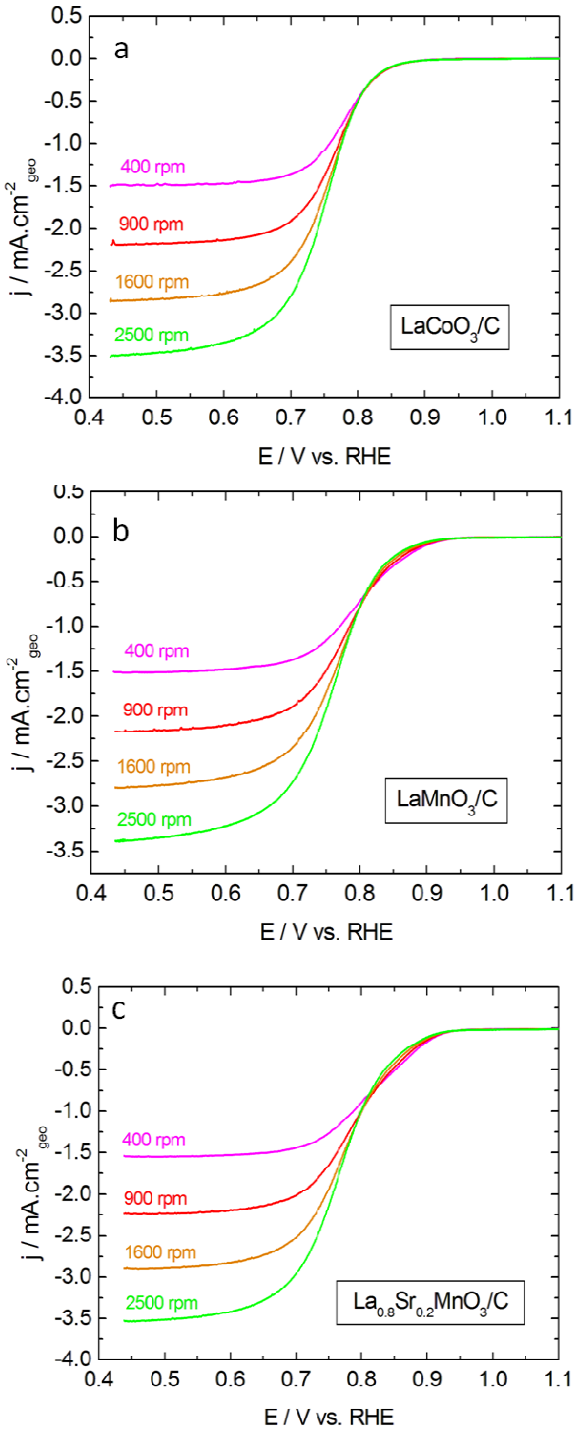

Figure 32 : *Positive scans of the RDE voltammograms of GC-supported thin films of (a) $LaCoO_3$ + Sibunit carbon, (b) $LaMnO_3$+ Sibunit carbon, (c) $La_{0.8}Sr_{0.2}MnO_3$+ Sibunit carbon, in O_2-saturated 1M NaOH electrolyte at various rotation rates and at 10 $mV.s^{-1}$. Measurements were performed with 91 $\mu g.cm^{-2}_{geo}$ perovskite and 37 $\mu g.cm^{-2}_{geo}$ Sibunit carbon. Color codes for rotation rates: 400 rpm (pink), 900 rpm (red), 1600 rpm (orange) and 2500 rpm (green). Currents are normalized to the geometric area of the electrode and corrected to the background currents measured in the N_2 atmosphere.*

Typical positive scans of the RDE voltammograms at 900 rpm for electrodes containing various quantities of carbon are shown in Figure 33 and compared with the activity of GC, Pt/C, and electrodes containing variable amounts of carbon. Only one representative curve is presented for each electrode while repeated independent experiments were performed to check the reproductibility of the results. Some of the repeated RDE voltammograms can be seen in Appendix 1 (Figure 95).

Figure 33,b,c,d indicates that electrodes containing perovskites without carbon show very low ORR onset potentials due to the insufficient access to perovskite active sites. This is especially true for $LaCoO_3$ whose onset potential is close to that of glassy carbon (Figure 33,b). Moreover, it can be observed that the ORR current densities of perovskite electrodes without carbon do not reach the diffusion limiting plateau. Similar RDE data were observed for $La_{1-x}Sr_xMnO_3$ perovskites by Tulloch et al. [85] and for $La_{0.6}Ca_{0.4}CoO_3$ perovskites by Li et al. [82] without carbon addition to the electrode layer. One may see that addition of carbon strongly increases the activity of the perovskite thin film electrodes which shows up a systematic shift of the RDE voltammograms towards positive potentials, and an increase in the absolute value of the limiting current density. Interestingly, the evolution of voltammograms is similar for composite and for pure carbon electrodes (Figure 33,a).

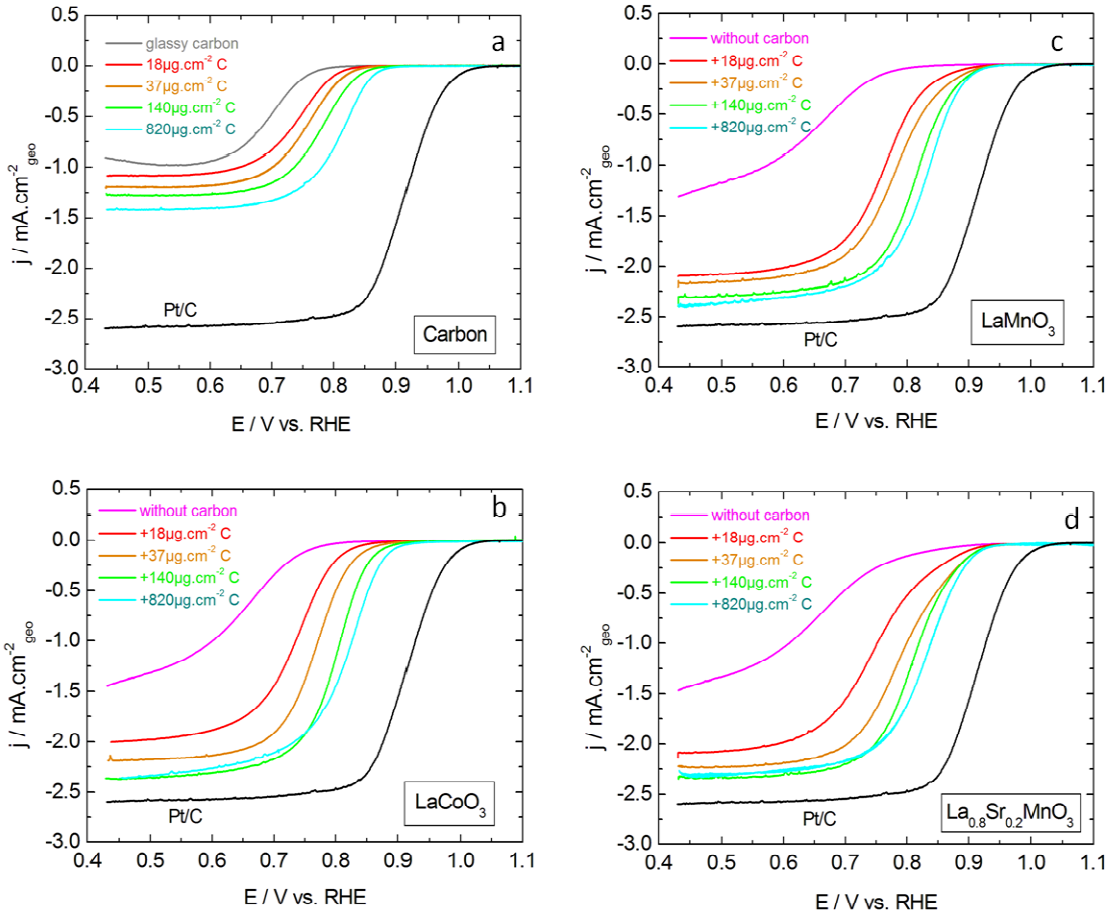

Figure 33 : *Positive scans of the RDE voltammograms of GC-supported thin films of (a) Sibunit carbon, (b) $LaCoO_3$ + Sibunit carbon, (c) $LaMnO_3$+ Sibunit carbon, (d) $La_{0.8}Sr_{0.2}MnO_3$+ Sibunit carbon, in O_2-saturated 1M NaOH electrolyte at 900 rpm and 10 $mV.s^{-1}$. Measurements were performed with a constant amount of perovskite (91 $\mu g.cm^{-2}_{geo}$), except for carbon electrodes which do not contain perovskite, and variable amount of Sibunit carbon. Color codes for Sibunit carbon loading: 0 (pink), 18 (red), 37 (orange) and 140 µg.cm-2geo (green). Grey and black lines show RDE curves for GC and Pt/C, respectively. Currents are normalized to the geometric area of the electrode and corrected to the background currents measured in the N_2 atmosphere.*

Hence, the discussion is started with the analysis of the ORR data for GC and for carbon film electrodes. This will then help in the understanding of the results for perovskite/carbon composites. For the GC electrode (Figure 33,a), one may notice a particular shape of the RDE voltammogram which shows a broad maximum around 0.55 V vs. RHE and, as discussed below, does not attain the diffusion limiting current density in the potential window studied. This was also observed by Tammeveski et al. [19,20,212] and explained by the surface functional group mediated oxygen reduction to hydrogen peroxide. The most active sites responsible for the positive onset of the ORR and the maximum in the RDE are limited in

number, and were attributed to quinone groups. The RDE shape was quantitatively modeled [20] with an EC mechanism with the first step being reversible reduction of quinone to semiquinone surface groups. The latter chemically react with molecular oxygen to form superoxide radical which is transformed into HO_2^- either in a chemical or in an electrochemical consecutive step. The onset and the shape of the RDE voltammogram thus depend on the type and the red-ox potential of active surface groups on the GC surface.

When a Sibunit carbon film is deposited on the GC electrode, the RDE curve shifts positive as expected due to the increase of the active surface area (Table 8). Then an increase of the amount of deposited carbon results in a systematic positive shift of the ORR onset and half-wave potential $E_{1/2}$ and in an increase of the absolute value of the limiting current density. The RDE voltammograms of carbon electrodes and their positive shift with an increasing amount of carbon are in agreement with the well known fact that carbon materials are active catalysts of the ORR in alkaline media [209,210].

Figure 34,a shows the Koutecky-Levich plots of the limiting current densities – at +0.5 V vs. RHE - for GC and for carbon film electrodes with various loadings. For the highest carbon loading of 820 $\mu g.cm^{-2}_{geo}$, the measured limiting current density is in reasonable agreement with the theoretical value calculated using the Levich equation with a number of electrons of 2. This is consistent with the current understanding of the ORR on carbon electrodes which predominantly proceeds to hydrogen peroxide in the investigated potential interval [20,209,213].

It should be noted however that nonzero y intercepts are observed for carbon electrodes with carbon loading below 820 $\mu g.cm^{-2}_{geo}$ as well as for GC Figure 34,a. Various reasons can be proposed to account for this phenomenon, namely (i) an inhomogeneity of the catalyst distribution on the current collector, (ii) a diffusion resistance in the ionomer film [82,88,149,154], (iii) an O_2 concentration gradient within a thick catalyst film [214,215], or (iv) a limited number of active sites leading to the adsorption limitation [215,216].

The linearity of Koutecky-Levich plots, even at high rotation rates, ensures that the characteristic size of eventual inhomogeneities of the electrode layers is inferior to the thickness of the diffusion layer, which allows to discard the first hypothesis. The apparent thickness of the ionomer film in this work was estimated as ca. 15 nm, which makes the second hypothesis very unlikely. The third option does not seem realistic either since the intercept drops down with the thickness of the carbon film. Finally, the most likely explanation of the nonzero y intercept decreasing with the film thickness is a limited number of active sites on the carbon surface. As the loading of carbon increases, the number of active

sites increases as well, and the current density attains the diffusion limiting value determined by the Levich equation. This explanation is also in agreement with the data for GC reported in this work as well as in the literature [20].

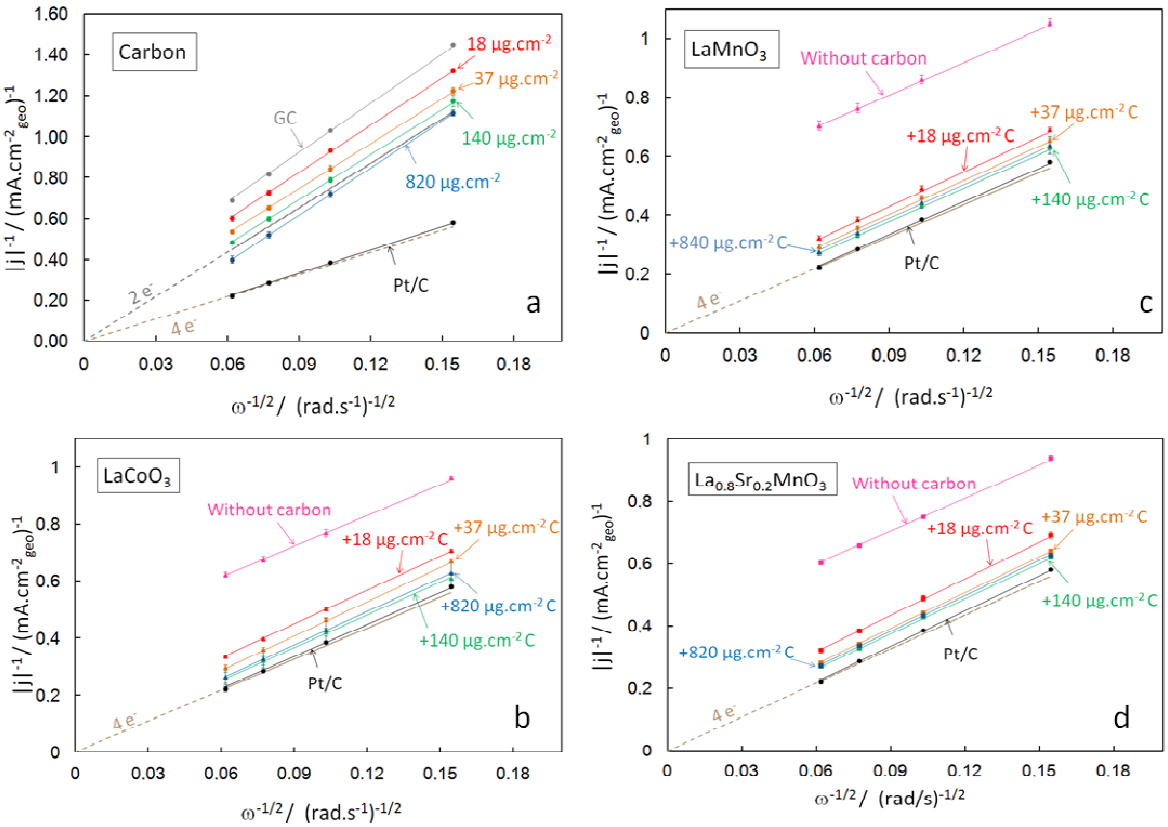

Figure 34 : *Koutecky-Levich plots of the ORR current measured at +0.5 V vs. RHE by thin layer RDE method in O_2 saturated 1M NaOH at 10 mV.s^{-1} for (a) Sibunit carbon, (b) $LaCoO_3$ + Sibunit carbon, (c) $LaMnO_3$ + Sibunit carbon and (d) $La_{0.8}Sr_{0.2}MnO_3$+ Sibunit carbon. Measurements were performed with a constant amount of perovskite (91 µg.cm$^{-2}_{geo}$) for (b), (c) and (d), and variable amount of Sibunit carbon. Color codes: 0 (pink), 18 (red), 37 (orange), 140 (green) and 820 µg cm$^{-2}_{geo}$ (light blue). Grey and black symbols stand for GC and Pt/C electrodes, respectively. Dotted lines represent theoretical current values for 2 and 4 electrons in 1 M NaOH at 25 ◦C. Currents are normalized to the geometric area of the electrode and corrected to the background currents measured in N_2 atmosphere. Error bars represent standard deviation from at least two independent repeated measurements.*

Now the discussion is turned to the analysis of the ORR on perovskite oxides. The most striking influence of the addition of perovskites to carbon is the increase of the absolute value of the limiting current density, which for perovskite/carbon composites approaches the value observed for Pt/C electrode, corresponding to the transfer of 4e-. The slopes of Koutecky-Levich plots (Figure 34,b,c,d) for perovskite-based electrodes confirm the transfer of 4e- in the overall ORR reaction. Similar numbers of transferred electrons were reported in the

literature for perovskite cathodes [82,88,103]. Contrary to carbon materials, transition metal oxides, and perovskites in particular, are known to be active catalysts of the catalytic hydrogen peroxide decomposition [121-127], as well as its electrocatalytic reduction [72,131,132]. In addition, perovskites may also be active in the first steps of the ORR by activating the O_2 molecule [72,84,85]. For a 4 electron mechanism, experimental data do not allow the clear differentiation between an OH^- transformation via intermediate HO_2^- without desorption, i.e. without possible detection by the ring of RRDE, or via the so-called "direct" $4e^-$ pathway occurring through O_2/O^{2-} splitting. Nevertheless, the "series" pathway with adsorbed HO_2^- seems to be more likely on perovskite oxides since the mechanism proposed by Suntivich et al. [84] was further validated by Wang et al. [217] using density functional theory (DFT) calculations. This will be studied in more details in section 5.

As for carbon electrodes, composite electrodes present nonzero y intercepts on the Koutecky-Levich plots (Figure 34,b,c,d). This can be due to an adsorption limitation as mentioned above, either on carbon sites or on perovskite sites since carbon addition increases the access to perovskite sites. Moreover, the hypothesis of an O_2 concentration gradient in the catalyst film can be reasonable in this case. Indeed, for perovskite electrodes with carbon loading higher than 140 $\mu g.cm^{-2}_{geo}$, the absolute value of the limiting current density does not increase with the electrode thickness anymore, in agreement with [214].

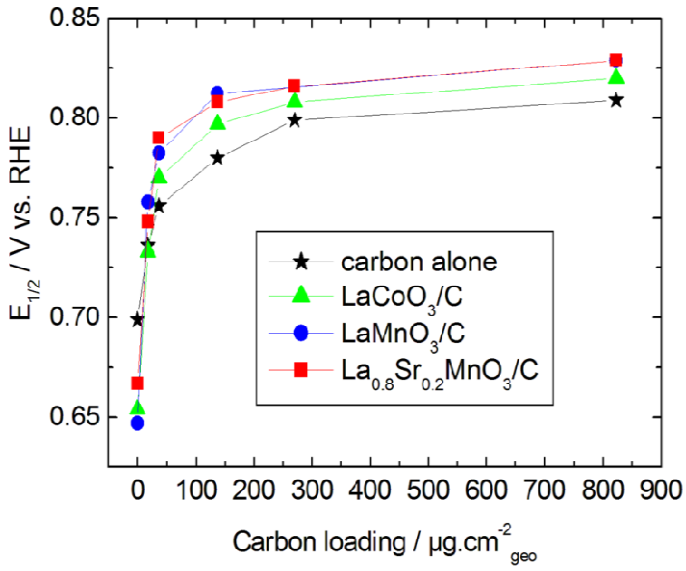

Figure 35 : *ORR halfwave potential of RDE voltammograms at 900 rpm (*Figure 33*) of GC-supported perovskite/carbon thin films in O_2-saturated 1M NaOH electrolyte. Color codes: Sibunit carbon (black stars), electrodes with 91 $\mu g.cm^{-2}_{geo}$ $LaCoO_3$ + Sibunit carbon (green triangles), electrodes with 91 $\mu g.cm^{-2}_{geo}$ $LaMnO_3$ + Sibunit carbon (blue circles) and electrodes with 91 $\mu g.cm^{-2}_{geo}$ $La_{0.8}Sr_{0.2}MnO_3$ + Sibunit carbon (green).*

In order to better understand the observed behavior with carbon addition, the evolution of the half-wave potential $E_{1/2}$ for composite electrodes and for the electrodes containing carbon alone were compared. Figure 35 shows $E_{1/2}$ versus the carbon loading. First of all, these results indicate that Mn-perovskites have higher mass activities in the ORR compared to $LaCoO_3$. Then, it can be observed that the three perovskites present higher half-wave potentials than carbon alone, but the evolution with the carbon quantity is similar to that observed for pure carbon. Moreover, while the maximum difference of $E_{1/2}$ for pure perovskites and composite electrodes amounts to more than 250 mV, the difference between $E_{1/2}$ for pure carbon and composites reaches at most 37 mV for $La_{0.8}Sr_{0.2}MnO_3$ with 37 $\mu g.cm^{-2}_{geo}$ carbon, and 33 mV for $LaMnO_3$ and 18 mV for $LaCoO_3$ with 140 $\mu g.cm^{-2}_{geo}$ carbon. This confirms that the carbon contribution to the ORR on composite perovskite / carbon electrodes cannot be neglected.

4.3.2. Influence of perovskite loading

In order to better understand the role of perovskite oxides in the ORR, electrodes with a constant amount of carbon (37 $\mu g.cm^{-2}_{geo}$) and various quantities of perovskites (Table 9) were studied (Figure 36).

Table 9 : *Loading, roughness factors and estimated thickness of RDE thin layers with constant carbon loading*

Electrodes	**Constant carbon loading**			
Perovskite loading ($\mu g.cm^{-2}_{geo}$)	0	46	91	180
Carbon loading ($\mu g.cm^{-2}_{geo}$)	37	37	37	37
Content of perovskite in the composite (wt%)	0	56	71	83
Estimated layer thickness (μm)	0.9	1.6	2.3	3.7

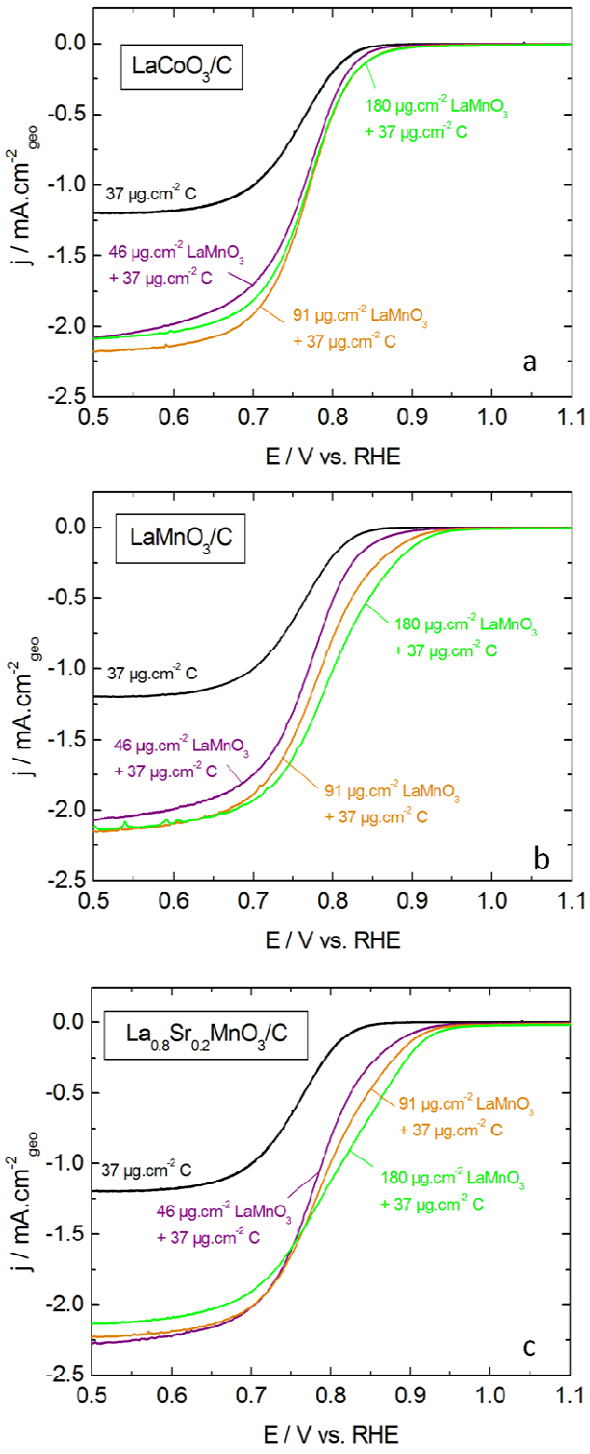

Figure 36 : *Positive scans of the RDE voltammograms of GC-supported thin films of (a) $LaCoO_3$ + Sibunit carbon, (b) $LaMnO_3$ + Sibunit carbon, and (c) $La_{0.8}Sr_{0.2}MnO_3$ + Sibunit carbon in O_2-saturated 1 M NaOH at 900 rpm and 10 $mV.s^{-1}$. Measurements were performed with a constant amount of Sibunit carbon (37 $\mu g.cm^{-2}_{geo}$) and variable amount of perovskite. Color codes for perovskite loading: 0 (black), 46 (purple), 91 (orange), 180 $\mu g.cm^{-2}_{geo}$ (green). Currents are normalized to the geometric area of the electrode and corrected to the background currents measured in N_2 atmosphere.*

The results displayed in Figure 36,a suggest that an addition of 46 $\mu g.cm^{-2}_{geo}$ $LaCoO_3$ to the carbon electrode results in doubling the ORR current density in the kinetic and mixed region, while further increase of the $LaCoO_3$ loading to 91 and then 180 $\mu g.cm^{-2}_{geo}$ leads to a marginal increase of the current density in the kinetic and mixed region. Such a behavior is consistent with an increase of the rate constant of the chemical disproportionation step as shown by the modeling work of Jaouen [214]. The catalytic activity of perovskites in the HO_2^- disproportionation has been demonstrated in numerous publications [121-127]. One should note however that the same effect is expected if $LaCoO_3$ were active in the electrochemical HO_2^- reduction. This suggests that once HO_2^- is produced on the carbon component of a composite electrode, the role of $LaCoO_3$ is largely reduced to the catalysis of HO_2^- transformations, either in the chemical disproportionation or in the electrochemical reduction reaction. More detailed mechanistic studies are required to differentiate between these possibilities and will be performed in the next chapter (see section 5). Therefore, for $LaCoO_3$/carbon composites, the first steps of the ORR are mainly electrocatalyzed by carbon. This is in part due to the lower specific surface area of $LaCoO_3$ compared to carbon (Table 8), and in part due to its fairly low specific ORR electrocatalytic activity [91,92]. Experiments were also performed by replacing the usual Sibunit carbon (S_{BET} = 65.7 $m^2.g^{-1}$) by a Sibunit carbon with lower specific surface area (S_{BET} = 6 $m^2.g^{-1}$) to diminish differences in surface area between the perovskite and the carbon. The results are presented in (Figure 37). Identical effect – current of $LaCoO_3$/carbon composites equal to the double of current of carbon alone – was observed, confirming the low activity of $LaCoO_3$ for O_2 activation.

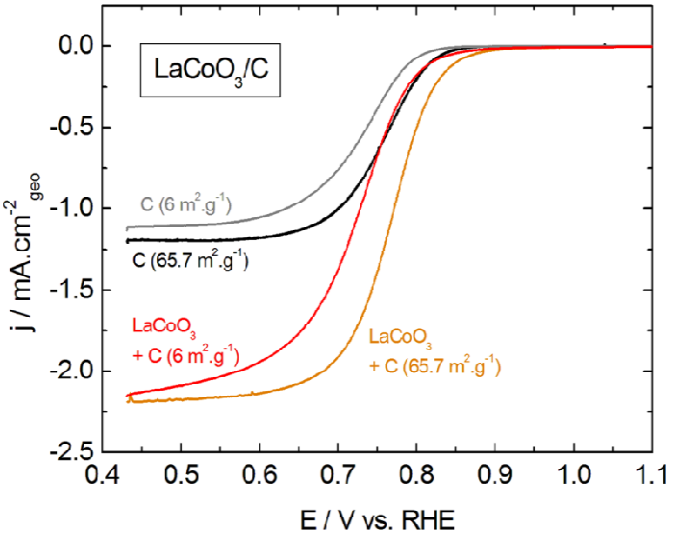

Figure 37 : *Positive scans of the RDE voltammograms of GC-supported thin films of $LaCoO_3$ + Sibunit carbon in O_2-saturated 1 M NaOH at 900 rpm and 10 mV.s^{-1}. Measurements were performed with 91 µg.cm$^{-2}_{geo}$ perovskite and 37 µg.cm$^{-2}_{geo}$ Sibunit carbon of various surface area. Color codes: Sibunit carbon 65.7 m^2.g^{-1} (black), Sibunit carbon 6 m^2.g^{-1} (grey), $LaCoO_3$ + Sibunit carbon 65.7 m^2.g^{-1} (orange), $LaCoO_3$ + Sibunit carbon 6 m^2.g^{-1} (red). Currents are normalized to the geometric area of the electrode and corrected to the background currents measured in N_2 atmosphere.*

The composite electrode may thus be considered as a bifunctional catalyst with carbon catalyzing the ORR into HO_2^-, and perovskite catalyzing further HO_2^- chemical / electrochemical transformations. Ultimately, O_2 on a composite electrode is reduced to OH^-, while carbon alone is only capable to support the reduction to HO_2^-. Similar mechanism was proposed for $La_{0.6}Ca_{0.4}CoO_3$ [82,90,133], for $LaNiO_3$ [88], for $CoFe_2O_4$ [218] and for MnO_x [36,37] in oxide/carbon composite electrodes. However, unlike this work, the oxide to carbon ratio was not varied systematically in the mentioned studies, the assumptions being based on the ORR activities of only one amount of oxide and carbon.

Very recently, after publication of our results [211], the bifunctionnal behavior of perovskite/carbon electrodes was confirmed by Malkhandi et al. [219]. The authors studied the ORR activities of various composite electrodes containing (i) different perovskite to carbon ratio, (ii) different conductive additives including various carbon materials and gold nanoparticles, (iii) oxides containing different transition metals. First of all, it was observed that the ORR activity of perovskite is significantly increased with the addition of carbon, in agreement with the present thesis. By varying the nature of the conductive additives, it was

demonstrated that the role of carbon is not limited to the improvement of electrical contact but also includes an active participation of carbon in the ORR. Indeed, the addition of gold nanoparticles – less active for the ORR but highly conductive - does not lead to an enhancement of the ORR activity while carbon does. The authors concluded, with the help of an RRDE study of the ORR and study of HO_2^- reduction and decomposition reactions for various electrode compositions, that oxygen is reduced into HO_2^- on carbon sites, and HO_2^- is further decomposed on a perovskite.

For $LaMnO_3$ and $La_{0.8}Sr_{0.2}MnO_3$, the behavior is quite different (Figure 36,b,c). The RDE curve is shifted more positive compared to carbon and $LaCoO_3$, and the increase of the amount of perovskite has a pronounced influence on the ORR onset. Similar behavior was observed for $LaMnO_3$ in literature [83,87]. This may be attributed to the contribution of Mn-perovskites to the first steps of the ORR. It can also be noticed that both Mn-perovskites, and in particular $La_{0.8}Sr_{0.2}MnO_3$, show a significant modification of the RDE shape with the perovskite/carbon ratio (Figure 36,b,c). At high potentials, ORR occurs on Mn-perovskite sites while at lower potentials, ORR is predominantly catalysed on carbon sites. Thus the modification of the RDE shape is most probably linked to the percentage of carbon contribution in the ORR. For low perovskite loadings, the surface area of carbon is larger than the one of perovskite (Table 8). It is therefore reasonable to imagine that a large amount of O_2 molecules are reduced on carbon sites rather than on perovskite sites, and conversely for electrodes with high perovskite loadings. Differences between $LaMnO_3$ and $La_{0.8}Sr_{0.2}MnO_3$ can then either be related to the specific surface area of the perovskite - $La_{0.8}Sr_{0.2}MnO_3$ has a higher BET surface area – or to the perovskite activity for the O_2 activation.

4.4. How to evaluate the intrinsic electrocatalytic activity of perovskite in perovskite/carbon composites?

4.4.1. Subtraction of carbon contribution

The above discussion shows that carbon actively participates in the ORR on perovskite/carbon composites. Thus, the ORR on the carbon and the oxide components must be considered as coupled (or tandem) reactions. Depending on the catalytic activity of perovskite materials in the various steps of the multistep ORR mechanism, different mechanisms may be expected. This poses problems for the evaluation of the intrinsic electrocatalytic activity of perovskites. In the literature, the participation of carbon in the ORR on perovskite/carbon composites is often neglected and the specific ORR activity may be calculated by normalizing the kinetic current to the surface area of a perovskite material [84,103]. However, this work demonstrates that the contribution of carbon to the ORR cannot be ignored.

In case of a minor coupling of reactions on oxide and on carbon, the contribution of the latter could be removed by subtracting the ORR current measured on pure carbon electrodes. In order to elucidate the applicability of such an approach to carbon/perovskite composites, the following procedure was employed. In the first place, kinetic currents I_k were calculated by performing the mass transport correction (Equation 38) to the ORR faradaic currents, obtained from capacity-corrected positive-going RDE scans. Considering that diffusion limited currents are accessible only for some samples, the theoretical values of I_D (normalized to the geometric surface area) of 2.71 and 1.36 $mA.cm^{-2}_{geo}$ were applied for the four and two electron reactions, respectively. Then, the current density of the ORR on perovskites j_k^p was calculated by using (Equation 73):

$$j_k{}^p = \frac{(I_k{}^{p+c} - I_k{}^c)}{A_{BET}{}^p} \quad \text{(Equation 73)}$$

Here I_k^{p+c} is the kinetic current of perovskite/carbon composite determined using (Equation 38), I_k^c is the corresponding kinetic current of carbon alone determined for the same quantity

of carbon, and A_{BET}^{p} is the surface area (in cm^2_{oxide}) of perovskite calculated from the BET data (Table 5). Tafel plots calculated with the said procedure for composites and Tafel plots for pure carbon normalized to the carbon surface area are presented in Figure 38.

It can be observed that Tafel plots for carbon electrodes in the interval of loadings from 18 to 140 $\mu g.cm^{-2}_{geo}$ are almost superposed (Figure 38,a). Glassy carbon shows slightly higher kinetic current densities, which is probably due to an underestimation of its active surface area that was assumed to be equal to the geometric area. The electrode with the highest amount of carbon presents slightly lower current densities than other carbon electrodes. This can be explained by (Equation 74):

$$I_k = I_k^{th} * u_f \quad \text{(Equation 74)}$$

with I_k^{th}, the kinetic current without mass-transport or ohmic limitations in the layer, and u_f the utilization factor [220]. For thin layers, the utilization factor is equal to 1. For thick layers however, it is inferior to 1, due to the mass transport hindrance of oxygen molecules within the catalytic layer [3,215,220].

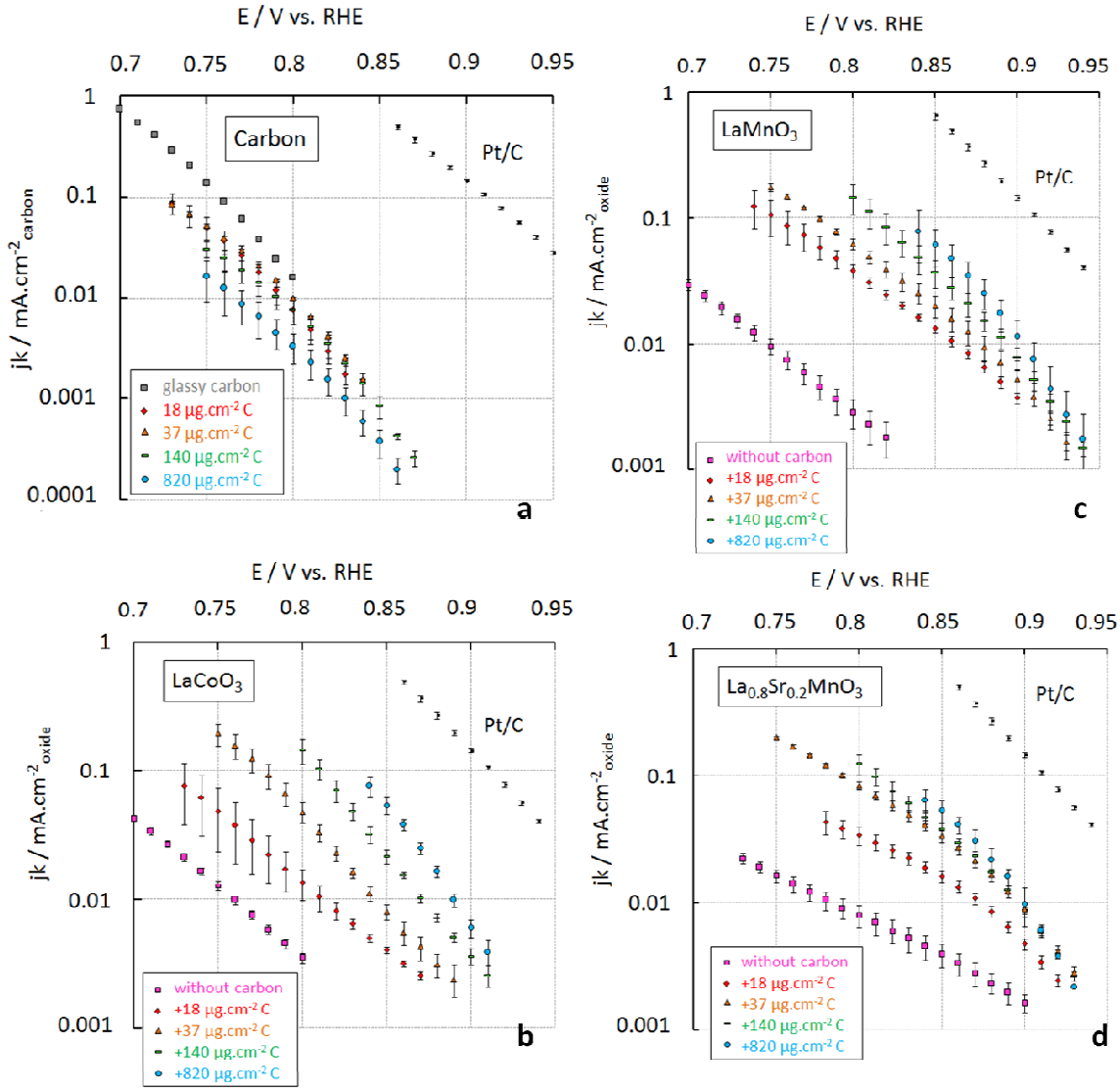

Figure 38 : *Tafel plots from mass-transport corrected positive-going scans of GC supported thin film RDE in O_2-saturated 1 M NaOH at 10 mV.s^{-1}. (a) Sibunit carbon, (b) $LaCoO_3$ + Sibunit carbon, (c) $LaMnO_3$ + Sibunit carbon, (d) $La_{0.8}Sr_{0.2}MnO_3$ + Sibunit carbon. Measurements were performed with a constant amount of perovskite (91 µg.cm$^{-2}_{geo}$) for (b), (c) and (d), and variable amounts of carbon. Color codes: 0 (pink squares), 18 (red diamonds), 37 (orange triangles), 140 (green rectangles) and 820 µg.cm$^{-2}_{geo}$ (light blue circles). Grey symbols stand for the GC electrode, while black for the Pt/C electrode. Error bars represent standard deviation from at least two independent repeated measurements. Currents are normalized to the specific surface area of carbon for carbon electrodes, to the BET surface area of perovskites after subtraction of the kinetic ORR current on carbon for composite electrodes, to the platinum electrochemical active surface area for Pt/C, and to the geometric surface area for GC.*

For $LaCoO_3$, Tafel plots with various amounts of carbon are not superposed (Figure 38,b). Indeed, it is observed that the higher the quantity of carbon added to the composite electrode, the higher is the kinetic current density. It is instructive to compare the degree of the kinetic

current density enhancement with the increase of the charge which is proportional to the number of accessible active sites, shown in Figure 31. For example, an increase of the amount of carbon from 18 to 140 $\mu g.cm^{-2}_{geo}$ leads to ca. factor of 2 enhancement of the total charge and ca. factor of 10 increase of the kinetic current density at +0.8 V vs. RHE. In agreement with the discussion above, this confirms that the role of carbon extends beyond the improvement of the layer conductivity, and involves also its active participation in the mechanism of the catalytic ORR reduction. This suggests that subtracting the ORR current in the absence of perovskite (Equation 73) does not allow to properly account for the carbon contribution.

In the case of $La_{0.8}Sr_{0.2}MnO_3$ (Figure 38,d), for electrodes containing more than 29% of carbon (37 $\mu g.cm^{-2}_{geo}$), Tafel plots are almost superposed confirming, on the one hand, that this amount of carbon is sufficient to achieve a good electrical contact between $La_{0.8}Sr_{0.2}MnO_3$ particles, and, on the other hand, that the catalytic activity of this perovskite material in the electrochemical ORR is much superior of that of carbon.

$LaMnO_3$ electrodes display an intermediate behavior (Figure 38,c). In the presence of carbon, their kinetic current densities are dependent on the carbon loading, but less significantly than for $LaCoO_3$ electrodes. This can either be due to a participation of carbon in the ORR mechanism or to a non sufficient electrical contact. Indeed, the strong difference between electrodes with carbon and electrodes without carbon suggest a low conductivity of this perovskite.

Convergence of Tafel plots for $La_{0.8}Sr_{0.2}MnO_3$ at high carbon loadings and high overpotentials indicates that (Equation 73) may be applied for estimating the intrinsic catalytic activity of this oxide material for a certain range of carbon/perovskite ratios. However, this conclusion cannot be generalized to all types of perovskite/carbon composite electrodes since, as discussed above, a mechanism consisting of carbon catalyzed reduction of O_2 into HO_2^- followed by a perovskite catalyzed HO_2^- transformation would also be able to account for a significant positive shift of the onset of the ORR even if the oxide were inactive for the ORR electrocatalysis.

4.4.2. ORR activity: function of oxide nature and composition

4.4.2.1. Role of B cation in the ORR activity

For each electrode composition, Mn-perovskites are more active than $LaCoO_3$, as seen from ORR mass activities (Figure 35). For example, at the typical benchmark condition of 0.9 V vs. RHE [3], and for an electrode containing 60% of carbon (140 $\mu g.cm^{-2}_{geo}$), the current density is 3.6, 7.7 and 8.7 $\mu A.cm^{-2}_{oxide}$ for $LaCoO_3$, $LaMnO_3$ and $La_{0.8}Sr_{0.2}MnO_3$, correspondingly. These values can hardly be compared to the data from the literature for several reasons: (i) the mass transport correction is not always performed [72,73,95,100,101,172], (ii) the quantity and the type of carbon in the composite electrodes, if any, is not always similar to the one used in the present work [82,84,89,95,100,101] and it was shown in this study that it has a strong influence on ORR activities, (iii) contribution of carbon support is never substracted to the activity of the composite electrodes [82,84,89,95,100,101], and (iv) the kinetic currents are sometimes not normalized to the oxide surface area, and the latter is not always precisely measured. Therefore, it is only possible to compare electrodes without carbon to the literature.

Without carbon, the current density at 0.9 V vs. RHE is 1.6 $\mu A.cm^{-2}_{oxide}$ for $La_{0.8}Sr_{0.2}MnO_3$, while Bockris et al. [74] found around 0.1 $\mu A.cm^{-2}_{oxide}$ for $La_{1-x}Sr_xMnO_3$ pellets (~0.1 $mA.cm^{-2}_{electrode}$ with a reported roughness factor ~10^3 $cm^2_{oxide}/cm^2_{electrode}$). Differences are probably related to the ohmic resistance and to the mass transport losses in the pellets, and show that the thin film approach based on the application of oxide/carbon composite layers leads to a better utilization of the surface of oxide particles. Tulloch et al. studied ORR activities of thin layers of $La_{1-x}Sr_xMnO_3$ without carbon and measured a current density of ca. 10 $\mu A.cm^{-2}_{oxide}$ at 0.9 V vs. RHE for $La_{0.8}Sr_{0.2}MnO_3$. This value is somewhat higher than the activity measured in this work. However, these authors also found strong differences (more than one order of magnitude) between doped and non-doped Mn-perovskites [85]. This is not in agreement with this work, neither with other publications [73,172,221] in which $La_{1-x}Sr_xMnO_3$ perovskites with x below 0.2 display close activities.

The Tafel slopes in $mV.decade^{-1}$ were calculated from Tafel plots (Figure 38) and are presented in Table 10 for various composite electrodes.

Table 10 : *Tafel slopes calculated from Tafel plots (Figure 38) of GC supported thin film RDE in O_2-saturated 1 M NaOH at 10 mV.s^{-1}. Measurements were performed with a constant amount of perovskite (91 µg.cm$^{-2}_{geo}$) except for carbon electrodes which do not contain perovskite, and variable amounts of carbon. η stands for overpotential.*

Electrodes	**Electrode composition and corresponding Tafel slopes**				
Carbon loading (µg.cm$^{-2}_{geo}$)	0	18	37	140	820
Carbon electrodes Tafel slope (mV.decade^{-1})	-59 (GC)	-80 (high η) -51 (low η)	-71 (high η) -49 (low η)	-78 (high η) -53 (low η)	-69 (high η) -48 (low η)
$LaCoO_3$ electrodes Tafel slope (mV.decade^{-1})	-91	-93	-69	-62	-53
$LaMnO_3$ electrodes Tafel slope (mV.decade^{-1})	-97	-106	-103 (high η) -69 (low η)	-81 (high η) -57 (low η)	-71 (high η) -48 (low η)
$La_{0.8}Sr_{0.2}MnO_3$ electrodes Tafel slope (mV.decade^{-1})	-153	-150 (high η) -75 (low η)	-125 (high η) -67 (low η)	-95 (high η) -60 (low η)	-81 (high η) -46 (low η)

For the glassy carbon support, a Tafel slope of 60 mV.decade^{-1} is measured. This value is consistent with Tammeveski et al. [20]. Thanks to the grafting of quinone groups on the GC surface and with the help of mathematical modeling, the authors attributed this slope to the EC mechanism with the first step being the reversible one electron reduction of quinone to semiquinone. These semiquinone species further react with oxygen to form adsorbed superoxide radical through a slow chemical step.

For Sibunit carbon electrodes, the Tafel slope is ca. 50 mV.decade^{-1} at low overpotentials and ca. 70/80 mV.decade^{-1} at high overpotentials. The slopes at low overpotentials are similar to those measured for other types of carbon (Vulcan XC72R and Chezacarb SH) in alkaline solutions by Moureaux et al. [38]. But, as reported in section 1.2.2.2, there is no general agreement on the rate determining step of the ORR on carbon materials.

$LaCoO_3$ electrodes display Tafel slopes of ca. -90 mV.decade^{-1} for electrodes without carbon and with low quantities of carbon, and of ca. -60 mV.decade^{-1} with higher carbon quantities. This is in very good agreement with Malkhandi et al. [219] and with Li et al. [82] who studied Co-based perovskites. The authors suggested that the rate determining step is the first electron transfer between the adsorbed species $O_{2,ads}$ and $O_{2,ads}^-$ on carbon sites in the presence of carbon or on perovskite sites in the absence of carbon. In parallel, similar Tafel slopes (-60 mV.decade^{-1}) were also observed for ORR on various perovskite/carbon electrodes – including $LaMnO_3$/C and $LaCoO_3$/C - by Suntivich et al. [103]. These authors attributed this slope to the slow replacement of OH_{ads} by $O_{2,ads}^-$ species accompanied by the oxidation of B cation.

At low overpotentials and with high amounts of carbon, Mn-perovskites also display Tafel slopes of ca. -50/-60 mV.decade^{-1}. This is consistent with the work of Suntivich et al. [103] mentioned above and it is also in agreement with literature data on Mn oxides [33-35,199,222]. Nevertheless, the mechanism responsible for this slope on Mn oxides is unclear. On the one hand, from the slope dependence on pH and on the oxygen partial pressure, Cao et al. [34] and Roche et al. [33] proposed that the ORR on MnO_x electrodes is a direct 4 electron pathway with the intervention of the redox couple Mn^{4+}/Mn^{3+} in the ORR mechanism and a one electron transfer as a rate determining step. However, the authors disagree on the nature of this step. Roche et al. mentioned the electrosplitting of O_2 adsorbed species as the slowest step, while Cao et al. suggested that the rate determining step is OH^- formation from adsorbed O^- species and Mn oxidation. Besides, Su et al. [223] performed DFT calculations on Mn oxides and demonstrated that the theoretical rate determining step for a direct ORR mechanism is the reduction of adsorbed OH into OH^- species. On the other hand, Lima et al. [35,199] combined *in-situ* XANES with an ORR study and concluded that the ORR on MnO_x electrode is a "series" pathway with the rate determining step being the reversible redox transition of Mn^{4+} into Mn^{3+} followed by a slow electron transfer between Mn cations and $O_{2,ads}$.

One should note that, despite the disagreement on the ORR mechanism, the quoted authors proposed that O_2 reacts with Mn^{3+}. This is consistent with the work of Stoerzinger et al. [221] who, by comparing the ORR activities of nanometer thin films of single crystal of $LaMnO_3$, $La_{0.67}Sr_{0.33}MnO_3$ and $CaMnO_3$, found that the ORR active site is Mn^{3+}.

In the present work, for Mn-perovskite electrodes with high amounts of carbon, the Tafel slope at high overpotentials is lower than that at low overpotentials. This suggests that the rate

determining step is different in the two potential regions. Although the reasons of the presence of these two disctinct Tafel slopes are not understood yet, it can be mentioned that this may result from (i) potential dependent kinetic constants, (ii) activation/deactivation of perovskite sites with the potential, (iii) contribution of carbon in the ORR kinetics in a given potential window. The latter is supported by the fact that different Tafel slopes are obtained for the electrodes with various carbon loadings. For low carbon loadings and without carbon, the lower Tafel slopes may indicate a lower participation of carbon in the ORR, or the effect of a poor electrical contact in the catalytic layer. Indeed, it can be supposed that without carbon in the layer, the electron transfer is slower and the redox transitions are irreversible.

4.4.2.2. Role of A cation in the ORR activity

It was observed that the choice of the B cation is significant for ORR activities of La-based perovskites, in agreement with Bockris et al. [74]. In order to investigate the role of the A cation in this ORR electrocatalysis, the perovskites $PrCoO_3$, $PrMnO_3$ and $La_{0.8}Ca_{0.2}MnO_3$ were investigated with an intermediate amount of carbon (37 $\mu g.cm^{-2}_{geo}$). The obtained RDE voltammograms and carbon corrected Tafel plots are presented in Figure 39.

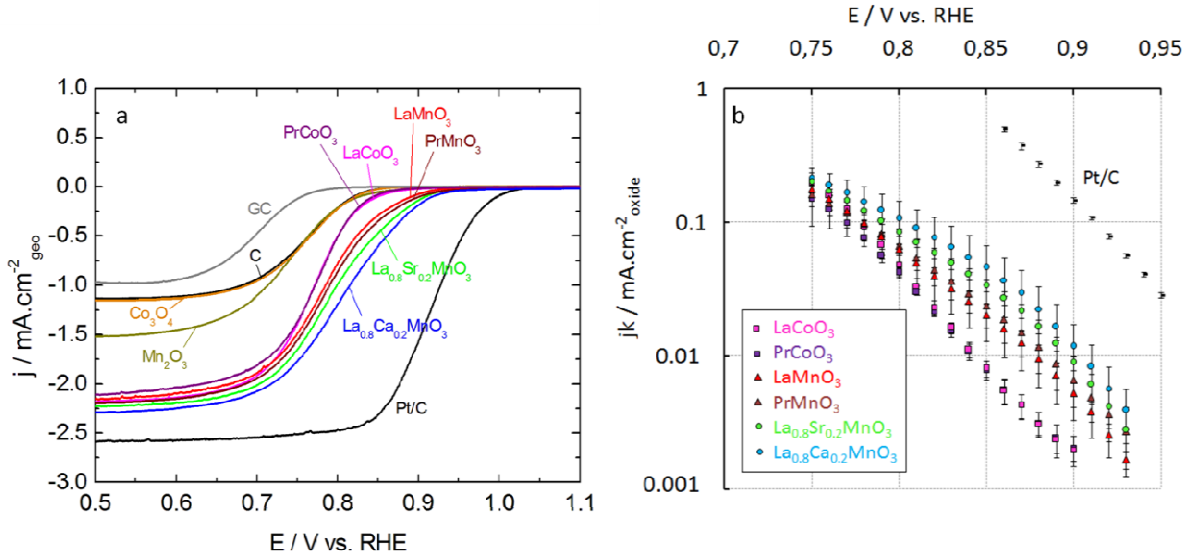

Figure 39 : *(a) Positive scans of the RDE voltammograms and (b) Tafel plots from mass-transport corrected positive-going scans of GC-supported thin films of oxide + Sibunit carbon in O_2-saturated 1M NaOH electrolyte at 900 rpm and 10 mV.s^{-1}. Measurements were performed with 91 µg.cm$^{-2}_{geo}$ oxide + 37 µg.cm$^{-2}_{geo}$ Sibunit carbon. Color codes: $LaCoO_3$ + Sibunit carbon (pink), $PrCoO_3$+ Sibunit carbon (purple), $LaMnO_3$ + Sibunit carbon (red), $PrMnO_3$ + Sibunit carbon (brown) $La_{0.8}Sr_{0.2}MnO_3$ + Sibunit carbon (green) and $La_{0.8}Ca_{0.2}MnO_3$ + Sibunit carbon (blue). Grey and black lines show RDE curves for GC and Pt/C, respectively. Black symbols on Tafel plots stand for the Pt/C electrode. RDE currents are normalized to the geometric area of the electrode and corrected to the background currents measured in the N_2 atmosphere. Kinetic currents of Tafel plots are normalized to the BET surface area of perovskites after subtraction of the kinetic ORR current on carbon for perovskite electrodes, and to the platinum electrochemical active surface area for Pt/C. Error bars represent standard deviation from at least two independent repeated measurements.*

From this figure, it is observed that the voltammogram shapes and the onset potentials as well as the kinetic current densities and the Tafel slopes seem to be significantly dependent of the nature and the oxidation state of the B cation. Indeed, there is stong similarity between non doped Co-perovskite ($LaCoO_3$ and $PrCoO_3$), non doped Mn-perovskites ($LaMnO_3$ and $PrMnO_3$) and doped Mn-perovskites ($La_{0.8}Sr_{0.2}MnO_3$ and $La_{0.8}Ca_{0.2}MnO_3$), respectively. Independently of the nature of A cation and a fortiori of the structure symmetry, Mn-perovskites display higher ORR activities than Co-perovskites. It should be noted that all Mn-perovskites demonstrate more pronounced voltammetric peaks than Co-perovskites in the potential interval of interest on CV in N_2-purged electrolyte (Figure 26), so their higher ORR activity might be due to easier redox transition of the oxide itself (see section 4.4.2.1). It can also be related to the higher amount of carbonates species on surface of Co-perovskites than on Mn-perovskites (see section 3.2.4.3).

One may notice that the specific ORR activities of perovskite-based electrodes are still inferior (ca. one order of magnitude) to the activity of the state of the art Pt/C catalyst, the latter reaching 150 $\mu A.cm^{-2}_{Pt}$ at 0.9V vs. RHE (Figure 39) – close to the value obtained in the same media for Pt/C (40% Pt) by Genies et al. [12]. It should be noted however that, contrary to noble metals, the loading of which is constrained by the cost considerations, the loading of non-precious metal oxide catalysts is only limited by the thickness constraints because of the decline of the utilization factor caused by ohmic and mass transport limitations in thick layers [3,215,220]. Thus, to compensate the lower specific activity, one may envisage higher loadings of metal oxide catalysts. Also, it will be interesting to increase the surface area of the catalysts to get high activities with low loadings. Moreover, it is expected that fine tuning of the perovskite composition will in the future allow to significantly increase the specific activity of this promising class of materials [84].

4.4.2.3. Role of oxide structure in the ORR activity

The perovskites oxides were also compared to the simple oxides Co_3O_4 and Mn_2O_3 to investigate the importance of the perovskite structure on the ORR activities (Figure 39).

As observed on CV in N_2-purged electrolyte (Figure 26), the currents displayed by these electrodes are very low compared to carbon electrodes. This is attributed on the one hand to low oxide conductivity of these oxides. Indeed, the resistivity at 25°C of Mn_2O_3 was reported to be ca. 10^5 Ω.cm [205], and that of Co_3O_4, ca. 10^4 Ω.cm [204], i.e. a conductivity around four orders of magnitude below that of perovskite oxides. On the other hand, the observed low activity of simple oxides may be due to their low specific surface area (BET of ca. 2 $m^2.g^{-1}$) compared to carbon. It is clear from RDE voltammograms that these simple oxides have lower activity than Sibunit carbon for O_2 reduction into HO_2^-. Tafel plots can therefore not be calculated by substracting carbon activity.

Whereas Co_3O_4 does not lead to any additional current compared to carbon, Mn_2O_3 electrodes show cathodic current at low potential values. From Koutecky-Levich plots (not shown), it was found that about 3.5 electrons were exchanged on Mn_2O_3/carbon electrodes. This suggests that Mn_2O_3 can transform HO_2^- in OH^-, either through a chemical disproportionation or through an electrochemical reduction, contrary to carbon. This conclusion is in agreement with the literature on Mn oxides [32,36,37,39,222,224-226].

As simple oxide studied in this work consists of larger particle agglomerates than perovskite oxides (see section 3.2.2.1), one may suggest that selection of a more appropriate quantity and type of carbon might improve the oxide layer conductivity and lead to higher currents. Even more promising is the utilization of carbon-supported nanosized oxide particles. For example, Liang et al. [30] reported enhanced ORR activities for grapheme supported Co_3O_4 nanocrystals (see section 1.2.2.3.1).

4.5. Conclusions of Chapter 4

This work shows that carbon is required in the catalytic layers containing perovskite oxides in order to achieve high ORR activity and that perovskite/carbon electrodes catalysed a overall 4 electron ORR process. Carbon in the catalytic layer plays a dual role. On the one hand, it is required to improve the electrical contact between perovskite particles and the current collector, and to ensure maximum utilization of the perovskite surface. On the other hand, carbon plays an active role in the ORR by catalyzing O_2 reduction to HO_2^-. The ORR on the carbon and the oxide components of composite electrodes must be considered as coupled reactions whose contributions cannot be always separated. Depending on the type and the surface area of perovskite and of carbon, but also on the electronic conductivity of the perovskite material, carbon may fully take over the catalytic role of the electrochemical O_2 activation. In such a case the role of perovskite is reduced to either chemical disproportionation or electrochemical reduction of HO_2^- to achieve a global 4 electron process. Then, calculation of the electrocatalytic activity by normalizing the measured kinetic current to the surface area of perovskite (with or without subtraction of the carbon contribution) will lead to erroneous results. In this work, carbon contribution is more pronounced for Co-perovskites than for Mn-perovskites, which display higher ORR activities, while the nature of A cation has only a minor influence on the electrode performance.

Thus, development of perovskite materials for SAFC should go along with the understanding of the mutual influence of perovskite and carbon in the catalytic layer and an improvement of the composition and morphology of carbon/perovskite composites. It also requires the understanding of the participation of carbon and perovskite materials in the various ORR steps. Further detailed RRDE studies of the ORR, as well as investigations of the HO_2^- chemical and electrochemical reactions on perovskites were performed in section 5 to conclude on “direct” 4e- vs. “series” 2e-+2e- ORR process on composite electrodes. Note that the ORR on carbon materials cannot be fully neglected even if perovskite materials are highly active in the “direct” 4 electron ORR. Indeed, if carbon is part of the cathode layer, HO_2^- produced on its surface must be either decomposed or reduced in order to prevent corrosion of the electrode layer and the membrane. Thus, along with the ORR activity, perovskites must possess significant activity in the HO_2^- transformation.

Chapter 5 :
ORR mechanism on perovskite/carbon composites

5.1. Introduction

In section 4, it was shown by the RDE study that 4 electrons are globally involved in the ORR on perovskite/carbon electrodes. However, despite numerous studies, the exact ORR mechanism on perovskites is still unclear. As mentioned in section 1.4.3.1, both "direct" [88] and "series" pathway occurring via the HO_2^- intermediate [82,90] were proposed for perovskite cathodes. Therefore, the ORR mechanism was investigated with the RRDE method for various electrode compositions, in order to unveil the influence of the perovskite/carbon ratio as well as the electrode thickness on the nature of the ORR pathway.

Since RRDE experiments confirmed that the HO_2^- intermediate is indeed formed on various perovskite oxides, it was necessary to study the kinetics of the HO_2^- reduction and decomposition reactions to identify the nature of the second ORR step, i.e. the HO_2^- transformation, occurring on perovskite oxides. Moreover, the RDE study of the ORR on perovskite/carbon composites has shown that carbon plays an active role in the ORR by catalyzing O_2 reduction to HO_2^- (see section 4). HO_2^- intermediate produced on the carbon surface can lead to the corrosion of the electrode layer and of the membrane in fuel cells. It is therefore necessary that perovskites have the ability to rapidly transform HO_2^- to avoid accumulation of this species in a fuel cell. Thus, in order to investigate the activity of perovskite for these transformations, both HO_2^- chemical decomposition and HO_2^- electrochemical reduction on perovskite oxides will be studied in this section in H_2O_2 containing electrolytes.

The studies of this section were performed on three selected perovskites: $LaCoO_3$, $LaMnO_3$ and $La_{0.8}Sr_{0.2}MnO_3$, representing a non doped Co-perovskite, a non doped Mn-perovskite and a doped Mn-perovskite, respectively, since they displayed distinct behaviors for the ORR (see section 4).

Based on the experimental results both in O_2 and H_2O_2 containing electrolytes, a model was constructed by Dr. Antoine Bonnefont (Institut de Chimie, Université de Strasbourg) to support the data interpretation and to better identify the differences between various perovskites (see section 5.5).

5.2. RRDE study in O_2-saturated electrolyte: quantification of the HO_2^- formation during the ORR

In order to quantify the HO_2^- production during the ORR and to conclude on "direct" vs. "series" (with HO_2^- intermediate) ORR process on composite electrodes, the rotating ring-disk electrode (RRDE) method was applied. Catalysts were deposited in the form of thin layers on a GC disk [154]. In order to understand the role of carbon and perovskite oxides in the HO_2^- production, various thin layer compositions, as indicated in (Table 11), were investigated. Considering that the probability of the H_2O_2 detection depends on the catalyst loading [164,214,227], the catalyst loading was varied from 23 to 91 $\mu g.cm^{-2}_{geo}$.

Table 11 : *Loading and estimated thickness (calculated with (Equation 19)) of RRDE thin layers*

Electrode	**RRDE experiments**					
	Constant perovskite or carbon loadings			**Constant carbon/perovskite ratio**		
Perovskite loading ($\mu g.cm^{-2}_{geo}$)	46	0	46	23	46	91
Carbon loading ($\mu g.cm^{-2}_{geo}$)	0	19	19	9	19	37
Content of perovskite in the composite (wt%)	100	0	71	71	71	71
Estimated layer thickness (µm)	0.8	0.4	1.2	0.6	1.2	2.3

5.2.1. Impact of the electrode composition on the HO_2^- release

5.2.1.1. Influence of the perovskite/carbon ratio

Previous experiments showed that the presence of carbon in the perovskite catalytic layer enhances the ORR (see section 4) electrocatalysis by improving the electrical contact between perovskite particles. Moreover, carbon may be directly involved in the ORR mechanism by electrocatalyzing the O_2 reduction into HO_2^-, especially in the case of perovskite oxides with low activity in the ORR (the case of $LaCoO_3$) (see section 4). Thus, the presence of carbon is expected to strongly affect the quantity of HO_2^- formed during the ORR. To investigate this, RRDE experiments were performed on electrodes containing perovskite alone, carbon alone or both perovskite and carbon, in O_2-saturated electrolyte (Table 11). The obtained disk and ring currents, as well as the amount of HO_2^- produced during the ORR (HO_2^- yield) calculated by (Equation 46), are shown in Figure 40 for glassy carbon support, $LaCoO_3$ and $La_{0.8}Sr_{0.2}MnO_3$ electrodes and in Figure 41 for electrodes containing perovskite alone, containing carbon alone and composite electrodes. The blue curves of Figure 41 corresponds to Figure 40.

One may notice that ring currents are normalized by the collection factor to facilitate their comparison with the disc current. The percentage of HO_2^- is not shown for high potentials where very low disk and ring currents result in a high error of the HO_2^- yield determination. Figures show representative results of RRDE studies. It should be noticed however that at least two (but often 3 or 4) independent experiments were performed for each electrode to check the reproductibility of the results. Some of the repeated RRDE voltammograms can be seen in Appendix 1 (Figure 96).

The effect of the rotation rates on the ORR currents and HO_2^- yield is studied in section 5.2.1.2.

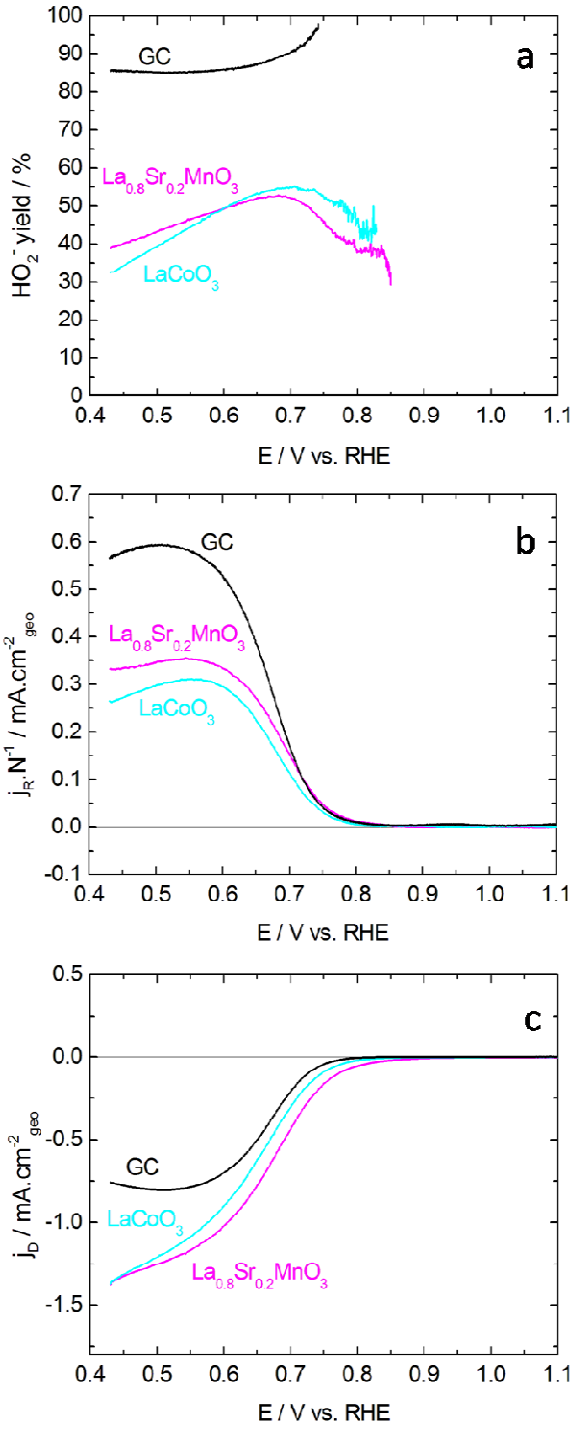

Figure 40 : *Positive scans of the RRDE voltammograms of GC-supported thin films of perovskites in O_2-saturated 1M NaOH at 900 rpm and 10 mV.s^{-1} : (a) percentage of HO_2^- formed, (b) ring currents at 1.23V vs. RHE versus disk potential, (c) disk voltammograms. Color codes for the electrode composition: glassy carbon alone (black), 46 µg.cm$^{-2}_{geo}$ $LaCoO_3$ (light blue), 46 µg.cm$^{-2}_{geo}$ $La_{0.8}Sr_{0.2}MnO_3$ (pink). Disk currents are normalized to the geometric area of the disk electrode and corrected to the background currents measured in the N_2 atmosphere. Ring currents are normalized to the geometric area of the disk electrode and to the collection factor.*

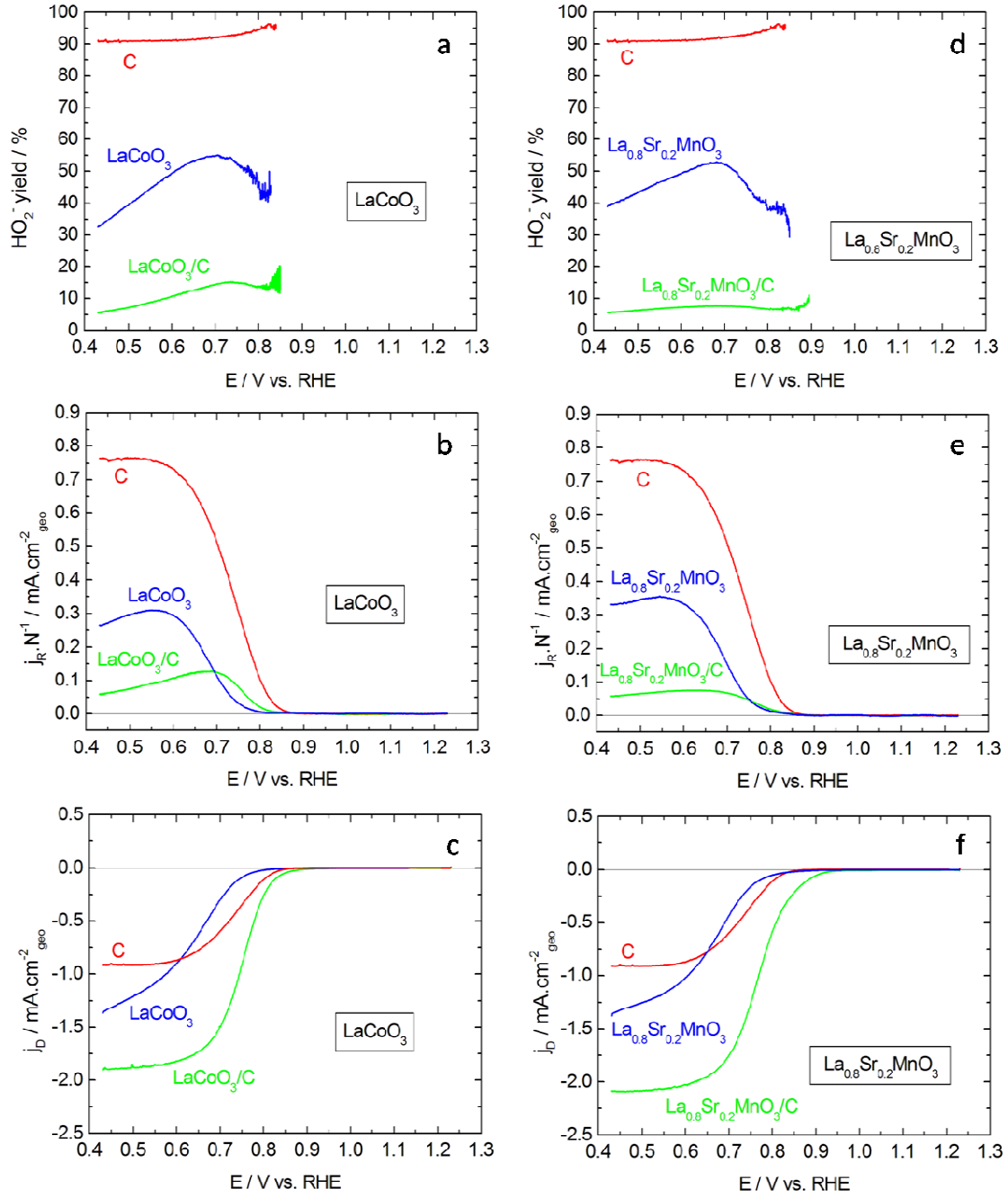

Figure 41 : *Positive scans of the RRDE voltammograms of GC-supported thin films of (a,b,c) $LaCoO_3$ and (d,e,f) $La_{0.8}Sr_{0.2}MnO_3$ in O_2-saturated 1M NaOH at 900 rpm and 10 $mV.s^{-1}$: (a,d) percentage of HO_2^- formed, (b,e) ring currents at 1.23V vs. RHE versus disk potential, (c,f) disk voltammograms. Measurements were performed for electrodes containing only perovskite, for electrodes containing only Sibunit carbon, and for composite perovskite + Sibunit carbon electrodes. Color codes for electrode composition: 46 $\mu g.cm^{-2}_{geo}$ perovskite (blue), 46 $\mu g.cm^{-2}_{geo}$ perovskite + 19 $\mu g.cm^{-2}_{geo}$ Sibunit carbon (green), 19 $\mu g.cm^{-2}_{geo}$ Sibunit carbon (red). Disk currents are normalized to the geometric area of the disk electrode and corrected to the background currents measured in the N_2 atmosphere. Ring currents are normalized to the geometric area of the disk electrode and to the collection factor.*

For layers containing perovskites only, the currents measured at the disk (Figure 40,c) and at the ring (Figure 40,b) result in a quantity of HO_2^- produced during the ORR of more than 30% (Figure 40,a). Taking into account that some amount of HO_2^- may stay adsorbed or be reduced or decomposed before being detected at the ring, and thus, that the true HO_2^- quantity may be even higher than measured, it can be argued that the ORR on the studied perovskite oxides is mainly a "series" pathway occurring via HO_2^- intermediate. Similar results were also obtained for $LaMnO_3$ (Figure 99 in Appendix 3) and are consistent with data of Tulloch et al. [85] who studied Mn-containing perovskites without carbon addition and found up to 80% of HO_2^- using the RRDE.

From the HO_2^- yield plots (Figure 40,a), it can be observed that the percentage of HO_2^- depends on the potential applied to the disk, suggesting that an electrochemical step may be involved in the HO_2^- transformation. For both $LaCoO_3$ and $La_{0.8}Sr_{0.2}MnO_3$, a maximum seems to be reached around +0.7V vs. RHE. For potentials above this value, one cannot discard the probability that the detected HO_2^- species are formed on the GC support surface. Indeed, the low perovskite loading does not lead in a full GC coverage and the ring onset potential of perovskite electrodes is similar to the one of GC (Figure 40,b). At lower potentials, the decrease of HO_2^- yield may result from a reduction of HO_2^- on the perovskite surface. As $LaCoO_3$ and $La_{0.8}Sr_{0.2}MnO_3$ display very close HO_2^- yield plots without carbon, it seems that they have similar activity for the HO_2^- reduction (decomposition) in the absence of carbon.

For glassy carbon (GC) support (Figure 40, black curves) and for electrodes containing carbon only (Figure 41, red curves), more than 85% of HO_2^- are detected at the ring. This is in agreement with the low activity of carbon for HO_2^- reduction and decomposition reported by several authors [20,209,213,218,228] and experimentally confirmed in this work (see section 5.3 and 5.4). However the HO_2^- yield does not reach 100% as expected. This may be due to a partial chemical disproportionation of HO_2^- before reaching the ring [33], either non catalytically in the electrolyte or catalytically on impurity traces. Indeed, despite the careful cleaning performed before all experiments, one cannot exclude some remaining oxide impurities on the insulating Teflon ring.

As carbon is only active for the reduction of O_2 into HO_2^-, one might expect that the addition of carbon in the catalytic layer increases the amount of HO_2^- formed during the ORR. However, the opposite effect was observed. Indeed, by adding 19 $\mu g.cm^{-2}_{geo}$ carbon (i.e. 29

wt% carbon) to the perovskite powder, the disk current increases (Figure 41,c,f) and the ring current decreases (Figure 41,b,e), leading in a drop of the HO_2^- yield below 15% for $LaCoO_3$ composites, and below 8% for $La_{0.8}Sr_{0.2}MnO_3$ composites (Figure 41,a,d, green curves). Similar effect was observed by Li et al. [82] on $La_{0.6}Ca_{0.4}CoO_3$ electrodes with carbon addition. As observed in Figure 31, the addition of 29 wt% of carbon to the perovskite powder (corresponding to 91 $\mu g.cm^{-2}_{geo}$ perovskite + 37 $\mu g.cm^{-2}_{geo}$ carbon) leads to a multiplication of the pseudocapacitive charge after carbon correction by more than a factor of 2, suggesting that at least 2 times more perovskite sites are electrically accessible thanks to the improvement of the contact between the oxide particles and the current collector. Thus, the decrease of the HO_2^- yield with the carbon addition can be attributed to a faster electrocatalysis of the HO_2^- reduction on perovskite oxides.

Both the decrease of the HO_2^- yield with the improvement of the electrical contact and its dependence to the electrode potential suggest that an electrochemical step is involved in the HO_2^- transformation on perovskite electrodes. Nevertheless, the shape of the ring current for perovskite/carbon electrodes, similar to the one observed on $La_{0.6}Ca_{0.4}CoO_3$/carbon electrodes by Li et al. [82] et Malkhandi et al. [219], does not correspond to the slope expected for a reaction limited by an electrochemical step, as demonstrated by modeling by Ruvinskiy et al. [229]. This shows that the reduction of HO_2^- is rather a complex multistep mechanism with an eventual chemical step as a rate determining step.

Additionnaly to the global decrease of the HO_2^- yield, it is interesting to note that the addition of carbon results in a positive shift of the onset of the ring current (Figure 41,b,e). This is partially due to an increase of the number of perovskite sites, leading to a positive shift of the ORR onset on the disc too (Figure 41,c,f). It may also be due to the formation of HO_2^- on carbon sites, especially for $LaCoO_3$/carbon electrodes (see section 4). In any case, the addition of carbon results in a global decrease of the HO_2^- yield compared to a perovskite alone suggesting fast reduction (decomposition) of HO_2^- on perovskite sites.

5.2.1.2. Influence of the perovskite composition

Figure 42 shows the mass transport dependence of the ORR and the HO_2^-formation for $LaCoO_3$ and $La_{0.8}Sr_{0.2}MnO_3$ electrodes. The results for $LaMnO_3$ electrodes are shown in Figure 100 in Appendix 3.

As expected, the faster the rotation rate, the higher are the measured currents at the disk and at the ring. Regardless the nature of the perovskite, the formation of HO_2^- in the catalytic layers is confirmed by the increase of the HO_2^- yield with the rotation rate, observed in Figure 42,a,d. Indeed, at high rotation rate, HO_2^- diffuses faster away from the electrode, therefore more HO_2^- can be detected at the ring, as proved by modeling by Jaouen [214].

Figure 42 also shows that in the presence of carbon the quantity of HO_2^- detected during the ORR is strongly dependent on the perovskite nature, contrary to the behavior of the perovskite alone (see section 5.2.1.1). One of the possible causes for this is the difference between the two perovskites in terms of the ORR activity. It was shown in section 4 that for $LaCoO_3$/C composites the first steps of the ORR mainly occur on carbon sites, while Mn-perovskites were able to catalyse O_2 activation at higher potentials than carbon. This is confirmed by the current measured at the disk and at the ring (Figure 43,a) which show that both the ORR and the HO_2^- formation start at higher electrode potentials for $La_{0.8}Sr_{0.2}MnO_3$/C than for $LaCoO_3$/C. Thus, for $La_{0.8}Sr_{0.2}MnO_3$, both the HO_2^- formation and the reduction (decomposition) of HO_2^- to OH^- occur on the perovskite surface (either on the same or on two different types of active sites). Meanwhile, for $LaCoO_3$, HO_2^- intermediate is first formed on carbon, and should then desorb and diffuse to perovskite sites to be further transformed. This way, some HO_2^- can diffuse out of the electrode thin layer and be detected at the ring, leading to a high HO_2^- yield. This also explains why differences in the HO_2^- yield were observed for Mn-based and Co-based perovskite/carbon electrodes and not for perovskite electrodes without carbon. Another explanation of the differences in the HO_2^- yield observed for the two perovskites would be a different catalytic activity for HO_2^- transformation in the presence of carbon. This will be further verified in section 5.3.

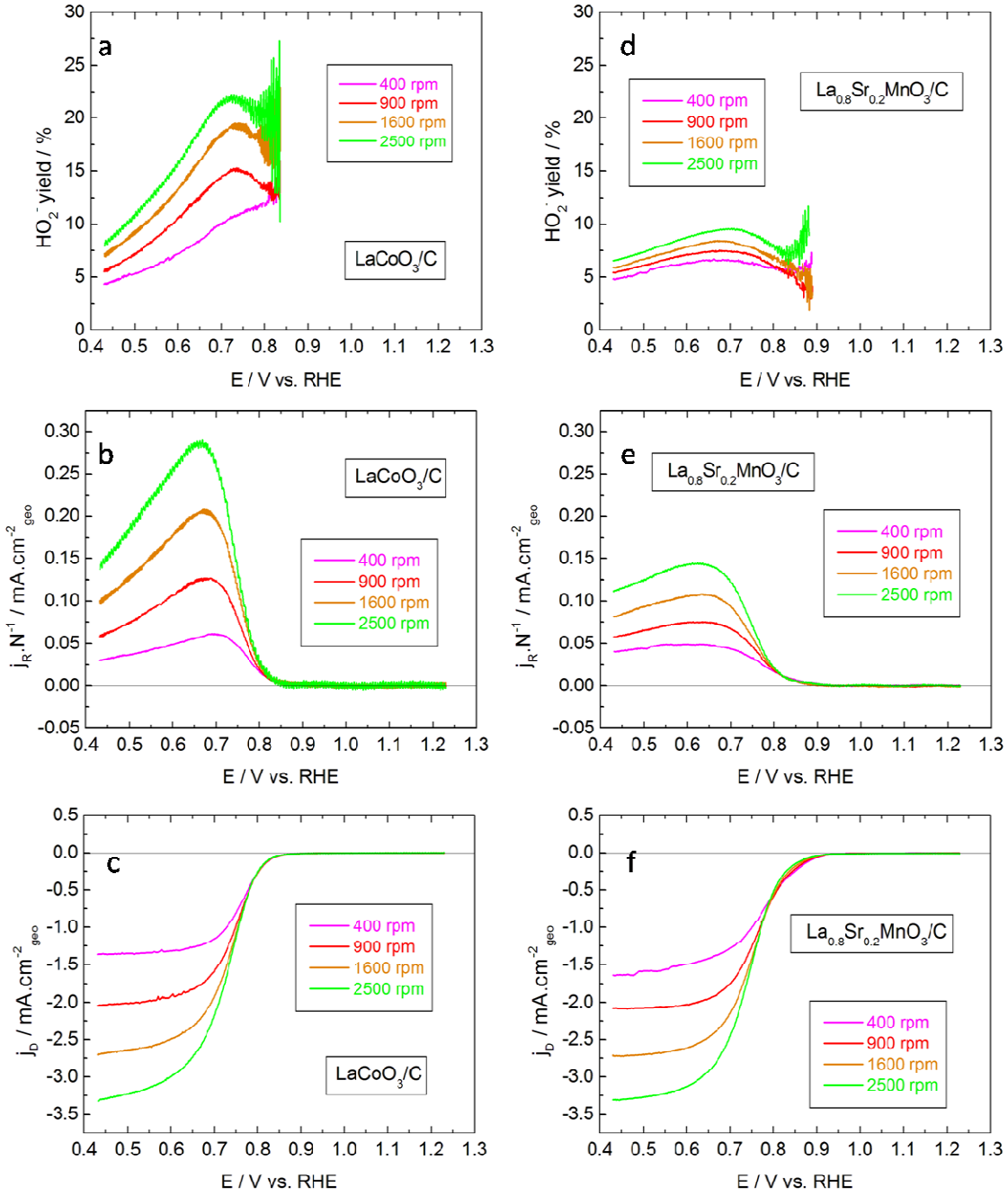

Figure 42 : *Positive scans of the RRDE voltammograms of GC-supported thin films of (a,b,c) $LaCoO_3$ + Sibunit carbon and (d,e,f) $La_{0.8}Sr_{0.2}MnO_3$ + Sibunit carbon in O_2-saturated 1M NaOH at various rotation rates and 10 $mV.s^{-1}$: (a,d) percentage of HO_2^- formed, (b,e) ring currents at 1.23V vs. RHE versus disk potential, (c,f) disk voltammograms. Measurements were performed with 46 $\mu g.cm^{-2}_{geo}$ perovskite and 19 $\mu g.cm^{-2}_{geo}$ Sibunit carbon. Color codes for electrode rotation rate: 400 rpm (pink), 900 rpm (red), 1600 rpm (orange) and 2500 rpm (green). Disk currents are normalized to the geometric area of the disk electrode and corrected to the background currents measured in the N_2 atmosphere. Ring currents are normalized to the geometric area of the disk electrode and to the collection factor.*

In order to investigate the effect of the electrode surface state on the HO_2^- release during the ORR, negative and positive scans of the RRDE voltammograms are presented in Figure 43. The discussion is started with the ring shape (Figure 43,a) for which $La_{0.8}Sr_{0.2}MnO_3$ displays a hysteresis between the anodic and the cathodic scans. The lower current, i.e. the lower amount of HO_2^- detected at the ring (Figure 43,c), measured on the positive scans compared to negative scans suggested that the reduced form of the perovskite is more efficient to reduce HO_2^- than the oxidized form of the perovskite.

On disk voltammograms, however, the hysteresis can hardly be noticed. As the ORR onset potential coincids with the peak assigned to the Mn^{4+}/Mn^{3+} couple (Figure 43,b,d), one may suggest that Mn^{3+} is involved in the O_2 activation step. This is in agreement with the mechanisms proposed for simple Mn oxides in which ORR occurs through oxidation of Mn^{3+} into Mn^{4+} [33-35,199] (see section 4.4.2).

Besides, the ORR on $LaCoO_3$ electrodes leads to negligible current hysteresis at the ring and at the disk. This may be related to the very small redox peaks observed in the CV in inert atmosphere (Figure 43,d), showing the little effect of the potential on the surface state.

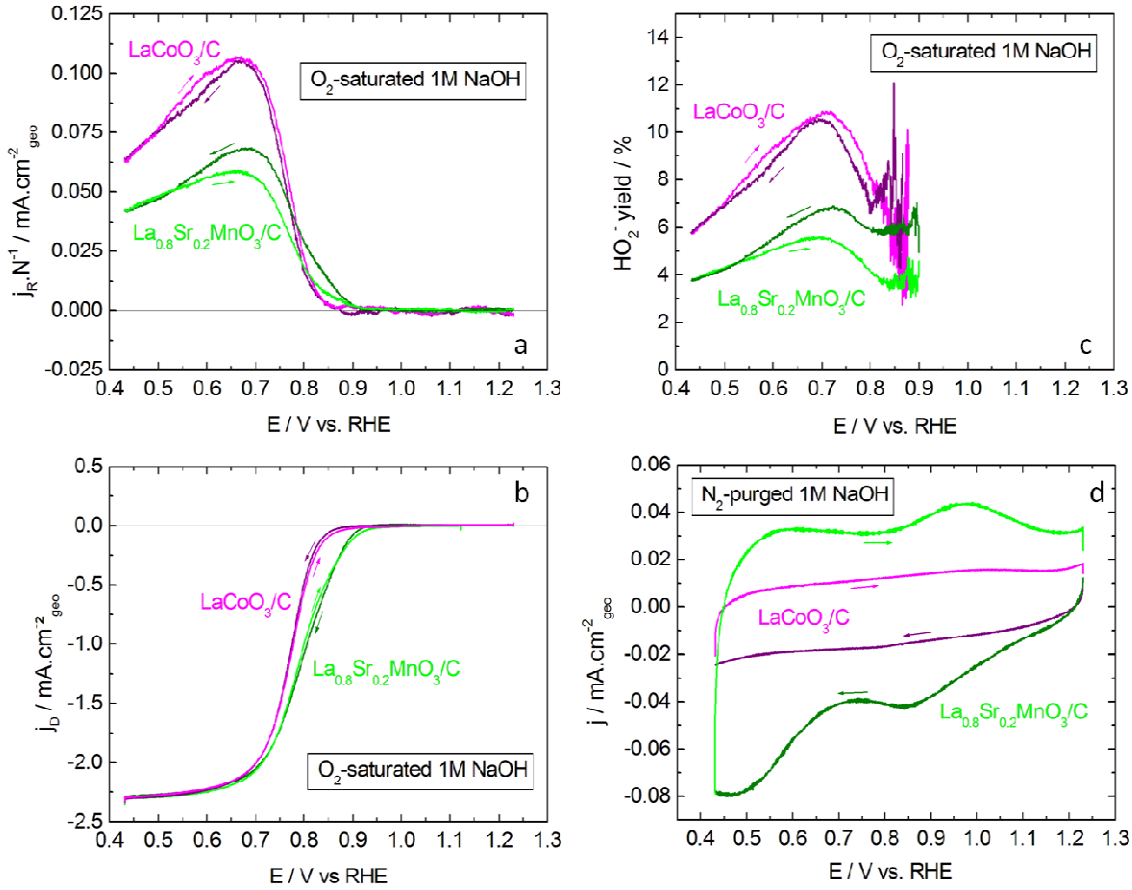

Figure 43 : *Negative and positive scans of RRDE voltammograms in O_2-saturated 1M NaOH at 900 rpm: (a) ring currents at 1.23V vs. RHE versus disk potential, (b) disk voltammograms, (c) percentage of HO_2^- formed, and (d) CV in N_2-purged 1M NaOH at 0 rpm, of GC-supported thin films of perovskite + Sibunit carbon at 10 mV.s^{-1}. Measurements were performed with 91 µg.cm$^{-2}_{geo}$ perovskite + 37 µg.cm$^{-2}_{geo}$ Sibunit carbon. Color codes: $LaCoO_3$ (pink for positive scan and purple for negative scan) and $La_{0.8}Sr_{0.2}MnO_3$ (green for positive scan and olive for negative scan), the arrows indicate the scan direction. Disk currents are normalized to the geometric area of the disk electrode and corrected to the background currents measured in the N_2 atmosphere. Ring currents are normalized to the geometric area of the disk electrode and to the collection factor.*

5.2.2. Impact of the catalyst loading on the HO_2^- detection

The catalyst loading, i.e. the number of active sites, is known to have a great influence on the detection of H_2O_2 by RRDE for platinum [229-231] as well as for non noble catalysts [214,227,232].

Indeed, if the density of active sites on the disk is high (high loading for thin layer electrodes), the HO_2^- intermediate has high probability to be further reduced or decomposed on the disk to ultimately form OH^-. As a consequence, for electrodes with high active site density, a "series" ORR mechanism cannot be distringuished from a "direct" 4 electrons ORR mechanism. Consequently, literature data reporting on the "direct" 4 electrons ORR mechanism must be taken with caution if high catalyst loadings are utilized.

In order to learn more about the contribution of the "series" versus "direct" ORR pathways for Co-based on Mn-based perovskite-type electrodes, composite electrodes with various perovskite loading and a constant perovskite/carbon ratio were tested (Table 11) (Figure 44). The green curves of Figure 44 correspond to the green curves of Figure 41 (46 $\mu g.cm^{-2}_{geo}$ perovskite + 19 $\mu g.cm^{-2}_{geo}$ carbon).

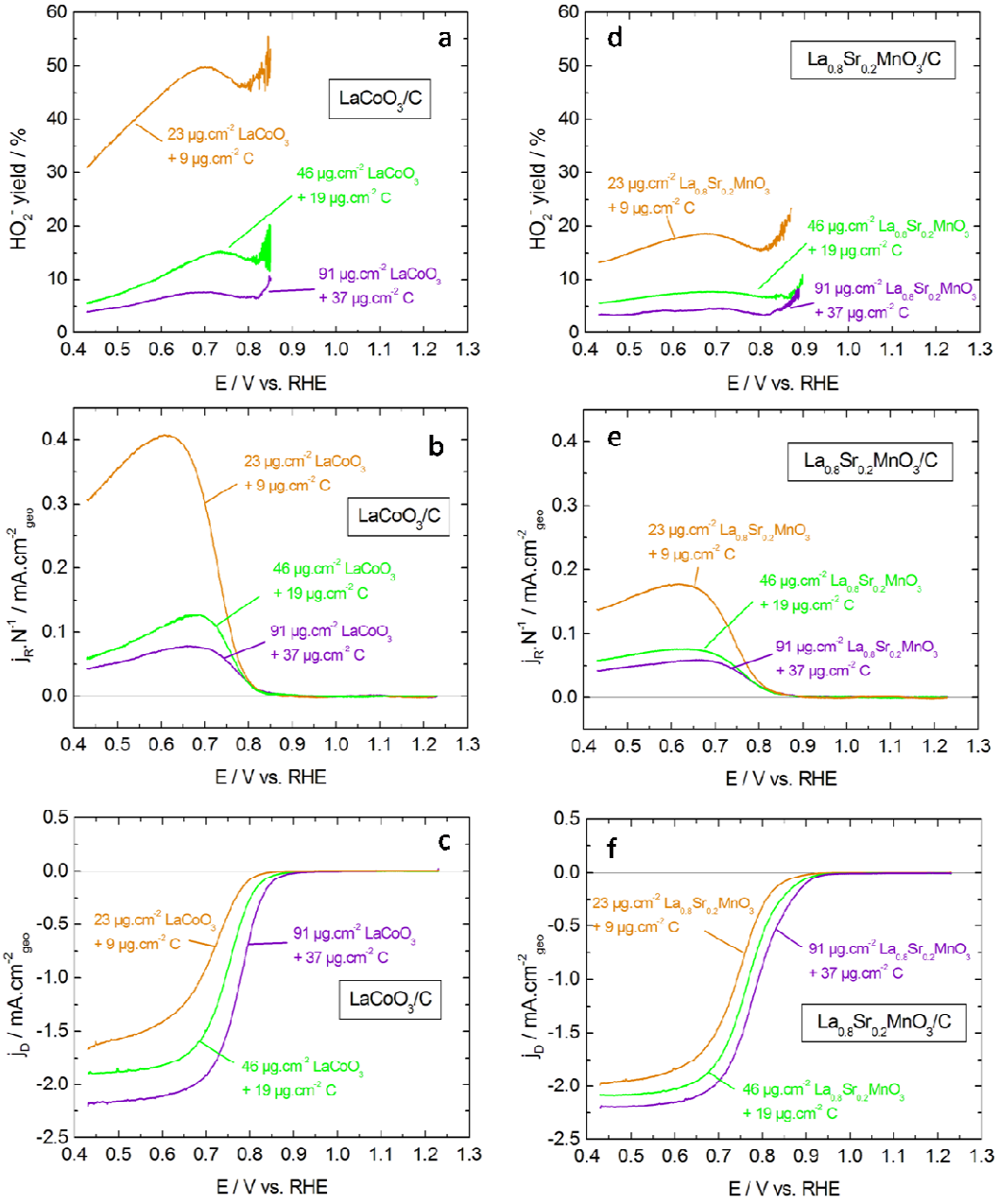

Figure 44 : *Positive scans of the RRDE voltammograms of GC-supported thin films of (a,b,c) $LaCoO_3$ + Sibunit carbon and (d,e,f) $La_{0.8}Sr_{0.2}MnO_3$ + Sibunit carbon in O_2-saturated 1M NaOH at 900 rpm and 10 $mV.s^{-1}$: (a,d) percentage of HO_2^- formed, (b,e) ring currents at 1.23V vs. RHE versus disk potential, (c,f) disk voltammograms. Measurements were performed for electrodes containing constant perovskite/carbon ratio (71 wt.% perovskite + 29 wt.% Sibunit carbon, Table 11) and various catalyst loadings. Color codes for electrode loading: 23 $\mu g.cm^{-2}_{geo}$ perovskite + 9 $\mu g.cm^{-2}_{geo}$ Sibunit carbon (orange), 46 $\mu g.cm^{-2}_{geo}$ perovskite + 19 $\mu g.cm^{-2}_{geo}$ Sibunit carbon (green), 91 $\mu g.cm^{-2}_{geo}$ perovskite + 37 $\mu g.cm^{-2}_{geo}$ Sibunit carbon (purple). Disk currents are normalized to the geometric area of the disk electrode and corrected to the background currents measured in the N_2 atmosphere. Ring currents are normalized to the geometric area of the disk electrode and to the collection factor.*

It was observed that for both perovskites the amount of HO_2^- detected at the ring increases systematically as the loading of perovskites is decreased from 91 to 23 $\mu g.cm^{-2}_{geo}$ (Figure 44). Such an increase of the HO_2^- yield suggests a significant contribution of a "series" ORR mechanism for both perovskite composite electrodes. Hermann et al. [90] investigated the ORR on $La_{0.6}Ca_{0.4}CoO_3$/carbon cathodes with a channel flow cell and also concluded on a predominant "series" pathway for composite electrodes.

In a "series" ORR mechanism, HO_2^- formed in a 2 electron ORR reaction may either desorb and diffuse to be ultimately detected at the ring, or readsorb and further react to OH^-. The probability of the HO_2^- detection at the ring thus depends on the ratio between the HO_2^- desorption and reduction rate constants, and, as explained above, decreases with the number of active sites and the catalytic layer thickness. This efficient transformation of HO_2^- within thick layers leads to a low HO_2^- yield (Figure 44, purple curves), i.e. an apparent 4 electrons pathway, as found by Koutecky-Levich plots in Figure 34. Thus, the low quantity of this intermediate reported for some perovskite/carbon cathodes in the literature [88] may be due to a "series" ORR pathway within a thick catalytic layer with high catalyst loading (a loading of ca. 160 $\mu g.cm^{-2}_{geo}$ perovskite + 40 $\mu g.cm^{-2}_{geo}$ carbon was used by the mentioned authors) rather than the "direct" 4 electron ORR process proposed by the authors. Also Malkhandi et al. [219] measured a very low amount of HO_2^- formed during the ORR on perovskite electrodes with and without carbon and attributed it to a fast HO_2^- decomposition on perovskite sites. However, the loading was very high (400 $\mu g.cm^{-2}_{geo}$ perovskite).

It can be noticed that current of the ring starts to increase at ca. +0.8 V vs. RHE, independently of the thickness of the catalytic layer, whereas the onset of the ORR at the disc increases with the active site loading. One may suggest that the ORR occurs through a "direct" 4 electron pathway on some perovskite sites at high potentials - above +0.8 V vs. RHE - whereas the "series" pathway is potential-dependent and its contribution increases as the electrode potential is shifted towards the negative [229]. However, a "series" pathway in the whole potential range will also result in the observed behavior, as it will be shown in section 5.5 thanks to modeling.

As mentioned previously, the higher HO_2^- yield detected for $LaCoO_3$ compared to $La_{0.8}Sr_{0.2}MnO_3$ is likely to be related to either larger carbon contribution in the HO_2^- formation for the former or faster HO_2^- reduction kinetics on the latter. This last hypothesis will be studied in the following section.

5.3. RDE study in the presence of H_2O_2: kinetics of the HO_2^- reduction/oxidation

RRDE study showed that ORR predominantly occurs through the formation of HO_2^- intermediate which is further transformed on perovskite sites. While several researchers studied the catalytic HO_2^- decomposition kinetics on perovskite oxides (see section 1.4.3), very few published results can be found for the study of the electrochemical reduction of HO_2^- on perovskite oxides [72,131,132] and these are unfortunately not detailed.

Thus, in order to investigate the kinetics of the HO_2^- reduction/oxidation on perovskite oxides which is important for the understanding of the ORR and is missing in the literature, a RDE study was performed in a N_2-purged electrolyte containing H_2O_2.

As mentioned in section 1.2.1.2, H_2O_2 transforms into HO_2^- with contact of alkaline solution according to (Equation 5). Four reactions can theoretically occur in the presence of HO_2^-: HO_2^- reduction into OH^- (Equation 75), HO_2^- oxidation into O_2 (Equation 76), and the inverse reactions, OH^- oxidation into HO_2^- (Equation 75) and O_2 reduction into HO_2^- (Equation 76).

$$HO_2^- + 2e^- + H_2O \rightleftarrows 3OH^-, E° = 1.71\ V_{RHE} \text{ at pH } 14 \quad \text{(Equation 75)}$$

$$HO_2^- + OH^- \rightleftarrows O_2 + H_2O + 2e^-, E° = 0.77\ V_{RHE} \text{ at pH } 14 \quad \text{(Equation 76)}$$

Regarding the standard potential of HO_2^-/OH^- couple, the OH^- oxidation into HO_2^- has very little chance to occur in the studied potential range. Thus, the activities of the perovskite electrodes for the three other reactions will determine the current-potential curve in a H_2O_2 containing electrolyte.

5.3.1. Characteristics of HO_2^- reduction/oxidation reactions

In this section, various rotation rates of the RDE were used to study whether the HO_2^- reactions are limited by mass transport or by kinetics. Also, the influence of the presence of O_2 in the electrolyte and of the H_2O_2 concentration will be studied in section 5.3.1.2.

All these experiments were performed with carbon addition to ensure sufficient conductivity of the catalytic layer (see section 4). In order to evaluate the effect of carbon on the HO_2^- reactions, the electrocatalytic activity of various electrode compositions including perovskite without addition of carbon will be investigated in section 5.3.1.3.

As for the ORR study, at least two independent experiments were performed for each electrode to check the reproductibility of the results. Some of the repeated RDE voltammograms in the presence of H_2O_2 can be seen in Appendix 1 (Figure 97).

5.3.1.1. Effect of the rotation rate and number of involved electrons

First of all, the effect of the electrode rotation rate on HO_2^- reactions was studied using RDE in N_2-purged 1M NaOH containing 0.84 mM H_2O_2. Typical positive scans of RDE voltammograms at various rotation rates are shown in Figure 45 for $LaCoO_3$/carbon, $LaMnO_3$/carbon and $La_{0.8}Sr_{0.2}MnO_3$/carbon electrodes, as well as for Pt/C electrode. These curves are corrected from the background CV in N_2-purged 1M NaOH.

For each electrode, an increase of the current in cathodic region at low potentials and in anodic region at high potentials can be observed with H_2O_2 addition compared to the background CV. Moreover, the current densities increase with the rotation rates. This demonstrates that the studied electrodes are active for HO_2^- reduction into OH^- at low potentials and HO_2^- oxidation into O_2 at high potentials.

The RDE curves in the presence of H_2O_2 cross the zero y-axis at a mixed potential where the sum of all currents is equal to zero [233-235]. In this study, it is observed that the mixed potential is mass transport dependent for both perovskite and Pt electrodes (Figure 45). Indeed, the RDE curves at various rotation rates seem to cross each other at a negative current value, corresponding to negative shift of the mixed potential with the increase of the rotation rate. The same behavior was observed by Kastounaros et al. on Pt electrodes [234]. Below (and above) the potential where the RDE curves at various rotation rates cross each other, i.e. below (and above) ca. +0.93V vs. RHE, the currents vary with the rotation rate and with the potential, suggesting a mixed region, limited by both HO_2^- reduction (oxidation) kinetics and HO_2^- mass transport.

At potentials below +0.6 V and above +1.1 V vs. RHE, HO_2^- reduction and oxidation currents, respectively, reach a plateau on Pt/C electrode, suggesting that currents approach the diffusion limiting values. This may be proven by plotting j^{-1} vs. $\omega^{-1/2}$ (Koutecky-Levich plots,

Figure 46). Furthermore, such plots allow the determination of the number of electrons involved in the studied reactions using Levich equation (Equation 36).

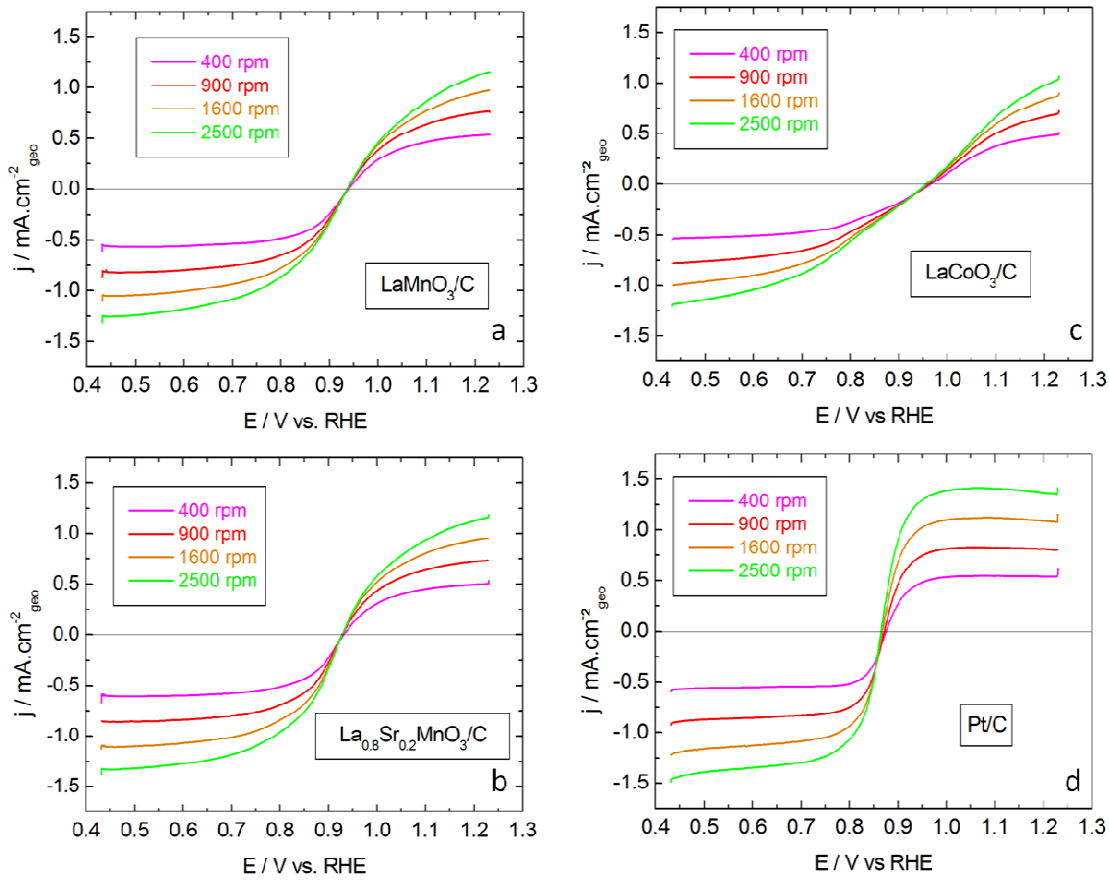

Figure 45 : *Positive scans of the RDE voltammograms of GC-supported thin films of (a) $LaCoO_3$ + Sibunit carbon, (b) $LaMnO_3$+ Sibunit carbon and (c) $La_{0.8}Sr_{0.2}MnO_3$+ Sibunit carbon, in N_2-purged 1M NaOH + 0.84 mM H_2O_2 at various rotation rates and at 10 mV.s^{-1}. Measurements were performed with 91 µg.cm$^{-2}_{geo}$ perovskite and 37 µg.cm$^{-2}_{geo}$ Sibunit carbon. Color codes for rotation rates: 400 rpm (pink), 900 rpm (red), 1600 rpm (orange) and 2500 rpm (green). Currents are normalized to the geometric area of the electrode and corrected to the background currents measured in the N_2 atmosphere without H_2O_2 presence.*

The Koutecky-Levich plots of HO_2^- reduction at +0.5 V vs. RHE and HO_2^- oxidation at +1.2 V vs. RHE are shown in Figure 46,a and Figure 46,b, respectively, for perovskite/carbon composites and for Pt/C electrodes. For both reactions, the plots obtained for Pt/C are linear, with identical slopes, and cross the origin. This confirms that the reactions are diffusion-limited at the studied potentials on Pt/C. As it is known that 2 electrons are involved for each reaction on platinum electrodes [8,234,235] and knowing the H_2O_2 concentration in the electrolyte (C_{H2O2} = 8.4 x 10^{-7} mol.cm^{-3}), one can determine the diffusion coefficient of HO_2^- using Levich equation (Equation 36). Thus, the diffusion coefficient of HO_2^- in 1M NaOH at

25°C was estimated as 7.3 10^{-6} $cm^2.s^{-1}$. This value is close to the value found in the same electrolyte by Paliteiro et al. [236,237], i.e. 5.5 10^{-6} $cm^2.s^{-1}$, and from the value found in 1M KOH by Van den Brink et al. [238], i.e. 8.4 10^{-6} $cm^2.s^{-1}$.

For the three studied perovskite/carbon composites, Koutecky-Levich plots at +0.5V vs. RHE are linear and their slopes are close to those of Pt/C (Figure 46,a). This shows that two electrons are involved in the HO_2^- reduction on perovskite oxides too. For $LaMnO_3$ and $La_{0.8}Sr_{0.2}MnO_3$, the plots cross the origin showing that the HO_2^- reduction is diffusion-limited at low potentials on Mn-perovskite electrodes. This means that, at these low potentials, the studied reaction is not controlled by the charge transfer, and thus, HO_2^- is rapidly reduced. For $LaCoO_3$ electrodes, the Koutecky-Levich plots do not cross the origin showing a positive intercept. Thus, for $LaCoO_3$, due to a slower HO_2^- reduction kinetics, the diffusion limiting current is not reach at +0.5V vs. RHE. This explains why the amount of HO_2^- detected at the ring of the RRDE fro Mn-based perovskites is smaller than for $LaCoO_3$ (see section 5.2).

Contrary to HO_2^- reduction, the plots for HO_2^- oxidation (Figure 46,b) do not cross zero for the three perovskites. This demonstrated that the reaction is controlled by the charge transfer at the studied potential on perovskite electrodes – and especially for $LaCoO_3$ - and is therefore slower than on Pt/C. Nevertheless the slope of the plots is similar to that of Pt/C showing that 2 electrons are also involved in that reaction on the perovskite composites.

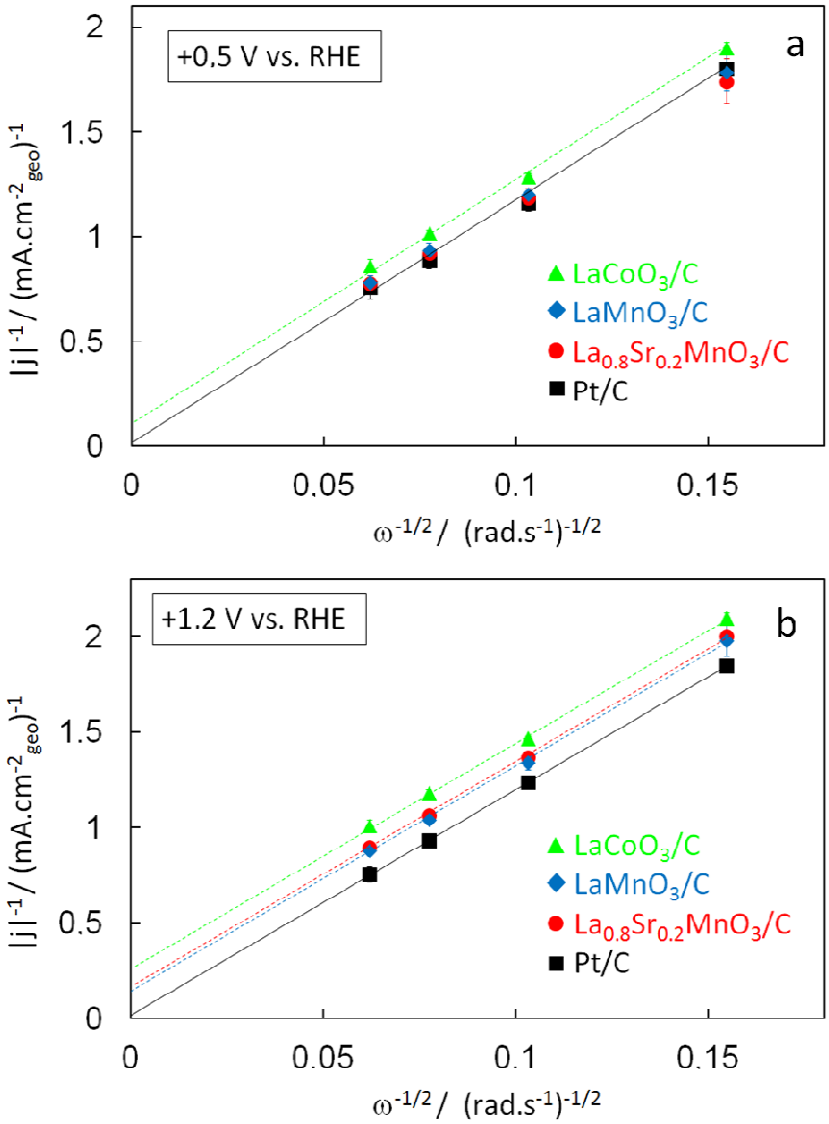

Figure 46 : *Koutecky-Levich plots of (a) the HO_2^- reduction current measured at +0.5 V vs. RHE and (b) the HO_2^- oxidation current measured at +1.2 V vs. RHE by thin layer RDE method in N_2-purged 1M NaOH + 0.84 mM H_2O_2 at 10 mV.s^{-1}. Measurements were performed with 91 µg.cm$^{-2}_{geo}$ perovskite and 37 µg.cm$^{-2}_{geo}$ Sibunit carbon. Color codes: $LaCoO_3$ + Sibunit carbon (green), $LaMnO_3$ + Sibunit carbon (blue), $La_{0.8}Sr_{0.2}MnO_3$ + Sibunit carbon (red), Pt/C (black). Currents are normalized to the geometric area of the electrode and corrected to the background currents measured in the N_2 atmosphere without H_2O_2 presence. Error bars represent standard deviation from at least two independent repeated measurements.*

5.3.1.2. Dependence on the H_2O_2 and O_2 concentrations

In order to check if the cathodic current observed in Figure 45 on perovskite composite electrodes is really due to the HO_2^- reduction or rather to the reduction of oxygen formed via HO_2^- oxidation, experiments were performed in O_2-saturated 1M NaOH with addition of H_2O_2. The results are displayed in Figure 47 (brown curves) and compared to experiments in O_2-saturated 1M NaOH in absence of H_2O_2 (usual ORR experiment, Figure 47 (black curves)) and to experiments in N_2-purged 1M NaOH in presence of H_2O_2 (usual H_2O_2 experiment Figure 47 (orange curves)). In O_2-saturated 1M NaOH, it is clear that the absolute value of the cathodic limiting current is higher in the presence of H_2O_2 than in the absence of H_2O_2. Thus, the additional current observed with H_2O_2 cannot be due to the ORR (since the electrolyte is saturated with O_2) and really represents the HO_2^- reduction current. One may also see that the HO_2^- mixed potential is more positive than the ORR onset confirming that the polarization curve observed on the H_2O_2-containing electrolyte is indeed due to the HO_2^- reduction. Furthermore, one may see that the polarization curve obtained in the presence of both H_2O_2 and O_2 is (within the experimental error) a sum of the HO_2^- and O_2 reduction currents for both perovskites. Indeed, the curve (Figure 47, red curves) obtained by subtracting the current obtained in N_2-purged 1M NaOH with 0.84 mM H_2O_2 (Figure 47, orange curves) from the current obtained in O_2-saturated 1M NaOH with 0.84 mM H_2O_2 (Figure 47, brown curves) is almost superposed to the current measured in O_2-saturated 1M NaOH without H_2O_2 (Figure 47, black curves).

As mentioned above, the onset potential of the ORR is lower than the mixed potential in the presence of HO_2^- for the studied electrodes. This suggests that HO_2^- intermediates eventually formed during the ORR can be reduced into OH^- on perovskite composite electrodes, in agreement with the RRDE results (see section 5.2). Moreover, the mixed potential might represent the highest onset potential that perovskite/carbon electrodes can reach for the ORR in case the ORR follows a "series" pathway, even after the electrode composition optimization. Indeed, at potentials higher that the mixed potential, HO_2^- eventually produced in the ORR would be oxidized, resulting in an overall zero ORR current.

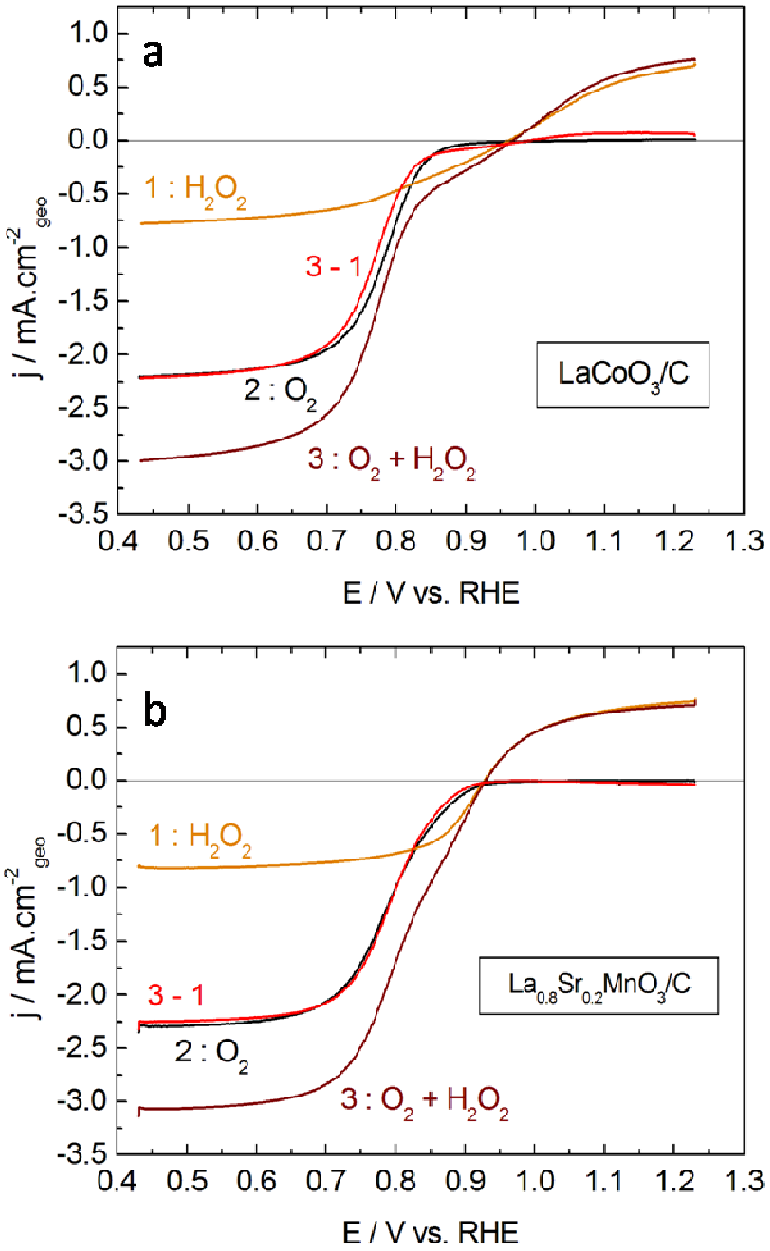

Figure 47 : *Positive scans of the RDE voltammograms of GC-supported thin films of (a) $LaCoO_3$ + Sibunit carbon and (b) $La_{0.8}Sr_{0.2}MnO_3$+ Sibunit carbon, in 1M NaOH electrolyte containing H_2O_2 and/or O_2 at 900 rpm and 10 mV.s^{-1}. Measurements were performed with 91 µg.cm$^{-2}_{geo}$ perovskite and 37 µg. cm$^{-2}_{geo}$ Sibunit carbon. Color codes for electrolyte composition: 1: N_2-purged 1M NaOH + 0.84 mM H_2O_2 (orange), 2: O_2-saturated 1M NaOH (black) and 3: O_2-saturated 1M NaOH + 0.84 mM H_2O_2 (brown). The curve in red was obtained by substracted curve 1 (orange) to curve 3 (brown). Currents are normalized to the geometric area of the electrode and corrected to the background currents measured in the N_2 atmosphere without H_2O_2 presence.*

The concentration of H_2O_2 usually chosen in this study - 0.84 mM – corresponds to the concentration of O_2 in an O_2-saturated 1M NaOH electrolyte. It therefore corresponds to the maximal concentration of HO_2^- that can be formed during the ORR in the corresponding electrolyte. In fact, even lower HO_2^- concentrations are expected near the electrode surface since HO_2^- formed during the ORR can further react to form OH^-. Thus, a lower H_2O_2 concentration – 0.42 mM – was also tested for the HO_2^- reduction/oxidation RDE study. Figure 48 shows the positive scans of the RDE voltammograms of perovskite/carbon electrodes in N_2-purged 1M NaOH with 0.84 mM H_2O_2 (orange curves) and with 0.42 mM H_2O_2 (green curves).

When the concentration of H_2O_2 is decreased by a factor of 2, the voltammogram shapes remain the same and the limiting current is divived by 2, in agreement with the Levich theory. However, the mixed potential is slightly dependent on the H_2O_2 concentration since it is shifted positively by about 10 mV when H_2O_2 concentration is divided by 2. This indicates that the HO_2^- reduction and the HO_2^- oxidation reactions have different concentration dependence on the perovskite oxides. This will be further corroborated with the help of mathematical models in section 5.5.

With the purpose to link the HO_2^- reduction/oxidation experiments to the HO_2^- decomposition measurements (see section 5.4), higher quantities of H_2O_2 (0.03M and 0.1M H_2O_2 in 1M NaOH) were tested. However, in such media, the rotation rate of the RDE did not have the expected effect: the current densities of HO_2^- reduction were almost superposed for different rotation rates tested on perovskite electrodes. This was probably due to a limitation by the number of available active sites of the reaction or to the blocking of the surface by the oxygen gas bubbles formed during HO_2^- oxidation, since the quantity of the catalyst was small (ca. 10 µg of perovskite on a RDE), and the concentration of H_2O_2, high. Thus, studies of HO_2^- reduction/oxidation reactions wih high H_2O_2 concentrations were abandoned.

Nevertheless, it can be noticed that the minor influence of the mass transport on the reduction currents observed by Hermann et al. [133] for $La_{0.6}Ca_{0.4}CoO_3$ perovskite may be due to a too high H_2O_2 concentration compared to the number of active sites.

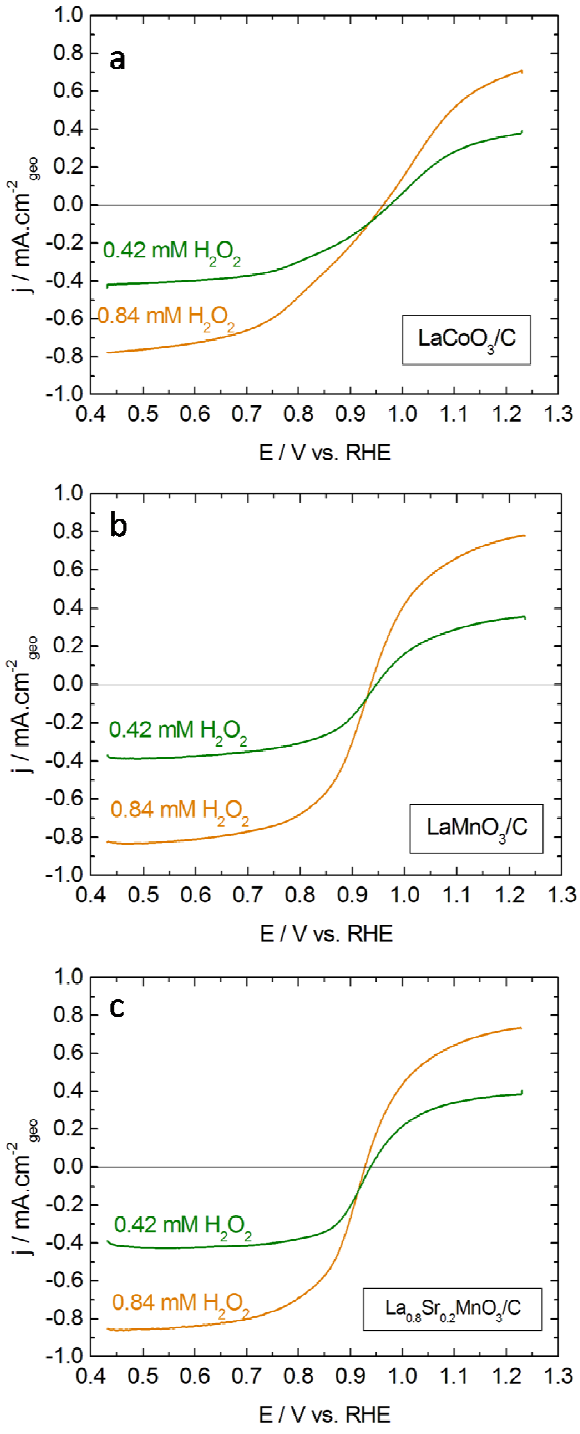

Figure 48 : *Positive scans of the RDE voltammograms of GC-supported thin films of (a) $LaCoO_3$ + Sibunit carbon, (b) $LaMnO_3$+ Sibunit carbon and (c) $La_{0.8}Sr_{0.2}MnO_3$+ Sibunit carbon, in N_2-purged 1M NaOH with various H_2O_2 concentrations at 900 rpm and 10 $mV.s^{-1}$. Measurements were performed with 91 $\mu g.cm^{-2}_{geo}$ perovskite and 37 $\mu g.\ cm^{-2}_{geo}$ Sibunit carbon. Color codes for H_2O_2 concentration: 0.42 mM H_2O_2 (green), 0.84 mM H_2O_2 (orange). Currents are normalized to the geometric area of the electrode and corrected to the background currents measured in the N_2 atmosphere in the absence of H_2O_2.*

5.3.1.3. Influence of the carbon loading

The experiments presented above were performed with the addition of carbon to the catalytic layers. However, it was demonstrated in section 4 that carbon plays a dual role in the perovskite/carbon composite electrodes for the ORR electrocatalysis. Also, the RRDE study showed that the presence of carbon leads to an increase of the HO_2^- reduction kinetics on the studied perovskite oxides (see section 5.2.1.1). Thus, in order to determine the role of carbon for the HO_2^- reduction/oxidation reactions, the carbon loading in the composite electrodes was varied and the RDE voltammograms in the presence of H_2O_2 were investigated.

Figure 49 shows the positive scans of the RDE voltammograms of perovskite/carbon composite thin layer electrodes in the presence of H_2O_2 for various carbon loadings. It is evident that perovskite electrodes without carbon, and especially non-doped $LaCoO_3$ and $LaMnO_3$ perovskites, show little activity for the HO_2^- reduction/oxidation (Figure 49, pink curves). For all studied perovskites, addition of carbon in the catalytic layer leads to an enhancement of the electrocatalysis of HO_2^- reactions (Figure 49, red, orange and green curves). Carbon (Figure 49, grey curves) shows a small activity for the HO_2^- oxidation, but is inactive for the HO_2^- reduction – the observed cathodic current may be due to the reduction of O_2 formed via HO_2^- oxidation. Thus, the enhancement of the electrocatalysis in HO_2^- reactions observed upon addition of carbon to perovskite oxides is attributed to an improved access to perovskite sites, especially for the non-doped perovskites which displayed lower conductivity and thus require more carbon to achieve a sufficient layer quality (see section 4.2). Thanks to the improvement of the electrical contact in the catalytic layer, HO_2^- intermediate can be reduced into OH^- on perovskite sites, whereas in the absence of carbon the reduction can hardly occur due to the low conductivity of the layers. This confirms that the decrease of the HO_2^- yield with the carbon addition observed in the RRDE study of the ORR (see section 5.2.1.1) is achieved thanks to a faster electrocatalysis of the HO_2^- reduction on perovskite oxides.

It is noticed that the more carbon in the electrode, the faster is the electrocatalysis. Nevertheless, regarding little differences between various perovskites, the role of the carbon loading seems to be less important for HO_2^- than for the O_2 reaction electrocatalysis. The role of carbon for HO_2^- reduction/oxidation electrocatalysis is limited to the improvement of the electrical contact in the layer and a concomitant increase in the number of active sites, contrary to the ORR electrocatalysis where it is also involved directly in the reaction

mechanism. One can observe that for the highest amount of carbon (140 $\mu g.cm^{-2}_{geo}$) (Figure 49, green curves), the limiting plateau measured on perovskite/carbon electrodes appears at lower absolute current values than for lower carbon loadings for which the limiting currents were very close to those of Pt/C electrode. This is linked to the HO_2^- mass transport losses in a thick catalytic layer, such that the HO_2^- concentration in the vicinity of the outer surface of the thick layer is above zero. Therefore the intermediate quantity of 37 $\mu g.cm^{-2}_{geo}$ (at least for the 65.7 $m^2.g^{-1}$ Sibunit carbon utilized in this work) seems to be an optimum loading for HO_2^- reactions and was kept at this value for other experiments.

While Mn-based perovskite electrodes display similar mixed potential with and without carbon in the catalytic layer, the mixed potential for $LaCoO_3$ electrodes is shifted positively with the carbon addition. For $LaMnO_3$ and $La_{0.8}Sr_{0.2}MnO_3$, the addition of carbon results in the increase of the perovskite utilization, and thus of a simultaneous enhancement of the electrocatalytic activity for the HO_2^- reduction, the HO_2^- oxidation and the ORR on perovskite sites. Therefore the mixed potential is not affected. However, in the case of $LaCoO_3$/carbon composites, the increase of the perovskite utilization only enhances the HO_2^- reaction electrocatalysis and the ORR now occurs on the carbon added to the catalytic layer (see section 4), leading to a positive shift of the mixed potential.

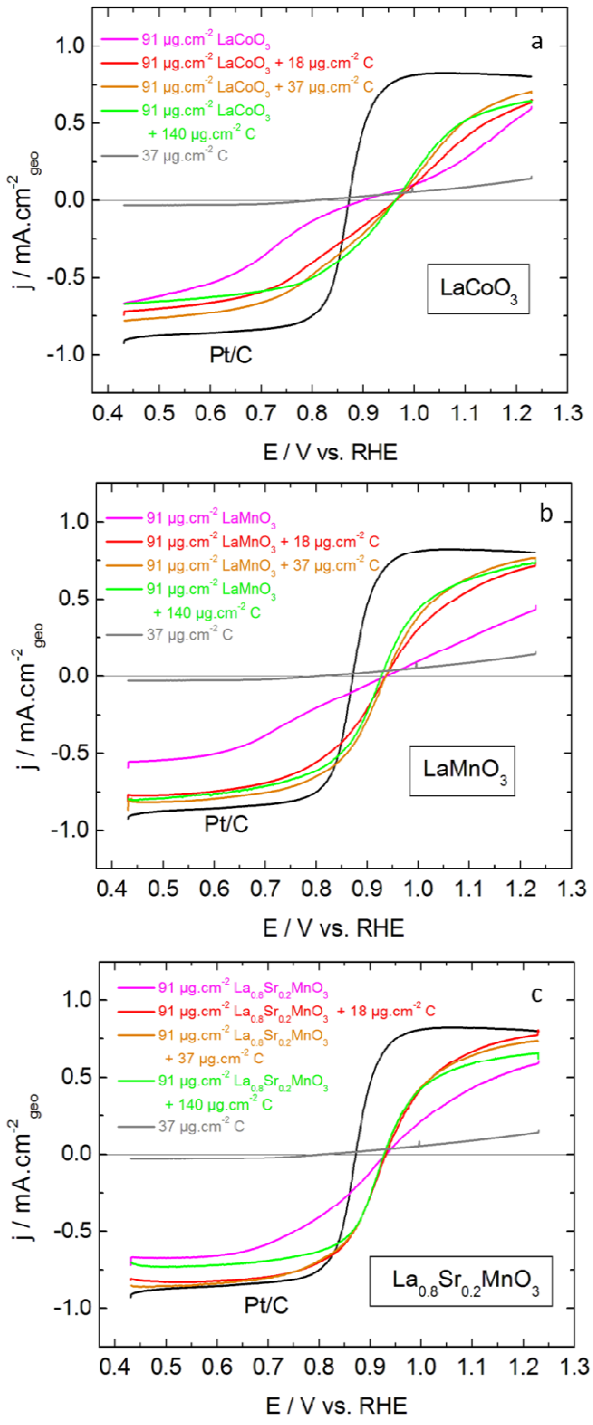

Figure 49 : *Positive scans of the RDE voltammograms of GC-supported thin films of (a) $LaCoO_3$ + Sibunit carbon, (b) $LaMnO_3$+ Sibunit carbon and (c) $La_{0.8}Sr_{0.2}MnO_3$+ Sibunit carbon, in N_2-purged 1M NaOH + 0.84 mM H_2O_2 at 900 rpm and 10 mV.s^{-1}. Measurements were performed with a constant amount of perovskite (91 µg.cm$^{-2}{}_{geo}$) and variable amount of Sibunit carbon. Color codes for carbon loading: 0 (pink), 18 (red), 37 (orange) and 140 µg.cm$^{-2}{}_{geo}$ (green). Black lines show RDE curves for Pt/C. Currents are normalized to the geometric area of the electrode and corrected to the background currents measured in the N_2 atmosphere without H_2O_2 presence.*

5.3.2. Study of the influence of the electrode composition on the HO_2^- reduction/oxidation kinetics

A comparison of the electrocatalytic activity of the three studied perovskites/carbon composites for the HO_2^- reduction/oxidation is shown in Figure 50. As observed previously (see section 5.3.1.1), these perovskite electrodes almost reach the limiting current of Pt/C electrodes (Figure 50, black curves). However, they all display a mixed potential higher than Pt/C.

From the current slope near the mixed potential and from the reported modeling of the oxidation and reduction contributions of the voltammograms on Pt electrodes [239], it appears that H_2O_2 reactions are reversible for Pt/C. Thus, the positive shift of the mixed potential for oxides compared to Pt may be due to a slow HO_2^- oxidation, i.e. which requires high overpotential, on the perovskite electrodes. This is consistent with the Koutecky-Levich plots of HO_2^- oxidation (see section 5.3.1.1). On carbon electrodes (Figure 50, grey curves), the mixed potential is lower than on perovskite/carbon electrodes. This is due to the very small – almost inexistent – activity of carbon for the HO_2^- reduction compared to its activity for the HO_2^- oxidation.

One can notice that, for Pt/C electrodes, the mixed potential for HO_2^- reduction/oxidation (Figure 50, black curves) is lower than the ORR onset potential (Figure 39, black curves). This means that HO_2^- eventually formed by O_2 reduction above the mixed potential would be oxidized back into O_2, resulting in an apparent zero current. Thus, the current measured above the mixed potential might be a sign of "direct" ORR process without an HO_2^- intermediate. This is consistent with the work of Ruvinskiy et al. [229] who demonstrated by combining experiments and modeling that the ORR on Pt nanoparticles occurs via a direct ORR pathway close to the onset potential and through HO_2^- intermediate at lower potentials.

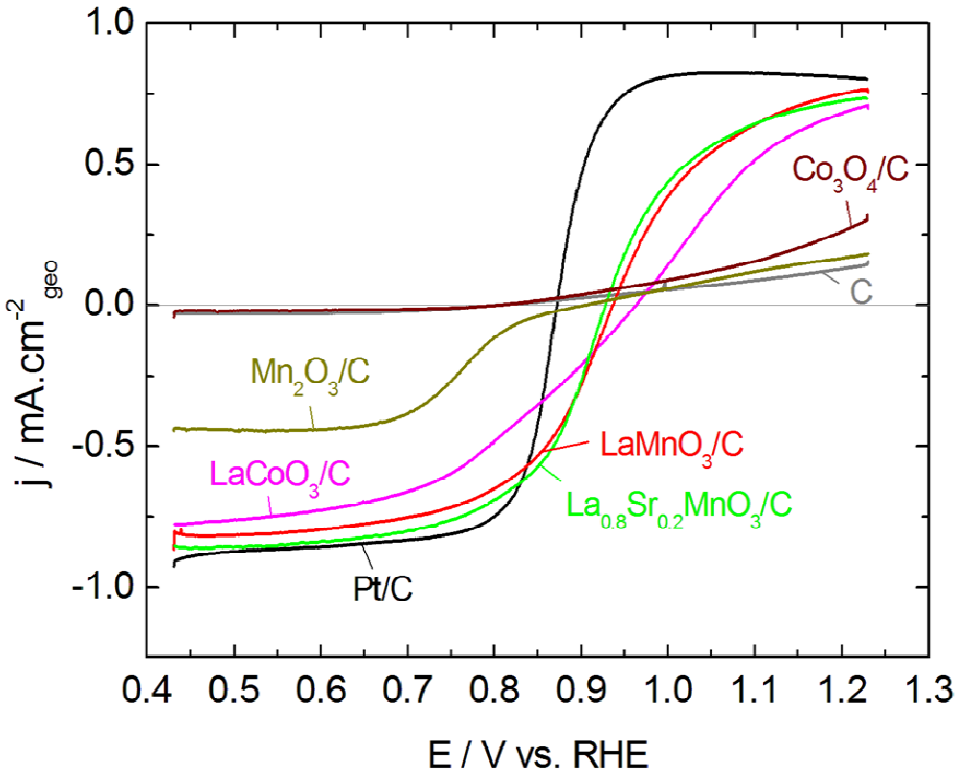

Figure 50 : *Positive scans of the RDE voltammograms of GC-supported thin films of oxide + Sibunit carbon in N_2-purged 1M NaOH + 0.84 mM H_2O_2 at 900 rpm and 10 mV.s^{-1}. Measurements were performed with 91 µg.cm$^{-2}_{geo}$ oxide + 37 µg.cm$^{-2}_{geo}$ Sibunit carbon. Color codes: $LaCoO_3$ + Sibunit carbon (pink), $LaMnO_3$ + Sibunit carbon (red), $La_{0.8}Sr_{0.2}MnO_3$+ Sibunit carbon (green), Mn_2O_3 + Sibunit carbon (khaki), and Co_3O_4 + Sibunit carbon (brown). Grey and black lines show RDE curves for 37 µg.cm$^{-2}_{geo}$ Sibunit carbon and Pt/C, respectively. Currents are normalized to the geometric area of the electrode and corrected to the background currents measured in the N_2 atmosphere without H_2O_2 presence.*

The Mn-based $LaMnO_3$ and $La_{0.8}Sr_{0.2}MnO_3$ perovskites display close mixed potentials, in agreement with works on $La_{1-x}Sr_xMnO_3$ [131], and very similar activity for HO_2^- reduction/oxidation with the optimum carbon loading (37 µg.cm$^{-2}_{geo}$ carbon) in the catalytic layer (Figure 50, red and green curves). This similarity for the HO_2^- reduction/oxidation reactions is in agreement with the similarity observed between their activities for the ORR (see section 4.4). Above (see section 5.3.1.1), it was discussed that $LaCoO_3$ is less active than either $LaMnO_3$ or $La_{0.8}Sr_{0.2}MnO_3$ for the HO_2^- reaction electrocatalysis. The comparison of the current slope near the mixed potential for various perovskites (Figure 50) is consistent with this hypothesis. As the mixed potential of $LaCoO_3$ is positively shifted compared to Mn-perovskites, it seems in particular that HO_2^- oxidation is slower on the cobalt perovskite.

From experimental curves, one can notice that two slopes are visible on the cathodic current of RDE voltammograms in H_2O_2 containing electrolyte for $LaCoO_3$ electrodes (Figure 50, pink curves). This indicates that at least two steps are involved in the HO_2^- reduction reaction, such as a chemical step followed by an electrochemical step, in agreement with the ring slope observed in the RRDE study of the ORR (see section 5.2.1.1). Howerer, at this stage, the nature of the chemical step is unknown but might be linked to an interaction between the perovskite surface and the adsorbed HO_2^-. This hypothesis will be further corroborated in section 5.5 with the help of the mathematical modeling.

The electrode surface composition has a great influence on the HO_2^- reduction/oxidation electrocatalysis. Indeed, it was reported that both the shape and the potential at zero current of H_2O_2 reduction/oxidation curves are function of the sweep direction for Pt electrodes [8,233-235,239,240]. This was linked to the potential-dependent oxide coverage of Pt surfaces, and points out to the influence of the surface oxidation state for the H_2O_2 reaction [241]. Furthermore, Savinova et al. found that the reaction rate of HO_2^- reduction on silver electrodes is strongly dependent on the surface state of silver [242].

As already mentioned, the nature of the B cation of the perovskite oxide has a strong influence on the voltammetric peaks observed in the supporting electrolyte (Figure 51,a). In order to investigate the effect of these redox transitions on the electrocatalytic activity, Figure 51,b presents the negative and the positive scan of the RDE voltammograms in the H_2O_2-containing electrolyte for $LaCoO_3$ and $La_{0.8}Sr_{0.2}MnO_3$ perovskites, after the background correction. The behavior of $LaMnO_3$ was similar to $La_{0.8}Sr_{0.2}MnO_3$ (Figure 101 in Appendix 3).

$La_{0.8}Sr_{0.2}MnO_3$ which displays more pronounced voltammetric peaks than $LaCoO_3$ also displays stronger hysteresis in the presence of H_2O_2. Indeed, for $La_{0.8}Sr_{0.2}MnO_3$, the positive scan is shifted positively by ca. 25 mV compared to the negative scan while $LaCoO_3$ presents almost superposed positive and negative scans. This shows that there is a “memory effect” of the surface state of Mn oxides on the HO_2^- activity. Based on these results and according to section 3.3.2, the following hypotheses may be proposed: perovskite in the oxidized state is more active for oxidation – negative shift of the mixed potential - thanks to the presence of Mn in the 4+ oxidation state, while perovskite in the reduced state is more active for reduction – positive shift of the mixed potential – thanks to the presence of Mn in the 3+ oxidation state and eventual modification of the surface and/or near surface structure and formation of oxygen vacancies. This is in agreement with the RRDE results (see section 5.2.1). As the

nature of the redox transitions occuring in Mn-perovskites is not fully understood, the exact active sites for HO_2^- reduction electrocatalysis cannot be identified yet.

It should be mentioned that the involvement of the redox couple Mn^{4+}/Mn^{3+} as an active site for the HO_2^- decomposition is discussed in the literature for Mn-based perovskites [125,126,130] and simple Mn oxides [243]. If this reaction is assumed as being the sum of HO_2^- reduction and HO_2^- oxidation, it can be tentatively proposed that Mn^{4+} favorises HO_2^- oxidation reaction and Mn^{3+}, HO_2^- reduction reaction. On the other hand, one may also suppose that oxygen vacancies – accompagnying the reduction of Mn - are involved in the mechanism, as mentioned by Matsumoto et al. [72] for HO_2^- reduction on $LaNiO_3$ perovskites and by Lee et al. [127] for HO_2^- decomposition on $A_{1-x}\ A'_xMnO_3$ perovskites (A=La, Nd, A'=K, Sr).

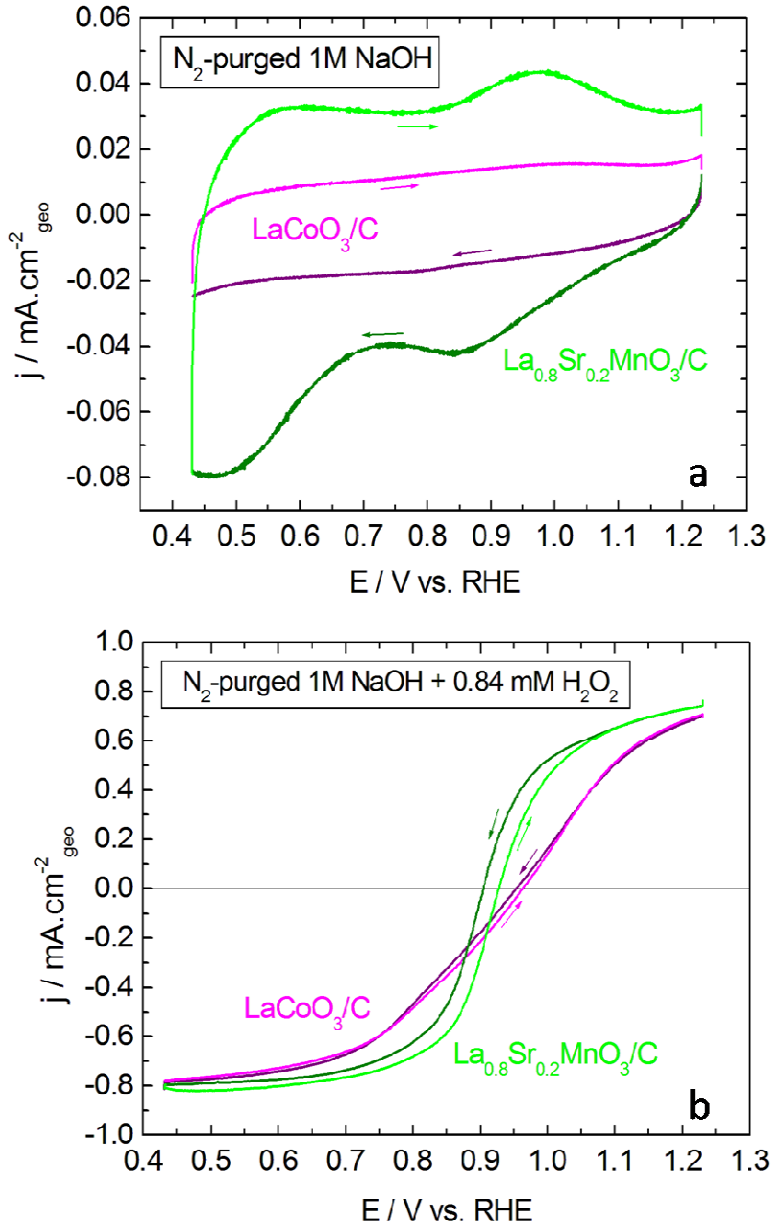

Figure 51 : *Negative and positive scans of (a) CV in N_2-purged 1M NaOH at 0 rpm and (b) RDE voltammograms in N_2-purged 1M NaOH + 0.84mM H_2O_2 at 900rpm, of GC-supported thin films of perovskite + Sibunit carbon at 10 mV.s^{-1}. Measurements were performed with 91 µg.cm$^{-2}_{geo}$ perovskite + 37 µg.cm$^{-2}_{geo}$ Sibunit carbon. Color codes: $LaCoO_3$ + Sibunit carbon (pink for positive scan and purple for negative scan) and $La_{0.8}Sr_{0.2}MnO_3$ + Sibunit carbon (green for positive scan and olive for negative scan), the arrows indicate the scan direction. Currents are normalized to the geometric area of the electrode. For RDE voltammograms in N_2-purged 1M NaOH + 0.84mM H_2O_2, the currents are corrected to the background currents measured in the N_2 atmosphere without H_2O_2 presence.*

Composite electrodes of simple oxides of cobalt and manganese were also studied in order to identify the role of the perovskite structure and of the transition metal in the electrocatalysis of HO_2^- reduction/oxidation reactions. On the one hand, it appears that Co_3O_4 is not active for the HO_2^- reduction (Figure 50, brown curves), but the increase of the current at high potentials shows that it is slightly more active than carbon (Figure 50, grey curves) for the HO_2^- oxidation. On the other hand, Mn_2O_3 is not very active for the HO_2^- oxidation since the current at high potential for Mn_2O_3/C composites (Figure 50, khaki curves) is similar to the current displayed by carbon alone (Figure 50, grey curves), but the currents measured at low potentials suggest some activity for the HO_2^- reduction, consistent with the literature data for Mn oxides [32,226] and RDE results for the ORR (see section 4.4.2.3). From these results, it seems that both the nature of the transition metal – in agreement with data for perovskite oxides - and the oxide structure are determining the activity for the HO_2^- reduction/oxidation. Nevertheless, as mentioned previously (see section 4.4.2.3), the low electrocatalytic activity of simple oxides may be related to their low conductivity and low surface area and might be enhanced by improving the catalytic layer quality. This is supported by the fact that improved structures such as vertically aligned Co_3O_4 nanowalls [244] demonstrated activity for HO_2^- reduction/oxidation in the literature.

5.4. Study of the catalytic HO_2^- decomposition

In section 5.3, it was demonstrated that perovskite oxides are active for HO_2^- reduction and oxidation reactions. In order to complement the study of the oxygen and HO_2^- reactions, the catalytic decomposition of HO_2^- was also studied using the volumetric method presented in section 2.4.2.

The establishement of the method (including the design of the setup, the establishement of the experiment procedure, and the choice of H_2O_2 concentrations and the catalyst masses) were performed by the author of the present thesis. Further experiments on the study of the HO_2^- decomposition were carried out by the master trainees Maximilien Huguenel (ECPM) and Elaine Dahlen (University of Savoie) under the supervision of the author of the present thesis.

5.4.1. Non catalytic HO_2^- decomposition: limits of the method

Hydrogen peroxide is known to decompose in time, even in the absence of a catalyst, and this process is faster in alkaline media. In order to estimate the rate of the non catalytic decomposition, experiments were performed without a catalyst and with various concentrations of H_2O_2.

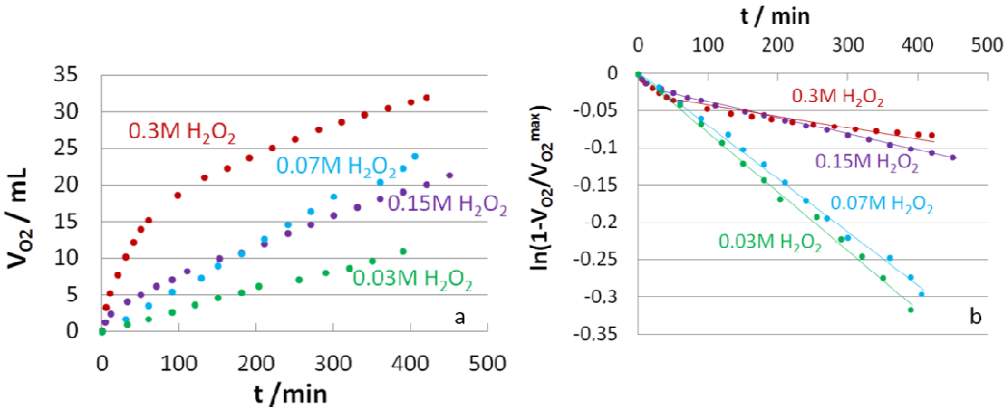

Figure 52 : *a. The volume of evolved O_2 (V_{O2}) and b. the corresponding plots of* $ln\left(1-\frac{V_{O_2}}{V_{O_{2max}}}\right)$ *vs. the time for a solution of O_2-saturated 1M NaOH + various concentrations of H_2O_2. Color codes for H_2O_2 concentrations: 0.03 (green), 0.07 (blue), 0.015 (purple) and 0.3M (dark red).*

As the plots V_{O2} versus time are not superposed for the different H_2O_2 concentrations (Figure 52,a), the zero order reaction is excluded. For all concentrations, $\ln\left(1-\frac{V_{O_2}}{V_{O_{2max}}}\right)$ relationship gives a linear plot in function of the time (Figure 52,b), as expected for a first order reaction (Equation 64). However, depending on the H_2O_2 concentration, two distinct first order constants were found. For low H_2O_2 concentrations (0.03M and 0.07M) the constant was ca. $1.3\ 10^{-5}\ s^{-1}$, while for higher H_2O_2 concentrations (0.15M and 0.3M) it was ca. $3.3\ 10^{-6}\ s^{-1}$.
The reasons of these differences are unknown but might be linked to the presence of remaining catalyst traces in the Teflon cell. Indeed, despite the careful cleaning procedure using piranha solution, a complete removal of catalysts is difficult to achieve due to the porosity of Teflon. In the presence of catalyst traces, a certain amount of HO_2^- would therefore be decomposed on the catalyst, reaction which is faster than the non catalytic decomposition. One may suppose that, for high H_2O_2 concentrations, the percentage of non catalytic reaction is larger than the percentage of the catalytic decomposition due to a limited number of catalyst sites. This would therefore lead in a global kinetic rate lower than for lower H_2O_2 concentrations which are less affected by the catalyst site number.

This shows the limits of the method to measure very low kinetic constants. Therefore, the higher constant obtained without catalyst ($1.3\ 10^{-5}\ s^{-1}$) was taken as an estimation of the error for the calculation of the first order rate constant.
In the following, the experiments were repeated three times (or twice when reproducibility was good). Then, a typical evolution of the volume of evolved O_2 is presented in the Figures "a", and the plots of $\ln\left(1-\frac{V_{O_2}}{V_{O_{2max}}}\right)$ in the Figures "b" are calculated from the average values of the repeated experiments. The errors bars in these plots were estimated from the reproductibility of the experiments and were in general larger than the error estimated from non catalytic decomposition. The first order rate constants were then determinated within the largest error.

5.4.2. Reaction order of the catalytic HO_2^- decomposition

In order to determine the reaction order of the catalytic HO_2^- decomposition on perovskite oxides, experiments were performed on a chosen perovskite ($LaMnO_3$) with various catalyst masses and H_2O_2 concentrations.

5.4.2.1. Dependence of the HO_2^- decomposition on the H_2O_2 concentration

The volumes of evolved O_2 during HO_2^- decomposition on $LaMnO_3$ in the presence of various concentrations of H_2O_2 are displayed in Figure 53,a. For each concentration, the theoretical maximum volume of O_2 V_{O2}^{max} calculated from perfect gas law (Equation 60) – 14 mL for 0.01M, 27 mL for 0.02M and 41 mL for 0.03M H_2O_2 – is reached.

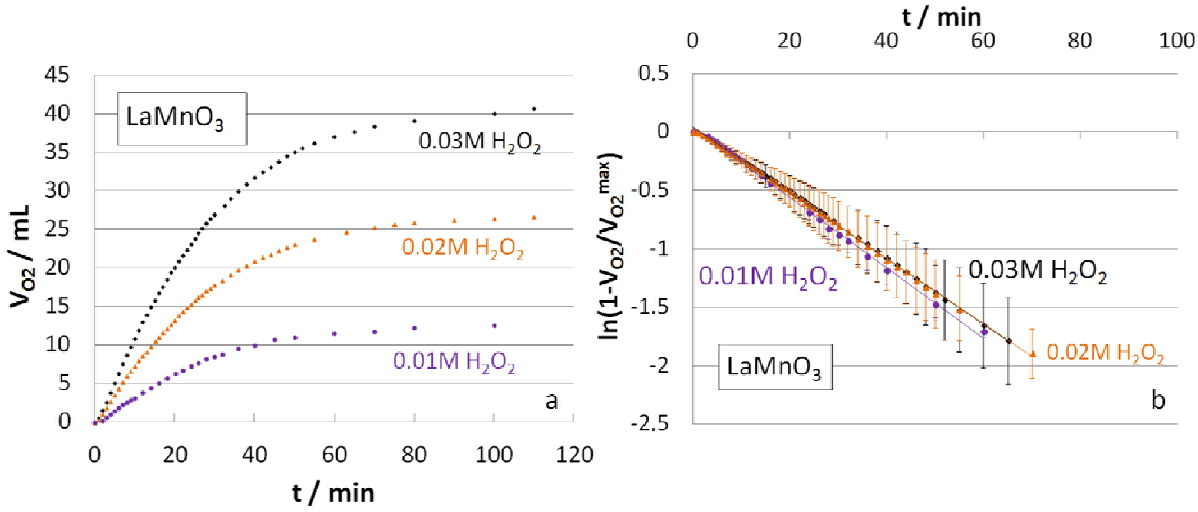

Figure 53 : *a. The volume of evolved O_2 (V_{O2}) and b. the average plots of* $ln\left(1-\frac{V_{O_2}}{V_{O_{2max}}}\right)$ *vs. the time for 10 mg of $LaMnO_3$ powder in O_2-saturated 1M NaOH + various concentrations of H_2O_2. Error bars represent standard deviation from at least two independent repeated measurements. Color codes for H_2O_2 concentrations: 0.01 (purple), 0.02 (orange) and 0.03M (black).*

Figure 53,b shows $\ln\left(1-\frac{V_{O_2}}{V_{O_{2max}}}\right)$ in function of the time. The good linearity with a correlation coefficient higher than 0.99 indicates that the reaction rate is first order with respect to H_2O_2 concentration. This is in agreement with literature data on perovskites [121-

125,127,133,189]. The first order constant k was then determined from the slope of this plot (Equation 64) and is presented in Table 12 for various H_2O_2 concentrations. All concentrations display similar k values within the experimental errors, as expected for a first order reaction.

Then, the heterogenous constant k_{het} was calculated using (Equation 65) with S_{BET} = 14 $m^2.g^{-1}$ ($LaMnO_3$, Table 5), m = 10 mg and $V_{solution}$ = 110 mL. For all H_2O_2 concentrations, k_{het} is close to 3.7 10^{-5} $cm.s^{-1}$ (Table 12). This demonstrates the ability of perovskite to catalytically decompose HO_2^-.

Table 12 : *First order constant k and heterogeneous constant k_{het} of H_2O_2 decomposition for 10 mg of $LaMnO_3$ powder in O_2-saturated 1M NaOH + various concentrations of H_2O_2. Errors were estimated from non catalytic decomposition measurements or from the reproducibility of the experiments (see section 5.4.1).*

H_2O_2 concentration (M)	**k (10^{-4} s^{-1})**	**k_{het} (10^{-5} $cm.s^{-1}$)**
0.03	4.7 ±1.1	3.7 ±0.9
0.02	4.5 ±0.8	3.5 ±0.7
0.01	5.0 ±0.2	3.9 ±0.2

5.4.2.2. Dependance of the HO_2^- decomposition on the mass of the catalyst

The volumes of O_2 evolved during the decomposition of 0.03M H_2O_2 in the presence of different amounts of $LaMnO_3$ are displayed in Figure 54,a. It is clear that the decomposition kinetics is dependent on the catalyst loading. The higher the catalyst mass, the higher is the O_2 volume, reaching V_{O2}^{max} more rapidly.

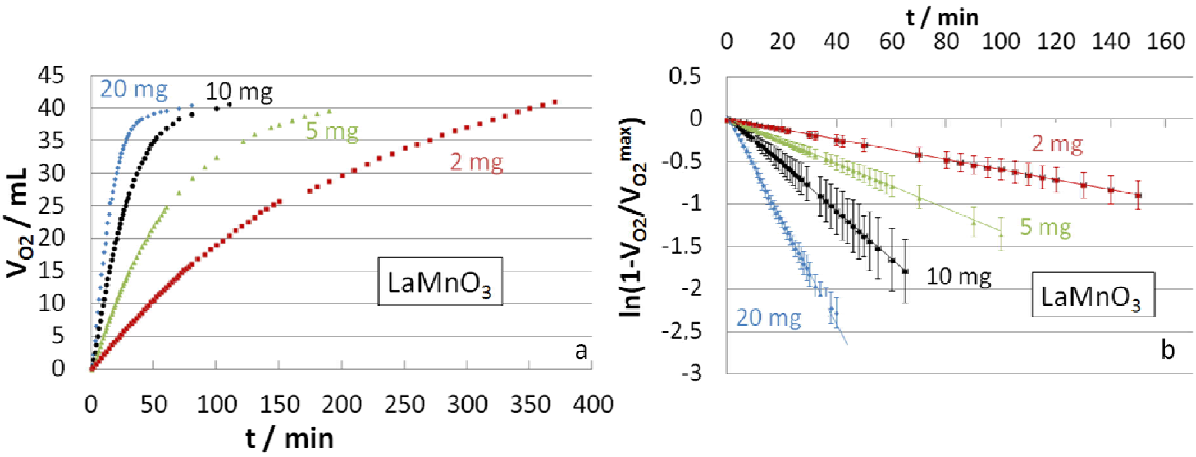

Figure 54 : *a. The volume of evolved O_2 (V_{O2}) and b. the average plots of* $ln\left(1-\frac{V_{O_2}}{V_{O_{2max}}}\right)$ *vs. the time for various masses of $LaMnO_3$ powder in O_2-saturated 1M NaOH + 0.03M H_2O_2. Error bars represent standard deviation from at least two independent repeated measurements. Color codes for perovskite masses: 2 (red), 5 (green), 10 (black) and 20 mg (blue).*

Figure 54,b points out that $\ln\left(1-\frac{V_{O_2}}{V_{O_{2max}}}\right)$ decreases linearly with the time, with a correlation coefficient higher than 0.99. The first order constant k was then determined from the slope of this plot (Equation 64).

Table 13 : *First order constant k and heterogeneous constant k_{het} of H_2O_2 decomposition for various masses of $LaMnO_3$ powder in O_2-saturated 1M NaOH + 0.03M H_2O_2. Errors were estimated from non catalytic decomposition measurements or from the reproducibility of the experiments (see section 5.4.1).*

Mass of catalyst (mg)	**k (10^{-4} s^{-1})**	**k_{het} (10^{-5} cm.s^{-1})**
20	10.2 ±0.9	4.0 ±0.4
10	4.7 ±1.1	3.7 ±0.9
5	2.3 ±0.4	3.6 ±0.6
2	1.0 ±0.2	3.9 ±0.8

It is evident that k increases with the catalyst mass (Table 13), consistent with the work of Lee et al. [127] on $La_{0.7}Sr_{0.3}MnO_3$ perovskite.

The heterogeneous constant k_{het} was then determined from (Equation 65) with S_{BET} = 14 $m^2.g^{-1}$ and $V_{solution}$ = 110 mL. For all $LaMnO_3$ masses, k_{het} is close to 3.7 10^{-5} cm.s^{-1} (Table 13), as found for various H_2O_2 concentrations on the same perovskite oxide (see section 5.4.2.1).

Thus, the similarity of k_{het} values between the various perovskite masses suggests that the catalytic HO_2^- decomposition reaction is indeed limited by the reaction kinetics rather than by mass transport or number of active sites.

5.4.3. Heterogeneous constant of the HO_2^- decomposition on various oxide catalysts

Figure 55 shows the volume of evolved O_2 and the $\ln\left(1-\frac{V_{O_2}}{V_{O_{2max}}}\right)$ relationship in function of the time for HO_2^- decomposition on various oxide catalysts in the presence of 0.03M H_2O_2. The linearity displayed in Figure 55,b confirms the first order of the catalytic HO_2^- decomposition reaction on perovskite oxides, as demonstrated in section 5.4.2 for $LaMnO_3$, and reported in the literature [121-125,127,133,189].

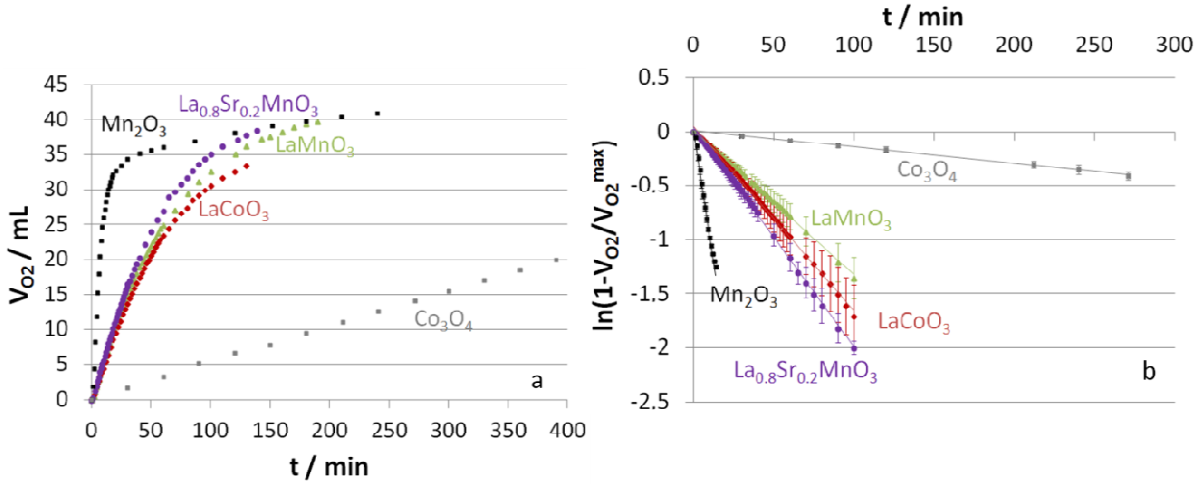

Figure 55 : *a. The volume of evolved O_2 (V_{O2}) and b. the average plots of $\ln\left(1-\frac{V_{O_2}}{V_{O_{2max}}}\right)$ vs. the time for 5 mg of various catalysts in O_2-saturated 1M NaOH + 0.03M H_2O_2. Error bars represent standard deviation from at least two independent repeated measurements. Color codes: $LaCoO_3$ (red), $LaMnO_3$ (green), $La_{0.8}Sr_{0.2}MnO_3$ (purple), Co_3O_4 (grey), Mn_2O_3 (black).*

Table 14 : *Specific surface of catalyst, and first order constant k and heterogeneous constant k_{het} of H_2O_2 decomposition for 5 mg of catalyst in O_2-saturated 1M NaOH + 0.03M H_2O_2. Errors were estimated from non catalytic decomposition measurements or from the reproducibility of the experiments (see section 5.4.1).*

Catalyst	$S_{specific}$ ($m^2.g^{-1}$)	k (10^{-4} s^{-1})	k_{het} (10^{-5} $cm.s^{-1}$)
$LaCoO_3$	10	2.8 ±0.5	6.2 ±1.0
$LaMnO_3$	14	2.3 ±0.4	3.6 ±0.6
$La_{0.8}Sr_{0.2}MnO_3$	17	3.3 ±0.3	4.3 ±0.3
Co_3O_4	2	0.2 ±0.1	2.0 ±1
Mn_2O_3	3	15.8 ±0.1	120 ±1
Sibunit carbon	66	0.2 ±0.1	0.06 ±0.04
Pt/C	28 (Pt)	12 ±1.0 (1 mg Pt)	48 ±5.0

The heterogenous constant k_{het} was calculated using (Equation 65) with $S_{specific}$ equal to S_{BET} for oxides (Table 5), to the surface provided by the supplier for C, and to the electrochemical active surface area for Pt/C (see section 2.3.4.3), with m = 5 mg (except for Pt/C : m = 1 mg Pt) and with $V_{solution}$ = 110 mL.

The Mn-perovskites studied for the decomposition reaction – $LaMnO_3$ and $La_{0.8}Sr_{0.2}MnO_3$ - display a k_{het} of ca. 4 10^{-5} $cm.s^{-1}$ (Table 14). This is consistent with the value found by Soleymani et al. [125] for $La_{1-x}Ca_xMnO_3$ (k_{het} between 5 and 7 10^{-5} $cm.s^{-1}$). $LaCoO_3$ is slightly more active in this study with a k_{het} of ca. 6 10^{-5} $cm.s^{-1}$ (Table 14), close to the value found by Hermann [133] for $La_{0.6}Ca_{0.4}CoO_3$ (ca. 10 10^{-5} $cm.s^{-1}$ with S_{BET} = 18 $m^2.g^{-1}$ and $V_{solution}$ = 50 mL). This suggests that HO_2^- decomposition is not responsible for the lower ORR activity observed on Co perovskites compared to Mn perovskites.

Since its first order constant is very close to the one of a non catalytic reaction, one may conclude that Sibunit carbon has low activity for the catalytic decomposition of HO_2^- (Table 14), in agreement with literature data for other carbon materials [209,218,228]. This confirms that perovskite oxides are much more active than carbon to decompose HO_2^-.

The H_2O_2 decomposition mechanism is not yet understood, a large variety of pathways having been proposed for different catalysts. Some authors proposed that H_2O_2 decomposition occurs through a chemical pathway [214,245,246], while others suggest that the decomposition reaction is the sum of electrochemical reduction and oxidation of H_2O_2 [247,248]. Both may

involve the redox transition of a metal cation. For example, FeOOH was widely studied and different authors proposed either chemical [246] or electrochemical [248] H_2O_2 decomposition mechanism with the participation of Fe^{3+}/Fe^{2+} redox couple. For perovskite oxides too, the redox transitions of metal cation were mentioned as being involved in the HO_2^- decomposition mechanism for Ni-based [121-124] as well as for Mn-based perovskites [125,126,130] (see section 1.4.3.2). Based on the latter publications, one can reasonably assume that the redox transitions of Mn participate in the HO_2^- decomposition mechanism on $LaMnO_3$ and $La_{0.8}Sr_{0.2}MnO_3$, as for ORR and HO_2^- reduction reaction.

As for carbon, the first order constant of Co_3O_4 is very close to the one for non catalytic reaction, proving low activity of this catalyst for the catalytic decomposition of HO_2^- (Table 14). Co_3O_4 catalysts were also studied by several authors, and their activity appears to be low in the absence of either doping or a carbon carrier [166,228,249]. For exemple, Deraz [249] found a heterogenous constant of ca. 10^{-6} $cm.s^{-1}$ (with a reaction rate constant per unit surface area of ca. 5 10^{-2} $min^{-1}.m^{-2}$ and $V_{solution}$=10.5 mL) for Co_3O_4 without ZnO doping, and up to 10^{-5} $cm.s^{-1}$ with ZnO doping. The authors proposed that this improvement is due to an increased number of ions pairs (Co^{3+}–Co^{2+} and Co^{3+}–Zn^{2+}) at the catalyst surface, and thus to the enhancement of the redox pathway involved in the HO_2^- decomposition reaction. According to Jiang et al. [228], an improvement of the catalyst morphology by precipitating the cobalt oxide directly on graphite surface can strongly increase the catalytic activity for HO_2^- decomposition. Moreover, Goldstein et al. [250] showed that the surface area of cobalt oxide catalysts has a strong impact on the heterogeneous activity – i.e. after surface normalization - for HO_2^- decomposition. Indeed, in their work, cobalt oxides with low surface area display significantly lower heterogeneous activities that high surface area oxides and a zero order reaction instead of a first order reaction due to the high HO_2^- concentration compared to available active sites.

Therefore the low conductivity (see section 4.4.2.3) as well as the low accessible surface area due to strong particle agglomeration (see section 3.2) of Co_3O_4 used in this study may be the cause of its low catalytic activity for HO_2^- decomposition. Regarding the linear relationship observed between V_{O2} and the time in Figure 55, and contrary to the previous approximation as a first order reaction, HO_2^- decomposition on Co_3O_4 may be a zero order reaction, as found by Goldstein et al. [250]. Then, the volume of oxygen is linked to the zero order constant k_0 by (Equation 77) :

$$k_0 t = C_{H_2O_2}{}^{o} \left(\frac{V_{O_2}}{V_{O_2}{}^{max}} \right)$$ (Equation 77)

Thus, k_0 = 6.4 10^{-7} M.s^{-1} for Co_3O_4 and the corresponding heterogenous constant is 7 10^{-6} mol.m^{-2}.s^{-1}.

However, Mn_2O_3, which shows similar microstructure to Co_3O_4 and low conductivity too, displays a very high catalytic activity – ca. 20 times higher than perovskite oxides - for the studied reaction. High catalytic activity was also observed in previous works on Mn oxides [224,225], but is not consistent with the low activity of Mn_2O_3 for HO_2^- reduction and especially for HO_2^- oxidation observed in this work. Thus, it suggests that the HO_2^- decompositon occurs predominantly via a chemical rather an electrochemical mechanism on this simple oxide. One should also note that HO_2^- reactions are probably dependent on the H_2O_2 concentrations (see section 5.3.1.2 and 5.4.1). In this work, high H_2O_2 concentrations (≥ 0.01 M) were used for HO_2^- decomposition study for technical reasons (see section 2.4.2) while electrochemical reactions were investigated at lower concentrations (≤ 0.084 mM).

The differences of the HO_2^- decomposition activity between Mn_2O_3 and Mn-based perovskites can be due to (i) different mechanisms such as an electrochemical pathway for perovskite oxides and a chemical mechanism for the simple oxide, which is less conductive and/or to (ii) an underestimation of the active surface for Mn_2O_3. Indeed, it is known that redox transitions of Mn propagate into the bulk of Mn simple oxides (while the CV charges suggest that they occur only on the surface of the perovskite oxides (see sections 3.3.3 and 4.2), therefore the BET surface is not suitable to evaluate its active surface.

Regardless its origin, the activity of Mn_2O_3 for HO_2^- decomposition confirms that this catalyst can transform HO_2^- formed on carbon into OH^-, leading to an ORR process of more than 2 electrons on Mn_2O_3/carbon electrodes, as found in section 4.4.2.3. In this work, Mn_2O_3 is even more active for HO_2^- decomposition than Pt/C which displays a heterogenous constant of ca. 48 10^{-5} cm.s^{-1}. This value is three times smaller than the one found by Venketachalapathy et al. [247] in 1M KOH (144 10^{-5} cm.s^{-1}). It is certainly due to differences in the platinum type - the mentioned authors studied Pt/C with 10 m^2.g^{-1} Pt - and thus in differences in particle size and presence of defects which affect the catalytic activity.

5.5. General discussion of the ORR on perovskite/carbon composites

In the previous sections of this chapter, an interpretation of the experimental data was presented. It should be noted however that this interpretation was not solely based on the experiments but was much inspired by numerous discussions with Dr. Antoine Bonnefont (Institut de Chimie, Université de Strasbourg) who, based on the experimental data, set up a kinetic model aimed at reproducing, semiquantitatively, the ORR and the HO_2^- reduction/oxidation currents obtained for $LaCoO_3$ and $La_{0.8}Sr_{0.2}MnO_3$ perovskites.
In this section, this model will be presented. In the first part of this section, the chosen mechanism and the corresponding kinetic equations are described, while the simulated curves are compared to the experimental data in the second part in order to validate the model assumptions.

5.5.1. The model

The model was developed as follows. First of all, the mechanism was chosen considering both the literature and the experimental results. Secondly, the kinetic equations were written and simplified following the electrochemical kinetic laws [155,156]. Then, the rate constants were varied such as to reproduce semiquantitatively the experimental data. This procedure was first applied to electrocatalysis on carbon. Secondly, the simulation parameters of the perovskite and perovskite/carbon curves were adjusted taking into account the contribution of carbon.
Since there are many unknown parameters, the rate constants of the model were chosen to reproduce the experimental trends of all experimental data, namely RRDE voltammograms (ORR disk current, HO_2^- ring current and HO_2^- yield) for various electrode compositions, as well as RDE voltammograms in electrolytes containing different concentrations of H_2O_2.
At this stage, the aim of the modeling is to better understand the ORR electrocatalysis on the composite electrodes and to identify the contribution of perovskite and of carbon to the ORR steps, rather than to precisely determine the kinetic rate constants. The development of the

model is still under progress, therefore the rate constants and the potentials chosen for the kinetic equations are preliminary

5.5.1.1. Tentative ORR mechanism on carbon

As mentioned in section 1.2.2.2, there is no common view on the ORR pathways occurring on carbon materials. Moreover, the understanding of the ORR mechanism on carbon is beyond the purpose of the present thesis. Therefore, it was chosen to use the simplest mechanism description for the ORR on carbon. The same mechanism was used for glassy carbon and for Sibunit carbon.

It was demonstrated in this work that carbon is able to reduce O_2 into HO_2^-. Thus, the first ORR step occurring on carbon may be the adsorption of O_2 on free sites of carbon (Equation 78):

$$\text{Step 1, carbon}: \ O_2 + * \rightleftarrows O_{2,ads} \quad \text{(Equation 78)}$$

where * is a free site on the carbon surface, and "ads" stands for an adsorbed species. The kinetics of this step can be written as (Equation 79):

$$\upsilon_{1,C} = k_{1,C} C_{O2}^{x=0} \left(1 - \theta_{O2,C} - \theta_{HO2-,C}\right) - k_{-1,C} \theta_{O2,C} \quad \text{(Equation 79)}$$

where $k_{1,C}$ and $k_{-1,C}$ are the rate constants of O_2 adsorption and desorption on carbon, respectively, $C_{O2}^{x=0}$ represents the O_2 concentration at the electrode surface in $mol.cm^{-3}$ and $\theta_{O2,C}$ and $\theta_{HO2-,C}$ are, correspondingly, the coverage of O_2 and HO_2^- species on the carbon surface. Thus $(1- \theta_{O2,C} - \theta_{HO2-,C})$ is the fraction of free carbon sites while $\theta_{O2,C}$ is the fraction of carbon sites covered by O_2 which can desorb through the inverse reaction. The unit of the reaction rate υ is s^{-1}.

To reproduce the experimentals curves, the following rate constants were chosen: $k_{1,C} = 10^8$ $cm^3.mol^{-1}.s^{-1}$ and $k_{-1,C} = 5\ 10^2\ s^{-1}$. Three time higher rate constants were used for the ORR modeling on Pt nanoparticles attached to vertically aligned carbon nanofilaments (Pt/VACNF) by Ruvinskiy et al. [229].

Then, the adsorbed O_2 is reduced into the adsorbed HO_2^- through a two electron charge transfer step (Equation 80). This step is in fact the sum of at least two individual electron charge transfers.

$$\text{Step 2, carbon}: \ O_{2,ads} + H_2O + 2e^- \rightleftarrows {HO_2^-}_{ads} + OH^- \text{(Equation 80)}$$

According to the Bulter-Volmer theory, for a one electron rate determining step, the kinetics can be expressed as (Equation 81):

$$\upsilon_{2,C} = k_{2,C}\theta_{O2,C} \exp\left(\frac{-(1-\alpha)F(E-E_2°)}{RT}\right) - k_{2,C}\theta_{HO2-,C}\exp\left(\frac{\alpha F(E-E_2°)}{RT}\right) \text{(Equation 81)}$$

with $k_{2,C}$, the rate constant, and α, the symmetry factor of the charge transfer in the oxidation direction. The choice of the potential $E_2°$ is given in Table 15.

From experimental curves, it was observed that, while the ORR is relatively fast on carbon (see section 4), the oxidation of HO_2^- hardly occurs (see section 5.3.1.3). Thus a symmetry factor of 0.3 was chosen for the oxidation reaction.

The rate constant was chosen as $k_{2,C} = 0.01\ s^{-1}$ in order to reproduce the experimental data.

The present study confirms the well known fact that carbon is not able to catalyse HO_2^- reduction or decomposition. Thus the formed adsorbed HO_2^- is then desorbed and diffuses to the electrolyte according to the inverse reaction of (Equation 82):

$$\text{Step 3, carbon}: HO_2^- + * \rightleftarrows {HO_2^-}_{ads} \text{ (Equation 82)}$$

With the rate expressed by (Equation 83):

$$\upsilon_{3,C} = k_{3,C}C_{HO2-}^{x=0}\left(1 - \theta_{O2,C} - \theta_{HO2-,C}\right) - k_{-3,C}\theta_{HO2-,C} \text{ (Equation 83)}$$

where $k_{3,C}$ and $k_{-3,C}$ stand for the rate constants of HO_2^- adsorption and desorption on carbon, respectively, and $C_{HO2-}^{x=0}$ represents the HO_2^- concentration at the electrode surface in $mol.cm^{-3}$.

The experimental data could be reproduced using $k_{3,C} = 10^7\ cm^3.mol^{-1}.s^{-1}$ and $k_{-3,C} = 50\ s^{-1}$.

It was shown in section 4 that carbon is involved in the ORR mechanism on perovskite/carbon electrodes. Therefore the contribution of the above mechanism was used not only for carbon electrodes but also for composite electrodes.

5.5.1.2. Tentative ORR mechanism on perovskites

The mechanism of the ORR on perovskites was inspired by the work of Suntivich et al. [84] validated by the density functional theory (DFT) calculations of Wang et al. [217] and adapted in order to reproduce the experimental findings of this work.

The proposed mechanism is in agreement with the behavior observed in this work and discussed in sections 4 and 5: (i) ORR is a "series" pathway, (ii) the HO_2^- intermediate is reduced through a chemical step followed by an electrochemical step, (iii) the redox transitions of the B cations are involved in the mechanism (this will be further confirmed in section 6).

The first ORR step on perovskites is expected to be an electrosorption step, i.e. an adsorption/desorption step coupled with a charge transfer, to replace OH_{ads} adsorbed on an active site by $O_{2,ads}$ (Equation 84):

$$\text{Step 1, perovskite}: \ O_2 + OH_{ads} + e^- \rightleftarrows O_{2,ads} + OH^- \quad \text{(Equation 84)}$$

This reaction is potential activated and depends on the concentration of O_2 (Equation 85):

$$\upsilon_{1,P} = k_{1,P} C_{O2}^{x=0} \left(1 - \theta_{O2,P} - \theta_{HO2,P} - \theta_{O,P}\right) \exp\left(\frac{-(1-\alpha)F(E-E_1^\circ)}{RT}\right) - k_{-1,P}\theta_{O2,P} \exp\left(\frac{\alpha F(E-E_1^\circ)}{RT}\right)$$

(Equation 85)

where $(1- \theta_{O2,P} - \theta_{HO2,P} - \theta_{O,P})$ is the fraction of perovskite sites covered by OH (these are all sites which are not occupied by O_2, HO_2 or O species) and $\theta_{O2,P}$ is the fraction of sites covered by O_2.

It is postulated that $O_{2,ads}$ is further reduced through a one electron charge transfer to form HO_2 species (Equation 86):

$$\text{Step 2, perovskite}: \ O_{2,ads} + H_2O + e^- \rightleftarrows HO_{2,ads} + OH^- \quad \text{(Equation 86)}$$

with (Equation 87):

$$\upsilon_{2,P} = k_{2,P}\theta_{O2,P} \exp\left(\frac{-(1-\alpha)F(E-E_2^\circ)}{RT}\right) - k_{2,P}\theta_{HO2,P} \exp\left(\frac{\alpha F(E-E_2^\circ)}{RT}\right) \quad \text{(Equation 87)}$$

The experiments showed that $LaCoO_3$ is less active than $La_{0.8}Sr_{0.2}MnO_3$ for the ORR and for the H_2O_2 oxidation. Therefore a factor of ca. 3 was chosen between the rate constants of the two perovskites for the 1st and 2nd steps, and for the corresponding inverse reactions.

The rate constants used to reproduce the experimental data are presented in Table 16. As a first attempt, the symmetry factors were all taken equal to 0.5. Table 15 gives the corrected standard potentials utilized in the kinetic equations.

The formed $HO_{2,ads}$ may then desorb from the perovskite surface in favor of OH_{ads}. Also, HO_2^- species, for example formed on carbon surface (see section 5.5.1.1) or placed in the electrolyte, can be adsorbed on the perovskite surface (Equation 88):

$$\text{Step 3, perovskite}: HO_2^- + OH_{ads} \rightleftarrows HO_{2,ads} + OH^- \quad \text{(Equation 88)}$$

The kinetics of this adsorption/desorption step is described by (Equation 89):

$$\upsilon_{3,P} = k_{3,P} C_{HO2-}^{x=0} \left(1 - \theta_{O2,P} - \theta_{HO2,P} - \theta_{O,P}\right) - k_{-3,P} \theta_{HO2,P} \quad \text{(Equation 89)}$$

For a first attempt of modeling, identical rate constants were chosen for the two perovskites for this reaction (Table 16).

It was demonstrated that, contrary to carbon, perovskite oxides are able to reduce $HO_{2,ads}$ into OH^- to ensure a global transfer of 4 electrons in the ORR. Moreover, the current slope at the ring and the RDE voltammogram shape in the presence of H_2O_2 suggest that the reduction of $HO_{2,ads}$ probably occurs through a chemical step followed by an electrochemical step. The chemical step may be the splitting of HO_2 and OH into O species on the perovskite surface (Equation 90).

$$\text{Step 4, perovskite}: HO_{2,ads} + OH_{ads} \rightarrow 2\,O_{ads} + H_2O \quad \text{(Equation 90)}$$

This step is irreversible and does not depend on the applied potential. Therefore the reaction kinetics is described by (Equation 91):

$$\upsilon_{4,P} = k_{4,P} \theta_{HO2,P} \left(1 - \theta_{O2,P} - \theta_{HO2,P} - \theta_{O,P}\right) \quad \text{(Equation 91)}$$

For this reaction, identical rate constants were chosen for the two perovskites as well (Table 16).

Finally, O_{ads} is electrochemically reduced into OH_{ads} through step 5 (Equation 92):

$$\text{Step 5, perovskite}: O_{ads} + H_2O + e^- \rightleftarrows OH_{ads} + OH^- \quad \text{(Equation 92)}$$

This reaction is potential dependent (Equation 93), hence the HO_2^- yield varies with the potential.

$$\upsilon_{5,P} = k_{5,P} \theta_{O,P} \exp\left(\frac{-(1-\alpha)F(E-E_5^\circ)}{RT}\right) - k_{5,P}\left(1 - \theta_{O2,P} - \theta_{HO2,P} - \theta_{O,P}\right)\exp\left(\frac{\alpha F(E-E_5^\circ)}{RT}\right) \quad \text{(Equation 93)}$$

This reaction (Equation 92) also described redox transitions of $B^{(m+1)+}$/ B^{m+} (Co^{3+}/Co^{2+} or Mn^{4+}/ Mn^{3+}) occurring with the polarization and observed in CVs in N_2 atmosphere. O

species are supposed to be adsorbed on $B^{(m+1)+}$ (B=O) and OH species, on B^{m+} (B-OH). Indeed, these intermediates – OH and O - are known to be strongly adsorbed on the perovskite surface according to DFT calculations [217].

The RDE voltammograms in H_2O_2-containing electrolyte and the HO_2^- yield during the ORR suggested that $LaCoO_3$ is less active for the HO_2^- reduction reaction than Mn-perovskites. Also, the redox transition of the former perovskite are less pronounced than the latter. This may be due to a slightly weaker adsorption on $LaCoO_3$ [137]. Thus, a lower rate constant was chosen for the $LaCoO_3$ perovskite.

In order to investigate the choice of the value of this constant on the results, the modeling was also performed with identical constants for both perovskites and is presented in Appendix 4.

It can be noticed that, in this model, O_2 reacts with Mn in the 3+ oxidation state (Mn-OH, Mn-O_2) for Mn-perovskites, which is consistent with literature data on Mn oxide (see section 4.4.2.1).

Table 15 : *Corrected standard potentials used in the mathematical model.*

$E_i°$	V vs. RHE	Correction
$E_1°$	1.13	Potential of O_2/HO_2^- couple corrected to the solubility of O_2 in 1M NaOH for step 1
$E_2°$	0.953	Potential of O_2/HO_2^- couple corrected to the solubility of O_2 in 1M NaOH for step 2
$E_5°$	0.98	Potential of the redox of $B^{(m+1)+}/B^{m+}$ couple

Table 16 : *ORR rate constants used in the mathematical model to fit the experimental curves of $LaCoO_3$ and $La_{0.8}Sr_{0.2}MnO_3$ electrodes.*

ORR steps	$LaCoO_3$	$La_{0.8}Sr_{0.2}MnO_3$
Step 1 : electrosorption of $O_{2,ads}$ (Equation 84)	$k_{1,P} = 5\ 10^2\ cm^3.mol^{-1}.s^{-1}$ $k_{-1,P} = 5\ 10^2\ s^{-1}$ $\alpha = 0.5$ (Equation 85)	$k_{1,P} = 1.4\ 10^3\ cm^3.mol^{-1}.s^{-1}$ $k_{-1,P} = 1.4\ 10^3\ s^{-1}$ $\alpha = 0.5$ (Equation 85)
Step 2 : reduction of $O_{2,ads}$ (Equation 86)	$k_{2,P} = 10\ s^{-1}$ $\alpha = 0.5$ (Equation 87)	$k_{2,P} = 30\ s^{-1}$ $\alpha = 0.5$ (Equation 87)
Step 3 : adsorption of $HO_{2,ads}$ (Equation 88)	$k_{3,P} = 5\ 10^7\ cm^3.mol^{-1}.s^{-1}$ $k_{-3,C} = 20\ s^{-1}$ (Equation 89)	$k_{3,P} = 5\ 10^7\ cm^3.mol^{-1}.s^{-1}$ $k_{-3,C} = 20\ s^{-1}$ (Equation 89)
Step 4 : splitting into O_{ads} (Equation 90)	$k_{4,P} = 30\ s^{-1}$ (Equation 91)	$k_{4,P} = 30\ s^{-1}$ (Equation 91)
Step 5 : reduction of O_{ads} (Equation 92)	$k_{5,P} = 0.1\ s^{-1}$ ($k_{5,P} = 0.2\ s^{-1}$ in Appendix 4) $\alpha = 0.5$ (Equation 93)	$k_{5,P} = 0.2\ s^{-1}$ $\alpha = 0.5$ (Equation 93)

5.5.1.3. Equation simplifications and approximations

With the RDE technique, the mass transport phenomena are controlled and the processes occur under stationary conditions. Therefore, several simplifications can be applied and relationships between different terms can be found.

In particular, within the diffusion layer thickness δ given by (Equation 37), a linear concentration profile is assumed (Equation 94):

$$\frac{\partial C_i}{\partial x} = \frac{C_i* - C_i(0)}{\delta} \quad \text{(Equation 94)}$$

The diffusion coefficients of O_2 and HO_2^- in 1M NaOH were determined with Pt/C electrodes as $D_{O2} = 1.5\ 10^{-5}$ $cm^2.s^{-1}$ and $D_{HO2-} = 0.8\ 10^{-5}$ $cm^2.s^{-1}$, respectively. Thus, the diffusion layer thickness at 900 rpm is 19 µm for O_2 and 15 µm for HO_2^-. The electrode thickness is assumed to be sufficiently small to keep this linear concentration profile. Also, it is assumed that the perovskite and carbon are well mixed in the catalytic layer and that the concentration of O_2 (or HO_2^-) is the same in the vicinity of carbon and perovskite sites.

At the electrode surface, the consumption of O_2 and HO_2^- is related to the reaction rates of the corresponding adsorption and electrosorption steps (Equation 95)(Equation 96):

$$D_{O2}\left(\frac{\partial C_{O2}}{\partial x}\right) = \Gamma_{geo,C}\upsilon_{1,C} + \Gamma_{geo,P}\upsilon_{1,P} \quad \text{(Equation 95)}$$

$$D_{HO2-}\left(\frac{\partial C_{HO2-}}{\partial x}\right) = \Gamma_{geo,C}\upsilon_{3,C} + \Gamma_{geo,P}\upsilon_{3,P} \quad \text{(Equation 96)}$$

where Γ_{geo} stands for the number of active sites per geometric area of the electrode.

The number of active sites per specific area $\Gamma_{specific}$ was taken as $4.14\ 10^{-10}$ $mol.cm^{-2}_{oxide}$ considering the atomic structure of perovskites. It is one order of magnitude less than the number of Pt active sites on Pt electrode ($2.2\ 10^{-9}$ $mol.cm^2_{Pt}$).

Then, the number of active sites per geometric area Γ_{geo} in the perovskite electrode can be approximated knowing the catalyst loading l and the specific surface area, i.e. the BET surface area S_{BET}, of the perovskite (Equation 97).

$$\Gamma_{geo} = S_{BET} * \Gamma_{specific} * l \text{ (Equation 97)}$$

For example, for an electrode containing 46 $\mu g.cm^{-2}_{geo}$ of $La_{0.8}Sr_{0.2}MnO_3$, the number of active sites is $\Gamma_{geo,La0.8Sr0.2MnO3} = (17\ 10^4) * (4.14\ 10^{-10}) * (46\ 10^{-6}) = 3.2\ 10^{-9}$ $mol.cm^{-2}_{geo}$. For an electrode containing 91 $\mu g.cm^{-2}_{geo}$ or 23 $\mu g.cm^{-2}_{geo}$ perovskite, the number of active sites is multiplied or divided by 2, respectively.

However, this approximation is only valid for electrodes with an optimal carbon loading. For perovskite electrodes without carbon, the electrical contact is not sufficient to ensure participation of all active sites in electrochemical processes. Therefore, a lower value of Γ_{geo} was used, in agreement with the charge measured by CV in N_2 atmosphere for electrodes with an insufficient amount of carbon (Figure 31).

For the first attempt of modeling, the number of active sites per specific area $\Gamma_{specific}$ of carbon was assumed to be comparable to that of a perovskite. Then, Γ_{geo} was calculated using a roughness factor of 1 for glassy carbon, and using the specific surface area and loading for Sibunit carbon.

The values of Γ_{geo} used in the model for carbon and perovskite are listed in Table 17 for electrodes containing 46 µg.cm$^{-2}_{geo}$ perovskite and/or 19 µg.cm$^{-2}_{geo}$ carbon.

Table 17 : *Number of carbon and perovskite ORR active sites per geometric area used in the mathematical model to fit the experimental curves of $LaCoO_3$ and $La_{0.8}Sr_{0.2}MnO_3$ electrodes containing 46 µg.cm$^{-2}_{geo}$ perovskite and/or 19 µg.cm$^{-2}_{geo}$ carbon*

Quantity of carbon in the catalytic layer	**Number of carbon sites**	**Number of $LaCoO_3$ sites (46 µg.cm$^{-2}_{geo}$)**	**Number of $La_{0.8}Sr_{0.2}MnO_3$ sites (46 µg.cm$^{-2}_{geo}$)**
Without Sibunit carbon	4 10^{-10} mol.cm$^{-2}_{geo}$ (glassy carbon)	8 10^{-10} mol.cm$^{-2}_{geo}$	8 10^{-10} mol.cm$^{-2}_{geo}$
With 19 µg.cm$^{-2}_{geo}$ Sibunit carbon	10^{-8} mol.cm$^{-2}_{geo}$	1.9 10^{-9} mol.cm$^{-2}_{geo}$	3.2 10^{-9} mol.cm$^{-2}_{geo}$

The temporal variation of the site coverage by a given species can be calculated from the rate of the reactions involving this species. Under stationary conditions, the temporal variation is equal to zero and this therefore gives relationships between the reaction rates. The mentioned relationships are: (Equation 98) (Equation 99) on carbon,

$$\frac{d\theta_{O2}}{dt} = \upsilon_{1,C} - \upsilon_{2,C} = 0 \quad \text{(Equation 98)}$$

$$\frac{d\theta_{HO2-}}{dt} = \upsilon_{2,C} + \upsilon_{3,C} = 0 \quad \text{(Equation 99)}$$

and (Equation 100)(Equation 101)(Equation 102) on perovskite.

$$\frac{d\theta_{O2}}{dt} = \upsilon_{1,P} - \upsilon_{2,P} = 0 \quad \text{(Equation 100)}$$

$$\frac{d\theta_{HO2}}{dt} = \upsilon_{2,P} + \upsilon_{3,P} - \upsilon_{4,P} = 0 \quad \text{(Equation 101)}$$

$$\frac{d\theta_{O}}{dt} = 2\upsilon_{4,P} - \upsilon_{5,P} = 0 \quad \text{(Equation 102)}$$

Finally, according to the Faraday law, the ORR current density measured at the disk J_{ORR} is (Equation 103):

$$J_{ORR} = -F\left(2\Gamma_{geo,C}\upsilon_{2,C} + \Gamma_{geo,P}(\upsilon_{1,P} + \upsilon_{2,P} + \upsilon_{5,P})\right) \quad \text{(Equation 103)}$$

and the corresponding HO_2^- ring current $J_{escape,HO2-}$ is – assuming a collection factor of 1 - (Equation 104):

$$J_{escape,HO2-} = -2FD_{HO2-}\left(\frac{\partial C_{HO2-}}{\partial x}\right) \quad \text{(Equation 104)}$$

Thus, several relationships relate the unknown terms.

5.5.2. Comparison of modeling and experimental results

In this section, the curves obtained by mathematical modeling are compared to the experimental results obtained in this work. The reader should note that the experimental curves shown in this section were already shown in section 5.2 for RRDE data, in section 4.4 for Tafel data and in section 5.3 for HO_2^- reduction/oxidation data and are only presented here for comparison with the modeling.

The discussion is started with the RRDE study of the ORR. The simulated (plots on the left hand side) and experimental (plots on the right hand side) results are shown in Figure 56 for $LaCoO_3$ and Figure 57 for $La_{0.8}Sr_{0.2}MnO_3$ electrodes, with and without carbon.
The model well reproduces the experimental features. The perovskite alone displayed quite low ORR activity, and this electrocatalytic activity is increased with the addition of carbon in the catalytic layer. Moreover, the HO_2^- yield is decreased when carbon is added, even if high amount of HO_2^- species is formed on carbon. This is due to the increase of perovskite utilization which allows a faster HO_2^- reduction. In addition, the HO_2^- yield is dependent on the potential, as for experimental data.
Similar modeling results were obtained when the rate of the O_{ads} reduction on $LaCoO_3$ was doubled (Figure 102) (see Appendix 4).

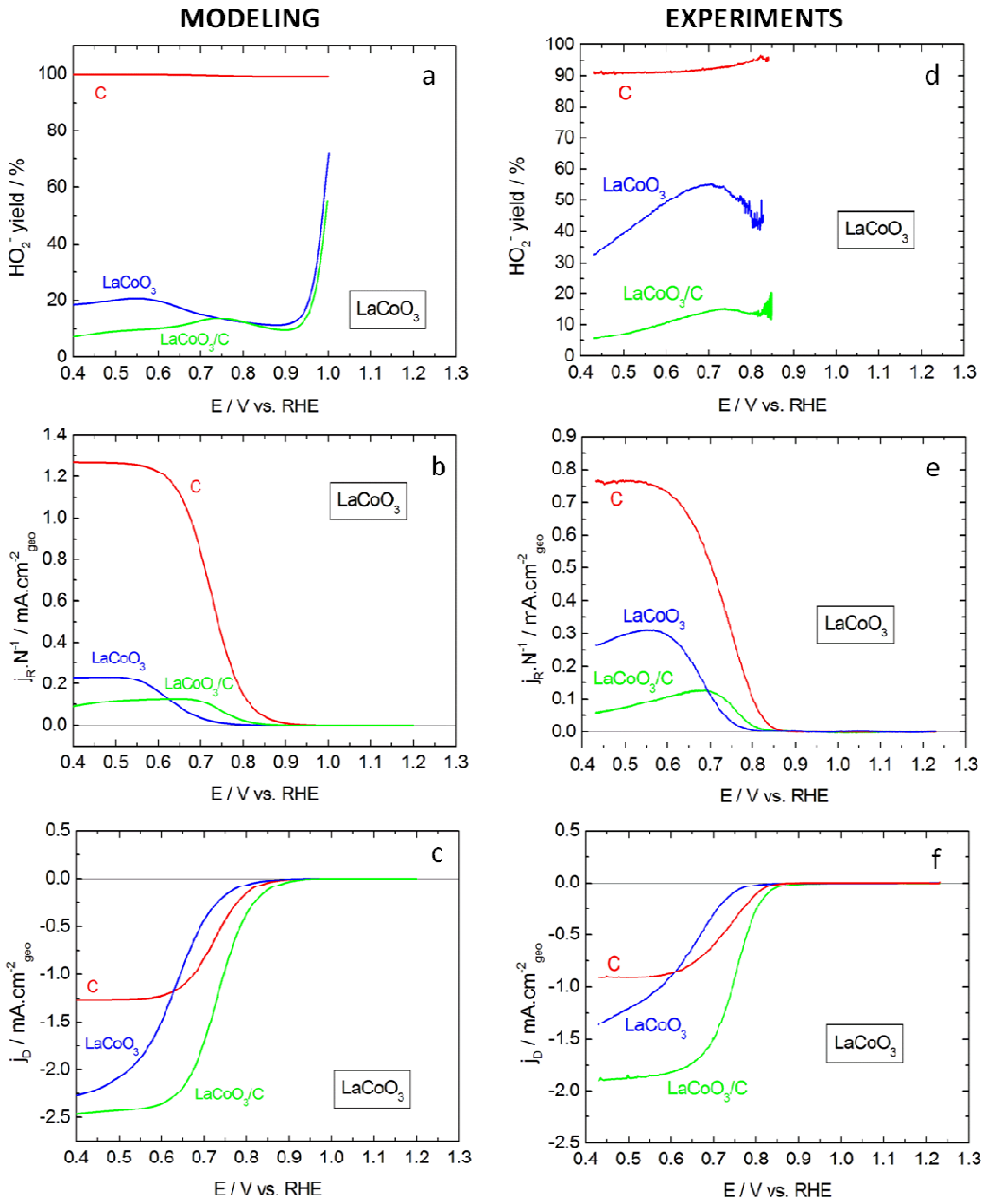

Figure 56 : *RRDE voltammograms of GC-supported thin films of $LaCoO_3$ + Sibunit carbon in O_2-saturated 1M NaOH at 900 rpm: (a,b,c) simulated curves with $k_{5,P}$ = 0.1 s^{-1} and (d,e,f) experimental positive scans at 10 $mV.s^{-1}$. (a,d) Percentage of HO_2^- formed, (b,e) ring currents versus disk potential, (c,f) disk voltammograms. Measurements were performed for electrodes containing only perovskite, for electrodes containing only Sibunit carbon, and for composite perovskite + Sibunit carbon electrodes. Color codes for electrode composition: 46 $\mu g.cm^{-2}_{geo}$ perovskite (blue), 46 $\mu g.cm^{-2}_{geo}$ perovskite + 19 $\mu g.cm^{-2}_{geo}$ Sibunit carbon (green), 19 $\mu g.cm^{-2}_{geo}$ Sibunit carbon (red). Disk currents are normalized to the geometric area of the disk electrode and corrected to the background currents measured in the N_2 atmosphere for the experimental curves. Ring currents are normalized to the geometric area of the disk electrode and to the collection factor.*

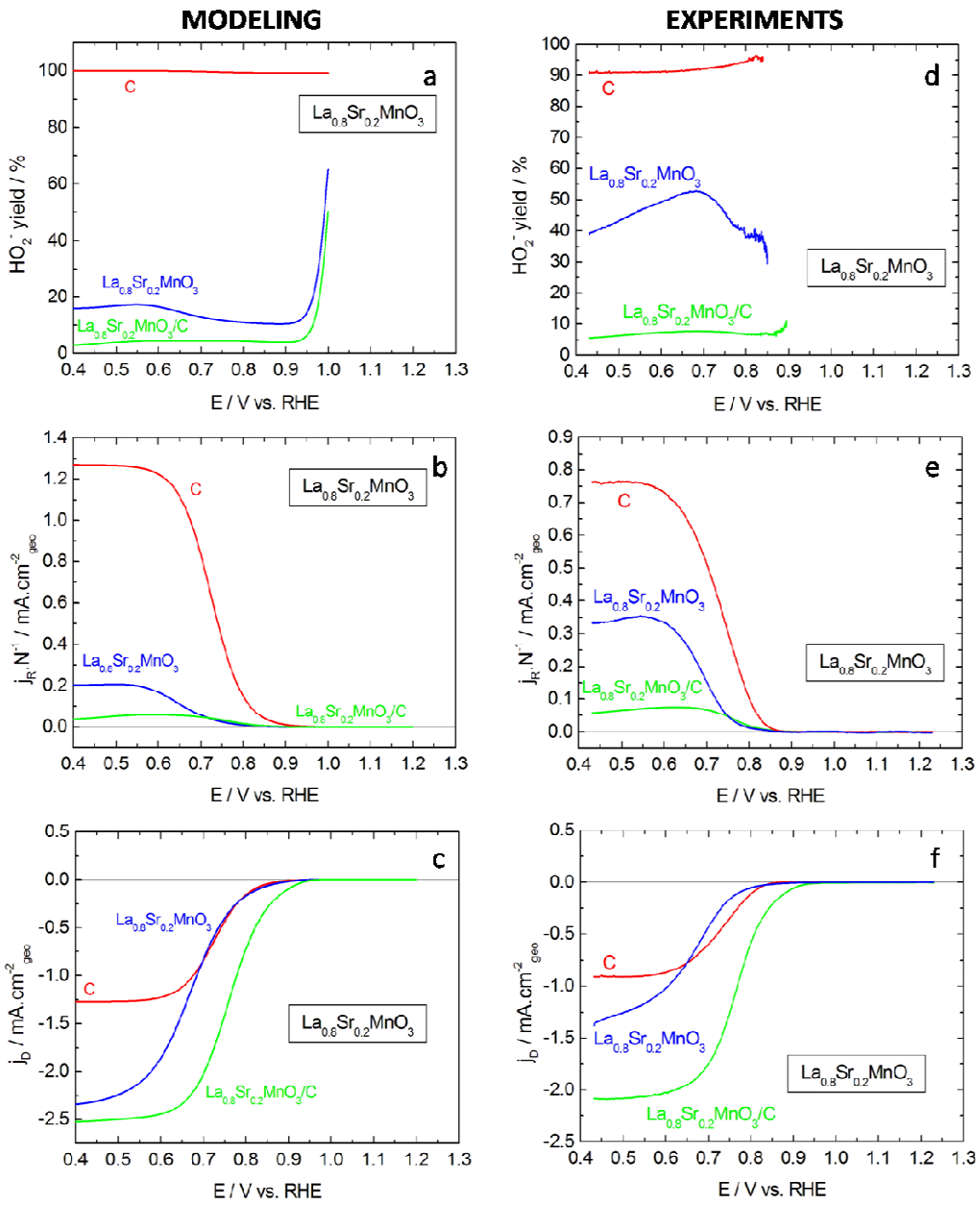

Figure 57 : *RRDE voltammograms of GC-supported thin films of $La_{0.8}Sr_{0.2}MnO_3$ + Sibunit carbon in O_2-saturated 1M NaOH at 900 rpm: (a,b,c) simulated curves and (d,e,f) experimental positive scans at 10 $mV.s^{-1}$. (a,d) Percentage of HO_2^- formed, (b,e) ring currents versus disk potential, (c,f) disk voltammograms. Measurements were performed for electrodes containing only perovskite, for electrodes containing only Sibunit carbon, and for composite perovskite + Sibunit carbon electrodes. Color codes for electrode composition: 46 $\mu g.cm^{-2}_{geo}$ perovskite (blue), 46 $\mu g.cm^{-2}_{geo}$ perovskite + 19 $\mu g.cm^{-2}_{geo}$ Sibunit carbon (green), 19 $\mu g.cm^{-2}_{geo}$ Sibunit carbon (red). Disk currents are normalized to the geometric area of the disk electrode and corrected to the background currents measured in the N_2 atmosphere for the experimental curves. Ring currents are normalized to the geometric area of the disk electrode and to the collection factor.*

The simulated ORR currents for perovskite/carbon composites presented in Figure 56,c, green curves, and in Figure 57,c, green curves take into account the ORR activity on perovskite (with high perovskite utilization thanks to the presence of carbon) and on carbon. Tafel plots were then constructed from the simulated ORR currents on perovskite only, normalized to the specific surface area of perovskite and presented in Figure 58,a.

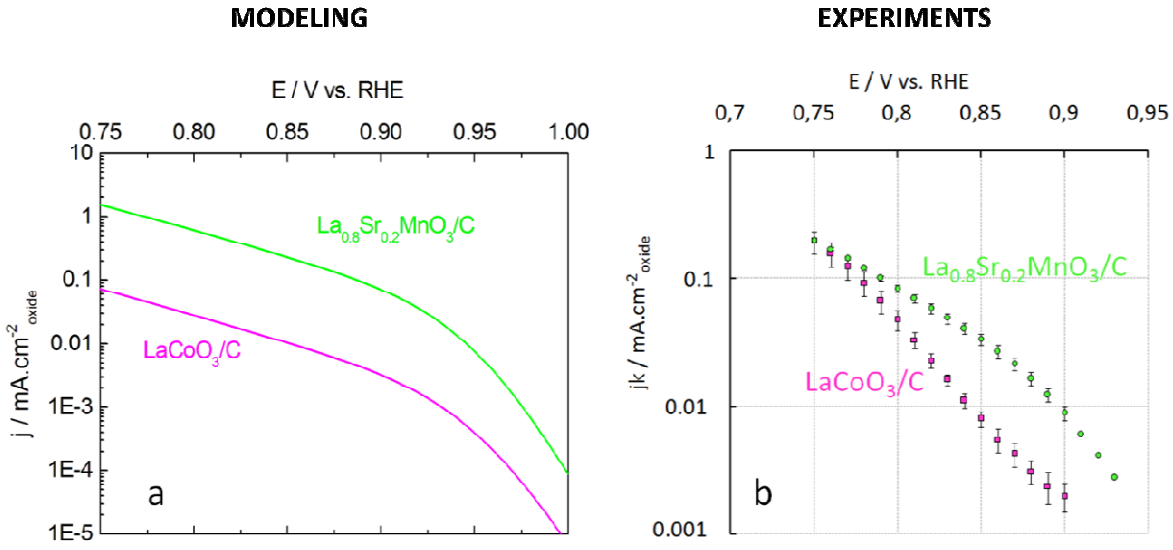

Figure 58 : *Tafel plots from mass-transport corrected scans voltammograms of GC-supported thin films of perovskite + Sibunit carbon in O_2-saturated 1M NaOH: (a) simulated curves without ORR contribution of carbon and (b) experimental positive scans at 10 mV.s^{-1} after subtraction of the kinetic ORR current on carbon. Measurements were performed with 71 wt.% perovskite + 29 wt.% Sibunit carbon. Color codes: $LaCoO_3$ + Sibunit carbon (pink) and $La_{0.8}Sr_{0.2}MnO_3$ + Sibunit carbon (green). Kinetic currents of Tafel plots are normalized to the BET surface area of perovskites. Error bars represent standard deviation from at least two independent repeated measurements.*

The change of Tafel slopes observed in experimental curves for $La_{0.8}Sr_{0.2}MnO_3$ electrodes is also seen on the simulated curves (Figure 58,b,green curves), showing that the mechanism chosen for the model is consistent. For $LaCoO_3$, however, the simulated Tafel plot is different from the experimental plot since no Tafel slope change was observed experimentally.

By varying the values of the rate constants, it was observed that the ratio $k_{1,P}$:$k_{2,P}$ determines the Tafel slopes. For a low $k_{1,P}$:$k_{2,P}$ ratio, i.e. for a slow 1st step, only a slope of 120 mV.decade^{-1} was observed in the studied potential range. On the other hand, the higher the $k_{1,P}$:$k_{2,P}$ ratio, i.e. the slower the 2nd step, the more pronounced change of slope was observed –

up to 120 mV.decade^{-1} at high overpotentials and 35 mV.decade^{-1} at low overpotentials were calculated – and the lower is the potential where this change of the slope occurs.
Therefore, the careful observation of the effect of these rate constants on the Tafel slopes – and thus, on the rate determining step - and on HO_2^- currents will allow a more precise determination of the model.

The influence of the catalyst loading was also modeled with the mechanism presented above by varying the number of accessible active sites on the perovskite surface. The corresponding simulated results (plots on the left hand side) are shown in Figure 59 for $LaCoO_3$ and Figure 60 for $La_{0.8}Sr_{0.2}MnO_3$ and compared to the experimental one (plots on the right hand side). Once again, the model very well reproduces the tendency observed in the experiments. Indeed, the electrodes with a low catalyst loading display high HO_2^- release, while those with high loading present low HO_2^- yield due to efficient reduction of HO_2^- species on the abundant active sites.
One can note that the onset potentials of the ring current are identical for different catalyst loadings with the "series" pathway used in the model. This shows that a zero current on the ring is not necessarily a sign of a "direct" ORR pathway.
When the rate of the O_{ads} reduction on $LaCoO_3$ was doubled, similar catalyst loading effects were observed (Figure 103) (see Appendix 4). Moreover, the HO_2^- yield was still higher than that observed on $La_{0.8}Sr_{0.2}MnO_3$ while the HO_2^- reduction rates were identical in that case ($k_{4,P}$ = 30 s^{-1}, $k_{5,P}$ = 0.2 s^{-1}). For example, for the electrode with the lowest loading (23 µg.cm$^{-2}_{geo}$ perovskite + 9 µg.cm$^{-2}_{geo}$ carbon), ca. 20% of HO_2^- were detected for $LaCoO_3$/C electrodes (Figure 103) and only 10% for $La_{0.8}Sr_{0.2}MnO_3$/C electrodes (Figure 60). This points out that the high HO_2^- yield observed for $LaCoO_3$ is predominantly due to its low activity for the ORR, and thus, to the formation of HO_2^- on carbon sites.

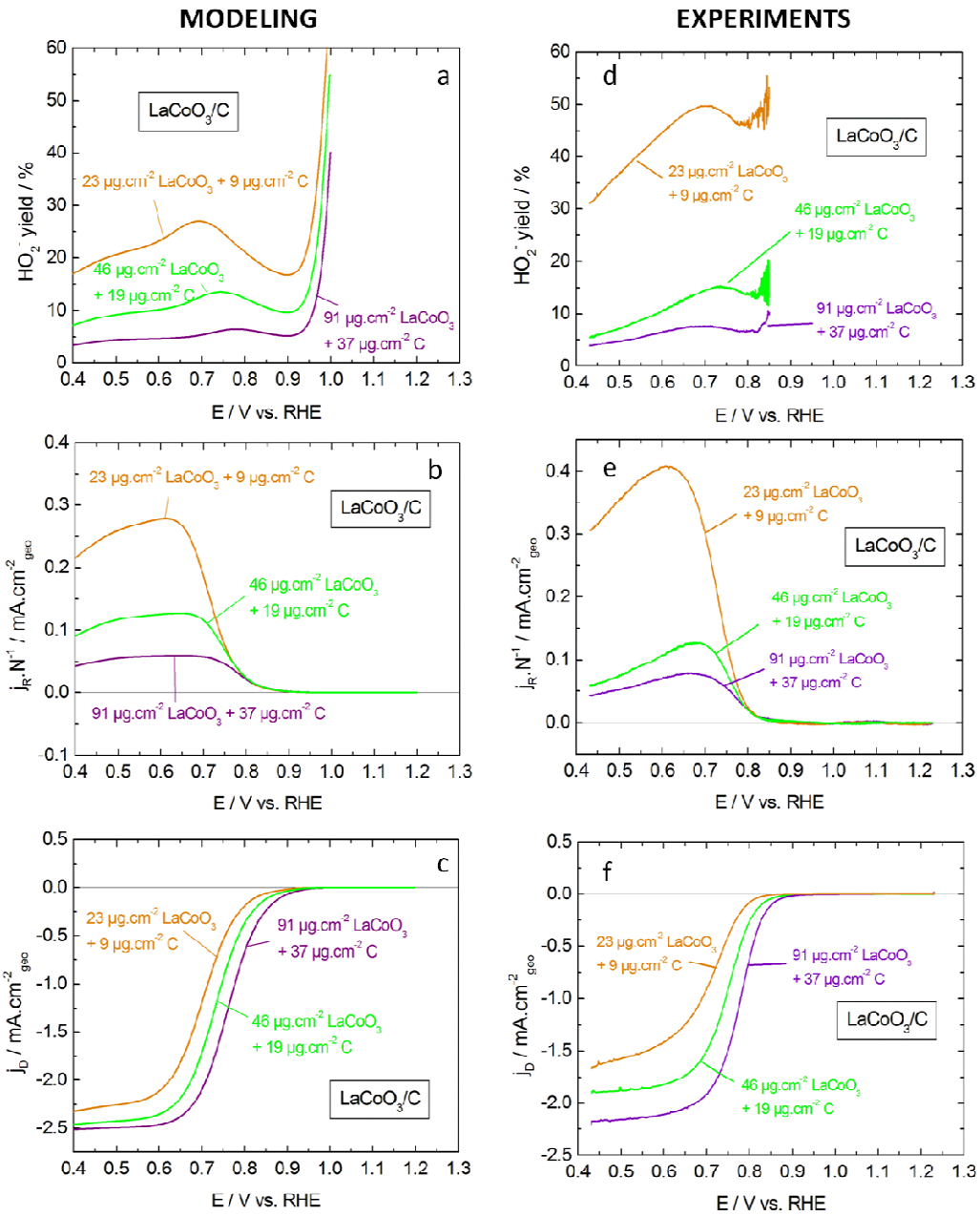

Figure 59 : *RRDE voltammograms of GC-supported thin films of $LaCoO_3$ + Sibunit carbon in O_2-saturated 1M NaOH at 900 rpm: (a,b,c) simulated curves with $k_{5,P} = 0.1\ s^{-1}$ and (d,e,f) experimental positive scans at 10 $mV.s^{-1}$. (a,d) Percentage of HO_2^- formed, (b,e) ring currents versus disk potential, (c,f) disk voltammograms. Measurements were performed for electrodes containing constant perovskite/carbon ratio (71 wt.% perovskite + 29 wt.% Sibunit carbon,) and various catalyst loadings. Color codes for electrode loading: 23 $\mu g.cm^{-2}_{geo}$ perovskite + 9 $\mu g.cm^{-2}_{geo}$ Sibunit carbon (orange), 46 $\mu g.cm^{-2}_{geo}$ perovskite + 19 $\mu g.cm^{-2}_{geo}$ Sibunit carbon (green), 91 $\mu g.cm^{-2}_{geo}$ perovskite + 37 $\mu g.cm^{-2}_{geo}$ Sibunit carbon (purple). Disk currents are normalized to the geometric area of the disk electrode and corrected to the background currents measured in the N_2 atmosphere for the experimental curves. Ring currents are normalized to the geometric area of the disk electrode and to the collection factor.*

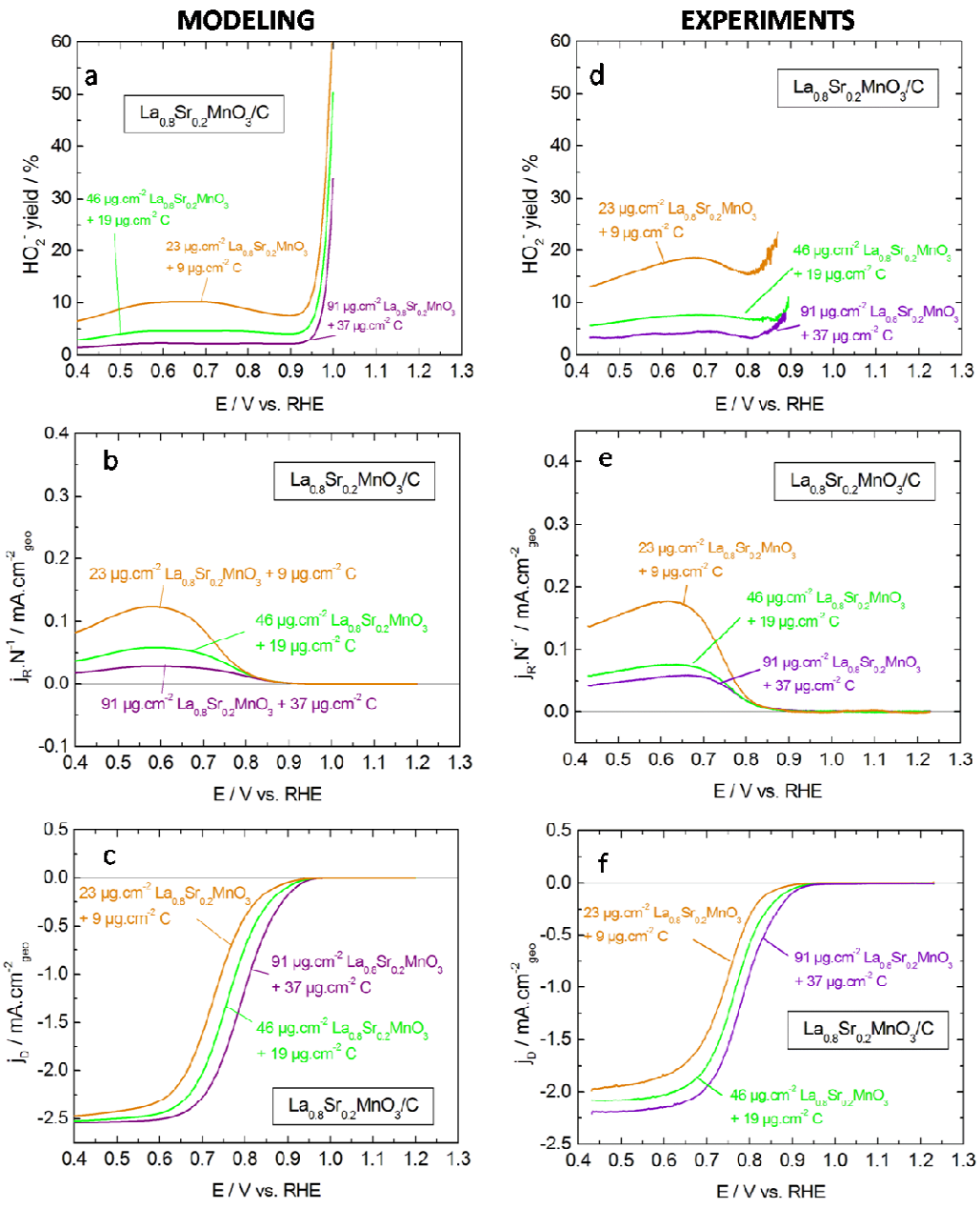

Figure 60 : *RRDE voltammograms of GC-supported thin films of $La_{0.8}Sr_{0.2}MnO_3$ + Sibunit carbon in O_2-saturated 1M NaOH at 900 rpm: (a,b,c) simulated curves and (d,e,f) experimental positive scans at 10 $mV.s^{-1}$. (a,d) Percentage of HO_2^- formed, (b,e) ring currents versus disk potential, (c,f) disk voltammograms. Measurements were performed for electrodes containing constant perovskite/carbon ratio (71 wt.% perovskite + 29 wt.% Sibunit carbon,) and various catalyst loadings. Color codes for electrode loading: 23 $\mu g.cm^{-2}_{geo}$ perovskite + 9 $\mu g.cm^{-2}_{geo}$ Sibunit carbon (orange), 46 $\mu g.cm^{-2}_{geo}$ perovskite + 19 $\mu g.cm^{-2}_{geo}$ Sibunit carbon (green), 91 $\mu g.cm^{-2}_{geo}$ perovskite + 37 $\mu g.cm^{-2}_{geo}$ Sibunit carbon (purple). Disk currents are normalized to the geometric area of the disk electrode and corrected to the background currents measured in the N_2 atmosphere for the experimental curves. Ring currents are normalized to the geometric area of the disk electrode and to the collection factor.*

Then, the modeling of the HO_2^- reduction/oxidation reactions was performed. The RDE voltammograms of perovskite composite electrodes in H_2O_2-containing electrolyte are the sum of three main contributions, as shown on the simulated curves in Figure 61. The anodic branch is composed by the HO_2^- oxidation into O_2, while the cathodic branch consists of the HO_2^- reduction into OH^- and the reduction of the O_2 formed during the HO_2^- oxidation. The contribution of the HO_2^- oxidation and of the ORR on carbon to the overall current is negligible according to the modeling.

The deconvolution of the whole current into these individual contribution shows that the kinetic currents of the HO_2^- reduction cannot be directly obtained from the total currents, contrary to what was performed in the literature [133,251].

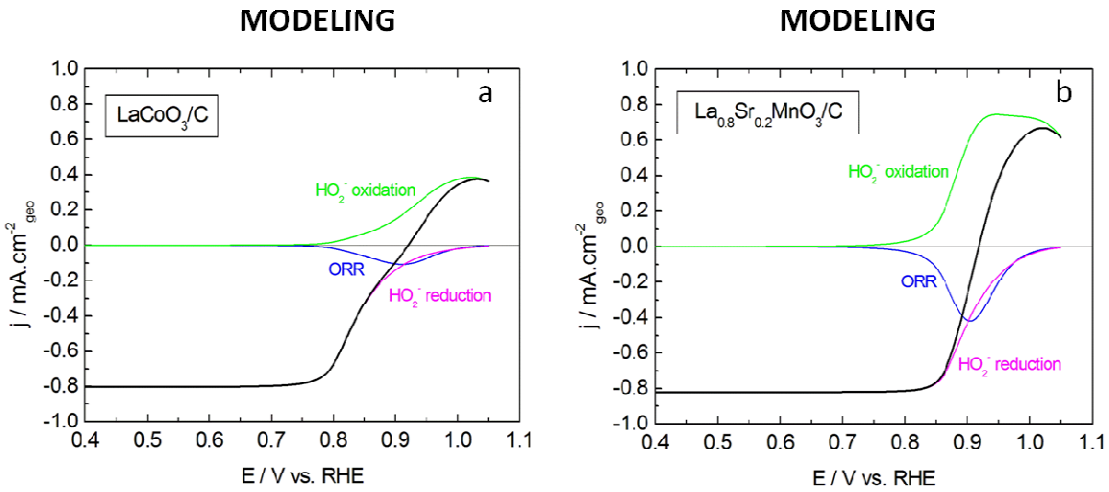

Figure 61 : *Simulated RDE voltammograms of GC-supported thin films of (a) $LaCoO_3$ + Sibunit carbon and (b) $La_{0.8}Sr_{0.2}MnO_3$ + Sibunit carbon in N_2-purged 1M NaOH + 0.84 mM H_2O_2 at 900 rpm. Measurements were modeled with 91 $\mu g.cm^{-2}_{geo}$ perovskite + 37 $\mu g.cm^{-2}_{geo}$ Sibunit carbon. Color codes for the individual contributions: HO_2^- reduction contribution (pink), O_2 reduction contribution (blue), HO_2^- oxidation contribution (green) and total current obtained by the addition of the previously mentioned contributions (black). Currents are normalized to the geometric area of the electrode.*

The total current obtained by this model (Figure 62,a, black curves) well reproduces the experimental voltammograms of $LaCoO_3$ and $La_{0.8}Sr_{0.2}MnO_3$ composite electrodes (Figure 62,b). Indeed, an almost reversible voltammogram is calculated for $La_{0.8}Sr_{0.2}MnO_3$ while $LaCoO_3$ displays significantly smaller currents. Moreover, a change in the current slope is visible for $LaCoO_3$, as for experimental curves. The only noticeable difference between the simulated and the experimental curves is the decrease of the HO_2^- oxidation current at high

potentials for the model. It is caused by the decrease of the number of active B^{m+} sites in favor of the formation of $B^{(m+1)+}$ cations. In practice, one may suppose that some B^{m+} cations are still present at these high potentials.

Interestingly, it was noticed that, when the O_{ads} reduction rate was doubled and thus the HO_2^- reduction was accelerated, the global current calculated on $LaCoO_3$ electrode was still lower than that of $La_{0.8}Sr_{0.2}MnO_3$ (Figure 104) (see Appendix 4), in agreement with the high HO_2^- yield measured on the former (Figure 103) (see Appendix 4). This is due to the smaller number of active sites on the Co-based perovskite and to its low activity for ORR and HO_2^- oxidation.

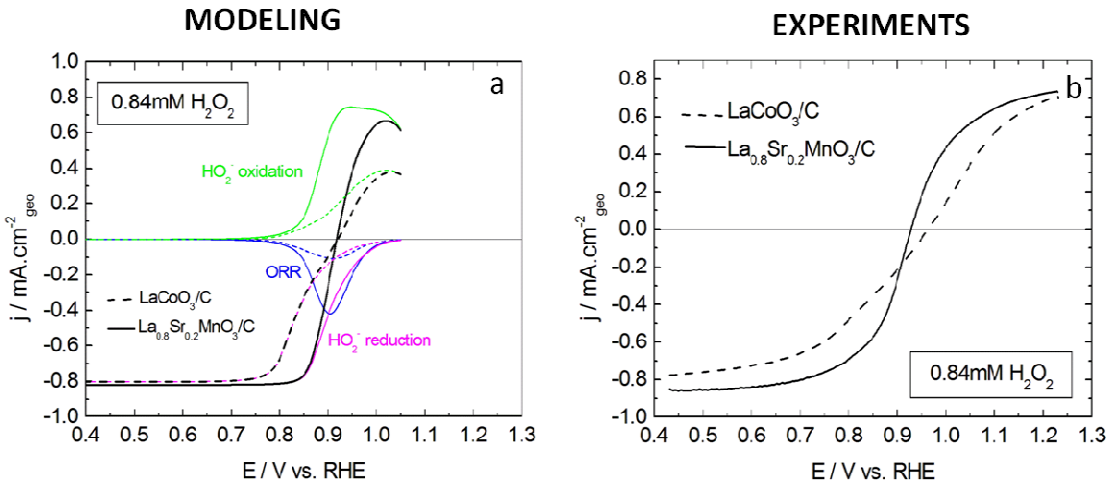

Figure 62 : *RDE voltammograms of GC-supported thin films of $La_{0.8}Sr_{0.2}MnO_3$ + Sibunit carbon (solid lines) or of $LaCoO_3$ + Sibunit carbon (dash lines) in N_2-purged 1M NaOH + 0.84 mM H_2O_2 at 900 rpm: (a) simulated curves and (b) experimental positive scans at 10 $mV.s^{-1}$. Measurements were performed with 91 $\mu g.cm^{-2}_{geo}$ perovskite + 37 $\mu g.cm^{-2}_{geo}$ Sibunit carbon. Color codes for the model contributions: HO_2^- reduction contribution (pink), O_2 reduction contribution (blue), HO_2^- oxidation contribution (green) and total current obtained by the addition of the previous mentioned contributions (black). Currents are normalized to the geometric area of the electrode and corrected to the background currents measured in the N_2 atmosphere in the absence of H_2O_2 for the experimental curves.*

The influence of the H_2O_2 concentration on the RDE voltammograms was also investigated using the mathematical modeling. The results are displayed in Figure 63,a. Besides the normal decrease of the diffusion limiting current, a positive shift of the mixed potential is observed when the concentration is decreased (Figure 63,a,black curves), similar to the experimental results (Figure 63,b).

Varying the H_2O_2 concentration directly affects the reaction rate of the adsorption/desorption of HO_{2-} (Equation 89) and therefore the site coverage by HO_2^- species ($\theta_{HO2,P}$). On the

cathodic branch, the decrease of the HO_2^- concentration does not lead to a strong slowing down of the splitting into O_{ads} species since the splitting rate depends on both $\theta_{HO2,P}$ and $\theta_{OH,P}$ (=1- $\theta_{O2,P}$ – $\theta_{HO2,P}$ - $\theta_{O,P}$) (Figure 63,a,pink curves). On the other hand, in the anodic direction, the decrease of $\theta_{HO2,P}$ causes a reduction in the speed of formation of $O_{2,ads}$ from $HO_{2,ads}$, the step which depends on the potential. Thus, the onset potential is shifted positively (Figure 63,a,green curves) and therefore, the mixed potential too (Figure 63,a,black curves).

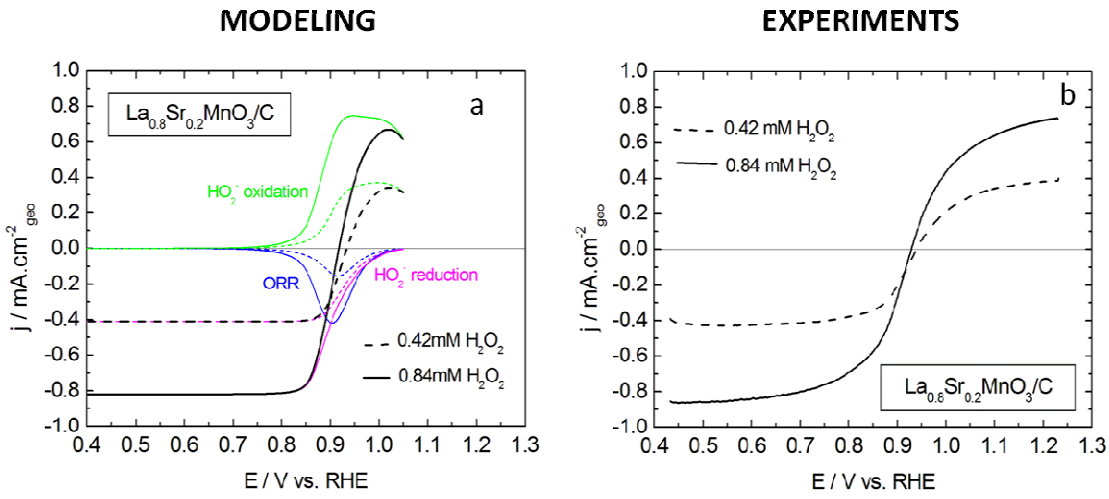

Figure 63 : *RDE voltammograms of GC-supported thin films of $La_{0.8}Sr_{0.2}MnO_3$ + Sibunit carbon in N_2-purged 1M NaOH with 0.84 mM H_2O_2 (solid lines) or 0.42 mM H_2O_2 (dash lines) at 900 rpm: (a) simulated curves and (b) experimental positive scans at 10 mV.s^{-1}. Measurements were performed with 91 µg.cm$^{-2}_{geo}$ perovskite and 37 µg. cm$^{-2}_{geo}$ Sibunit carbon. Color codes for the model contributions: HO_2^- reduction contribution (pink), O_2 reduction contribution (blue), HO_2^- oxidation contribution (green) and total current obtained by the addition of the previous mentioned contributions (black). Currents are normalized to the geometric area of the electrode and corrected to the background currents measured in the N_2 atmosphere in the absence of H_2O_2 for the experimental curves.*

The model used in this work helped in the understanding of the ORR mechanism on perovskite electrodes. However, at the time of writing, the adjustement of the rate constants is still in progress. Indeed, model parameters will be adjusted thanks to additional on-going experiments with other H_2O_2 concentrations and with the careful study of the effect of the choice of kinetic constants on the Tafel slopes.

5.6. Conclusions of Chapter 5

In this section, the interpretation of the experiment features was combined with a mathematical model developed by Dr. Antoine Bonnefont (Institut de Chimie, Université de Strasbourg) and allowed to propose a tentative ORR mechanism on perovskite electrodes.

It was demonstrated that, on perovskite as well as on perovskite/carbon electrodes, ORR is mainly a "series" pathway with formation of the HO_2^- intermediate. This intermediate species is further reduced on perovskite sites, likely through its splitting into O species, followed by an electrochemical reduction of O_{ads} into OH^-, with the help of redox transitions of the B cation of the perovskite. The amount of HO_2^- detected at the ring of the RRDE strongly depends on (i) the perovskite loading (thick layers leading to an apparent "direct" ORR mechanism due to an efficient HO_2^- reduction), (ii) the carbon addition (which affects both the perovskite utilization and the HO_2^- production), and (iii) the nature of the perovskite.

Indeed, studied perovskite electrodes showed significant activity for HO_2^- reduction/oxidation reactions in the investigated potential range, but $LaCoO_3$ showed lower reaction rates than Mn perovskites. This is due to the low electrocatalytic activity of the former perovskite for the ORR and for HO_2^- oxidation, but probably also to the easier redox transitions of Mn compared to Co cation. As for the ORR, the addition of carbon to perovskite thin layer electrodes significantly enhanced the reaction rate of the HO_2^- reduction by increasing the catalyst utilization, which leads to a lower HO_2^- detection at the RRDE ring.

In addition to the activity for HO_2^- reduction, perovskite oxides demonstrated significant activity for the HO_2^- decomposition compared to carbon. This reaction appeared to be a first order reaction on the studied oxides and the heterogeneous rate constant for this reaction shows only slight differences between Co and Mn-based perovskites. The study of HO_2^- reactions of Mn_2O_3 points out that HO_2^- decomposition is a chemical pathway rather than an electrochemical pathway, at least on this oxide.

In conclusion, HO_2^- species can be transformed on perovskite sites and therefore will not survive in a fuel cell, provided that sufficiently thick catalytic layers are utilized.

Chapter 6 :
Stability of perovskites as ORR catalyst

6.1. Introduction

The perovskites studied in this work show promising ORR activity for fuel cell applications. However, fuel cell components should display sufficient stability to ensure their long term performance. This chapter is therefore focused on the study of the stability of perovskite oxides.

First of all, the effect of the storage under ambient conditions and successive thermal treatments on the state of the perovskite surface was studied by XPS. XPS was also applied to check the oxide surface stability in the suspensions used for electrochemical measurements. In fuel cells, perovskite oxides will be in contact with either concentrated alkaline media or an OH^- conducting membrane which is also strongly basic. Thus, the stability of their structure and composition after immersion in alkaline solutions was investigated using XRD, ICP and XPS techniques. The immersion duration was extended up to one month.

Secondly, the durability of the ORR activity was studied by chronoamperometries at various applied pontentials for perovskite and perovskite/carbon electrodes. The effect of the electrocatalytic reaction on the interfacial properties of perovskites was investigated by CV under N_2 atmosphere at the end of the measurements. Also, as HO_2^- is formed during the ORR on perovskite electrodes (see section 5), similar experiments were performed for the HO_2^- reduction. In order to visualize eventual modifications of the bulk structure, the electrode morphophogy and the surface composition of perovskites, and to understand the evolution of their electrocatalytic activity, electrodes were studied using XRD, SEM/EDX and XPS analysis after electrocatalysis.

6.2. Chemical stability of perovskite oxides

6.2.1. Surface modification under the atmospheric storage and after the thermal treatment

XPS data (see section 3.2.4) showed that La:Co ratio on the surface and near-surface region of $LaCoO_3$ stored under ambient conditions significantly exceeds the theoretical 1:1 ratio characteristic of the ABO_3 structure. Moreover, the analysis of the O1s and C1s spectra indicated the presence of carbonates on the sample surface. From these observations, it was concluded on the presence of $La_2(CO_3)_3$ on the surface which is apparently formed via interaction with CO_2 from atmosphere.

With the purpose to remove these species, a thermal treatment was applied to the oxides as described in section 2.5.1: the sample was kept during 1h at 650°C or 700°C in air. The treated perovskites were then studied by XPS, CV and RDE under O_2 atmosphere to investigate the impact of the thermal treatment on the surface composition, the interfacial properties and the ORR activity, respectively. Figure 64 presents the XPS spectra of $LaCoO_3$ before and after the thermal treatment. The corresponding La3d, Co2p, C1s and O1s peak binding energies and atomic ratios are shown in Table 18 and Figure 65. In the following, the XPS peak attributions are similar to that of section 3.2.4.

First of all, it is noticed that the peaks of the La3d spectra are better defined and shifted towards lower binding energies after the thermal treatments (Figure 64,a and Table 18), suggesting the removal of lanthanum carbonates (see section 3.2.4.1 and Appendix 2, Figure 98). It is observed that the fraction of carbonates indeed decreases with the thermal treatment by comparing the peak areas of carbonates to other components in the O1s spectrum (Figure 64,c,d and Table 18). Similar decrease of the carbonate quantity was observed for $LaMnO_3$ and $La_{0.8}Sr_{0.2}MnO_3$ after the thermal treatment at 650°C (not shown).

Thermal treatment at 650°C in air results in the decrease of the amount of $La_2(CO_3)_3$ and a partial recovery of the ABO_3 perovskite structure for $LaCoO_3$. However, electrochemical measurements have shown that the decrease of the amount of carbonate species on the surface

does not lead to changes either in the CV under N_2 or RDE voltammograms in O_2-saturated electrolyte. This means either that $La_2(CO_3)_3$ – which itself is inactive in the ORR - forms on the surface a porous layer which does not block an access of O_2 to the active sites, or that this carbonate layer is destroyed (or dissolved) either during the thin layer electrode preparation or during the contact with the alkaline electrolyte. Considering that $La_2(CO_3)_3$ is not soluble in NaOH (tested in laboratory), the latter hypothesis in unlikely. Meanwhile, XPS measurement of $LaCoO_3$ after an ultrasonic treatment in an aqueous suspensions indeed suggest a partial decomposition/dissolution of the carbonate species (see section 6.2.2)

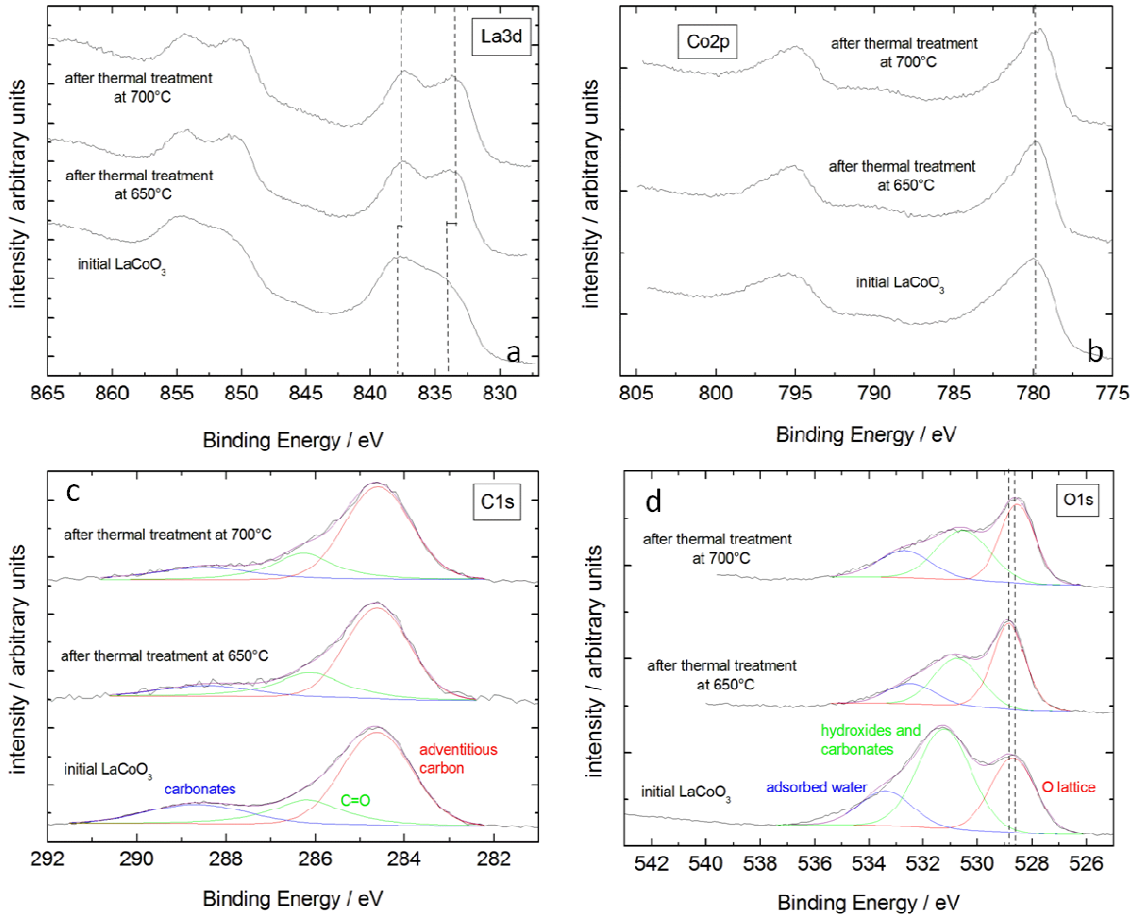

Figure 64 : *XPS spectra of (a) La3d, (b) Co2p, (c) C1s and (d) O1s of $LaCoO_3$ before and after thermal treatment, and corresponding peak deconvolution. Lines are guides for the eye and indicate the experimental positions.*

Table 18 : *Binding energies (in eV) of XPS peaks and atomic ratios (in brackets) for $LaCoO_3$ before and after thermal treatment*

$LaCoO_3$	$La3d_{5/2}$	$Co2p_{3/2}$	C1s			O1s		
			Adventious carbon	C=O	Carbonate	O lattice	Carbonate and hydroxide	Adsorbed water
Initial $LaCoO_3$	833.2 834.1 838.1 (13%)	779.9 (7%)	284.6 (26%)	286.2 (9%)	288.7 (8%)	528.6 (12%)	531.3 (20%)	533.7 (5%)
After thermal treatment at 650°C	833.4 837.5 (14%)	779.9 (6%)	284.6 (21%)	286.2 (7%)	288.7 (4%)	528.7 (23%)	531.0 (19%)	533.7 (7%)
After thermal treatment at 700°C	833.4 837.5 (9%)	779.9 (4%)	284.6 (31%)	286.3 (9%)	288.7 (8%)	528.6 (16%)	531.0 (14%)	533.7 (7%)

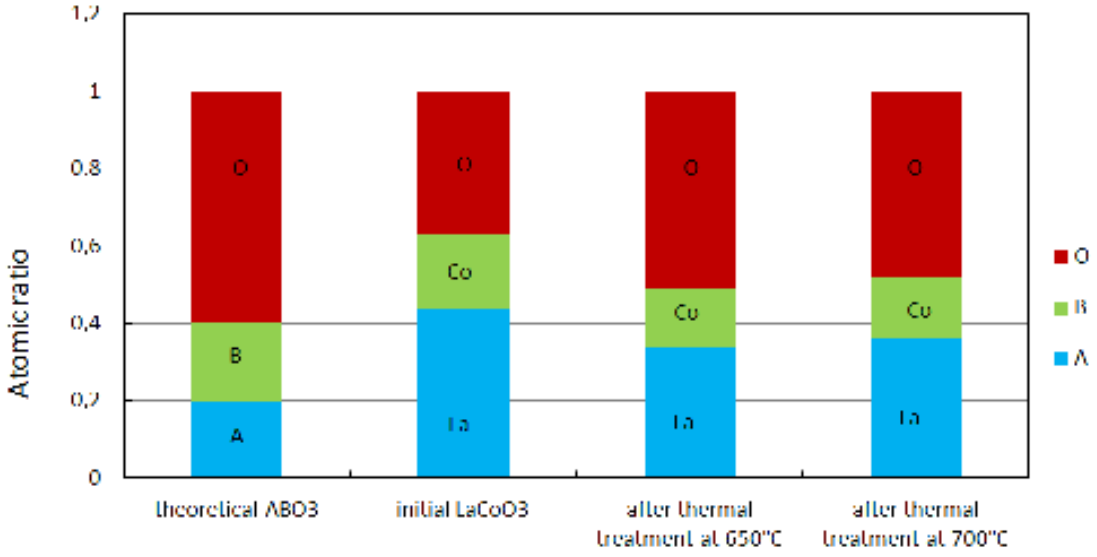

Figure 65 : *XPS atomic ratio of La (blue), Co (green) and O from perovskite lattice (red) in $LaCoO_3$ before and after thermal treatment, calculated with Scofield factors after background correction of XPS spectra.*

6.2.2. Surface modification in aqueous suspensions

Usually, perovskite is ground and aqueous suspensions are freshly prepared before electrochemical studies, as described in section 2.3.2.2. This procedure was developed after an observation of modifications in the behavior of suspensions of $LaCoO_3$ with the time.

Indeed, after several utilizations – and therefore successive ultrasonic treatments - and storage during few days under atmospheric conditions, the colour of the $LaCoO_3$ suspension changes from black to yellow-brown, even when protected from light. Moreover, the CV was significantly affected by the freshness of the suspension, as can be observed from Figure 66. "Old" suspension leads to additional current peaks at high potentials, suggesting the presence of new redox couples.

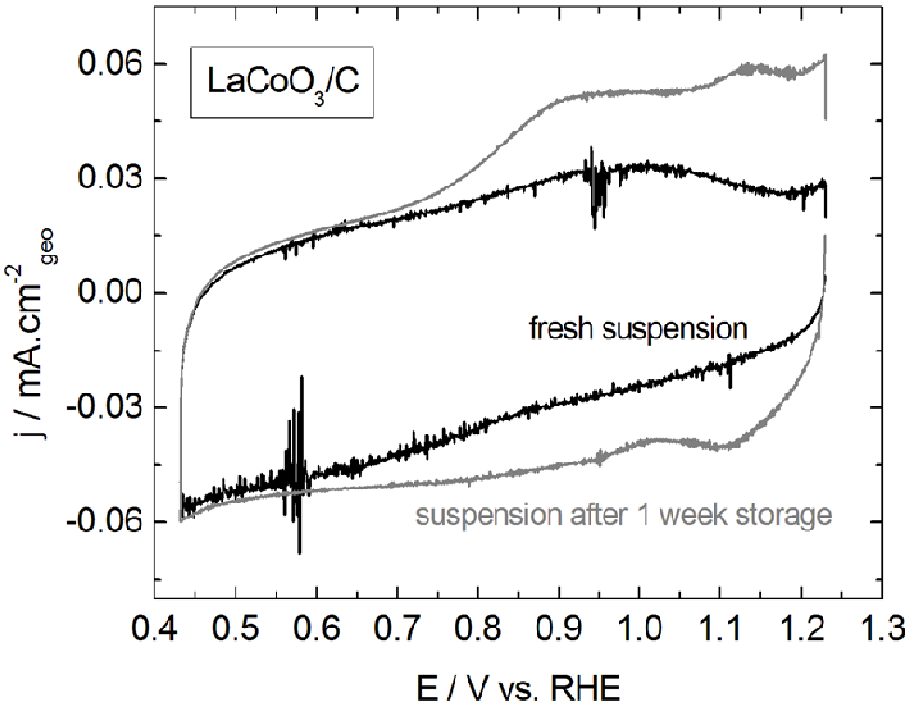

Figure 66 : *CV at 0 rpm and 10 mV.s^{-1} of CP-supported thin films of $LaCoO_3$ + Sibunit carbon in N_2-purged 1M NaOH. Measurements were performed with 180 µg.cm$^{-2}_{geo}$ perovskite + 74 µg.cm$^{-2}_{geo}$ Sibunit carbon. Color codes: fresh suspension (black), suspension after one week storage under atmospheric conditions (grey). Currents are normalized to the geometric area of the electrode.*

In order to investigate the modification of the perovskite surface in aqueous suspensions, various suspensions of $LaCoO_3$ in ultrapure water were prepared as described in section 2.5.2, drop cast on carbon scotch placed on an XPS sample holder and studied by XPS. The obtained XPS spectra are presented in Figure 67, and the corresponding binding energies of the elements and their atomic ratios, in Table 19 and Figure 68.

By comparing the XPS data from fresh perovskite suspensions to data of the initial powder, it is observed that La3d spectrum shows better defined peaks (Figure 67,a), appearing at lower binding energies (Table 19), for fresh $LaCoO_3$ suspension. Moreover, the ratio La:Co proves that the excess of La is less pronounced for perovskite suspension than for the $LaCoO_3$ powder stored in air (Figure 68). This suggests a decrease of the quantity of lanthanum carbonate on the perovskite surface after sonication in ultrapure water. This might be caused by the slightly acidic pH of this water with contact of CO_2 of air [252] or to the ultrasonic treatment.

All the fresh suspensions – with ground and not ground powder, and with various durations of ultrasonic treatment – show (i) similar XPS spectra (Figure 67), (ii) similar peak binding energies (Table 19) and, (iii) within the experimental error, similar atomic ratios of the La, Co and O (Table 19 and Figure 68). This proved that the powder grinding in a mortar as well as a longer ultrasonic treatment do not significantly affect the perovskite surface.

After storage of the suspension during one week under ambient conditions, several changes in the XPS spectra can be observed. First of all, the La3d spectrum is significantly modified with high peak intensities at high binding energies. The origin of this modification is not understood yet but might suggest that lanthanum is not in the perovskite phase at the oxide surface. However, lanthanum carbonates and oxides are excluded since the La3d spectrum is different from the commercial $La_2(CO_3)_3$ and La_2O_3 (Figure 21,a).
Cobalt also seems to be affected by the storage. Indeed, the $Co2p_{3/2}$ peak is slighty shifted towards higher binding energies (Figure 67,b and Table 19), and the atomic ratio evidences a larger amount of cobalt on the perovskite surface than either in the initial powder or fresh suspensions (Figure 68). This cobalt is probably not only in the perovskite structure since the fraction of O from the perovskite lattice is very low (Figure 68). In fact, the O1s peak ratio suggests a high amount of carbonates and/or hydroxide species compared to perovskite without suspension storage (Figure 67,d). Therefore hydroxide and/or carbonate of cobalt are probably formed during this storage.

Although the presence of carbonates is suggested from O1s and C1s spectra (Figure 67,c,d), $Co(CO_3)$ is unlikely because no satellite peaks corresponding to Co^{2+} can be observed in the Co2p spectra (Figure 67,b). Similarly, $Co(OH)_2$ should be discarded. Also, one can see that the Co2p spectra of the stored suspension (Figure 67,b) is different from the spectrum of the commercial $Co(OH)_2$ (Figure 22,a). On the other hand, if the high oxidation state Co^{4+} was formed to compensate the loss of lanthanum carbonates on the perovskite surface mentioned for the fresh suspensions, it could not explain the modification of the CV (Figure 66) since according to Pourbaix diagrams [195] redox transitions of Co^{4+}/Co^{3+} occur at potentials higher than the potentials studied in this work. The most probable specie present on the perovskite surface is therefore either $Co(OH)_3$ or CoOOH. Then, the redox peaks observed in the CV (Figure 66) can be attributed to Co^{3+}/Co^{2+} redox couple from different phases (perovskite, hydroxide…). Also, a little shift observed in the Co2p spectra can be related to a change of the chemical bonds and the coordination number of Co. In addition, the formation of $Co(OH)_3$ or CoOOH species can be at the origin of the color change of the suspension.
As $Co(OH)_3$ is not active for the ORR [253], the ORR activity of $LaCoO_3$ from old suspensions was investigated. Interestingly, it was observed that the activity was not affected by the freshness of the suspension since fresh and old suspensions lead to superposed RDE voltammograms (not shown). Moreover, the CV after electrocatalysis from old suspensions displays a similar shape to the CV of fresh suspensions (not shown), suggesting that the initial interfacial properties are recovered. Therefore, it seems that the ORR and/or the HO_2^- reactions lead to a removal of the eventual $Co(OH)_3$ or CoOOH layer.

For Mn perovskites, no significant CV or color changes were observed after the suspension storage, suggesting higher stability of Mn-containing perovskites compared to Co-containing perovskites. This is consistent with the higher stability of the $LaMnO_3$ structure compared to the $LaCoO_3$ structure [138] (see 1.4.4.1).

To ensure high reproductibility, only fresh suspensions were used for electrocatalytic studies for all perovskites.

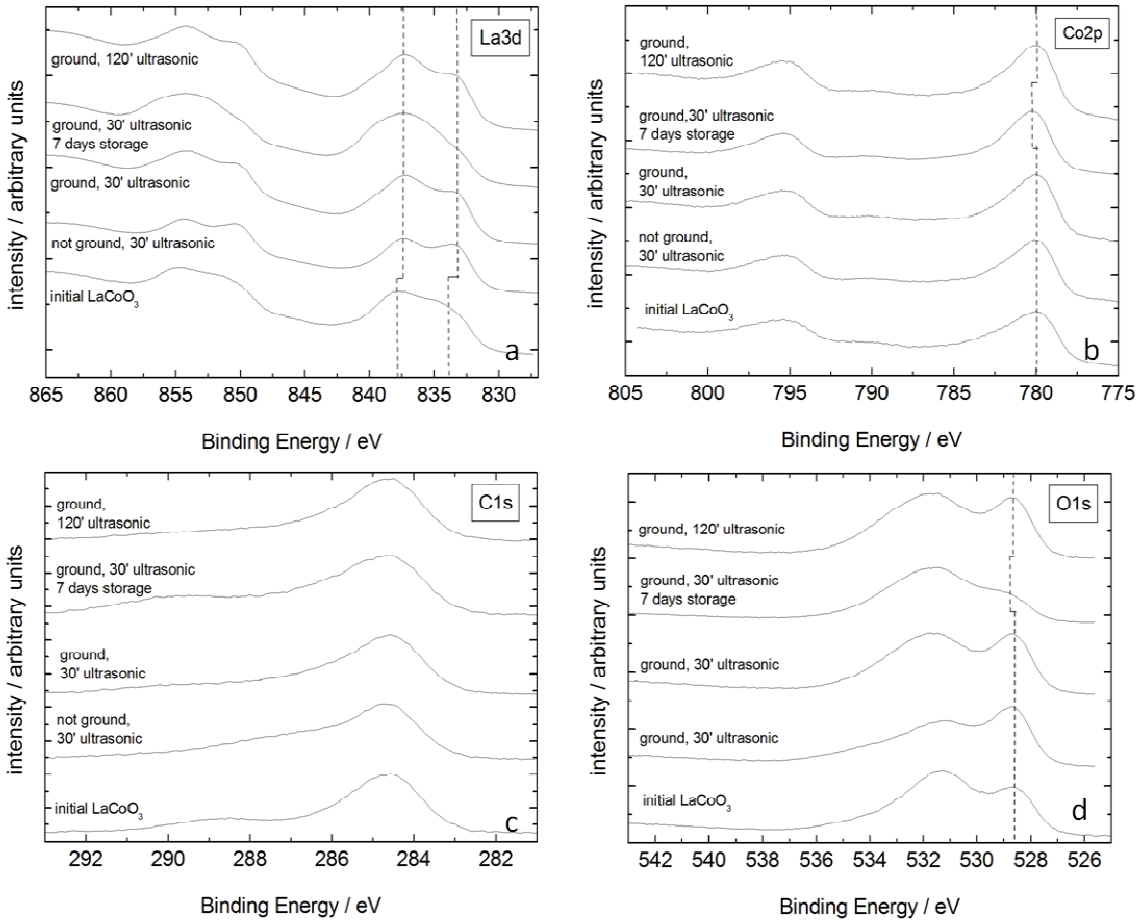

Figure 67 : *XPS spectra of (a) La3d, (b) Co2p, (c) C1s and (d) O1s of various suspensions of $LaCoO_3$. Lines are guides for the eye and indicate the experimental positions.*

Table 19 : *Binding energies (in eV) of XPS peaks and atomic ratios (in brackets) for $LaCoO_3$ of various suspensions*

$LaCoO_3$	$La3d_{5/2}$	$Co2p_{3/2}$	C1s			O1s		
			Adventious carbon	C=O	Carbonate	O lattice	Carbonate and hydroxide	Adsorbed water
Initial $LaCoO_3$	833.2 834.1 838.1 (10%)	779.9 (4%)	284.6 (25%)	286.2 (8%)	288.7 (7%)	528.6 (8%)	531.3 (36%)	533.7 (2%)
not milled, 30' in ultrasonic bath	833.2 837.5 (9%)	779.9 (6%)	284.6 (27%)	286.7 (8%)	288.2 (8%)	528.6 (13%)	531.0 (21%)	533.8 (8%)
milled, 30' in ultrasonic bath	833.2 837.5 (9%)	779.9 (4%)	284.6 (27%)	286.5 (11%)	289.2 (7%)	528.6 (11%)	531.5 (29%)	533.6 (2%)
milled, 30' in ultrasonic bath, 7 days storage	833.2 837.5 839.8 (8%)	780.2 (6%)	284.6 (18%)	286.5 (8%)	289.5 (9%)	528.7 (6%)	531.5 (40%)	533.2 (5%)
milled, 120' in ultrasonic bath	833.2 837.5 (8%)	779.9 (4%)	284.6 (29%)	286.5 (10%)	289.5 (7%)	528.6 (10%)	531.5 (27%)	533.2 (5%)

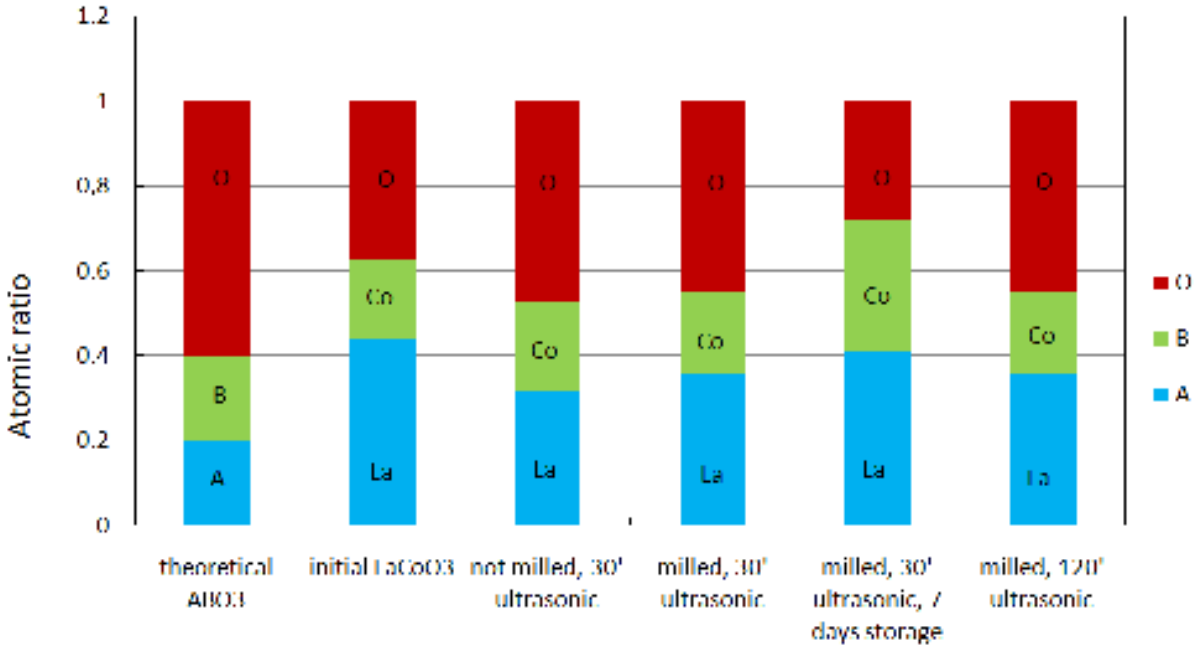

Figure 68 : *XPS atomic ratio of La (blue), Co (green) and O from perovskite lattice (red) in $LaCoO_3$ of various suspensions, calculated with Scofield factors after background correction of XPS spectra.*

6.2.3. Properties of perovskite oxides after immersion in 1M NaOH

In order to investigate the stability of the perovskite oxides in alkaline media, $LaCoO_3$, $LaMnO_3$ and $La_{0.8}Sr_{0.2}MnO_3$ were studied after storage in 1M NaOH for various durations using XRD, ICP-MS and XPS.

6.2.3.1. Structure of the bulk and perovskite dissolution after immersion in 1M NaOH

XRD was used to check the presence of the perovskite phase. After immersion in 1M NaOH and for all the studied perovskites, the perovskite structure remained and no additional peaks could be observed in XRD patterns (Figure 69 for $LaCoO_3$), showing the stability of this structure in alkaline media for at least one month.

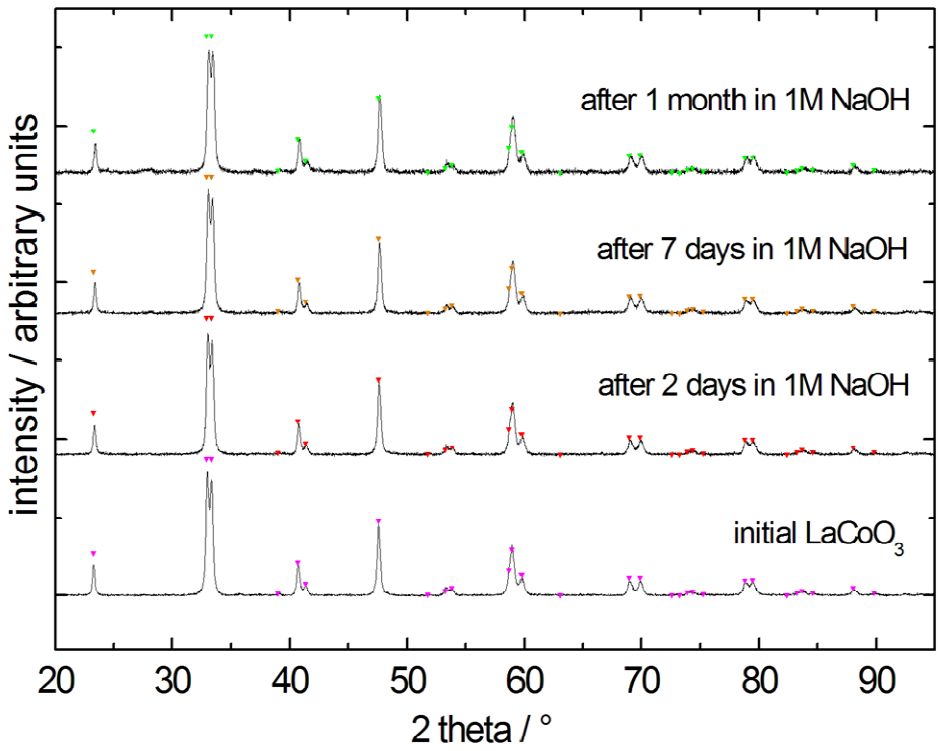

Figure 69 : *X-Ray powder diffraction pattern (step size = 0.0223°, time step = 1s) of $LaCoO_3$ powder before and after immersion in 1M NaOH. The triangle symbols indicate the ICDD reference card LaCoO3 – 01-084-0848. The diffraction patterns were corrected from the background signal.*

The alkaline solution in which the perovskite powder was immersed was analysed by ICP-MS to quantify eventual dissolved species. While La, Co and Mn were stable in the three studied perovskites with an amount of corresponding dissolved species below the detection limit, it was observed that ca. 3 wt.% of the initial mass of Sr contained in $La_{0.8}Sr_{0.2}MnO_3$ was dissolved after two days in alkaline media. No additional dissolution occured for longer immersions. The bulk structure was not affected by this dissolution since the expected perovskite structure was still observed by XRD, as mentioned above. However, one can expect that the loss of Sr should be compensated locally, either by a change in the oxidation state of Mn or by the formation of oxygen vacancies.

The higher extent of dissolution of Sr compared to La, Co and Mn species can be related to the higher solubility of Sr^{2+} hydroxides in alkaline media compared to those of La^{3+}, Mn^{3+} and Co^{3+}. Indeed, the logarithm of the solubility product in alkaline media of $Sr(OH)_2$ (-3.5) is higher than that of $La(OH)_3$ (-18.7), $Co(OH)_3$ (-43.8) or $Mn(OH)_3$ (-36) [254].

Despite the fact that, according to the XRD analysis, the bulk phase composition did not change, the perovskite surface may be degradated. Indeed, it was noticed that the bottle containing $LaCoO_3$ changes from white to brown after long immersion of the perovskite in 1M NaOH, while the bottles containing Mn-based perovskites kept their white color during the whole tests. Thus, the brown color is attributed to the surface degradation and formation of a new Co phase during alkaline immersion.

6.2.3.2. Surface composition after the immersion in 1M NaOH

An eventual modification of the surface composition of the perovskites after the immersion in alkaline media was studied by XPS. In the following, the behavior of each perovskite is analysed separately.

6.2.3.2.1. $LaCoO_3$

Figure 70 shows the XPS spectra of $LaCoO_3$ after various durations in 1M NaOH. The discussion of XPS spectra is started for samples after storage for periods up to 18 days. The data obtained after 1 month in 1M NaOH will be discussed later.

After alkaline treatment, the La3d peaks are better defined but appear at higher binding energies than expected for $LaCoO_3$ perovskite (Figure 70,a). By comparing the La3d spectrum and its peak binding energies (Table 20) to XPS data of commercial La_2O_3 and $La_2(CO_3)_3$ (Figure 21,a and Table 7), it is reasonnable to believe that there is formation of oxide, hydroxide and/or carbonate of lanthanum on $LaCoO_3$ surface, already largely covered by lanthanum carbonates before the alkaline treatment (see section 3.2.4). The formation of lanthanum hydroxide after immersion in alkaline media of Co-based perovskites was also reported in the literature [94,139] and may negatively affect the ORR activity of the perovskite [94,253].

Besides, the atomic ratio of La:Co shows that the immersion in alkaline solution also leads to an increase of the quantity of cobalt on the perovskite surface (Figure 71). The Co2p spectrum displays assymetric peaks slightly shifted to higher binding energies (Figure 70,b and Table 20), consistent with the formation of Co^{4+} or Co^{3+} from non perovskite phases such as oxides (e.g. CoO_2 which is however not supposed to be stable at OCP) or hydroxides (e.g. $Co(OH)_3$).

Moreover, these new phases can be at the origin of the change of the bottle color mentioned previously (see section 6.2.3.1). The absence of satellite peaks proves that Co^{2+}, and in particular $CoCO_3$, is not formed during the immersion in alkaline media.
Small fraction of the lattice oxygen compared to the fraction of La and Co (Figure 71) confirms that both cations are not in the perovskite form at the surface. From O1 spectrum (Figure 70,d) and the atomic ratio (Table 20), it is clear that the predominant species are carbonates and/or hydroxides on the $LaCoO_3$ surface. In addition to La and Co species, the presence of Na_2CO_3 or NaOH is suggested by the atomic ratio (Table 20).
Indeed, the sample was directly analysed after immersion in 1M NaOH without rinsing. As mentioned in section 2.5.3, the effect of the rinsing was investigated but the results were not reproducible probably due to the longer storage under atmospheric conditions which is required to performe the rinsing and which could modify the perovskite surface composition.

After 1 month in 1M NaOH, all the spectra display significant shape change. This is probably due to a charge effect with the formation of the insulating phases mentioned above on the perovskite surface.

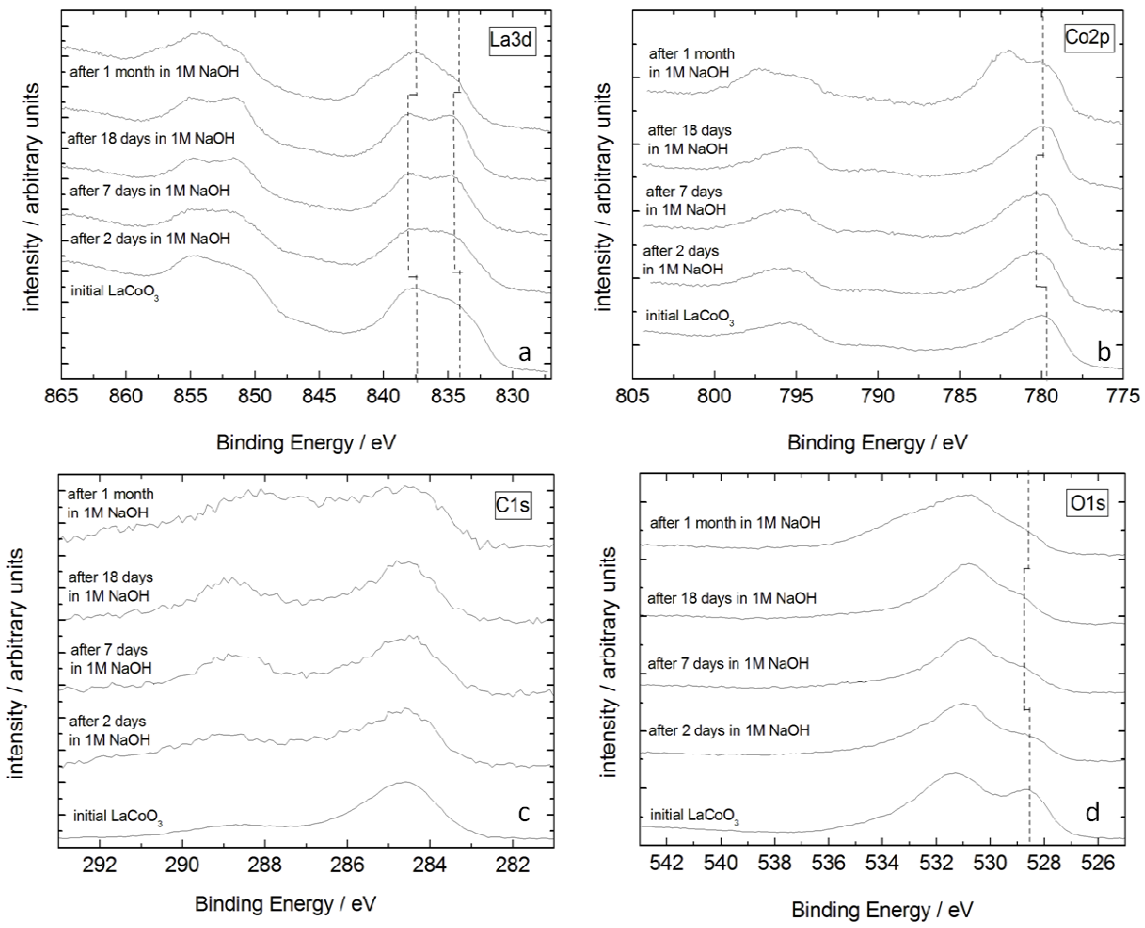

Figure 70 : *XPS spectra of (a) La3d, (b) Co2p, (c) C1s and (d) O1s of $LaCoO_3$ before and after immersion in 1M NaOH. Lines are guides for the eye and indicate the experimental positions.*

Table 20 : *Binding energies (in eV) of XPS peaks and atomic ratios (in brackets) for $LaCoO_3$ before and after immersion in 1M NaOH*

$LaCoO_3$	$La3d_{5/2}$	$Co2p_{3/2}$	C1s			O1s			Na1s
			Adventious carbon	C=O	Carbonate	O lattice	Carbonate and hydroxide	Adsorbed water	
Initial $LaCoO_3$	833.2 834.1 838.1 (10%)	779.9 (4%)	284.6 (25%)	286.2 (8%)	288.7 (7%)	528.6 (8%)	531.3 (36%)	533.7 (2%)	-
After 2 days in 1M NaOH	834.6 838.1 (9%)	780.4 (6%)	284.6 (10%)	286.2 (4%)	288.9 (11%)	528.6 (5%)	530.8 (39%)	533.6 (9%)	1071.3 (8%)
After 7 days in 1M NaOH	834.6 838.1 (9%)	780.4 (7%)	284.6 (11%)	286.2 (2%)	288.9 (11%)	528.8 (6%)	530.8 (33%)	533.6 (11%)	1071.3 (9%)
After 18 days in 1M NaOH	834.6 838.1 (10%)	779.9 (7%)	284.6 (10%)	286.2 (2%)	288.9 (11%)	528.8 (5%)	530.8 (37%)	533.6 (10%)	1071.3 (8%)
After 1 month in 1M NaOH	834.1 837.5 840.6 (11%)	779.9 782.1 (7%)	284.6 (7%)	286.5 (2%)	288.4 (19%)	528.6 (2%)	530.9 (36%)	533.6 (11%)	1073.6 (5%)

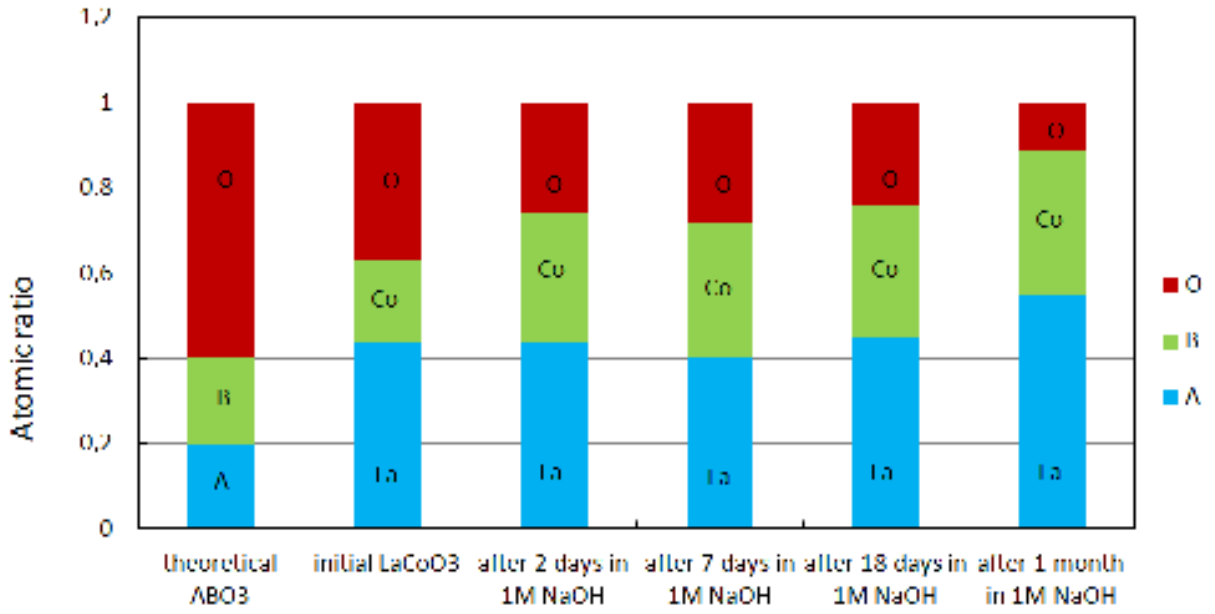

Figure 71 : *XPS atomic ratio of La (blue), Co (green) and O from perovskite lattice (red) in $LaCoO_3$ before and after immersion in 1M NaOH, calculated with Scofield factors after background correction of XPS spectra.*

6.2.3.2.2. $LaMnO_3$

For $LaMnO_3$, a similar negative shift of 0.4 eV is observed in La3d, Mn2p and O1s spectra after immersion in alkaline media (Figure 72,a,b,d, Table 21) and no significant modification of the spectra shape is visible. Thus, the shift is probably due to charging rather than to surface modification. Also, the atomic ratio (Figure 73) shows that the surface of $LaMnO_3$ is rather stable after a long immersion in 1M NaOH, contrary to $LaCoO_3$, probably due to the higher stability of the former perovskite structure [138].

Only the formation of some carbonates species occurs. Indeed, the presence of carbonates is highlighted in C1s and O1s spectra (Figure 72,c,d) and the atomic ratio of carbonates from C1s to carbonates and hydroxides from O1s is ca. 1:3 (Table 21), consistent with presence of CO_3^{2-} species. In fact, the presence of Na in the XPS scan (not shown) as well as the atomic ratio Na:carbonates (Table 21) suggest that a large part of the carbonates present on the perovskite surface are Na_2CO_3 formed during perovskite storage in 1M NaOH.

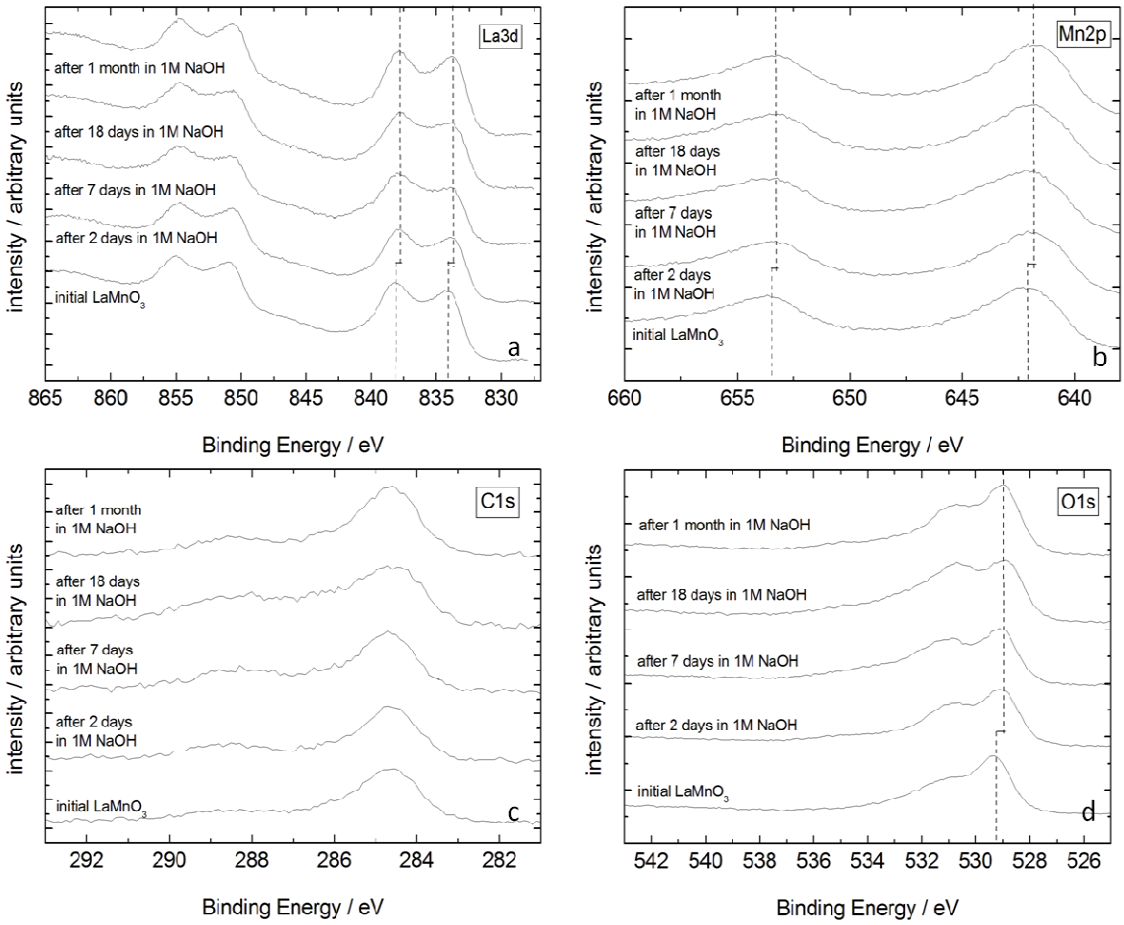

Figure 72 : *XPS spectra of (a) La3d, (b) Mn2p, (c) C1s and (d) O1s of $LaMnO_3$ before and after immersion in 1M NaOH. Lines are guides for the eye and indicate the experimental positions.*

Table 21 : *Binding energies (in eV) of XPS peaks and atomic ratios (in brackets) for $LaMnO_3$ before and after immersion in 1M NaOH*

$LaMnO_3$	$La3d_{5/2}$	$Mn2p_{3/2}$	C1s			O1s			Na1s
			Adventious carbon	C=O	Carbonate	O lattice	Carbonate and hydroxide	Adsorbed water	
Initial $LaMnO_3$	834.1 838.1 (14%)	642.1 (9%)	284.6 (17%)	286.2 (6%)	288.7 (5%)	529.3 (22%)	531.0 (21%)	532.8 (7%)	-
After 2 days in 1M NaOH	833.7 837.7 (10%)	641.8 (8%)	284.6 (13%)	286.2 (2%)	288.5 (7%)	528.9 (20%)	530.9 (20%)	533.0 (10%)	1071.3 (10%)
After 7 days in 1M NaOH	833.7 837.7 (10%)	641.8 (8%)	284.6 (11%)	286.2 (6%)	288.5 (6%)	528.9 (16%)	531.0 (18%)	533.0 (14%)	1071.3 (10%)
After 18 days in 1M NaOH	833.7 837.7 (9%)	641.8 (7%)	284.6 (9%)	286.2 (6%)	288.5 (7%)	528.9 (13%)	530.9 (21%)	533.0 (14%)	1071.3 (12%)
After 1 month in 1M NaOH	833.7 837.7 (9%)	641.8 (7%)	284.6 (13%)	285.9 (8%)	288.5 (7%)	528.9 (18%)	530.9 (18%)	533.0 (9%)	1071.3 (10%)

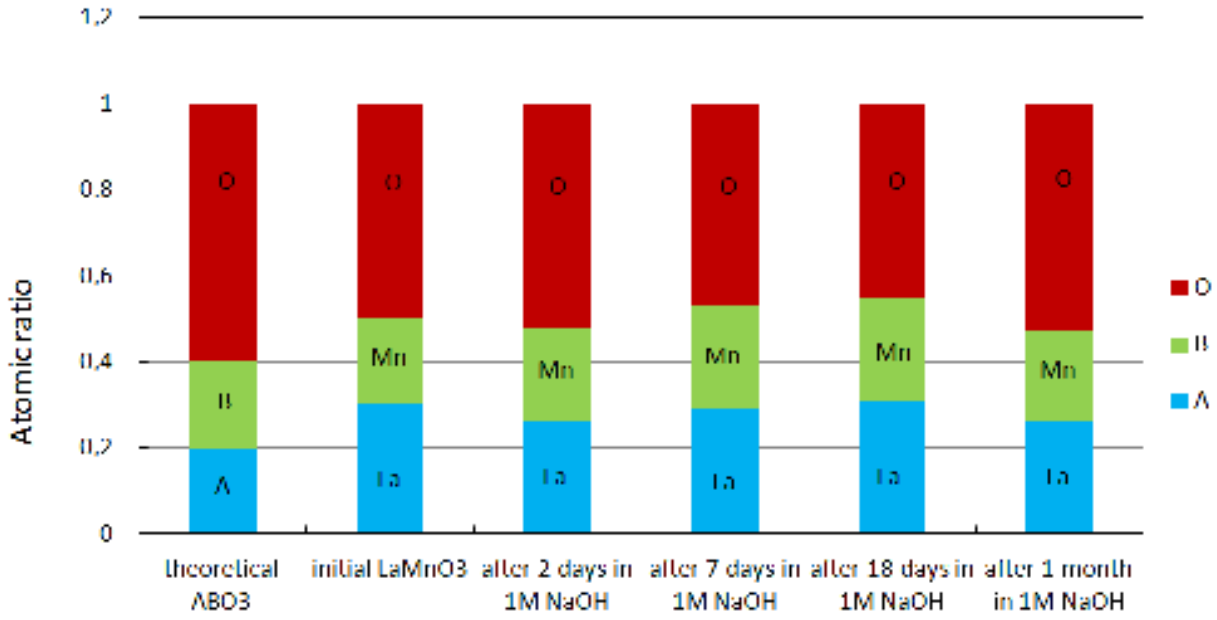

Figure 73 : *XPS atomic ratio of La (blue), Mn (green) and O from perovskite lattice (red) in $LaMnO_3$ before and after immersion in 1M NaOH, calculated with Scofield factors after background correction of XPS spectra.*

6.2.3.2.3. $La_{0.8}Sr_{0.2}MnO_3$

After immersion in the alkaline solution, no modification of the La3d spectra is noticed for $La_{0.8}Sr_{0.2}MnO_3$ (Figure 74,a), but a small shift towards lower binding energies is observed in Mn2p spectra (Figure 74,b and Table 22). This is likely related to a decrease of the amount of high oxidation state Mn^{4+} in the perovskite as a consequence of the dissolution of Sr^{2+} from the perovskite observed by ICP-MS (see section 6.2.3.1) and probably responsible for the slight modification of the Sr3d spectra shape (Figure 74,c). However, the quantity of dissolved Sr species (3 wt.%) is smaller than the XPS error (ca. 10%) and is therefore not clearly visible in the atomic ratio (Figure 75).

As for $LaMnO_3$, XPS results evidences the presence of Na_2CO_3 regarding the atomic ratio of Na and carbonates species (Table 22). Nevertheless, regarding the negligible changes in the spectra shape, peak binding energies and atomic ratio (Figure 75) with the immersion in alkaline solution, the surface of $La_{0.8}Sr_{0.2}MnO_3$ seems to be rather stable after long immersion in 1M NaOH, similar to the non doped $LaMnO_3$.

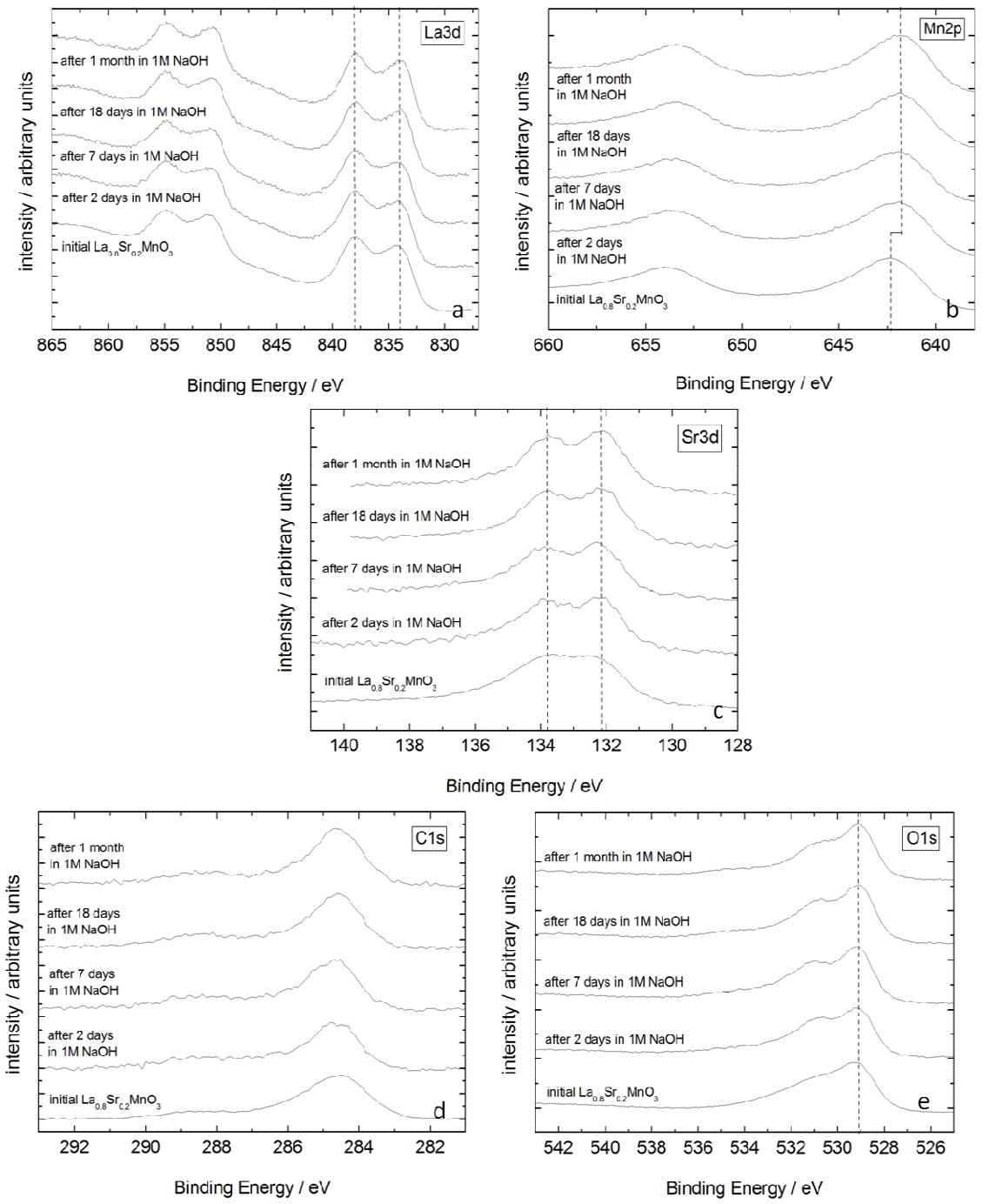

Figure 74 : *XPS spectra of (a) La3d, (b) Mn2p, (c) Sr3d, (d) C1s and (e) O1s of $La_{0.8}Sr_{0.2}MnO_3$ before and after immersion in 1M NaOH. Lines are guides for the eye and indicate the experimental positions.*

Table 22 : *Binding energies (in eV) of XPS peaks and atomic ratios (in brackets) for $La_{0.8}Sr_{0.2}MnO_3$ before and after immersion in 1M NaOH*

$La_{0.8}Sr_{0.2}MnO_3$	La3d$_{5/2}$	Sr3d$_{5/2}$	Mn2p$_{3/2}$	C1s			O1s			Na1s
				Adventious carbon	C=O	Carbonate	O lattice	Carbonate and hydroxide	Adsorbed water	
Initial $La_{0.8}Sr_{0.2}MnO_3$	834.1 838.1 (8%)	132.3 (6%)	642.4 (8%)	284.6 (22%)	286.1 (5%)	288.5 (5%)	529.2 (22%)	531.0 (13%)	532.7 (9%)	-
After 2 days in 1M NaOH	834.1 838.1 (7%)	132.3 (4%)	641.8 (9%)	284.6 (13%)	286.4 (5%)	288.5 (4%)	529.2 (22%)	531.0 (11%)	532.7 (16%)	1071.3 (9%)
After after 7 days in 1M NaOH	834.1 838.1 (8%)	132.3 (5%)	641.8 (9%)	284.6 (14%)	286.4 (4%)	288.5 (6%)	529.2 (20%)	531.0 (12%)	532.7 (14%)	1071.3 (8%)
After after 18 days in 1M NaOH	834.1 838.1 (8%)	132.3 (3%)	641.8 (9%)	284.6 (16%)	286.1 (5%)	288.5 (5%)	529.0 (21%)	531.0 (15%)	532.9 (11%)	1071.3 (9%)
After after 1 month in 1M NaOH	834.1 838.1 (8%)	132.3 (5%)	641.8 (9%)	284.6 (17%)	286.1 (4%)	288.5 (5%)	529.0 (21%)	531.0 (14%)	532.9 (9%)	1071.3 (9%)

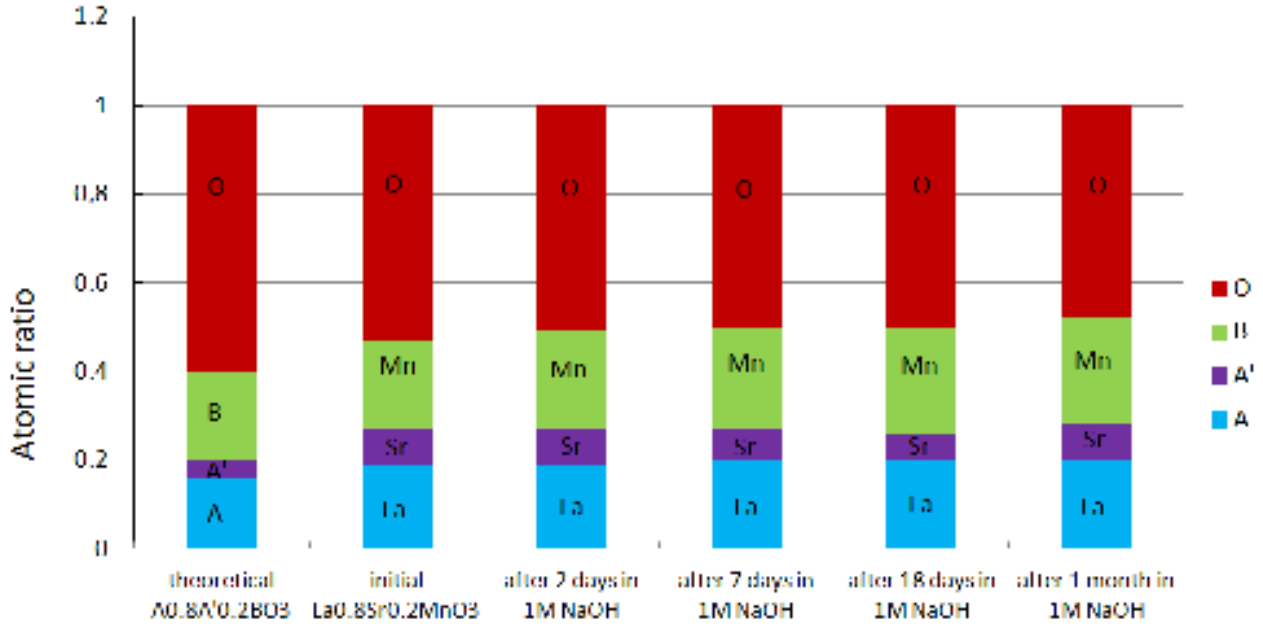

Figure 75 : *XPS atomic ratio of La (blue), Sr (purple), Mn (green) and O from perovskite lattice (red) in $La_{0.8}Sr_{0.2}MnO_3$ before and after immersion in 1M NaOH, calculated with Scofield factors after background correction of XPS spectra.*

6.3. Electrochemical stability of perovskite electrodes

In the previous section, it was observed that Mn-perovskites present rather stable surface in alkaline medium, whereas $LaCoO_3$ is significantly affected with probable formation of lanthanum and cobalt hydroxide species.

During the ORR electrocatalysis in alkaline medium, the electrode polarization, as well as the interaction of the perovskite surface with O_2 and HO_2^- – since ORR occurs through a "series" pathway – may also affect the stability of the perovskite oxides. Thus, in order to study the electrochemical stability of perovskite electrodes, the stability of the electrocatalytic activities and interfacial properties were studied in the first place, and then, the material properties of the perovskites were investigated.

6.3.1. Stability of the electrocatalytic activity

The stability of the electrocatalytic activity of perovskite electrodes was evaluated by chronoamperometry at various potentials, as described in section 2.5.5, both in the presence and in the absence of carbon in the catalytic layer. Distinct behaviors were found for Co-based and for Mn-based perovskites and are presented in sections 6.3.1.1 and 6.3.1.2, respectively.

Each experiment was repeated at least two times. Only reproducible results are presented in this section.

6.3.1.1. Stability of Co-based perovskite electrodes

6.3.1.1.1. Without carbon in the catalytic layer

Figure 76,a presents a typical RDE voltammogram of GC-supported thin film of 91 $\mu g.cm^{-2}_{geo}$ $LaCoO_3$ in O_2-saturated 1M NaOH. The potentials of interest, i.e. in the kinetic region

(ORR current of ca. 0.01 mA), in the mixed kinetic-diffusion region (ORR halfwave potential), and in the diffusion region (lower potential limit) are +0.76 V, +0.67 V and +0.43 V vs. RHE, respectively, and are indicated in the voltammogram in O_2-saturated electrolyte (Figure 76,a), as well as in the voltammogram in H_2O_2-containing electrolyte (Figure 76,d). The chronoamperometries at the mentioned potentials are shown in Figure 76,b for ORR and in Figure 76,e for HO_2^- reduction. For comparison, Figure 76,c,f presents these chronoamperometries after normalization by the current value at the end of the measurement at t=167 min in order to better visualize and compare the activity loss[1]. In addition, RDE voltammograms were performed before and after each chronoamperometry to better visualize the stability of the activity. The obtained voltammograms are displayed in Figure 77.

[1] It should be noted that normalization to the current at t=0 was not feasible due to a strong initial current drop.

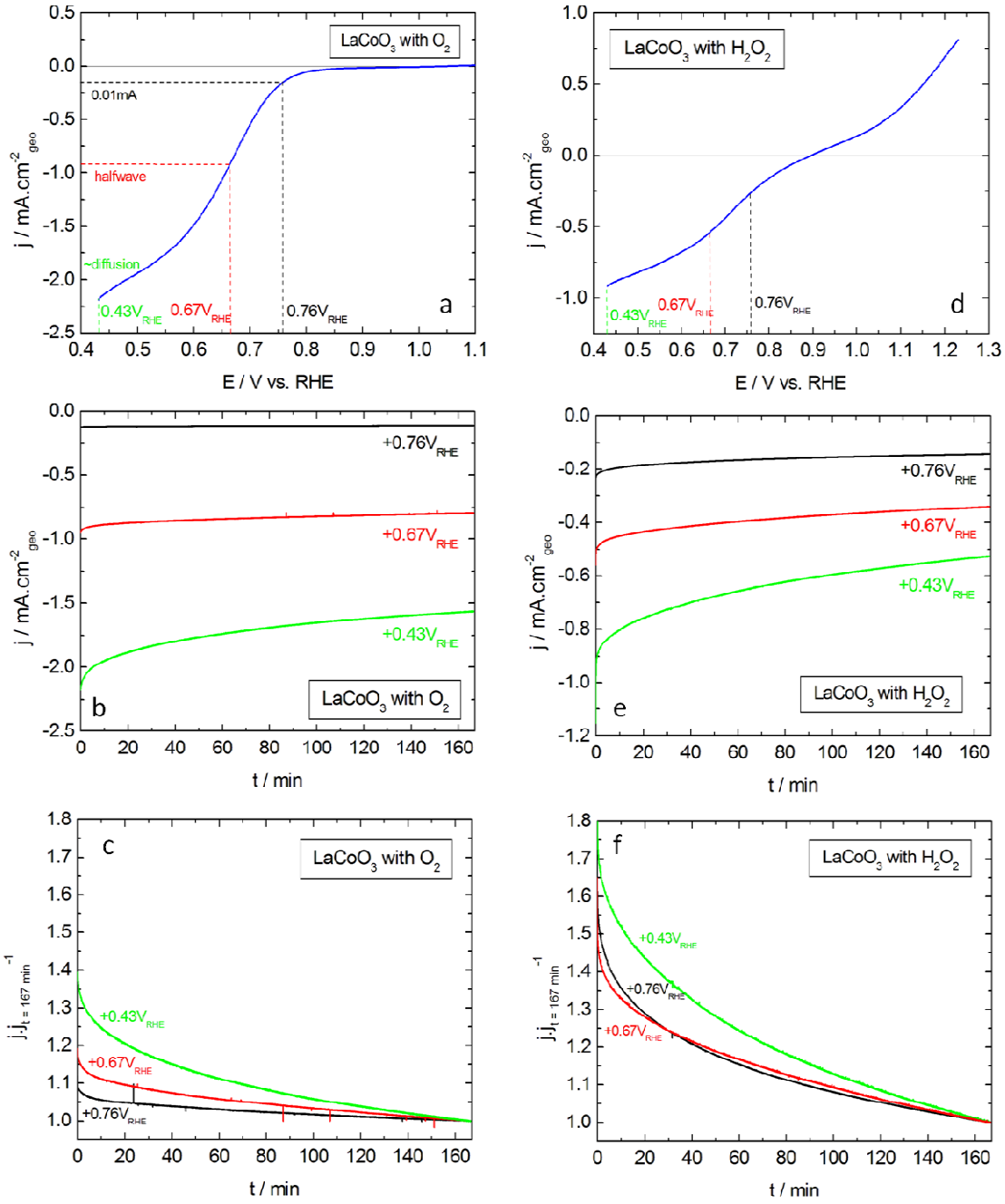

Figure 76 : *(a,d) Positive scans of RDE voltammograms at 10 mV.s^{-1}, (b,e) chronoamperometry at various potentials and (c,f) corresponding normalization by the last current value of GC-supported thin films of $LaCoO_3$ at 2500 rpm in (a,b,c) O_2-saturated 1M NaOH and (d,e,f) N_2- purged 1M NaOH + 0.84mM H_2O_2. Measurements were performed with 91 µg.cm$^{-2}_{geo}$ perovskite. Color codes for applied potential: +0.76 V vs. RHE (black), +0.67 V vs. RHE (red) and +0.43 V vs. RHE (green). Currents are normalized to the geometric area of the electrode.*

The discussion is started with the stability of the ORR activity. After 10,000 seconds of chronoamperometry at +0.76 V, +0.67 V and +0.43 V vs. RHE in O_2-containing electrolyte, the remaining ORR currents are ca. -120 $\mu A.cm^{-2}_{geo}$, -800 $\mu A.cm^{-2}_{geo}$ and -1.6 $mA.cm^{-2}_{geo}$, respectively (Figure 76,b). This corresponds to a total current loss of ca. 10, 15 and 25%, correspondly, with the half of the loss occurring during the first 20 min (Figure 76,c). Thus, the lower the applied potential, or in other words the higher the overpotential, the less stable the ORR current is.

The comparison of the ORR RDE voltammograms before and after each chronoamperometry measurements (Figure 77,a,b,c) shows that the currents at high potentials were not affected. This proves the stability of the ORR kinetic currents on $LaCoO_3$ electrode. On the other hand, the currents at low potentials decrease significantly after chronoamperometry, in particular when the applied potential is low (+0.43 V vs. RHE).

First of all, the O_2 consumption in the ORR was estimated to check whether the observed current decrease might be due to the O_2 concentration drop. The variation of molar quantities of O_2 Δn_{O2} was roughly estimated using the Faraday law (Equation 105)

$$\Delta n_i = \frac{\nu_i}{\nu_e F} Q \quad \text{(Equation 105)}$$

where ν_i is the stoichiometric number of the reactant (1 for O_2), ν_e is the number of involved electrons (4 for ORR), and Q is the faradic charge (Equation 106):

$$Q = |I|\Delta t \text{ (Equation 106)}$$

with I, the current, and Δt, the duration of the reaction.

Therefore, the maximal quantity of O_2 consumed during chronoamperometry – corresponding to the maximal measured current - at +0.43 V vs. RHE in O_2-containing electrolyte is (Equation 107):

$$\Delta n_{O2} = \frac{1*2.2\ mA.cm^{-2}_{geo}*0.071\ cm^{-2}_{geo}*10000\ s}{4*96485\ C.mol^{-1}} = 0.004\ mmol \quad \text{(Equation 107)}$$

This corresponds to a decrease of at most 5% of the initial amount of O_2 (0.84 mM in 100 mL = 0.084 mmol). O_2 consumption can therefore not explain the loss of 25% of the ORR current.

Then, two hypotheses can be proposed to explain the loss of currents at low potentials. The first one is the formation of a non conductive layer on the perovskite surface - such as lanthanum or cobalt hydroxides formed throug contact with the alkaline media (see section 6.2.3.2) - during the ORR. Then, the layer ohmic drop will be more pronounced at high currents, leading to stronger effect on the current transients at high overpotentials.

The second explanation of the instability of currents at high overpotentials can be the degradation of the active sites for HO_2^- transformation, if it is supposed that different active sites are responsible for the ORR and for the HO_2^- reduction reaction on $LaCoO_3$ electrodes. For example, ORR could occur on the GC surface and HO_2^- formed on GC is further transformed on perovskite sites (see section 5.2.1.1). The currents at low overpotential are therefore not affected because the sites actives for the ORR (carbon sites) are relatively stable, while the number of actives sites for the HO_2^- reduction reaction (perovskite sites) decreases, which leads to a decrease of the currents at high overpotentials.

One shoud note that the two hypotheses could be linked. Indeed, the formation of insulating phases such as $La(OH)_3$ or $Co(OH)_3$, non active for ORR [94,253] would decrease the perovskite surface area and lead to a decrease of activity.

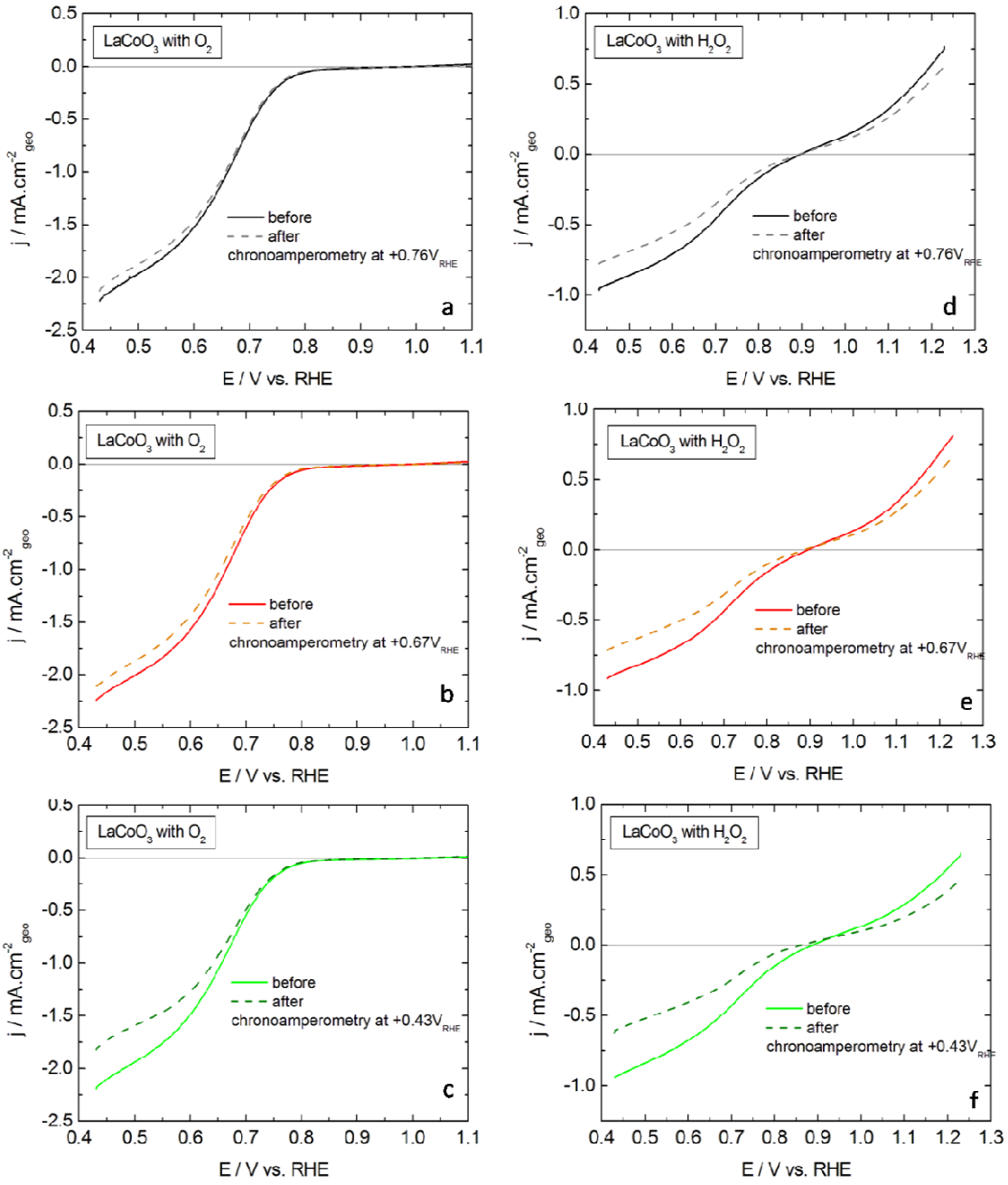

Figure 77 : *Positive scans of RDE voltammograms at 2500 rpm and 10 mV.s^{-1} of GC-supported thin films of $LaCoO_3$ in (a,b,c) O_2-saturated 1M NaOH and (d,e,f) N_2- purged 1M NaOH + 0.84mM H_2O_2 before and after chronoamperometry at various potentials* (Figure 76). *Measurements were performed with 91 µg.cm$^{-2}_{geo}$ perovskite. Color codes for applied potential: +0.76 V vs. RHE (before : black, after : dash grey), +0.67 V vs. RHE (before : red, after : dash orange) and +0.43 V vs. RHE (before : green, after : dash olive). Currents are normalized to the geometric area of the electrode and corrected to the background currents measured in the N_2 atmosphere in the absence of H_2O_2.*

In order to investigate the stability of $LaCoO_3$ sites versus HO_2^- reduction, chronoamperometry measurements were performed in H_2O_2-containing electrolytes. In this case, the remaining currents after 10,000 seconds of chronoamperometry at +0.76 V, +0.67 V and +0.43 V vs. RHE are ca. -140 $\mu A.cm^{-2}_{geo}$, -340 $\mu A.cm^{-2}_{geo}$ and -530 $\mu A.cm^{-2}_{geo}$, respectively (Figure 76,e). This corresponds to a total current loss of ca. 35% at low overpotentials and 40% at high overpotentials, with the half of loss occurring during the first 30 minutes (Figure 76,f). This loss is significantly stronger than in the presence of O_2 (Figure 76,c).

With the purpose to quantify the amount of HO_2^- consumed during chronoamperometry, the Faraday law is applied for HO_2^- reduction with ν_i, the stoichiometric number of reactant (1 for HO_2^-) and ν_e, the number of involved electrons (2 for HO_2^- reduction) (Equation 108):

$$\Delta n_{H2O2} = \frac{1*0.9\ mA.cm^{-2}_{geo}*0.071\ cm^{-2}_{geo}*10000\ s}{2*96485\ C.mol^{-1}} = 0.003\ mmol \quad \text{(Equation 108)}$$

Thus, ca. 4% of the initial amount of HO_2^- (0.84 mM in 100 mL = 0.084 mmol) is consumed by electrochemical reduction.

One should also take into account that a part of HO_2^- can be consumed by catalytic decomposition on perovskite sites. For $LaCoO_3$, the heteregenous constant of HO_2^- decomposition is 6.2 10^{-5} $cm.s^{-1}$ (see section 5.4.3). On the RDE electrode used for chronoamperometry, the perovskite mass is 6.4 µg (91µg.cm^{-2}geo * 0.071 cm^2_{geo}), which corresponds to a perovskite surface of 0.64 $cm^2_{perovskite}$ ($S_{BET}(LaCoO_3)$ = 10 $m^2.g^{-1}$ (see section 3.2.3)). Therefore, from (Equation 65), the first order constant k is (Equation 109):

$$k = \frac{6.2*10^{-5}cm.s^{-1}*0.64\ cm^2}{100\ cm^3} = 4*10^{-7}s^{-1} \text{ (Equation 109)}$$

Based on (Equation 63), the H_2O_2 consumption by catalytic HO_2^- decomposition on $LaCoO_3$ electrode during chronoamperometry is (Equation 110):

$$1 - \frac{C_{H_2O_2}}{C_{H_2O_2}{}^{0}} = 1 - \exp(-4*10^{-7}s^{-1}*10000\ s) = 0.4\% \quad \text{(Equation 110)}$$

which is negligible. Clearly, the maximal HO_2^- consumption – ca. 4.4% all in all - is not sufficient to justify the strong current losses observed in chronoamperometries.

The observation of the RDE voltammograms in H_2O_2-containing electrolyte (Figure 77,d,e,f), indicates a global decrease of the HO_2^- reduction after chronoamperometries. This is consistent with the hypothesis of an irreversible modification of the active sites for the HO_2^- reduction, i.e. of the perovskite sites. Also, as the HO_2^- reduction/oxidation currents are affected more than the ORR, it confirms that different types of active sites are involved for the

O_2 and for the HO_2^- reactions: probably glassy carbon for the former and perovskite for the latter.

However, no significant differences were observed between the CV before and after chronoamperometries (not shown) which could support the possible degradation of the interfacial properties of $LaCoO_3$.

6.3.1.1.2. With carbon in the catalytic layer

In the previous section, it was mentioned that the ORR may lead to an increase of the ohmic drop in the electrode. As the addition of carbon is known to have a great impact on the electrical contact into the perovskite layer, the effect of its presence on the electrocatalytic stability was investigated.

However, carbon is corroded in the presence of H_2O_2 [209,255], and this corrosion may induce a degradation of the catalytic layer. For instance, Kinumoto et al. [255] observed that the carbon corrosion in the presence of H_2O_2 causes the agglomeration of Pt particles and a fortiori the decrease of the active surface area.

Thus, in order to study the effect of carbon presence on the electrochemical and electrocatalytic stability of perovskite electrodes, chronoamperometries were also performed on perovskite/carbon composites. Figure 78,a presents a typical RDE voltammogram of GC-supported thin film of 91 $\mu g.cm^{-2}_{geo}$ $LaCoO_3$ + 37 $\mu g.cm^{-2}_{geo}$ carbon in O_2-saturated 1M NaOH. The potentials of interest, i.e. in the kinetic region, in the mixed kinetic-diffusion region and in the diffusion region are +0.85 V, +0.78 V and +0.43 V vs. RHE, respectively, for $LaCoO_3$/C composite, and are indicated in the voltammogram in O_2-saturated electrolyte (Figure 78,a), as well as in the voltammogram in H_2O_2-containing electrolyte (Figure 78,d). The chronoamperometries at the mentioned potentials are shown in Figure 78,b for ORR and in Figure 78,e for HO_2^- reduction, and Figure 78,c,f presents these chronoamperometries after normalization by the current value at the end of the measurement at t=167 min. The RDE voltammograms obtained before and after each chronoamperometry are displayed in Figure 79.

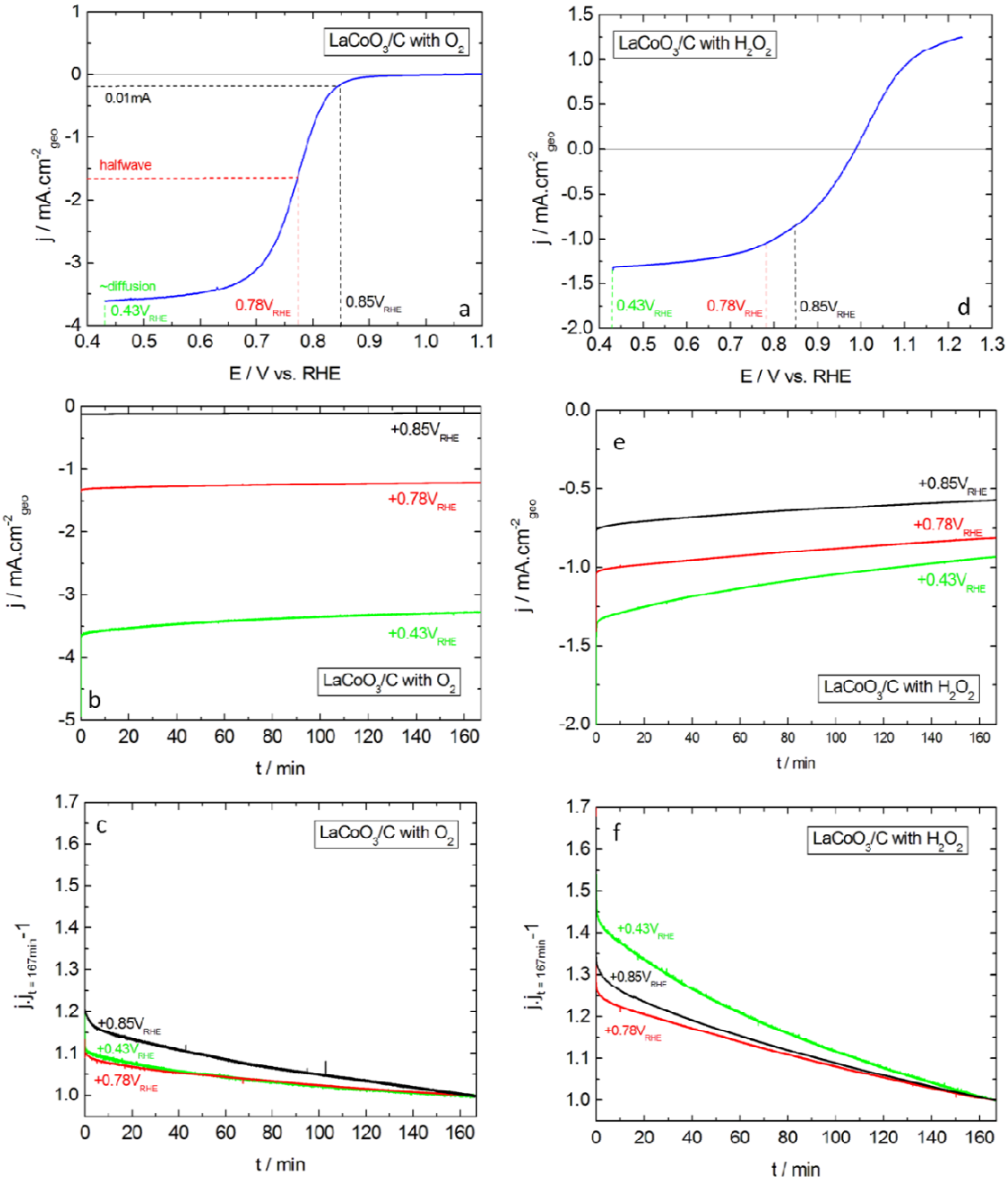

Figure 78 : *(a,d) Positive scans of RDE voltammograms at 10 mV.s^{-1}, (b,e) chronoamperometry at various potentials and (c,f) corresponding normalization by the last current value of GC-supported thin films of $LaCoO_3$ + Sibunit carbon at 2500 rpm in (a,b,c) O_2-saturated 1M NaOH and (d,e,f) N_2- purged 1M NaOH + 0.84mM H_2O_2. Measurements were performed with 91 µg.cm$^{-2}_{geo}$ perovskite + 37 µg.cm$^{-2}_{geo}$ Sibunit carbon. Color codes for applied potential: +0.85 V vs. RHE (black), +0.78 V vs. RHE (red) and +0.43 V vs. RHE (green). Currents are normalized to the geometric area of the electrode.*

First of all, it can be noticed on the chronoamperometry results that the ORR currents are rather stable in the presence of carbon (Figure 78,b,c). Also, the ORR RDE voltammograms are not significantly affected by the chronoamperometries (Figure 79,a,b,c). Indeed, only a little decrease of the diffusion limited current can be observed and may be attributed to the O_2 consumption – ca. 8% at +0.43 V vs. RHE.

In the presence of H_2O_2 (Figure 78,e,f), the current losses are somewhat stronger than in the presence of O_2 (Figure 78,b,c), but are less pronounced than for electrodes without carbon (Figure 76,e,f).

In the RDE voltammogramms after long HO_2^- reduction, it is observed that the currents have decreased and that the mixed potential is shifted toward lower potentials (Figure 79,d,e,f). A part of the current decrease is a consequence of the HO_2^- consumption, evaluated as ca. 5% at +0.43 V vs. RHE, but the negative shift of the mixed potential indicates that the reaction rate of HO_2^- reduction has decreased. This is probably due to the degradation of perovskite active sites mentioned previously, but one can also not exclude corrosion of some carbon particles due to the presence of H_2O_2 in the electrolyte [209,255]. Then, the carbon corrosion would cause a deterioration of the electrical contact within the catalytic layer [1] and therefore to a lower perovskite utilization.

To conclude, the following hypothesis is made. During the ORR, an electrochemically inactive and insulating phase is formed on $LaCoO_3$ sites. This leads to (i) an increase of the ohmic drop in the layer, which can be minimized with the addition of carbon and (ii) a decrease of the accessible perovskite area and thus, a decrease of the electrocatalytic activity. As carbon is more active than $LaCoO_3$ for the ORR, the ORR kinetic currents are not affected. However, the activity for the HO_2^- reduction which occurs on perovskite sites is decreased.

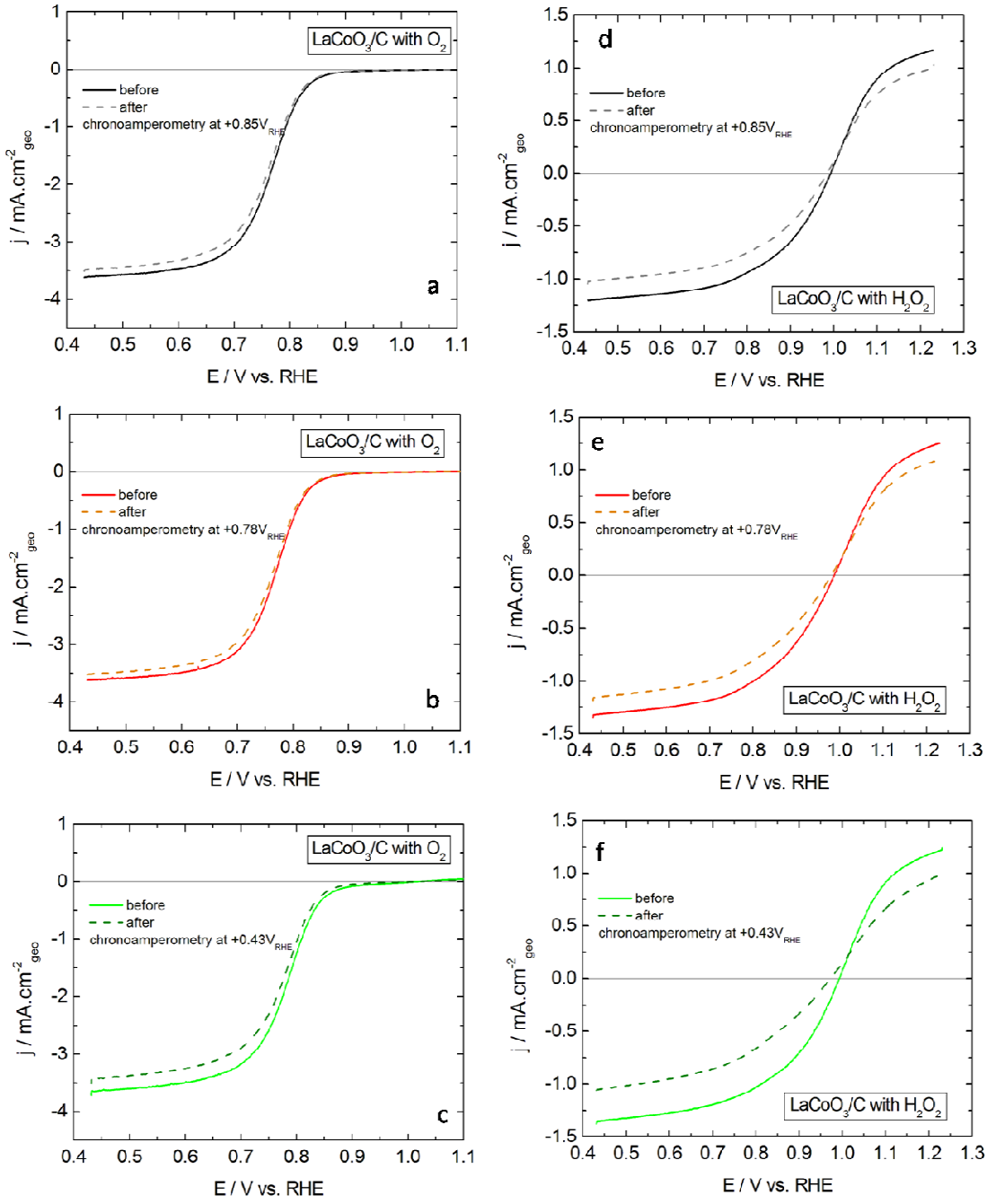

Figure 79 : *Positive scans of RDE voltammograms at 2500 rpm and 10 mV.s^{-1} of GC-supported thin films of $LaCoO_3$ + Sibunit carbon in (a,b,c) O_2-saturated 1M NaOH and (d,e,f) N_2- purged 1M NaOH + 0.84mM H_2O_2 before and after chronoamperometry at various potentials* (Figure 78). *Measurements were performed with 91 µg.cm$^{-2}_{geo}$ perovskite + 37 µg.cm$^{-2}_{geo}$ Sibunit carbon. Color codes for applied potential: +0.85 V vs. RHE (before : black, after : dash grey), +0.78 V vs. RHE (before : red, after : dash orange) and +0.43 V vs. RHE (before : green, after : dash olive). Currents are normalized to the geometric area of the electrode and corrected to the background currents measured in the N_2 atmosphere in the absence of H_2O_2*

6.3.1.2. Stability of Mn-based perovskite electrodes

The behaviors observed for $LaMnO_3$ and $La_{0.8}Sr_{0.2}MnO_3$ perovskites concerning electrochemical and electrocatalytic stability were similar to each other. Therefore, only data for $La_{0.8}Sr_{0.2}MnO_3$ are presented in this section.

6.3.1.2.1. Without carbon in the catalytic layer

Figure 80,a presents a typical RDE voltammogram of GC-supported thin film of 91 $\mu g.cm^{-2}_{geo}$ $La_{0.8}Sr_{0.2}MnO_3$ in O_2-saturated 1M NaOH. The potentials of interest, i.e. in the kinetic region, in the mixed kinetic-diffusion region, and in the diffusion region are +0.83 V, +0.69 V and +0.43 V vs. RHE, respectively, and are indicated on the voltammogram in O_2-saturated electrolyte (Figure 80,a), as well as on the voltammogram in H_2O_2-containing electrolyte (Figure 80,d). The current transients at the mentioned potentials are shown in Figure 80,b for ORR and in Figure 80,e for HO_2^- reduction, and Figure 80,c,f presents these current transients after normalization by the current value at the end of the measurement at t=167 min. The RDE voltammograms obtained before and after each chronoamperometry are displayed in Figure 81.

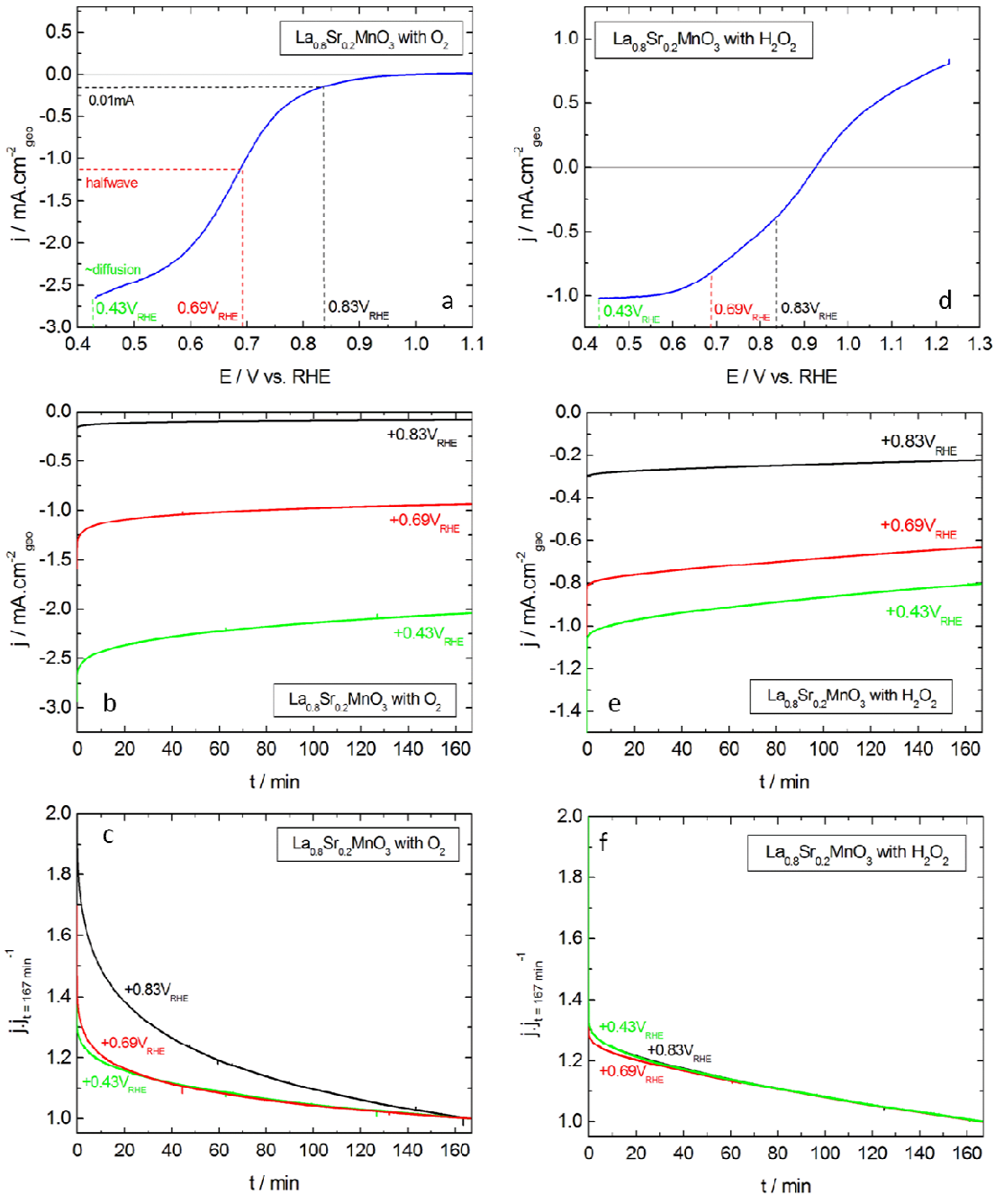

Figure 80 : *(a,d) Positive scans of RDE voltammograms at 10 mV.s^{-1}, (b,e) chronoamperometry at various potentials and (c,f) corresponding normalization by the last current value of GC-supported thin films of $La_{0.8}Sr_{0.2}MnO_3$ at 2500 rpm in (a,b,c) O_2-saturated 1M NaOH and (d,e,f) N_2- purged 1M NaOH + 0.84mM H_2O_2. Measurements were performed with 91 µg.cm$^{-2}{}_{geo}$ perovskite. Color codes for applied potential: +0.83 V vs. RHE (black), +0.69 V vs. RHE (red) and +0.43 V vs. RHE (green). Currents are normalized to the geometric area of the electrode.*

The discussion is started with the stability of $La_{0.8}Sr_{0.2}MnO_3$ versus the ORR. From chronoamperometries, it is observed that the ORR currents are strongly affected (Figure 80,b). The remaining current densities are -84 $\mu A.cm^{-2}_{geo}$, -940 $\mu A.cm^{-2}_{geo}$ and -2.0 $mA.cm^{-2}_{geo}$ at +0.83 V, +0.69 V and +0.43 V vs. RHE, respectively. In particular, it corresponds to a loss of ca. 45% in the kinetic region, significantly higher than the ca. 25% losses in mixed and diffusion regions (Figure 80,c). From the RDE voltammograms (Figure 81,a,b,c), it is observed that, regardless the applied potential during the chronoamperometries, the kinetic currents are indeed decreased. This suggests an irreversible modification of the active sites for O_2 activation followed by a decrease of the ORR kinetics.
After chronoamperometry at +0.43 V vs. RHE, the whole currents are decreased, and in particular at low potentials. The origin of this loss is not understood yet but may be due to a decrease in the active site number.

During the HO_2^- reduction, ca. 25% of the current is lost whatever the applied potential is (Figure 80,f). Then, the remaining current densities after 10,000 s chronoamperometry are -220 $\mu A.cm^{-2}_{geo}$, -630 $\mu A.cm^{-2}_{geo}$ and -800 $\mu A.cm^{-2}_{geo}$ at +0.83 V, +0.69 V and +0.43 V vs. RHE, respectively (Figure 80,e). Then, for all the applied potentials, the RDE voltammograms present a global decrease of the current densities and a positive shift of the mixed potential (Figure 81,d,e,f). This is not only due to the decrease of the HO_2^- concentration (ca. 4% loss) and may indicate, among others, a decrease of the HO_2^- oxidation reaction rate, the inverse reaction of the ORR.

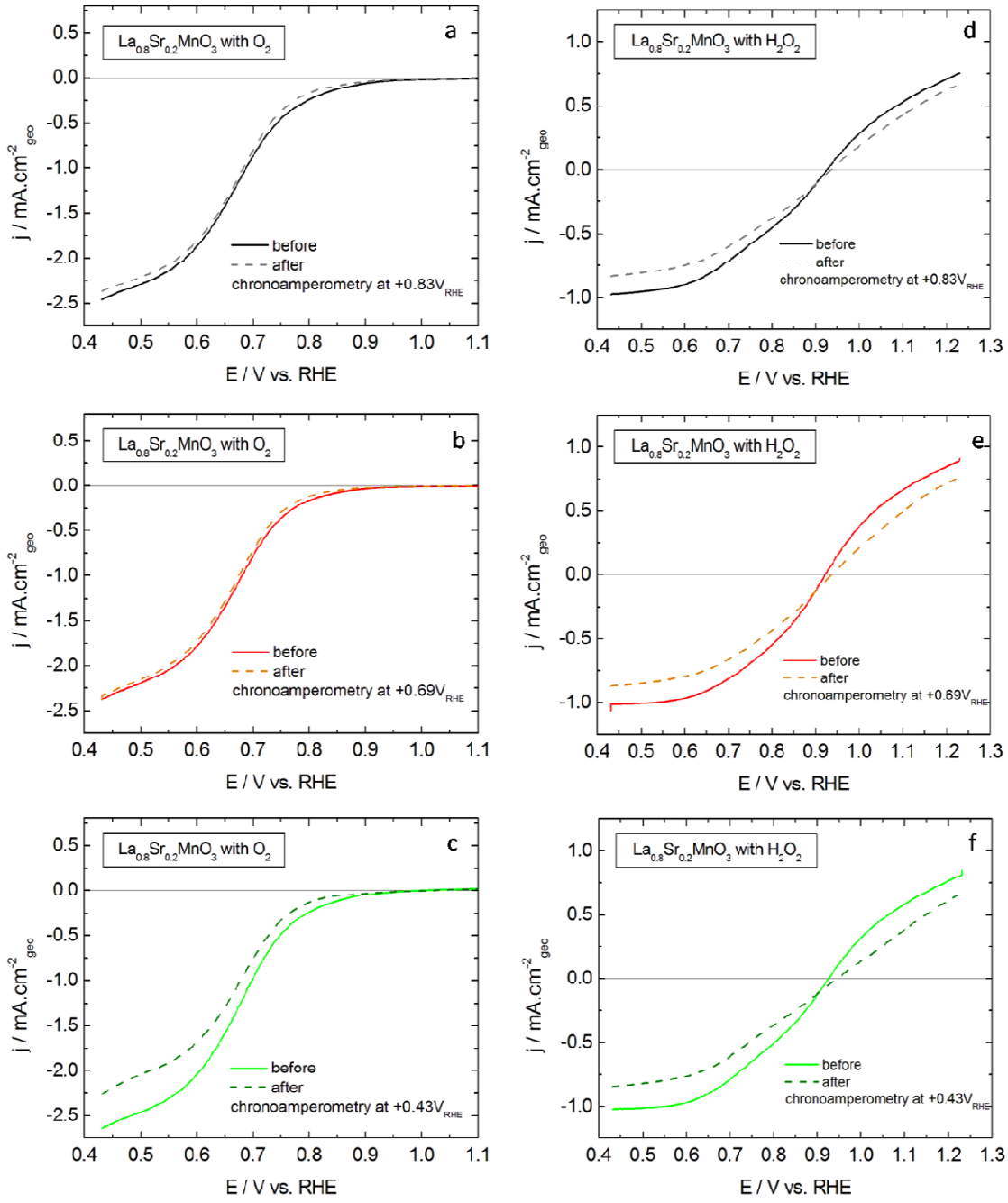

Figure 81 : *Positive scans of RDE voltammograms at 2500 rpm and 10 mV.s^{-1} of GC-supported thin films of $La_{0.8}Sr_{0.2}MnO_3$ in (a,b,c) O_2-saturated 1M NaOH and (d,e,f) N_2-purged 1M NaOH + 0.84mM H_2O_2 before and after chronoamperometry at various potentials* (Figure 80). *Measurements were performed with 91 µg.cm$^{-2}{}_{geo}$ perovskite. Color codes for applied potential: +0.83 V vs. RHE (before : black, after : dash grey), +0.69 V vs. RHE (before : red, after : dash orange) and +0.43 V vs. RHE (before : green, after : dash olive). Currents are normalized to the geometric area of the electrode and corrected to the background currents measured in the N_2 atmosphere in the absence of H_2O_2.*

In order to investigate the eventual modifications of the interfacial properties of $La_{0.8}Sr_{0.2}MnO_3$, CVs were performed before and after chronoamperometries in N_2-purged electrolyte (Figure 82).

For each applied potential, and after both ORR and HO_2^- reduction, the CVs are significantly affected with a strong decrease of the charge and less defined redox peaks. This supports the previous idea that the perovskite sites are degraded in the course of the O_2 and HO_2^- reactions. Moreover, the potential splitting between the anodic and the cathodic peaks increases, suggesting an increase of the ohmic drop in the catalytic layer. This may be caused by the formation of insulating phases on the surface during reactions. Also, the increase of the ohmic drop in the perovskite layer might partially explain the decrease of the electrocatalytic currents, strongly dependent on the electrical contact.

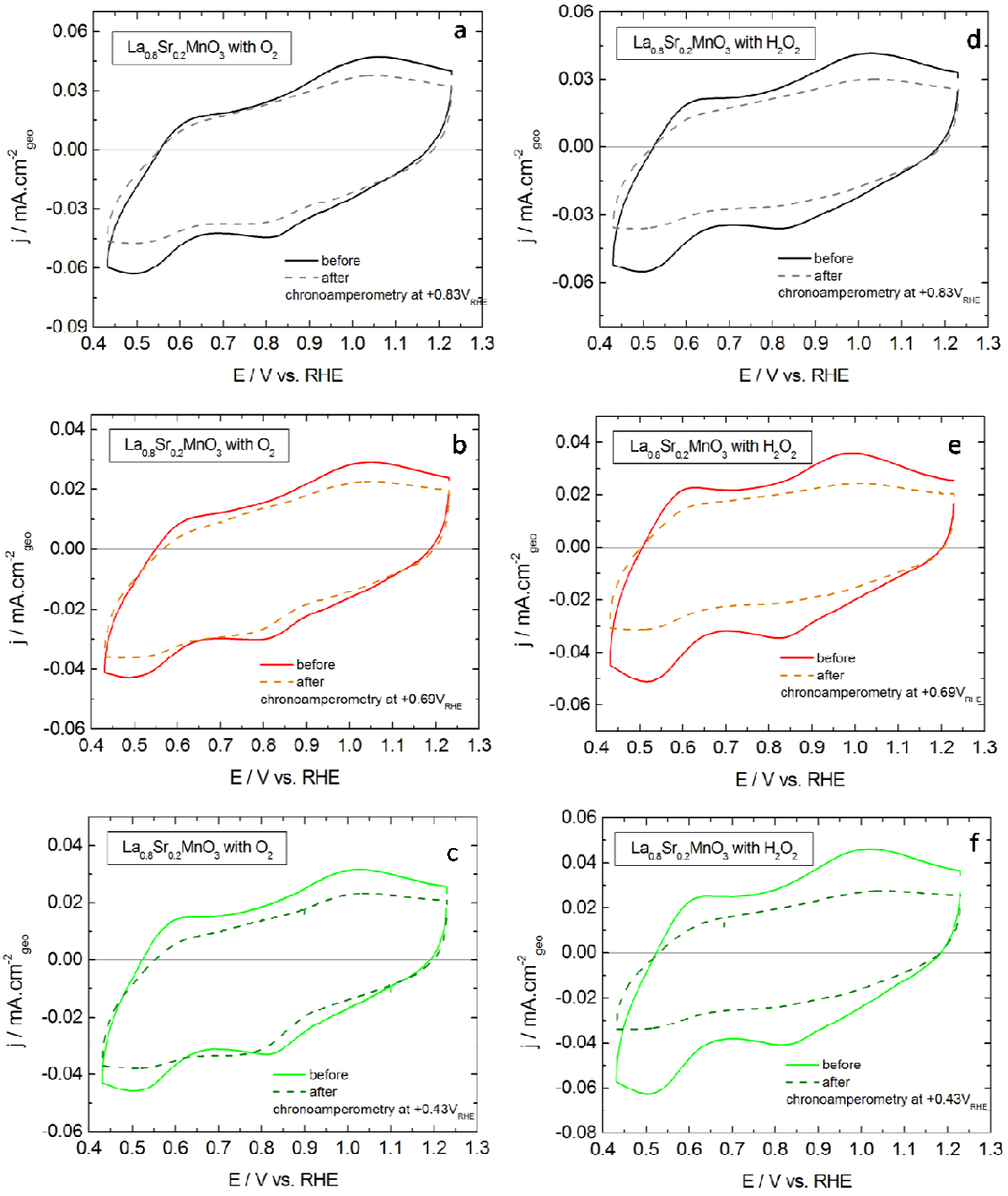

Figure 82 : *CV at 0 rpm and 10 mV.s^{-1} of GC-supported thin films of $La_{0.8}Sr_{0.2}MnO_3$ in N_2-purged 1M NaOH before and after chronoamperometry at various potentials in (a,b,c) O_2-saturated 1M NaOH and (d,e,f) N_2-saturated 1M NaOH + 0.84mM H_2O_2* (Figure 80). *Measurements were performed with 91 µg.cm$^{-2}_{geo}$ perovskite. Color codes for applied potential: +0.83 V vs. RHE (before : black, after : dash grey), +0.69 V vs. RHE (before : red, after : dash orange) and +0.43 V vs. RHE (before : green, after : dash olive). Currents are normalized to the geometric area of the electrode.*

6.3.1.2.2. With carbon in the catalytic layer

In order to study the effect of the electrical contact on the electrocatalytic stability and to better understand the modifications occurring in Mn-perovskites, carbon was added to the catalytic layer and the electrochemical and electrocatalytic stability of $La_{0.8}Sr_{0.2}MnO_3$ electrodes was investigated. Figure 83,a presents a typical RDE voltammogram of GC-supported thin film of 91 $\mu g.cm^{-2}_{geo}$ $La_{0.8}Sr_{0.2}MnO_3$ + 37 $\mu g.cm^{-2}_{geo}$ carbon in O_2-saturated 1M NaOH. The potentials of interest, i.e. in the kinetic region, in the mixed kinetic-diffusion region, and in the diffusion region are +0.9 V, +0.8 V and +0.43 V vs. RHE, respectively, and are indicated on the voltammogram in O_2-saturated electrolyte (Figure 83,a), as well as on the voltammogram in H_2O_2-containing electrolyte (Figure 83,d). The chronoamperometries at the mentioned potentials are shown in Figure 83,b for ORR and in Figure 83,e for HO_2^- reduction, and Figure 83,c,f presents these chronoamperometries after normalization by the current value at the end of the measurement at t=167 min. The RDE voltammograms and the CV in N_2-purged electrolyte obtained before and after each chronoamperometry are displayed in Figure 84 and in Figure 85, respectively.

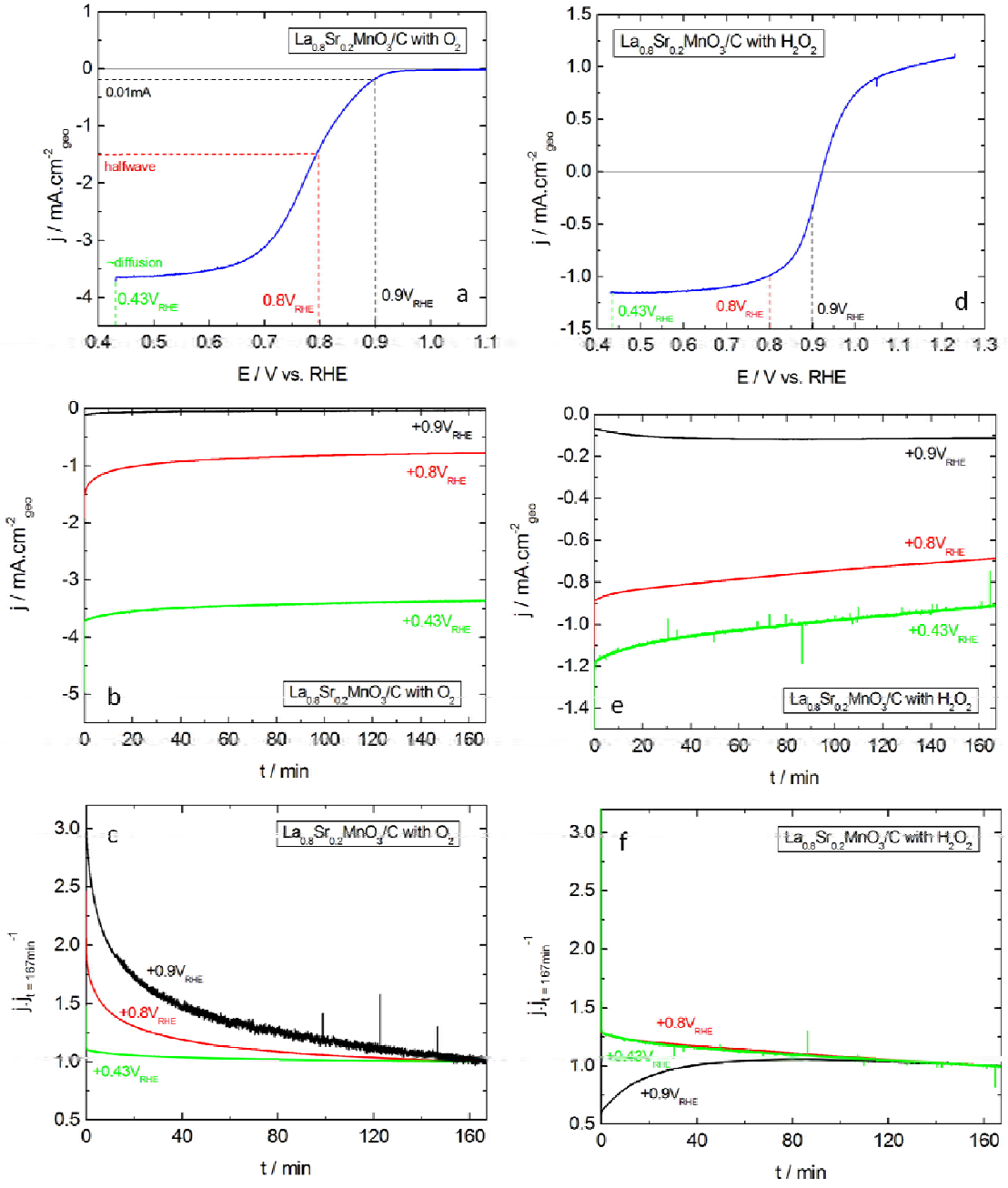

Figure 83 : *(a,d) Positive scans of RDE voltammograms at 10 mV.s^{-1}, (b,e) chronoamperometry at various potentials and (c,f) corresponding normalization by the last current value of GC-supported thin films of $La_{0.8}Sr_{0.2}MnO_3$ + Sibunit carbon at 2500 rpm in (a,b,c) O_2-saturated 1M NaOH and (d,e,f) N_2- purged 1M NaOH + 0.84mM H_2O_2. Measurements were performed with 91 µg.cm$^{-2}_{geo}$ perovskite + 37 µg.cm$^{-2}_{geo}$ Sibunit carbon. Color codes for applied potential: +0.9 V vs. RHE (black), +0.8 V vs. RHE (red) and +0.43 V vs. RHE (green). Currents are normalized to the geometric area of the electrode.*

From chronoamperometries in O_2-saturated electrolyte, it is noticed that the higher the applied potential, the stronger the current loss is (Figure 83,b,c). Indeed, ca. 70% of the current is lost after 10,000 s at +0.9 V vs. RHE. On the other hand, a decrease of only ca. 10% of the ORR current is observed for chronoamperometry at +0.43 V vs. RHE.

The RDE voltammograms confirm the current loss in the kinetic region (Figure 84,a,b,c), in agreement with stability tests on $La_{0.8}Sr_{0.2}MnO_3$ electrodes without carbon. Besides the negative shift of the onset potential, one can notice the modification of the voltammogram shape. This suggests a decrease of the participation of perovskite sites for the ORR in favour of carbon sites (see section 4.3.2). In other words, the number of perovskite sites is decreased, leading to a lower ORR current on perovskite, while the number of carbon sites, and thus the ORR current on carbon, remains the same and then becomes predominant. This also explains the onset potential shift observed in RDE voltammograms with various rotation rates (Figure 32): after each cycle (and a fortori each rotation), the onset potential is decreased due to the degradation of perovskite sites.

However, from the small current loss observed in the current transient at low potential (Figure 83,b,c) and from the slight decrease of the limiting plateau in RDE voltammograms (Figure 84,a,b,c), the number of electrons involved in the ORR does not seem to be affected. Indeed, the loss of current is consistent with the consumption of O_2 (ca. 8% for chronoamperometry at +0.43 V vs. RHE). Therefore, it means that, despite the possible degradation of the perovskite most active sites for the ORR, the intermediate HO_2^- – for example formed on carbon sites – is invariably reduced on perovskite sites. In fact, at low potentials, the HO_2^- reduction is quite fast on $La_{0.8}Sr_{0.2}MnO_3$ since it occurs in the diffusion limited regime, and therefore the decrease of the number of active sites may not affect the limiting current value.

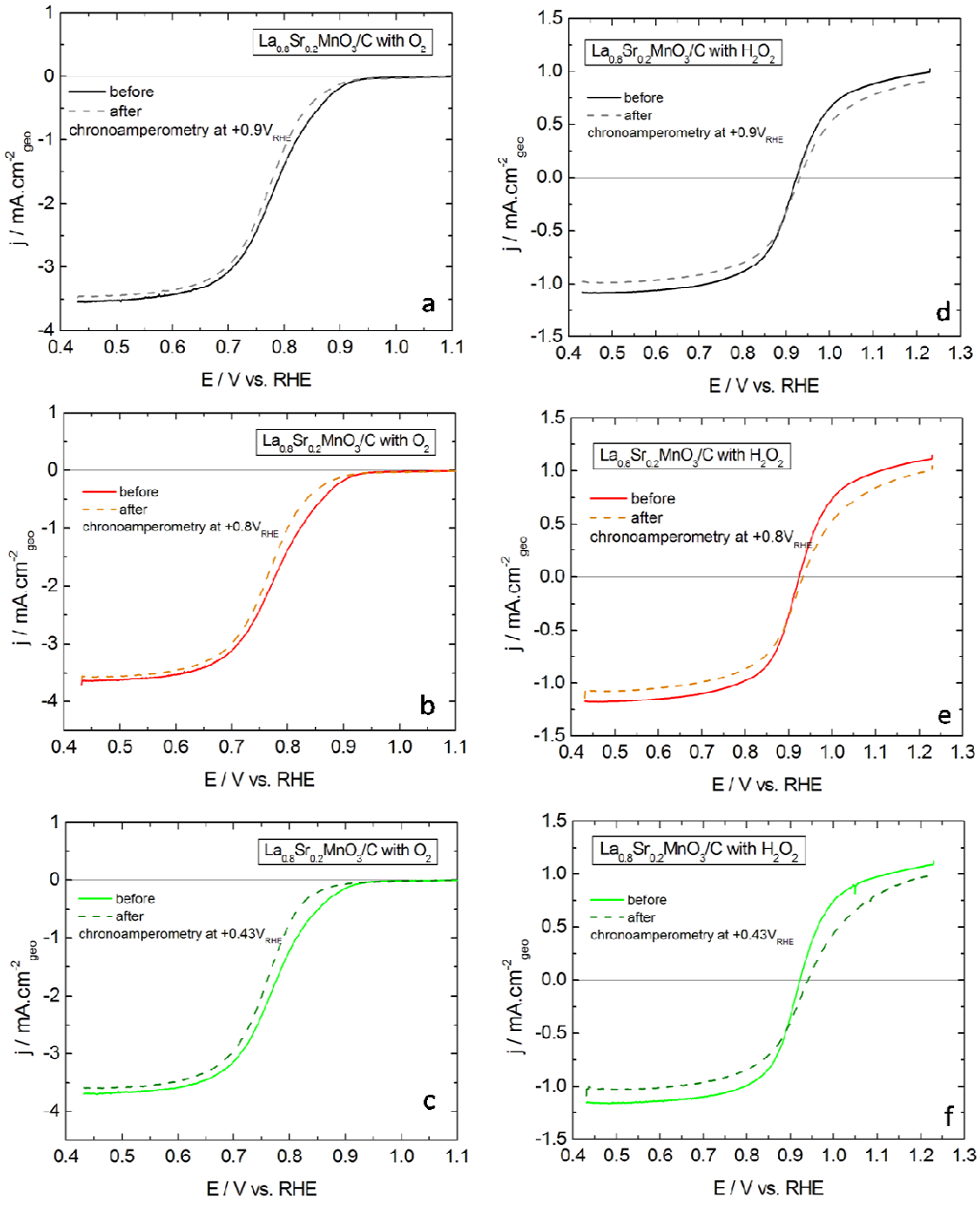

Figure 84 : *Positive scans of RDE voltammograms at 2500 rpm and 10 mV.s^{-1} of GC-supported thin films of $La_{0.8}Sr_{0.2}MnO_3$ + Sibunit carbon in (a,b,c) O_2-saturated 1M NaOH and (d,e,f) N_2-purged 1M NaOH + 0.84mM H_2O_2 before and after chronoamperometry at various potentials* (Figure 83). *Measurements were performed with 91 µg.cm$^{-2}_{geo}$ perovskite + 37 µg.cm$^{-2}_{geo}$ Sibunit carbon. Color codes for applied potential: +0.9 V vs. RHE (before : black, after : dash grey), +0.8V vs. RHE (before : red, after : dash orange) and +0.43 V vs. RHE (before : green, after : dash olive). Currents are normalized to the geometric area of the electrode and corrected to the background currents measured in the N_2 atmosphere in the absence of H_2O_2*

The discussion is now turned to the stability of perovskite oxides versus HO_2^- reduction. First of all, one can notice that the current at +0.9 V vs. RHE surprisingly increased with the time (Figure 83,e,f). As the applied potential is very close to the mixed potential of HO_2^- reactions (Figure 83,d), the current increase may be due to a positive shift of this mixed potential. At other applied potentials, the currents decrease with time, with a loss of ca. 25% (Figure 83,e,f).

On RDE voltammograms after chronoamperometry (Figure 84,d,e,f), the global current is decreased and the mixed potential is slightly shifted towards higher potentials, as suggested above. These two effects are partially the consequence of the decrease of the HO_2^- concentration (see sections 5.3.1.2 and 5.5). However, the chronoamperometry at +0.9 V vs. RHE shows that the shift of the mixed potential occurs rapidly, already in the first 10 min of the reaction and, considering the small overall current at +0.9 V, could hardly be solely due to the concentration change. This may suggest that the currents are also affected by a decrease of the HO_2^- oxidation rate due to a degradation of perovskite sites. Neverthess, the loss of the global current is less pronounced than for experiments without carbon thanks to the better electrical contact in the catalytic layer.

From the CVs after chronoamperometries in O_2 and H_2O_2 containing electrolytes (Figure 85), it is clear that $La_{0.8}Sr_{0.2}MnO_3$ irreversibly changes during these reactions. One may notice that the strongest current drop is observed in the potential range of the redox peaks, while the capacitance does not seem to decrease much. The latter allows one to discard loss of catalyst as a possible reason for the observed CV changes. Modification of the redox transitions of the perovskite and/or formation of electrochemically inactive phases seems more likely. The latter would explain the increase of the ohmic drop observed in electrodes without carbon. In both cases, this shows that the electrocatalytic activity is closely related to the redox behavior of the catalyst.

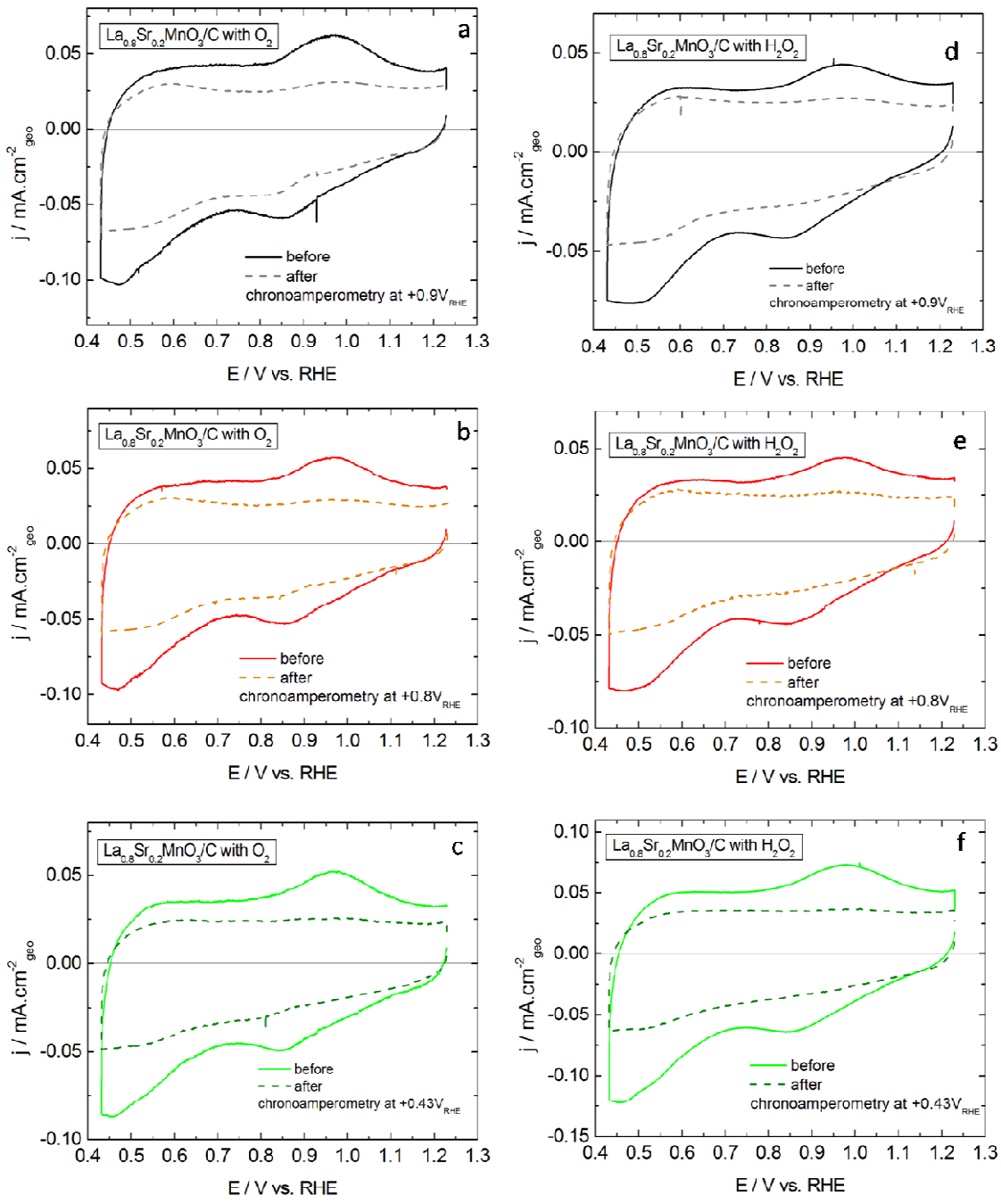

Figure 85 : *CV at 0 rpm and 10 mV.s^{-1} of GC-supported thin films of $La_{0.8}Sr_{0.2}MnO_3$ + Sibunit carbon in N_2-purged 1M NaOH before and after chronoamperometry at various potentials in (a,b,c) O_2-saturated 1M NaOH and (d,e,f) N_2-saturated 1M NaOH + 0.84mM H_2O_2* (Figure 83). *Measurements were performed with 91 µg.cm$^{-2}_{geo}$ perovskite + 37 µg.cm$^{-2}_{geo}$ Sibunit carbon. Color codes for applied potential: +0.9 V vs. RHE (before : black, after : dash grey), +0.8 V vs. RHE (before : red, after : dash orange) and +0.43 V vs. RHE (before : green, after : dash olive). Currents are normalized to the geometric area of the electrode.*

In order to discard the electrode polarization as the possible cause of the observed modifications, chronoamperometries were also performed in N_2-purged electrolyte, in absence of O_2 or H_2O_2, at the same potentials (+0.9 V, +0.8 V and +0.43 V vs. RHE) during 10,000 s. The CVs were measured before and after these chronoamperometries and are presented in Figure 86. The pseudocapacitance is slightly decreased but the redox peaks are still visible and the differences are clearly less evident than after ORR or HO_2^- reductions. Thus, it is justified to attribute the perovskite degradation to electrocatalytic reactions rather than to the electrode polarization alone. Dissolution of the Mn in low oxidation state reported in the literature for simple Mn oxides [200,206] seems unlikely since the CV modifications are not more pronounced after chronoamperometry at low potentials where Mn is reduced to Mn^{2+}.

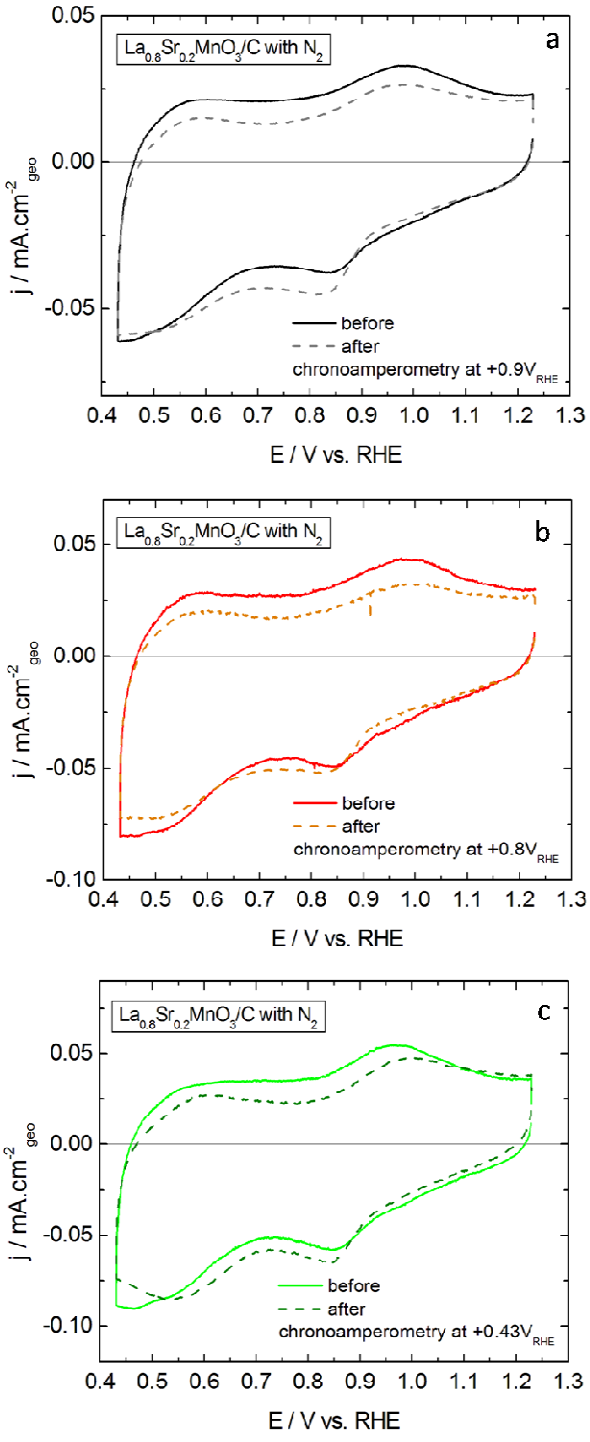

Figure 86 : *CV at 0 rpm and 10 mV.s^{-1} of GC-supported thin films of $La_{0.8}Sr_{0.2}MnO_3$ + Sibunit carbon in N_2-purged 1M NaOH before and after chronoamperometry at various potentials in N_2-purged 1M NaOH. Measurements were performed with 91 µg.cm$^{-2}{}_{geo}$ perovskite + 37 µg.cm$^{-2}{}_{geo}$ Sibunit carbon. Color codes for applied potential: +0.9 V vs. RHE (before : black, after : dash grey), +0.8 V vs. RHE (before : red, after : dash orange) and +0.43 V vs. RHE (before : green, after : dash olive). Currents are normalized to the geometric area of the electrode.*

Interestingly, instabilities versus ORR were also reported for MnO_x/C electrodes. Indeed, Wu et al. [40] performed accelerated aging tests by performing up to 2500 CV cycles in O_2-saturated 0.1M NaOH and observed (i) a negative shift of the ORR onset potential, (ii) a decrease of the absolute value of the limiting current and (iii) a decrease of the peak area of a CV in inerte atmosphere. With the support of XRD and XPS analysis before and after the accelerated aging tests, the authors attributed these modifications to a decrease of the number of ORR active sites with the formation of an inactive Mn_3O_4 phase. The formation of Mn_3O_4 on MnO_x electrodes during the ORR was also observed thanks to XPS and *in-situ* XANES studies in reference [190]. Moreover, TEM studies by Wu et al. [40] and Roche et al. [256] highlight a change in the morphology of MnO_x/C electrodes after the ORR, i.e. particle agglomeration and increase of the particle size which result in a lower accessible surface area. The increase of the particle size was confirmed by XRD [256]. In addition, the chemical analysis of the alkaline electrolyte where MnO_x/C electrodes were prematurely aged at 80°C in the presence of O_2 revealed a partial dissolution of the active material [256].
The similarity of the behavior of these simple oxides with the Mn-perovskites studied in this work show that the mentioned modifications probably occur on Mn-perovskites too. While the increase of particle size in unlikely regarding the large particle size of perovskites in this work and since a minor decrease of the double layer capacitance observed in CVs allows one to discard the dissolution of the active material, the formation of Mn_3O_4 phase seems to be a reasonable explanation of the electrocatalytic activity loss. Indeed, this phase is electrochemically irreversible, thus it can explain the loss of redox peaks in CVs. Characterisation of the perovskite after electrocatalysis will be performed in the following section to confirm or discard this hypothesis.

One should note that comparison of the activity degradation with literature data on perovskite oxides (see section 1.4.4) is hardly possible since the applied potential or current may be different. Indeed, it was shown in this section that disctint potentials (or currents) lead to completely different stability behaviors.

6.3.2. Catalyst properties after electrocatalysis

It was observed that the ORR and HO_2^- reduction electrocatalysis strongly affect the perovskite interfacial properties and electrocatalytic activites. To investigate in more detail the modifications occurring on perovskite electrodes, electrodes were analysed after electrocatalysis using XRD, SEM/EDX and XPS.

6.3.2.1. Electrocatalytic response

To allow material characterization, electrodes with more suitable geometries than a GC RDE were built using carbon paper, as described in section 2.5.4. The carbon paper covered with a layer of perovskite/carbon was attached to a gold wire which served as a current collector and CVs were performed in a N_2-purged electrolyte, O_2-saturated electrolyte or N_2-purged electrolyte containing H_2O_2.
HO_2^- reduction/oxidation and O_2 reduction currents are observed on carbon paper electrodes even in the absence of an oxide (Figure 87,a). However, currents in the presence of perovskite oxides are higher and occur at lower overpotentials (Figure 87,b,c).

The CVs were stable during at least 30 cycles. In particular, the kinetic currents of Mn-perovskites were not shifted towards lower potentials with the time, as it was observed for thin film RDE electrodes. This suggests that under the applied experimental conditions, degradation of perovskite is negligible.
To check it, CVs in N_2-purged electrolyte were measured after a CV in O_2-saturated electrolyte and are shown in Figure 88. The pseudocapacitance is slightly decreased but the redox peaks are still visible and the modifications are not as impressive as for the RDE (Figure 85). This may be partially due to the lower overall charge passing through the CP electrode. For one cycle, i.e. for 160 s (potential window of 1.6 V and sweep rate of 10 $mV.s^{-1}$), the maximal current measured on the CP electrode is 0.5 $mA.cm^2_{geo}$. Thus, the maximal charge involved in one cycle is: 0.5 $mA.cm^2_{geo}$ * 160 s = 80 $mC.cm^2_{geo}$. As the CP contains 180 $\mu g.cm^{-2}_{geo}$ perovskite, the charge passed per perovskite unit of the perovskite mass is 440 $C.g^{-1}_{perovskite}$. For RDE however, the maximal charge involved in one cycle of 160 s at the

lowest rotation rate (400 rpm) for an electrode containing 91 $\mu g.cm^{-2}_{geo}$ perovskite (+37 $\mu g.cm^{-2}_{geo}$ carbon) is ca. 1.5 $mA.cm^{2}_{geo}$ * 160 s = 240 $mC.cm^{2}_{geo}$, which corresponds to a charge per perovskite units of 2700 $C.g^{-1}_{perovskite}$. This is almost one order of magnitude higher than for CP electrodes thanks to the faster mass transport. For CP electrodes, electrolyte agitation could not be performed due to a fragile connection between the gold wire and the carbon paper. Also, the nature and the morpholohy of the carbon support are different in the two approaches and this certainly affects the electrical connection between the perovskite particles, and thus may affect the degradation of the electrode.

Unfortunately, this observation implies that the modifications occurring during the ORR and the HO_2^- reduction for RDE electrodes of Mn-perovskites will probably not be observable with carbon paper electrodes.

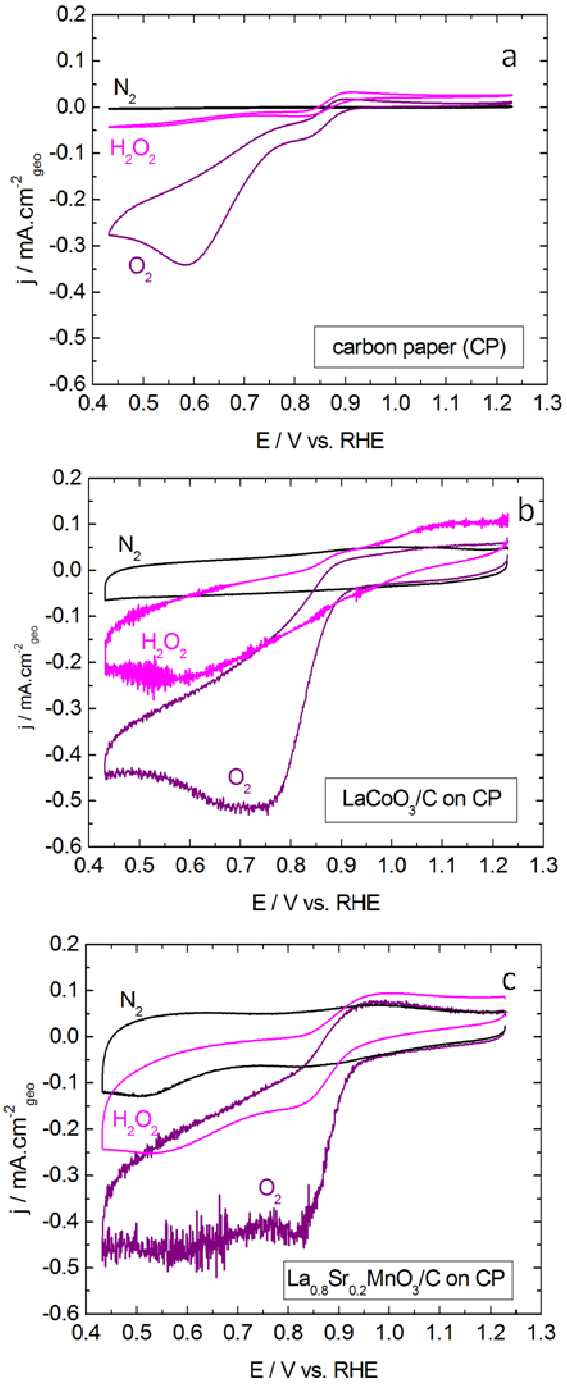

Figure 87 : *CV at 10 mV.s^{-1} of (a) carbon paper (CP) and CP-supported thin films of (b) $LaCoO_3$ + Sibunit carbon and (c) $La_{0.8}Sr_{0.2}MnO_3$ + Sibunit carbon in various electrolytes. Measurements were performed with 180 µg.cm$^{-2}{}_{geo}$ perovskite + 74 µg.cm$^{-2}{}_{geo}$ carbon. Color codes: N_2-purged 1M NaOH (black), N_2-purged 1M NaOH + 0.84M H_2O_2 (pink) and O_2-saturated 1M NaOH (purple). Currents are normalized to the geometric area of the electrode.*

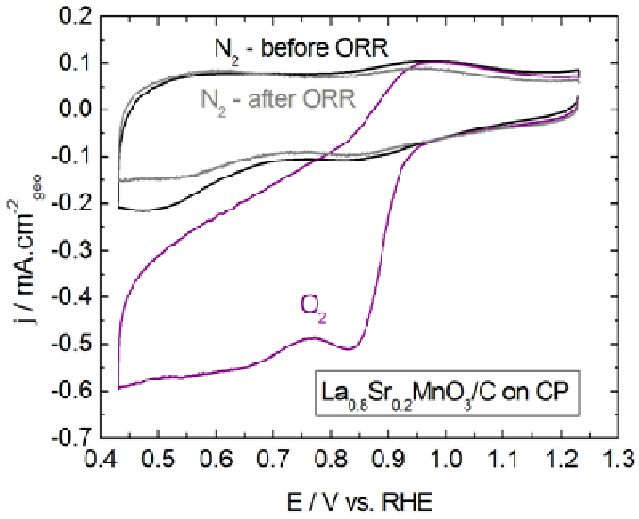

Figure 88 : *CV at 10 mV.s^{-1} of CP-supported thin films of $La_{0.8}Sr_{0.2}MnO_3$ + Sibunit carbon before, during and after ORR. Measurements were performed with 180 µg.cm$^{-2}_{geo}$ perovskite + 74 µg.cm$^{-2}_{geo}$ carbon. Color codes: N_2-purged 1M NaOH, initial scan (black), O_2-saturated 1M NaOH (purple) and N_2-purged 1M NaOH, scan after ORR (grey). Currents are normalized to the geometric area of the electrode.*

6.3.2.2. Structure of the bulk after electrocatalysis

First of all, the crystalline structure of perovskites supported on carbon paper electrodes was investigated using XRD after polarization (CV in N_2-purged 1M NaOH), HO_2^- reduction/oxidation (CV in N_2-purged 1M NaOH + 0.84 mM H_2O_2) and ORR (CV in O_2-saturated 1M NaOH), and compared to electrodes without treatment and after an alkaline treatment (storage in 1M NaOH during 3h), and to pristine perovskite powder. These comparisons allow one to separate the effects due to electrocatalysis from those due to the polarization alone – which may change the perovskite into hydroxide species [141] - and those due to contact with an alkaline solution (see also section 6.2.3.2).
The obtained XRD patterns are displayed in Figure 89,a for $LaCoO_3$ and in Figure 89,b for $La_{0.8}Sr_{0.2}MnO_3$.

First of all, it is noticed that the peaks attributed to the perovskite structure are visible for all samples, whatever the treatment was, showing that the perovskite phase is still present after electrochemistry.

Compared to the initial $LaCoO_3$ powder, the XRD pattern of perovskite/carbon layer on carbon paper shows additional peaks and a shoulder at ca. 26°, 43° and 54°. They are attributed to the carbon paper support which displays similar XRD peaks, as shown in Figure 89.

No additional peaks were visible after the chemical treatment in NaOH electrolyte, electrode polarization or HO_2^- reduction/oxidation. However, the ORR leads to the appearance of new XRD peaks, e.g. at 32.3°, 34.3°, 35.2°, 38.0° and 39.0°, for both $LaCoO_3$ and $La_{0.8}Sr_{0.2}MnO_3$ electrodes. Interestingly, these peaks also appear on the carbon paper alone after the ORR. This shows that the new phases arise from a modification of the carbon paper support with O_2 rather than a modification of the perovskite itself. The nature of these new phases is not identified yet, but some peaks may be attributed to sodium carbonate species, as shown in Figure 89 by comparison with commercial Na_2CO_3 (>99.5%, SDS). The high amount of this species on the carbon paper after the ORR is likely to be due to the increased wettability of carbon paper after the ORR [209]. Indeed, one can guess that the NaOH electrolyte easily enters into the pores of the hydrophilic carbon paper. Then, the drying of the alkaline electrolyte present in the electrode results in the formation of sodium carbonate species.

However, no traces of $La(OH)_3$ or $Co(OH)_3$ eventually formed upon contact with the alkaline solution (see section 6.2.3) could be distinguished for $LaCoO_3$, and no XRD peaks of Mn_3O_4 could be observed for $La_{0.8}Sr_{0.2}MnO_3$. This suggests that these species, if formed, are only present on the perovskite surface.

As shown in section 3.2.1.2, XRD data also allow an estimation of the crystallite size thanks to Scherrer equation. Before and after the electrochemical treatment, the crystallite sizes were ca. 30 nm for $LaCoO_3$ and ca. 20 nm for $La_{0.8}Sr_{0.2}MnO_3$. Thus, the perovskite particle size does not seem to be affected by the ORR electrocatalysis, contrary to Pt [255] or MnOx (40)(256) [40,256]. This is likely to be due to the large crystallite size of the perovskite oxides.

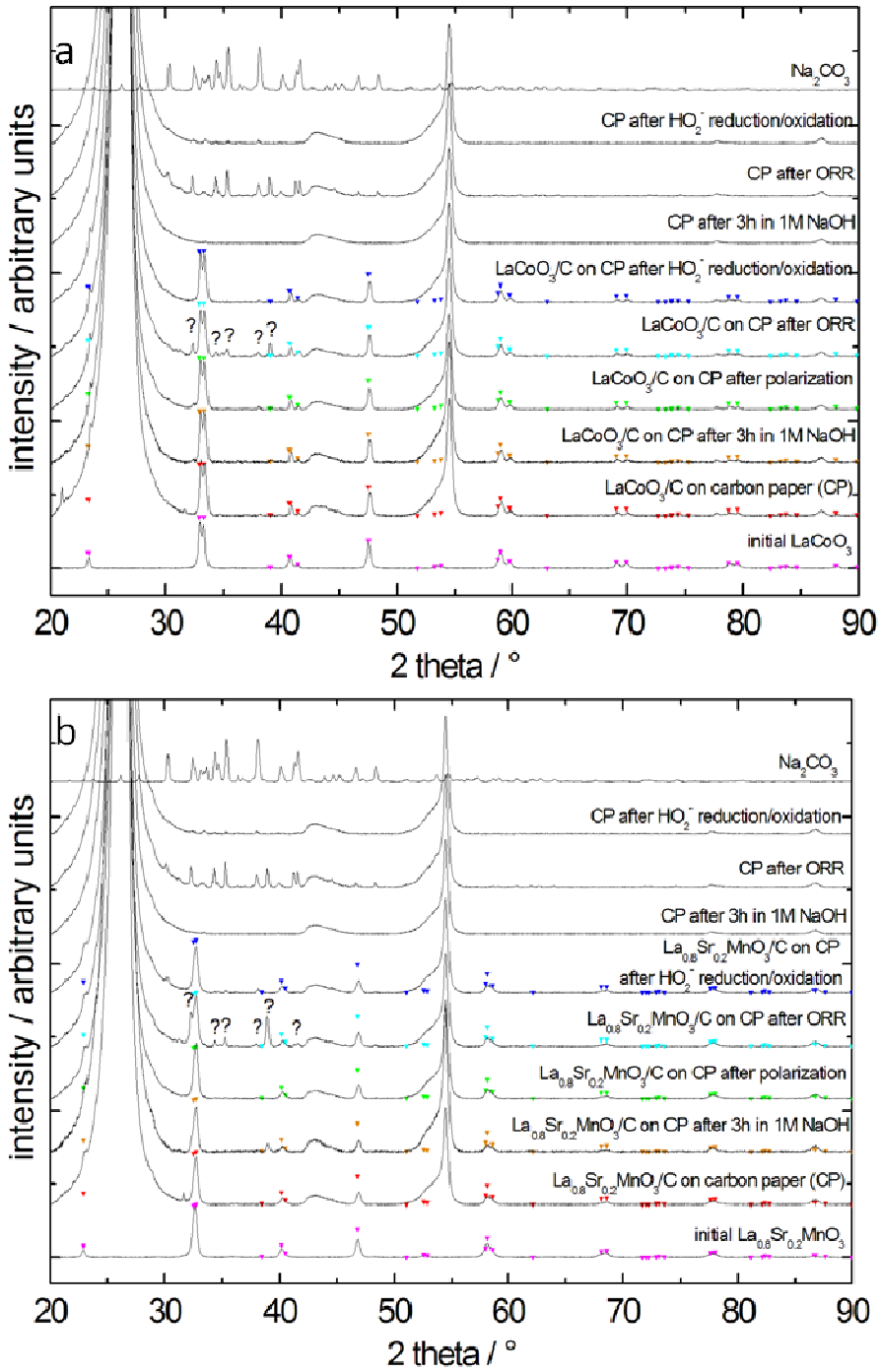

Figure 89 : *X-Ray diffraction pattern (step size = 0.0223°, time step = 8s) of CP-supported thin films of (a) $LaCoO_3$ + Sibunit carbon and (b) $La_{0.8}Sr_{0.2}MnO_3$ + Sibunit carbon before and after chemical and electrochemical treatments. The symbols indicate the ICDD reference card of (a) LaCoO3 – 01-084-0848, (b) $La_{0.7}Sr_{0.3}MnO_3$ 01-089-4461. Measurements were performed with 180 $\mu g.cm^{-2}_{geo}$ perovskite + 74 $\mu g.cm^{-2}_{geo}$ Sibunit carbon. X-Ray diffraction patterns of carbon paper after chemical and electrochemical treatments as well as commercial Na_2CO_3 (>99.5%, SDS) are given as comparison. The diffraction patterns were corrected from background signal.*

6.3.2.3. Electrode morphology after electrocatalysis

In order to complement XRD results and verify whether the perovskite particle morphology is indeed not affected by the ORR electrocatalysis, SEM analysis coupled with EDX was applied to carbon paper supported perovskite electrodes before and after the ORR. EDX was used to identify the elemental composition. Typical SEM images are shown in Figure 90 for $LaCoO_3$. Similar observations were made for Mn-perovskites (not shown).

First of all, EDX analysis (not shown) confirmed the presence of perovskite components (La, Sr, Co, Mn, depending on the perovskite) on the carbon paper electrodes before and after various treatments. The dispersion of the particles of perovskite and Sibunit carbon on the fibers of the carbon papers is similar before and after electrocatalysis (Figure 90,a,d). In particular, the particle agglomeration is not more pronounced after the ORR than initially (Figure 90,b,e) and no significant morphological change due to carbon corrosion in alkaline media [209] could be dinstinguished. SEM images at high magnification (Figure 90,c,f) show that, in agreement with the XRD data, the size of perovskite particles does not increase after electrocatalysis. Thus, the electrochemical instabilities observed in section 6.3.1 cannot be explained by a morphological change of the perovskite oxides.

Thanks to the EDX, the large component observed in Figure 90,e was identified as being mainly composed of Na. Other morphologies of Na components were observed, such as needles (not shown). EDX method does not allow an exact identification of these phases, but, from XRD analysis, one may invoke formation of sodium carbonate and probably some NaOH deposits.

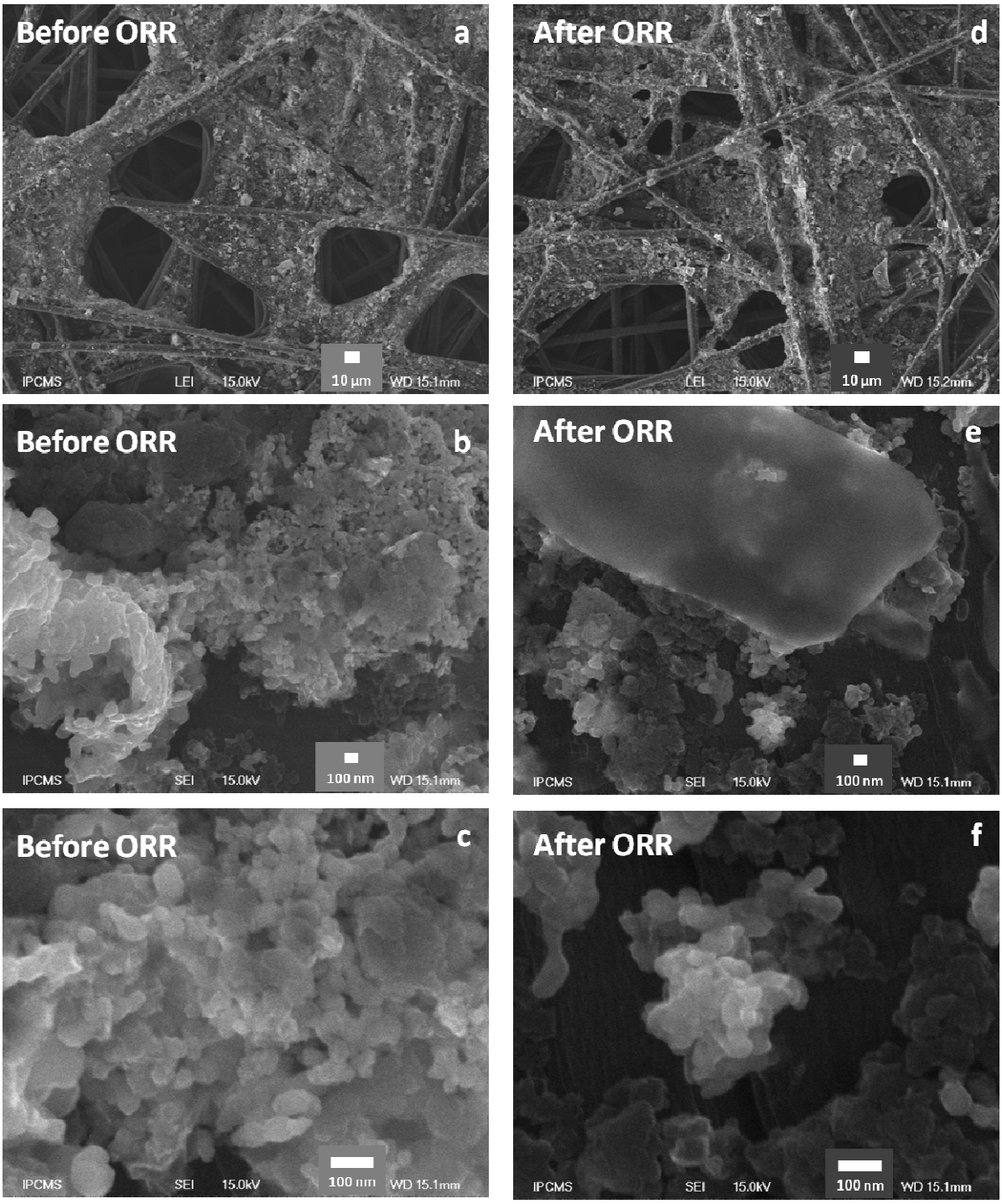

Figure 90 : *SEM image (a,d : LEI, b,c,e,f : SEI) of CP-supported thin films of $LaCoO_3$ + Sibunit carbon before (a,b,c) and after (d,e,f) ORR. Measurements were performed with 180 $\mu g.cm^{-2}_{geo}$ perovskite + 74 $\mu g.cm^{-2}_{geo}$ Sibunit carbon.*

6.3.2.4. Surface composition after electrocatalysis

XRD analysis showed that the bulk structure of perovskite oxides is stable after electrochemical treatments (see section 6.3.2.2). However, this does not mean that no changes occur on the perovskite surface. To check eventual surface modifications, XPS was applied on carbon paper electrodes after electrochemical treatments and anlayzed in the following sections.

6.3.2.4.1. $LaCoO_3$

XPS spectra of carbon-supported thin layers of $LaCoO_3$/carbon are presented in Figure 91. The corresponding peak binding energies and atomic ratios are reported in Table 23.The electrochemical treatment of $LaCoO_3$/C electrodes leads to a shift toward higher binding energies of La3d spectra (Figure 91,a and Table 23) probably due to an increased amount of lanthanum hydroxides or carbonates. Besides, the Co2p spectrum (Figure 91,b) is not affected by electrochemical treatments. In particular, no evidences of cobalt hydroxide formation upon contact with the alkaline solution could be observed neither after soaking in 1M NaOH nor after electrochemical treatments. This is probably due to too the short duration of the experiment. Regarding the very small fraction of La3d and Co2p compared to other components, the atomic La:Co ratio cannot be precisely determined.

Among all the electrode treatments, only the ORR has an effect on the C1s spectrum (Figure 91,c). Indeed, the intensity of the peak corresponding to C=O bonds is significantly increased after the ORR. The relative amount of carbonate species also seems to be higher after the ORR than after the other treatments.

The O1s spectrum (Figure 91,d) of the pristine electrode shows a strong peak of adsorbed water, related to water from the aqueous suspension. After chemical and electrochemical treatment of the electrodes, new peaks appear at high binding energies (ca. 536 eV). By comparing the O1 spectra of the carbon paper electrodes to the commercial Na_2CO_3 (Figure 91,d), these peaks were identified as being Na Auger peaks. Indeed, high amount of Na is present on the electrode surface according to the atomic ratio of Na1s, and especially after the ORR (Table 23). O1s spectra also show that a high relative amount of hydroxide and carbonate species covered the perovskite surface (Figure 91,d). Regarding the atomic ratios of the various surface components (Table 23), the major surface species are sodium carbonates

rather than lanthanum hydroxides or carbonates. In agreement with XRD and SEM/EDX results, the concentration of sodium carbonates is increased after the ORR, likely due to the wettability of the carbon paper, as mentioned previously (see section 6.3.2.2).

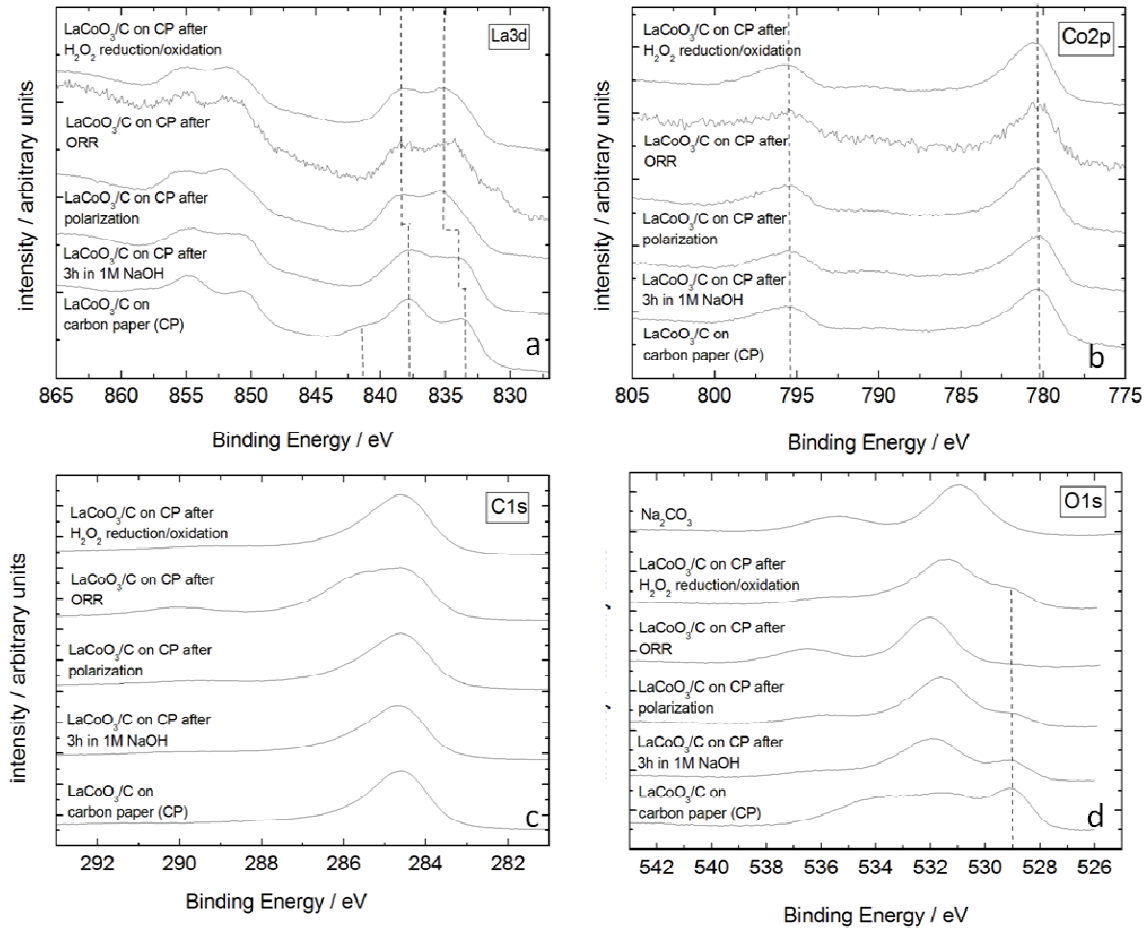

Figure 91 : *XPS spectra of (a) La3d, (b) Co2p, (c) C1s and (d) O1s of $LaCoO_3$ before and after chemical and electrochemical treatments. Measurements were performed with 180 $\mu g.cm^{-2}_{geo}$ perovskite + 74 $\mu g.cm^{-2}_{geo}$ Sibunit carbon. O1s XPS spectrum of commercial Na_2CO_3 (>99.5%, SDS) is given as comparison. Lines are guides for the eye and indicate the experimental positions.*

Table 23 : *Binding energies (in eV) of XPS peaks and atomic ratios (in brackets) for $LaCoO_3$ before and after chemical and electrochemical treatments*

$LaCoO_3$/C on CP	$La3d_{5/2}$	$Co2p_{3/2}$	C1s			O1s			Na1s
			Adventious carbon	C=O	Carbonate	O lattice	Carbonate and hydroxide	Adsorbed water or Na Auger	
Without treatment	833.5 837.8 841.3 (4%)	795.5 (2%)	284.6 (57%)	286.1 (10%)	287.8 (4%)	529.0 (6%)	531.1 (6%)	533.6 (11%)	-
After 3h in 1M NaOH	834.0 837.8 (2%)	795.5 (1%)	284.6 (46%)	286.1 (19%)	289.3 (7%)	529.0 (3%)	531.9 (15%)	536.0 (2%)	1072.1 (5%)
After polarization	833.5 835.2 838.4 (2%)	795.5 (1%)	284.6 (42%)	285.9 (21%)	289.5 (7%)	529.0 (1%)	531.6 (16%)	535.8 (3%)	1072.0 (6%)
After ORR	834.3 838.4 (0.4%)	795.5 (0.3%)	284.6 (22%)	285.9 (32%)	289.9 (8%)	529.0 (0.2%)	532.1 (18%)	536.4 (7%)	1072.2 (13%)
After HO_2^- reduction / oxidation	833.5 835.2 838.4 (2%)	795.5 (2%)	284.6 (47%)	286.1 (11%)	289.0 (9%)	529.0 (2%)	531.4 (19%)	535.6 (2%)	1072.0 (6%)

6.3.2.4.2. $LaMnO_3$

For $LaMnO_3$, La3d and Mn2p spectra are similar before and after electrochemical experiments (Figure 92,a,b and Table 24). This proves that La and Mn are not significantly modified by the ORR and HO_2^- reduction/oxidation electrocatalysis.

After the ORR, the peak corresponding to C=O is significantly increased in the C1 spectrum of CP-supported $LaMnO_3$ (Figure 92,c and Table 24), as for CP-supported $LaCoO_3$. In addition, an increase of the relative amount of hydroxide and carbonate species is visible after the ORR in O1s and C1s spectra (Figure 92,c,d). Regarding the high amount of Na (Table 24), it is clear that species such as NaOH or Na_2CO_3 are covering the perovskite surface after the ORR electrocatalysis, resulting in a very low relative amount of O from the perovskite lattice (Figure 92,d and Table 24), as well as La and Mn (Table 24). The same effect – formation of sodium carbonates and hydroxides on perovskite surface - was also observed but to a lesser extent after the HO_2^- reduction/oxidation and an alkaline treatment, compared to electrodes without any treatment (Figure 92,d and Table 24).

The origin of the negative shift of the peak lattice oxygen in the O1s spectra (Figure 92,d and Table 24) after electrochemical treatment is not understood yet, but it cannot be related to oxygen vacancies formation since they are not stable in $LaMnO_3$ (oxygen excess is more likely).

In summary, besides the formation of sodium species, no clear evidence of perovskite surface modifications could be observed after electrocatalysis.

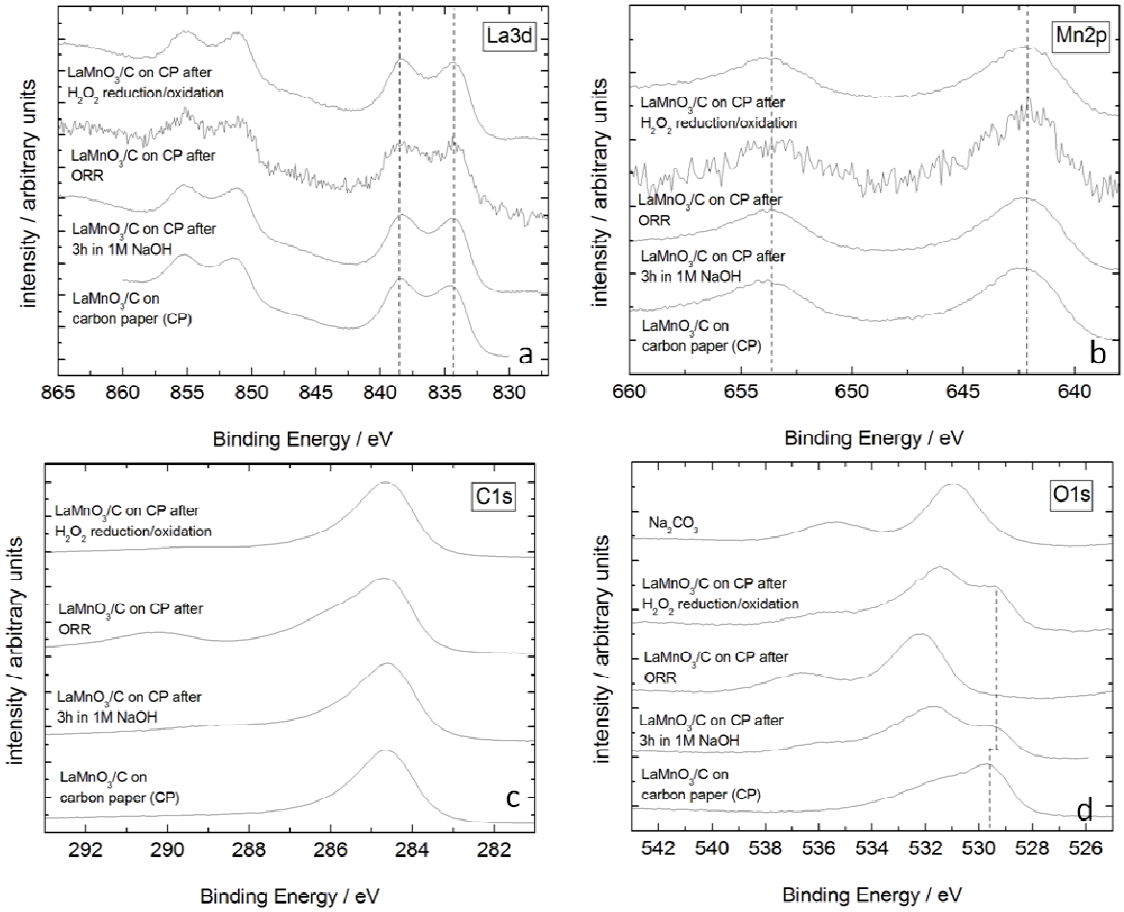

Figure 92 : *XPS spectra of (a) La3d, (b) Mn2p, (c) C1s and (d) O1s of $LaMnO_3$ before and after chemical and electrochemical treatments. Measurements were performed with 180 $\mu g.cm^{-2}_{geo}$ perovskite + 74 $\mu g.cm^{-2}_{geo}$ Sibunit carbon. O1s XPS spectrum of commercial Na_2CO_3 (>99.5%, SDS) is given as comparison. Lines are guides for the eye and indicate the experimental positions.*

Table 24 : *Binding energies (in eV) of XPS peaks and atomic ratios (in brackets) for $LaMnO_3$ before and after chemical and electrochemical treatments*

$LaMnO_3$/C on CP	La3d$_{5/2}$	Mn2p$_{3/2}$	C1s			O1s			Na1s
			Adventious carbon	C=O	Carbonate	O lattice	Carbonate and hydroxide	Adsorbed water or Na Auger	
Without treatment	834.3 838.5 (4%)	642.1 (3%)	284.6 (45%)	285.6 (23%)	288.0 (7%)	529.6 (8%)	531.4 (6%)	533.0 (4%)	-
After 3h in 1M NaOH	834.3 838.5 (2%)	642.1 (1%)	284.6 (40%)	285.9 (18%)	288.3 (14%)	529.3 (2%)	531.7 (14%)	535.7 (3%)	1072.1 (5%)
After ORR	834.3 838.5 (0.3%)	642.1 (0.2%)	284.6 (23%)	286.0 (21%)	290.2 (9%)	529.3 (0.3%)	532.2 (21%)	536.4 (9%)	1072.3 (16%)
After HO_2^- reduction / oxidation	834.3 838.5 (2%)	642.1 (2%)	284.6 (46%)	286.0 (20%)	289.5 (6%)	529.3 (3%)	531.4 (14%)	535.6 (3%)	1072.1 (6%)

6.3.2.4.3. $La_{0.8}Sr_{0.2}MnO_3$

The XPS results for $La_{0.8}Sr_{0.2}MnO_3$ are very similar to those of $LaMnO_3$. Indeed, (i) La3d, Mn2p, Sr3d are not affected by electrocatalysis (Figure 93, Table 25), (ii) the ratio of hydroxides and carbonates are increased after soaking in NaOH, electrode polarizarion and HO_2^- reduction/oxidation, and even more increased after the ORR, leading to a small fraction of O lattice in the O1s spectrum (Figure 93, Table 25), (iii) Na is present in high amount in the treated samples, and in particular after the ORR (Table 25). This shows that, after treatment and especially after the ORR, $La_{0.8}Sr_{0.2}MnO_3$ is covered by a layer of sodium hydroxide and carbonate species, probably due to the increase wettability of the carbon paper support. Also, as for $LaMnO_3$, a shift of the lattice oxygen towards lower binding energies is observed, but its cause could not be identified.

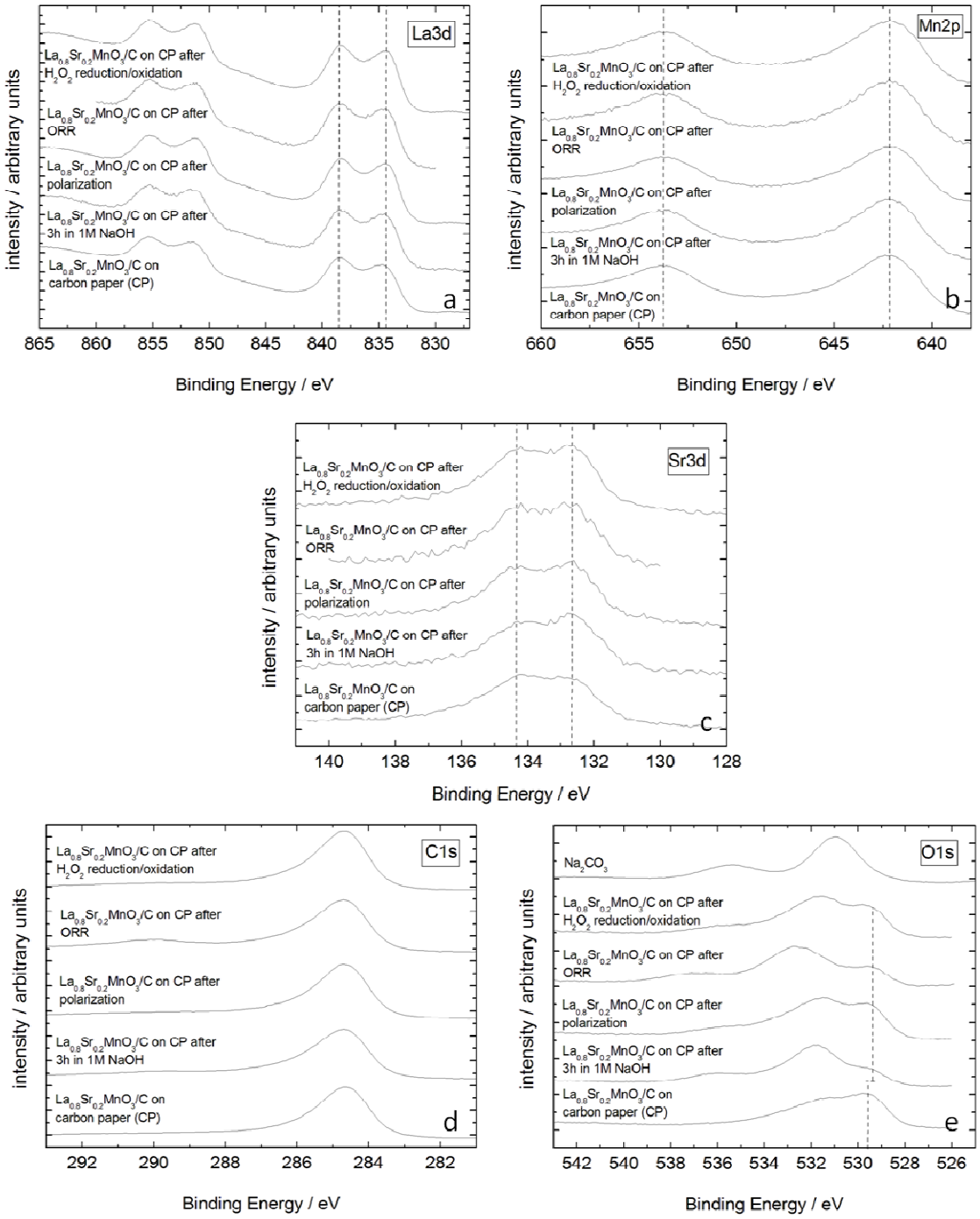

Figure 93 : *XPS spectra of (a) La3d, (b) Mn2p, (c) Sr3d, (d) C1s and (e) O1s of $La_{0.8}Sr_{0.2}MnO_3$ before and after chemical and electrochemical treatments. Measurements were performed with 180 $\mu g.cm^{-2}_{geo}$ perovskite + 74 $\mu g.cm^{-2}_{geo}$ Sibunit carbon. O1s XPS spectrum of commercial Na_2CO_3 (>99.5%, SDS) is given as comparison. Lines are guides for the eye and indicate the experimental positions.*

Table 25 : *Binding energies (in eV) of XPS peaks and atomic ratios (in brackets) for $La_{0.8}Sr_{0.2}MnO_3$ before and after chemical and electrochemical treatments*

$La_{0.8}Sr_{0.2}MnO_3$ /C on CP	$La3d_{5/2}$	$Sr3d_{5/2}$	$Mn2p_{3/2}$	C1s			O1s			Na1s
				Adventious carbon	C=O	Carbonate	O lattice	Carbonate and hydroxide	Adsorbed water or Na Auger	
Without treatment	834.3 838.5 (2%)	132.6 (2%)	642.3 (2%)	284.6 (46%)	285.7 (26%)	289.6 (6%)	529.5 (5%)	531.2 (5%)	533.0 (4%)	-
After 3h in 1M NaOH	834.3 838.5 (1%)	132.6 (1%)	642.3 (1%)	284.6 (43%)	286.2 (21%)	289.6 (6%)	529.4 (2%)	531.8 (14%)	535.9 (3%)	1072.1 (7%)
After polarization	834.3 838.5 (2%)	132.6 (1%)	642.3 (2%)	284.6 (43%)	285.9 (22%)	289.5 (5%)	529.4 (3%)	531.5 (13%)	535.2 (3%)	1071.1 (6%)
After ORR	834.3 838.5 (2%)	132.6 (1%)	642.3 (2%)	284.6 (30%)	286.1 (22%)	290.4 (7%)	529.4 (3%)	532.5 (20%)	537.2 (3%)	1072.8 (11%)
After HO_2^- reduction / oxidation	834.3 838.5 (2%)	132.6 (1%)	642.3 (2%)	284.6 (47%)	285.9 (22%)	289.4 (2%)	529.4 (4%)	531.6 (12%)	535.2 (3%)	1072.1 (6%)

In conclusion, no clear evidence of perovskite surface modifications which could explain the irreversible changes of the perovskite interfacial properties and the decrease of ORR activity observed with RDE for Mn perovskites (see section 6.3.1.2) could be distinguised with XPS. Several reasons could be proposed to explain this result. First of all, XPS might not be an adequate method to observe the occurring modifications. Indeed, different oxidation states of Mn and Co are hardly discernable with this method and therefore the perovskite modification might not be visible. Secondly, the XPS analysis was performed several minutes after the electrochemical treatment, after the transfer of the sample from an electrochemical cell into the XPS spectrometer under ambient condition. Then, modification of the surface could happen between the electrocatalytic test and the material characterization. *In-situ* measurements would be more suitable to investigate electrode surface changes with electrocatalysis but were not available for the present work. Finally, as mentionned in section 6.3.2.1, the ORR activity and the interfacial properties of Mn perovskites on carbon paper were not modified to the same extent as for the RDE. Therefore future measurements should be performed with electrodes showing similar ORR currents and electrode morphology to RDE to expect the same behavior, and thus, the same modifications.

6.4. Conclusion of Chapter 6

In this section, it was shown that the lanthanum carbonate species formed on perovskite surface during storage under ambient conditions can be partially removed by thermal treatment and are probably destroyed during sonication in aqueous suspension. It was also observed that $LaCoO_3$ is very sensitive to its chemical environment. Indeed, the extended immersion of this perovskite in ultrapure water leads to the formation of cobalt hydroxide layer which affects the CV response of the electrode. Also, the long immersion of $LaCoO_3$ in alkaline solution causes the transformation of the perovskite surface to cobalt and lanthanum hydroxide species. The surface of Mn-perovskites is more stable, no significant modifications of Mn being visible by XPS after the immersion in alkaline medium. Only a slight dissolution of Sr species could be detected by ICP for $La_{0.8}Sr_{0.2}MnO_3$ but does not affect the bulk which preserves its perovskite structure for all the studied samples after one month exposure in 1M NaOH.

The study of the stability of the electrocatalytic activity showed that the ORR electrocatalysis leads to a decrease of the number of perovskite sites. This probably occurs through the formation of an electrochemically inactive phase on the perovskite surface. This does not affect the ORR kinetic currents on $LaCoO_3$/C electrodes since the ORR predominatly occurs on carbon sites in these electrodes, but only decreases their HO_2^- reduction activity. On the other hand, the ORR activity of $La_{0.8}Sr_{0.2}MnO_3$/C electrodes is strongly reduced with the decrease of the active site number, the remaining kinetic current being largely ensured by carbon sites. The relationship observed between the decrease of the activity and the disappearance of the redox peaks in the CV in N_2 points out to the role of the redox transitions in electrocatalysis. Nevertheless, the high activity of $La_{0.8}Sr_{0.2}MnO_3$ for the HO_2^- reduction ensures a 4 global electron pathway even with a lower number of active sites. For both studied perovskites, it was observed that the ohmic drop caused by the formation of the insulating layer on the perovskite surface may be minimized with addition of carbon in the catalytic layer.

However, the XPS analysis did not detect changes of the Co and Mn cations on the perovskite surface after electrocatalysis. Moreover, no significant modifications of the bulk structure and electrode morphology were observed. Only the formation of sodium carbonates from carbon support hydrophilization is visible after the ORR. Nevertheless, the method used for the

electrode characterization has its limitations and might not be suitable to observe possible degradations which lead to the ORR activity loss.

General conclusion and Outlook

The aim of the present thesis was to check if the perovskite oxides are suitable ORR catalysts for SAFC applications in terms of activity and stability, and to clarify the ORR mechanism on these oxides.

In order to pursue these objectives, the thin layer approach was used and the experiments were performed in liquid electrolyte to allow a control of the mass transport and electrochemical phenomena and a better understanding of the mechanisms.

The present thesis demonstrates that electrodes made of perovskite oxides are active for the ORR and can therefore potentially be used as cathode material in SAFC.

The studies of the catalysis of the ORR and the HO_2^- transformations on various perovskite/carbon composites with various compositions and loadings proves that, on these electrodes, O_2 is reduced to OH^- via a "series" ORR pathway with the HO_2^- intermediate. Based on the experimental data and with the help of mathematical modeling, the following tentative mechanism was proposed for the ORR on perovskites, including the participation of the redox transition of the transition metal B of the perovskite.

O_2 is reduced through the two following steps:

$$O_2 + OH, ads + e^- \rightleftarrows O_2, ads + OH^-$$

$$O_2, ads + H_2O + e^- \rightleftarrows HO_2, ads + OH^-$$

The formed HO_2 species are further reduced through a slow chemical step followed by an electrochemical step:

$$HO_2, ads + OH, ads \rightarrow 2\,O, ads + H_2O$$

$$O, ads + H_2O + e^- \rightleftarrows OH, ads + OH^-$$

or might desorb from the electrode through:

$$HO_2, ads + OH^- \rightleftarrows HO_2^- + OH, ads$$

It should be stressed that the nature of the reaction intermediates is hypothetical, since the only intermediate detected in this work is HO_2^-. The reaction rates appear to be significantly lower on $LaCoO_3$ than either on $LaMnO_3$ or on $La_{0.8}Sr_{0.2}MnO_3$ perovskites, leading to a lower ORR onset potential, higher HO_2^- yield, and slower HO_2^- reduction/oxidation reactions for the former. The reason of this reaction rate differences is probably due to distinct redox transition behaviors of Co and Mn-based perovskites. The HO_2^- yield not only depends on the nature and the loading of perovskite, high perovskite loadings allowing a more efficient HO_2^- reduction, but also on the carbon loading.

Indeed, by carefully studying the impact of the carbon loading in the perovskite/carbon composite electrodes on the electrocatalytic activity, it was proved that the carbon plays a

dual role. First of all, it increases the perovskite utilization by improving the electrical contact in the catalytic layer. This results in an increased electrocatalytic activity for ORR and HO_2^- reduction/oxidation, leading to a lower HO_2^- yield. In addition, carbon is involved in the ORR mechanism by catalyzing the reduction of O_2 into HO_2^-, especially for perovskites with low activity for this reaction such as $LaCoO_3$. Therefore, it shows that the contribution of carbon cannot be neglected in the activity measurement, and that the intrinsic activity of the perovskite may not be directly measurable if it is used in the form of oxide/carbon composites. Moreover, the HO_2^- produced on carbon may either desorb from the surface and diffuse into the bulk of the electrolyte or be readsorbed on adjacent perovskite sites to be further reduced.

Besides, it was observed that the ORR electrocatalysis leads to a decrease of the number of perovskite active sites. The nature of this degradation is not fully understood yet but results in distinct behaviors depending on the activity of the perovskite for the ORR. Indeed, for $LaCoO_3$, which is less active than carbon for the ORR, currents at low overpotentials are not affected by this degradation since the ORR predominantly occurs on carbon sites. However, a current decrease at high overpotentials is observed due to slowing down the HO_2^- reduction with the decrease of the perovskite site number. On Mn-perovskites, the ORR onset potential is significantly shifted towards lower potentials due to the degradation of the highly active Mn sites. This also results in the disappearance of the redox peaks on the CV in the N_2-atmosphere.

Even if this work answered numerous questions about the ORR on perovskite oxides, there are still aspects to clarify and to improve in the future.

First of all, it appears that *in-situ* measurements are required, on the one hand to better understand the ORR mechanism and the involvement of the redox transitions of the perovskites, and on the other hand, to investigate the degradation of the catalyst during the electrocatalysis. These may be performed using X-ray absorption spectroscopies (XAS), but Raman spectroscopy is also a good tool to study the modifications of the catalysts and the adsorbed species. However, this will require the design of an *in-situ* cell as well as the development of a method to separate the bulk from the surface contribution. Moreover, such measurements may result in a local heating which might affect the properties of the catalysts, the nature and the coverage of adsorbates. The *in-situ* studies should be performed on oxides with different oxidation states of the transition metals (e.g. doped and undoped perovskites,

simple oxides) to allow the full understanding of the participation of the redox transitions in electrocatalysis. Also, to complete the degradation study, it might be interesting to build a flow cell with ICP or IR measurements downstream to detect the dissolved species in function of the potential applied on the working electrode.
Thanks to the results of *in-situ* studies, together with the careful investigation of the effect of the choice of kinetic rate constants on the voltammogram shapes and with the help of eventual additional experiments (e.g. RDE study of HO_2^- reduction/oxidation with other H_2O_2 concentrations), the mathematical model introduced in Chapter 5 to explain the ORR mechanism could be improved to be as close as possible to the reality.

For the future, it will be interesting to further improve the catalytic layer composition targeting maximum the perovskite utilization and high catalytic activity per unit mass.
For example, it is important to synthesize perovskites with higher specific surface area to reach high activities without increasing the loading. Also, it might be useful to have a control over the size of oxide crystallites, as well as the size of oxide or oxide-on-carbon agglomerates (the latter could be achieved by using a sieve).
As perovskite and carbon work as a tandem in composite electrodes, one can expect that higher activities will be reached with a better perovskite to carbon contact using carbon-supported perovskite catalysts. In addition, promising bifunctionnal catalysts can be built by combining a material very active for the reduction of O_2 to a perovskite highly active for the reduction of HO_2^-. The former may be carbon material, as in this work, or another material as soon as it is (i) inexpensive, (ii) electrically conductive to ensure electronic contact in the layer, (iii) active for the reduction of O_2 into HO_2^-, (iv) stable. Eventually, by varying the nature of the transition metal cations of the perovskites, one may find complementary perovskites.

In order to validate the application of perovskites as SAFC cathode materials, fuel cell tests will be required. This includes (i) the optimization of the catalytic layers and membrane-electrode assemblies (MEAs), (ii) the management of water and hydroxide flows in the fuel cell, (iii) the activity measurement and (iv) long-term stability tests. To optimize the catalytic layers, an optimized ratio of perovskite, carbon and ionomer will have to be chosen to ensure the triple contact. Besides the composition, also the procedure utilized for the preparation of MEAs is of primary importance to insure high mass transport and ion transport rates, high catalyst utilization, and ultimately, high performance and durability. This has to be performed

together with the choice of the alkaline membrane which will serve as a hydroxide ion conductor. This kind of membrane is strongly alkaline and may accelerate the degradation of the catalyst layer. Therefore, the stability of the performance has to be investigated and the duration of the stability tests should be comparable to real fuel cell operation, i.e. several months. Also, post-mortem analysis of the MEA might be useful to better understand degradation processes occurring in the fuel cell.

References

1. **Li, J.** 23. Catalyst layer degradation, diagnosis and failure mitigation. [auteur du livre] J. Zhang. *PEM Fuel Cell Electrocatalysts and Catalyst Layers: Fundamentals and Applications.* London : Springer, 2008, pp. 1041-1094.

2. **Varcoe, J.R., Slade, C.T.** Prospects for alkaline anion-exchange membranes in low temperature fuel cells. *Fuel Cells.* 2005, Vol. 5, 187-200.

3. **Gasteiger, H.A., Kocha, S.S., Sompalli, B., Wagner, F.T.** Activity benchmarks and requirements for Pt, Pt-alloy, and non-Pt oxygen reduction catalysts for PEMFCs. *Applied Catalysis B: Environmental.* 2005, Vol. 56, 9-35.

4. **Wroblowa, H.S., Yen-Chi-Pan, Razumney, G.** Electroreduction of oxygen. A new mechanistic criterion. *Journal of Electroanalytical Chemistry.* 1976, Vol. 69, 195-201.

5. **Kinumoto, T., Inaba, M., Nakayama, Y., Ogata, K., Umebayashi, R., Tasaka, A., Iriyama, Y., Abe, T., Ogumi, Z.** Durability of perfluorinated ionomer membrane against hydrogen peroxide. *Journal of Power Sources.* 2006, Vol. 158, 1222-1228.

6. **Ramaswamy, N., Hakim, N., Mukerjee, S.** Degradation mechanism study of perfluirinated proton exchange membrane under fuel cell operating conditions. *Electrochimica Acta.* 2008, Vol. 53, 3279-3295.

7. **Dobos, D.** *Electrochemical Data.* Budapest : Akademiai Kiado, 1978.

8. **Markovic, N.M., Gasteiger, H.A., Ross, P.N.** Oxygen reduction on platinum low-index single-crystal surfaces in alkaline solution: rotating ring disk Pt(hkl) studies. *Journal of Physical Chemistry.* 1996, Vol. 100, 6715-6721.

9. **Schmidt, T.J., Stamenkovic, V., Ross Jr, P.N., Markovic, N.M.** Temperature dependent surface electrochemistry on Pt single crystals in alkaline electrolyte. *Physical Chemistry Chemical Physics.* 2003, Vol. 5, 400-406.

10. **Paliteiro, C., Batista, L.** Electroreduction of dioxygen on plycrystalline platinum in alkaline solution. I. Platinum surface pretreated by potential cycling between 40 and 1450 mV. *Journal of the Electrochemical Society.* 2000, Vol. 147, 3436-3444.

11. **Paliteiro, C., Correia, E.** Electroreduction of dioxygen on plycrystalline platinum in alkaline solution. I. Platinum surface modified by hydrogen evolution. *Journal of the Electrochemical Society.* 2000, Vol. 147, 3445-3455.

12. **Genies, L., Faure, R., Durand, R.** Electrochemical reduction of oxygen on platinum nanoparticles in alkaline media. *Electrochimica Acta.* 1998, Vol. 44 , 1317-1327.

13. **Lima, F.H.B., Zhang, J., Shao, M.H., Sasaki, K., Vukmirovic, M.B., Ticianelli, E.A., Adzic, R.R.** Catalytic activity-d band center correlation for the O2 reduction reaction on platinum in alkaline solutions. *Journal of Physical Chemistry.* 2007, Vol. 111, 404-410.

14. **Spendelow, J.S., Wieckowski, A.** Electrocatalysis of oxygen reduction and small oxidation in alkaline media. *Physical Chemistry Chemical Physics.* 2007, Vol. 9, 2654-2675.

15. **Markovic, N.M., Schmidt, T.J., Stamenkovic, V., Ross, P.N.** Oxygen reduction reaction on Pt and Pt bimetallic surfaces : a selective review. *Fuel Cells.* 2001, Vol. 1, 105-116.

16. **Sljukic, B., Banks, C.E., Compton, R.G.** An overview of the electrochemical reduction of oxygen at carbon-based modified electrodes. *Journal of the Iranian Chemical Society.* 2005, Vol. 2, 1-25 .

17. **Brito, P.S.D., Sequeira, C.A.C.** Cathodic oxygen reduction on noble metal and carbon electrodes. *Journal of the Power Sources.* 1994, Vol. 52, 1-16.

18. **Xu, J., Huang, W., McCreery, R.L.** Isotope and surface preparation effects on alkaline dioxygen reduction at carbon electrodes. *Journal of Electroanalytical Chemistry.* 1996, Vol. 410, 235-242.

19. **Vaik, K., Schiffrin, D.J., Tammeveski, K.** Electrochemical reduction of oxygen on anodically pre-treated and chemically grafted glassy carbon electrodes in alkaline solution. *Electrochemistry Communications.* 2004, Vol. 6, 1-5.

20. **Tammeveski, K., Kontturi, K., Nichols, R.J., Potter, R.J., Schiffrin, D.J.** Surface redox catalysis for O2 reduction on quinone-modified glassy carbon electrodes. *Journal of Electroanalytical Chemistry.* 2001, Vol. 515, 101-112.

21. **Pan, F., Jin, J., Fu, X., Liu, Q., Zhang, J.** Advanced oxygen reduction electrocatalyst based on nitrogen-doped graphene derived from edible sugar and urea. *Applied Materials and Interfaces.* 2013, Vol. 5, 11108-11114.

22. **Liu, Z.W., Peng, F., Wang, H.-J., Yu, H., Zheng, W.X., Yang, J.** Phosphorous-doped graphite layers with high electrocatalytic activity for the O2 reduction in alkaline medium. *Angewandte Chemie.* 2011, Vol. 50, 3257-3261.

23. **Yang, S., Feng, X., Wang, X., Mullen, K.** Graphene-based carbon nitride nanosheets as efficient metal-free electrocatalysts for oxygen reduction reactions. *Angewandte Chemie.* 2011, Vol. 50, 5339-5343.

24. **Heller-Ling, N., Prestat, M., Gautier, J.L., Koenig, J.F., Poillerat, G., Chartier, P.** Oxygen electroreducton mechanism at thin NixCo3-xO4 spinel films in a double channel electrode flow cell (DCEFC). *Electrochimica Acta.* 1997, Vol. 42, 197-202.

25. **Bagotzky, V.S., Shumilova, N.A., Khrushcheva, E.I.** Electrochemical oxygen reduction on oxide catalysts. *Electrochimica Acta.* 1976, Vol. 21, 919-924 .

26. **Burshtein, R.H., Vilinskaya, V.S., Tarasevich, M.R., Bulavina, N.G.** Electrocatalytic properties of oxide catalysts on a carbon carrier. *Reaction Kinetics and Catalysis Letters.* 1976, Vol. 4, 159-165.

27. **De Koninck, M., Marsan, B.** MnxCu1-xCo2O4 used as bifunctional electrocatalyst in alkaline medium. *Electrochimica Acta.* 2008, Vol. 53, 7012-7021.

28. **Ortiz, J., Gautier, J.L.** Oxygen reduction on copper chromium manganites. Effect of oxide composition on the reaction mechanism in alkaline solution. *Journal of Electroanalytical Chemistry.* 1995, Vol. 391, 111-118.

29. **Ponce, J., Rehspringer, J.L., Poillerat, G., Gautier, J.L.** Electrochemical study of nickel-aluminium-manganese spinel NixAl1-xMn2O4. Electrocatalytical properties for the oxygen evolution reaction and oxygen reduction reaction in alkaline media. *Electrochimica Acta.* 2001, Vol. 46, 3373-3380.

30. **Liang, Y., Li, Y., Wang, H., Zhou, J., Wang, J., Regier, T., Dai, H.** Co3O4 nanocrystals on graphene as a synergistic catalyst for oxygen reduction reaction. *Nature Material.* 2011, Vol. 10 , 780-786.

31. **Liang, Y., Wang, H., Zhou, J., Li, Y., Wang, J., Regier, T., Dai, H.** Covalent hybrid of spinel manganese-cobalt oxide and graphene as advanced oxygen reduction electrocatalysts. *Journal of the American Chemical Society.* 2012, Vol. 134 , 3517-3523.

32. **Tan, Y., Xu, C., Chen, G., Fang, X., Zheng, N., Xie, Q.** Facile synthesis of manganese-oxide-containing mesoporous nitrogen-doped carbon for efficient oxygen reduction. *Advanced Functional Materials.* 2012, Vol. 22, 4584-4591.

33. **Roche, I., Chainet, E., Chatenet, M., Vondrak, J.** Carbon-supported manganese oxide nanoparticles as electrocatalysts for the oxygen reduction reaction (ORR) in alkaline medium: physical characterizations and ORR mechanism. *Journal of Physical Chemistry C.* 2007, Vol. 111, 1434-1443.

34. **Cao, Y.L., Yang, H.X., Ai, X.P., Xiao, L.F.** The mechanism of oxygen reduction on MnO2-catalyzed air cathode in alkaline solution. *Journal of Electroanalytical Chemistry.* 2003, Vol. 557, 127-134 .

35. **Lima, F.H.B., Calegaro, M.L., Ticianelli, E.A.** Investigations of the catalytic properties of manganese oxides for the oxygen reduction reaction in alkaline media. *Journal of Electroanalytical Chemistry.* 2006, Vol. 590, 152-160.

36. **Matsuki, K., Kamada, H.** Oxygen reduction electrocatalysis on some manganese oxides. *Electrochimica Acta.* 1986, Vol. 31, 13-18.

37. **Wu, J., Zhang, D., Wang, Y., Wan, Y.** Manganese oxide-graphene composite as an efficient catalyst for 4-electron reduction of oxygen in alkaline media. *Electrochimica Acta.* 2012, Vol. 75, 305-310.

38. **Moureaux, F., Stevens, P., Chatenet, M.** Effect of lithium and potassium cations on the electrocatalytic properties of carbon and manganese oxide electrocatalysts towards the oxygen reduction reaction in concentrated alkaline electrolyte. *Electrocatalysis.* 2013, Vol. 4, 123-133.

39. **Sun, W., Hsu, A., Chen, R.** Carbon supported tetragonal MnOOH catalysts for oxygen reduction reaction in alkaline media. *Journal of Power Sources.* 2011, Vol. 196, 627-635.

40. **Wu, Q., Jiang, L., Tang, Q., Liu, J., Wang, S., Sun, G.** Activity and stability of the Ni(OH)2-MnOx/C composite for oxygen reduction reaction in alkaline solution. *Electrochimica Acta.* 2013, Vol. 91, 314-322.

41. **Saito, M., Saito, Y., Konishi, T., Kawai, H., Kuwano, J., Shiroishi, H., Uchimoto, Y.** Electrocatalytic O2 reduction properties of pyrochlore-type oxides for alkaline DAFCs. *ECS Transactions.* 2008, Vol. 16, 891-900.

42. **Konishi, T., Kawai, H., Saito, M., Kuwano, J., Shiroishi, H., Okumura, T., Uchimoto, Y.** Electrocatalytic activity of pyrochlores Ln2M2O7-delta (Ln=lanthanoids) for oxygen reduction reaction. *Topics of Catalysis* . 2009, Vol. 52, 896-902.

43. **Gao, Z., Wang, R.** Catalytic activity for methane combustion of the perovskite-type La1-xSrxCoO3-delta oxide prepared by the urea decomposition method. *Applied Catalysis B: Environmental.* 2010, Vol. 98, 147-153.

44. **Ponce, S., Pena, M.A., Fierro, J.L.G.** Surface properties and catalytic performance in methane combustion of Sr-substituted lanthanum manganites. *Applied Catalysis B: Environmental.* 2000, Vol. 24, 193-205.

45. **Ciambelli, P., Cimino, S., De Rossi, S., Faticanti, M., Lisi, L., Minelli, G., Pettiti, P., Porta, P., Russo, G., Turco, M.** AMnO3 (A=La,Nd,Sm) and Sm1-xSrxMnO3 perovskites as combustion catalysts : structural, redox and catalytic properties. *Applied Catalysis B : Environmental.* 2000, Vol. 24, 243-253 .

46. **Milt, V.G., Spretz, R., Ulla, M.A., Lombardo, E.A.** The nature of active sites for the oxidation of methane on La-based perovskites. *Catalysis Letters.* 1996, Vol. 42, 57-63.

47. **O'Connell, M., Norman, A.K., Huttermann, C.F., Morris, M.A.** Catalytic oxidation over lanthanum-transition metal perovskite materials. *Catalysis Today.* 1999, Vol. 47, 123-132.

48. **Ferri, D., Forni, L.** Methane combustion on some perovskite-like mixed oxides. *Applied Catalysis B: Environmental.* 1998, Vol. 16, 119-126.

49. **Royer, S., Duprez, D., Kaliaguine, S.** Role of bulk and grain boundary oxygen mobility in the catalytic oxidation activity of LaCo1-xFexO3. *Journal of Catalysis.* 2005, Vol. 234, 364-375.

50. **Pecchi, G., Reyes, P., Zamora, R., Campos, C., Cadus, L.E., Barbero, B.P.** Effect of the preparation method on the catalytic activity of La1-xCaxFeO3 perovskite-tytpe oxides . *Catalysis Today.* 2008, Vol. 133-135, 420-427.

51. **Garcia de la Cruz, R.M., Falcon, H., Pena, M.A., Fierro, J.L.G.** Role of bulk and surface structures of La1-xSrxNiO3 perovskite-type oxides in methane combustion. *Applied Catalysis B: Environmental.* 2001, Vol. 33, 45-55.

52. **Kucharczyk, B., Tylus, W.** Effect of Pd or Ag additive on the activity and stability of monolithic LaCoO3 perovskites for catalytic combustion of methane. *Catalysis Today.* 2004, Vol. 90, 121-126.

53. **Lee, Y.N., Lago, R.M., Fierro, J.L.G., Cortes, V., Sapina, F., Martinez, E.** Surface properties and catalytic performance for ethane combustion of La1-xKxMnO3+delta perovskites. *Applied Catalysis A: General.* 2001, Vol. 207, 17-24.

54. **Merino, N.A., Barbero, B.P., Eloy, P., Cadus, L.E.** La1-xCaxCoO3 perovskite-type oxides: identification of the surface oxygen species by XPS. *Applied Surface Science.* 2006, Vol. 253, 1489-1493.

55. **Merino, N.A., Barbero, B.P., Ruiz, P., Cadus, L.E.** Synthesis, characterisation, catalytic activity and structural stability of LaCo1-yFeyO3+/-delta perovskite catalysts for combustion of ethanol and propane. *Journal of Catalysis.* 2006, Vol. 240, 245-257.

56. **Bedel, L., Roger, A.C., Rehspringer, J.L., Zimmermann, Y., Kiennemann, A.** La1-yCo0.4Fe0.6O3-delta perovskite oxides as catalysts for Fischer-Tropsch synthesis. *Journal of Catalysis.* 2005, Vol. 235, 279-294.

57. **Bedel, L., Roger, A.C., Estournes, C., Kiennemann, A.** Co0 from partial reduction of La(Co,Fe)O3 perovskites for Fischer-Tropsch synthesis. *Catalysis Today.* 2003 , Vol. 85, 207-218.

58. **Najjar, H., Batis, H.** La-Mn perovskite-type oxide prepared by combustion method: catalytic activity in ethanol oxidation. *Applied Catalysis A: General.* 2010, Vol. 383, 192-201.

59. **Rousseau, S., Loridant, S., Delichere, P., Boreave, A., Deloume, J.P., Vernoux, P.** La1-xSrxCo1-yFeyO3 perovskites prepared by sol-gel method : characterization and

relationships with catalytic properties for total oxidation of toluene. *Applied Catalysis B: Environmental.* 2009, Vol. 88, 438-447.

60. **Natile, M.M., Ugel, E., Maccato, C., Glisenti, A.** LaCoO3 : effect of synthesis conditions on properties and reactivity. *Applied Catalysis B : Environmental.* 2007, Vol. 72, 351-362.

61. **Yang, W., Zhang, R., Chen, B., Bion, N., Duprez, D., Royer, S.** Activity of perovskite-type mixed oxides for the low-temperature CO oxidation: evidence of oxygen species participation from the solid. *Journal of Catalysis.* 2012, Vol. 295, 45-58.

62. **Petrovic, S., Rakic, V., Jovanovic, D.M., Baricevic, A.T.** Oxidation of CO over Ru containing perovskite type oxides. *Applied Catalysis B: Environmental.* 2006, Vol. 66, 249-257.

63. **Yakovleva, I.S., Isupova, L.A., Rogov, V.A., Sadykov, V.A.** Forms of oxygen in La1-xCaxMnO3+delta (x=0-1) perovskites and their reactivities in oxidation reactions. *Kinetics and Catalysis.* 2008, Vol. 49, 261-270.

64. **Yokoi, Y., Uchida, H.** Catalytic activity of perovskite-type oxide catalysts for direct decomposition of NO: correlation between cluster model calculations and temperature-programmed desoprtion experiments. *Catalysis Today.* 1998, Vol. 42, 167-174.

65. **Kumar, S., Vinu, A., Subrt, J., Bakardjieva, S., Rayalu, S., Teraoka, Y., Labhsetwar, N.** Catalytic N2O decomposition on Pr0.8Ba0.2MnO3 type perovskite catalyst for industrial emission control. *Catalysis Today.* 2012, Vol. 198, 125-132.

66. **Krkljus, I., Brankovic, Z., Duris, K., Vukotic, V., Brankovic, G.** The electrophoretic deposition of lanthanum manganite powders for a cathode-supported solid oxide fuel cell in planar and tubular configurations. *International Journal of Applied Ceramic Technology.* 2008, Vol. 5, 548-556.

67. **Liu, B., Zhang, Y., Tang, L.** X-ray photoelectron spectroscopic studies of Ba0.5Sr0.5Co0.8Fe0.2O3-delta cathode for solid oxide fuel cells. *International Journal of Hydrogen Energy.* 2009, Vol. 34, 435-439.

68. **Hrovat, M., Katsarakis, N., Reichmann, K., Bernik, S., Kuscer, D., Holc, J.** Characterisation of LaNi1-xCoxO3 as a possible SOFC cathode material. *Solid State Ionics.* 1996, Vol. 83, 99-105.

69. **Yan, A., Maragou, V., Arico, A., Cheng, M., Tsiakaras, P.** Investigation of a Ba0.5Sr0.5Co0.8Fe0.2O3-delta based cathode SOFC. II. The effect of CO2 on the chemical stability. *Applied Catalysis B: Environmental.* 2007, Vol. 76, 320-327.

70. **Hjalmarsson, P., Soggard, M., Mogensen, M.** Electrochemical behavior of (La1-xSrx)sCo1-yNiyO3-delta as porous SOFC cathodes. *Solid State Ionics.* 2009, Vol. 180, 1395-1405 .

71. **Choi, Y.M., Lin, M.C., Liu, M.** Computational study on the catalytic mechanism of oxygen reduction on La0.5Sr0.5MnO3 in solid oxide fuel cells. *Angewandte Chemie.* 2007, Vol. 119, 7352-7357.

72. **Matsumoto, Y., Yoneyama, H., Tamura, H.** The mechanism of oxygen reduction at a LaNiO3 electrode. *Bulletin of the Chemical Society of Japan.* 1978, Vol. 51, 1927-1930.

73. **Matsumoto, Y.** *Electrochemical studies on transition metal oxides with electronic conductivity.* Osaka : s.n., 1977.

74. **Bockris, J.O'M, Otagawa, T.** Mechanism of Oxygen Evolution on Perovskites. *Journal of Physical Chemistry.* 1983, Vol. 87, 2960-2971.

75. —. The Electrocatalysis of Oxygen Evolution on Perovskites. *Journal of the Electrochemical Society.* 1984, Vol. 131, 290-302.

76. **Singh, N.K., Tiwari, S.K., Singh, R.N.** Electrocatalytic properties of lanthanum manganites obtained by a novel malic acid-aided route. *International Journal of Hydrogen Energy.* 1998, Vol. 23, 775-780.

77. **Poznyak, S.K., Kharton, V.V., Frade, J.R., Yaremchenko, A.A., Tsipis, E.V., Yakovlev, S.O., Marozau, I.P.** Behavior of (La,Sr)CoO3- and La2NiO4-based ceramic anodes in alkaline media: compositional and microstructural factors . *Journal of Solid State Electrochemistry.* 2008, Vol. 12, 15-30.

78. **Suntivich, J., May, K.J., Gasteiger, H.A., Goodenough, J.B., Shao-Horn, Y.** A Perovskite oxide optimized for oxygen evolution catalysis from molecular orbital principles. *Science.* 2011, Vol. 334, 1383-1385.

79. **Grimaud, A., May, K.J., Carlton, C.E., Lee, Y.L., Risch, M., Hong, W.T., Zhou, J., Shao-Horn, Y.** Double perovskites as a family of highly active catalysts for oxygen evolution in alkaline solution. *Nature Communications.* 2013, Vol. 4, 2439.

80. **Singh, R.N., Lal, B.** High surface area lanthanum cobaltate and its A and B sites substituted derivatives for electrocatalysis of O2 evolution in alkaline solution. *International Journal of Hydrogen Energy.* 2002, Vol. 27, 45-55.

81. **Kahoul, A., Hammouche, A., Poillerat, G., De Doncker, R.W.** Electrocatalytic activity and stability of La1-xCaxCoO3 perovskite-type oxides in alkaline medium. *Catalysis Today.* 2004, Vol. 89, 287-291.

82. **Li, X., Qu, W., Zhang, J, Wang, H.** Electrocatalytic Activities of La0.6Ca0.4CoO3 and La0.6Ca0.4CoO3-Carbon Composites Toward the Oxygen Reduction Reaction in Concentrated Alkaline Electrolytes. *Journal of The Electrochemical Society.* 2011 , Vol. 158, A597-A604.

83. **Hayashi, M., Uemura, H., Shimanoe, K., Miura, N., Yamazoe, N.** Reverse micelle assisted dispersion of lanthanum manganite on carbon support for oxygen reduction cathode. *Journal of the Electrochemical Society.* 2004, Vol. 151, A158-A163.

84. **Suntivich, J., Gasteiger, H.A., Yabuuchi, N., Nakanishi, H., Goodenough, J.B., Shao-Horn, Y.** Design principles for oxygen-reduction activity on perovskite oxide catalysts for fuel cells and metal-air batteries . *Nature Chemistry.* 2011, Vol. 3, 546-550.

85. **Tulloch, J., Donne, S.W.** Activity of perovskite La1-xSrxMnO3 catalysts towards oxygen reduction in alkaline electrolytes. *Journal of Power Sources.* 2009, Vol. 188, 359-366.

86. **Yuasa, M., Tachibana, N., Shimanoe, K.** Oxygen reduction activity of carbon-supported La1-xCaxMn1-yFeyO3 nanoparticles. *Chemistry of Materials.* 2013, Vol. 25, 3072-3079.

87. **Lukaszewicz, J., Imaizumi, S., Yuasa, M., Shimanoe, K., Yamazoe, N.** New approach towards preparation of efficient gas diffusion-type oxygen reduction electrode. *Journal of Material Science.* 2006, Vol. 41, 6215-6220.

88. **Sunarso, J., Torriero, A.J., Zhou, W., Howlett, P.C., Forsyth, M.** Oxygen reduction reaction activity of La-based perovskite oxides in alkaline medium : a thin-film rotating ring-disk electrode study. *Journal of Physical Chemistry C.* 2012, Vol. 116, 5827-5834.

89. **Miyazaki, K., Kawakita, K.-I., Abe, T., Fukutsuka, T., Kojima, K., Ogumi, Z.** Single-step synthesis of nano-sized perovskite-type oxide/carbon nanotube composites and their electrocatalytic oxygen-reduction activites. *Journal of Materials Chemistry.* 2011, Vol. 21, 1913-1917.

90. **Hermann, V., Dutriat, D., Müller, S., Comninellis, Ch.** Mechanistic studies of oxygen reduction at La0.6Ca0.4CoO3-activated carbon electrodes in a channel flow cell. *Electrochimica Acta.* 2000, Vol. 46, 365-372.

91. **Hammouche, A., Kahoul, A., Sauer, D.U., De Doncker, R.W.** Influential factors on oxygen reduction at La1-xCaxCoO3 electrodes in alkaline electrolyte. *Journal of Power Sources.* 2006, Vol. 153, 239-244.

92. **Kahoul, A., Hammouche, A., Naamoune, F., Chartier, P., Poillerat, G., Koenig, J.F.** Solvent effect on synthesis of perovskite-type La1-xCaxCoO3 and their electrochemical properties for oxygen reactions. *Materials Research Bulletin.* 2000, Vol. 35, 1955-1966.

93. **Yuan, X.-Z., Li, X., Qu, W., Ivey, D.G., Wang, H.** Electrocatalytic activity of non-stoichiometric perovskites toward oxygen reduction reaction in alkaline electrolytes . *ECS Transactions.* 2011, Vol. 35, 11-20.

94. **Hyodo, T., Hayashi, M., Mitsutake, S., Miura, N., Yamazoe, N.** Praseodymium-calcium manganites (Pr1-xCaxMnO3) as electrode catalyst for oxygen reduction in alkaline solution. *Journal of Applied Electrochemistry.* 1997, Vol. 27, 745-746.

95. **Wang, X., Sebastian, P.J., Smit, M.A., Yang, H., Gamboa, S.A.** Studies on the oxygen reduction catalyst for zinc-air battery electrode. *Journal of Power Sources.* 2003, Vol. 124, 278-284.

96. **Eom, S.-W., Ahn, S.-Y., Kim, I.-J., Sun, Y.-K., Kim, H.-S.** Electrochemical evaluation of La1-xCaxCoO3 cathode material for zinc air batteries application. *Journal of Electroceramics.* 2009, Vol. 23, 382-386.

97. **Weidenkaff, A., Ebbinghaus, S.G., Lippert, T.** Ln1-xAxCoO3 (Ln = Er, La ; A = Ca, Sr)/carbon nanotube composite materials applied for rechargeable Zn/air batteries. *Chemistry of Materials.* 2002, Vol. 14, 1797-1805.

98. **Malkhandi, S., Yang, B., Manohar, A.K., Manivannan, A., Surya Prakash, G.K., Narayanan.** Electrocatalytic properties of nanocrystalline calcium-doped lanthanum cobalt oxide for bifunctional oxygen electrodes. *Journal of Physical Chemistry Letters.* 2012, Vol. 3, 967-972.

99. **Wu, N.-L., Liu, W.-R., Su, S.-J.** Effect of oxygenation on electrocatalysis of La0.6Ca0.4CoO3-x in bifunctional air electrode. *Electrochimica Acta.* 2003, Vol. 48, 1567-1571.

100. **Zhuang, S., Huang, K., Huang, C., Huang, H., Liu, S., Fan, M.** Preparation of silver modified La0.6Ca0.4CoO3 binary electrocatalyst for bi-functional air electrodes in alkaline medium. *Journal of Power Sources.* 2011, Vol. 196, 4019-4025.

101. **Bursell, M., Pirjamali, M., Kiros, Y.** La0.6Ca0.4CoO3, La0.1Ca0.9MnO3 and LaNiO3 as bifunctional oxygen electrodes. *Electrochimica Acta.* 2002, Vol. 47, 1651-1660.

102. **Muller, S., Striebel, K., Haas, O.** La0.6Ca0.4CoO3 : a stable and powerful catalyst for bifunctional air electrodes. *Electrochimica Acta.* 1994, Vol. 39, 1661-1668.

103. **Suntivich, J., Gasteiger, H.A., Yabuuchi, N., Shao-Horn, Y.** Electrocatalytic measurement methodology of oxide catalysts using a thin-film rotating disk electrode. *Journal of the Electrochemical Society.* 2010, Vol. 157, B1263-B1268.

104. **Davies, P.K., Wu, H., Borisevich, A.Y., Molodetsky, I.E., Farber, L.** Crystal chemistry of complex perovskites: new cation-ordered dielectric oxides. *Annual Review of Material Research.* 2008, Vol. 38, 369-401 .

105. **Bhalla, A.A., Guo, R., Roy, R.** The perovskite structure - a review of its role in ceramic science and technology. *Materials Research Innovation.* 2000, Vol. 4, 3-26.

106. **Goodenough, J.B.** Electronic and ionic transport properties and other physical aspects of perovskites. *Reports on Progress in Physics.* 2004 , Vol. 67, 1915-1993.

107. **Goldschmidt, V.M.** Die Gesetze der Krystallochemie. *Die Naturwissenschaften.* 1926, Vol. 21, 477-485.

108. **Glazer, A.M.** The classification of tilted octahedra in perovskites. *Acta Crystallographica.* 1972, Vol. B28, 3384-3392.

109. —. Simple ways of determining perovskite structures. *Acta Crystallographica.* 1975, Vol. A31, 756-762.

110. **Woodward, P.M.** Octahedral tilting in perovskites. I. Geometrical considerations . *Acta Crystallographica.* 1997, Vol. B53, 32-43 .

111. —. Octahedral tilting in perovskites. II. Structure stabilizing forces. *Acta Crystallographica.* 1997, Vol. B53, 44-66.

112. **Antipov, E.V., Abakumov, A.M., Istomin, S.Y.** Target-aimed synthesis of anion-deficient perovskites. *Inorganic Chemistry* . 2008, Vol. 47, 8543-8552 .

113. **Abakumov, A.M., Hadermann, J., Van Tendeloo, G., Antipov, E.V.** Chemistry and structure of anion-deficient perovskites with translational interfaces. *Journal of American Ceramic Society.* 2008, Vol. 91, 1807-1813.

114. **Pena, M.A., Fierro, J.L.G. /.** Chemical structures and performance of perovskite oxides. *Chemical Reviews.* 2001, Vol. 101, 1981-2017.

115. **Thiele, D., Zuttel, A.** Electrochemical characterisation of air electrodes based on La0.6Sr0.4CoO3 and carbon nanotubes. *Journal of Power Sources.* 2008, Vol. 183, 590-594.

116. **Chang, Y.-M., Hsieh, Y.-C., Wu, P.-W., Lai, C.-H., Chang, T.-Y.** Enchancement of bifunctional catalysis by Ir doping of La0.6Ca0.4CoO3 perovskites. *Materials Letters.* 2008, Vol. 62, 4220-4222.

117. **El Baydi, M., Tiwari, S.K., Singh, R.N., Rehspringer, J.-L., Chartier, P., Koenig, J.-F., Poillerat, G.** High specific surface area nickel mixed oxide powders LaNiO3 (perovskite) and NiCo2O4 (spinel) via sol-gel type routes for oxygen electrocatalysis in alkaline media. *Journal of Solid State Chemistry.* 1995 , Vol. 116 , 157-169.

118. **Carbonio, R.E., Fierro, C., Tryk, D., Scherson, D., Yeager, E.** Perovskite-type oxides : oxygen electrocatalysis and bulk structure. *Journal of Power Sources.* 1988, Vol. 22, 387-398.

119. **Kudo, T., Obayashi, H., Yoshida, M.** Rare earth cobaltites as oxygen electrode materials for alkaline solution. *Journal of the Electrochemical Society.* 1977, Vol. 124, 321-325.

120. **Suntivich, J., Perry, E.E., Gasteiger, H.A., Shao-Horn, Y.** The influence of the cation on the oxygen reduction and evolution activities of oxide surfaces in alkaline electrolyte. *Electrocatalysis.* 2013, Vol. 4, 49-55.

121. **Ariafard, A., Aghabozorg, H.R., Salehirad, F.,.** Hydrogen peroxide decomposition over La0.9Sr0.1Ni1-xCrxO3 perovskites. *Catalysis Communications.* 2003, Vol. 4, 561-566.

122. **Falcon, H., Carbonio, R.E.** Study of the heterogeneous decomposition of hydrogen peroxide: its application to the development of catalysts for carbon-based oxygen cathodes. *Journal of Electroanalytical Chemistry.* 1992, Vol. 339, 69-83.

123. **Falcon, H., Carbonio, R.E., Fierro, J.L.G.** Correlation of oxidation states in LaFexNi1-xO3+delta oxides with catalytic activity for H2O2 decomposition. *Journal of Catalysis.* 2001, Vol. 203, 264-272.

124. **Alonso, J.A., Martinez-Lope, M.J., Falcon, H., Carbonio, R.E.** On the correlation of Ni oxidation states and electronic conductivity of (R,A)NiO3-delta (R = lanthanides, A = alkaline earths, Th) perovskites with catalytic activity for H2O2 decomposition. *Physical Chemistry Chemical Physics.* 1999, Vol. 1, 3025-3030.

125. **Soleymani, M., Moheb, A., Babakhani, D.** Hydrogen peroxide decomposition over nanosized La1-xCaxMnO3 (0<x<0.6) perovskite oxides. *Chemical Engineering and Technology.* 2011, Vol. 34, 49-55.

126. **Yang, H., Zhang, T., Tian, H., Tang, J., Xu, D., Yang, W., Lin, L.** Effect of Sr substitution on catalytic activity of La1-xSrxMnO3 (0<x<0.8) perovskite-type oxides for catalytic decomposition of hydrogen peroxide. *Reaction Kinetics and Catalysis Letters.* 2001, Vol. 73, 311-316.

127. **Lee, Y.N., Lago, R.M., Fierro, J.L.G., Gonzalez, J.** Hydrogen peroxide decomposition over Ln1-xAxMnO3 (Ln=La or Nd and A=K or Sr) perovskites. *Applied Catalysis A: General.* 2001, Vol. 215, 245-256.

128. **Ge, L., Zhu, Z., Shao, Z., Wang, S., Liu, S.** Effects of preparation methods on the oxygen nonstoichiometry B-site cation valences and catalytic efficiency of perovskite La0.6Sr0.4Co0.2Fe0.8O3-delta. *Ceramics International .* 2009, Vol. 35, 3201-3206.

129. **Magalhaes, F., Moura, F.C.C., Ardisson, J.D., Lago, R.M.** LaMn1-xFexO3 and LaMn0.1-xFe0.9MoxO3 perovskites : synthesis, characterization and catalytic activity in H2O2 reactions. *Materials Research.* 2008, Vol. 11, 307-312.

130. **Moura, F.C.C., Araujo, M.H., Ardisson, J.D., Macedo, W.A.A., Albuquerque, A.S., Lago, R.M.** Investigation of the solid state reaction of LaMnO3 with Fe° and its effect on the catalytic reactions with H2O2 . *Journal of the Brazilian Chemical Society.* 2007, Vol. 18, 322-329.

131. **Wang, G., Bao, Y., Tian, Y., Xia, J., Cao, D.** Electrocatalytic activity of perovskite La1-xSrxMnO3 towards hydrogen peroxide reduction in alkaline medium. *Journal of Power Sources.* 2010, Vol. 195, 6463-6467.

132. **Zhuang, S., Liu, S., Huang, C., Tu, F., Zhang, J., Li, Y.** Electrocatalytic activity of nanoporous perovskite La1-xCaxCoO3 towards hydrogen peroxide reduction in alkaline medium. *International Journal of Electrochemical Science.* 2012, Vol. 7, 338-344.

133. **Hermann, V.** *Préparation et caractérisation d'électrodes à base de La0.6Ca0.4CoO3 pérovskite: application à la réduction de l'oxygène en milieu alcalin.* Lausanne : EPFL - PhD thesis, 2000.

134. **Shimizu, Y., Komatsu, H., Michishita, S., Miura, N., Yamazo, N.** Sensing characteristics of hydrogen peroxide sensor using carbon-based electrode loaded with perovskite-type oxide. *Sensors and Actuators B.* 1996, Vol. 34, 493-498 .

135. **Luque, G.L., Ferreyra, N.F., Leyva, A.G., Rivas, G.A.** Characterization of carbon paste electrodes modified with manganese based perovskites-type oxides from amperometric determination of hydrogen peroxide. *Sensors and Actuators B.* 2009, Vol. 142, 331-336.

136. **Ahn, D.T.V., Olthuis, W., Bergveld, P.** Sensing properties of perovskite oxide La0.5Sr0.5CoO3-delta obtained by using pulsed laser deposition. *Sensors and Actuators B.* 2004 , Vol. 103, 165-168.

137. **Fernandez, E.M., Moses, P.G., Toftelund, A., Hansen, H.A., Martinez, J.I., Abild-Pedersen, F., Kleis, J., Hinnemann, B., Rossmeisl, J., Bligaard, T., Norskov, J.K.** Scaling relationships for adsorption energies on transition metal oxide, sulfide, and nitride surfaces. *Angewandte Chemie.* 2008, Vol. 47, 1-5.

138. **Calle-Vallejo, F., Martinez, J.I., Garcia-Lastra, J.M., Mogensen, M., Rossmeisl, J .** Trends in stability of perovskite oxides. *Angewandte Chemie.* 2010, Vol. 49, 7699-7701.

139. **Hyodo, T., Shimizu, Y., Miura, N., Yamazoe, N.** Investigation of materials for gas diffusion-type oxygen cathode aiming at electric power-saving brine electrolysis. *Denki Kagaku.* 1993, Vol. 62, 158-164.

140. **Lucas, C., Eiroa, I., Nunes, M.R., Russo, P.A., Ribeiro Carrott, M.M.L., da Silva Pereira, M.I., Melo Jorge, M.E.** Preparation and characterization of Ca1-xCexMnO3 perovskite electrodes. *Journal of Solid State Electrochemistry.* 2009 , Vol. 13, 943-950.

141. **Karlsson, G.** Reduction of oxygen on LaNiO3 in alkaline solution. *Journal of Power Sources.* 1983, Vol. 10, 319-331.

142. **Napolskiy, F.** *(PhD thesis under progress).* Moscow : Moscow State University - PhD thesis.

143. **Douy, A.** Polyacrilamide gel: an efficient tool for easy synthesis of multicomponent oxide precursors of ceramics and glasses. *International Journal of Inorganic Materials.* 2001, Vol. 3, 699-707.

144. **Larson, A.C., Von Dreele, R.B.** *General Structure Analysis System (GSAS).* s.l. : Los Alamos National Laboratory Report , 2004 . LAUR 86-748.

145. **Toby, B.H.** EXPGUI, a graphical user interface for GSAS. *Journal of Applied Crystallography.* 2001, Vol. 34, 210-213.

146. **Brunauer, S., Emmett, P.H., Teller, E.** Adsorption of gases in molecular layers. *Journal of the American Chemical Society.* 1938, Vol. 60, 309-319.

147. **Moulder, J.F., Stickle, W.F., Sobol, P.E., Bomben, K.D.** *Handbook of X-ray Photoelectron Spectroscopy.* MN, USA : Perkin-Elmer Corporation, Physical Electronics Division, Eden Prairie, 1992.

148. **Scofield, J.H.** Hartree-slater subshell photoionization cross-sections at 1254 and 1487 eV. *Journal of Electron Spectroscopy and Related Phenomena.* 1976, Vol. 8, 129-137.

149. **Schmidt, T.J., Gasteiger, H.A., Stab, G.D., Urban, P.M., Kolb, D.M., Behm, R.J.** Characterization of high-surface-area electrocatalysts using a rotationg disk electrode configuration. *Journal of Electrochemical Society.* 1998, Vol. 145, 2354-2358.

150. **Yermalov, Yu.I., Surovikin, V.F., Plasksin, G.V., Semikolenov, V.A., Likholobov, V.A., Chuvilin, L.V., Bogdanov, S.V.** New carbon material as support for catalysts. *Reaction Kinetics and Catalysis Letters.* 1987, Vol. 33, 435-440.

151. **Maillard, F., Simonov, P.A., Savinova, E.R.** Carbon materials as supports for fuel cell electrocatalysts. [auteur du livre] P. Serp et J.L. Figueiredo. *Carbon Materials for Catalysis.* New Jersey : John Wiley & Sons, 2009.

152. **Rao, V., Simonov, P.A., Savinova, E.R., Plaksin, G.V., Cherepanova, S.V., Kryukova, G.N., Stimming, U.** The influence of carbon support porosity on the activity of PtRu/Sibunit anode catalysts for methanol oxidation. *Journal of Power Sources.* 2005, Vol. 145, 178-187.

153. **Fukuta, K. (Tokuyama Corporation).** Electrolyte Material for AMFCs and AMFC performance. *AMFC Workshop.* [En ligne] 8th May 2011. [Citation : 30th July 2013.] http://www1.eere.energy.gov/hydrogenandfuelcells/pdfs/amfc_050811_fukuta.pdf.

154. **Paulus, U.A., Schmidt, T.J., Gasteiger, H.A., Behm, R.J.** Oxygen reduction on a high-surface area Pt/Vulcan carbon catalyst: a thin-film rotating ring-disk electrode study. *Journal of Electroanalytical Chemistry.* 2001, Vol. 495, 134-145.

155. **Bard, A.J., Faulkner, L.R.** *Electrochemical Methods - Fundamentals and Applications - 2nd Edition.* Phoenix, USA : Wiley, 2001. ISBN 978-0-471-04372-0.

156. **Diard, J.-P., Le Gorrec, B., Montella, C.** *Cinétique électrochimique.* Paris, France : Hermann, 1996. ISBN 2 7056 6295 2.

157. **Schmidt, T.J., Ross, P.N., Markovic, N.M.** Temperature-dependent surface electrochemistry on Pt single crystals in alkaline electrolyte: Part 1: CO oxidation. *Journal of Physical Chemistry B.* 2001, Vol. 105, 12082-12086.

158. **Sheng, W., Gasteiger, H.A., Shao-Horn, Y.** Hydrogen oxidation and evolution reaction kinetics on platinum: acid vs alkaline electrolytes. *Journal of The Electrochemical Society.* 2010, Vol. 157, B1529-B1536.

159. **Ramaswamy, N., Mukerjee, S.** Fundamental mechanistic understanding of electrocatalysis of oxygen reduction on Pt and non-Pt surfaces: acid versus alkaline media. *Advances in Physical Chemistry.* 2012, Vol. 2012, Article ID 491604.

160. **Trasatti, S., Petrii, O.A.** Real surface area measurements in electrochemistry. *Journal of Electroanalytical Chemistry.* 1992, Vol. 327, 353-376.

161. **Lefrou, C., Fabry, P., Poignet, J.-C.** *L'électrochimie – Fondamentaux avec exercices corrigés.* Grenoble, France : EDP Sciences, 2009. ISBN 978-2-7598-0425-2.

162. **Zhang, D., Wang, K., Sun, D., Xia, X., Chen, H.** Potentiodynamic deposition of Prussian blue from a solution containing single component of ferricyanide and its mechanism investigation. *Journal of Solid State Electrochemistry.* 2003, Vol. 7, 561-566.

163. **Chatenet, M., Aurousseau, M., Durand, R.** Electrochemical measurement of the oxygen diffusivity and solubility in concentrated alkaline media on rotation ring-disk and disk electrodes – application to industrial chlorine-soda electrolyte. *Electrochimica Acta.* 2000, Vol. 45, 2823-2827.

164. **Ruvinskiy, P.** *Development of novel catalytic layers with controlled architecture based on aligned carbon nano-filaments for fuel cell applications.* Strasbourg : Strasbourg University - PhD thesis, 2011.

165. **Deren, J., Haber, J., Podgorecka, A., Burzyk, J.** Physicochemical and catalytic properties of the system chromium oxides-oxygen-water. *Journal of Catalysis.* 1963, Vol. 2, 161-175.

166. **Minami, T., Ravindranathan, P., Patil, K.C.** Catalytic decomposition of hydrogen peroxide on fine particle ferrites and cobaltites. . *Proceedings of the Indian Academy of Science.* 1987, Vol. 99, 209-215.

167. **Popa, M., Frantti, J., Kakihana, M.** Characterization of LaMeO3 (Me=Mn, Co, Fe) perovskite powders obtained by polymerizable complex method. *Solid State Ionics.* 2002, Vol. 154-155, 135-141.

168. **Royer, S. Levasseur, B., Alamdari, H., Barbier Jr., J., Duprez, D., Kaliaguine, S.** Mechanism of stearic acid oxidation over nanocrystalline La1-xA'xBO3 (A'=Sr, Ce ; B=Co, Mn) : the role of oxygen mobility. *Applied Catalysis B : environmental.* 2008, Vol. 80, 51-61.

169. **Pecchi, G., Campos, C. Pena, O., Cadus, E.** Structural, magnetic and catalytic properties of perovskite-type mixed oxides LaMn1-yCoyO3 (y = 0.0, 0.1, 0.3, 0.5, 0.7, 0.9, 1.0). *Journal of Molecular Catalysis A: Chemical.* 2008, Vol. 282, 158-166.

170. **Navarro, R.M., Alvarez-Galvan, M.C, Villoria, J.A., Gonzalez-Jimenez, I.D., Rosa, F., Fierro, J.L.G.** Effect of Ru on LaCoO3 perovskite-derived catalyst properties tested in oxidative reforming of diesel. *Applied Catalysis B: Environmental.* 2007, Vol. 73, 247-258.

171. **Niu, J., Deng, J., Liu, W., Zhang, L., Wang, G., Dai, H., He, H., Zi, X.** Nanosized perovskite-type oxides La1-xSrxMO3-delta (M = Co, Mn ; x = 0, 0.4) for the catalytic removal of ethylacetate. *Catalysis Today.* 2007, Vol. 126, 420-429.

172. **Singh, R.N., Malviya, M., Anindita, Sinha, A.S.K., Chartier, P.** Polypyrrole and La1-xSrxMnO3 (0<x<0.4) composite electrodes for electroreduction of oxygen in alkaline medium. *Electrochimica Acta.* 2007, Vol. 52, 4264-4271.

173. **Coey, J.M.D., Viret, M., von Molnar, S.** Mixed-valence manganites. *Advances in Physics.* 1999, Vol. 48, 167-293.

174. **Galenda, A., Natile, M.M., Krishnan, V., Bertagnolli, H., Glisenti, A.** LaSrCoFeO and Fe2O3/LaSrCoFeO powders : synthesis and characterisation. *Chemistry of Materials.* 2007 , Vol. 19, 2796-2808.

175. **Nie, M, Shen, P.K., Wu, M., Wei, Z., Meng, H.** A study of oxygen reduction on improved Pt-WC/C electrocatalysts. *Journal of Power Sources.* 2006, Vol. 162 , 173-176.

176. **Park, K.-H., Oh, S.-J.** Electron-spectroscopy study of rare-earth trihalides. *Physical Review B.* 1993, Vol. 48, 14833-14842.

177. **Galenda, A., Natile, M.M., Nodari, L., Glisenti, A.** La0.8Sr0.2Ga0.8Fe0.2O3-delta: Influence of the preparation procedure on reactivity toward methanol and ethanol. *Applied Catalysis B: Environmental.* 2010, Vol. 97, 307-322.

178. **Wang, P., Yao, L., Wang, M., Wu, W.** XPS and voltammetric studies on La1-xSrxCoO3-delta perovskite oxide electrodes. *Journal of Alloys and Compounds.* 2000, Vol. 311, 53-56.

179. **Sunding, M.F., Hadidi, K., Diplas, S., Lovvik, O.M., Norby, T.E., Gunnaes, A.E.** XPS characterisation of in situ treated lanthanum oxide and hydroxide using tailored charge referencing and peak fitting procedures. *Journal of Electron Spectroscopy and Related Phenomena.* 2011, Vol. 184, 399-409.

180. **Moggia, J.M., Milt, V.G., Ulla, M.A., Cornaglia, L.M.** Surface characterization of Co,K/La2O3 catalysts used for the catalytic combustion of diesel soot. *Surface and Interface Analysis.* 2003, Vol. 35, 216-225.

181. **Yaremchenko, A.A., Patricio, S.G., Frade, J.R.** Thermochemical behavior and transport properties of Pr-substituted SrTiO3 as potential solid oxide fuel cell anode. *Journal of Power Sources.* 2014, Vol. 245, 557-569.

182. **Kimura, S.-I., Arai, F., Ikezawa, M.** Mixed valence of praseodymium oxides. *Journal of Electron Spectroscopy and Related Phenomena.* 1996, Vol. 78, 135-138.

183. **Konysheva, E.Y., Francis, S.M.** Identification of surface composition and chemical states in composites comprised of phases with fluorite and perovskite structures by X-ray photoelectron spectroscopy. *Applied Surface Science.* 2013, Vol. 268, 278-287.

184. **Milt, V.G., Ulla, M.A., Lombardo, E.A.** Zirconia-supported cobalt as a catalyst for methane combustion. *Journal of Catalysis.* 2001, Vol. 200, 241-249.

185. **Casella, I.G., Guascito, M.R.** Anodic electrodeposition of conducting cobalt oxyhydroxide films on a gold surface. XPS study and electrochemical behaviour in neutral and alkaline solution. *Journal of Electroanalytical Chemistry.* 1999, Vol. 476, 54-63.

186. **Petitto, S.C., Marsh, E.M., Carson, G.A., Langell, M.A.** Cobalt oxide surface chemistry : the interaction of CoO(100), Co3O4(110) and Co3O4(111) with oxygen and water. *Journal of Molecular Catalysis A: Chemical.* 2008, Vol. 281, 49-58.

187. **Biesinger, M.C., Payne, B.P., Grosvenor, A.P., Lau, L.W.M., Gerson, A.R., Smart, R.St.C.** Resolving surface chemical states in XPS analysis of first row transition metals, oxides and hydroxides: Cr, Mn, Fe, Co and Ni. *Applied Surface Science.* 2011, Vol. 257, 2717-2730.

188. **Bi, L., Kim, H.-S., Dionne, G.F., Ross, C.A.** Structure, magnetic properties and magnetoelastic anisotropy in epitaxial Sr(Ti1-xCox)O3 films. *New Journal of Physics.* 2010, Vol. 12, 1-15.

189. **Yang, W., Salim, J., Li, S., Sun, C., Chen, L., Goodenough, J.B., Kim, Y.** Perovskite Sr0.95Ce0.05CoO3-delta loaded with copper nanoparticles as a bifunctional catalyst for lithium-air batteries. *Journal of Materials Chemistry.* 2012, Vol. 22, 18902-18907.

190. **Gorlin, Y., Lassalle-Kaiser, B., Benck, J.D., Gul, S., Webb, S.M., Yachandra, V.K., Yano, J., Jaramillo, T.F.** In situ X-ray absoprtion spectroscopy investigation of a bifunctional manganese oxide catalyst with high activity for electrochemical water oxidation and oxygen reduction. *Journal of the American Society.* 2013, Vol. 135, 8525-8534.

191. **Falcon, H., Barbero, J.A., Araujo, G., Casais, M.T., Martinez-Lope, M.J., Alonso, J.A., Fierro, J.L.G.** Double perovskite oxides A2FeMoO6-delta (A=Ca, Sr and Ba) as catalysts for methane combustion. *Applied Catalysis B: Environmental.* 2004, Vol. 53, 37-45.

192. **Norman, C., Leach, C.** In situ high temperature X-ray photoelectron spectroscopy study of barium strontium iron cobalt oxide. *Journal of Membrane Science.* 2011, Vol. 382, 158-165.

193. **Vovk, G., Chen, X., Mims, C.A.** In situ XPS studies of perovskite oxide surfaces under electrochemical polarization. *Journal of Physical Chemistry B.* 2005, Vol. 109, 2445-2454.

194. **Wullens, H., Leroy, D., Devillers, M.** Preparation of ternary Bi-La and Bi-Pr oxides from polyaminocarboxylate complexes. *International Journal of Inorganic Materials.* 2001, Vol. 3, 309-321.

195. **Pourbaix, M.** *Atlas of Electrochemical Equilibria in Aqueous Solutions.* Houston, USA : NACE, 1974. ISBN 978-0915567980.

196. **Suzuki, T., Mori, M., Matsunaga, K., Tanaka, I.** Pourbaix diagrams of alkaline earth metal elements by combination of first principles calculations and thermochemical data. *Journal of Physics : Condensed Matter.* 2010, Vol. 22, 384206 (5pp).

197. **Sis, L.B., Wirtz, G.P., Sorenson, S.C.** Structure and properties of reduced LaCoO3. *Journal of Applied Physics.* 1973 , Vol. 44, 5553-5559.

198. **Ferreira, B.M., Melo Jorge, M.E., Lopes, M.E., Nunes, M.R., da Silva Pereira, M.I.** Properties of Ca1-xHoxMnO3 perovskite-type electrodes. *Electrochimica Acta.* 2009, Vol. 54, 5902-5908.

199. **Lima, F.H.B., Calegaro, M.L., Ticianelli, E.A.** Electrocatalytic activity of manganese oxides prepared by thermal decomposition for oxygen reduction. *Electrochimica Acta.* 2007 , Vol. 52, 3732-3738.

200. **Messaoudi, B., Joiret, S., Keddam, M., Takenouti, H.** Anodic behavior of manganese in alkaline medium. *Electrochimica Acta.* 2001, Vol. 46, 2487-2498.

201. **Ruetschi, P., Giovanoli, R.** Cation vacancies in MnO2 and their influence on electrochemical reactivity. *Journal of Electrochemical Society.* 1988, Vol. 135, 2663-2669.

202. **Balachandran, D., Morgan, D., Ceder, G.** First principles study of H-insertion in MnO2 . *Journal of Solid State Chemistry.* 2002, Vol. 166, 91-103.

203. **Pitteloud, C., Nagao, M., Itoh, K., Kanno, R.** The structure of manganese dioxide and position of proton studied by neutron diffraction with isotopic substitution. *Journal of Solid State Chemistry.* 2008, Vol. 181, 467-472.

204. **Appandairajan, N. K., Gopalakrishnan, J.** A study of Co3-xNixO4 (0<x<1) system. *Proceedings of the Indian Academy of Science A.* 1978, Vol. 87, 115-120.

205. **Klose, P.H.** Electrical Properties of Manganese Dioxide and Manganese Sesquioxide. *Journal of Electrochemical Society.* 1970, Vol. 117, 854-858.

206. **Nam, K.-W., Kim, M.G., Kim, K.-B.** In situ Mn K-edge X-ray absorption spectroscopy studies of electrodeposited manganese oxide films for electrochemical capacitors. *Journal of Physical Chemistry C.* 2007, Vol. 111, 749-758.

207. **Singh, R.N., Sharma, T., Singh, A., Anindita, Mishra, D., Tiwari, S.K.** Perovskite-type La2-xSrxNiO4 (0<x<1) as active anode materials for methanol oxidation in alkaline solutions. *Electrochimica Acta.* 2008, Vol. 53, 2322-2330.

208. **Levine, S., Smith, A.L.** Theory of the differential capacity of the oxide/aqueous electrolyte interface. *Discussions of the Faraday Society.* 1971, Vol. 52, 290-301.

209. **Kinoshita, K.** *Carbon - Electrochemical and Physicochemical Properties* . New York : Wiley, 1988. ISBN 978-0471848028.

210. **Song, C., Zhang, J.** 2. Electrocatalytic oxygen reduction reaction. [auteur du livre] J. Zhang. *PEM Fuel Cell Electrocatalysts and Catalyst Layers: Fundamentals and Applications.* London : Springer, 2008, pp. 89-134.

211. **Poux, T., Napolskiy, F.S., Dintzer, T., Kéranguéven, G., Istomin, S.Ya., Tsirlina, G.A., Antipov, E.V., Savinova, E.R.** Dual role of carbon in the catalytic layers of perovskite/carbon composites for the electrocatalytic oxygen reduction reaction. *Catalysis Today.* 2012, Vol. 189, 83-92.

212. **Sarapuu, A., Vaik, K., Schiffrin, D.J., Tammeveski, K.** Electrochemical reduction of oxygen on anthraquinone-modified glassy carbon electrodes in alkaline solution. *Journal of Electroanalytical Chemistry.* 2003, Vol. 541, 23-29.

213. **Baez, V.B., Plechter, D.** Preparation and characterization of carbon/titanium dioxide surfaces – the reduction of oxygen. *Journal of Electroanalytical Chemistry.* 1995, Vol. 382, 59-64.

214. **Jaouen, F.** O2 reduction mechanism on non-noble metal catalysts for PEM fuel cells. Part II: a porous-electrode model to predict the quantity of H2O2 detected by rotating ring-disk electrode. *Journal of Physical Chemistry C.* 2009, Vol. 113, 15433-15443.

215. **Ruvinskiy, P.S., Bonnefont, A., Houlle, M., Pham-Huu, C., Savinova, E.R.** Preparation, testing and modeling of three-dimensionally ordered catalytic layers for electrocatalysis of fuel cell reactions. *Electrochimica Acta.* 2010, Vol. 55, 3245-3256.

216. **Dong, Q., Santhanagopalan, S., White, R.E.** Simulation of the Oxygen Reduction Reaction at an RDE in 0.5 M H2SO4 Including an Adsorption Mechanism. *Journal of The Electrochemical Society.* 2007, Vol. 154, A888-A899.

217. **Wang, Y., Cheng, H.-P.** Oxygen reduction activity on perovskite oxide surfaces : a comparative first-principles study of LaMnO3, LaFeO3, and LaCrO3. *Journal of Physical Chemistry C.* 2013, Vol. 117, 2106-2112.

218. **Goldstein, J.R., Tseung, A.C.C.** Kinetics of oxygen reduction on graphite/cobalt-iron oxide electrodes with coupled heterogeneous chemical decomposition of H2O2. *The Journal of Physical Chemistry.* 1972, Vol. 76, 3646-3656.

219. **Malkhandi, S., Trinh, P., Manohar, A.K., Jayachandrabu, K.C., Kindler, A., Sury Prakash, G.K., Narayanan, S.R.** Electrocatalytic activity of transition metal oxide-carbon composites for oxygen reduction in alkaline batteries and fuel cells. *Journal of the Electrochemical Society.* 2013, Vol. 160, F943-F952.

220. **Gloaguen, F., Andolfatto, F., Durand, R., Ozil, P.** Kinetic study of electrochemical reactions at catalyst-recast ionomer interfaces from thin active layer modelling. *Journal of Applied Electrochemistry.* 1994, Vol. 24, 863-869.

221. **Stoerzinger, K.A., Risch, M., Suntivich, J., Lu, W.M., Zhou, J., Biegalski, M.D., Christen, H.M., Ariando, Venkatesan, T., Shao-Horn, Y.** Oxygen electrocatalysis on (001)-oriented manganese perovskite films: Mn valency and charge transfer at the nanoscale. *Energy and Environmental Science.* 2013, Vol. 6, 1582-1588.

222. **Gyenge E.L., Drillet, J.F.** The electrochemical behavior and catalytic activity for oxygen reduction of MnO2/C-Toray gas diffusion electrodes. *Journal of the Electrochemical Society.* 2012, Vol. 159, F23-F34.

223. **Su, H.Y., Gorlin, Y., Man, I.C., Calle-Vallejo, F., Norskov, J.K., Jaramillo, T.F., Rossmeisl, J.** Identifying active surface phases for metal oxide electrocatalysts: a study of

manganese oxide bi-functional catalysts for oxygen reduction and water oxidation catalysis. *Physical Chemistry Chemical Physics.* 2012, Vol. 14, 14010-14022.

224. **Park, J.-N., Shon, J.K., Jin, M., Hwang, S.H., Park, G.O., Boo, J.-H., Han, T.H., Kim, J.M.** Highly ordered mesoporous alpha-Mn2O3 for catalytic decomposition of H2O2 at low temperatures. *Chemical Letters.* 2010, Vol. 39, 493-495.

225. **Zhang, W., Wang, H., Yang, Z., Wang, F.** Promotion of H2O2 decompostion activity over beta-MnO2 nanorod catalysts. *Colloids and Surface A : Physicochemical Engineering Aspects.* 2007, Vol. 304, 60-66.

226. **Chen, W., Wang, N., Liu, L., Cui, Y., Cao, X., Chen, Q., Guo, L.** Facile synthesis of manganite nanowires: phase transitions and their electrocatalysis performance. *Nanotechnology.* 2009, Vol. 20, 445601 (8pp).

227. **Jaouen, F., Dodelet, J.-P.** O2 reduction mechanism on non-noble metal catalysts for PEM fuel cells. Part I: experimental rates of O2 electroreduction, H2O2 electroreduction, and H2O2 disproportionation. *Journal of Physical Chemistry C.* 2009, Vol. 113, 15422-15432.

228. **Jiang, S.P., Lin, Z.G., Tseung, A.C.C.** Homogeneous and heterogeneous catalytic reactions in cobalt oxide/graphite air electrodes. I. Chemical kinetics of peroxide decomposition by Co(II) ions in alkaline solutions. *Journal of Electrochemical Society.* 1990, Vol. 137, 759-764.

229. **Ruvinskiy, P.S., Bonnefont, A., Pham-Huu, C., Savinova, E.R.** Using ordered carbon nanomaterials for shedding light on the mechanism of the cathodic oxygen reduction reaction. *Langmuir.* 2011 , Vol. 27, 9018–9027.

230. **Shih, Y.-H., Sagar, G.V., Lin, S.D.** Effect of electrode Pt loading on the oxygen reduction reaction evaluated by rotating disk electrode and its implication on the reaction kinetics. *Journal of Physical Chemistry C.* 2008, Vol. 112, 123-130 .

231. **Inaba, M., Yamada, H., Tokunaga, J., Tasaka, A.** Effect of agglomeration of Pt/C catalyst on hydrogen peroxide formation. *Electrochemical and Solid-State Letters.* 2004, Vol. 7, A474-A476.

232. **Bonakdarpour A., Lefevre, M., Yang, R., Jaouen, F., Dahn, T., Dodelet, J.-P., Dahn, J.R.** Impact of loading in RRDE experiments on Fe-N-C catalysts: two- or four-electron oxygen reduction ? . *Electrochemical and Solid-State Letters.* 2008, Vol. 11, B105-B108.

233. **Prabhu, V.G., Zarapkar, L.R., Dhaneshwar, R.G.** Electrochemical studies of hydrogen peroxide at a platinum disc electrode. *Electrochimica Acta* . 1981, Vol. 26, 725-729 .

234. **Katsounaros I., Schneider, W.B., Meier, J.C., Benedikt, U., Biedermann, P.U., Auer, A.A., Mayrhofer, J.J.** Hydrogen peroxide electrochemistry on platinum: towards understanding the oxygen reduction reaction mechanism. *Physical Chemistry Chemical Physics.* 2012, Vol. 14, 7384-7391.

235. **Gomez-Marin, A.M., Schouten, K.J.P., Koper, M.T.M., Feliu, J.M.** Interaction of hydrogen peroxide with a Pt(111) electrode. *Electrochemistry Communications.* 2012, Vol. 22, 153-156.

236. **Paliteiro, C., Hamnett, A., Goodenough, J.B.** The electroreduction of dioxygen on thin films of gold in alkaline solution. *Journal of Electroanalytical Chemistry.* 1987, Vol. 234, 193-211 .

237. —. The electroreduction of oxygen on pyrolytic graphite. *Journal of Electroanalytical Chemistry.* 1987, Vol. 233, 147-159.

238. **Van den Brink, F., Visscher, W., Barendrecht, E.** Electrocatalysis of cathodic oxygen reduction by metal phthalocyanines. Part III. Iron phthalocyanine as electrocatalyst: experimental part. *Journal of Electroanalytical Chemistry.* 1984, Vol. 172, 301-325.

239. **Sitta, E., Gomez-Marin, A.M., Aldaz, A., Feliu, J.M.** Electrocatalysis of H2O2 reduction/oxidation at model platinum surfaces. *Electrochemistry Communications.* 2013, Vol. 33, 39-42.

240. **Hall, S.B., Khudaish, E.A., Hart, A.L.** Electrochemical oxidation of hydrogen peroxide at platinum electrodes. Part II : effect of potential. *Electrochimica Acta.* 1998, Vol. 43, 2015-2024.

241. **Bianchi, G., Mazza, F., Mussini, T.** Catalytic decomposition of acid hydrogen peroxide solutions on platinum, iridium, palladium and gold surfaces. *Electrochimica Acta.* 1962, Vol. 7, 457-473.

242. **Savinova, E.R, Wasle, S., Doblhofer, K.** Structure and activity relations in the hydrogen peroxide reduction at silver electrodes in alkaline NaF/NaOH electrolytes. *Electrochimica Acta.* 1998, Vol. 44, 1341-1348 .

243. **Kanungo, S.B., Parida, K.M., Sant, B.R.** Studies on MnO2 – III. The kinetics and the mechanism for the catalytic decomposition of H2O2 over different crystalline modifications of MnO2. *Electrochimica Acta.* 1981, Vol. 26, 1157-1167.

244. **Jia, W., Guo, M., Zheng, Z., Yu, T., Rodriguez, E.G., Wang, Y., Lei, Y.** Electrocatalytic oxidation and reduction of H2O2 on vertically aligned Co3O4 nanowalls electrode : towards H2O2 detection. *Journal of Electroanalytical Chemistry.* 2009, Vol. 625, 27-32.

245. **Lousada, C.M., Johansson, A.J., Brinck, T., Jonsson, M.** Mechanism of H2O2 decomposition on transition metal oxide surfaces. *Journal of Physical Chemistry C.* 2012, Vol. 116, 9533-9543.

246. **Lin, S.-S., Gurol, M.D.** Catalytic decomposition of hydrogen peroxide on iron oxide: kinetics, mechanism, and implications. *Environmental Science and Technology.* 1998, Vol. 32, 1417-1423.

247. **Venkatachalapathy, R., Davila, G.P., Prakash, J.** Catalytic decomposition of hydrogen peroxide in alkaline solutions . *Electrochemistry Communications.* 1999, Vol. 1, 614-617.

248. **Fu, D., Keech, P.G., Shoesmith, D.W., Wren, J.C.** An electrochemical study of H2O2 decomposition on single-phase gamma-FeOOH films. *Electrochimica Acta.* 2010, Vol. 55, 3787-3796.

249. **Deraz, N.A.M.** Catalytic decomposition of H2O2 on promoted cobaltic oxide catalysts. *Materials Letters.* 2002, Vol. 57, 914-920.

250. **Goldstein, J.R., Tseung, A.C.C.** The kinetics of hydrogen peroxide decomposition catalyzed by cobalt-iron oxides. *Journal of Catalysis.* 1974, Vol. 32, 452-465.

251. **Cao, D., Sun, L., Wang, G., Lv, Y., Zhang, M.** Kinetics of hydrogen peroxide electroreduction on Pd nanoparticles in acidic medium. *Journal of Electroanalytical Chemistry.* 2008, Vol. 621, 31-37.

252. **Riche, E., Carrié, A., Andin, N., Mabic, S.** *High-purity water and pH.* s.l. : American Laboratory News, 2006. http://www.millipore.com/references/files/pmc_url/$file/highpuritywater.pdf.

253. **Zagrebin, P.** Unpublished results.

254. **Dean, J.** *Lange's Handbook of Chemistry - 15th edition* . New York : McGraw-Hill, 1999.

255. **Kinumoto, T., Takai, K., Iriyama, Y., Abe, T., Inaba, M., Ogumi, Z.** Stability of Pt-catalyzed highly oriented pyrolytic graphite against hydrogen peroxide in acid solution. *Journal of the Electrochemical Society.* 2006 , Vol. 153, A58-A63.

256. **Roche, I, Chainet, E., Chatenet, M., Vondrak, J.** Durability of carbon-supported manganese oxide nanoparticles for the oxygen reduction reaction (ORR) in alkaline medium. *Journal of Applied Electrochemistry.* 2008, Vol. 38, 1195-1201.

Appendix

Appendix 1 : Reproducibility of some electrochemical experiments

In this section, the reproductibity of some electrochemical experiments are shown. However, it should be noted that numerous other experiments were performed – each of the experiments shown in this thesis was made at least twice – but are not shown to limit the number of pages.

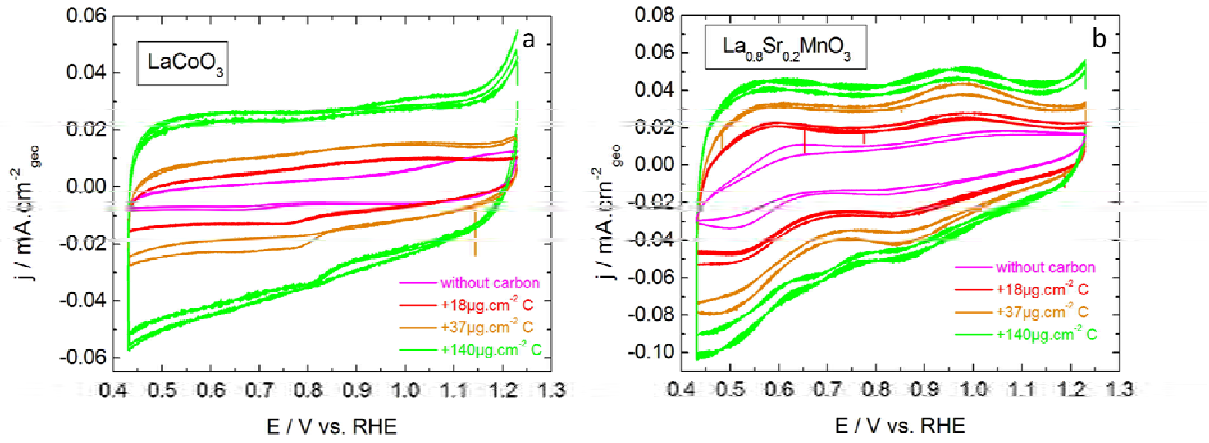

Figure 94 : *Reproducibility of CV of GC-supported thin films of (a) $LaCoO_3$ + Sibunit carbon and (b) $La_{0.8}Sr_{0.2}MnO_3$+ Sibunit carbon in N_2-purged 1M NaOH electrolyte at 10 mV.s^{-1}. Measurements were performed with a constant amount of perovskite (91 µg.cm$^{-2}_{geo}$) and variable amount of carbon. Color codes for carbon loading: 0 (pink), 18 (red), 37 (orange) and 140 µg.cm$^{-2}_{geo}$ (green). Currents are normalized to the geometric area of the electrode.*

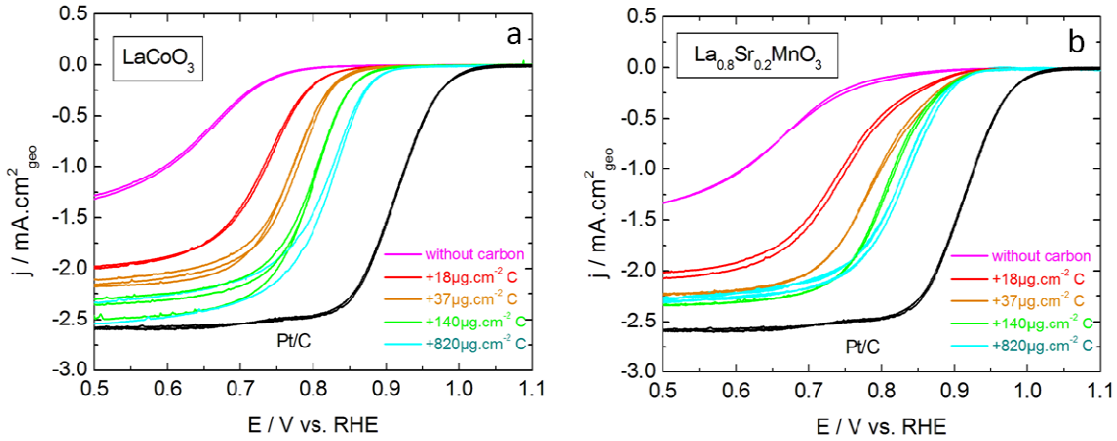

Figure 95 : *Reproducibility of positive scans of the RDE voltammograms of GC-supported thin films of (a) $LaCoO_3$ + Sibunit carbon and (b) $La_{0.8}Sr_{0.2}MnO_3$+ Sibunit carbon, in O_2-saturated 1M NaOH electrolyte at 900 rpm and 10 $mV.s^{-1}$. Measurements were performed with a constant amount of perovskite (91 $\mu g.cm^{-2}_{geo}$) and variable amount of carbon. Color codes for carbon loading: 0 (pink), 18 (red), 37 (orange) and 140 µg.cm-2geo (green). Black lines show RDE curves for Pt/C. Currents are normalized to the geometric area of the electrode and corrected to the background currents measured in the N_2 atmosphere.*

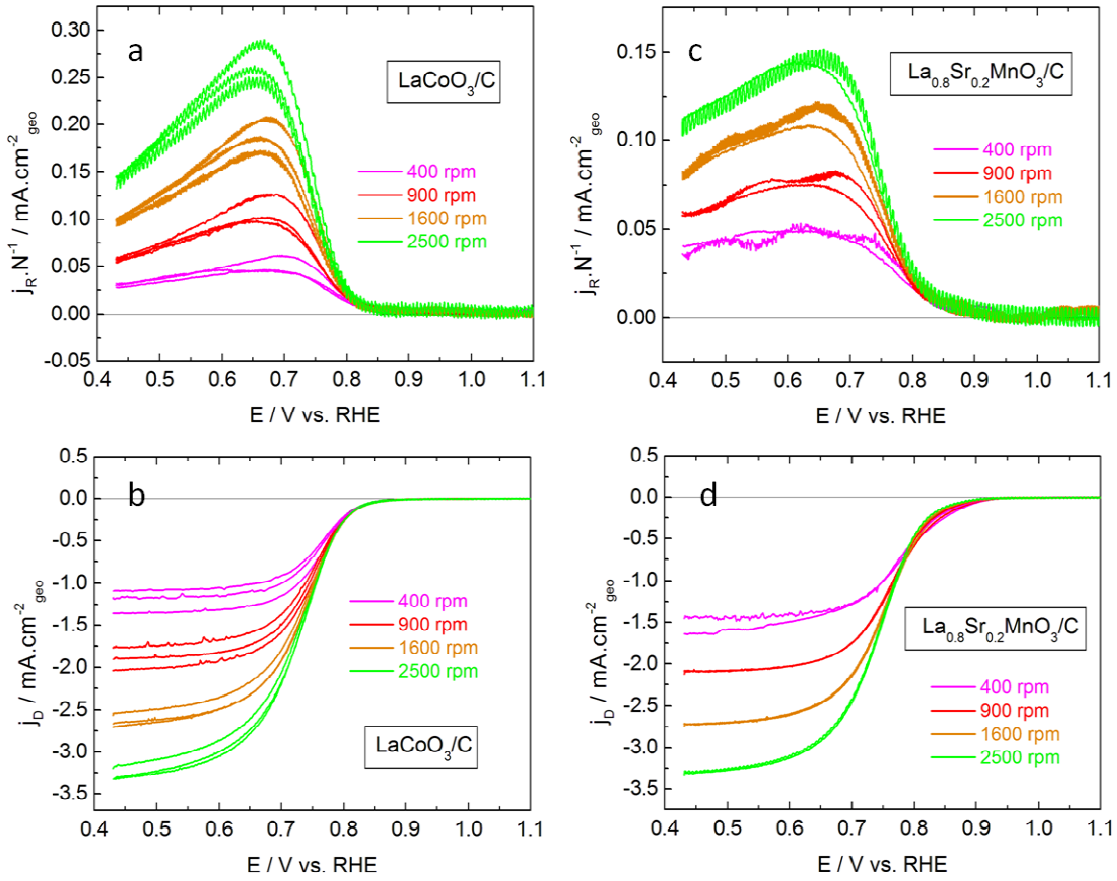

Figure 96 : *Reproducibility of positive scans of the RRDE voltammograms of GC-supported thin films of (a,b) $LaCoO_3$ + Sibunit and (c,d) $La_{0.8}Sr_{0.2}MnO_3$ + Sibunit in O_2-saturated 1M NaOH at various rotation rates and 10 mV.s^{-1} : (a,c) ring currents at 1.23V vs. RHE versus disk potential, (b,d) disk voltammograms. Measurements were performed with 46 µg.cm$^{-2}_{geo}$ perovskite and 19 µg.cm$^{-2}_{geo}$ carbon. Color codes for electrode rotation rate: 400 rpm (pink), 900 rpm (red), 1600 rpm (orange) and 2500 rpm (green). Disk currents are normalized to the geometric area of the disk electrode and corrected to the background currents measured in the N_2 atmosphere. Ring currents are normalized to the geometric area of the disk electrode and to the collection factor.*

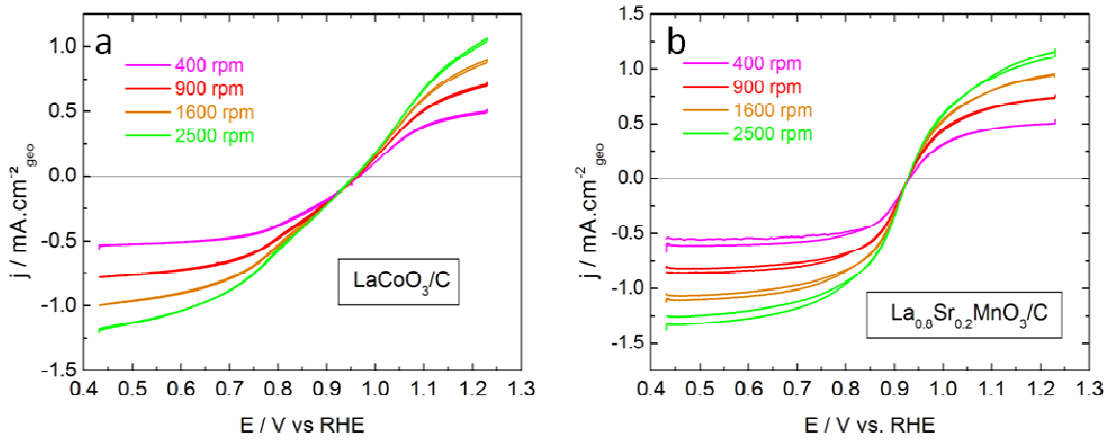

Figure 97 : *Reproducibility of positive scans of the RDE voltammograms of GC-supported thin films of (a) $LaCoO_3$ + Sibunit carbon and (b) $La_{0.8}Sr_{0.2}MnO_3$+ Sibunit carbon, in N_2-purged 1M NaOH + 0.84 mM H_2O_2 at various rotation rates and at 10 mV.s^{-1}. Measurements were performed with 91 µg.cm$^{-2}_{geo}$ perovskite and 37 µg.cm$^{-2}_{geo}$ carbon. Color codes for rotation rates: 400 rpm (pink), 900 rpm (red), 1600 rpm (orange) and 2500 rpm (green). Currents are normalized to the geometric area of the electrode and corrected to the background currents measured in the N_2 atmosphere without H_2O_2 presence.*

Appendix 2 : La3d XPS spectrum of perovskite oxide – Literature data

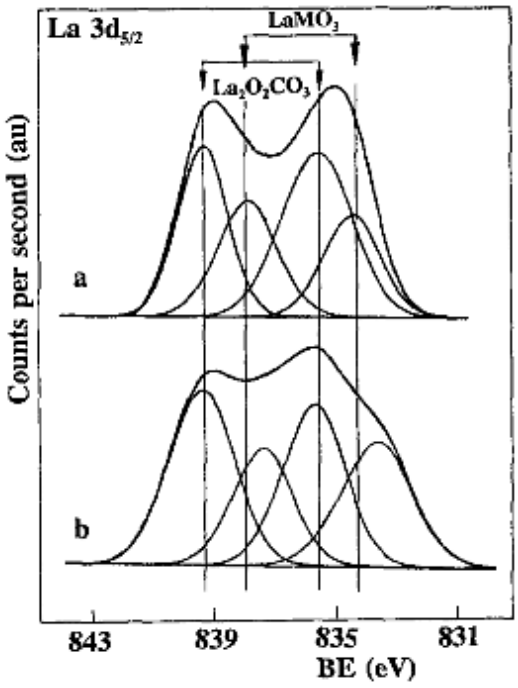

Figure 98 : *Literature data reprinted from [46] with the permission of Springer.*

La $3d_{5/2}$ core level spectra of: (a) $LaFeO_3$; and (b) $LaCoO_3$. The two arrow sets correspond to $LaMO_3$ (M=Fe,Co) and $La_2O_2CO_3$ species.

Appendix 3 : ORR and HO_2^- reduction on $LaMnO_3$

In this section, the RRDE study of ORR and the RDE study of HO_2^- reduction/oxidation reactions are presented for $LaMnO_3$ electrodes.

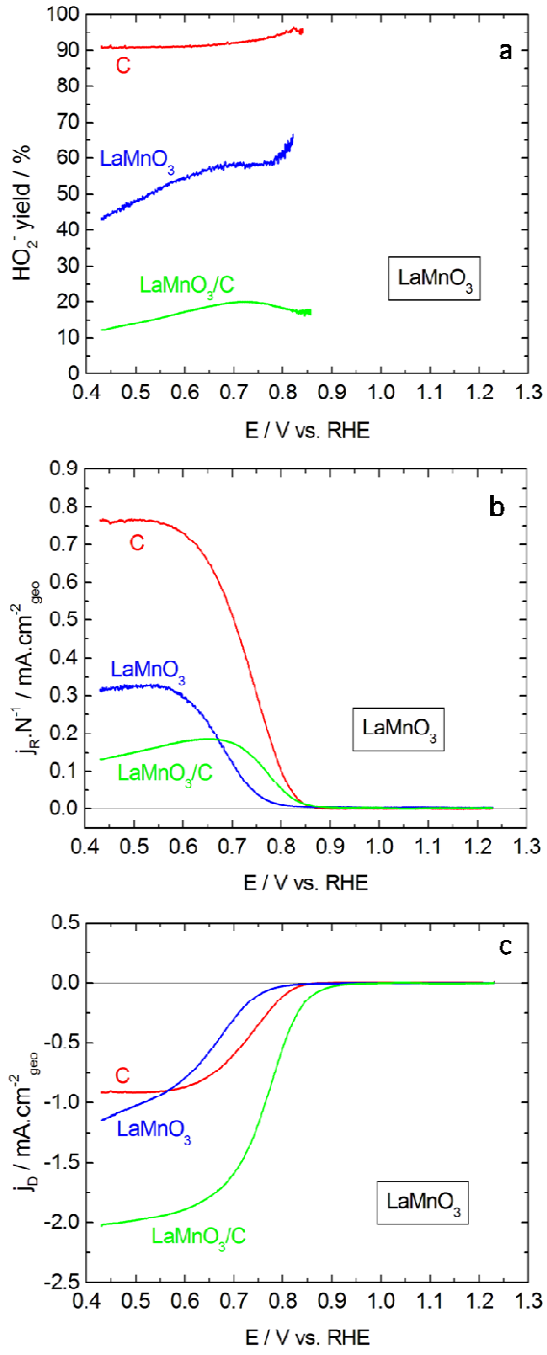

Figure 99 : *Positive scans of the RRDE voltammograms of GC-supported thin films of $LaMnO_3$ in O_2-saturated 1M NaOH at 900 rpm and 10 mV.s^{-1} : (a) percentage of H_2O_2 formed, (b) ring currents at 1.23V vs. RHE versus disk potential, (c) disk voltammograms. Measurements were performed for electrodes containing only perovskite, for electrodes containing only carbon, and for composite perovskite/carbon electrodes. Color codes for electrode composition: 46 µg.cm$^{-2}_{geo}$ perovskite (blue), 46 µg.cm$^{-2}_{geo}$ perovskite + 19 µg.cm$^{-2}_{geo}$ carbon (green), 19 µg.cm$^{-2}_{geo}$ carbon (red). Disk currents are normalized to the geometric area of the disk electrode and corrected to the background currents measured in the N_2 atmosphere. Ring currents are normalized to the geometric area of the disk electrode and to the collection factor.*

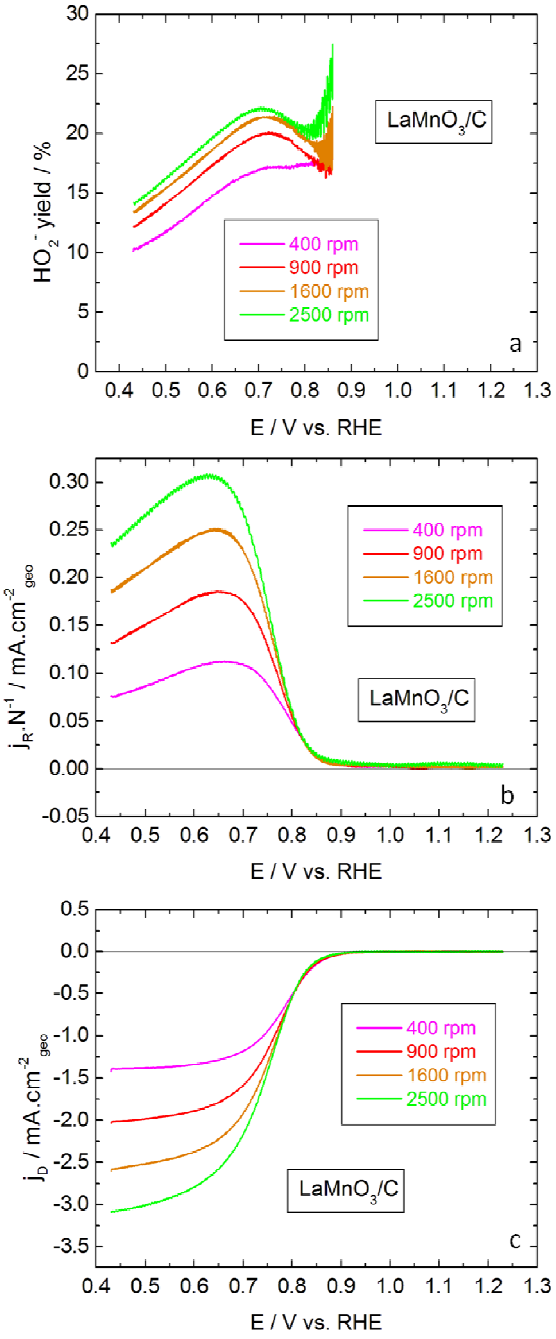

Figure 100 : *Positive scans of the RRDE voltammograms of GC-supported thin films of $LaMnO_3$ + Sibunit in O_2-saturated 1M NaOH at various rotation rates and 10 mV.s^{-1} : (a) percentage of H_2O_2 formed, (b) ring currents at 1.23V vs. RHE versus disk potential, (c) disk voltammograms. Measurements were performed with 46 µg.cm$^{-2}_{geo}$ perovskite and 19 µg.cm$^{-2}_{geo}$ carbon. Color codes for electrode rotation rate: 400 rpm (pink), 900 rpm (red), 1600 rpm (orange) and 2500 rpm (green). Disk currents are normalized to the geometric area of the disk electrode and corrected to the background currents measured in the N_2 atmosphere. Ring currents are normalized to the geometric area of the disk electrode and to the collection factor.*

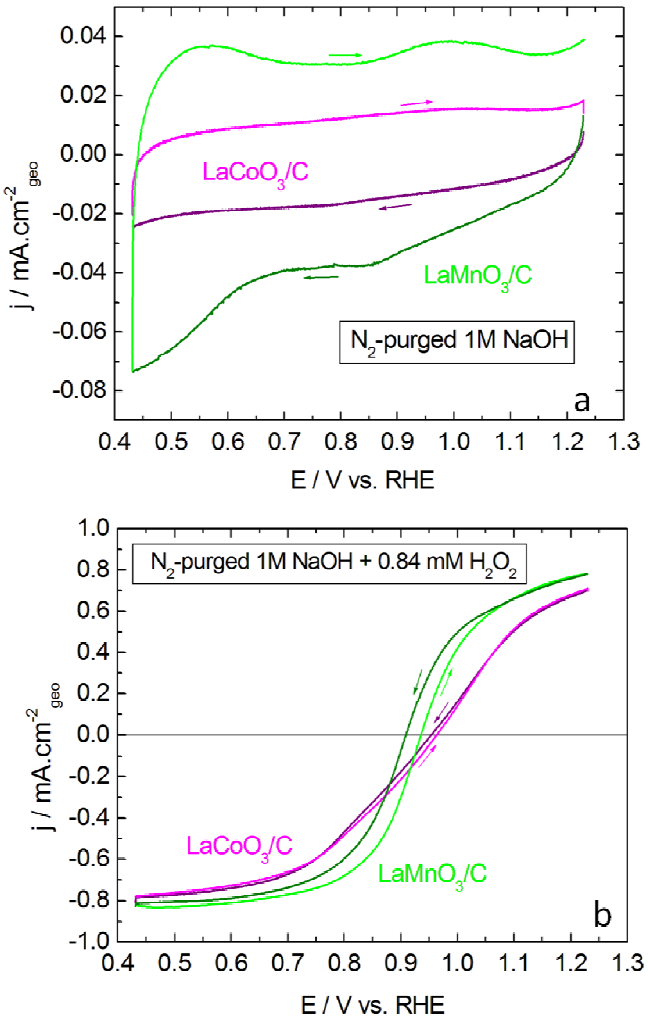

Figure 101 : *Negative and positive scans of (a) CV in N_2-purged 1M NaOH at 0 rpm and (b) RDE voltammograms in N_2-purged 1M NaOH + 0.84mM H_2O_2 at 900rpm, of GC-supported thin films at 10 mV.s^{-1}. Measurements were performed with 91 µg.cm$^{-2}_{geo}$ perovskite + 37 µg.cm$^{-2}_{geo}$ carbon. Color codes: $LaCoO_3$ (pink for positive scan and purple for negative scan) and $LaMnO_3$ (green for positive scan and olive for negative scan), the arrows indicate the scan direction. Currents are normalized to the geometric area of the electrode. For RDE voltammograms in N_2-purged 1M NaOH + 0.84mM H_2O_2, the currents are corrected to the background currents measured in the N_2 atmosphere without H_2O_2 presence.*

Appendix 4 : Modeling of ORR on $LaCoO_3$ electrodes with faster HO_2^- reduction

This section presents the modeling of ORR on $LaCoO_3$ electrode using $k_{5,P} = 0.2\ s^{-1}$, i.e. the same rate constant as $La_{0.8}Sr_{0.2}MnO_3$ for the O_{ads} reduction reaction.

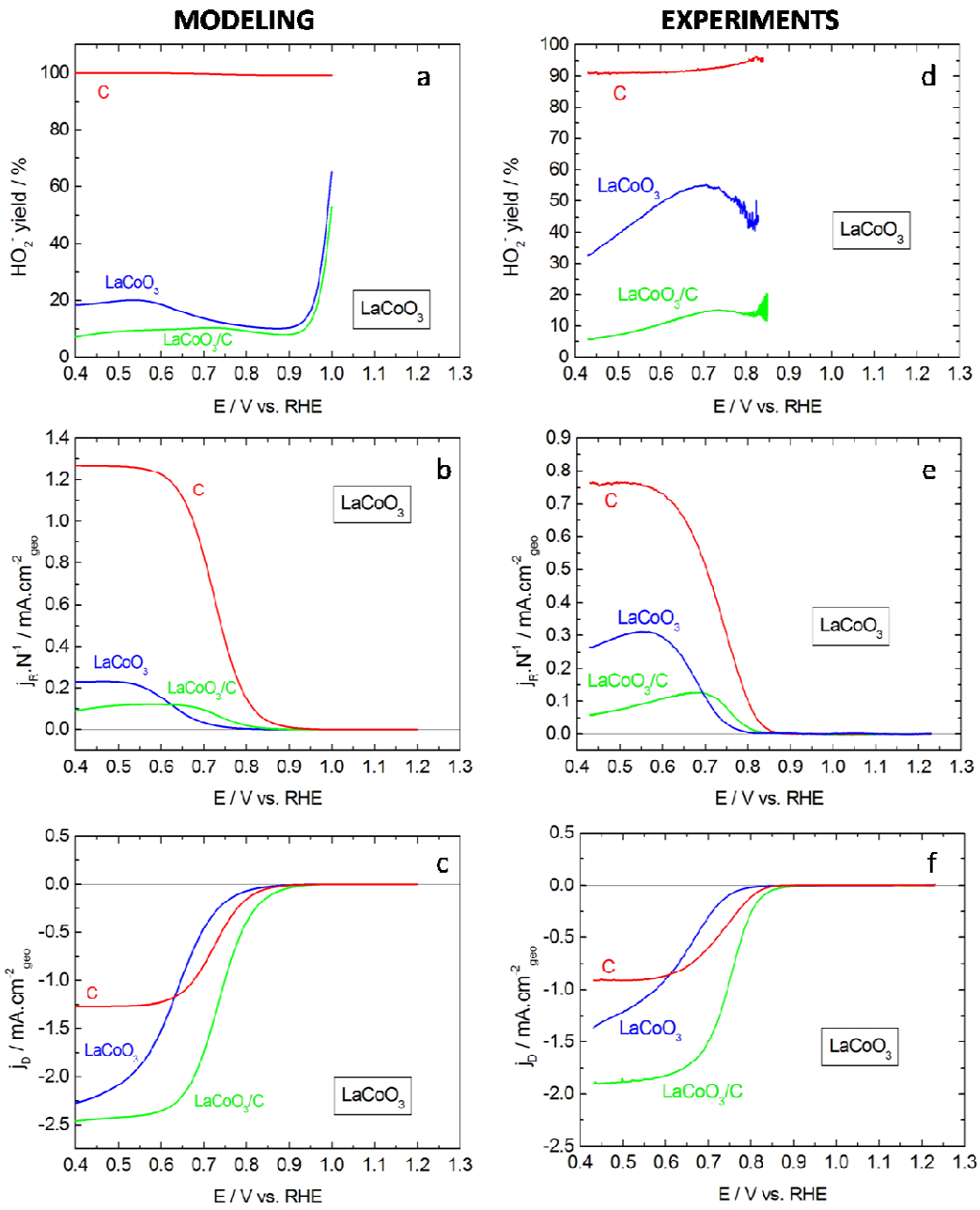

Figure 102 : *RRDE voltammograms of GC-supported thin films of $LaCoO_3$ + Sibunit carbon in O_2-saturated 1M NaOH at 900 rpm: (a,b,c) simulated curves with $k_{5,P}$ = 0.2 s^{-1} and (d,e,f) experimental positive scans at 10 $mV.s^{-1}$. (a,d) Percentage of HO_2^- formed, (b,e) ring currents versus disk potential, (c,f) disk voltammograms. Measurements were performed for electrodes containing only perovskite, for electrodes containing only Sibunit carbon, and for composite perovskite + Sibunit carbon electrodes. Color codes for electrode composition: 46 $\mu g.cm^{-2}_{geo}$ perovskite (blue), 46 $\mu g.cm^{-2}_{geo}$ perovskite + 19 $\mu g.cm^{-2}_{geo}$ Sibunit carbon (green), 19 $\mu g.cm^{-2}_{geo}$ Sibunit carbon (red). Disk currents are normalized to the geometric area of the disk electrode and corrected to the background currents measured in the N_2 atmosphere for the experimental curves. Ring currents are normalized to the geometric area of the disk electrode and to the collection factor.*

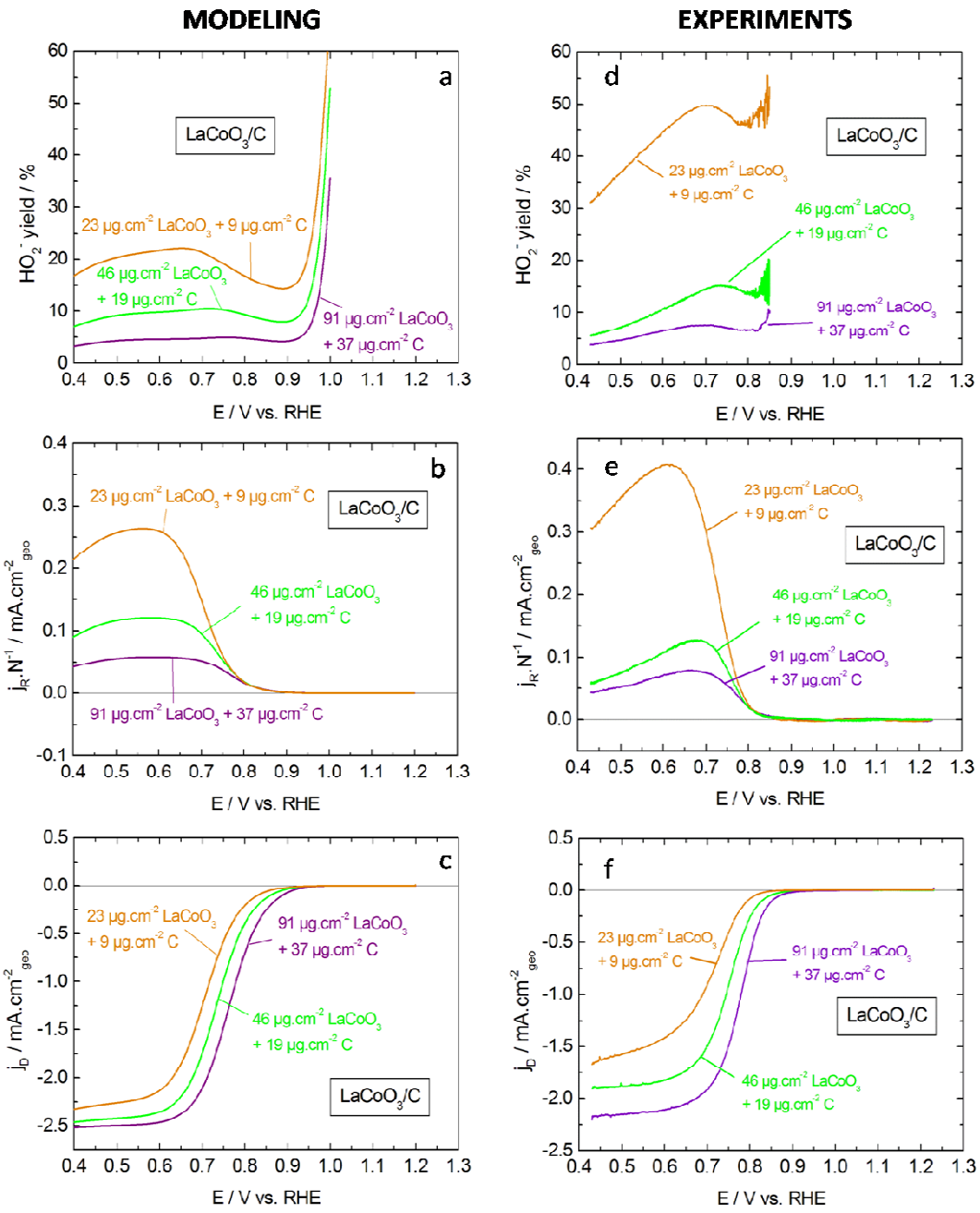

Figure 103 : *RRDE voltammograms of GC-supported thin films of $LaCoO_3$ + Sibunit carbon in O_2-saturated 1M NaOH at 900 rpm: (a,b,c) simulated curves with $k_{5,P}$ = 0.2 s^{-1} and (d,e,f) experimental positive scans at 10 $mV.s^{-1}$. (a,d) Percentage of HO_2^- formed, (b,e) ring currents versus disk potential, (c,f) disk voltammograms. Measurements were performed for electrodes containing constant perovskite/carbon ratio (71 wt.% perovskite + 29 wt.% Sibunit carbon,) and various catalyst loadings. Color codes for electrode loading: 23 $\mu g.cm^{-2}_{geo}$ perovskite + 9 $\mu g.cm^{-2}_{geo}$ Sibunit carbon (orange), 46 $\mu g.cm^{-2}_{geo}$ perovskite + 19 $\mu g.cm^{-2}_{geo}$ Sibunit carbon (green), 91 $\mu g.cm^{-2}_{geo}$ perovskite + 37 $\mu g.cm^{-2}_{geo}$ Sibunit carbon (purple). Disk currents are normalized to the geometric area of the disk electrode and corrected to the background currents measured in the N_2 atmosphere for the experimental curves. Ring currents are normalized to the geometric area of the disk electrode and to the collection factor.*

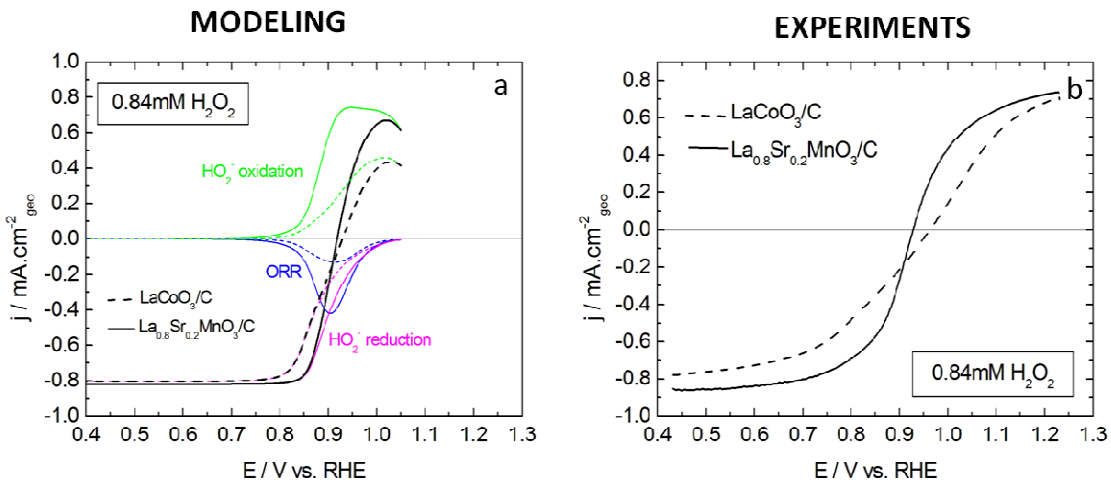

Figure 104 : *RDE voltammograms of GC-supported thin films of $La_{0.8}Sr_{0.2}MnO_3$ + Sibunit carbon (solid lines) or of $LaCoO_3$ + Sibunit carbon (dash lines) in N_2-purged 1M NaOH + 0.84 mM H_2O_2 at 900 rpm: (a) simulated curves with $k_{5,P} = 0.2\ s^{-1}$ and (b) experimental positive scans at 10 $mV.s^{-1}$. Measurements were performed with 91 $\mu g.cm^{-2}_{geo}$ perovskite + 37 $\mu g.cm^{-2}_{geo}$ Sibunit carbon. Color codes for the model contributions: HO_2^- reduction contribution (pink), O_2 reduction contribution (blue), HO_2^- oxidation contribution (green) and total current obtained by the addition of the previous mentioned contributions (black). Currents are normalized to the geometric area of the electrode and corrected to the background currents measured in the N_2 atmosphere in the absence of H_2O_2 for the experimental curves.*

Résumé détaillé

A. Introduction et objectifs

Face au besoin croissant d'énergie et au souci de l'environnement, les piles à combustible représentent une technologie de conversion d'énergie attractive. Parmi les piles existantes et en cours de développement, la pile à combustible alcaline à membrane échangeuse d'anion (SAFC) est un système prometteur qui permet l'utilisation de matériaux peu couteux.
Bien que la réaction de réduction de l'oxygène (ORR) en milieu alcalin soit souvent plus rapide qu'en milieu acide, il s'agit tout de même d'un procédé très lent qui limite largement les performances des piles. Ainsi, de nombreuses études ont été effectuées dans le but de trouver les catalyseurs les plus actifs et stables pour cette réaction.
En milieu alcalin, comme en milieu acide, les métaux nobles sont très actifs pour l'ORR. Cependant, contrairement au milieu acide, de nombreux matériaux dont certains sans métaux nobles comme le carbone [a,b] et des oxydes de métaux de transition ont démontré des activités notables pour l'ORR en milieu alcalin. Parmi ces matériaux, les oxydes de type pérovskite apparaissent comme des catalyseurs prometteurs vis-à-vis de leur activité pour l'ORR et de leur prix [c,d]. Le présent travail de doctorat est donc focalisé sur l'étude de ces oxydes dont le comportement catalytique n'est pas encore complétement compris.

La structure flexible des pérovskites tolère une large gamme de compositions $A_{1-x}A'_xB_{1-y}B'_yO_3$ et offre donc la possibilité d'adapter les propriétés physico-chimiques des oxydes [e,f]. Ces oxydes ont ainsi démontré des propriétés intéressantes pour la catalyse hétérogène, les piles à combustible à hautes températures (SOFC), ainsi que pour l'ORR et l'OER à basses températures [g,h]. Il est désormais accepté que la nature du cation en position B a une grande influence sur l'activité vis-à-vis de l'ORR et le dopage du cation en position A par un cation de plus petite valence peut augmenter la cinétique de l'ORR. Parmi les diverses compositions de pérovskites, les pérovskites à base de Mn et de Co font partie des oxydes les plus actifs. Il a donc été choisi dans ce travail de se focaliser sur les pérovskites dopées et non dopées de Mn et Co afin de déterminer les relations entre leurs propriétés intrinsèques et leurs activités catalytiques.
Dans la littérature, une large gamme de configuration d'électrodes a été utilisée pour mesurer l'activité pour l'ORR des pérovskites comme les pastilles, les couches de diffusion de gaz ou les couches minces. Cependant, seule l'approche couche mince est compatible avec les techniques d'électrode à disque tournant (RDE) et d'électrode tournante à disque-anneau

(RRDE) [c,i]. Grâce à ces techniques en milieu liquide, les courants cinétiques peuvent être mesurés de manière précise et des informations concernant le mécanisme de l'ORR peuvent être obtenues. Ainsi, un électrolyte liquide et des couches minces de pérovskites ont été utilisés dans ce travail.

Cependant, les électrodes à base de pérovskite souffrent généralement d'une grande résistance entre les particules (ou agglomérats) d'oxydes. Ceci limite non seulement l'étude de l'ORR mais aussi l'intégration de ces oxydes comme matériaux de cathode dans les piles à combustible. L'ajout de carbone augmente de façon significative la conductivité, et donc la performance, des électrodes de pérovskite [j,k]. Néanmoins, le carbone est également actif pour l'ORR en milieu alcalin [a,b] et son activité peut interférer avec celle des pérovskites. Dans ce travail de doctorat, le rôle du carbone dans le mécanisme de l'ORR sur les électrodes composites pérovskite/carbone a été étudié en variant de manière systématique le rapport pérovskite:carbone. L'évaluation de l'activité intrinsèque des pérovskites pour l'ORR est également une question abordée dans ce travail.

L'ORR suit un mécanisme complexe qui implique la formation de l'intermédiaire HO_2^- s'il a lieu via le mécanisme « en série ». Dans la littérature, quelques contradictions ont été soulevées à propos du mécanisme ayant lieu sur les électrodes à base de pérovskites. En effet, certains auteurs mentionnent un mécanisme « direct », c'est-à-dire sans formation d'HO_2^- [l], alors que d'autres suggèrent un mécanisme « en série » [m,n]. Ceci peut être le résultat de l'utilisation de différentes configurations d'électrodes, différentes compositions d'oxydes et/ou différentes quantités de catalyseurs. Pour éclaircir ce point, l'impact de la composition de l'électrode en termes de quantité de pérovskite et de carbone ainsi que de nature de l'oxyde sur la production d'HO_2^- lors de l'ORR a été étudiée au cours de cette thèse grâce à la technique RRDE.

Si l'ORR est effectivement un mécanisme « en série » avec production d'HO_2^-, la mesure de la cinétique de transformation de cet intermédiaire est nécessaire pour la compréhension du mécanisme. Des travaux antérieurs ont montré que la cinétique de décomposition d'HO_2^- est fortement dépendante de la nature du cation en position B de la pérovskite. Par contre, très peu de résultats ont été rapportés sur la réduction électrochimique d'HO_2^- sur les pérovskites, la cinétique de cette réaction reste donc aujourd'hui inconnue. Le présent travail inclut l'étude des réactions de réduction/oxydation et de décomposition d'HO_2^- sur diverses pérovskites afin d'étendre la compréhension de l'ORR.

Enfin, dans le but d'utiliser les oxydes de type pérovskites comme matériaux de pile à combustible, une stabilité sur le long terme est requise. D'une part, il a été rapporté dans la littérature que certaines pérovskites se dégradent en milieu alcalin [o]. D'autre part, la stabilité de l'activité électrocatalytique n'est pas étudiée de manière systématique, bien qu'indispensable pour une application industrielle. Ainsi, les stabilités chimiques et électrochimiques des oxydes ont été explorées dans cette étude. Ceci implique non seulement le suivi de l'activité électrocatalytique au cours du temps, mais aussi la caractérisation des matériaux après éventuelle dégradation.

Pour résumer, cette thèse regroupe des études cinétiques, mécanistiques et de stabilité pour diverses compositions d'électrodes. Dans la littérature, ces études sont rarement combinées mais permettent une complète compréhension de l'électrocatalyse de l'ORR. Ce travail permet donc de relier des études fondamentales de l'ORR à des applications potentielles des pérovskites comme matériaux de cathodes dans les SAFC.

B. Propriétés des oxydes de type pérovskite

Les pérovskites utilisées dans ce travail ont été synthétisées par chimie douce par des partenaires de l'Université de Moscou. Les pérovskites choisies étaient principalement $LaCoO_3$, $LaMnO_3$ et $La_{0.8}Sr_{0.2}MnO_3$ afin d'étudier l'influence de la nature du cation B et de l'effet du dopage du cation A par un cation de plus petite valence sur l'ORR. Afin de vérifier l'effet de la nature du cation A, les propriétés des pérovskites $La_{0.8}Ca_{0.2}MnO_3$, $PrCoO_3$ et $PrMnO_3$ ont également été analysées.

Avant d'être utilisés comme catalyseurs de l'ORR, les oxydes ont été caractérisés par diverses techniques physico-chimiques afin de pouvoir relier leur comportement catalytique à leurs propriétés.
Grâce à la diffraction aux rayons X (DRX), il a été montré que les oxydes utilisés dans ce travail présentaient effectivement la structure pérovskite sans traces des précurseurs. Cette structure est stable après stockage dans des conditions atmosphériques durant plusieurs mois, seuls quelques traces de carbonates ont pu être observées après vieillissement. La symétrie de la structure est apparue comme étant dépendante de la taille du cation A. En effet, les

pérovskites à base de La et Sr étaient de structure rhombohédrale alors que celles à base de Pr et Ca, cations de plus petits rayons, étaient de structure orthorhombique.

La microscopie électronique à balayage (MEB) a été utilisée pour étudier la morphologie des catalyseurs utilisés dans ce travail. L'analyse par MEB a notamment permis de montrer que les pérovskites étaient constituées de petites particules de 50-100 nm agglomérées dans des agrégats de quelques micromètres. Cette agglomération entraine une surface spécifique – mesurée par BET - de l'ordre de 10 à 20 $m^2.g^{-1}$ pour les oxydes étudiés, ce qui est plus faible que la surface estimée par DRX pour des cristallites non agglomérées. Toutefois, cette surface reste supérieure à celle obtenue pour les pérovskites synthétisées à hautes températures et permet donc d'atteindre des activités électrocatalytiques plus élevées avec la même quantité de catalyseurs.

La morphologie des couches minces de pérovskite/carbone utilisées pour les mesures électrochimiques a également pu être observée par MEB. Les cartographies élémentaires du carbone et du cobalt ont prouvé que les deux éléments étaient bien dispersés sur $LaCoO_3$/C, démontrant que la pérovskite était globalement bien mélangée au carbone (Figure A).

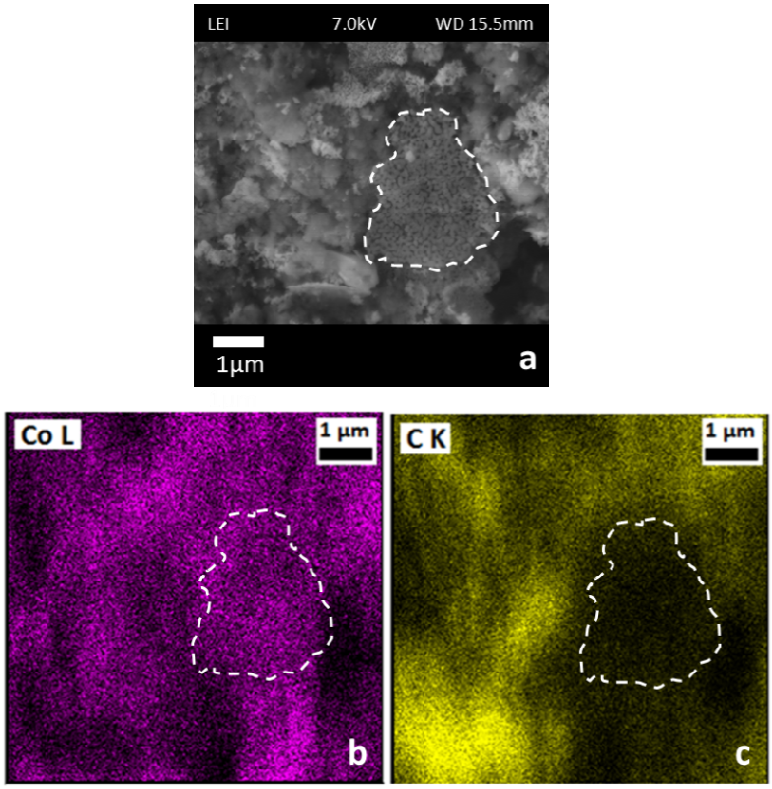

Figure A : *(a) Image MEB et cartographies élémentaires de (b) Co et (c) C d'un composite $LaCoO_3$ + carbone Sibunit déposé sur un support de carbone vitreux. Les pointillés délimitent un agglomérat de particules de $LaCoO_3$*

La composition de surface des oxydes, déterminante pour l'électrocatalyse, a été identifiée par spectrométrie photoélectronique par rayons X (XPS). La présence des éléments de la pérovskite a été confirmée puisque les énergies de liaisons des cations A, B et de l'oxygène correspondaient à ceux rapportés dans la littérature pour des oxydes de type pérovskite. Cependant, le rapport atomique de ces éléments n'était pas stœchiométrique. Toutes les pérovskites, et en particulier celles à base de Co, ont présenté un enrichissement en cation A à leur surface. Ceci est probablement dû à la présence de carbonates de cation A à la surface des pérovskites. Ces espèces ont en effet été observées sur les spectres XPS de C1s et O1s.

Enfin, les propriétés interfaciales des oxydes ont été étudiées de manière électrochimique par voltamétrie cyclique (CV). Grâce à cette technique, il a été démontré que les pérovskites sont stables dans la plage de potentiel [0.43 ; 1.23 V vs. RHE] dans 1M NaOH. A des potentiels plus faibles, les oxydes de type pérovskite sont réduits de manière irréversible.
Dans la gamme de potentiel étudiée, les pics observés sur les voltammogrammes ont été attribués aux métaux de transitions B, la nature du cation A n'ayant pas d'influence significative sur les voltammogrammes (Figure B). Pour les pérovskites à base de Co, les transitions redox n'étaient que faiblement visibles sur les CV (Figure B,a) alors que les pérovskites à base de Mn présentaient deux pics anodiques et deux pics cathodiques bien distincts (Figure B,b). Les couples impliqués dans ces pics sont probablement Mn^{4+}/Mn^{3+} à hauts potentiels et Mn^{3+}/Mn^{2+} à bas potentiels [p,q]. La première transition semble être réversible alors que la seconde est irréversible.

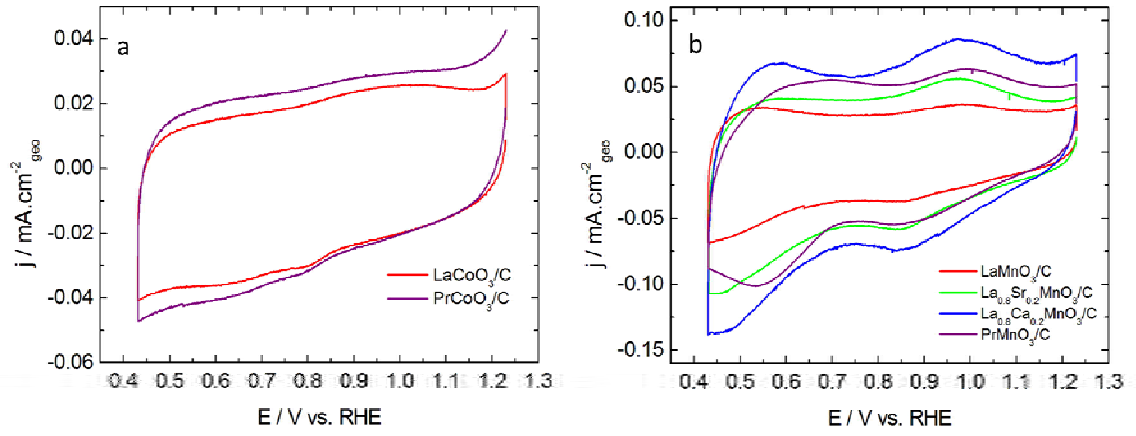

Figure B : *CV de composites à base de (a) Co ou (b) Mn déposés sur un support de carbone vitreux dans 1M NaOH désaéré, à 10mV.s^{-1}. Les électrodes contiennent 91µg/cm² de pérovskite et 37µg/cm² de carbone Sibunit.*

La voltamétrie cyclique dans une plage de potentiel restreinte où seuls des procédés capacitifs se produisent a permis de montrer que seule la surface de la pérovskite est impliquée dans les procédés électrochimiques. De plus, la rugosité calculée grâce à cette méthode était en accord avec la surface spécifique mesurée par BET.

Afin de démontrer l'intérêt de la structure pérovskite, les oxydes de type pérovskite ont été comparés à deux types d'oxydes simples de métaux de transitions : un oxyde de Co de type spinelle, Co_3O_4 et un oxyde de Mn, Mn_2O_3, de structure cubique. Il a été observé que leur surface spécifique était inférieure d'un facteur 5 par rapport à celles des pérovskites à cause d'une forte agglomération de particules. De plus, leur faible conductivité complique leur caractérisation par des méthodes électrochimiques.

C. Double rôle du carbone dans les couches catalytiques pérovskite/carbone

Pour identifier le rôle du carbone dans les composites pérovskite/carbone, le comportement électrochimique et électrocatalytique de différentes électrodes a été étudié. Dans un premier temps, la quantité de pérovskite a été fixée et la quantité de carbone a été variée. Des électrodes de différentes quantités de carbone (sans pérovskites) ont également été examinées en guise de référence. Le carbone choisi dans cette étude est le carbone Sibunit, obtenu par pyrolyse d'hydrocarbone, qui est de grande pureté et présente une conductivité élevée.

Les CV en milieu inerte ont montré une augmentation systématique de la capacitance avec la quantité de carbone. Afin d'identifier la contribution de chacun des composés de l'électrode, les CV d'électrodes de carbone seul ont été soustraites aux CV des composites (Figure C,a). Il est clair que la capacitance augmente avec la quantité de carbone même après correction. Ceci suggère que le carbone améliore le contact entre les particules de pérovskites, davantage de sites actifs étant accessibles électroniquement. On observe également que la différence de potentiel entre les pics anodiques et cathodiques des CV des pérovskites diminue avec la quantité de carbone grâce à une diminution de la résistance ohmique en présence de carbone. Pour la pérovskite la plus conductrice, $La_{0.8}Sr_{0.2}MnO_3$, la quantité de carbone nécessaire pour assurer un bon contact entre les particules d'oxydes est plus faible que pour les autres pérovskites : 29 %poids de carbone suffisent pour obtenir la capacitance maximale.

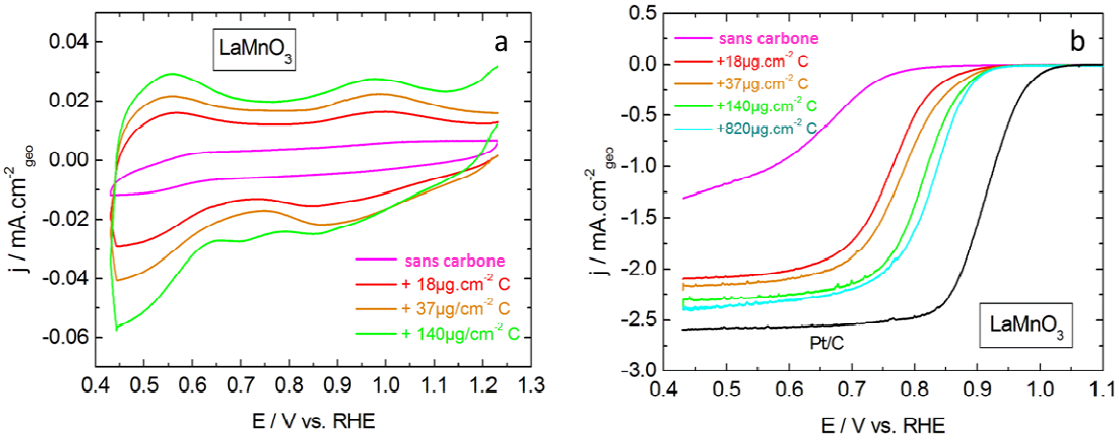

Figure C : *(a) CV corrigées par soustraction des CV du carbone aux CV des composites correspondants dans 1M NaOH désaéré et (b) courbes anodiques RDE à 900rpm dans 1M NaOH saturé en oxygène de composites $LaMnO_3$ + carbone Sibunit déposés sur un support de carbone vitreux à 10mV.s^{-1}. Les électrodes contiennent 91µg/cm² de pérovskite et des quantités variables de carbone Sibunit.*

L'activité électrocatalytique des différentes électrodes de quantité de pérovskite constante a ensuite été mesurée par RDE en milieu saturé en oxygène (Figure C,b). Sans carbone, l'activité des pérovskites vis-à-vis de l'ORR s'est avérée très faible et peu différente du carbone vitreux. Avec ajout de carbone, le potentiel de demi-vague et le courant limitant augmentent de manière systématique avec la quantité de carbone dans les électrodes contenant seulement du carbone et dans les électrodes composites. Ceci est lié à l'augmentation du nombre de sites actifs accessibles avec l'ajout de carbone. Il faut cependant noter que, lorsque la quantité de carbone est très élevée, la couche catalytique devient trop épaisse et la diffusion des molécules d'oxygène dans la couche devient l'étape limitante. Cela entraine une diminution du facteur d'utilisation de la surface.

L'équation de Levich qui relie le courant limitant à la vitesse de rotation de l'électrode donne alors une approximation du nombre d'électrons échangés. Contrairement au carbone qui ne fait intervenir que deux électrons, le nombre global d'électrons impliqués dans l'ORR sur des couches suffisamment épaisses de pérovskite est de quatre, comme sur le platine. Cependant, à ce stade, le mécanisme exact – « direct » ou « en série »- ne peut être identifié.

Pour mieux comprendre le mécanisme de l'ORR, des composites contenants une quantité constante de carbone et différentes quantités de pérovskite ont été testés. Deux comportements distincts ont été observés. A partir d'une certaine quantité de $LaCoO_3$, augmenter la quantité de pérovskite ne semble pas affecter le courant cinétique. Cela suggère,

de ce fait, que cette pérovskite est moins active que le carbone pour la réduction d'O_2 en HO_2^-. Cette étape est probablement principalement catalysée par le carbone. Le rôle de la pérovskite se limite alors à la réduction ou à la décomposition chimique d'HO_2^- pour obtenir un mécanisme global de quatre électrons. Pour les pérovskites au manganèse, $LaMnO_3$ et $La_{0.8}Sr_{0.2}MnO_3$, les courants cinétiques augmentent avec la quantité de pérovskite. Ces pérovskites sont donc plus actives que $LaCoO_3$ et que le carbone pour l'ORR. On peut également penser que le carbone contribue à la réduction d'O_2 en H_2O_2 lorsque les quantités de pérovskite sont faibles, i.e. lorsque la surface active de pérovskite est faible par rapport à celle du carbone.

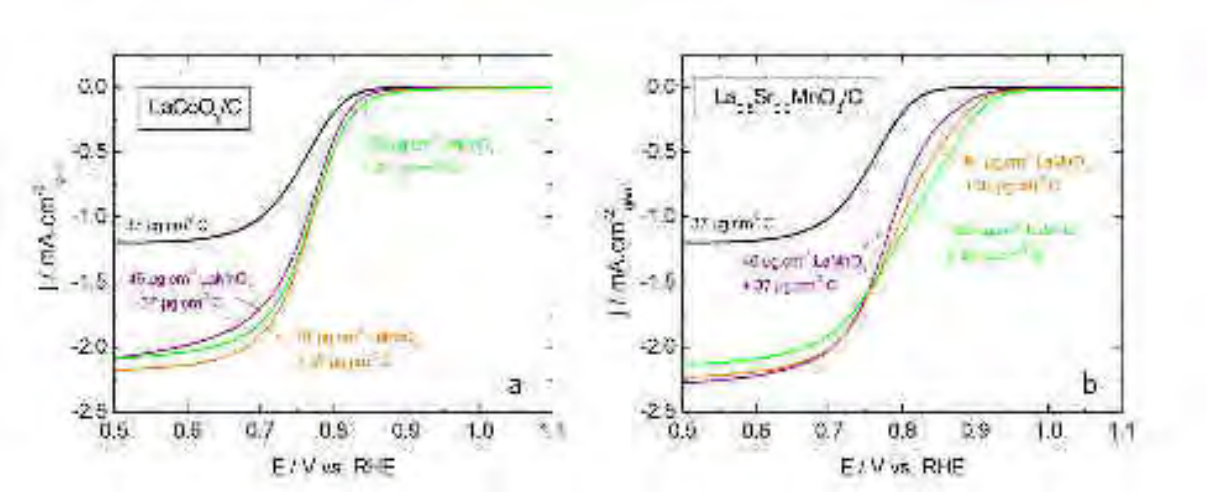

Figure D : *Courbes anodiques RDE de composites (a) $LaCoO_3$ + carbone Sibunit et (b) $La_{0.8}Sr_{0.2}MnO_3$ + carbone Sibunit déposés sur un support de carbone vitreux dans 1M NaOH saturé en oxygène à 900rpm et à 10mV.s^{-1}. Les électrodes contiennent 37 µg/cm² de carbone Sibunit et des quantités variables de pérovskite.*

Afin de quantifier l'activité de la pérovskite seule, il a été proposé dans cette thèse de soustraire les courants cinétiques du carbone aux courants cinétiques du composite (Figure E), mais cette correction n'est valable que si le carbone n'intervient pas directement dans le mécanisme de l'ORR. C'est le cas de la pérovskite $La_{0.8}Sr_{0.2}MnO_3$ pour laquelle le rôle du carbone est limité à l'amélioration du contact électronique (Figure E,a). A partir de la quantité de carbone optimale (37 µg.cm^{-1}), les courants cinétiques sont alors superposés après normalisation par la surface spécifique d'oxyde. Cependant, pour $LaCoO_3$, l'augmentation de l'activité avec la quantité de carbone est largement supérieure à l'augmentation de la charge observée à l'aide des CV (Figure E,b), ce qui suppose une synergie entre le carbone et la pérovskite dans le mécanisme de l'ORR. Dans tous les cas, la contribution du carbone dans la

détermination de l'activité de l'ORR ne doit pas être négligée contrairement à ce qui est parfois proposé dans la littérature.

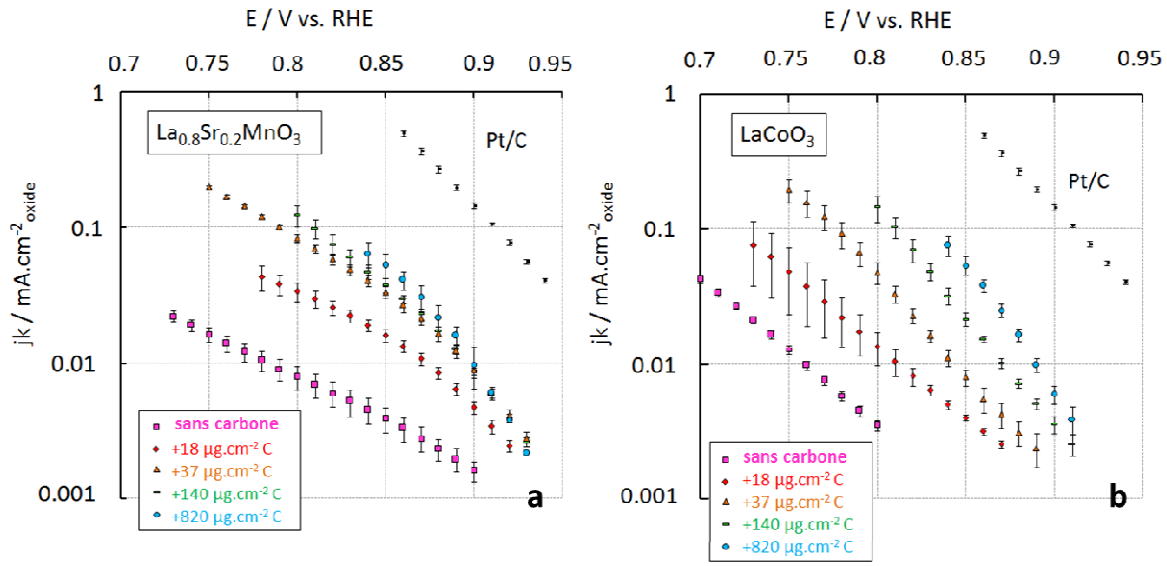

Figure E : *Courbes de Tafel de composites (a) $La_{0.8}Sr_{0.2}MnO_3$ + carbone Sibunit et (b) $LaCoO_3$ + carbone Sibunit déposés sur un support de carbone vitreux obtenues par correction du transport de masse des courbes anodiques RDE et soustraction de la contribution du carbone dans 1M NaOH saturé en oxygène à 10mV/s. Les électrodes contiennent 91µg/cm² de pérovskite et des quantités variables de carbone Sibunit. Les courants sont normalisés par la surface spécifique des oxydes.*

En comparant des perovskites contenant divers cations en position A, il a été démontré que l'activité pour l'ORR des pérovskites est principalement déterminée par la nature du cation en position B, les pérovskites à base de Mn étant plus actives que celle à base de Co. Les oxydes simples de ces deux métaux de transition Co_3O_4 et Mn_2O_3 ne sont quant à eux pas très actifs pour cette réaction à cause de leur faible conductivité. Cependant, il a été observé que le nombre d'électrons échangés sur Mn_2O_3 était supérieur à deux, ce qui suggère que cet oxyde est capable de catalyser la réduction ou la décomposition d'HO_2^-.

On peut noter qu'au potentiel de référence de 0.9 V_{RHE} [r], les pérovskites ont une activité électrocatalytique vis-à-vis de l'ORR à seulement un ordre de grandeur de celle des électrodes Pt/C (Figure E). Cela est intéressant puisque le faible coût des pérovskites offre la possibilité d'augmenter la quantité d'oxyde pour avoir une meilleure activité, contrairement aux catalyseurs à base de platine.

D. Mécanisme de l'ORR sur les composites pérovskite/carbone

Dans ce travail, l'étude RDE a montré que quatre électrons étaient globalement impliqués dans l'ORR sur les électrodes pérovskite/carbone. Cependant, ceci ne permet pas de conclure si l'ORR est un mécanisme « direct » ou « en série ». Pour éclaircir ce point, l'ORR a été étudié par RRDE pour différentes électrodes. Pour un mécanisme « en série », une partie de l'HO_2^- produit diffuse hors de l'électrode. Grâce à la technique RRDE, cet intermédiaire est réoxydé à l'anneau et peut donc être quantifié à partir des courants du disque et de l'anneau. La composition des électrodes a été variée afin d'étudier l'influence (i) de la présence de carbone, (ii) de la nature de la pérovskite, et (iii) de la charge de pérovskite sur l'électrode sur le mécanisme de l'ORR.

Tout d'abord, il a été prouvé que les électrodes composées exclusivement de pérovskite engendrent une grande quantité d'HO_2^- (Figure F, courbes bleues). Ceci prouve que l'ORR est principalement un mécanisme « en série » sur les pérovskites. Comme la quantité d'HO_2^- dépend du potentiel, la transformation d'HO_2^- implique probablement une étape électrochimique.

Le carbone seul catalyse la réduction d'O_2 en HO_2^- mais ne permet pas la transformation de cet intermédiaire (Figure F, courbes rouges). Pourtant, son ajout dans les couches de pérovskite diminue sensiblement la quantité d'HO_2^- détectée (Figure F, courbes vertes). Ceci a été attribué à une augmentation de l'activité pour la réduction d'HO_2^- grâce à l'amélioration du contact électronique en présence de carbone. Néanmoins, l'allure du courant à l'anneau indiquait que cette réduction n'était pas exclusivement électrochimique mais impliquait également une étape chimique lente.

Ce travail a montré que davantage d'HO_2^- était détecté pour les électrodes à base de $LaCoO_3$ que celles à base de $La_{0.8}Sr_{0.2}MnO_3$. Ceci a été attribué d'une part à la faible activité de $LaCoO_3$ pour la réduction d'HO_2^-, démontré par la suite, et d'autre part au fait que, pour cette pérovskite, l'HO_2^- est formé sur le carbone et doit donc diffuser vers les sites pérovskites afin d'être transformé. Une grande probabilité de diffuser hors de l'électrode et donc d'être détecté à l'anneau, en résulte de ce fait.

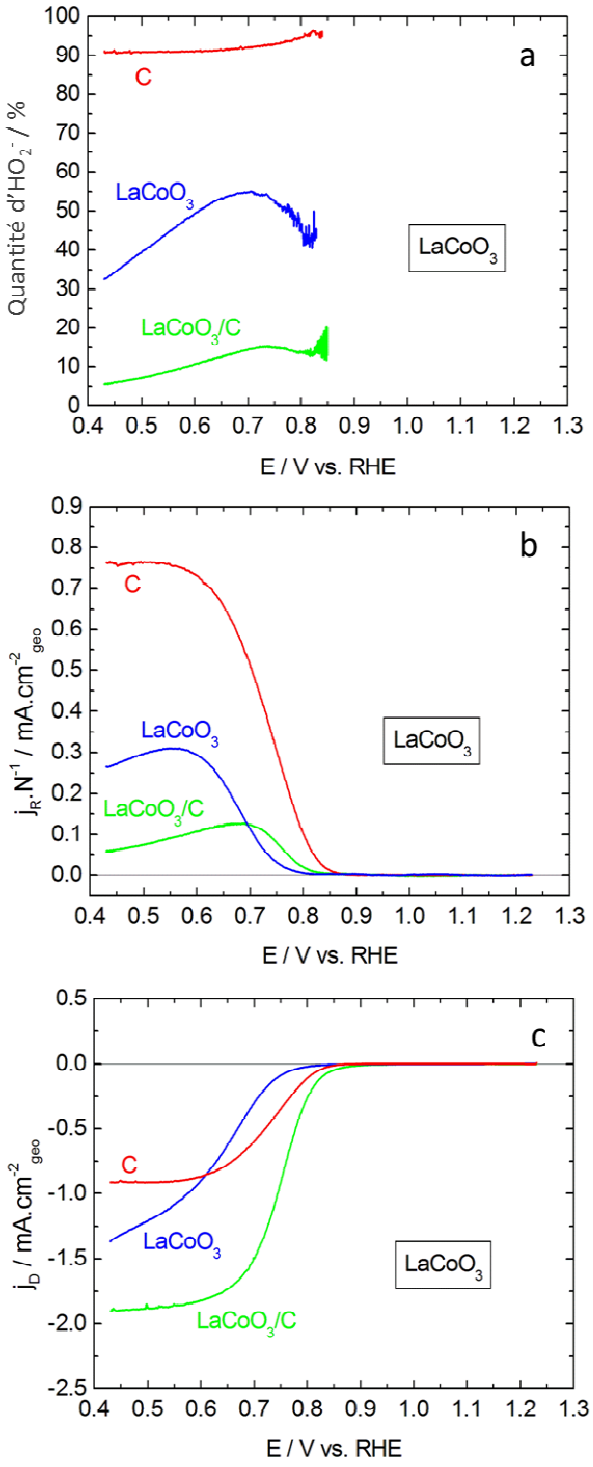

Figure F : *Courbes anodiques RRDE de composites $LaCoO_3$ + carbone Sibunit déposés sur un support de carbone vitreux dans 1M NaOH saturé en oxygène à 900rpm et à 10mV.s^{-1}.: (a) pourcentage d'HO_2^- formé, (b) courant à l'anneau, polarisé à 1.23V vs. RHE, (c) courant au disque. Les électrodes contiennent 37 µg/cm² de carbone Sibunit et /ou 91 µg/cm² de pérovskite.*

Il a aussi été observé que l'activité des pérovskites à base de Mn était sensible à l'état d'oxydation de Mn. En effet, la pérovskite réduite semblait plus active pour la transformation d'HO_2^- car la quantité d'HO_2^- détectée est plus faible après réduction électrochimique de la pérovskite. Ceci n'est pas le cas de $LaCoO_3$ pour laquelle peu de différences d'activité ont été observées entre la pérovskite réduite et la pérovskite oxydée.
Afin d'étudier l'influence de la charge de catalyseur sur le mécanisme de l'ORR [s], des électrodes de rapport pérovskite/carbone constant et de différentes charge de catalyseurs ont été étudiées par RRDE (voir Figure I,d,e,f). Il a été observé d'une part que les électrodes les plus fines – avec les plus faibles quantités de catalyseurs – entrainaient la détection d'une grande quantité d'HO_2^-, prouvant que l'ORR sur les électrodes composites est un mécanisme « en série ». D'autre part, lorsqu'on augmente le nombre de sites actifs, on augmente la probabilité de réduire ou décomposer HO_2^- dans la couche. Cela se traduit par une diminution du pourcentage d'HO_2^- détecté à l'anneau, soit un mécanisme apparent de quatre électrons. Cela peut expliquer pourquoi certains auteurs suggèrent un mécanisme direct sur les pérovskites.

Comme les expériences RRDE ont confirmé que l'intermédiaire HO_2^- est formé sur les différents oxydes de type pérovskite, il était également nécessaire d'étudier la cinétique de réduction et de décomposition de cette espèce afin de déterminer la nature de la transformation d'HO_2^- sur les pérovskites. De plus, l'étude RDE de l'ORR sur les composites pérovskite/carbone a montré que le carbone catalyse la réduction d'O_2 en HO_2^- dans ces électrodes. L'HO_2^- formé sur le carbone peut entrainer la corrosion de la couche catalytique et de la membrane de la pile à combustible. Il est donc nécessaire que la pérovskite utilisée dans la cathode soit capable de transformer rapidement cet intermédiaire afin d'éviter son accumulation dans la pile. Dans le but de déterminer l'activité des oxydes pour cette transformation, les réactions de réduction et de décomposition d'HO_2^- ont été étudiées dans des électrolytes contenant H_2O_2. En milieu alcalin, H_2O_2 est transformé en HO_2^-.
Dans 1M NaOH contenant H_2O_2 et dans la plage de potentiel étudiée, des courants cathodiques et anodiques ont été mesurés par RDE pour des électrodes de pérovskite (Figure G). Ceci prouve que les pérovskites sont actives pour la réduction et l'oxydation d'HO_2^- alors que le carbone ne l'est pas (Figure G, courbes grises). Comme pour l'ORR, l'ajout de carbone dans la couche catalytique augmente de façon considérable l'activité pour la réduction d'HO_2^- en augmentant l'utilisation du catalyseur. Ceci est à l'origine de la diminution de la quantité d'HO_2^- détectée par RRDE avec l'ajout de carbone (Figure F).

Les pérovskites sont apparues comme considérablement plus actives que les oxydes simples de Co et Mn pour les réactions électrochimiques avec HO_2^-. Elles sont néanmoins moins actives que le platine, notamment pour l'oxydation d'HO_2^-, ce qui résulte en un potentiel mixte plus positif pour les pérovskites (Figure G).

Le fait que les courants à bas potentiels se rapprochent du plateau de diffusion de Pt/C indique que deux électrons sont échangés lors de la réduction d'HO_2^- sur les pérovskites. Toutefois, cette réaction est composée de plusieurs étapes. En particulier, le changement de pente observé sur les voltammogrammes de $LaCoO_3$/C (Figure G) suggère une étape chimique lente suivie d'une étape électrochimique. Ceci est en accord avec l'évolution du courant de l'anneau de l'électrode RRDE avec le potentiel (Figure F). Comme $LaCoO_3$ atteint plus difficilement les plateaux de diffusion de Pt/C et comme les courants autour du potentiel mixte sont plus faibles que pour LaMnO3 ou $La_{0.8}Sr_{0.2}MnO_3$, la pérovskite à base de Co est moins active pour les réactions de réduction/oxydation d'HO_2^-. La plus grande quantité d'HO_2^- mesurée par RRDE pour cette pérovskite est, par conséquent, justifiée.

L'hystérèse observée entre le balayage cathodique et le balayage anodique pour les pérovskites à base de Mn dans un milieu contenant H_2O_2 a confirmé que la pérovskite réduite est plus active pour la réduction d'HO_2^- que la pérovskite oxydée. En revanche, aucune hystérèse n'a pu être observée pour $LaCoO_3$. Ces différences dans le comportement redox peuvent être à l'origine de la plus faible activité de $LaCoO_3$ par rapport aux pérovskites à base de Mn.

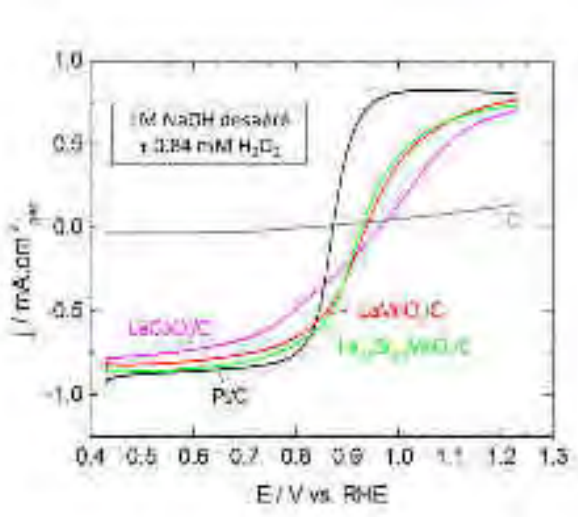

Figure G : *Courbes anodiques RDE de composites pérovskite + carbone Sibunit déposés sur un support de carbone vitreux dans 1M NaOH désaéré avec 0.84 mM H_2O_2 à 900rpm et à 10mV.s^{-1}. Les électrodes contiennent 91 µg.cm$^{-2}_{geo}$ de pérovskite et 37 µg/cm² de carbone Sibunit.*

La concentration d'H_2O_2 principalement utilisée dans ce travail était 0.84mM, correspondant à la concentration d'O_2 dans une solution de 1M NaOH saturée. Pour étudier l'effet de la concentration d'H_2O_2 sur le comportement des pérovskites, d'autres concentrations ont été testées. Lorsque la concentration était divisée par deux, les courants l'étaient également et le potentiel mixte était légèrement décalé vers les potentiels positifs. Un constat indiquant que les vitesses de réduction et d'oxydation d'HO_2^- n'ont pas la même dépendance avec la concentration d' H_2O_2.

Dans le but de comparer les résultats électrochimiques aux résultats de décomposition d'HO_2^- décrits ci-après, l'étude RDE a également été effectuée avec de plus grandes concentrations d'H_2O_2. Cependant, la cinétique de réaction dans ces milieux était très lente, probablement à cause d'un nombre limité de sites actifs.

Même si la réduction électrochimique d'HO_2^- semble être la réaction prédominante sur les pérovskites, l'activité de ces oxydes pour la décomposition chimique d'HO_2^- a également été étudiée par suivi volumétrique [t] de la formation d'O_2 après contact d'H_2O_2 avec le catalyseur.

En variant la concentration d'H_2O_2, il a été montré que le volume maximal d'O_2 formé est dépendant de cette concentration (Figure H,a) et que les relations de 1er ordre liant le volume d'O_2 au volume maximal sont linéaires dans le temps et superposées pour toutes les concentrations (Figure H,b). Ceci indique que la décomposition chimique d'HO_2^- sur les pérovskites est une réaction d'ordre 1 vis-à-vis de la concentration d'H_2O_2.

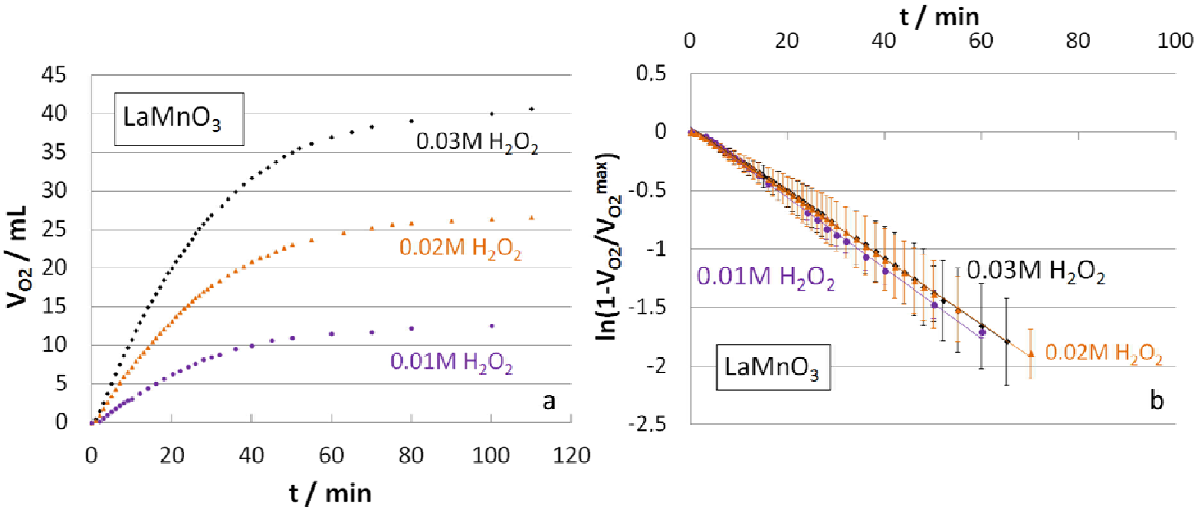

Figure H : *(a) Volume d'O_2 relâché et (b) courbes* $ln\left(1-\frac{V_{O_2}}{V_{O_{2max}}}\right)$ *en fonction du temps pour 10mg de poudre de $LaMnO_3$ dans 1M NaOH saturé en oxygène avec différentes concentrations d'H_2O_2.*

Il a également été observé que, quel que soit la masse de pérovskite ajoutée dans la cellule, les constantes hétérogènes obtenues par normalisation des constantes de 1er ordre par la masse de catalyseur étaient égales.

De plus, on a démontré que les pérovskites étaient beaucoup plus actives que le carbone pour la catalyse de cette réaction. Ainsi, que ce soit par réduction ou par décomposition, l'HO_2^- formé est rapidement transformé sur les pérovskites et ne peut donc survivre dans une pile.

$LaCoO_3$ est apparue légèrement plus active que les pérovskites au Mn : la constante hétérogène est d'environ 6 10^{-5} cm.s^{-1} pour la pérovskite au Co, et autour de 4 10^{-5} cm.s^{-1} pour celles au Mn.

De manière intéressante, il a été observé que l'oxyde simple Mn_2O_3 est très actif pour la décomposition d'HO_2^- avec une constante hétérogène de l'ordre de 10^{-3} cm.s^{-1} alors que l'oxyde simple Co_3O_4 n'est pas actif pour cette réaction. Le mécanisme de la réaction de décomposition est encore flou puisque certains auteurs proposent un mécanisme chimique et d'autres un mécanisme électrochimique. Mais la très grande activité de Mn_2O_3 pour la décomposition alors que ce même oxyde possède une faible activité pour la réduction électrochimique d'HO_2^-, de même que le fait que la pérovskite au Co moins active pour les réactions électrochimiques est plus active pour la réaction catalytique hétérogène que les pérovskites au Mn, tendent à prouver que la décomposition est plutôt un mécanisme chimique, en tout cas pour certains matériaux.

Afin de mieux comprendre le mécanisme de l'ORR ayant lieu sur les pérovskites, un modèle mathématique a été développé par A. Bonnefont (Institut de Chimie, Université de Strasbourg) à partir des données expérimentales obtenues au cours de ce doctorat. En utilisant un mécanisme « en série » avec réduction d'HO_2^- en deux étapes – une chimique et une électrochimique - sur les sites pérovskites, les courbes simulées (Figure I,a,b,c) reproduisaient de manière satisfaisante les courbes expérimentales (Figure I,d,e,f).

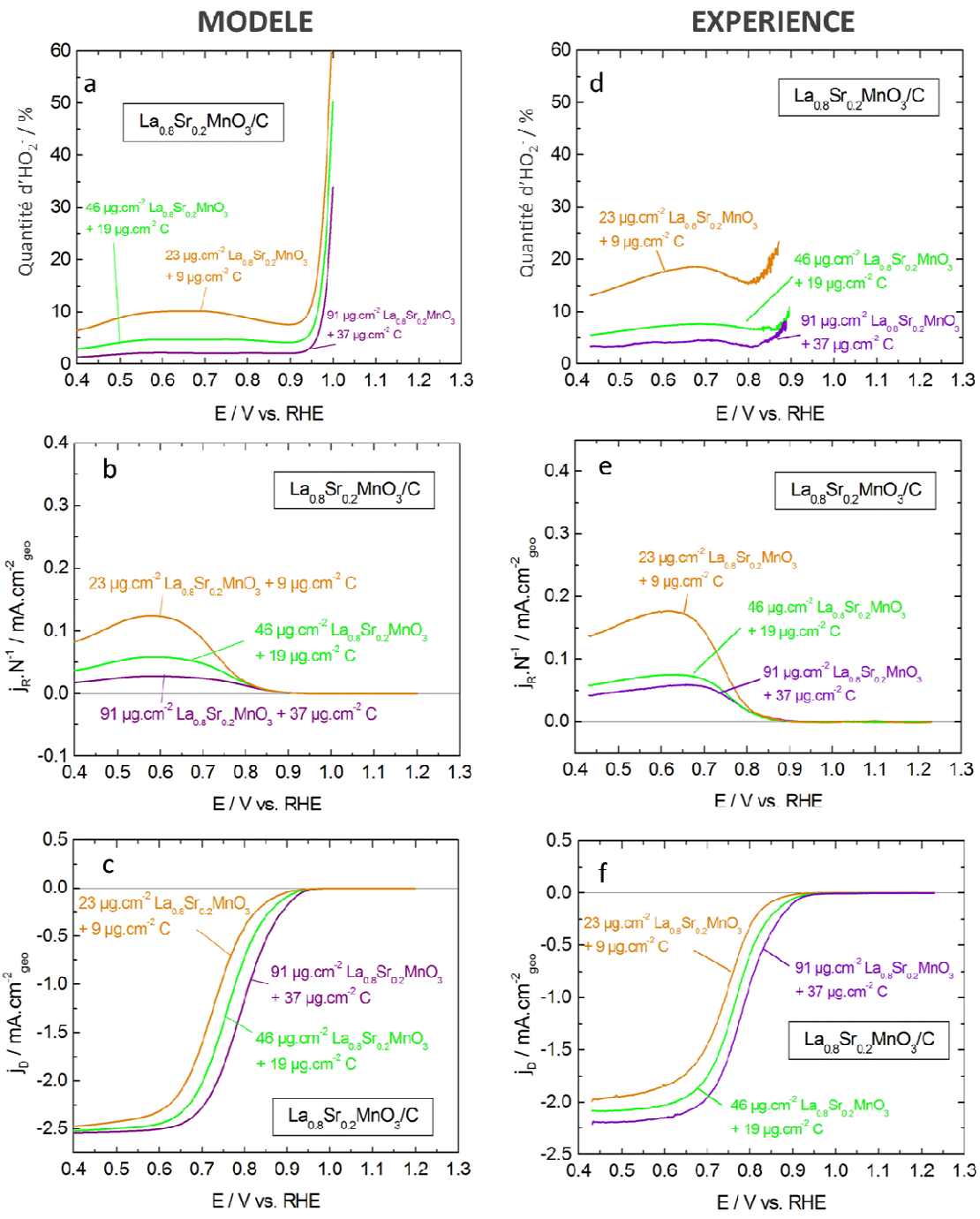

Figure I : *Courbes anodiques RRDE de composites $La_{0.8}Sr_{0.2}MnO_3$ + carbone Sibunit déposés sur un support de carbone vitreux dans 1M NaOH saturé en oxygène à 900rpm : (a,b,c) courbes simulées, (d,e,f) courbes anodiques expérimentales à 10mV.s^{-1}. (a) Pourcentage d'HO_2^- formé, (b) courant à l'anneau, polarisé à 1.23V vs. RHE, (c) courant au disque. Les électrodes contiennent un rapport pérovskite/carbone constant (71 %poids pérovskite + 29 %poids carbone Sibunit) et différentes charges d'électrode.*

E. Stabilité des oxydes de type pérovskite comme catalyseurs de l'ORR

Les pérovskites étudiées dans ce travail ont démontré des activités pour l'ORR prometteuses pour des applications en pile à combustible. Cependant, les composants des piles doivent être suffisamment stables pour assurer une performance durable sur le long terme.

Afin de valider ce point, plusieurs études de stabilité ont été effectuées au cours de cette étude. Tout d'abord, l'effet du traitement thermique sur la surface des oxydes après stockage a été analysé par XPS. Il a ainsi été montré que les carbonates de lanthane formés à la surface des pérovskites sous conditions atmosphériques peuvent être partiellement éliminés grâce à un traitement sous air à 650°C. Ces carbonates sont par ailleurs probablement détruits par ultrasons lors de la préparation des suspensions aqueuses de pérovskites pour les mesures électrochimiques puisque la proportion de carbonates observée par XPS était plus faible pour les suspensions que pour les poudres initiales.
Il a également été observé que $LaCoO_3$ est extrêmement sensible à son environnement chimique. En effet, une immersion prolongée de cette pérovskite dans de l'eau ultrapure entraine la formation d'une couche d'hydroxyde de cobalt (visible sur le spectre XPS Co2p) qui affecte la réponse voltamétrique de cette électrode. C'est pourquoi seules des suspensions fraiches de pérovskite ont été utilisées pour les tests électrochimiques dans ce travail. De plus, la longue immersion de $LaCoO_3$ dans une solution alcaline entraine la transformation de la surface de la pérovskite en hydroxyde de cobalt et de lanthane. Ceci suppose la dégradation du catalyseur au contact du milieu basique d'une pile à combustible alcaline.
La surface des pérovskites à base de Mn est plus stable. En effet, aucune modification significative n'a pu être observée par XPS après immersion dans de l'eau ultrapure ou dans un électrolyte alcalin. Seule une dissolution partielle du Sr de $La_{0.8}Sr_{0.2}MnO_3$ a pu être détectée par spectrométrie d'émission à plasma (ICP) après trempage dans la solution alcaline, les autres éléments étant stables. Néanmoins, aucune des modifications mentionnées n'affecte la structure des catalyseurs puisque l'analyse DRX a montré que la structure pérovskite est maintenue pour toutes les pérovskites étudiées, même après un mois dans 1M NaOH.

Par la suite, la stabilité de l'activité électrocatalytique pour l'ORR a été étudiée par chronoampérométrie à différents potentiels pour les électrodes à base de pérovskite, avec ou sans carbone, dans un électrolyte saturé en O_2.

Les courants obtenus pour des électrodes $LaCoO_3$/C ont été normalisés par la dernière valeur mesurée sur la Figure J,a. Ceci montre que l'activité pour l'ORR est relativement stable sur ces électrodes. En mesurant les voltammogrammes RDE avant et après la chronoampérométrie (Figure J,b), il a pu être observé que les courants cinétiques ne sont effectivement pas affectés. En revanche, les courants à bas potentiels ont diminué après chronoampérométrie, et la perte de courant est supérieure à la consommation d'O_2 lors de l'ORR. En effectuant les même expériences dans un milieu contenant H_2O_2, il a été constaté que les courants de réduction d'HO_2^- ont considérablement décru après chronoampérométrie (Figure J,c). Cet effet est encore plus prononcé en l'absence de carbone.

Il a donc été proposé dans ce travail qu'une phase électrochimiquement inactive et isolante est formée sur la surface de $LaCoO_3$ lors de l'ORR. Cela entraine (i) une augmentation de la chute ohmique dans la couche, qui peut être minimisée avec addition de carbone et (ii) une diminution de la surface de perovskite accessible, ce qui diminue l'activité électrocatalytique. Comme le carbone est plus actif que $LaCoO_3$ pour l'ORR, les courants cinétiques de l'ORR ne sont pas affectés. L'activité pour la réduction d'HO_2^- qui se produit sur la perovskite est cependant réduite.

Pour les électrodes à base de $La_{0.8}Sr_{0.2}MnO_3$, la perte de courant en présence d'O_2 est considérable, surtout dans la zone cinétique (Figure K,a,b). Ceci révèle une modification irréversible de la pérovskite, initialement active pour l'ORR. Le courant cinétique restant est alors assuré par le carbone qui devient plus actif que la pérovskite suite à la diminution du nombre de site de l'oxyde. Néanmoins, la grande activité de cette perovskite pour la réduction d'HO_2^- permet le maintien d'un mécanisme global de quatre électrons même avec une diminution du nombre de sites actifs.

L'effet de l'électrocatalyse sur les propriétés interfaciales a été étudié par CV en milieu inerte à la fin des mesures. Après l'ORR comme après la réduction d'HO_2^-, les CV de $La_{0.8}Sr_{0.2}MnO_3$ ont présenté une forte diminution de la charge et des pics redox moins bien définis (Figure K,c). Ceci confirme la dégradation de la pérovskite lors des réactions et pointe la relation entre ses transitions redox et son activité électrocatalytique. Le même comportement a été observé pour $LaMnO_3$.

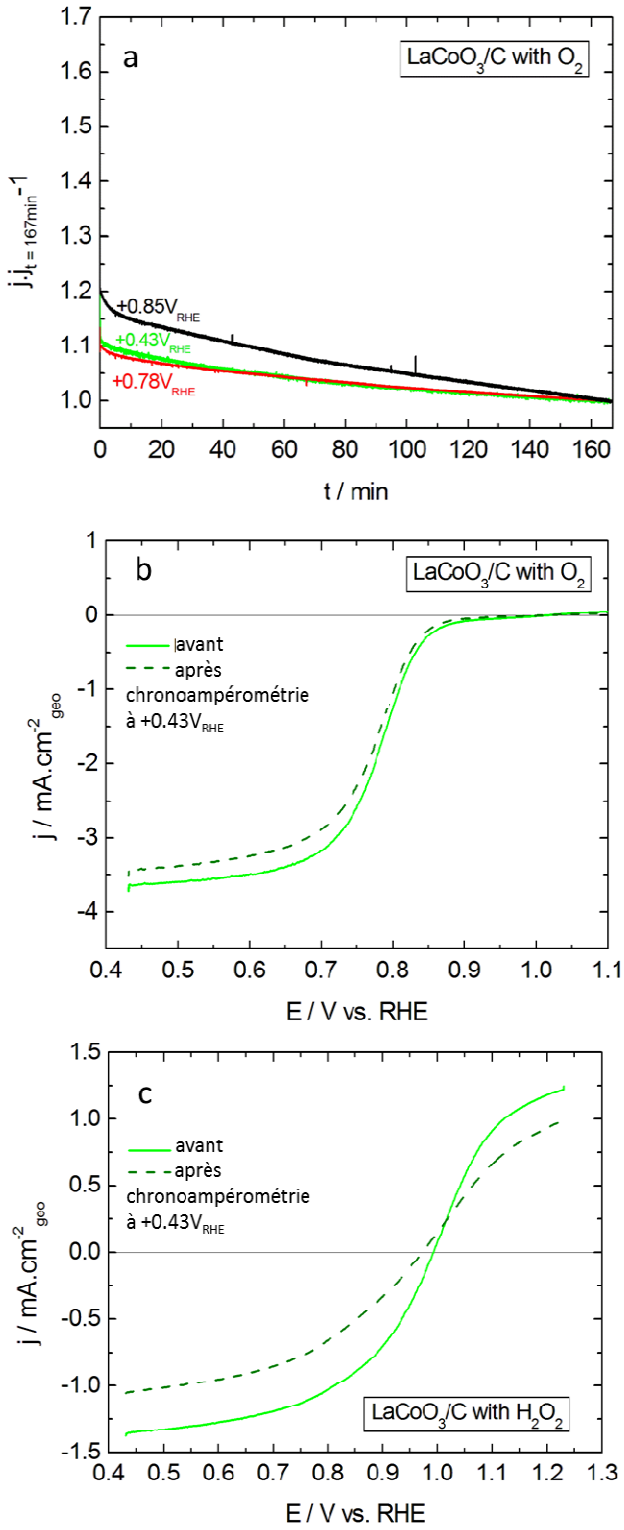

Figure J: *(a) Chronoampérométrie à divers potentiels à 2500rpm dans 1M NaOH saturé en oxygène avec normalisation par la dernière valeur de courant, et courbes anodiques RDE à 2500rpm et 10mV.s^{-1} avant et après chronoampérométrie à +0.43V $_{RHE}$ dans (b) 1M NaOH saturé en oxygène et (c) 1M NaOH désaéré avec 0.84 mM H_2O_2, de composites $LaCoO_3$ + carbone Sibunit déposés sur un support de carbone vitreux. Les électrodes contiennent 91 µg.cm^{-2} $_{geo}$ de pérovskite et 37 µg/cm² de carbone Sibunit.*

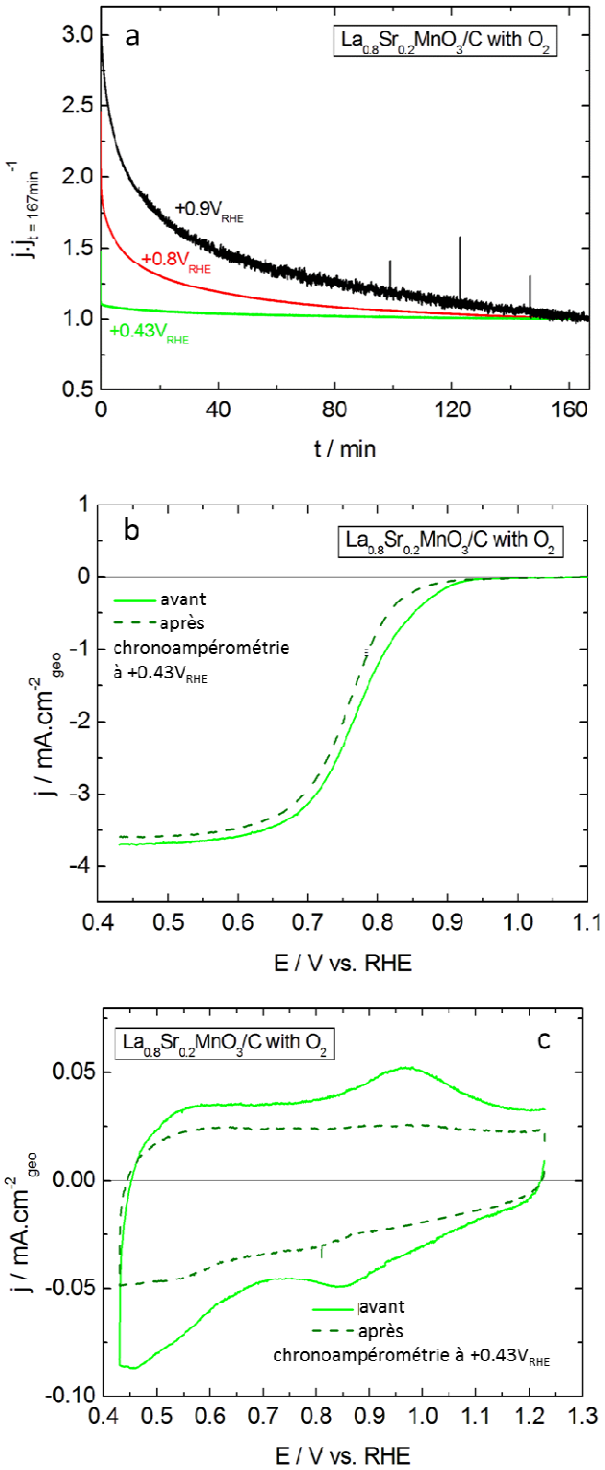

Figure K : *(a) Chronoampérométrie à divers potentiels à 2500rpm dans 1M NaOH saturé en oxygène avec normalisation par la dernière valeur de courant, (b) courbes anodiques RDE à 2500rpm et 10mV.s^{-1} avant et après chronoampérométrie à +0.43V $_{RHE}$ dans 1M NaOH saturé en oxygène et (c) CV à 10mV.s^{-1} dans 1M NaOH désaéré avant et après chronoampérométrie à +0.43V $_{RHE}$ dans 1M NaOH saturé en oxygène, de composites $La_{0.8}Sr_{0.2}MnO_3$ + carbone Sibunit déposés sur un support de carbone vitreux. Les électrodes contiennent 91 µg.cm$^{-2}{}_{geo}$ de pérovskite et 37 µg/cm² de carbone Sibunit.*

Afin de visualiser d'éventuelles modifications dans la structure, la morphologie et la composition de surface des catalyseurs et donc, de mieux comprendre la perte d'activité électrocatalytique, des électrodes ont été créées pour permettre l'analyse DRX, MEB et XPS.
Ces électrodes sont constituées de papier de carbone sur lequel est déposé un film mince de pérovskite et carbone.
Après plusieurs CV dans un milieu alcalin saturé en O_2 ou contenant H_2O_2 pour reproduire l'électrocatalyse de l'ORR ou de la réduction d'HO_2^-, ces électrodes ont été analysées. L'étude DRX a prouvé que la structure pérovskite est toujours présente après électrocatalyse. L'analyse MEB a montré qu'aucune agglomération particulière n'a lieu lors de l'electrocatalyse. Seules des traces de NaOH et Na_2CO_3 ont pu être observés par DRX et EDX après l'ORR, et résultent certainement du caractère hydrophile du papier de carbone dans ce milieu.
Bien que les CV des couches minces après chronoampérométrie aient suggéré un changement de la surface de la pérovskite avec les réactions, aucune altération notable de Co ou de Mn n'a pu être observée par XPS après électrocatalyse. Cependant, l'utilisation d'électrodes de papier de carbone pour la caractérisation des pérovskites a montré des limites et peut ne pas être adaptée pour observer la dégradation responsable de la perte d'activité pour l'ORR.

F. Conclusions

Cette thèse a démontré que les électrodes à base d'oxydes de type pérovskite étaient actives pour l'ORR et pouvaient donc être potentiellement utilisées comme matériaux de cathode dans les SAFC.
Les études de la catalyse de l'ORR et des transformations d'HO_2^- sur des composites pérovskite/carbone de diverses compositions ont montré que, sur ces électrodes, O_2 est réduit en OH^- via un mécanisme « en série » avec formation de l'intermédiaire HO_2^-. Basé sur les résultats expérimentaux et avec l'aide d'un modèle mathématique, un mécanisme a été proposé pour l'ORR sur les pérovskites.
O_2 est réduit via les deux étapes suivantes où « ads » signifie adsorbé:

$$O_2 + OH, ads + e^- \rightleftarrows O_2, ads + OH^-$$

$$O_2, ads + H_2O + e^- \rightleftarrows HO_2, ads + OH^-$$

L'espèce HO_2 peut ensuite être réduite par une étape chimique lente suivie d'une étape électrochimique:

$$HO_2, ads + OH, ads \rightarrow 2\ O, ads + H_2O$$

$$O, ads + H_2O + e^- \rightleftarrows OH, ads + OH^-$$

ou désorbée de l'électrode:

$$HO_2, ads + OH^- \rightleftarrows HO_2^- + OH, ads$$

La nature des intermédiaires est hypothétique, puisque le seul intermédiaire détecté dans ce travail est HO_2^-. Cependant, le mécanisme est inspiré de la littérature [u,v] et notamment de calculs DFT sur les pérovskites [w].

Les vitesses de réactions sont considérablement plus faibles sur $LaCoO_3$ que sur $LaMnO_3$ ou $La_{0.8}Sr_{0.2}MnO_3$. Ceci entraine une plus grande surtension, un relâchement plus important d'HO_2^- et des réactions de réduction/oxydation d'HO_2^- plus lentes sur la pérovskite au Co que sur celles au Mn. Ceci est probablement dû à un comportement redox différent des deux métaux de transition. La quantité d'HO_2^- relâchée lors de l'ORR dépend non seulement de la nature et de la quantité de pérovskite, de grandes quantités permettant l'efficace réduction d'HO_2^-, mais également de la quantité de carbone.

En effet, en étudiant soigneusement l'impact de la quantité de carbone dans les composites pérovskite/carbones sur l'activité électrocatalytique, il a été montré dans cette thèse que le carbone joue un double rôle. Tout d'abord, il permet l'augmentation de l'utilisation de la pérovskite en améliorant le contact électrique dans la couche catalytique. Il en résulte une augmentation de l'activité électrocatalytique pour l'ORR et pour la réduction d'HO_2^-, entrainant une diminution du relâchement d'HO_2^-. Ensuite, le carbone est impliqué dans le mécanisme de l'ORR en catalysant la réduction d'O_2 en d'HO_2^-, surtout pour les pérovskites ayant une faible activité pour l'ORR comme $LaCoO_3$. Ceci montre que la contribution du carbone ne peut être négligée dans la mesure de l'activité, et que l'activité intrinsèque de la pérovskite n'est pas directement mesurable dans les électrodes composites. De plus, l'HO_2^- formé sur le carbone peut désorber pour diffuser dans l'électrolyte ou se réadsorber sur des sites pérovskites adjacents pour être réduit.

Parallèlement, il a été observé que l'électrocatalyse de l'ORR entraine une diminution du nombre de sites actifs sur les pérovskites. La nature de cette dégradation est encore floue mais son impact dépend de l'activité de la pérovskite étudiée pour l'ORR. En effet, pour $LaCoO_3$ qui est moins actif que le carbone pour l'ORR, les courants à faible surtensions ne sont pas affectés par la dégradation puisque l'ORR se produit principalement sur le carbone. En revanche, une diminution du courant à grandes surtensions est observée suite au

ralentissement de la réduction d'HO_2^- avec la diminution du nombre de sites de la pérovskite. Sur les pérovskites au Mn, le potentiel de début de réaction est considérablement déplacé vers les potentiels plus négatifs avec la dégradation des sites les plus actifs. Ceci entraine également la disparition des pics redox sur les CV en milieu inerte.

G. Références

a. **Kinoshita, K.** Carbon - Electrochemical and Physicochemical Properties. New York : Wiley, 1988. ISBN 978-0471848028.

b. **Tammeveski, K., Kontturi, K., Nichols, R.J., Potter, R.J., Schiffrin, D.J.** Journal of Electroanalytical Chemistry. 2001, Vol. 515, 101-112.

c. **Suntivich, J., Gasteiger, H.A., Yabuuchi, N., Shao-Horn, Y.** Journal of the Electrochemical Society. 2010, Vol. 157, B1263-B1268.

d. **Tulloch, J., Donne, S.W.** Journal of Power Sources. 2009, Vol. 188, 359-366.

e. **Goodenough, J.B.** Reports on Progress in Physics. 2004, Vol. 67, 1915-1993.

f. **Pena, M.A., Fierro, J.L.G.** Chemical Reviews. 2001, Vol. 101, 1981-2017.

g. **Matsumoto, Y., Yoneyama, H., Tamura, H.** Bulletin of the Chemical Society of Japan. 1978, Vol. 51, 1927-1930.

h. **Bockris, J.O'M, Otagawa, T.** Journal of Physical Chemistry. 1983, Vol. 87, 2960-2971.

i. **Schmidt, T.J., Gasteiger, H.A., Stab, G.D., Urban, P.M., Kolb, D.M., Behm, R.J.** Journal of Electrochemical Society. 1998, Vol. 145, 2354-2358.

j. **Thiele, D., Zuttel, A.** Journal of Power Sources. 2008, Vol. 183, 590-594.

k. **Hayashi, M., Uemura, H., Shimanoe, K., Miura, N., Yamazoe, N.** Journal of the Electrochemical Society. 2004, Vol. 151, A158-A163.

l. **Sunarso, J., Torriero, A.J., Zhou, W., Howlett, P.C., Forsyth, M.** Journal of Physical Chemistry C. 2012, Vol. 116, 5827-5834.

m. **Hermann, V., Dutriat, D., Müller, S., Comninellis, Ch.** Electrochimica Acta. 2000, Vol. 46, 365-372.

n. **Li, X., Qu, W., Zhang, J, Wang, H.** Journal of the Electrochemical Society. 2011, Vol. 158, A597-A604.

o. **Hyodo, T., Shimizu, Y., Miura, N., Yamazoe, N.** Denki Kagaku. 1993, Vol. 62, 158-164.

p. **Pourbaix, M.** Atlas of Electrochemical Equilibria in Aqueous Solutions. Houston, USA : NACE, 1974. ISBN 978-0915567980.

q. **Lima, F.H.B., Calegaro, M.L., Ticianelli, E.A.** Electrochimica Acta. 2007 , Vol. 52, 3732-3738.

r. **Gasteiger, H.A., Kocha, S.S., Sompalli, B., Wagner, F.T.** Applied Catalysis B: Environmental. 2005, Vol. 56, 9-35.

s. **Jaouen, F.** Journal of Physical Chemistry C. 2009, Vol. 113, 15433-15443.

t. **Minami, T., Ravindranathan, P., Patil, K.C.** Proceedings of the Indian Academy of Science. 1987, Vol. 99, 209-215.

u. **Suntivich, J., Gasteiger, H.A., Yabuuchi, N., Nakanishi, H., Goodenough, J.B., Shao-Horn, Y.** Nature Chemistry. 2011, Vol. 3, 546-550.

v. **Ruvinskiy, P.S., Bonnefont, A., Pham-Huu, C., Savinova, E.R.** Langmuir. 2011, Vol. 27, 9018–9027.

w. **Wang, Y., Cheng, H.-P.** Journal of Physical Chemistry C. 2013, Vol. 117, 2106-2112.

Tiphaine POUX

Étude de la réduction d'oxygène sur les oxydes de type pérovskite en milieu alcalin

Résumé

La cinétique lente de la réduction de l'oxygène (ORR) est en grande partie responsable de la perte d'énergie de nombreux systèmes de conversion tels que les piles à combustible. Parmi les possibles catalyseurs de l'ORR, les oxydes de type pérovskite sont des candidats prometteurs en milieu alcalin. La présente thèse est consacrée à l'étude de l'activité, du mécanisme et de la stabilité de pérovskites à base de Co et Mn pour l'ORR. Grâce aux techniques d'électrode tournante à disque et disque-anneau (R(R)DE), les études de l'ORR et des transformations d'HO_2^- sur les couches minces de pérovskite/carbone dans une solution de NaOH ont montré qu'O_2 est réduit en OH^- via un mécanisme « en série » avec formation d'HO_2^- intermédiaire. Pour des quantités d'oxyde suffisantes, HO_2^- est ensuite réduit, ce qui résulte en un mécanisme apparent de 4 électrons. Dans ces électrodes, le carbone joue un double rôle. Il augmente l'activité électrocatalytique en améliorant le contact électrique et il est impliqué dans le mécanisme de l'ORR en catalysant la réduction d'O_2 en HO_2^-, surtout pour les pérovskites à base de cobalt qui sont considérablement moins actives que celles à base de Mn. Néanmoins, l'électrocatalyse de l'ORR semble dégrader les sites actifs des pérovskites.

Mots-clés : pérovskites; réaction de réduction d'oxygène (ORR); électrolyte alcalin; electrocatalyse; carbone; réduction et oxydation du peroxyde d'hydrogène; décomposition du peroxyde d'hydrogène; électrode à disque tournant (RDE); électrode tournante à disque-anneau (RRDE); cinétique et mécanisme de l'ORR; couche mince; voltamétrie cyclique (CV)

Résumé en anglais

The sluggish kinetics of the oxygen reduction reaction (ORR) is largely responsible for the energy losses in energy conversion systems such as fuel cells. Among possible inexpensive catalysts for the ORR, perovskite oxides are promising electrocatalysts in alkaline media. The present thesis is devoted to the investigation of the ORR activity, mechanism and stability of some Co and Mn-based perovskites. The rotating (ring) disk electrode (R(R)DE) studies of the ORR and the HO_2^- transformations on perovskite/carbon thin layers in NaOH electrolyte prove that O_2 is reduced to OH^- via a "series" pathway with the HO_2^- intermediate. For high oxide loadings, the formed HO_2^- species are further reduced to give a global 4 electron pathway. In these electrodes, carbon plays a dual role. It increases the electrocatalytic activity by improving the electrical contact and it is involved in the ORR mechanism by catalyzing the reduction of O_2 into HO_2^-, especially for Co-based perovskites which display lower reaction rates than Mn-based perovskites.

Keywords : perovskite oxides; oxygen reduction reaction (ORR); alkaline electrolyte; electrocatalysis; carbon; hydrogen peroxide reduction and oxidation; hydrogen peroxide decomposition; rotating disk electrode (RDE); rotating ring-disk electrode (RRDE); ORR kinetics and mechanism; thin layer; cyclic voltammetry (CV)